S01010000-TR0001, R00

SPALLATION NEUTRON SOURCE
SECOND TARGET STATION
CONCEPTUAL DESIGN REPORT
VOLUME 1: OVERVIEW, TECHNICAL AND EXPERIMENT SYSTEMS

March 2020

Approved for public release.
Distribution is unlimited.

OAK RIDGE NATIONAL LABORATORY
MANAGED BY UT-BATTELLE FOR THE US DEPARTMENT OF ENERGY

S01010000-TR0001, R00

SECOND TARGET STATION PROJECT

SPALLATION NEUTRON SOURCE
SECOND TARGET STATION

CONCEPTUAL DESIGN REPORT
VOLUME 1: OVERVIEW, TECHNICAL AND EXPERIMENT SYSTEMS

March 2020

Prepared by
OAK RIDGE NATIONAL LABORATORY
Oak Ridge, TN 37831-6283
managed by
UT-BATTELLE, LLC
for the
US DEPARTMENT OF ENERGY
under contract DE-AC05-00OR22725

CONTENTS

LIST OF FIGURES

LIST OF TABLES

ABBREVIATIONS, ACRONYMS, AND INITIALISMS

µTCA	Micro Telecommunications Computing Architecture
ADARA	Accelerating Data Acquisition, Reduction, and Analysis
ADnED	areaDetector/nED plugins
AFF	adaptive feed-forward
AFM	antiferromagnetic
AHU	air handling unit
ALARA	as low as reasonably achievable
AMT	ammonia/ammonium transport channel
AMTb	ammonium transport protein
APS	Advanced Photon Source-Upgrade
ARR	Accelerator Readiness Review
ASC	application-specific controller
BCM	beam current monitor
BES	Office of Basic Energy Sciences
BESAC	Basic Energy Sciences Advisory Committee
BLM	beam loss monitor
BLP	bottom loading port
BPLS	beam power limiting system
BPM	beam position monitor
BPVC	(ASME) Boiler and Pressure Vessel Code
CA	Channel Access
CAA	Clean Air Act
CCD	charge-coupled device
CD-0	Critical Decision 0
CF	conventional facilities
CLO	Central Laboratory and Office
CMS	cryogenic moderator system
CNCS	Cold Neutron Chopper Spectrometer
CSNS	Chinese Spallation Neutron Source
CS-Studio	Control System Studio
CWA	Clean Water Act
DAGMC	Direct Accelerated Geometry Monte Carlo
DAQ	data acquisition
DI	deionized
DNP	dynamic neutron polarization
DOE	US Department of Energy
DOE HQ	US Department of Energy headquarters
DOE-SC	US Department of Energy Office of Science
DOF	degrees-of-freedom
DSP-T	data system packetizer and timing interface
EB	electron beam
EDA	ethylenediamine
EDM	Extensible Display Manager
EDmp	extraction dump

EL	event link
EMS	environmental management system
EPA	US Environmental Protection Agency
EPICS	Experimental Physics and Industrial Control System
ES&H	environment, safety, and health
ESS	European Spallation Source
FCM	field control module
FEIS	final environmental impact statement
FM	ferromagnetic
FMC	FPGA mezzanine card
FODO	focus-drift-defocus-drift
FPGA	field programmable gate array
FTS	First Target Station
FWHM	full-width-at-half-maximum
FY	fiscal year
GI	grazing incidence
GLS	gas/liquid separator
GUI	graphical user interface
HAP	hazardous air pollutant
HD	high-density
HDC	high-density concrete
HFIR	High Flux Isotope Reactor
HPM	high-power protection module
HPSS	high-performance storage system
HPV	hot process vault
HUR	hydrogen utility room
HVAC	heating, ventilation, and air conditioning
I&C	instrumentation and control
I/O	input/output
I/Q	in-phase/quadrature
IBC	International Building Code
ICS	Integrated Control Systems
IDF	instrument definition file
IDP	intrinsically disordered protein
IOC	input/output controller
IPPS	instrument Personnel Protection System
IPT	integrated project team
IR	infrared
IRP	inner reflector plug
ISM	(DOE) Integrated Safety Management Program
ISMS	Integrated Safety Management System
ISO	International Organization for Standardization
J-PARC	Japan Proton Accelerator Research Complex
KB	Kirkpatrick–Baez

LCLS	Linac Coherent Light Source-II
LLLW	low-level liquid waste
LLRF	low-level radio frequency
LLW	low-level waste
LPSD	linear position-sensitive tube detectors
LVDS	low-voltage differential signaling
MAWP	maximum allowable working pressure
MIT	metal-insulator transition
MLLW	mixed low-level waste
MOF	metal-organic framework
MP	membrane proteins
MPS	Machine Protection System
MRA	moderator reflector assembly
MUTS	Mock-up Test Stand
NCNR	NIST Center for Neutron Research
nED	Neutron Event Detector
NEMA	National Electrical Manufacturers Association
NEPA	National Environmental Policy Act
NESHAPs	National Emission Standards for Hazardous Air Pollutants
NeXus	neutron and x-ray scattering experiments
NIST	National Institute of Standards and Technology
NNSS	Nevada National Security Site
NPDES	National Pollutant Discharge Elimination System
NPH	natural phenomena hazard
NSF	non–spin flip
NSLS-II	National Synchrotron Light Source-II
NSOT	Néel spin-orbit torque
NTS	Nevada Test Site
OCC	optical communication card
ODB	optical distribution board
OEC	oxygen-evolving complex
OLCF	Oak Ridge Leadership Computing Facility
OPC	Other Project Costs
ORNL	Oak Ridge National Laboratory
ORR	Oak Ridge Reservation
OSO	ORNL Site Office
OTR	over-the-road
PBW	proton beam window
PDF	pair distribution function
PID	proportional-integral-derivative
PLC	programmable logic controller
PMAA	polymethacrylic acid
PPS	Personnel Protection System
PPU	proton power upgrade
PS	power supplies
PSD	position-sensitive detectors
PS-II	photosystem II

PTE	potential to emit
PVPON	polyvinylpyrrolidone
QA	quality assurance
QA&VP	quality assurance and validation process
QIKR	Quite Intense Kinetics Reflectometer
QMS	Quality Management System
QSL	quantum spin liquid
R&D	research and development
RCRA	Resource Conservation and Recovery Act
RF	radio frequency
rms	root mean square
ROC	read-out card
RRM	repetition rate multiplication
RSB	Ring Service Building
RTBT	Ring to Target Beam Transport
RTDL	real-time data link
RTST	ring-to-second-target beam transport line
RWP	radiological work permit
SAM	Survey, Alignment, and Metrology (team)
SANS	small-angle neutron scattering
SAXS	small-angle X-ray scattering
SBMS	Standards-Based Management System
SCE	secondary confinement exhaust
SDC	seismic design category
SEI	solid-electrolyte interphase
SFVS	sum-frequency vibrational spectroscopy
SiPM	silicon photomultipliers
SLS	Swiss Light Source
SMS	Streaming Management Service
SNS	Spallation Neutron Source
SSC	structure, system, and component
STP	sewage treatment plant
STPPS	second target Personnel Protection System
STS	Second Target Station
TCA	Tennessee Code Annotated
TDC	top-dead centers
TDEC	Tennessee Department of Environment and Conservation
TEC	Total Estimated Cost
TLP	top loading port
TOF	time-of-flight
TPC	total project cost
TPS	Target Protection System
TSCA	Toxic Substances Control Act
TSYNC	beam synchronous trigger
TVP	target viewing periscope
UTC	Coordinate Universal Time

VITA	VMEBus International Trade Association
VME	Versa Module Europa
WANS	wide-angle neutron scattering
WAXS	wide-angle X-ray scattering
WBS	Work Breakdown Structure
XPS	x-ray photoelectron spectroscopy

EXECUTIVE SUMMARY

INTRODUCTION

The Spallation Neutron Source (SNS) at Oak Ridge National Laboratory (ORNL), which began operating in April 2006, provides the United States with a world-leading source of pulsed neutrons for research. As currently configured, SNS delivers 60 Hz pulses of high-energy protons to a liquid mercury target, where bursts of neutrons are produced when protons collide with the nuclei of mercury atoms. This First Target Station (FTS) is optimized for the production of thermal neutrons (i.e., neutrons with wavelength $\lambda \approx$ 1.8 Å) that are ideal for spatial resolutions on the atomic scale and fast dynamics studies of materials.

The Second Target Station (STS) Project substantially expands the capabilities of SNS to meet global needs for a high-intensity source of cold (long-wavelength) neutrons and sustain US leadership in neutron scattering for decades to come. Planning for the STS began during the initial SNS project stage [Carpenter and Mason 2002], and Critical Decision 0 (CD-0) was approved in January 2009 for a facility with capabilities complementary to those of the FTS and optimized for the production of cold neutrons.

During the past decade, the design of the STS has evolved to meet the need for a facility that can probe the structure and dynamics of materials over extended length, time, and energy scales. Subcommittees empaneled by the US Department of Energy (DOE) Basic Energy Sciences Advisory Committee (BESAC) in 2013 and 2016 [Hemminger and Barletta 2013, DOE 2016] evaluated two proposed upgrades to SNS: construction of the STS, and an associated proton power upgrade (PPU) to double the power capability of the SNS accelerator. Both studies found that these upgrades were "absolutely central to contribute to world-leading science," and both called for the resolution of questions about the design and implementation of the STS and the distribution of proton pulses between the two target stations.

These questions have been resolved through extensive consultation with the research community. The PPU Project [ORNL 2018], initiated in FY 2018, will double the power of the SNS accelerator complex to 2.8 MW and provide the capabilities needed to divert every fourth proton pulse produced by the accelerator to a new beamline serving the STS. As outlined in this conceptual design report, the STS Project will provide researchers from a wide range of disciplines with a facility that offers wholly new experimental capabilities for addressing key questions across a range of scientific areas [ORNL 2019].

SCOPE

The STS Project includes the design, construction, installation, and commissioning of the facilities and equipment necessary to create a world-leading source of cold neutrons of unprecedented peak brightness at SNS. The project leverages the capacity of the existing SNS accelerator, accumulator ring, and infrastructure and takes full advantage of the performance gains delivered by the PPU Project. The following are the main scope elements of the STS Project:

- The accelerator systems, including a ring-to-second-target beam transport line operating at 15 Hz to transport proton pulses to the target
- A water-cooled, rotating, solid tungsten target with closely coupled compact moderators to optimize the production of high-brightness cold neutrons
- A suite of five world-class neutron scattering instruments, to be developed in consultation with the neutron user community

- Conventional facilities, including a target building, three instrument buildings, and a central utilities building

- The integrated control systems and computing infrastructure for all technical systems included in the STS

PERFORMANCE CHARACTERISTICS

The STS Project will deliver a world-leading facility that will produce beams of cold neutrons of unprecedented peak brightness, delivered in short pulses to an initial set of five instruments designed to take advantage of the ability of the STS to enable the examination of materials over broad ranges of length, energy, and time scales. The STS will incorporate advances in neutron instrumentation and technologies to make optimal use of the neutrons produced by this new source, opening the way to experiments that are not now possible anywhere in the world. High-level performance characteristics are listed in Table ES.1.

Table ES.1. High-level performance characteristics of the STS.

Proton beam power capability	0.70 MW
Proton pulse length on target	0.75 μs
Pulse repetition rate	15 Hz
Energy per pulse on target	47 kJ
Target material	Tungsten
Number of ambient/cold moderators	0/2
Initial instrument suite	5
Number of instrument positions	22

COST AND SCHEDULE

The current total project cost (TPC) for the STS Project is $1.67B.The cost estimate was established using a bottom-up approach based on analysis by subject matter experts, historical knowledge from SNS costs, recent instrument beamline and similar technical component costs and vendor estimates where possible. The estimates are escalated from fiscal year (FY) 2020. The TPC also includes 36% contingency for the Total Estimated Cost (TEC), which was estimated using a systematic evaluation of uncertainties and event risks, and 40% for Other Project Costs (OPC).

The current schedule will lead to the establishment of the performance measurement baseline (CD-2) in FY24, start of construction (CD-3) in FY25, and project completion (CD-4) in FY31 which includes a schedule contingency of 24 months.

ALTERNATIVES ANALYSIS and SELECTION

The Spallation Neutron Source (SNS) was completed in June 2006. The BESAC sub-panel that recommended the initial technical parameters of SNS also urged that flexibility be included in the design to enable a future increase in proton beam power and the capability to add additional target stations. Following their recommendation, SNS was constructed to accommodate future upgrades.

The CD-0 for the SNS (STS was approved in January 2009. In preparation for CD-1 approval, five potential alternatives to address the mission need for a high- brightness, long-wavelength neutron source have been considered and evaluated, with the most viable option being to build STS at the SNS and operate in short-proton pulse mode at 15Hz.

ACQUISITION STRATEGY

The lead contractor for the STS Project will be UT-Battelle LLC, which manages and operates ORNL for DOE. The design, fabrication, installation, testing, and commissioning of the STS Project will be largely performed by ORNL scientific and technical staff. Design and construction of conventional facilities and some hardware fabrication will be executed through subcontracts.

REFERENCES

Carpenter, J. M., and T. E. Mason 2002. *Technical Concepts for a Long Wavelength Target Station for the Spallation* Neutron Source, ANL-02/16 and ORNL/SNS-TM-2001/163, November 2002.

DOE (Department of Energy) 2016. *BESAC Report on Facility Upgrades,* US Department of Energy, June. Available at https://science.osti.gov/~/media/bes/besac/pdf/Reports/BESAC_Facility_Upgrade_Assessment_Approved_June_9_2016.pdf (accessed July 2019).

Hemminger, J. C., and W. Barletta (co-chairs) 2013. *Basic Energy Sciences Facilities Prioritization,* US Department of Energy, February. Available at https://science.osti.gov/~/media/bes/besac/pdf/Reports/BESAC_Facilities_Prioritization_Report_2013.pdf (accessed July 2019).

ORNL (Oak Ridge National Laboratory) 2018. *Conceptual Design Report: Proton Power Upgrade Project,* ORNL/TM-2016/672-R1, Oak Ridge National Laboratory, February. Available at https://info.ornl.gov/sites/publications/Files/Pub71531.pdf (accessed July 2019).

ORNL (Oak Ridge National Laboratory) 2019. *First Experiments: New Science Opportunities at the Spallation Neutron Source Second Target Station*, ORNL/SPR-2019/1407, Oak Ridge National Laboratory, December. Available at https://conference.sns.gov/event/193/attachments/276/2173/STS_FirstExperimentsReport_120219_r1.pdf (accessed March 2, 2020).

1. PROJECT OVERVIEW

1.1 INTRODUCTION

The use of neutrons to probe the structure and dynamics of materials at the atomic scale began in the 1940s, when the first generation of nuclear reactors made neutrons available in large enough numbers to verify that these fundamental particles could be diffracted by a crystal. Neutron diffraction was soon recognized as a potential "partner to the X-ray and electron diffraction techniques for studying crystal and molecular structure." [Wollan and Shull 1948]

With the development first of more powerful reactors and later of accelerator-based sources of neutrons, in combination with notable advances in instrumentation and techniques, neutron scattering emerged as a powerful tool for materials characterization. Today, more than a dozen major neutron scattering facilities are in operation worldwide, including both reactor-based and accelerator-based neutron sources [APS 2018]. In the United States, the US Department of Commerce supports a 20 MW reactor at the National Institute of Standards and Technology (NIST) Center for Neutron Research (NCNR), and the US Department of Energy (DOE) supports the 85 MW High Flux Isotope Reactor (HFIR) and the accelerator-based Spallation Neutron Source (SNS), both located at Oak Ridge National Laboratory (ORNL).

HFIR delivers steady-state neutron fluxes as high as those of any research reactor in the world. SNS provides the United States with a world-leading source of pulsed neutrons for research. As currently configured, SNS delivers 60 Hz pulses of high-energy protons to a liquid mercury target, where neutrons are produced when protons collide with the nuclei of mercury atoms. This First Target Station (FTS) is optimized for the production of thermal neutrons (wavelength $\lambda \approx 1.8$ Å) that are ideal for spatial resolutions on the atomic scale and fast dynamics studies of materials.

The increasing use of neutrons in broad areas of the physical, chemical, biological, and geological sciences, as well as materials development and human health, is driving demand both for additional resources and for improvements in the precision and resolution of measurements that can be made with neutrons. In particular, a source of high-brightness cold neutrons that can simultaneously access a broad range of energies and wavelengths would provide the scientific community with exciting new opportunities to examine, understand, and improve a variety of materials.

To respond to this demand, ORNL has proposed the construction of a Second Target Station (STS) at SNS. Planning for the STS began during the initial SNS project stage [Carpenter and Mason 2002], and Critical Decision 0 (CD-0) for a facility with capabilities complementary to those of the FTS and optimized for the production of cold neutrons (wavelength $\lambda \approx 5$ Å) was approved in January 2009.

During the past decade, the design of the STS has evolved to meet the need for a facility that can probe the structure and dynamics of materials over extended length, time, and energy scales. Subcommittees empaneled by the DOE Basic Energy Sciences Advisory Committee (BESAC) in 2013 and 2016 [Hemminger and Barletta 2013, DOE 2016] evaluated two proposed upgrades to SNS: construction of the STS, and an associated proton power upgrade (PPU) to double the power capability of the SNS accelerator. Both studies found that these upgrades were "absolutely central to contribute to world-leading science," and both called for the resolution of questions about the design and implementation of the STS and the distribution of proton pulses between the two target stations.

These questions have been resolved through extensive consultation with the research community. The PPU Project [ORNL 2018], which received CD-1 approval in FY 2018, will double the power of the SNS accelerator complex to 2.8 MW and provide the capabilities needed to divert every fourth proton pulse

produced by the accelerator to a new beamline serving the STS. As outlined in this conceptual design report, the STS Project will provide researchers from a wide range of disciplines with a facility that offers wholly new experimental capabilities for addressing key questions in science, engineering, and human health.

The STS project utilizes the existing SNS accelerator, storage ring, and infrastructure and takes full advantage of the performance gains delivered by the PPU Project. The following are the main scope elements of the STS Project:

- A water-cooled rotating solid tungsten target with closely coupled compact moderators.
- A ring-to-second-target beam transport line (RTST), operating at 15 Hz, to transport proton pulses to the STS target after separation of the beam at the first ring-to-target beam transport line with a pulsed kicker magnet, using standard quadrupole and dipole magnets.
- Five world-class neutron scattering instruments that leverage advances in neutron instrument design, methods, and technologies to multiply the >20× increase in cold neutron brightness relative to FTS and capitalize on neutrons with moderate wavelength resolution as a source for reflectometry, medium-resolution spectroscopy, and high-intensity instruments.
- Control systems and computing infrastructure for RTST proton extraction, neutron scattering instruments, and target systems; technical systems utilities for conventional facilities; and data acquisition software and hardware for the neutron scattering instruments.
- New building structures to house the second target, instrument halls, beam transport line, secondary facilities, and supporting systems and infrastructure.

The remaining sections of this chapter present

- A description of the Work Breakdown Structure (WBS) for the STS
- Initial cost and schedule estimates based on a preliminary total project cost (TPC) range of $1.34B – $2.25B.
- A description of the STS Project management organization

1.2 WORK BREAKDOWN STRUCTURE

The STS WBS contains a complete definition of the project scope and forms the basis for planning, executing, and controlling project activities. The project WBS to Level 3 is shown in Figure 1.1.

The WBS follows a logical breakdown of Project Management, Technical Systems, R&D, Pre-Ops, and Conceptual Design at Level 2. Each system is then broken down into lower levels to define sub-elements of the technical component systems. Costs and resources will be captured within the WBS elements for all systems and will relate directly to an integrated STS master schedule in which all of the WBS areas are linked via integrated project links. The WBS dictionary details the work scope and activities for each WBS element. The following is a high-level summary description of the Level 2 WBS elements:

- S.01—STS Project Management: includes the management, planning, procurement, and general administration of the project.

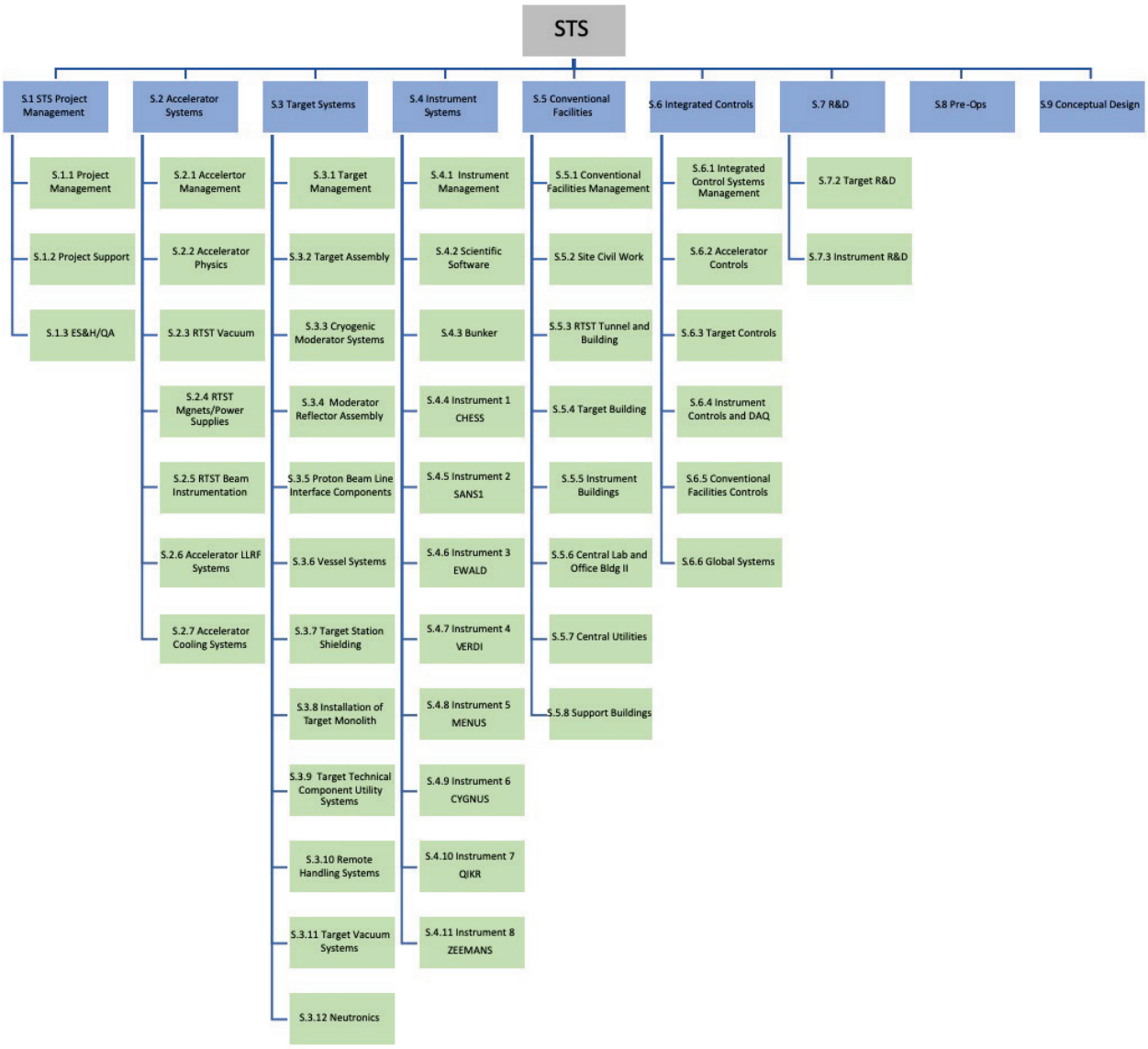

Figure 1.1. Work Breakdown Structure for STS Project, shown to Level 3.

- S.02—Accelerator Systems: includes all the labor, materials, and expenses necessary to design, procure, build, and install the RTST and its associated technical systems.

- S.03—Target Systems: includes all the labor, materials and expenses necessary to design, procure, build, and install the target monolith and shielding housing a rotating tungsten target and its associated technical systems.

- S.04—Instrument Systems: includes all the labor, materials, and expenses necessary to design, procure, build, and install a suite of world-class neutron instruments and their associated technical systems. Note: The STS project will build five initial neutron scattering instruments. For project planning purposes and to illustrate the science enabled at STS, concepts were developed for several instruments. However, community engagement in the final selection of project-built instruments is in process and anticipated to be complete by end of the 2020 calendar year. Five of these instrument

concepts are included in this report as representative of both the range of science enabled at STS and the range of complexity and physical and technical parameters anticipated for STS instruments. They include one inelastic spectrometer, two diffractometers, one reflectometer, and one small- and wide-angle neutron scattering instrument. Instrument lengths range from 18 to 90 M, essentially the shortest and longest instrument lengths that can be achieved at STS. Therefore the WBS and detailed cost and schedule developed for these five representative instruments are an appropriate basis for estimating cost.

- S.05—Conventional Facilities: includes all the labor, materials, and expenses required to design, procure, and construct a target building, three instrument buildings, a central utilities building, and an office building.

- S.06—Integrated Control Systems: includes all the labor, materials and expenses necessary to design, procure, build, and install the integrated control systems and computing infrastructure for all technical systems.

- S.07—R&D: includes all the labor, materials and expenses required to design, procure, and test components to support research and development (R&D) in accelerator, target, and instrument systems.

- S.08—Pre-Ops: includes all the labor and materials to complete the pre-ops portion of the project. Pre-ops is defined as starting after the accelerator and instrument readiness reviews are completed and signed off.

- S.9—Conceptual Design: includes all the labor, materials and expenses necessary to successfully complete conceptual design for all technical WBS elements.

The full WBS, down to the control account level, is available in the WBS document and the WBS dictionary. Development of the WBS and WBS dictionary is consistent with the requirements of DOE Order 413.3B, “Program and Project Management for the Acquisition of Capital Assets.”

1.3 COST AND SCHEDULE

1.3.1 Cost

The TPC point estimate is $1.67B. It was developed using a bottom-up estimate approach. The basis of the estimate strategy to establish a reasonable point estimate and range includes the following:

- Recent experience from SNS upgrade activities on the accelerator, target, and instrument beamlines
- Subject matter expert analysis
- Estimates from suppliers for commercial off-the-shelf items
- Experience from other facilities
- Historical information from similar deliverables
- Vendor estimates, where possible

The TPC point estimate is generated from the integrated master schedule and includes direct costs, indirect costs, escalation, and contingency. All cost estimates are based on the solutions required to satisfy the technical designs detailed in the technical sections within this report.

A bottom-up contingency estimate has been generated using a systematic approach to assess the uncertainty and event risks for all WBS elements. The established contingency is 36% of the Total

Estimated Cost (TEC), and 40% of the Other Project Costs (OPC). The cost contingency, although originally estimated based on individual cost elements, is not assigned and is held by the Federal Project Director.

1.3.2 Schedule

Table 1.1 shows proposed Level 1 milestones for the STS Project. The STS integrated schedule was developed from the detailed WBS elements, which include resource loading for all activities and inter-project links that link the various activities. Long lead procurements at stages CD-3A and CD-3B will be essential to move the project forward in a timely manner. These critical procurements will include site preparation, pile driving, initial concrete pours, and neutron guide procurement. The project schedule will be refined during preliminary design, and final milestones will be established at CD-2.

Table 1.1. Proposed Level 1 milestones for STS Project.

Proposed Level 1 Milestones	Schedule
CD-0, Approve Mission Need	Jan 2009 (A)
CD-1, Approve Alternative Selection and Cost Range	FY 2020 Q4
CD-3A, Approve Long Lead Procurement	FY 2023 Q2
CD-2/3b, Approve Performance Baseline and Long Lead Procurement	FY 2024 Q2
CD-3, Approve Start of Construction	FY 2025 Q2
CD-4, Approve Project Completion	FY 2031 Q3

Figure 1.2 shows a high-level summary of the current project schedule which is consistent with the preliminary baseline schedule. The schedule is consistent with the WBS and includes project activities, critical decision (Level 1) approval milestones, major procurement award dates, and the early finish date.

A detailed resource loaded schedule has been developed with approximately 7,000 logically linked activities and milestones. The project has adopted a 24 month schedule contingency resulting in a project completion date and approval of CD-4 in Q3 of FY 2031.

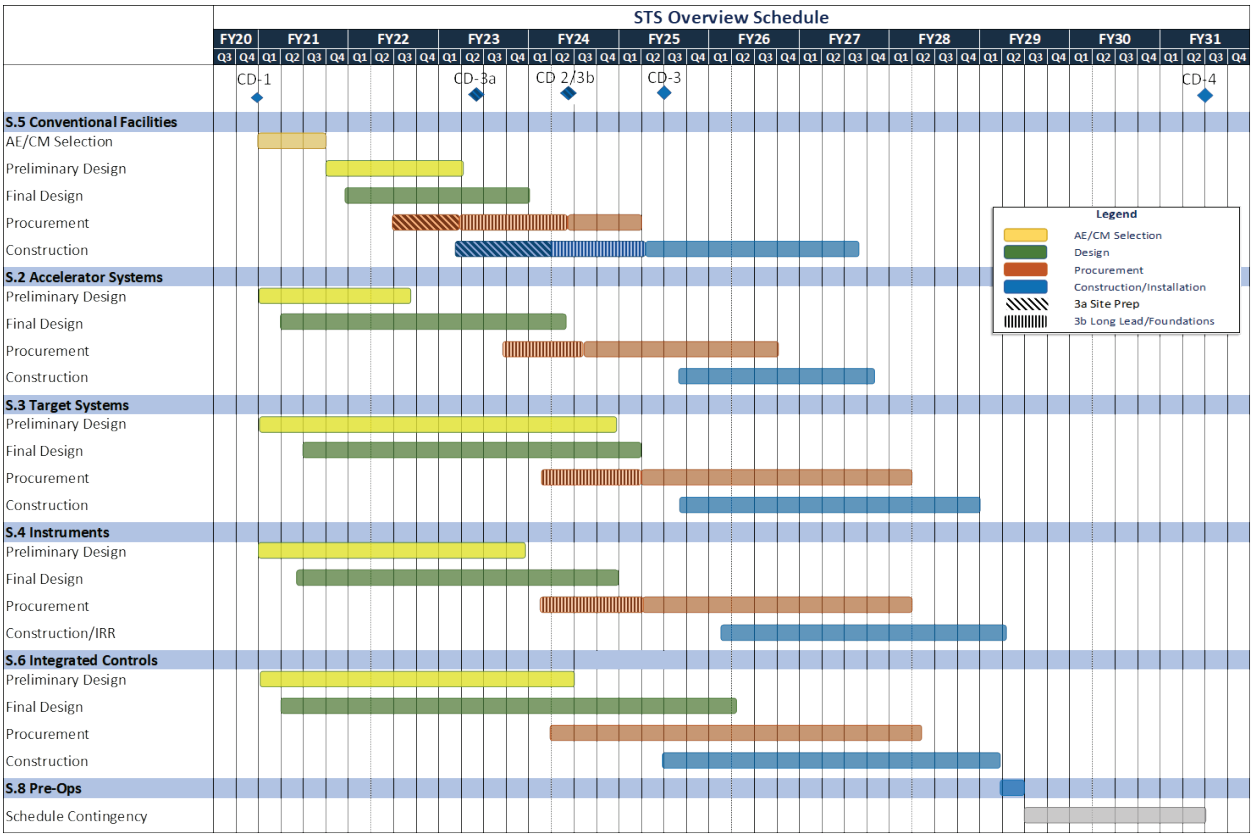

Figure 1.2. STS Project high-level summary schedule.

1.4 PROJECT MANAGEMENT

The DOE Office of Science (DOE-SC), Office of Basic Energy Sciences (BES), provides program direction and funding for the STS Project through the ORNL Site Office (OSO) to ORNL via work authorizations and approved financial plans and provides program-level oversight and coordination. Day-to-day oversight is provided by the OSO staff located at ORNL. As the management and operations contractor for ORNL, UT-Battelle LLC is accountable to DOE for carrying out the STS Project. An integrated project team (IPT) comprising DOE, ORNL, and other participants, when appropriate, has been established to accomplish this project. The IPT organization chart is shown in Figure 1.3.

The STS IPT, headed by the DOE federal project director, includes the following core members:

- DOE federal project director
- DOE/BES program manager
- STS Project director
- STS Project manager
- STS Project controls manager

The IPT holds regularly scheduled meetings to communicate STS Project progress, resolve issues, and provide coordinated management of the overall project. The project director and project manager manage the STS Project on behalf of UT-Battelle LLC. The project director reports directly to the ORNL laboratory director. The organizational chart is shown in Figure 1.4.

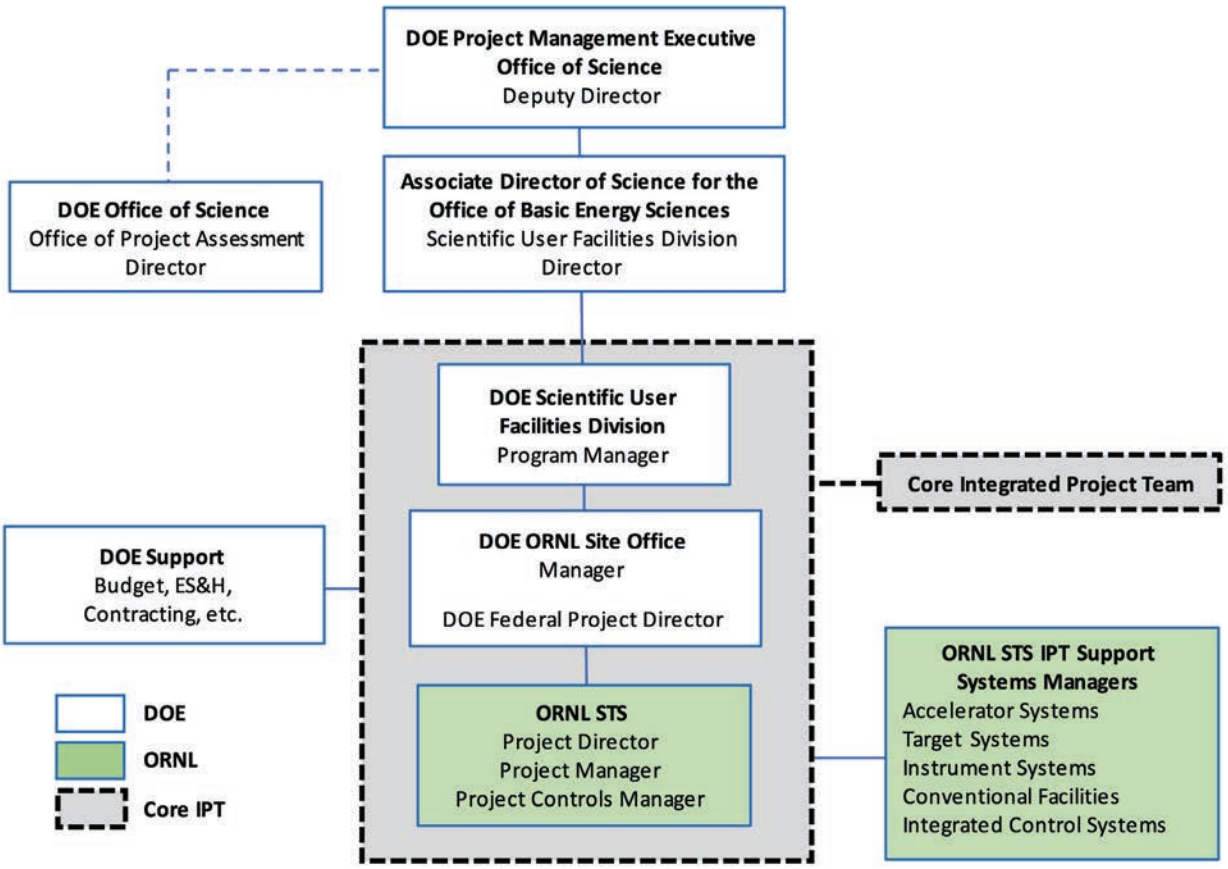

Figure 1.3. STS Project integrated project team.

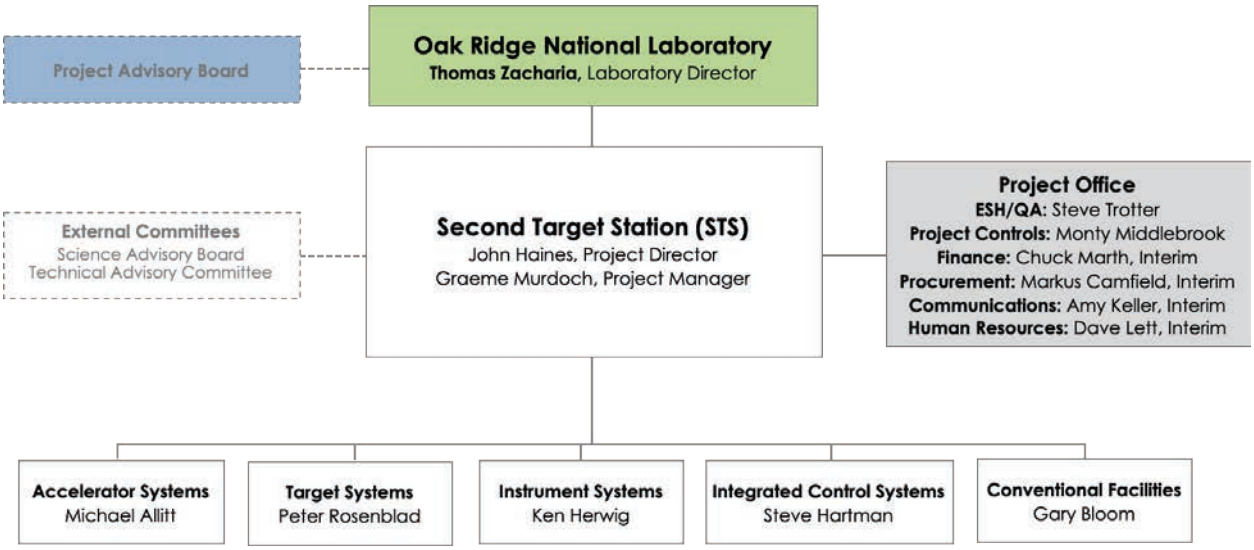

Figure 1.4. STS organizational chart.

1.5 REFERENCES

Wollan, E. O., and C. G. Shull. 1948. “Neutron diffraction and associated studies,” *Nucleonics* 3(1), 8–21.

APS (American Physical Society). 2018. *Neutrons for the Nation: Discovery and Applications while Minimizing the Risk of Nuclear Proliferation*, American Physical Society, College Park, MD, July.

Carpenter, J. M., and T. E. Mason. 2002. *Technical Concepts for a Long Wavelength Target Station for the Spallation* Neutron Source, ANL-02/16 and ORNL/SNS-TM-2001/163, November.

Hemminger, J. C., and W. Barletta (co-chairs). 2013. *Basic Energy Sciences Facilities Prioritization*, US Department of Energy, February 2013. Available at https://science.osti.gov/~/media/bes/besac/pdf/Reports/BESAC_Facilities_Prioritization_Report_2013.pdf (accessed February 2020).

DOE (Department of Energy). 2016. *BESAC Report on Facility Upgrades*, US Department of Energy, June. Available at https://science.osti.gov/~/media/bes/besac/pdf/Reports/BESAC_Facility_Upgrade_Assessment_Approved_June_9_2016.pdf (accessed February 2020).

ORNL (Oak Ridge National Laboratory). 2018. *Conceptual Design Report: Proton Power Upgrade Project*, ORNL/TM-2016/672-R1, Oak Ridge National Laboratory, February. Available at https://info.ornl.gov/sites/publications/Files/Pub71531.pdf (accessed February 2020).

2. SCIENCE AT THE STS

The ability to probe the structure and dynamics (internal motions) of materials, beginning at the atomic level and extending to objects well beyond the nanometer scale, is essential to the development of future technologies that will drive this nation's economy—new batteries and structural materials for transportation, new catalysts for efficient production of fuels and chemicals, next-generation polymers that make it possible to upcycle waste into new consumer products, and quantum materials to enable advances in computing and sensors. The STS will provide transformative new capabilities to examine materials over broad ranges of length, energy, and time scales and address the research community's need for bright beams of cold neutrons. Science opportunities enabled by the STS were illustrated in a report that describes examples of first experiments to be conducted at the STS [ORNL 2019]. This chapter is an abridged version of this longer report and is complemented by instrument-specific science cases defined in Chapter 5 of this document for the five instruments identified for concept development to support project planning.

The mission of the DOE Office of Science is to deliver scientific discoveries and major scientific tools to transform understanding of nature and advance the energy, economic, and national security of the United States. To carry out this mission, the Office of Science develops and operates a set of advanced scientific user facilities. These tools for scientific discovery and innovation, used by thousands of scientists annually, include some of the world's best resources for understanding and characterizing materials at the level of atoms and molecules. The Office of Science has developed powerful sources of x-rays and neutrons, including five x-ray light sources and two neutron scattering facilities, and provides additional capabilities at five nanoscale science research centers that include advanced electron microscopies. Experiments conducted using these scientific tools have extended the frontiers of science and led to new technologies with real-world applications.

Neutrons are a unique tool to study materials: because they carry no electrical charge, they interact directly with the nuclei in a material and are sensitive to light elements as well as isotopic differences; neutrons carry a magnetic moment and thus directly interact with magnetic structure and excitations; and, because they penetrate deep into materials, they can be used to study samples inside pressure or reaction vessels. Neutrons can be produced with a wide range of wavelengths suitable to probing structures from the atomic level through 100s of nanometers and beyond, while having energies that are well matched to studying collective excitations and individual atomic motions. Neutrons interact with nuclei and magnetic fields in quantitative ways that support direct comparison between experiment and theoretical and computational modeling. The two neutron sources in the United States supported by the DOE Office of Science, the HFIR and the SNS, are both located at ORNL.

HFIR produces continuous beams of either cold or thermal neutrons. It has 12 instruments available to the user community. At SNS, a 1.4 MW accelerator delivers high–peak-brightness neutrons, tailored for high wavelength resolution, to a suite of 19 instruments. An upgrade under way at SNS will double the power capability of its accelerator to 2.8 MW by 2024.

2.1 STS: SECURING US LEADERSHIP IN NEUTRON SCATTERING

The STS will produce beams of cold neutrons with world-leading peak brightness at a repetition rate of 15 Hz, providing broad energy/wavelength ranges that can be used simultaneously. Construction of the STS will provide transformative capabilities that allow thousands of users from national laboratories, universities, and industry to address grand scientific challenges [Hemminger 2015], advance energy research [BES 2019], and accelerate industrial innovations through the combination of

- Cold (long-wavelength) neutrons of unprecedented peak brightness (1.5×10^{15} n/s/cm^2/Å/ster at λ = 3 Å)

- Short neutron pulses with broad ranges of usable wavelengths or energy ($\Delta\lambda$ = 13.2 Å at 15 Hz at a distance of 20 m from the source)

This unique combination of neutron beam characteristics will open new avenues for examining materials and systems over greatly increased length, energy, and time scales. These characteristics—in combination with new instruments and sample environments, advances in neutron optics and detectors, and new computational methods—will make it possible to conduct a wide range of experiments not now possible anywhere in the world. Specifically, the STS will provide unique capabilities for experiments that require

- Time-resolved neutron measurements of chemical and physical processes, such as materials as they are being synthesized, processed, or self-assembled; chemical processes at interfaces; and changes in biological macromolecular complexes

- More intense neutron beams focused to explore smaller samples of newly discovered or synthesized materials, or materials under the extreme conditions of magnetic field, pressure, and temperature that are often encountered in energy technologies

- Simultaneous measurements of hierarchical architectures across an unprecedented range of length scales, from atomic scale to the micron and beyond, that will reveal how materials, such as polymers, self-assemble into hierarchical structures and how proteins interact in living biological cells

The STS will provide transformative new capabilities for many fields of research—materials science, physics, chemistry, geology, biology, and engineering, among others. Section 2.2, "Science Enabled by STS," presents examples of opportunities to apply these capabilities to challenges in five key areas of science: polymers and soft materials, quantum matter, materials synthesis and energy materials, structural materials, and biology and life sciences.

The capabilities offered by the STS instruments (22 when fully built out) will complement those of the FTS and HFIR, providing the United States with unparalleled resources for neutron scattering at the world's leading high–peak brightness cold neutron source, as shown in Figure 2.1.

2.1.1 The International Landscape for Accelerator-Based Neutron Sources

Powerful new accelerator-driven neutron sources in other nations include the neutron source at the Japan Proton Accelerator Research Complex (J-PARC), a short-pulse source operating at 25 Hz with a design power of 1 MW, and the European Spallation Source (ESS), a long-pulse source to be operated at 14 Hz and 2 MW when construction is completed in 2025 (with plans for an upgrade to 5 MW in the future). The lower repetition rates of J-PARC and ESS will allow the use of broader ranges of neutron energies in each pulse compared with FTS. The long pulses of neutrons at 14 Hz at ESS will provide both high peak brightness and a broad range of neutron energies (a strength of short-pulse spallation neutron sources with low repetition rates) and high time-averaged fluxes of both cold and thermal neutrons (a strength of reactor-based sources).

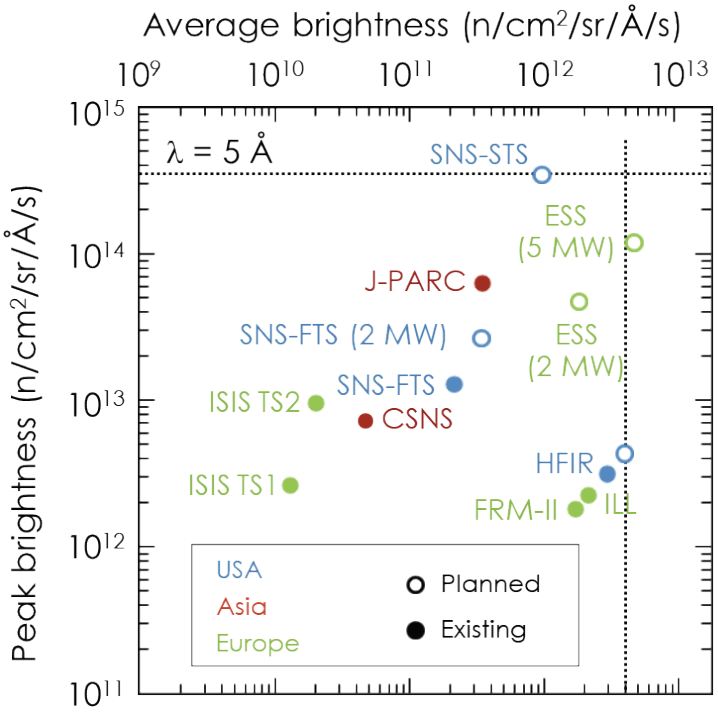

Figure 2.1. Peak and time-averaged brightness of existing (closed circles) and planned (open circles) sources of cold neutrons (wavelength λ = 5 Å). CSNS: China Spallation Neutron Source, China; ESS: European Spallation Source, Sweden; FRM-II: Forschungsreaktor München II, Germany; ILL: Institut Laue-Langevin, France; ISIS: ISIS Neutron and Muon Source, UK (TS: Target Station); J-PARC: Japan Proton Accelerator Research Complex, Japan.

2.2 SCIENCE ENABLED BY THE STS

The scientific community has evaluated opportunities to apply the capabilities of the STS to emerging challenges in a variety of fields. The examples presented in this section span polymers and soft materials, quantum matter, materials synthesis and energy materials, structural materials, and biology and life sciences, illustrating the extraordinary potential of the STS to impact a broad spectrum of scientific fields.

2.2.1 Polymers and Soft Materials

Polymers and soft matter self-organize through very weak interactions into larger structures, creating hierarchically structured materials with macroscopic properties stemming from the interplay of the structures found at different length scales. Because these structures can be altered through changes in temperature, pressure, stress or flow, soft materials are more readily tailored than most other materials, thereby affording new ways to create a desired structure or function.

Neutron scattering is a key tool for studying polymers and soft materials because neutrons can penetrate reaction vessels, allowing in situ measurements to monitor reaction processes, without destroying the relatively weak bonds in the materials. In addition, neutrons have strong sensitivity to both hydrogen and deuterium but can readily differentiate between the two to provide insight into reaction mechanisms and structure. These capabilities, combined with the high flux and broad energy range provided by the STS, will provide transformative capabilities to probe transient, time-dependent, and nonequilibrium processes in soft materials, with measurements completed in seconds or less, including

- high peak brightness and pulse structure that allow monitoring of the evolution of out-of-equilibrium states
- simultaneous characterization at length scales from the atomic level up to the emerging nanoscale and mesoscale hierarchical architectures
- simultaneous resolution of length and time scales, particularly when combined with specific contrast to identify soft molecular interactions and cooperativity

A fundamental question in polymer science and technology is

> *How can we control the assembly of soft matter to realize a wholly new generation of dynamic, hierarchical, polymorphic, and reconfigurable materials?*

Answering this question would allow scientists to design soft materials with functionality approaching that of natural systems or even to design polymers with superior properties that can be readily recycled to create new high-value materials.

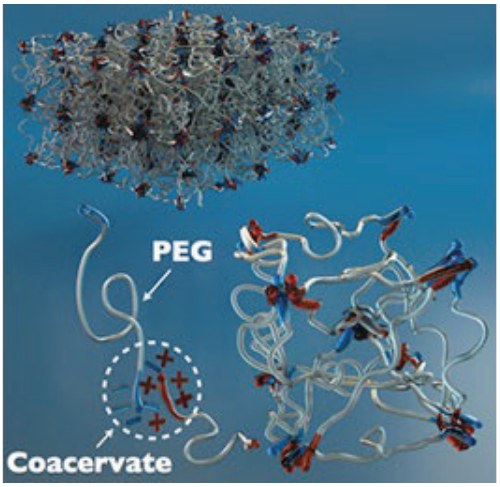

Figure 2.2. Schematic of an ABA block copolymer complex coacervate. The oppositely charged A blocks create the coacervate (lower left). The coacervate domains are bridged by the neutral B block (here polyethylene glycol, or PEG). The coacervate domains can adopt a loose gel-like structure (lower right) that can become very well ordered at the nanoscale (top left) if concentrations are high enough (*Source: Srivastava et al. Nat. Commun. 2017*). The time evolution of such systems will be observable with the capabilities available at the STS. *Source: Courtesy of Peter Allen, Institute for Molecular Engineering, University of Chicago.*

For example, coacervate complexes are formed from charged polymers that self-assemble (Figure 2.2) as a result of mainly electrostatic attraction between oppositely charged polymers. These materials are of high interest because they can respond to "triggers" in ways that cause their functionality to change. For instance, they could be employed to deliver specific "cargoes," such as ions in batteries (triggered with electric fields) or drugs for medical applications (triggered with changes in pH). These materials could form the foundation for production of robust smart materials that strengthen upon application of strain or self-heal by forming new chemical bonds.

Today, the processes by which polymer chains respond during coacervation remain largely unknown. But understanding the formation pathways is critical to being able to design these materials to provide desired functionality. Neutrons are well suited to probing such systems, but observing the relevant length scales with a time resolution of seconds or below is not currently possible. The capabilities of the STS, including a new generation of instrumentation, will enable the study of these processes over wide time and length scales with a real-time resolution of seconds. With these world-leading capabilities, researchers can finally decode this longstanding mystery and unlock our ability to predictively design these 3D structures to deliver highly functional coacervate materials.

2.2.1.1 New Scientific Opportunities

The new capabilities provided by the STS will revolutionize the ability to understand nanoscale changes in soft materials with neutrons. They will provide new opportunities for the study of time-resolved phenomena associated with the processing, 3D printing, or assembly of complex polymers, soft materials,

and nanomaterials. As a result, these next-generation instruments will lead to breakthroughs in the development of responsive, recyclable, and reconfigurable materials for future energy technologies such as photovoltaics, fuel cells, batteries, lightweight materials, lubrication, gas purification, water desalination, and microelectronics and computing.

2.2.2 Quantum Matter

Quantum materials hold exceptional promise for the development of next-generation computers, high-precision sensors, and new energy technologies. Examples of quantum materials include superconductors, in which electrons form a collective quantum state that carries electricity with no resistive heat losses; topological materials, in which the geometric connectivity of quantum states leads to a novel form of electron transport at surfaces; and superfluids, which can flow with zero viscosity.

Neutron scattering provides unique insight into the workings of these materials because of the sensitivity of the neutron to the magnetism, or spin, of electrons, and the ability of neutrons to probe low-energy fluctuations that determine the behavior of quantum states. The high brightness and wide energy bandwidth provided by the STS will enable studies of new quantum materials at the very earliest stages of discovery and will extend the application of neutron scattering to new classes of materials, such as artificially layered materials, interfaces, or assemblies of nanoparticles that are difficult to access with current neutron sources. Thus, the STS will accelerate the transformation of quantum materials into new technologies with the potential to strengthen national security, create unparalleled computing power, and enhance economic competitiveness.

One of the key questions in quantum materials research is

> *How can quantum fluctuations be controlled and exploited to design new materials for energy-relevant technologies?*

One intriguing example is a quantum spin liquid (QSL), a state in which the motions of highly entangled spins behave like new kinds of particles. Greater understanding of the behavior of these particles may make it possible to deploy them in future technologies. An excellent illustration is provided by a theoretical construct known as the Kitaev model, a network of spins on a honeycomb lattice. This QSL model gives rise to particle-like fluctuations, known as Majorana fermions, that could form the basis of a technology for quantum computing. As materials exhibiting the essential features of the Kitaev model are developed, neutrons will be an essential tool for characterizing and understanding their behavior. Majorana fermions (see Figure 2.3) produce a signature that can be seen in a neutron scattering measurement made with the unprecedented resolution, intense beams, and broad bandwidth that will be supplied by the STS.

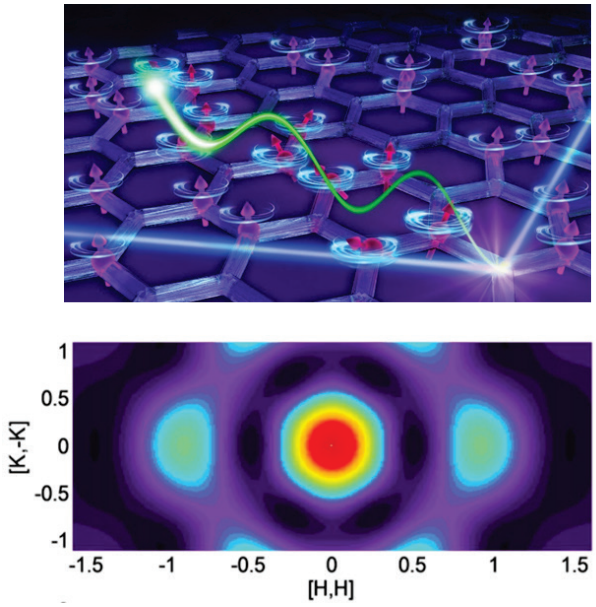

Figure 2.3. Using neutrons to explore Kitaev QSLs. Top: Artist's conception of a neutron exciting a Majorana fermion in a Kitaev QSL. *Image source: ORNL.* Bottom: Predicted inelastic neutron scattering pattern for a Kitaev QSL. *Source: Banerjee et al., Science 356, 2017.*

2.2.2.1 New Scientific Opportunities

The field of quantum materials is growing rapidly and goes far beyond QSLs to include emergent topological states in spin-orbit coupled metals, Weyl semi-metals, axion insulators, and topological Mott insulators. The key characteristics of the STS will enable unprecedented insights into the fundamental physics of these materials, which is critically important for opening pathways to new technologies. For example, the high peak brightness and highly focused beams of the STS will make it possible to perform neutron studies on smaller samples than are currently possible, allowing newly synthesized materials to be examined early in the discovery process. This sensitivity will also make it possible to study layered materials with interfaces designed to enhance quantum properties in devices, providing unprecedented understanding of thermal or magnetic transport across these designed interfaces.

The STS will also make it possible to study quantum materials under extremes of magnetic field or pressure. Under such extreme conditions, new and uniquely detailed information will be obtained on the types of interactions that determine a material's properties. Also, the high peak brightness and energy bandwidth attainable with the STS will facilitate fundamentally new ways of looking at quantum matter. The unrivaled peak brightness of STS will dramatically expand the ability to probe time-dependent processes in materials. For measurements on time scales of seconds or longer, the additional intensity will enable faster measurements with better time resolution. Stroboscopic measurements, when possible, will enable much faster time-resolution on the microsecond to the millisecond scales. Time-resolved measurements at the STS will enable an atomic-level view of quantum materials beyond thermal equilibrium, providing important insights into in operando behaviors that are crucial for the development and application of these materials in computing, sensors, and energy technologies.

2.2.3 Materials Synthesis and Energy Materials

Understanding the chemical processes involved in the synthesis of materials, as well as those associated with energy production, storage, and use, requires the ability to observe and characterize multiple processes simultaneously across broad length and time scales. For example, in the case of energy storage materials used in a battery or supercapacitor, charging and discharging, energy flow, and chemical reactions at the atomic scale are coupled to changes in the electrode structure and to performance of the device at much larger length scales.

Understanding how dissolved species that carry charge interact with the surrounding fluids is also of critical importance. For a battery, this is the interaction of charge-carrying species (e.g., lithium) with the electrolyte (typically an organic liquid). Because both charge carriers and electrolytes are made up of light elements, neutrons provide an exceptionally sensitive means of probing these processes. Further, uncertainties in the chemical reaction mechanisms that occur during the precipitation of solid phases from liquids (e.g., the formation of undesirable secondary phases in a battery that can shorten its lifetime or lead to catastrophic failure), and the subsequent assembly of small particles into macroscopic aggregates, hinder our ability to predict new device performance and develop new materials synthesis strategies.

Neutron scattering is essential to attaining a detailed understanding of materials characteristics and behaviors—including roles of disorder and defects, fluid flow and reactivity, kinetics, materials growth and synthesis, and performance in nonequilibrium and extreme conditions—and to understanding how components and integrated materials in devices function under real-world conditions. Such knowledge is a prerequisite for developing the next generation of energy technologies and understanding hierarchical and heterogeneous structures from the atomic scale to actual components and systems. And transitioning that knowledge to practical uses requires an integrated understanding of synthesis at the nano-, meso-, and macroscale. STS instruments will incorporate multiple modalities by combining different neutron scattering analyses made simultaneously on a single sample, and by combining neutron measurements

with those made using other analytical tools. The power and adaptability of the STS beamlines will allow significant advances in the ability to conduct complex experiments in situ and in real time.

Two key questions for designing new energy materials are

How are atomic-scale reactions in liquids linked to the macroscopic structure and transport within a material?

How we can take advantage of this linkage to design and control energy materials more efficiently?

The STS will provide wholly new capabilities to address these questions, including the ability to observe processes at different length scales simultaneously and over time. To gain a quantitative and mechanistic understanding of how macroscopic system performance over time is influenced by the atomic-scale structure and reactivity (and vice versa), measurements must be performed in one experiment (see Figure 2.4). In addition, increases in cold neutron brightness at STS will allow measurements on materials at far lower concentrations than can currently be studied, opening up these experiments to many more scientifically and technologically relevant material and chemical systems.

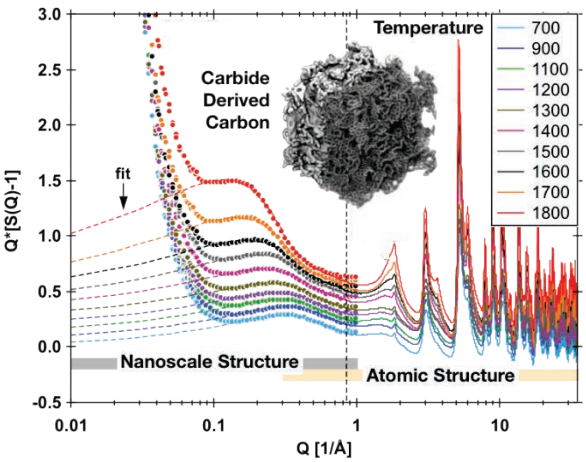

Figure 2.4. Simulated neutron scattering data for a potential energy storage electrode material made from carbide-derived carbon. Ex situ measurements of nanoscale and atomic structure have been artificially stitched together to simulate a single data set spanning the size range that will become accessible in a single, time-resolved in situ experiment on STS instruments. *Source: H.-W. Wang, ORNL; inset: Zhan et al. 2017, PubMed).*

2.2.3.1 New Scientific Opportunities

STS will offer transformative opportunities for capturing the structure and dynamics of complex materials systems in situ and in real time at a temporal resolution of minutes, allowing researchers to follow chemical reactivity self-assembly mechanisms at the atomic/molecular level through transport/aggregation/crystallization toward targeted architectures or functionalities. Doing so will make it possible to establish quantitative links between specific atomic-level solvation structures in solution and reaction pathways during liquid-solid transitions, and then extend these linkages to specific nanoscale morphologies, aggregation behavior, and the ultimate macroscopic crystal form. Without the ability to link relevant reaction and assembly mechanisms across length scales, it will be difficult to control hierarchical assembly and crystallization reactions to tailor specific properties or material morphologies.

Characterizing reactivity, selectivity, and kinetics associated with the reaction and separation of products in solution, under realistic conditions of temperature and pressure, will have a broad impact on DOE missions in science and energy and on the development of new materials and chemical processes for future applications in energy efficiency, production, and storage. The benefits of these new STS capabilities will extend to many processes in which complex aqueous solutions are used, such as treatment of contaminated slurries found in waste tanks, synthesis of materials inspired by biology, and understanding of geological processes [Zhan et al. 2017].

2.2.4 Structural Materials

Structural materials are ubiquitous in modern society as key components in automobiles, airplanes, buildings, bridges, and many more applications. However, today's structural materials realize only about 10% of their theoretical strength. A grand challenge in structural materials is how to increase strength to near-theoretical levels without sacrificing other essential properties, such as ductility and toughness. Solving this challenge would make it possible to realize a new generation of lightweight, high-strength materials. Improvements in the understanding of other aspects of structural materials, including their response to manufacturing and processing (e.g., additive and metamorphic manufacturing processes) and their degradation under extreme conditions (e.g., corrosion and irradiation), could also lead to substantial improvements in performance and to the development of new materials.

Neutrons provide valuable capabilities for studying structural materials, thanks to their deep penetrating power, their ability to monitor atomic-level changes during actual operating and processing conditions, their strong sensitivity to isotopic differences, and, in many cases, their ability to differentiate between elements that are indistinguishable by other characterization techniques. The high brightness and broad energy bandwidths of the STS will advance the study of structural materials by making it possible to

- probe smaller sample volumes to understand complexities and variations in chemistries and macro-structures/microstructure that typically control essential materials properties such as (ion) transport under corrosion conditions, strength, and ultimate functional performance and reliability

- observe transient, time-dependent, and nonequilibrium processes in structural materials, including capturing structural evolution during processing or operation with subsecond time-resolved measurements

- investigate complex and low-symmetry materials and characterize microstructural and crystallographic features across multiple length scales simultaneously

While there are well-established scientific methods for achieving ultrahigh strength in structural materials, in almost all cases they degrade ductility. Only a few notable exceptions have been discovered in which this strength–ductility trade-off is defeated. The exceptions involve either the dynamic generation of certain types of interfaces (twin or phase boundaries) during deformation, or use certain types of nanoscale precipitates or ordered complexes. Broadly speaking, the former approach is better suited for enhancing ductility and the latter for improving strength. A combination of the two is therefore needed to maximize strength and ductility: that is, an optimal distribution of precipitates in a metastable matrix that undergoes twinning and/or phase transformation when stressed or strained (Figure 2.5).

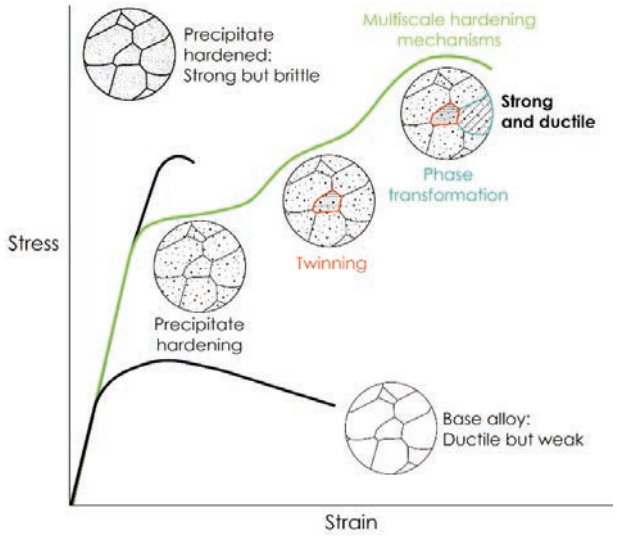

Figure 2.5. Strength and ductility. Schematic of interplay between spatial confinement due to precipitates and activation of multiscale hardening mechanisms to achieve high strength and ductility.

Although the broad outlines of how to accomplish this combination are known, important scientific questions need to be answered to develop a sound basis for alloy design:

Do twin and phase boundaries act merely to provide a steady (or increasing) source of work hardening and thus delay the onset of necking instability, or do they also provide additional deformation modes to accommodate the applied strain and thus enhance ductility?

How can the metastability of the matrix, and the volume fractions, morphologies, and sizes of the strengthening precipitates, be controlled to obtain the highest combination of strength and ductility?

What are the effects of spatial confinement due to grain boundaries or precipitates on the activation barriers for twinning and stress-induced phase transformations?

The STS will enable in situ neutron diffraction experiments to study the evolution of relevant microstructural features and load partitioning across length and time scales as a function of strain and temperature. Small-angle neutron scattering (SANS) techniques will provide quantitative measurements of critical precipitate distributions. In combination with theoretical calculations of phase stability and defect energies, these results will help develop broadly applicable scientific principles that can be used to design future generations of stronger and tougher alloys.

2.2.4.1 New Scientific Opportunities

The STS will provide exciting new capabilities for structural materials, because it will provide information at high resolution for specific regions in a material while also examining a material across broad length scales. This will allow simultaneous characterization of microstructures, including nucleation and growth of precipitates, metastable phases in complex alloys and composites, long-range order, and defects. The example highlighted in Figure 2.5 is a single example of how the STS can help clarify governing mechanisms in next-generation advanced materials, many of which will be increasingly complex and even hierarchically structured. The macroscopic properties of such materials result from multiscale interactions among features from the atomic scale to the microscale. Thus, probes are needed to simultaneously examine those features across those length scales as a function of time. The new capabilities of the STS will enable researchers to conduct entirely new experiments on these advanced materials. Simultaneous measurement of neutron diffraction and SANS data will eliminate the ambiguity of comparing measurements taken with different techniques on different samples. The ability to simultaneously observe these phenomena on time scales similar to those in actual applications is essential to advance our understanding of how a structural material responds to realistic conditions. These insights into structure-property relationships are critical for the design of a new generation of structural materials, improving both the reliability and performance of these materials in transportation, buildings, and many other applications.

2.2.5 Biology and Life Sciences

Natural systems demonstrate a mastery of chemical and physical principles that enables highly selective catalytic processes, efficient energy conversion, and optimized materials synthesis.

The unprecedented peak brightness and broader energy range of neutrons at the STS, with associated advances in neutron optics and detectors, will transform neutron scattering capabilities for biological research. The brightness and energy range of the STS will make it possible to observe changes in biological systems in real time, using smaller samples, and across the multiple length scales relevant to biological systems, from quantum biological phenomena up to cellular scales. Combining the capabilities of the STS with precision deuterium labeling, multimodal experimental environments (or techniques), and

high-performance computing will allow cinematic observations of collective motions in biomolecular systems and of cellular components as they interact in real time to form functional complexes and higher-order assemblies. A dynamic understanding of the function of complex, hierarchical biological systems will become possible, enabling advances in areas such as artificial photosynthesis, biocatalysis, and biopharmaceuticals

A major question in biological research is

> *Can the molecular basis of life's processes be understood to obtain a predictive understanding of the designs and mechanisms that underpin them?*

Obtaining this knowledge will make it possible to mimic the architectures and processes of living systems to create new bio-inspired materials and processes for developing new energy technologies. In addition, the information will provide insights into molecular and cellular processes that will enhance human health and quality of life.

For instance, nature uses sunlight to convert water into oxygen; most of the oxygen in the atmosphere is generated by plants, algae, and cyanobacteria through this reaction. Photosynthetic processes also convert atmospheric carbon dioxide (CO_2) into sugar. Understanding photosynthetic processes could open the way to the development of biomimetic processes to efficiently generate fuels and useful chemicals, such as photo-induced production of hydrogen or conversion of CO_2 to hydrocarbons.

Neutron scattering provides a number of advantages for the study of biological systems. First, neutrons are highly sensitive to hydrogen, so hydrogen atoms can be located and followed during biological processes to explore reaction pathways and chemical mechanisms. In addition, neutrons can readily distinguish hydrogen from its isotope deuterium, enabling a powerful experimental technique, isotopic contrast variation. Through the judicious substitution of deuterium for hydrogen, contrast can be increased or eliminated, making it possible either to highlight specific molecules or even parts of a living cell, or to make them invisible to neutrons. Finally, neutrons can probe delicate biological materials without damage.

As an example, for the case of the conversion of water into oxygen, the multi-subunit membrane protein photosystem II contains a small metal ion cluster, Mn_4CaO_5 (Figure 2.6), that catalyzes the oxidation of H_2O, forming an oxygen-oxygen bond. This light-induced reaction is thought to involve five intermediate states (illustrated on the right side of Figure 2.6). The oxidation state of the manganese atoms within the cluster alters during the reaction; and neutrons can probe both the structure and dynamics of the system during this critical process without interfering with it, unlike probes that can ionize the metal cluster. Further, with the new capabilities of the STS, it will be possible to obtain detailed insight into the water environment of the catalytic site. This information will provide critical information on light-induced changes in the hydrogen bonding network and protonation around the active site.

The new capabilities of STS will enable researchers to rapidly take snapshots throughout the photosystem II reaction cycle and thus map the proton transfer pathways, providing critical insight into the full range of chemical mechanisms involved. This foundational information will accelerate the development of bio-inspired catalysts with impacts on areas ranging from fuel cells and solar cells to carbon capture technologies.

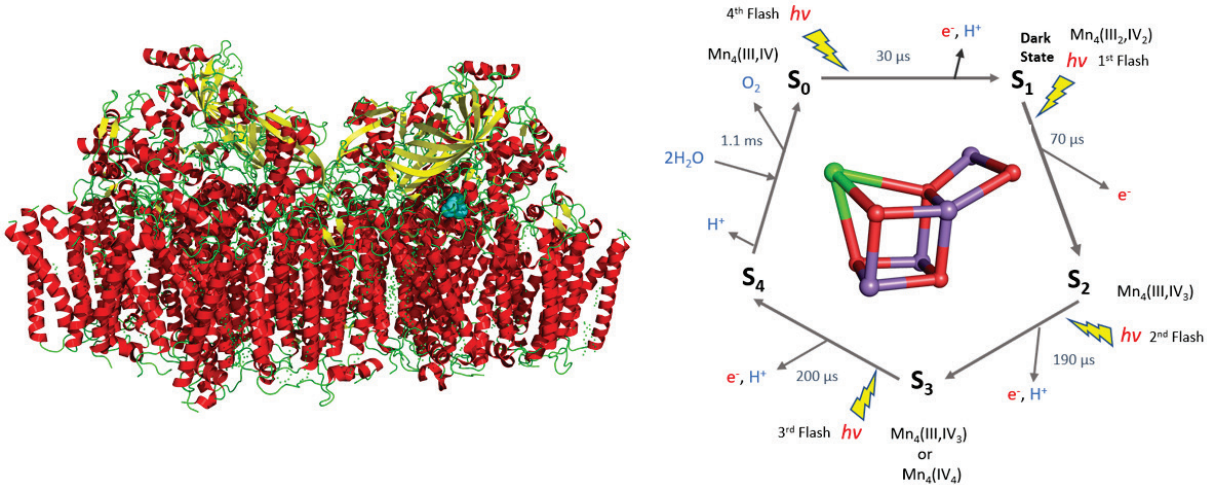

Figure 2.6. Photosystem II and the Kok cycle. At left, the structure of the multi-subunit photosystem II complex. At right, the classical Kok cycle with its five kinetic states (S_0 to S_4); a structural model of the oxygen-evolving cluster, an unusual metal cluster formed of manganese, calcium, and oxygen, is superimposed. The oxidation of H_2O is catalyzed via a series of light-induced transitions between the five kinetic states of the Kok cycle.

2.2.5.1 New Scientific Opportunities

The STS will dramatically extend the capabilities of neutron scattering for biological studies, revealing molecular events as they unfold over broad length and time scales. STS advances will enable the use of neutrons in a transformative way, integrating structural and dynamical descriptions of biological systems from the molecular to cellular levels. For instance, the dynamic assembly of many biological complexes involves networks of competing interactions, which constantly assemble and disassemble in response to their cellular environment. Gaining insight into these processes will provide researchers with opportunities to improve processes of importance to energy production, such as converting biomass to fuels and increasing drought resistance in crops, and processes key to human health, such as developing more effective treatments for diseases and producing bio-inspired materials for targeted drug delivery systems and biosensors.

2.3 CONCLUSION

The proposed STS will provide wholly new capabilities that will substantially extend this nation's current resources for neutron scattering. Specifically, the STS is designed to produce the highest peak brightness of cold (long-wavelength) neutrons in the world, providing the US research community with transformative opportunities to study the structure, dynamics, properties, and reactions of complex materials that have heterogeneity, interfaces, and disorder, as well as conducting temporally resolved, in situ and operando studies of materials and associated chemical processes.

The design of the STS will enable studies of materials systems across larger length scales—from the atomic scale to the micron scale and beyond—revealing, for example, how polymeric materials self-assemble into hierarchical structures or molecules interact in living biological cells. These capabilities will be available to the broad research community, including academic, industrial, and government laboratories, as part of the DOE Office of Science User Facility program. The STS will incorporate major advances in neutron instrumentation and technologies to make optimal use of the high–peak-brightness cold neutrons produced by this new source. It will be a transformative new tool for addressing grand challenges in fundamental science and for developing materials for next-generation energy technologies, national security, and other national needs.

2.4 REFERENCES

Banerjee, A., J.-Q. Yan, J. Knolle, et al. 2017. "Neutron scattering in the proximate quantum spin liquid α-$RuCl_3$," *Science 356*, 1055–1059.

BES (Office of Basic Energy Sciences) 2019. BES Workshop Reports. Series of reports available at https://science.osti.gov/bes/Community-Resources/Reports (accessed September 4, 2019).

Hemminger, J. C. (chair) 2015. *Challenges at the Frontiers of Matter and Energy: Transformative Opportunities for Discovery Science: A Report from the Basic Energy Sciences Advisory Committee*, U.S. Department of Energy, November. Available at https://science.osti.gov/-/media/bes/besac/pdf/Reports/Challenges_at_the_Frontiers_of_Matter_and_Energy_rpt.pdf (accessed March 2020).

ORNL (Oak Ridge National Laboratory) 2019. *First Experiments: New Science Opportunities at the Spallation Neutron Source Second Target Station*, ORNL/SPR-2019/1407, Oak Ridge National Laboratory, December. Available at https://conference.sns.gov/event/193/attachments/276/2173/STS_FirstExperimentsReport_120219_r1.pdf (accessed March 2, 2020).

Srivastava, S., M. Andreev, A. E. Levi, et al. 2017. "Gel phase formation in dilute triblock copolyelectrolyte complexes," *Nature Commun.* 8, 14131.

Zhan, C., C. Lian, Y, Zhang, et al. 2017. "Computational insights into materials and interfaces for capacitive energy storage," *Adv. Sci.* 4, 1700059.

3. ACCELERATOR SYSTEMS

The accelerator systems consist of a beamline from the present Ring to Target Beam Transport (RTBT) to the STS, the supportive equipment for the beamline in the Ring to Second Target (RTST) service building, and the low-level radio frequency (LLRF) upgrades for the linac that will allow separate pulse modes for the FTS and the STS.

3.1 RING TO SECOND TARGET BEAM TRANSPORT LINE

The RTST beamline is designed to operate in a “transparent” fashion with regard to the RTBT, e.g., the beam to each target station operates completely independently of the other. The RTST was further designed to provide low–beam-loss (<1 W/m) transport of beam from the RTBT to the STS and to meet beam-on-target specifications for the second target.

The design of the RTST beamline follows closely that of the existing RTBT [Holmes 2006, Plum 2007, Plum 2009, Henderson 2014, Cousineau 2011]. With the exception of a few magnets near the start of the RTST beamline, the magnets will have the same designs as those on the RTBT. The beam pipe diameter and beam acceptance will be the same as in the ring and RTBT. One difference between the RTBT and the RTST beamlines is that the RTST will not contain a beam dump but will instead use the extraction dump (EDmp) in the RTBT. This is possible because the RTST begins upstream of the EDmp. A second difference is that the new RTST will not contain a collimation system, since the RTBT collimation system is not used in operation.

3.1.1 RTST Physics Design

Beam to the second target will be deflected from the RTBT at 15 Hz. A pulsed kicker magnet will first deflect the beam horizontally to the beam left. The following quadrupole magnet will further deflect the beam to the left, and then an additional kicker will complete the initial separation of the RTBT and RTST beamlines. The remainder of the RTST beamline is standard bends and FODO (focus-drift-defocus-drift) lattices until just before the target, where four quadruple magnets will tailor the beam size to the target requirements. The top level parameters for the beamline are given in Table 3.1.

Table 3.1. Top level beam and beamline parameters for the RTST.

Parameter	Value
Beam power	700 kW
Beam energy	1.3 GeV
Repetition rate	15 Hz
Pulse length	700 ns
RTST length	239.3 m
Max Twiss Beta H	26 m
Max Twiss Beta V	26 m
H beam full width on Target	130 mm (95)
V beam height on target	48 mm (95%)
Aperture acceptance	> 480 (pi mm mrad)

A schematic of the new RTST beamline is shown in Figure 3.1. The beam will be deflected from the RTBT to the RTST beamline using a string of horizontal kicker magnets before and after the existing RTBT QH08 quadrupole magnet. The kicker magnets will not be water cooled and are assumed to be

similar to the injection kicker magnets. Four short kicker magnets, each about 82 cm long, were chosen rather than a combination of short and long magnets for the initial deflection of the beam destined for the second target. This arrangement allows easy fabrication of the ceramic vacuum chambers and flexibility in tuning of the beam deflection.

The kickers will deflect the beam to beam left. This will cause a large shift in the beam position, requiring that the quadrupole magnet RTBT:QV09 be replaced with another one with a larger aperture. This new quadrupole must be designed with a 40 cm aperture diameter to accommodate the kicked beam (see Figure 3.2). The next kicker magnet should provide the final deflection. This beam deflection will be sufficient to clear the next RTBT:QH10 quadrupole from the left side. This RTBT:QH10 quadrupole should be modified to a narrow quadrupole similar to the existing SNS ring quadrupoles in the injection and extraction regions, as in Figure 3.3. The next RTBT and the first RTST quadrupoles also should be the same narrow type of quadrupole to avoid RTBT and RTST beamline interference.

3.1.1.1 Extraction System Design

The kickers are designed to kick out every fourth bunch of protons from the RTBT and send it to the RTST line. The requirements for the kicker system are given in Table 3.2, and a simplified schematic is shown in Figure 3.4.

Pulser Design

The modulators produce full sine pulses, which reset the magnet core after each pulse. They are timed for the peak field in the magnet, aligning with the bunch that is to be kicked into the RTST line. The width of the pulse is set by the magnet inductance and the storage capacitor, Cs, and the values are selected so that the magnet current is zero for the next bunch. Figure 3.5 shows the timing of the magnet current in relation to the bunch train.

Ideally, the addition of the STS kickers should be transparent to the RTBT optics, and that requirement limits the placement of the kicker magnets. Figure 3.6 shows the extraction region of the RTBT and the RTST lines along with the approximate locations of four kicker magnets (K1, K2, K3, K4). The maximum magnet length for the kickers, to allow for flanges and bellows, is approximately 0.82 m. Longer magnets may be possible, but they would require moving existing sextupoles. Vacuum vessel supports between QV07 and QH08 and between QH08 and QV09 will likely have to be redesigned.

Kicker Magnet Design

A picture frame–type magnet (Figure 3.7) is adequate for the STS kickers. These magnets consist of a laminated steel core, copper windings, and a ceramic beam pipe coated with titanium or another conductive material to allow for a low-impedance image current return path.

The total bend angle for the four kicker magnets is 56 mrad; however, QH08 subtracts from the overall kicker, while QV09 adds to it. Therefore, the bend differs for K1 and K4. In addition, the width of the magnets grows as the kicked bunch of protons and the straight bunch diverge in the horizontal direction. A list of parameters for each of the kicker magnets is given in Table 3.3. The magnet current, voltage, and inductance are calculated for a magnet with 40 turns.

Figure 3.8 shows the magnitude of the magnetic field and flux lines, as well as the y-component of the field across the center of the aperture. Note that the field is flat to greater than 1% across the width of the aperture.

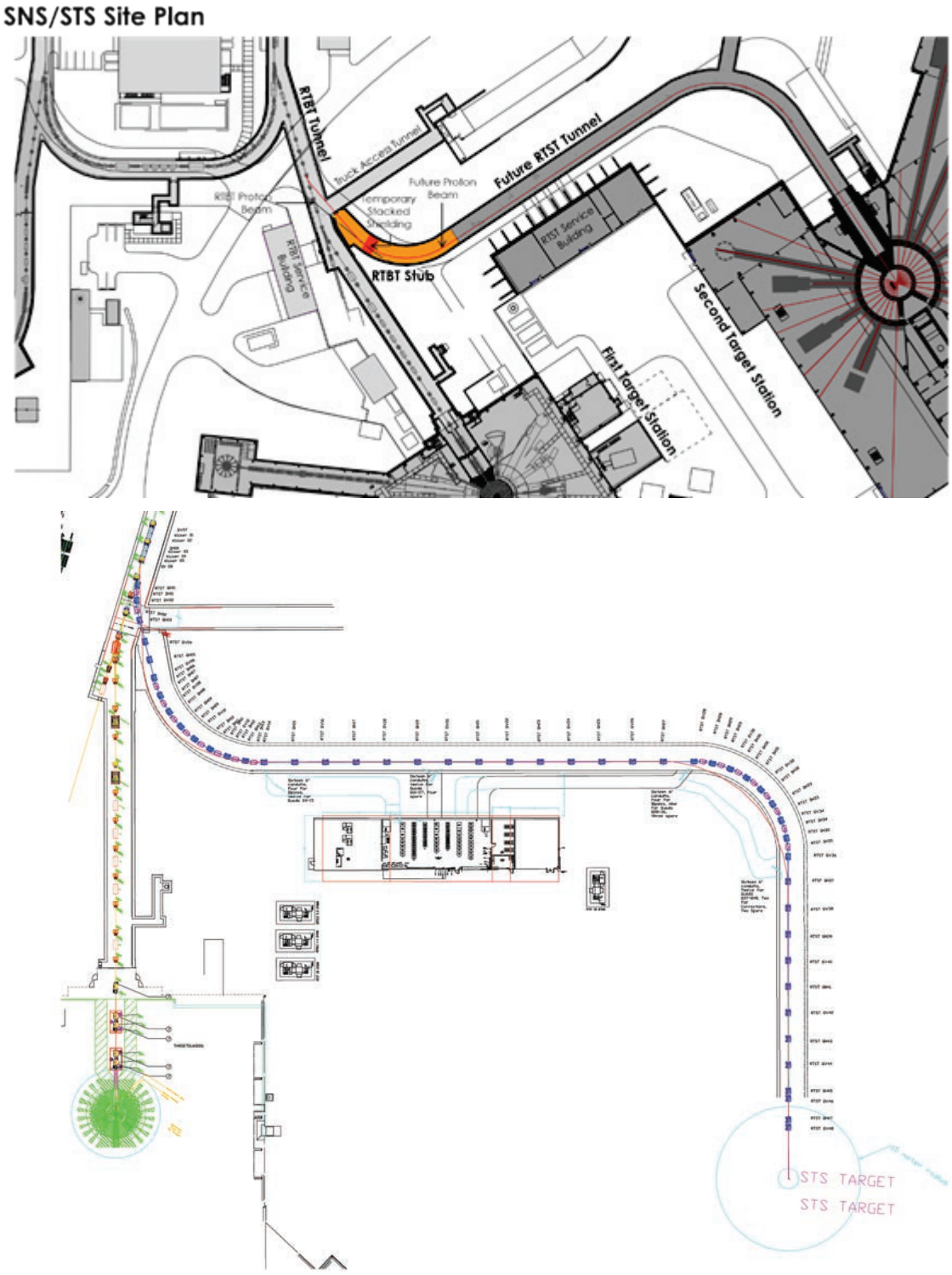

Figure 3.1. The new RTST shown together with the existing RTBT in a site layout drawing (top) and a beamline drawing (bottom).

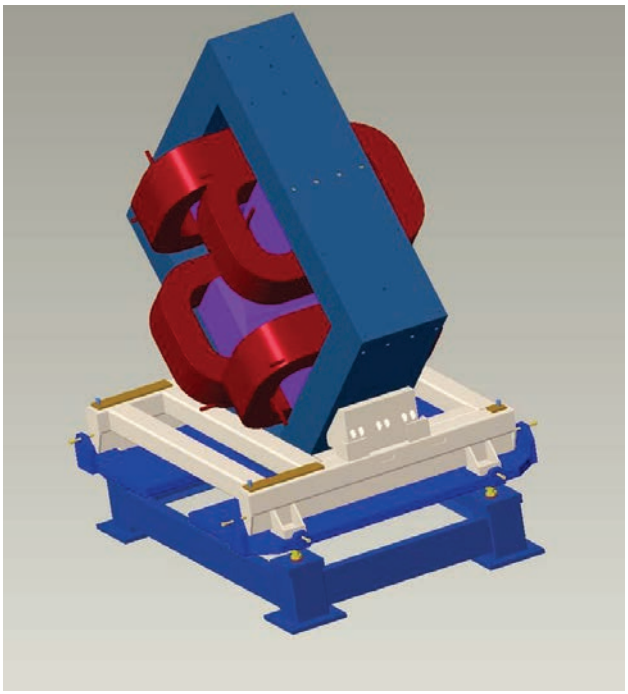

Figure 3.2. The large quadrupole 40Q40 concept design.

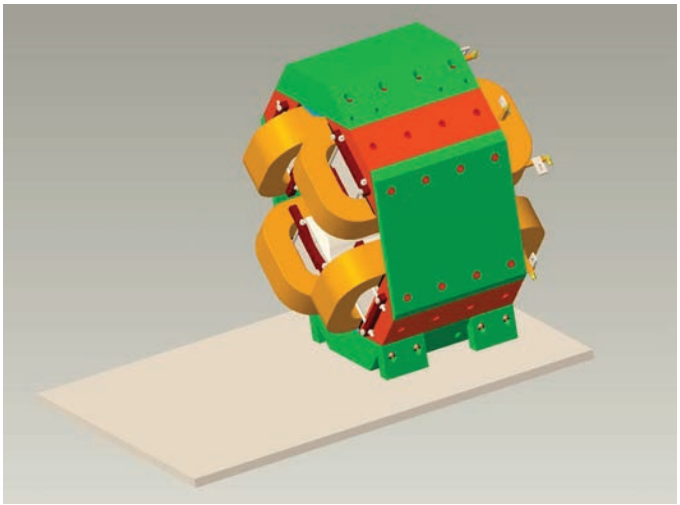

Figure 3.3. The 21Q40 quadrupole with a narrow design.

Table 3.2. Requirements for extraction to the RTST line.

Parameter	Value	Units
Beam energy	1.3	GeV
Bend angle	56	mrad
Rise/fall time	4.167	ms
Repetition rate	15	Hz
Field flat top	< ±10, 0.1%	Full scale
Pulse-to-pulse stability	< 0.1%	Full scale
Magnet length	Must fit between existing RTBT quadrupole magnets.	

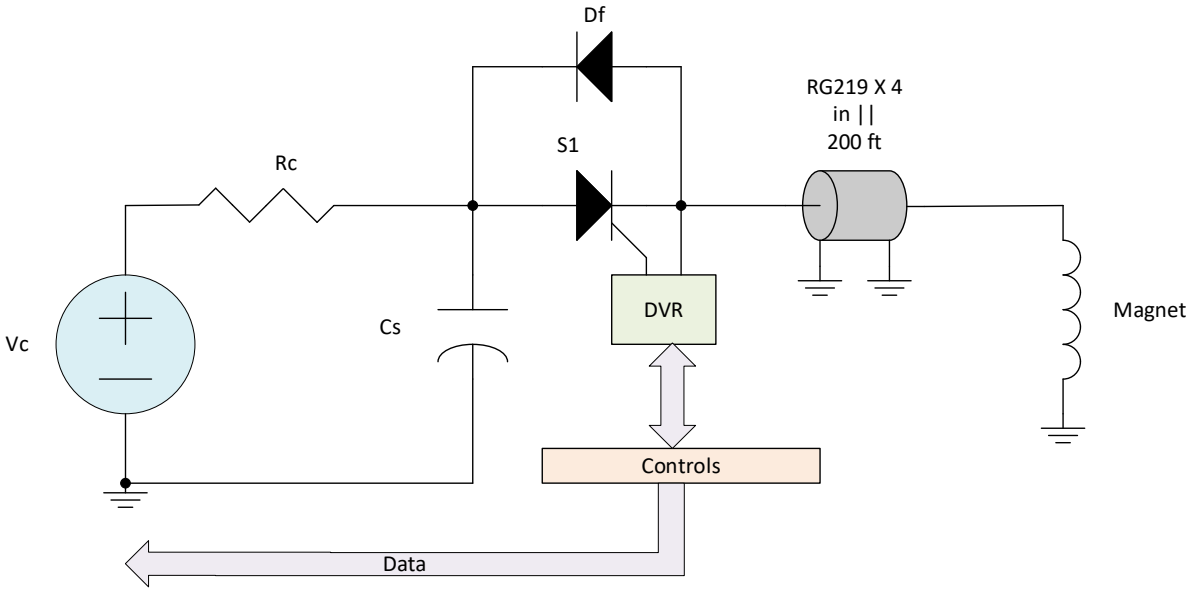

Figure 3.4. Simplified schematic of the STS kicker system.

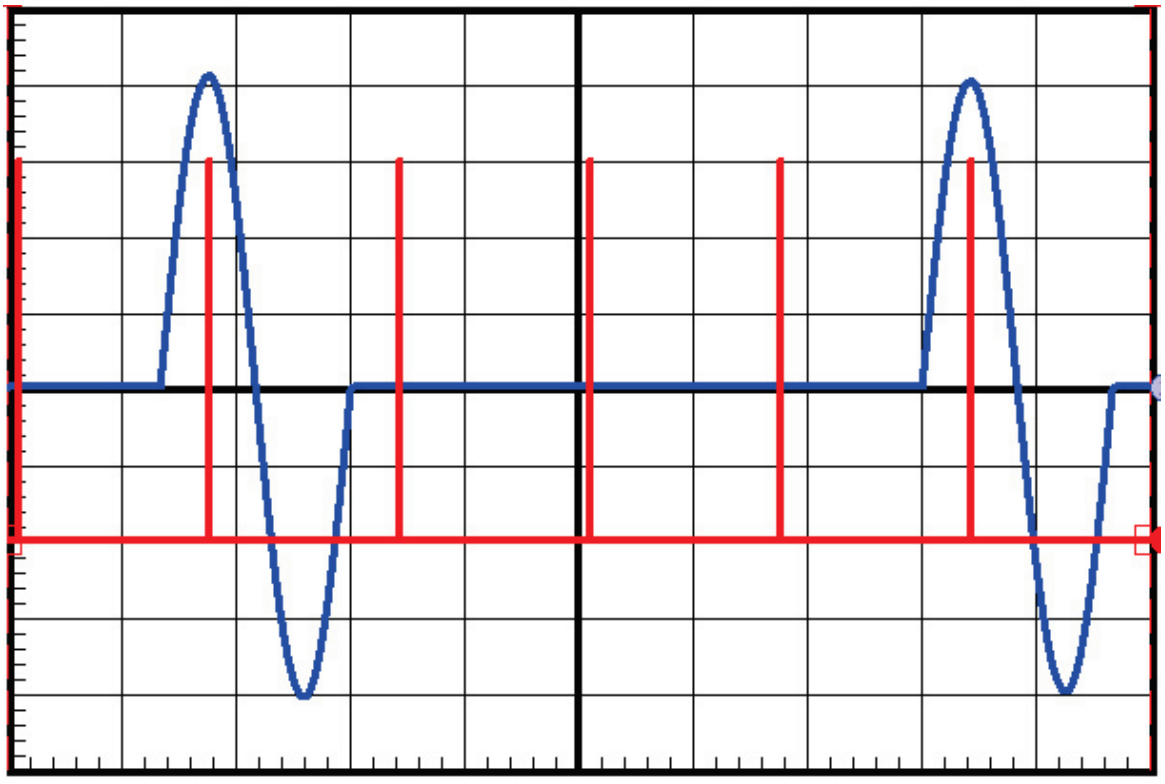

Figure 3.5. Timing of magnet current (blue) and bunches (red) in the RTBT line.

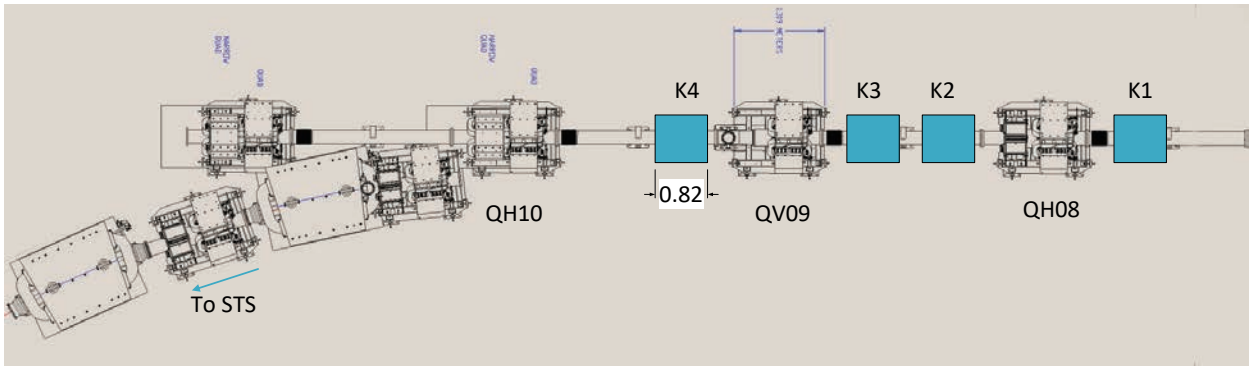

Figure 3.6. RTST extraction region showing approximate location of kicker magnets K1-K4.

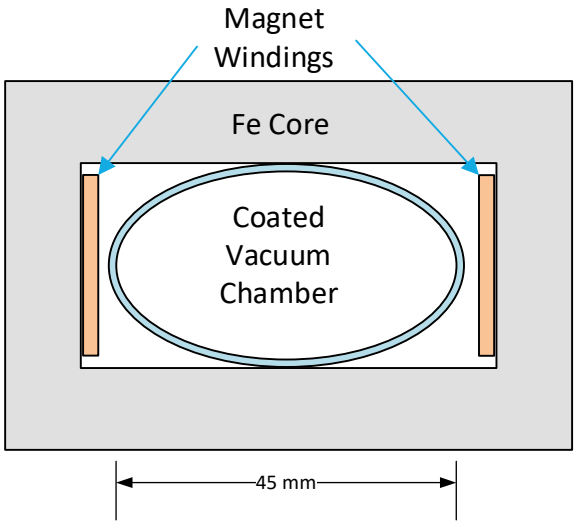

Figure 3.7. Cross section of STS kicker magnets.

Table 3.3. Magnet parameters with 40 turn windings.

Magnet	Magnetic length (m)	Aperture (V×H) (cm)	Bend angle (mrad)	B field (T)	Current (A)	Inductance (mH)	Magnet voltage (V)
K1	0.82	25×25	10	8.27e-2	411	1.65	256
K2	0.82	25×25	16.5	1.36e-1	678	1.65	422
K3	0.82	25×45	16.5	1.36e-1	678	2.97	759
K4	0.82	25×45	13	1.07e-1	534	2.97	580

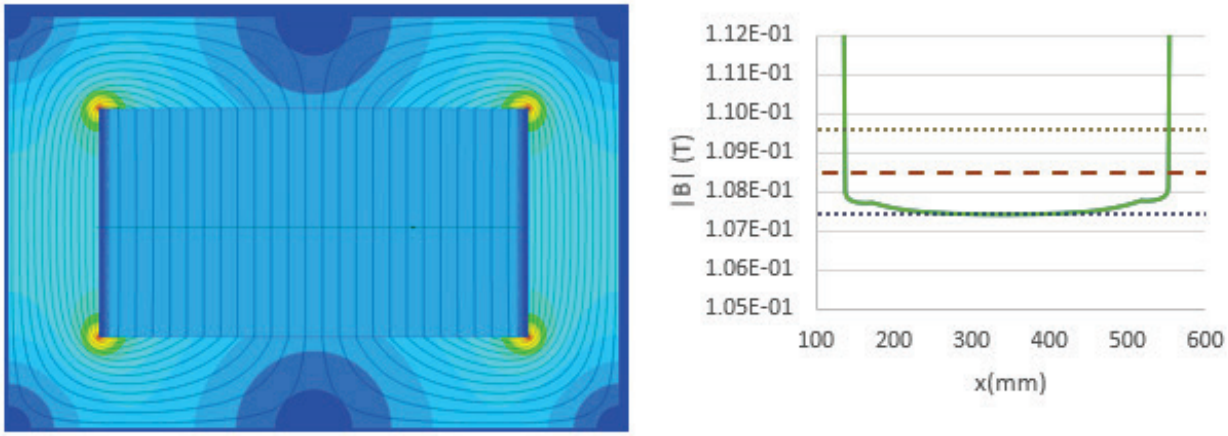

Figure 3.8. Finite element analysis results showing |B| and flux lines (left) and field flatness (right).

The design of the conductive coating involves finding a compromise between penetration of the kicking field and induced eddy currents, and low resistive heating and beam impedance. Most of the power dissipated in the coating is caused by the beam image current and can be calculated by the product of the coating reistance multiplied by the square of the rms current. A simplistic analysis assuming the beam is a square pulse train with a charge of 36 μC , 640 ns wide, at 60 Hz, results in an rms current of approximately 4 A. The SNS current has a 40 mΩ copper striped coating on a ceramic tube overlaid with Ti-N to prevent secondary electron emissions. Using a similar coating for the STS kickers results in a value of approximately 640 mW because of the beam image current. This analysis assumes a uniform current density in the coating, which is a good approximation because the skin depth of copper is greater than the thickness of the coating at the fundamental frequency. A 2D eddy current calculation was performed to estimate the field attenuation due to the coating; the results, shown in Figure 3.9, show an attenuation of approximately 3%.

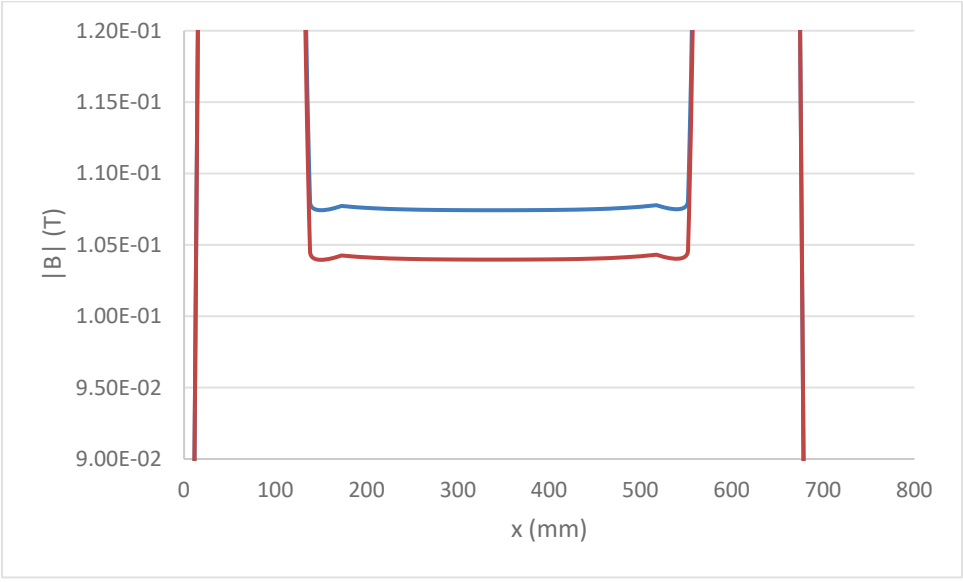

Figure 3.9. |B| across the center of the magnet aperture without coating (blue) and with coating (orange).

3.1.1.2 Kicker Power Supply Location

The closest building that could be used as a location for the kicker pulsers and controls, to minimize cable lengths, is the Ring Service Building (RSB) (Figure 3.10). Space exists in the tunnel for up to five racks for the kicker magnets, although the pulsers and controls are likely to require only two racks. The maximum cable length needed to reach the magnets from the RSB is approximately 122 m. Using four parallel RG218 coaxial cables per magnet, with ODs of 2.08 cm, will result in a cable voltage drop of approximately 36 V for K2 and K3. Figure 3.11 shows the rack profile of two pulsers, a DC power supply, and a programmable logic controller for all four kicker magnets.

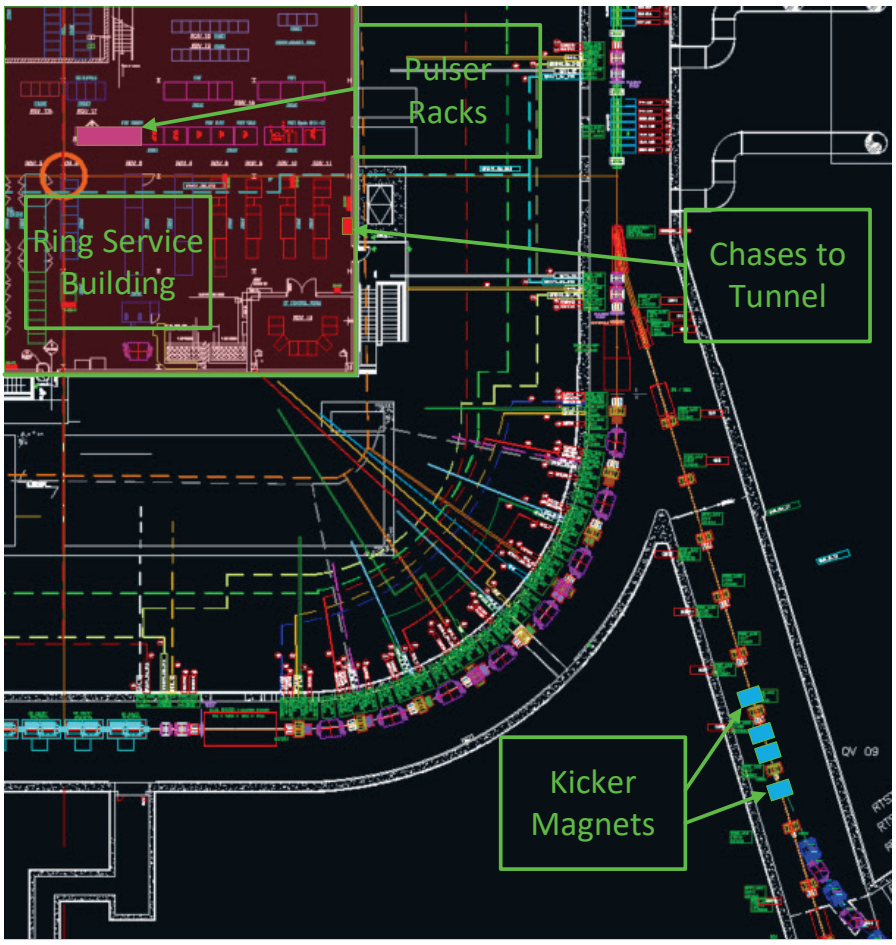

Figure 3.10. Layout of the Ring Service Building and SNS tunnel.

3.1.1.3 RTST Beamline

Once the beam exits the fifth kicker magnet, it will be well separated from the RTBT beamline. Standard dipole magnets and quadrupole magnets will then transport the beam to the second target. Renderings of the extraction region are shown in Figures 3.12 and 3.13. Custom magnet stands, as depicted in orange in Figure 3.12, will be designed to accommodate the spacing and orientation of the magnets. The quadrupole magnets throughout the RTST will be clones of the existing 21Q40 SNS magnets (see Figure 3.14). The dipole magnets will be clones of the SNS ring dipoles (Figure 3.15). After the two first dipole magnets transport the beam to the penetration point of the track entrance tunnel wall, the beam will go into the bending section and then into the straight section along the service building. The second set of dipole

magnets will point the beam toward the target, and then four quadrupole magnets at the end of the beamline will tailor the beam distribution to the target requirements.

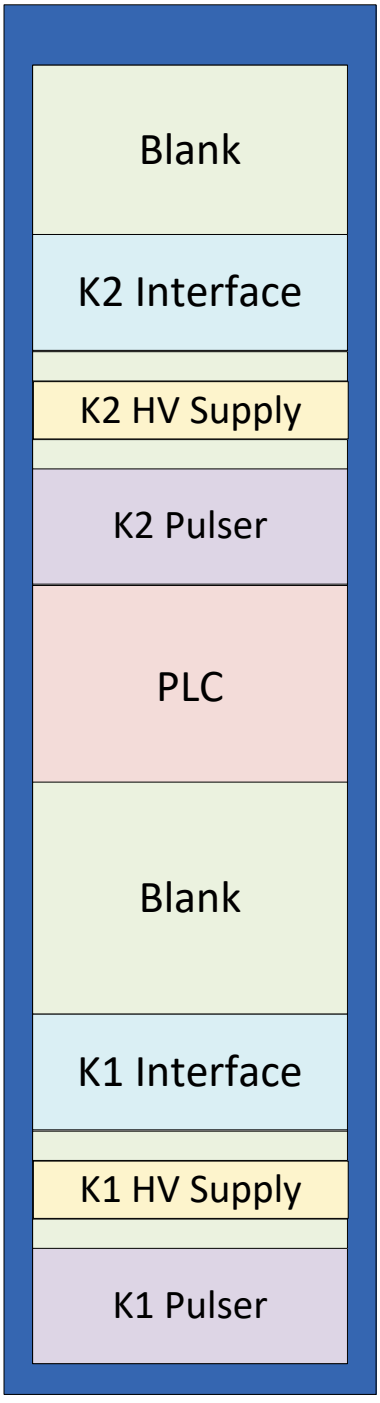

Figure 3.11. Rack profile of the K1 and K2 pulsers with a single programmable logic controller for system controls.

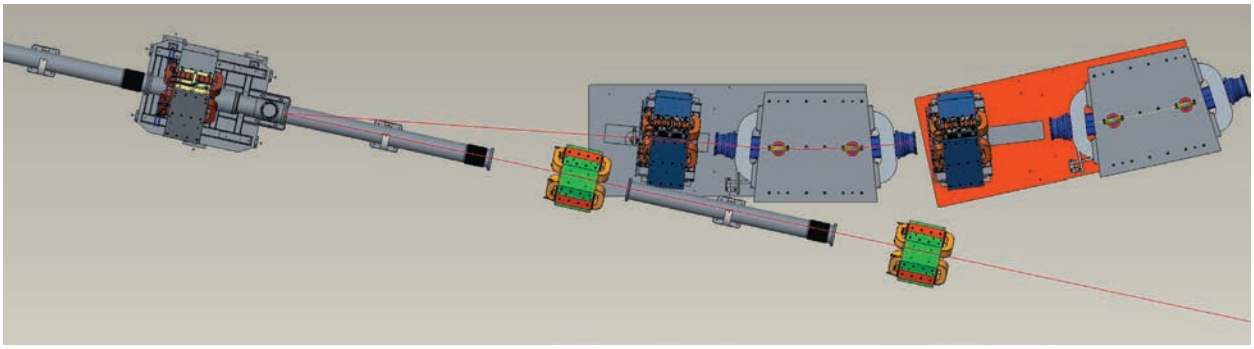

Figure 3.12. Extraction point into the RTST.

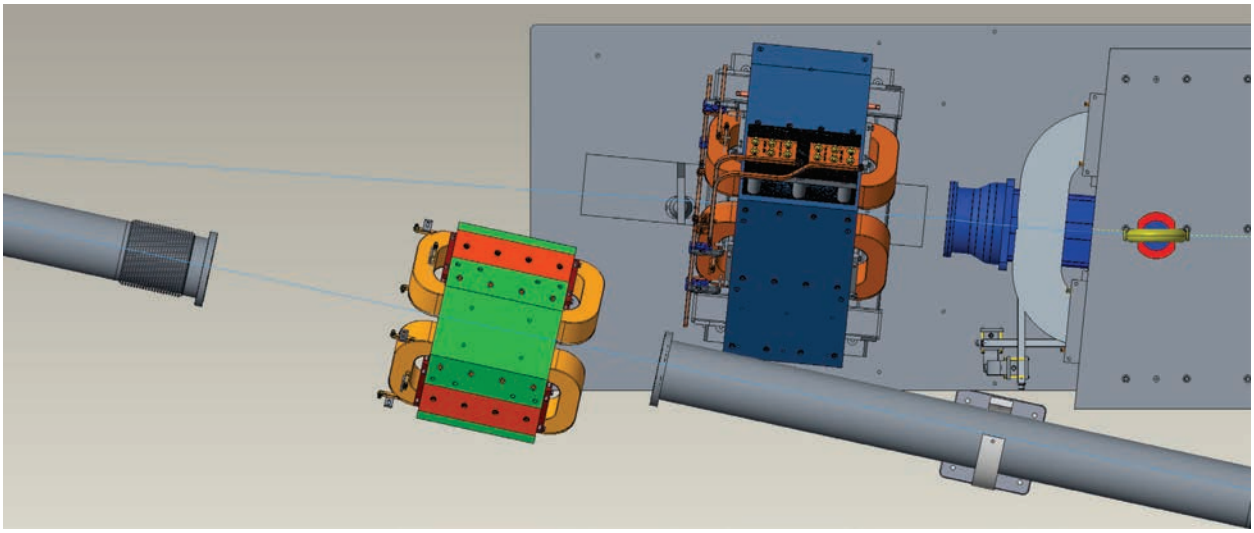

Figure 3.13. Zoom of the extraction point into the RTST.

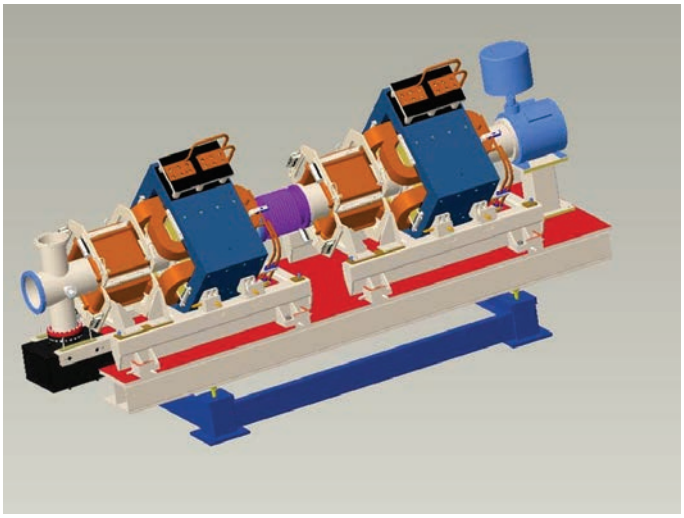

Figure 3.14. Nominal 21Q40 quadrupole doublet design.

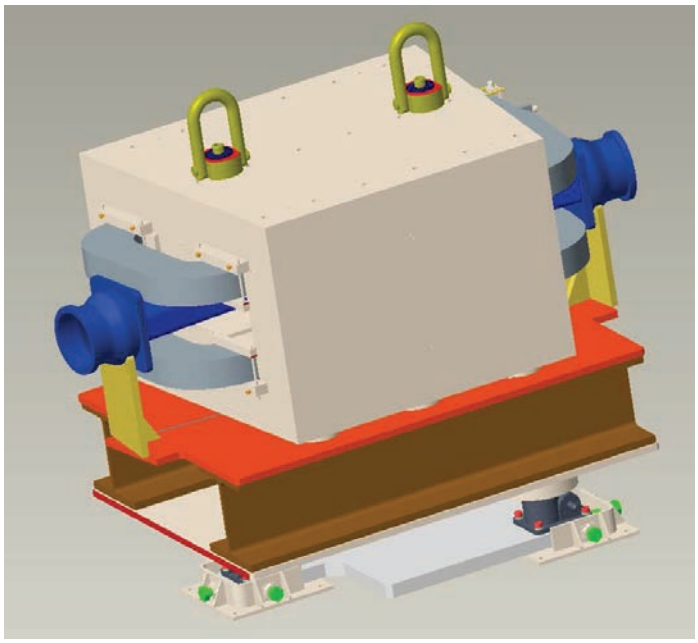

Figure 3.15. Dipole magnet design.

The quadrupole magnet spacing in the RTST beamline has been set to be close to the spacing in the RTBT, since the beam is essentially the same in each beamline. In the downstream portion of the RTBT, the quadrupole magnet spacing will be 5.8 m; in the RTST, it will vary from 5.8 to 6.3 m. The same type of quadrupole magnet (21Q40) will be used in each beamline. The beamline lattice functions are shown in Figures 3.16 and 3.17. Note that the dispersion in the current iteration is not fully optimized, but it will be zero at the location of the target in the final design.

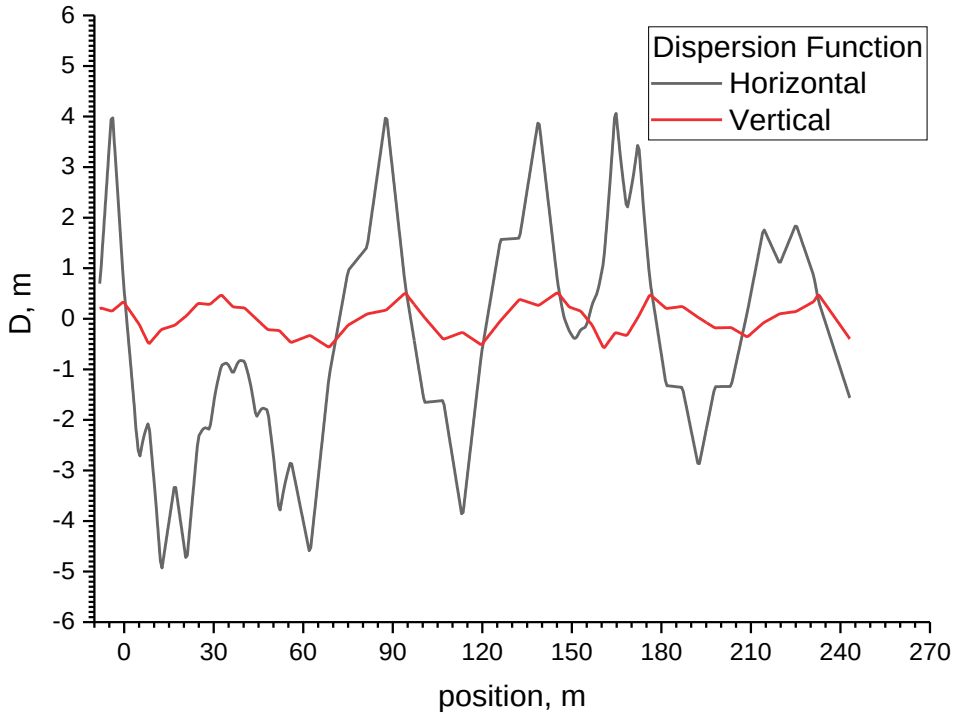

Figure 3.16. The RTST lattice dispersion function.

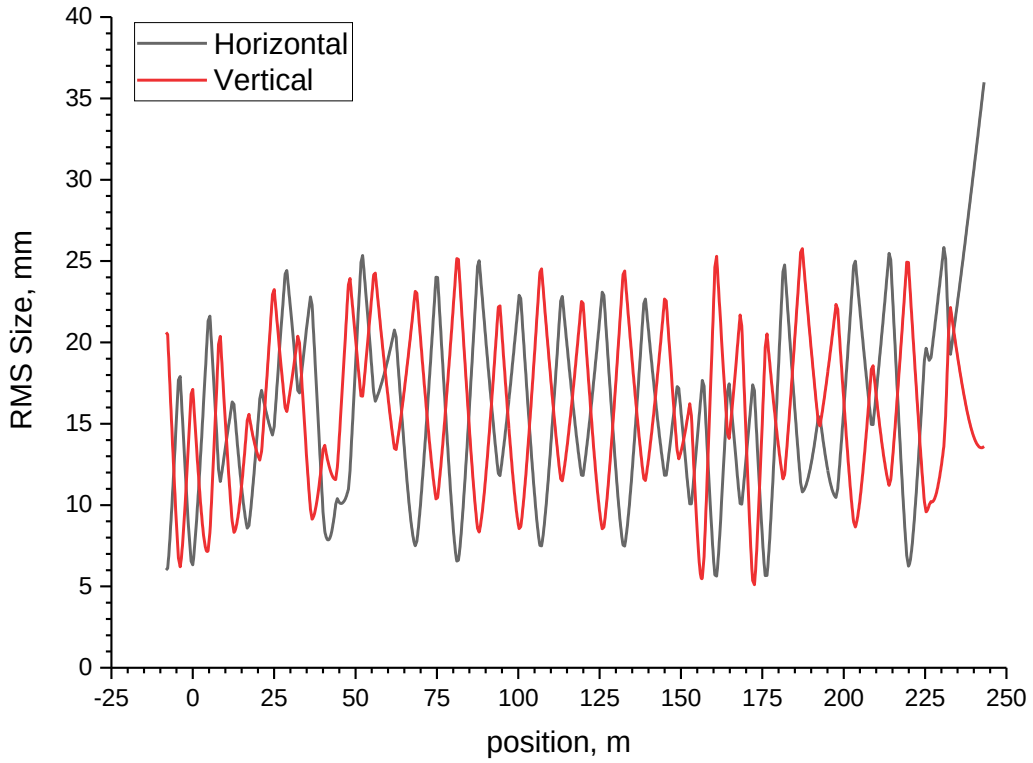

Figure 3.17. RMS beam sizes in the RTST beamline.

The beam in the RTST was simulated using the PyORBIT simulation code [Shishlo et al. 2015]. The pyORBIT code has been successfully benchmarked with beam profiles in the existing SNS RTBT, as shown in Figure 3.18.

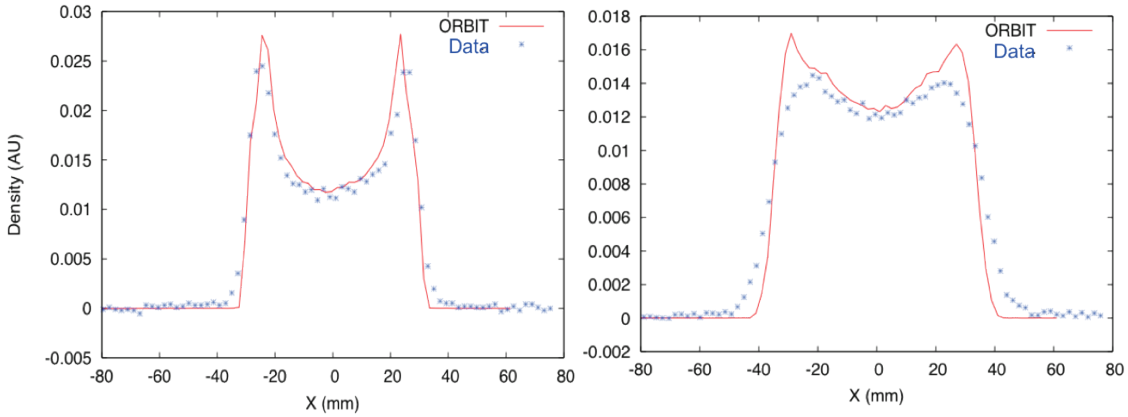

Figure 3.18. Benchmark of wire scanner profiles in the SNS RTBT with the code ORBIT (pyORBIT) for 0.35 μC of beam (left), and for 12 μC of beam (right). *Source:* Cousineau, S. 2011, "Status of High Intensity Effects in the SNS Accumulator Ring," *Proceedings of NAPAC11*, New York.

For the RTST simulations, the input distribution was created by simulating the turn-by-turn accumulation of beam in the ring, including all relevant physics effects (e.g., injection, space charge, nonlinear transport), and extracting it to the beginning point of the RTST. Simulated transport of the beam down the

RTST indicated that there will be no beam loss and that beam size specifications on the second target are correct. Figures 3.19 and 3.20 show the simulated distribution on the second target face.

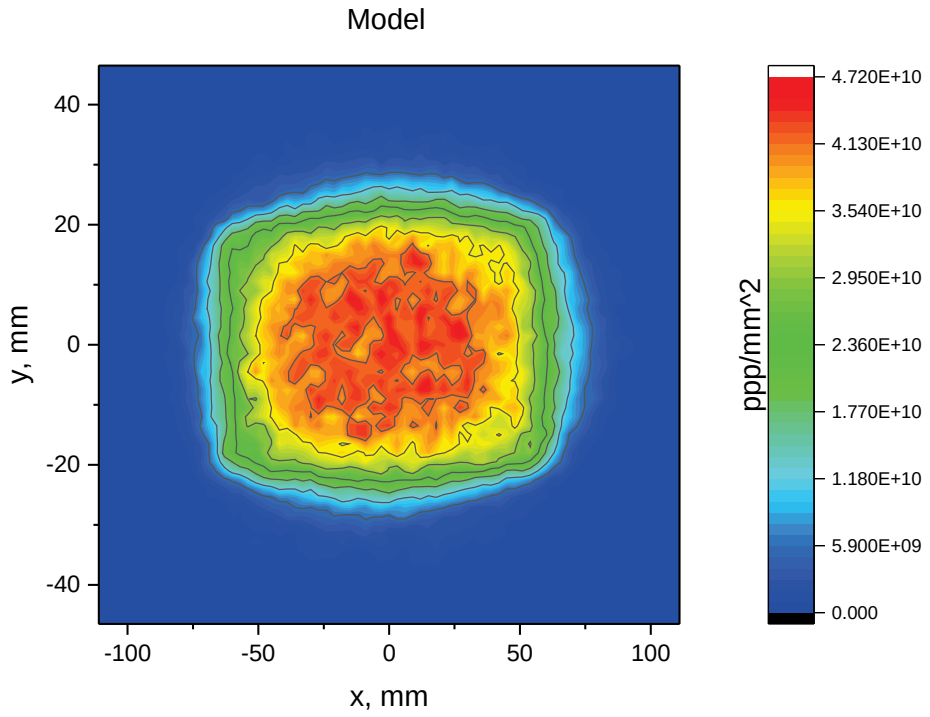

Figure 3.19. Simulated beam transverse distribution on the face of the target.

The Personnel Protection System (PPS) gate separating the ring segment from the RTBT segment will be extended to include the second dipole (RTST DH02) in addition to the first dipole (RTST DH01) and two of the quadrupole magnets (RTST QH01 and QV02) for consistency in lock/tag/verification. The third quadrupole magnet (RTST QH03) will be within the RTBT lock/tag/verify segment.

Table 3.4 lists equipment included in the RTST beamline. The items of equipment are, in general, copies of their counter-components in the existing beamline, to minimize development and maintenance issues. One notable difference from the RTBT beamline is the absence of a collimation system.

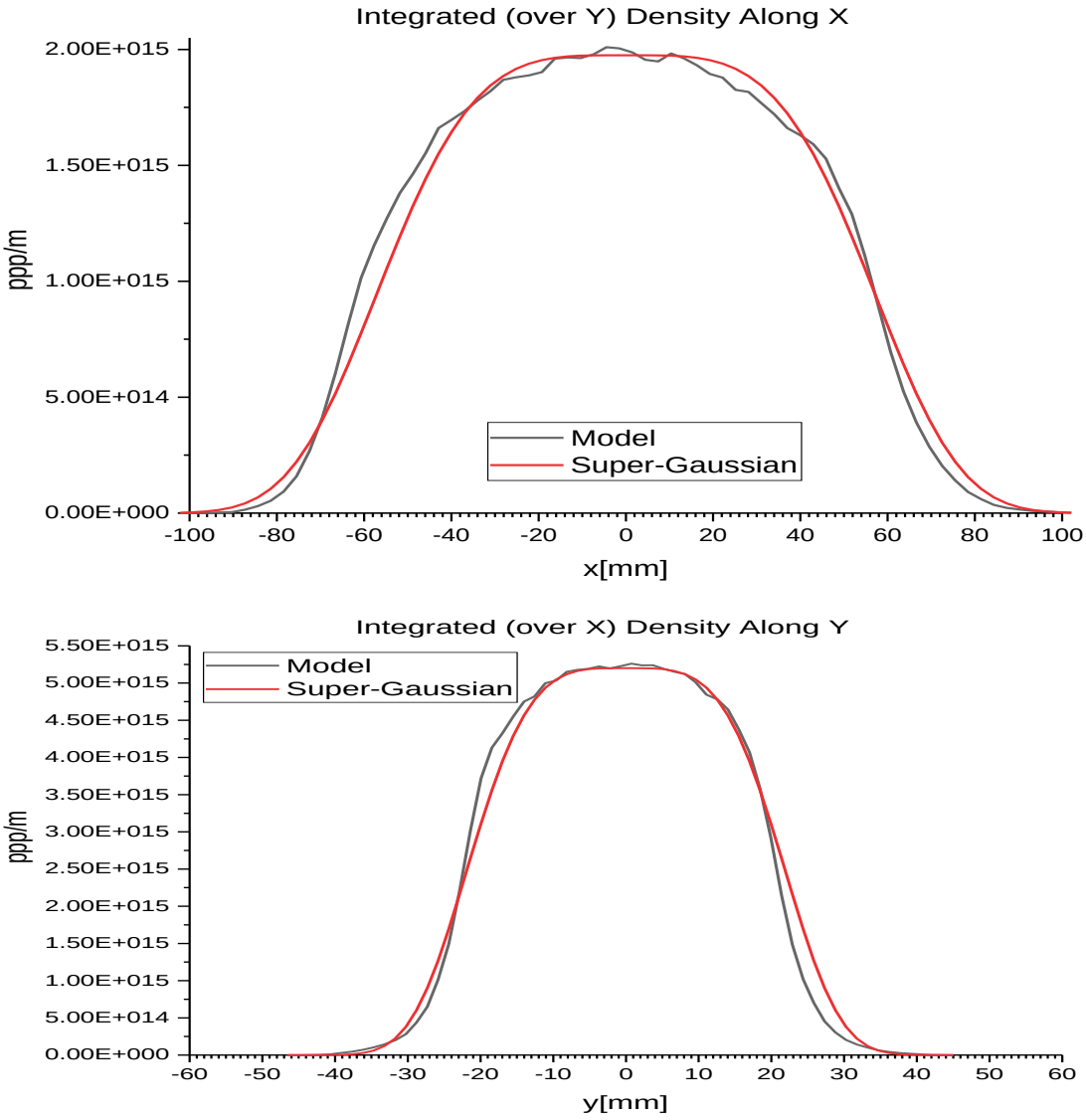

Figure 3.20. Corresponding to the optics in Figures 3.16 and 3.17, the density profiles of the horizontal (top) and vertical (bottom) beam distributions on the target (black line), compared with a perfect super gaussian fit (red line).

Table 3.4. Components included in the new RTST beamline.

Category	Type	Number installed	Water cooled	Comments
Magnets	21Q40 quadrupole magnet	48	Yes	Total number of new quads is 48
	40Q40 quadrupole magnet	1	Yes	RTBT QV09 replacement
	Dipole magnets in RTBT	2	Yes	17D120, 2.75° bend each
	Kicker magnets	4	Yes	Similar to ring injection kickers, 1.4° each
	Horizontal dipole magnets	16	Yes	17D120, 22° bend
	Dipole corrector magnets	32	No	Similar to existing RTBT dipole correctors
Power supplies	Power supplies (PS) for individual quadrupole magnets	29	Yes	30 V/1000 A, includes new power supplies for RTBT QV09 – QV11
	PS for 2, 3, or 4-quad strings	6	Yes	100 V/1000 A
	PS for 4-quad strings	4	Yes	50 V/1500 A
	PS for horizontal dipoles	2	Yes	1 PS per set of 8 dipoles 110 V/6000 A
	PS for RTBT dipoles	1	Yes	1 PS for dipole in RTBT 30 V/6000 A
	PS for kickers	4	Yes	1 PS per kicker, similar to ring injection kickers
	PS for dipole corrector magnets	52	No	Dual polarity, ±20 A; last 4 quads have 6 power supplies each
Diagnostics	Wire scanners	4		Similar to existing RTBT wire scanners
	Beam position monitors (BPMs)	27		Existing RTBT has about 2 BPMs for every 3 quadrupole magnets
	Beam current monitors (BCMs)	1		Similar to existing RTBT BCMs
	Beam loss monitors	40		One for every quad
	Harp	1		Downstream as far as possible
	Halo monitor	1		Mounted to proton beam window?
	Fast valve	1		
Vacuum	Vacuum gate valves in-line	7		
	Ion pumps	22		
	Turbo pumps (700 lps)	1		
	Cold cathode gauge	8		
	Convection enhanced Pirani gauge	8		
	IP controller	11		
	Fast valve	1		
	Beam pipe (~216 m)			

3.1.2 Beam Instrumentation

The beam instrumentation scope of work includes new beam diagnostics for the RTST and adaptation of the user interface of the existing SNS beam diagnostics to accommodate the dual beam timing requirements. The new beam diagnostics for the RTST are listed in Table 3.5.

Table 3.5. Beam loss diagnostics for the RTST.

	Number of pickups	Number of electronics crates
Beam loss monitors	48	3
Beam position monitors	24	3
Beam current monitors	2	2
Wire scanners	9	3
View screens	1	1

3.1.2.1 Beam Loss Monitors

Beam loss monitors (BLMs) are required for beam loss control and machine protection. The BLM system will consist of radiation detectors and data acquisition electronics. The proven standard SNS design of the detectors and electronics will be used for the RTST [Aleksandrov 2015] (Figure 3.21). Radiation detectors will be located at every RTST magnet.

Figure 3.21. Photo of the type of BLM to be used in the RTST beamline.

3.1.2.2 Beam Position Monitors

Beam position monitors (BPMs) will be used for the beam trajectory and position control on the target. The BPM system will consist of beamline pickups and data acquisition electronics. The proven standard SNS design of the pickups and ring-style electronics will be used for the RTST [Aleksandrov 2015] (Figure 3.22). The exact pickup locations along the RTST will be optimized based on the beam dynamics error analysis. The last four quadrupoles of the beamline will be equipped with BPMs to provide the required accuracy of beam position on the target. The individual BPM measurement accuracy is expected to be on the order of ±1.0 mm.

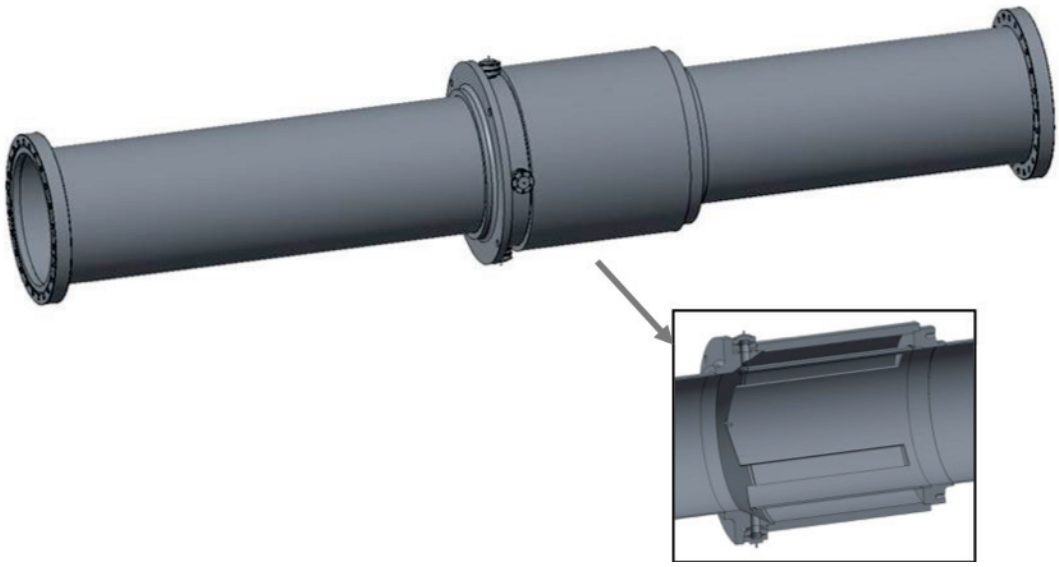

Figure 3.22. Engineering model of the BPM to be used in the RTST beamline.

3.1.2.3 Beam Current Monitors

Beam current monitors (BCMs) will be used for charge-to-target accounting purposes and to provide input to the PPS. The BCM system will consist of beamline current transformers and data acquisition electronics. The proven standard SNS design for transformers and electronics will be used for the RTST (Figure 3.23). The plan is to deploy two BCMs to provide the redundancy required by the PPS. The BCM accuracy is expected to be ~1%.

3.1.2.4 Wire Scanners

Wire scanners will be used to measure the transverse profile of the beam for control of the beam size in the beamline and on the target. The wire scanner system will consist of beamline wire actuators and data acquisition electronics. The proven standard SNS design for actuators and electronics will be used for the RTST (Figure 3.23). The exact locations of the nine wire scanners to be placed along the RTST will be optimized based on the beam dynamics error analysis.

3.1.2.5 View Screen

A luminescent view screen mounted on a pneumatic actuator will be located between the last quadrupole magnet and the proton beam window. A video camera with a telescopic lens will be located behind the last dipole magnet of the RTST. The view screen will be used with a low-power beam for precise calibration of the final focus of the BPMs. The need for the calibration system is dictated by tight requirements for the beam position control on the target. The viewscreen will be retracted from the beam during normal operation.

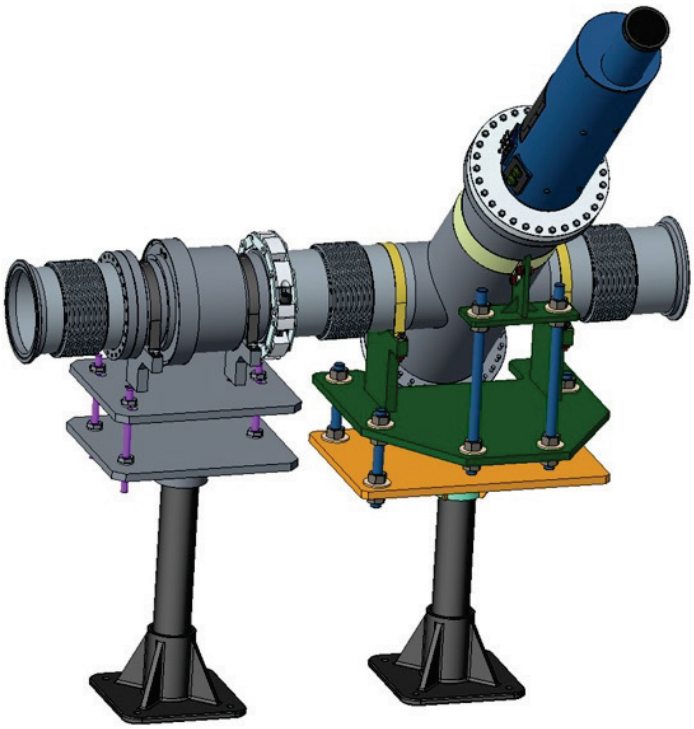

Figure 3.23. Engineering model of the BCM and wire scanner to be used in the RTST.

3.1.3 Power Supplies in the Ring Service Building for the Magnets in the RTBT Tunnel

Five 2000 A peak pulsed kickers (RTST Kick01-05), two 1000 A/30 V quadrupoles (RTST QH01, QV02), and one 6000 A/30 V dipole (RTST DH01-02) water-cooled power supply will be installed in row 20 on the main floor on the east side of the RSB. A new 1000 A/30 V power supply for RTBT QV09 will also be installed in row 20. This magnet is currently fed in series with the odd-numbered (vertical) quadrupole magnets QV05t11 and will be removed from the string to allow independent control. The output cables will be routed through the chases on the east wall, where they will run along the inside of the ring beamline to a point where they can pass between the two crane rails above the extraction septum. A new switch bucket will be installed in RN-SS1 to feed an 800 A electrical panel that will supply 3ϕ 480 VAC power for the power supplies in the RSB.

The third RTST quadrupole (RTST QH03) in the RTBT tunnel will be supplied from a power supply located in the RTBT service building. The output cables will pass through an existing conduit in the east wall chase to the RTBT tunnel (Figure 3.24).

The pulsed kicker systems to kick beam from RTBT to RTST will be custom-designed pulsed magnets and power supplies. A resonant circuit design is proposed that produces a sinusoidal pulse of a single period of less than 16 ms, consistent with the 60 Hz operation of the accelerator. The kicker magnet current will be zero when the FTS beam pulse is passing through and will be at the peak of the sinusoidal pulse during the STS pulse. The sinusoidal pulse will have a period large enough that the peak will be quasi-flat during the beam pulse, plus time allowed for timing errors. Development of this pulser will be performed during the preliminary design phase of the STS project.

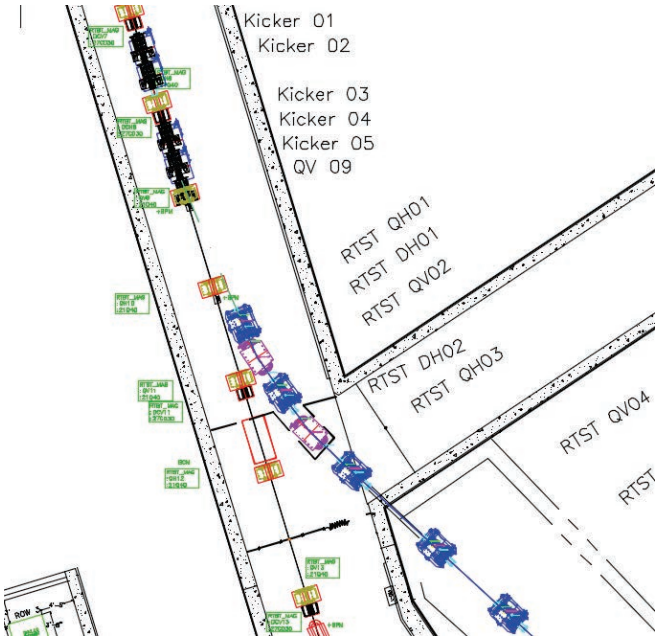

Figure 3.24. RTBT tunnel showing where the STS beam will penetrate the truck entrance wall.

3.1.4 Power Supplies in the RTST Service Building

The RTST service building will house 53 power supplies for the dipole, quadrupole, and corrector magnets in the RTST tunnel. Multiple quadrupoles will be supplied by a single power supply (two strings each of two quads, two strings each of three quads, and two strings each of four quads for a total of six power supplies), and the remaining magnets will have a single magnet per power supply. The eight left-bend dipole magnets and eight right-bend dipole magnets will have one power supply per bend, with each bend power supply supplying eight magnets in series. There will be 28 corrector power supplies, one for each magnet.

The water-cooled quadrupole power supply types will be 1000 A/30 V (quantity 23), 1000 A/75 V (quantity 4), 1000 A/125 V (quantity 2), and 1500 A/50 V (quantity 4). The two dipole magnet power supplies will be water cooled and rated at 6000 A/110 V, similar to the ¼ DH-main in the RSB. The corrector power supplies will be bipolar ±20 A/35 V, similar to the correctors used throughout the accelerator.

3.1.5 RTST Vacuum Systems

The RTST vacuum system will extend ~241 m from the existing RTBT to the STS. Five sector gate valves will be located strategically along this line for convenience during initial construction and to allow for isolation between segments for maintenance during operation. Twenty-two 300 l/s noble diode ion pumps will be used to achieve ultra-high vacuum, $\leq 1E^{-8}$ Torr. To achieve these pressures, stainless steel 304 beam pipes and all-metal seals (ConFlat flanges) will be specified and leak-checked at a rate of $<1E^{-9}$ torr·liter/second. Each beam pipe will be baked at 200°C before installation to reduce hydrocarbon contamination from manufacturing and handling. Various ports along the length of the line will exist for rough vacuum connections and gauging. Finally, a turbo pump system and a fast valve will be located near the STS to mitigate any back-streaming or catastrophic release of gases from the target into the RTST. Figure 3.25 shows the vacuum configuration and status screen for the existing RTBT. The RTST configuration will be based on this design, but without the EDmp.

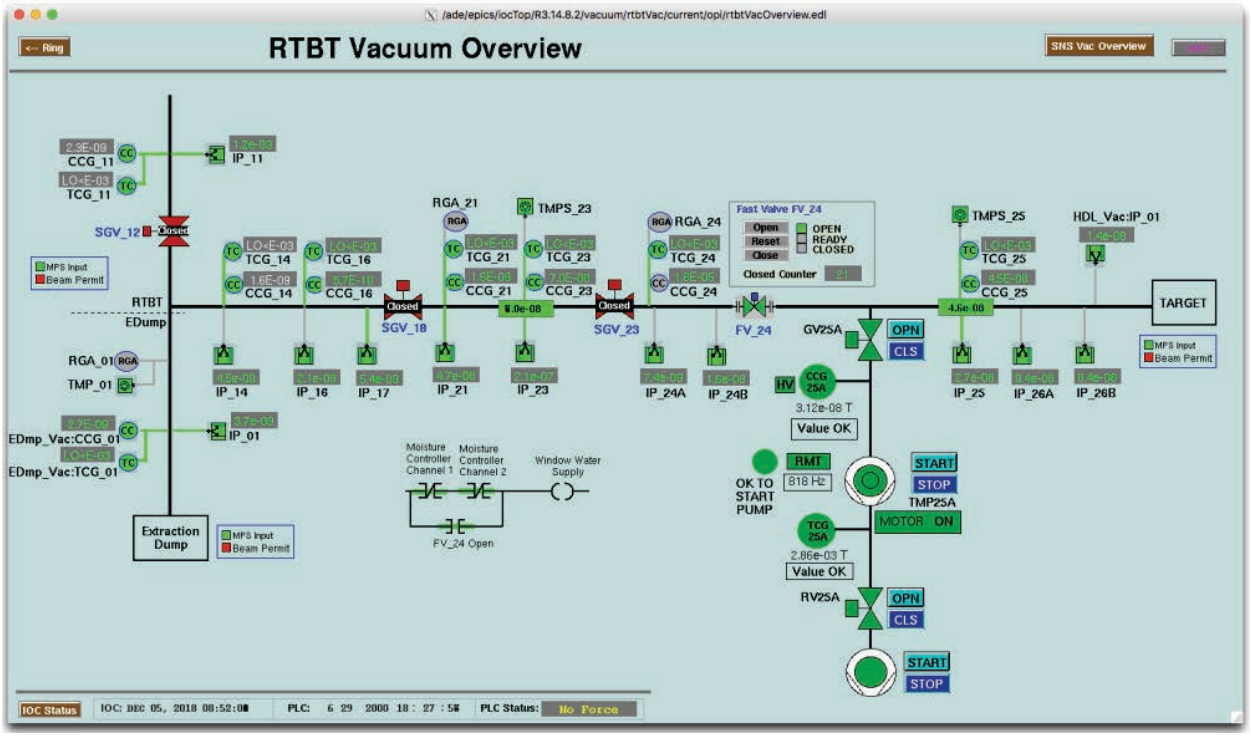

Figure 3.25. Vacuum status configuration for the existing RTBT.

3.1.6 RTST Alignment

The Survey, Alignment, and Metrology (SAM) team will have approximately 280 survey monuments installed in the floor and walls of the RTST tunnel. SAM will then measure the positions of these monuments relative to the rest of the SNS global survey network, with the same precision as the RTBT tunnel survey (i.e., capable of supporting 100-micron rms magnet offset tolerance, and 1-mrad rms magnet yaw, pitch, and roll tolerance). RTST components requiring high-precision alignment will be fiducialized by SAM or by the component manufacturer. Then, using the monuments and fiducial data, SAM will align the components in the tunnel to the position, orientation, and precision designated by the physics lattice and parameters list. In the following months and years, SAM will perform periodic deformation monitoring in the RTST tunnel to check the component alignment and monument coordinates, and realign if necessary.

3.1.7 RTST Utilities

3.1.7.1 RTST Tunnel Magnet Cooling System (RTST-01)

A new magnet cooling system will be installed in the RTST service building (Building 8560—provided by conventional facilities) with supply and return headers extended into the new RTST tunnel to cool the new magnets in the tunnel. The cooling system will consist of the standard duplex pump arrangement with a single heat exchanger and all ancillary equipment and instrumentation for reliable operation. Once the magnets are installed, the final connections to each magnet assembly will be made and the system will be balanced for optimum operation. Local flow indication is required to facilitate system balancing.

3.1.7.2 RTST Service Building Magnet Power Supply Cooling System (RTST-02)

A new magnet power supply cooling system will be installed in the RTST service building (8560—provided by conventional facilities) with supply and return headers extended into the power supply room to cool the new magnet power supplies. The cooling system will consist of the standard duplex pump arrangement with a single heat exchanger and all ancillary equipment and instrumentation for reliable operation. Once the magnet power supplies are installed, the final connections to each power supply assembly will be made and the system will be balanced for optimum operation.

3.1.7.3 RTBT Tunnel Magnet Addition

Several quadrupole magnets and extraction kicker magnets will be added to the existing RTBT tunnel lattice to provide beam to the RTST and the STS. The cooling requirements of these magnets will be satisfied by the new RTST-01 magnet cooling system. The supply and return headers will be extended from the RTST tunnel into the RTBT tunnel and to the new transition magnets. Once the magnets are installed, the final connections to each magnet assembly will be made and the system will be balanced for optimum operation.

3.1.7.4 RTBT Tunnel Magnet Power Supply Addition

The power supplies for the new quadrupole magnets and extraction kicker magnets will be located in the RSB (Building 8540).

The existing power supplies in the RSB are cooled by pump skid ring #3 (PS-RN-03). The Proton Power Upgrade (PPU) Project necessitates an upgrade to PS-RN-03. The increased demand from the additional extraction power supplies has been incorporated into the PS-RN-03 upgrade performance criteria.

3.1.7.5 RTBT Power Supply Cooling System

Only one new power supply will be installed at the RTBT service building (8550). This small cooling demand can be accommodated by the existing RTBT power supply cooling system.

3.2 LOW-LEVEL RADIO FREQUENCY SYSTEMS FOR THE STS

The STS will replace 96 units in the existing 96 cavities to be capable of alternating the LLRF control between two flavors on a pulse-to-pulse basis. The 28 new units to be installed during the PPU Project are being designed with this capability, eliminating the requirement to replace them during the STS Project. The STS Project will use the same design as the PPU Project.

The LLRF systems provide a low-power RF drive to the linac RF systems and, most important, control of the phase and amplitude of each cavity. The initial baseline stability requirements for this control are ±1.0° in phase and ±1.0% in amplitude. The existing LLRF control systems more than meet this specification, with ±0.5° in phase and ± 0.5% in amplitude routinely observed. A block diagram for the LLRF system is shown in Figure 3.26.

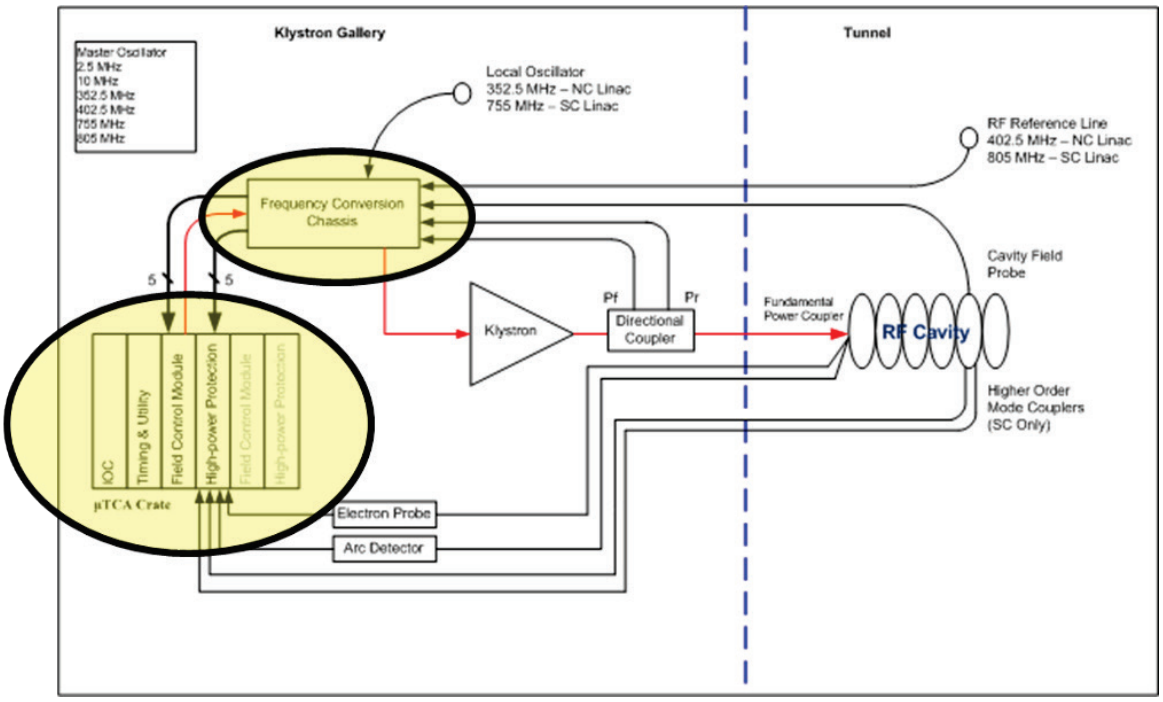

Figure 3.26. Block diagram of the SNS linac low-level control system.

The current LLRF system is a digital-control system that fundamentally realizes a proportional-integral feedback controller along with adaptive feed-forward (AFF) to support cavity filling and beam loading compensation. The heart of the system is the field control module (FCM), which digitizes four analog input channels (cavity field, reference, forward, and reflected signals), digitally processes the data stream, and produces an output signal at either 402.5 or 805 MHz, depending on the location in the linac. The FCM is a VXI bus module consisting of a motherboard and three daughter boards: the analog front end, digital front end, and RF output. The analog front end takes the analog signals and converts them to a differential pair for input to the ac-dc converters. The digital front end consists primarily of four high-speed, 14-bit A/D converters and a single field-programmable gate array responsible for the real-time processing. The RF output is responsible for receiving the I/Q (in-phase/quadrature) signals and generating the required RF drive. Communication with the outside world is via the input-output controller running the VxWorks operating system. The LLRF finite state machine is implemented as an Experimental Physics and Industrial Control System sequencer running on the input-output controller for capabilities such as ramping up RF power. The LLRF control system also provides high-power protection via the high-power protection module (HPM), which provides for fast shutdown of the drive in case of RF overpower; cavity quenches; arcs in the distribution system; poor vacuum; or “soft” interlocks such as cryo, coupler cooling, and high-power RF permit. Down-conversion of the reference and cavity signals is performed in a temperature-regulated chassis. The master oscillator provides low-noise, phase-coherent reference signals that are distributed throughout the Klystron Gallery and tunnel.

The LLRF control systems are currently installed with two control systems per rack, consisting of two FCM/HPM pairs with a shared timing card, utility card, and input-output controller.

The accelerator will operate with a pulse repetition rate of 60 Hz, with every fourth pulse delivered to the second target and the remaining pulse going to the first target. Each of the two targets requires different beam energy and chopping styles, requiring an additional beam loading AFF buffer in the LLRF systems. The additional AFF buffer will be designed, developed, and tested within the PPU scope of work, during which 28 additional superconducting linac LLRF systems will be installed.

3.3 REFERENCES

Aleksandrov, A. 2015. “SNS beam diagnostics: Ten years after commissioning,” in *Proceedings of IBIC2015*, Melbourne, Australia, September 13–17, 2015, p. 8.

Cousineau, S. 2011. “Status of High Intensity Effects in the SNS Accumulator Ring,” in *Proceedings of NAPAC11*, New York, 2011, p. 17.

Henderson, S. 2014. “The Spallation Neutron Source accelerator system design,” *Nucl. Instrum. Meth.* A763 (2014) 610-673.

Holmes, J. 2006. “Simulations for SNS Ring Commissioning,” in *Proceedings of EPAC06*, Edinburg, Scotland, 2006, p. 348.

Plum, M. 2007. “Commissioning of the Spallation Neutron Source Accelerator System,” in *Proceedings of PAC07*, Albuquerque, New Mexico, 2007, p. 2603.

Plum, M. 2009. “SNS Ring Operational Experience and Power Ramp Up Status,” in *Proceedings of PAC09*, Vancouver, Canada, 2009, p. 1952.

Shishlo, A., S. Cousineau, J. Holmes et al. 2015. “The particle accelerator simulation code PyORBIT,” *Procedia Computer Science* 5, 1272–1281.

4. TARGET SYSTEMS

4.1 INTRODUCTION

4.1.1 Target Systems Summary

The STS Target Systems are designed to produce high-brightness cold neutron beams, which will be accomplished by employing three coupled processes. First, the incoming proton beam at the STS target will be compressed by more than 50% relative to the FTS to a cross-section of 65 cm^2. Second, a solid rotating tungsten target will be employed that can support the higher proton flux. Finally, novel compact moderator designs will be optimally coupled to the resulting beam of neutrons. This source design, coupled with a short proton pulse that produces neutrons in a short period of time, will result in world-leading neutron peak brightness.

The proton pulses transported to the STS from the accumulator ring will impact the outer edge of the rotating tungsten target to spall neutrons that will be directed to an eventual total of 22 instruments (preliminary concepts described in Section 5). The target will be approximately 1.1 m in diameter and 6 cm thick. Figure 4.1 shows the target and moderator design. The target will consist of 21 separate stainless-steel segments, each housing a solid tungsten block that is encased in a layer of tantalum to protect the tungsten from any potential contact with cooling water. The stainless-steel segments will be welded to a central hub at the end of a 4 m long shaft extending above the core vessel. This shaft will connect to a drive system rotating the target. The target will be rotated to spread out the power load on the target and thus simplify the cooling requirements. The target will be cooled by water conveyed through the shaft and directed through the stainless steel housings around the tantalum-clad tungsten blocks. This design allows the incident proton energy to be spread across 21 target blocks, resulting in each block receiving the equivalent of 33 kW (700 kW ÷ 21 segments) of proton beam power at a repetition rate of 1 pulse every 1.4 s. If the target were stationary, the tungsten would have to be further segmented to allow greater water cooling. This additional segmentation of the target blocks would reduce the average density of the target material in the neutron production zone and consequently decrease neutron production in the vicinity of the moderators. Thus, the rotating target design enables a brighter neutron source.

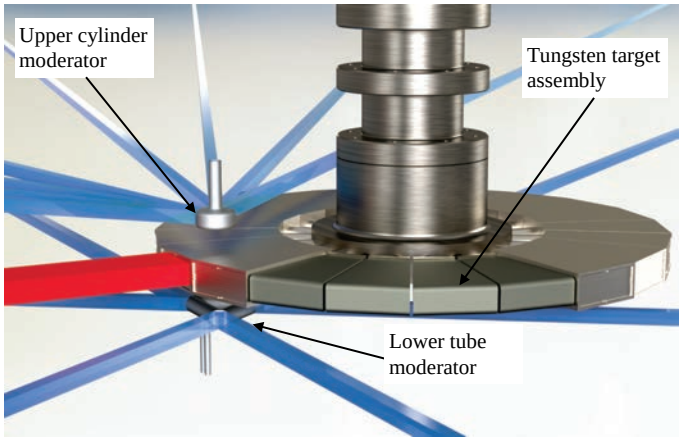

Figure 4.1. Rotating tungsten target and moderator configuration. The outer diameter of the target wheel is 1.1 m. The red beam illustrates the incident proton beam coming from the accelerator and the blue beams represent the outgoing neutron beams emitted from the two moderators. Neutron beam sizes are shown as 3 by 3 cm^2.

The spalled neutrons will then be moderated (reduced in energy) by a pair of compact moderators (30 mm tall), located above and below the target to optimize the production of high-brightness cold neutrons. Each moderator will contain hydrogen molecules that collide with neutrons and reduce their energy. They will be surrounded by 20 mm of light water that will act as a pre-moderator. The moderators will be operated at a temperature of 20 K and with high-purity para-hydrogen. These moderators will be four

times shorter than the 120 mm tall cold moderators at the FTS, resulting in much brighter beams of neutrons.

The top STS moderator will be a vertical cylinder (3 cm in height and 8.2 cm in diameter) that emits neutrons that will then enter guides to deliver neutrons to 16 instruments (for clarity, only 8 of the 16 emitted neutron beams/instrument paths are shown in Figure 4.1). This top moderator will have a narrower neutron pulse width for better neutron wavelength resolution. The bottom moderator will consist of three horizontal tubes (14–16 cm in length and three cm in diameter) that are connected to form a triangle; the neutrons will enter along the length of each tube and be restricted to focus the emitted neutron beam to serve six instruments. The bottom moderator will have the same peak brightness as the top moderator but produce somewhat broader neutron pulses with a correspondingly higher time-integrated brightness.

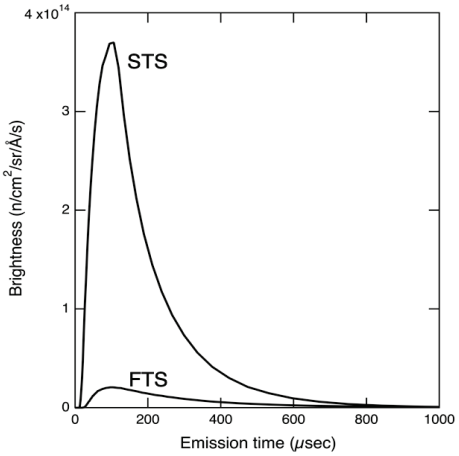

Figure 4.2. Pulse shapes emitted from FTS and STS cold, coupled moderators at a wavelength of 5 Å. Calculations are for STS operating at 15 Hz with 700 kW and FTS operating at 45 proton pulses per second and 2 MW.

Figure 4.2 shows the expected neutron brightness emitted from the STS coupled moderator design compared with its counterpart on FTS. The brightness of a beam of neutrons is defined as the number of neutrons of a certain wavelength (i.e., per Ångstrom) that pass through an area of 1 cm^2 in 1 s and that are traveling in a direction within a solid angle of 1 steradian (i.e., n/s·cm^{2}·Å·ster). Brightness differs from flux, which does not depend on the solid angle (divergence) of neutrons within the beam. For many experiments, brightness is a more important beam property than flux. However, higher brightness directly translates into higher neutron flux on the sample, which is the foundation for delivering the multiple orders of magnitude gains in instrument performance required to address the science challenges envisioned for STS.

In Figure 4.2, the height of the pulse shapes is the peak brightness, and the integral under the curve multiplied by the number of proton pulses per second (15 and 45 for STS and FTS, respectively) is the time-averaged brightness. Instrument performance scales with peak brightness if the width of the pulse is broad enough to deliver the wavelength resolution desired, which is true for most of the instruments envisioned for STS. That means that the higher the peak brightness, the better the performance of instruments at the STS. STS will provide beams of cold neutrons with the world's highest peak brightness.

4.1.2 Design Requirements

The primary design requirement of the target systems is the ability to convert the proton beam into cold neutrons directed toward 22 instrument guide ports. The following are the high-level design requirements:

- Accept 700 kW, 1.3 GeV, 15 Hz, proton beam.
- Convert to short high-intensity pulses of moderated neutrons.
- Distribute neutrons to 22 beamlines.
- Optimize performance for neutron scattering science.

- Allow for 5,000 h of operation per year and a lifetime of 40 years.
- Include a safe replacement scheme for all perishable components.
- Include a disposal path for all perishable components.
- Allow for 50 years of operation for remote handling equipment to accommodate decommissioning.
- Allow safe operation. Specifically, the design shall develop in conjunction with the facility safety analysis process to minimize and mitigate safety risk.

More detailed design requirements are listed in the following sections.

4.1.3 Target Building Configuration

The target and instrument complex at STS will be configured similarly to the FTS. To better clarify the functional uses of the spaces, the STS target and instrument areas are divided into four separate buildings, as shown in Figure 4.3. The Target Building is the central portion. The buildings directly north and south of the Target Building are the 50M Instrument Building and the 40M Instrument Building. The lengths indicate the approximate length of the longest instrument that could be located at the instrument port perpendicular to the proton beam. The 90M Instrument Building completes the target and instrument complex and houses the longest anticipated instruments. Section 8 includes more details and descriptions of the configuration and motivation for the three instrument buildings.

The central Target Building will house the target technical components and the necessary support systems. It will include three levels—basement, first floor, and high bay. Conventional Facilities, Section 8, describes the detailed layout of the building. This section highlights the technical components and areas most relevant to the target systems conceptual design.

1. The basement will include the technical utilities, maintenance areas, and other support areas.

2. The first floor will include the last section of the ring-to-STS, the target monolith, technical utilities, the service cell, and other support areas.

3. The high bay, or second floor, will house technical utility vaults.

Figure 4.4 shows an overhead view of the high bay with the building roof removed. To the west are the technical component utility (water cooling systems) cavities. In the center of the circular structure is the monolith, which will house the core of the Target Systems components. Surrounding the monolith are the instrument bunkers. The bunkers are described in detail in Section 5.3, Instrument Systems. The service cell is just east of the monolith. The Mock-up Test Stand (MUTS) sits adjacent to the truck bay on the east end of the building. MUTS will allow operations to conduct dry runs of critical remote handling maintenance activities. The MUTS is further described in Section 4.9.4.

Figure 4.5 shows a vertical cross section of the Target Building along the proton beam. To the west and above the ring-to-STS tunnel are the hydrogen utility room and helium compressor room, which house the majority of components for the cryogenic moderator system (CMS). Positioning the hydrogen utility room outside the main Target Building is inherently safe. This room includes specifically designed venting systems and blowout panels. Thus, failure of components in this area will not affect the general space within the Target Building. The proton beam can be seen leading to the monolith itself.

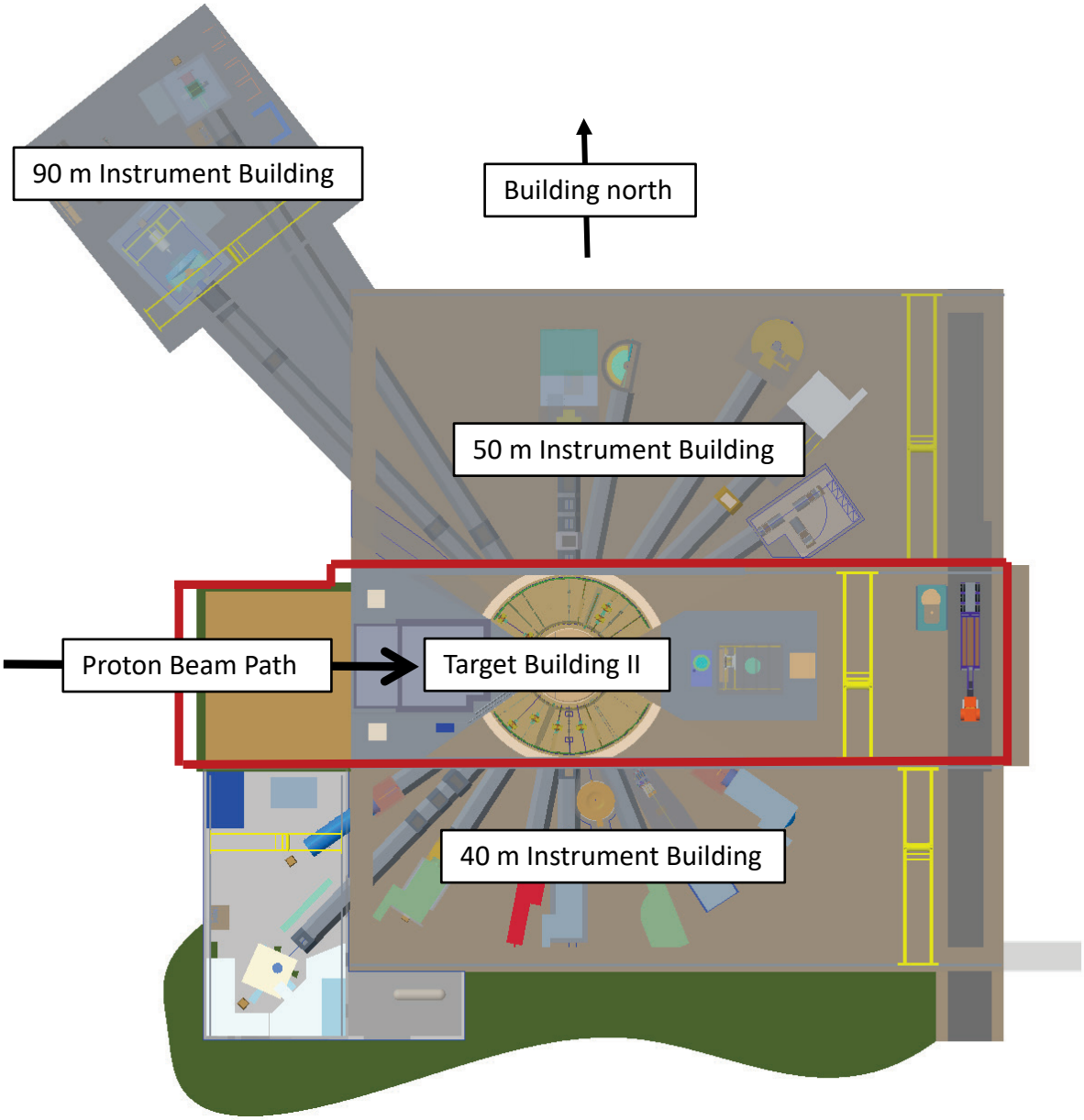

Figure 4.3. Target and instrument complex buildings.

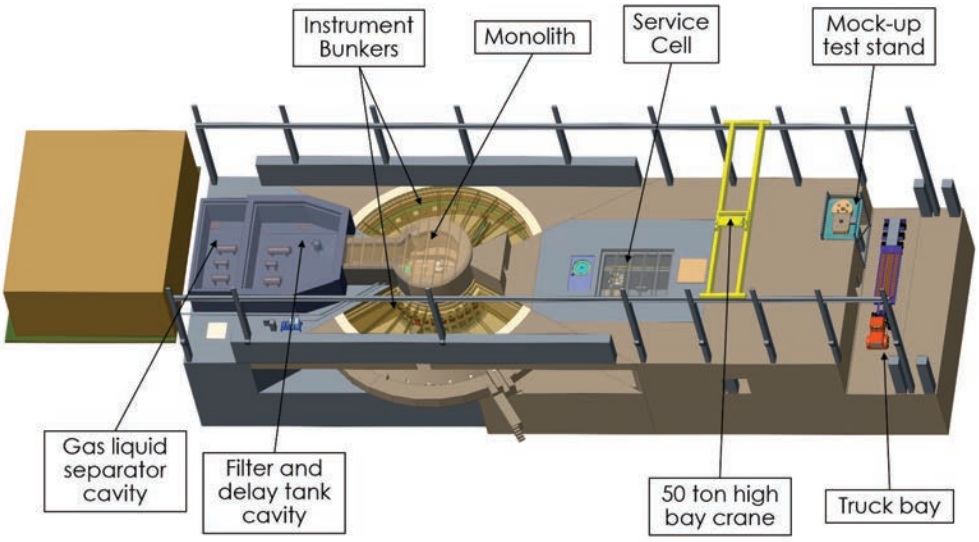

Figure 4.4. Overhead view of Target Building.

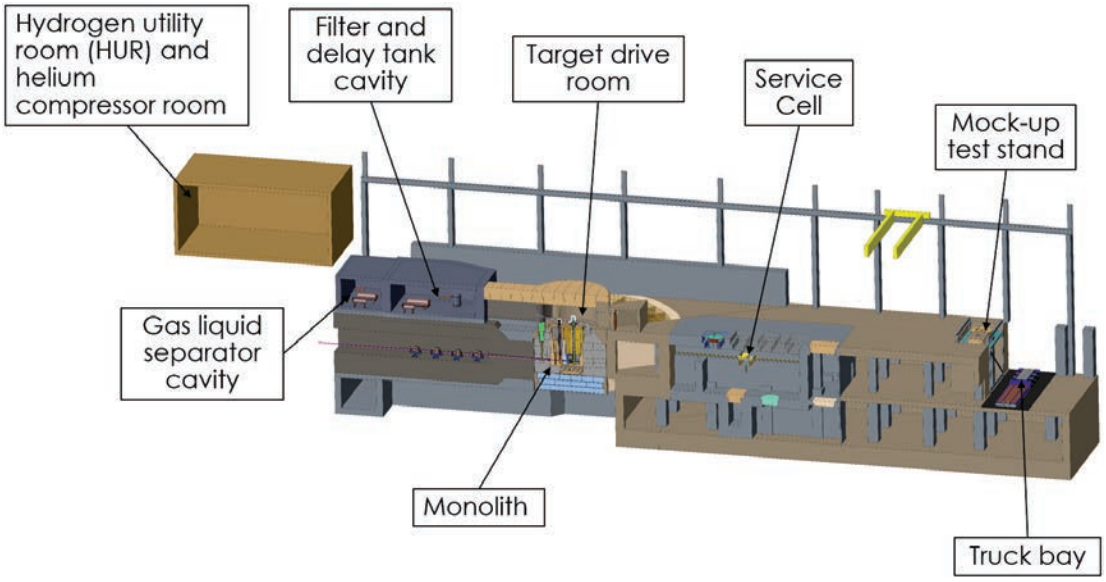

Figure 4.5. Vertical cross section showing Target Building layout.

4.1.4 Monolith Configuration

The target monolith (Figure 4.6) encloses the high-radiation area of the STS target facility. An 8.7 m diameter cylinder of iron shielding surrounded by a ~1.15 m thick, high-density concrete (HDC) wall will protect personnel and equipment. A core vessel in the center of the monolith will provide an inert atmosphere and enclose the functional target system components. The proton beam window (PBW) will separate the high-vacuum environment of the accelerator from the either low-vacuum or helium-backfilled atmosphere within the core vessel. The shielded target drive room above the monolith will provide access to the target drive and enable vertical handling of spent activated component assemblies. The 4.2 m height of the shielding between the target and the target bunker is based on the operating experience at FTS, where virtually no activation of components above the 4.2 m level has occurred after 14 years of operation. Eleven neutron beam lines will project through both sides of the monolith toward the instruments.

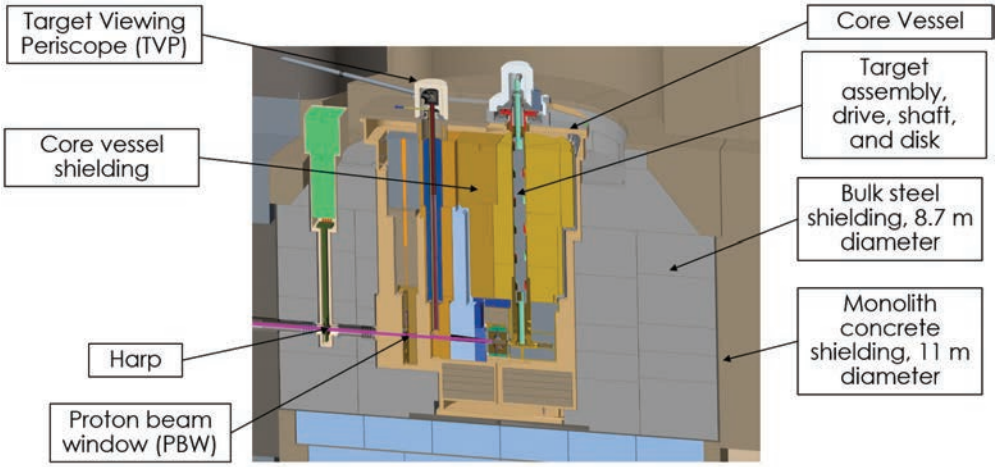

Figure 4.6. Monolith configuration.

4.1.5 Neutron Production Components

The STS will be optimized to produce high-brightness (relative to FTS and other spallation sources) pulsed beams of neutrons. The charge per pulse for STS will be the same as for FTS. Therefore, the increase in brightness (neutrons per unit of area per unit of time) will be achieved by reducing the sizes of the proton beam profile, the target material, and the moderators.

1. The STS nominal beam profile will be 48 mm tall by 130 mm wide, compared with 70 mm tall by 200 mm wide on FTS.

2. The STS target material will be 60 mm tall, compared with 98 mm at FTS. In addition, the shroud structure on FTS will be more compact, allowing the moderators to be closer to the target center.

3. The STS moderators will have a characteristic height of 30 mm, compared with 120 mm at FTS.

With these three items reduced in size, the neutron generation and resulting neutron beams will be more compact, resulting in higher brightness. In addition, STS will employ tungsten as the primary target material, which has a density of 19.3 g/cm^3 compared with the 13.6 g/cm^3 density of the FTS target mercury. Figure 4.7 shows the STS neutron production components on their own and provides a size comparison between FTS and STS.

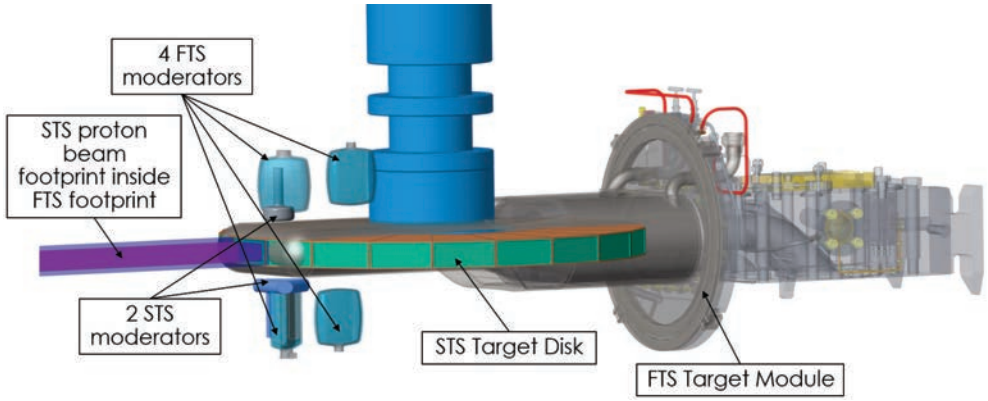

Figure 4.7. Overlay of STS target and moderator layout onto FTS target and moderator layout.

4.1.5.1 Target Assembly

The target itself will actually consist of 21 identical target segments arranged as a disk. The disk will rotate so that each subsequent proton beam pulse impacts the center of the next target segment. A target drive system will be located approximately 4 m above the target disk and will be connected to the target disk with a target drive shaft. The target drive shaft will also convey cooling water to and from the target disk. The complete target assembly is shown in Figure 4.8.

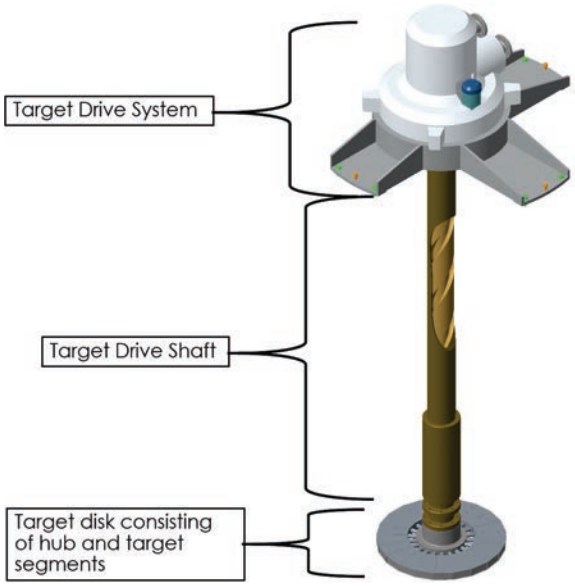

Figure 4.8. Target assembly.

Employing a rotating target provides benefits not provided by a fixed-position target. The beam energy is distributed over a larger volume of target material. This reduces the volume fraction of water cooling necessary in the neutron production zone, therefore increasing the neutron yield. In addition, the activation and residual heat is spread over the larger volume, reducing the maximum possible temperature during a loss-of-cooling accident and thus making the rotating target inherently safe, compared with a fixed target. Finally, since the target lifetime based on radiation damage to the stainless steel shroud structure, the nominal lifetime of a rotating target is increased from the order of 1 year to the order of 20 years. The choice of target configuration and material is discussed in detail in Section 4.3.2

4.1.5.2 Moderator Reflector Assembly

Because of the compact and coupled nature of the STS design, the moderators and reflector will be combined into a single assembly, as shown in Figure 4.9. The top moderator will be a 30 mm tall by 87 mm diameter cylinder. The bottom moderator will consist of three 30 mm diameter by ~150 mm deep tubes arranged in a triangle configuration. With the lower integrated power level of 700 KW on STS, the beryllium reflector can be edge cooled, further increasing the efficiency of neutron production.

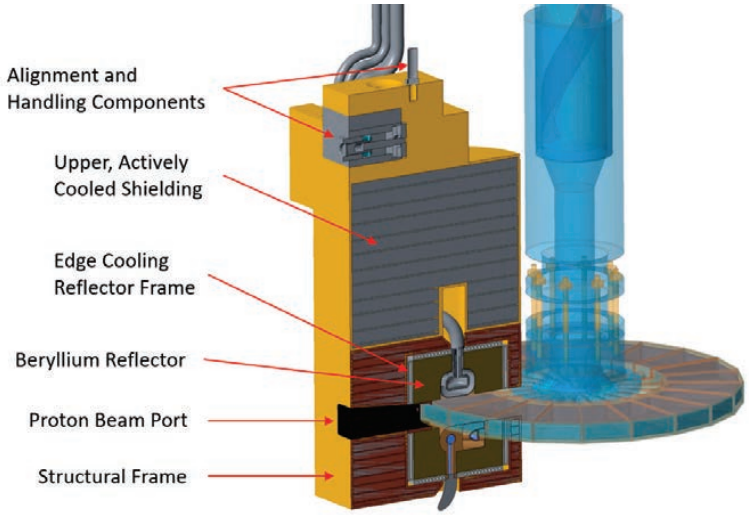

Figure 4.9. Moderator reflector assembly with target shown.

4.1.6 Physics Overview

4.1.6.1 Introduction

Production of neutrons in a spallation source starts with accelerating protons to high energy and directing the proton beam onto a target material, which is typically a high-Z material such as lead, mercury, or tungsten. Nuclear interactions of protons with target nuclei release dozens of neutrons with energies up to the energy of the impinging protons. The neutrons interact with a moderator material—typically a hydrogen or hydrogen-rich material at room or cryogenic temperature—and a reflector material, lose energy, and slow down. Thermal and cold neutrons with energies below ~0.1 eV and wavelengths of ~1Å and longer are directed toward instruments that provide a variety of capabilities to researchers across a broad range of disciplines, including physics, chemistry, biology, and materials science.

The existing neutron sources at ORNL, the High Flux Isotope Reactor (HFIR), and SNS, deliver outstanding performance for neutron science. HFIR produces neutron beams with high time-averaged cold neutron brightness, is comparable to the world's best reactor-based neutron sources, and is within a factor of 3 of the predicted performance of the European Spallation Source (ESS) currently under construction in Lund, Sweden. FTS excels in high neutron wavelength resolution provided by poisoned, decoupled moderators that produce very sharp in-time neutron pulses. The design objective for STS is to deliver cold neutrons with the highest peak brightness of any current or proposed neutron sources, and to use a low pulse repetition rate to provide wide dynamic range.

4.1.6.2 Scope of the Neutronics Analyses

"Neutronics analyses" for a spallation neutron source is a catch-all term that includes simulations of the physics of the proton beam interactions with target material and other structures, generation of secondary particles (e.g., neutrons, protons, photons) and simulations of their interactions with materials and structures. Neutronics analyses evaluate the impacts of design choices on STS performance: proton beam size and profile, target, moderators, and reflector material choices and configurations. Neutronics analyses also provide detailed information needed for engineering design, such as heating rates in and around the target during operation; radiation levels and shielding requirements; radiation damage in components and component lifetime estimates; and activation levels, decay heat, and radiation levels for planning the post-operation handling, maintenance, and disposal of components. A particularly important task of neutronics analyses is to evaluate moderators' parameters and optimize moderators for the performance required by science, such as peak and time-integrated moderator brightness and pulse shapes. In short, neutronics analyses provide input to, support, or guide most of the other STS design tasks.

4.1.6.3 Neutronics Analyses Tools

Traditional tools such as MCNPX and CINDER-90 which were used extensively for the FTS analysis are also being used for the STS design. Simulations of radiation transport were performed mostly with MCNPX versions 2.6 and 2.7 [Pelowitz 2008, Pelowitz 2011], with enhancements added by the SNS neutronics team, such as neutron mirrors [Gallmeier et al. 2009] and residual nuclides tally [Gallmeier et al. 2010b]. The activation calculations were performed mostly with the CINDER-90 code [Wilson et al. 2008]. CINDER 2008 [Popoval 2018] is the latest release in the CINDER data and code development effort and is a modern implementation of the CINDER-90 software package for activation calculations.

The "Gamma Source Perl Script" [Wohlmuther and Gallmeier 2008] was extensively used for post-processing of activation results and preparation of decay gamma-ray sources for MCNPX calculation of residual radiation fields.

More recent additions to the neutronics analyses tools include MCNP 6.1, DAGMC (Direct Accelerated Geometry Monte Carlo) [Tautges et al. 2009], SpaceClaim, Cubit, CINDER2008, and ADVANTG. The radiation transport code MCNP 6.1 [Pelowitz 2013], is a result of the merger of the MCNP5 and MCNPX codes. ADVANTG [Mosher et al. 2015] generates problem-specific space- and energy-dependent mesh-based weight-windows that provide efficient variance reduction in the radiation transport calculations with MCNPX.

The DAGMC toolkit, which requires the use of SpaceClaim and Cubit, is a toolkit implemented in MCNP 6.1. It is developed at the University of Wisconsin–Madison by a group headed by Paul Wilson. A workflow of the analysis with DAGMC is illustrated in Figure 4.10. DAGMC allows "automatic" conversion of engineering CAD models into MCNP models for neutronics analyses, which are performed with MCNP6.1 The process starts with the engineering CAD model generated in CREO, which is the CAD software used for STS design. This model is processed through SpaceClaim [ANSYS n.d.] and Cubit [SNL n.d.] to produce the MCNP model. In principle, the conversion could be automatic, with little human intervention. However, our experience is that complex target models always require iterations to produce functional MCNP models. The conversion produces "high fidelity" MCNP models, which closely match the engineering models, as illustrated in Figure 4.11.

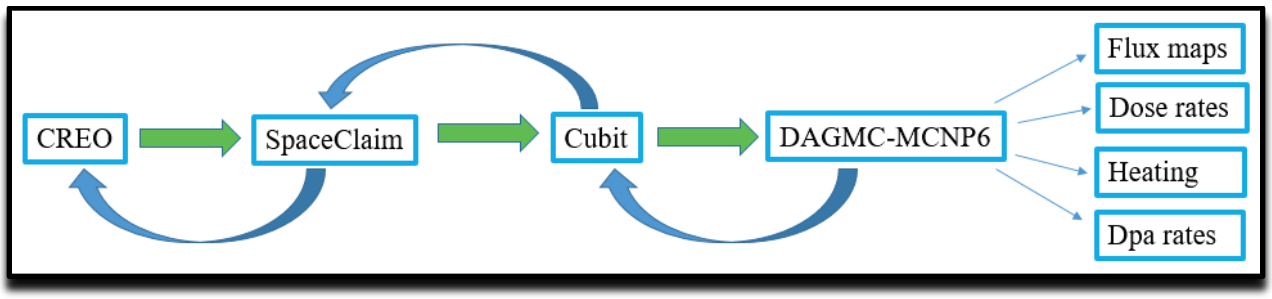

Figure 4.10. Workflow of DAGMC neutronics analysis.

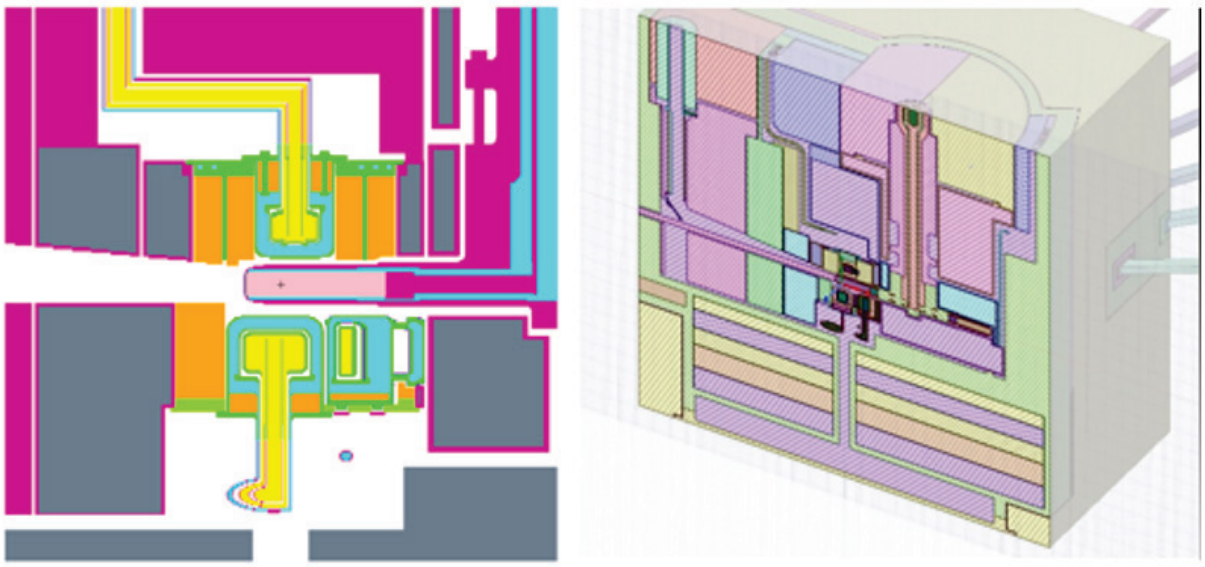

Figure 4.11. Section through the STS model in CREO (on the right side) and the model for neutronics analysis obtained with the DAGMC toolkit.

4.1.6.4 STS Target and Moderator Physics Concepts

Conceptual planning and investigation of the possible configurations for the STS started in 2002 [Carpenter and Mason 2002] and continued, albeit with interruptions and varying levels of intensity, to the present time [Herwig and Rennich 2017]. The pros and cons of operating the STS with short (~ 1 μs) and long (~ 1 ms) proton pulses were considered [Carpenter and Mason 2002, ORNL 2007, Gallmeier 2010a]. Different target materials and configurations were also investigated: a liquid mercury target, which would benefit from experience with the SNS FTS [Riemer et al. 2013]; a stationary target with tungsten plates [Galambos 2015] [Remec et al. 2015], similar to the FTS at ISIS [Broom 1995] and also planned for the Chinese Spallation Neutron Source [Wei et al. 2009]; and a water-cooled rotating tungsten target [McManamy et al. 2010, [Remec et al. 2018].

To fulfill the requirement to produce cold neutron beams with the highest peak brightness of any current or proposed neutron sources, and with the benefit of accumulated SNS experience and previous studies, the following design choices for the STS were made. Tungsten was selected as the target material. Tungsten has higher density than mercury and enables the creation of a more compact neutron production volume. For the same reason, a proton beam footprint as small as possible is required. However, a small beam footprint results in high energy deposition density during the short proton beam pulse and induces high stresses. To keep the stresses at acceptable levels it was necessary to increase the beam footprint from the originally targeted 30 cm^2 to ~ 60 cm^2. The target will be cooled with water flow on the top and bottom of the tantalum-clad tungsten plate; there are no cooling channels inside the target plate, so the high density will be maintained.

Moderators will be placed as close as possible to the high-intensity neutron production zone to obtain tight coupling and high neutron flux in the moderators. A relatively high proton beam power of 700 kW and high energy deposition in the moderator material constrain the selection of the moderator material to liquid hydrogen. Several studies were performed on hydrogen moderators at spallation sources [Russell et al. 2003, Kiyanagi 2006, Harada et al. 2007, Ooi et al. 2003, Kai et al. 2006, Lu et al. 2011, Gallmeier et al. 2016, Remec et al. 2015] that led us to adopt para-hydrogen as the cryogenic moderator material, with water as pre-moderator and a beryllium reflector. The studies also showed that moderators with smaller viewed areas produce significantly higher peak brightness. In addition, neutron scattering experiments show a trend to use increasingly smaller samples, which require a smaller beam footprints and allow smaller moderator viewed areas. A recent study by Gallmeier [2018] showed that a moderator with para-hydrogen in tubes arranged in a triangle and viewed at the corners in the direction along the tubes—a configuration nicknamed “tube moderator”—provides peak brightness equivalent to that of a cylindrical moderator. At the same time, it generates longer pulses and hence higher time-integrated brightness, which can benefit certain instruments. The current configuration of the STS moderators consists of one cylindrical moderator with four 30 by 30 mm^2 viewed areas, which will serve 16 beamlines; and 1 tube moderator with a para-hydrogen tube diameter of 30 mm, which will serve 6 beamlines. The present configuration of STS moderators, which is at the conceptual design level, will provide peak brightness about 25 times higher and time-integrated brightness 4 to 5 times higher than the brightness of the FTS coupled hydrogen moderator; those values are for the FTS as it operates currently—at 1.4 MW, 60 Hz, and proton energy of 1 GeV. The STS moderator brightness increase will be achieved via a more compact proton beam footprint and smaller moderators and viewed areas; however, it also will be due in part to the different FTS design requirements, which gave preference to decoupled moderators and an ortho-para-hydrogen mixture, rather than pure para-hydrogen.

Table 4.1 provides a short list of key FTS and STS parameters. Both targets are driven by short proton pulses, less than 1 μs long, with proton kinetic energy of 1.3 GeV. The energy delivered per pulse is also quite similar: 44.4 kJ per pulse for FTS and 46.7 kJ per pulse for STS. The repetition rate will be 45 pulses per second for the FTS and only 15 pulses per second for the STS. Consequently, the total proton

beam power delivered to the target will be 2 MW for FTS and 700 kW for STS. The FTS neutron producing material is liquid mercury, while for the STS it is tungsten. The proton beam footprint is ~140 cm^2 for the FTS and ~60 cm^2.

Additional selected STS target parameters are listed in Table 4.2; more details are provided in Section 4.3, Target Assemblies.

Table 4.1. Comparison of key parameters for the FTS and STS

FTS (upgraded)	STS
Short (<1 μs) proton pulses	Short (<1 μs) proton pulses
1.3 GeV protons	1.3 GeV protons
45 pulses/second	15 pulses/second
2 MW beam power	700 kW beam power
44.4 kJ per proton pulse	46.7 kJ per proton pulse
Large beam footprint: ~140 cm2	Smaller beam footprint: ~60 cm^2 (90% of the beam)
Mercury target (stationary steel shroud, water cooled)	Tungsten target (steel shroud, water cooled, rotating, segmented, synchronous)

Table 4.2. Selected STS target parameters

Target type	Rotating, synchronous
Rotational speed	1 turn in1.4 s
Number of segments	21
Target material	Tungsten
Tungsten width	163.7 mm
Tungsten height	58 mm
Tungsten length	250 mm
Clad material	Tantalum
Clad thickness	1 mm
Disk diameter	1156 mm
Shroud material	316L SS
Cooling	H_20

4.1.6.5 STS Target, Moderators, and Reflector Neutronics Models

The STS models used for the conceptual design neutronics studies are illustrated in Figures 4.12 to 4.15 Neutronics simulations were performed with STS “physics” models, which capture the STS design features important for the performance but do not try to model all details of the engineering design.

Figure 4.12 shows a horizontal section through the STS target disk midplane. Scales on the edges show dimensions in centimeters. Figure 4.13 depicts a vertical section through the STS model along the proton beam direction. Figure 4.14 shows a model of the target disk, shaft, cylindrical moderator and tube moderator with beryllium reflector, and neutron beam extraction channels. Figure 4.15 shows a model of the STS target with the moderators, beryllium reflector, and surrounding steel shielding. The inner part of the steel shielding, closer to the moderators, is cooled with heavy water, whereas the outer part of the steel shield is cooled with H_2O. In the model, the steel and coolant are homogenized.

Material specifications used neutron cross sections from ENDF/B-VI [McLane 1996] and ENDF/B-VII [Chadwick 2006]. Neutron scattering kernels for ambient temperature water, liquid para-hydrogen at 20 K temperature, and beryllium were taken from ENDF/B-VII.

Point detectors at 10 m from the moderators' viewed areas were implemented in the models to tally time- and energy-dependent neutron fluxes. Collimators were applied to ensure that only neutrons passing through viewed areas of the moderators contributed to the point detector tallies. Point detector neutron fluxes were used to determine moderator characteristics such as peak and time-integrated brightness and pulse shapes.

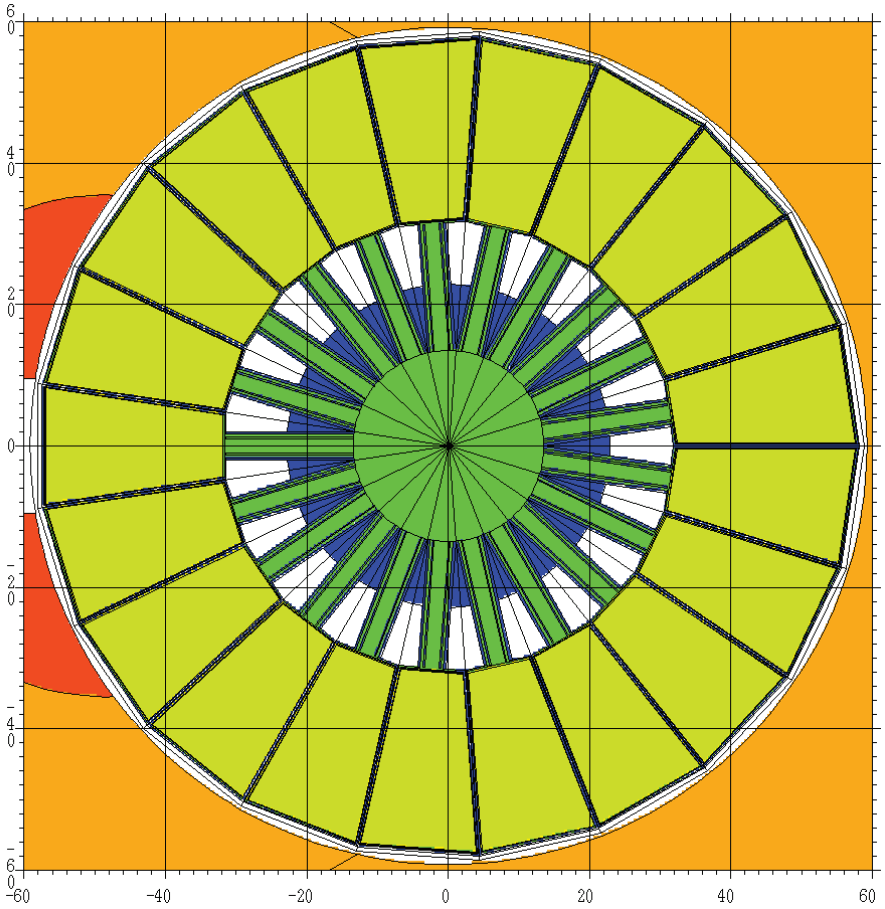

Figure 4.12. Horizontal section through the target disk midplane. Colors indicate materials: tungsten is light green, water is green, steel is blue, steel shielding is orange.

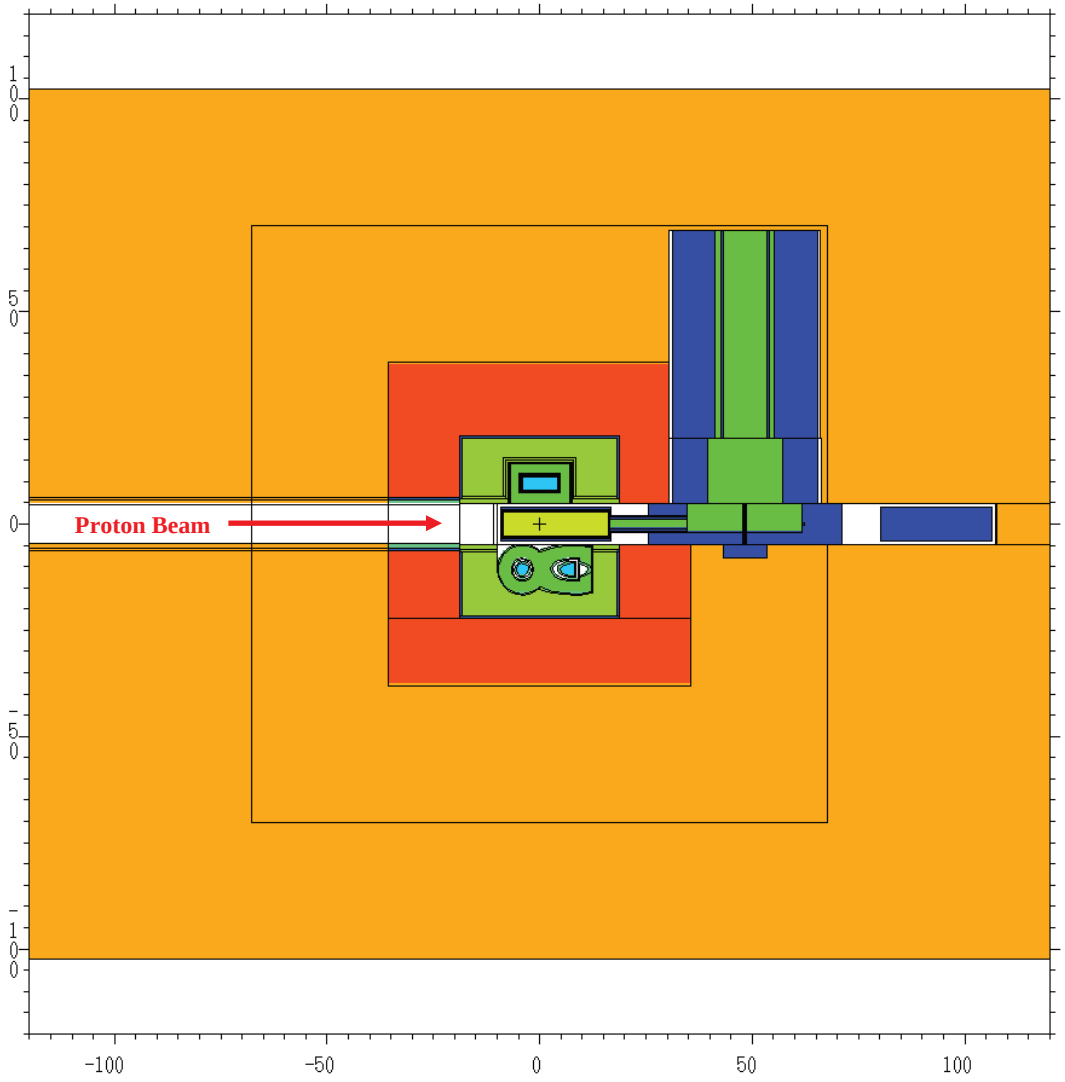

Figure 4.13. Vertical section through the STS model along the proton beam direction. Colors indicate materials: tungsten is light green, water is green, steel is blue, steel shielding is orange.

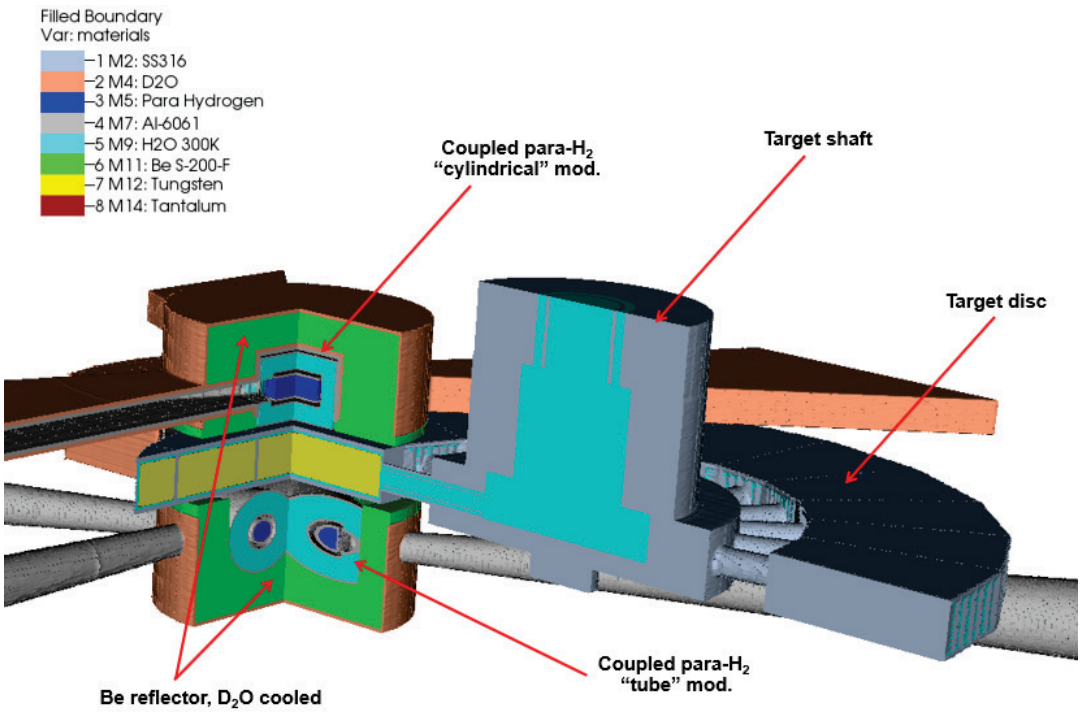

Figure 4.14. Shows model of the target disk, shaft, cylindrical moderator, and tube moderator with beryllium reflector and neutron beam extraction channels. A cutout through the target along the proton beam direction and another cutout at the center of the moderators perpendicular to the proton beam shows the structure inside. The steel shielding that surrounds the target is not shown.

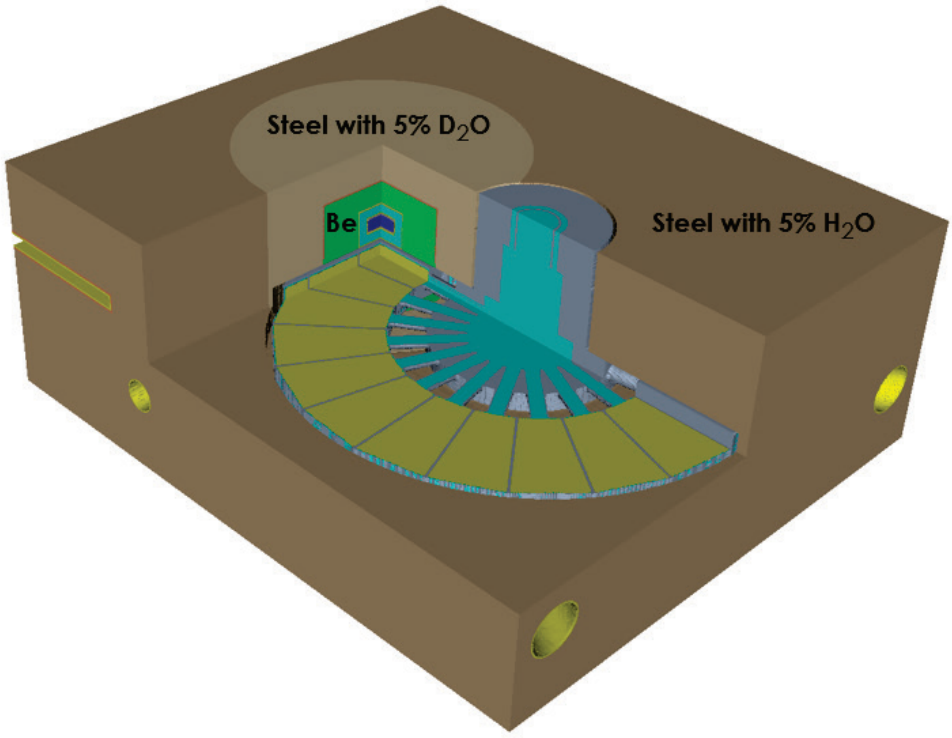

Figure 4.15. Model of the STS target with the moderators, beryllium reflector, and surrounding steel shielding.

4.1.6.6 Effect of Coolant: Heavy Water versus Water

The STS assemblies—target disk, target shaft, moderators, beryllium reflector, steel reflector, and PBW—receive intense heating from the 700 kW proton beam and secondary radiation emitted from the target material and thus require cooling. Using heavy water (D_2O) with lower neutron absorption is typically preferred to improve neutronics performance; however, using ordinary water (H_2O) significantly reduces the cost of operation. Therefore, it is necessary to evaluate the benefit obtained by using D_2O to cool a specific assembly.

Starting from a baseline configuration, shown in Figure 4.16, the coolant was changed to evaluate the impact. In the baseline configuration, all assemblies are D_2O cooled except the PBW (which is cooled by a homogeneous mixture of 76% Al, 24% by vol. H_2O) and the outer part of the stainless steel reflector (which is cooled by a homogeneous mixture of 95% SS-316 and 5% H_2O) , The configuration analyzed and the observed changes are summarized in Table 4.3.

There is no difference in the moderator performance if the PBW is cooled with H_2O or D_2O. Changing the target coolant from D_2O to H_2O reduced both the peak and time integrated brightness of both moderators by ~ 2%. When both the target and inner steel reflector are cooled with H_2O, the peak and time integrated brightness of both moderators decrease by ~ 5%. The largest effect is observed when the coolant of the inner steel reflector is changed to H_2O, coolant on the edge of Be is also changed to H_2O, the beryllium reflector is beryllium only (with no coolant homogenized in it), and the extraction channels of the cylindrical moderator are also H_2O cooled. In this case the peak brightness decreases by 5%-8% for the tube moderator and 5%-13% for the cylindrical moderator. The time-integrated brightness of the tube moderator decreases by 5%-8%, while the time-integrated brightness of the cylindrical moderator increases by 2% for the neutron energies below 20 meV and deceases by ~ 15% above ~100 meV.

Based on these results it was decided to cool the beryllium and inner steel reflector with D_2O and all the other assemblies with H_2O. The analyses of the effect of H_2O and D_2O, described in this section, were done with synchronous rotating target model (which predates the current design) and the proton beam footprint of ~ 44 cm^2, which was smaller than the current footprint of ~ 62.4 cm^2. Therefore; it is expected that these analyses will be repeated in the later stages of the STS design.

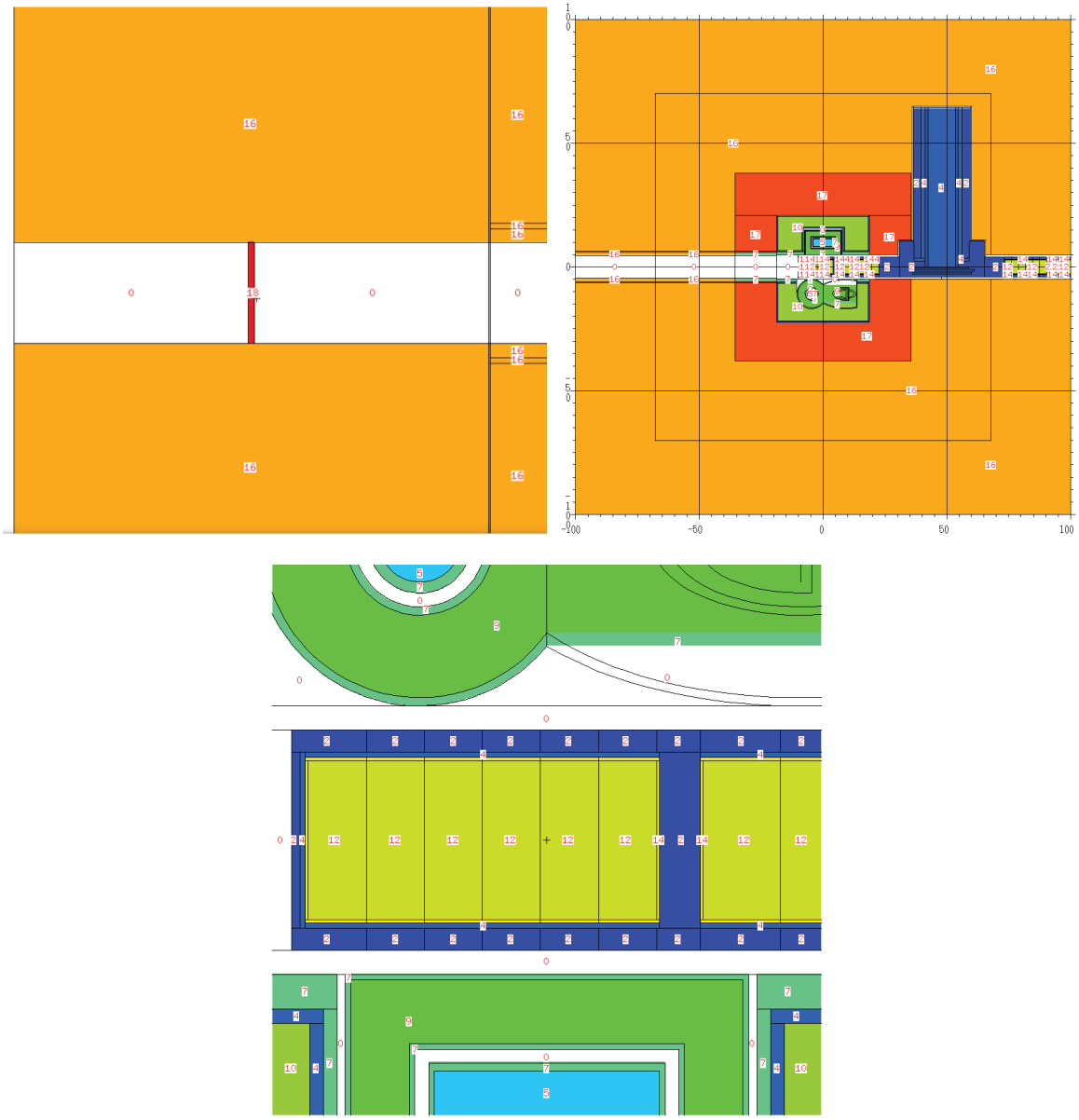

Figure 4.16. Details of the baseline model: top left—target, moderators, inner (dark orange) and outer (light orange) steel reflector; top right: PBW and steel reflector, bottom: detail of the target disk, moderators, and beryllium reflector. The numbers indicate materials: M4= D_2O; M7 = Al-6061; M9 = H_2O; M10 = Be with 2 % by vol D_2O; M16 = 95% SS-316 and 5% H_2O by volume; M17 = 95% SS-316 and 5% D_2O by volume; M18 = 76% Al-6061 and 24% H_2O (by volume).

Table 4.3. Effect of assemblies' coolant selection (D_2O or H_2O) on performance of the moderators.

Configuration	Description	Effect on moderator performance
Baseline	All assemblies are D_2O cooled, except the PBW (76% Al, 24% by vol. H_2O) and outer part of the stainless steel reflector (95% SS-316 and 5% H_2O). Be reflector contains 2% by volume D_2O.	
Target: H_2O	As baseline, but the target coolant will be H_2O	~ 2 % lower peak and time-integrated brightness for both the cylindrical and the tube moderator
Target-PBW-reflector: H_2O	Target and inner and outer reflector are water cooled (95% SS-316 and 5% H_2O), PBW is water cooled, Be reflector contains 2% by volume D_2O and is D_2O cooled. Extraction channels of the cylindrical moderator are also D_2O cooled.	~ 4 to 5 % lower peak and time-integrated brightness for both the cylindrical and the tube moderator
Reflector: H_2O	As baseline, but inner part of the steel reflector is H_2O cooled, coolant on the edge of Be is H_2O, and Be reflector is Be only. Extraction channels of the cylindrical moderator are also H_2O cooled.	Peak brightness decrease: • Tube mod. 5–8%, Cylindrical mod. 5–13% Tint brightness: • Tube mod decrease by 5–8%, • Cylindrical mod. increase by 2% below 20 meV, decease by ~ 15% above ~100 meV Full width at half maximum: increase for cylindrical moderator, no effect for tube moderator
Target-PBW: D_2O	The same as reflector, H_2O, but PBW is D_2O cooled (76% Al, 24% by vol. D_2O)	Changing PBW coolant from D_2O to H_2O has negligible effect on the moderator performance.

4.1.6.7 Radiation-induced Damage and Component Lifetime

Radiation-induced damage to the material causes degradation of material properties, such as mechanical strength, loss of ductility, and decreased thermal conductivity, and may limit the lifetimes of certain components of the STS. For steel, the established lifetime limit is 12 dpa (displacements per atom). For the aluminum components, the lifetime limit is either 40 dpa or a radiation-induced helium concentration of 2000 appm, whichever is reached first. For tungsten, there is no clearly established lifetime limit; but it is known that thermal conductivity decreases with increasing dpa, and this needs to be taken into account in the target design.

For these reasons, neutronics analyses were performed to calculate the atom displacement rates and helium production rates in different STS structures. Such analysis typically consists of calculating neutron and proton fluxes inside the structure of interest and folding the fluxes with the dpa or helium-production cross sections. Usually, a spatial mesh is applied to subdivide the structure and obtain a distribution of the dpa and/or helium production inside the structure.

The front part of the target shroud, through which the proton beam enters the target, is usually referred to as the "target window." At the STS, each of the 21 segments will have a target window consisting of a stainless steel plate about 160×60×2 mm (width × height × thickness). The distribution of neutron- and proton induced atom displacements in the target window is shown in Figure 4.17. The peak neutron-induced dpa rate is 0.2687 dpa/year and the peak proton-induced dpa rate is 0.1754 dpa/year, so the

combined total (neutron + proton) dpa rate is 0.444 dpa per year. The lifetime limit of 12 dpa is reached in approximately 27 years of operation. It is assumed that the target is operated in synchronization with the proton beam pulses, so that consecutive proton pulses hit the centers of the adjacent target segments, at full proton beam power of 700 kW for 5000 h per year. For comparison, for the stationary target operating at 700 KW, with a beam footprint about two times smaller, the lifetime is estimated to be only 0.7 years. For a rotating target operated in asynchronous mode, the location of the peak proton beam intensity would sweep the circumference of the target uniformly, thus spreading out the maximum damage over a larger surface and reaching the lifetime limit of 12 dpa in in an estimated ~51 years.

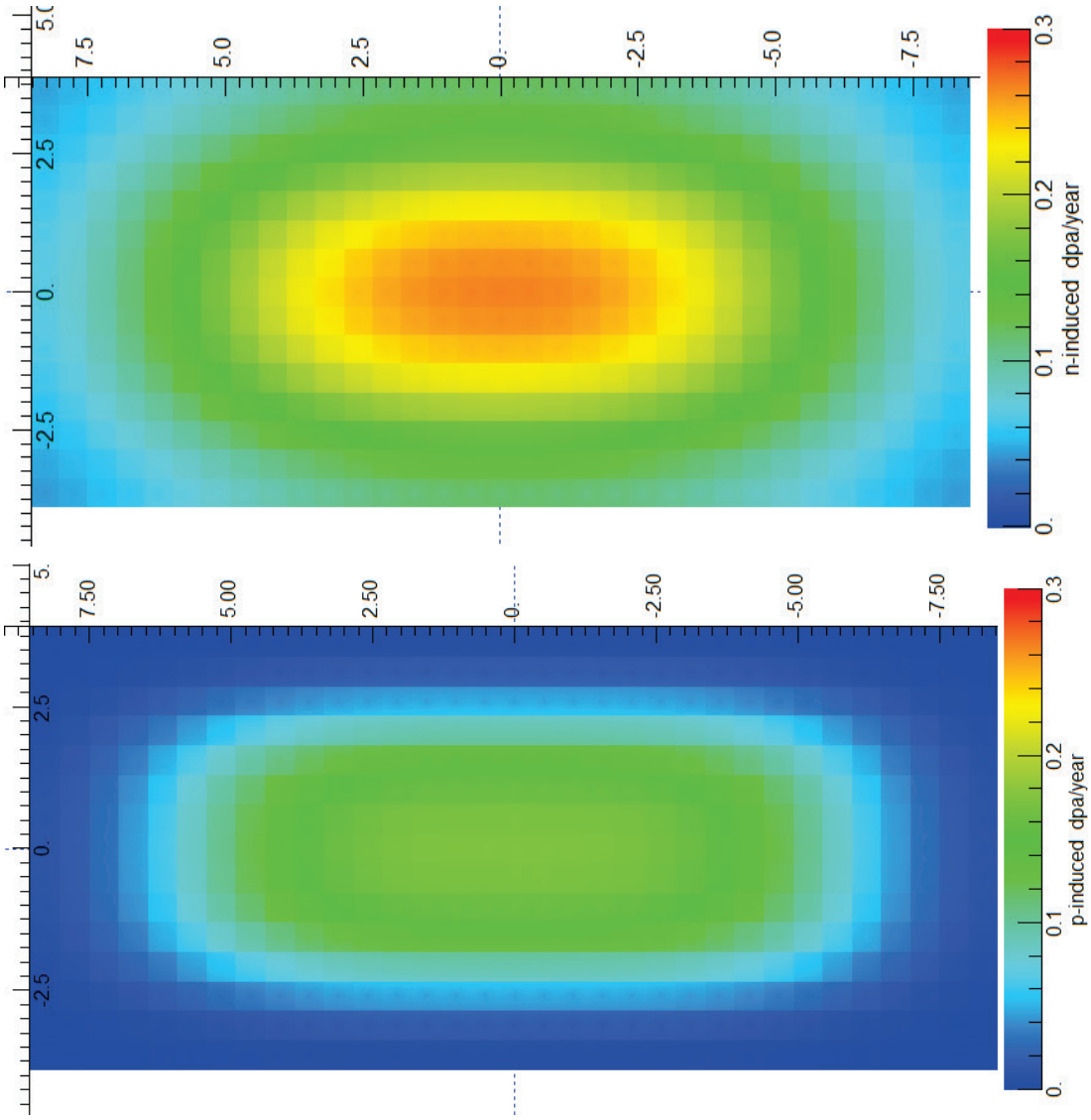

Figure 4.17. Distribution of neutron- (top) and proton-induced dpa rate in the target window.

The PBW is a water-cooled aluminum window that is located upstream of the target and separates the high vacuum of the proton beam guide from the rough vacuum or helium atmosphere of the core vessel. In the current neutronics STS model, the PBW is a 5.1 mm thick plate consisting of a homogeneous mixture of 76% Al 24% by vol. H_2O. Total helium production rate in PBW is ~ 616 appm/y; proton reactions contribute 609.5 appm/y while neutron reactions contribute only 7.75 appm/y. The 2000 appm limit is reached in 3.2 years of operation. The combined proton- and neutron-induced dpa rate is only 1.07

dpa/year and would allow operation for 37 years. The PBW lifetime is therefore limited by the helium production and is estimated to be 3.2 years. A map of the helium production in the PBW is shown in Figure 4.18.

Damage in the aluminum shell of the moderators was calculated with the mesh tally in the bottom plate of the cylindrical moderator, as shown in Figure 4.19. The highest neutron-induced dpa rate is 5.24 dpa/year, while the proton induced dpa rate is only 0.034 dpa/year. The lifetime limit of 40 dpa is reached in 7.6 years. The helium production rate is ~68 appm/year, which would allow the operation of the moderators for ~29 years.

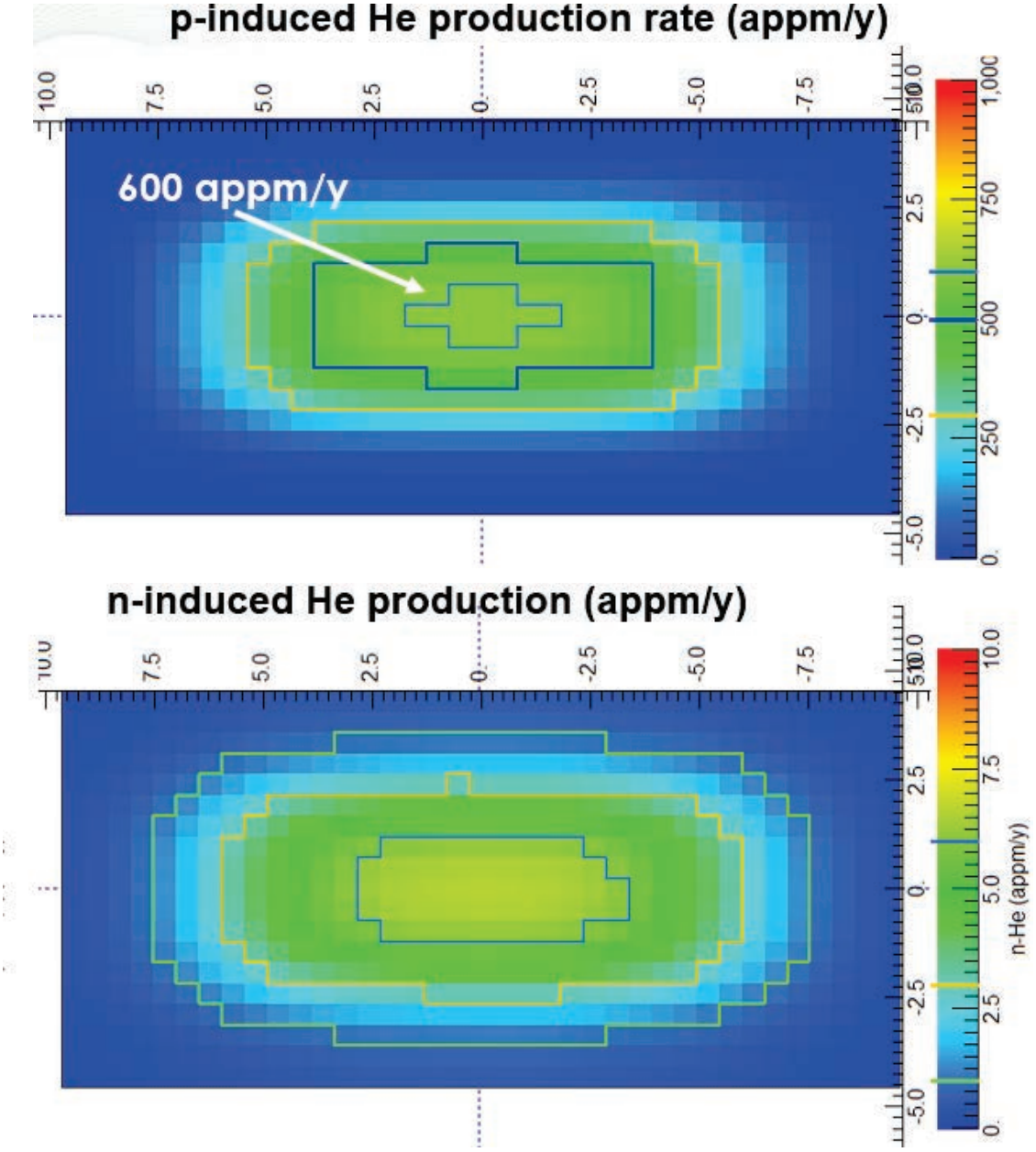

Figure 4.18. A map of the helium production in the PBW, proton-induced (top) and neutron-induced (bottom) helium production rate. STS operation with 700 kW proton beam power for 5000 h per year is assumed.

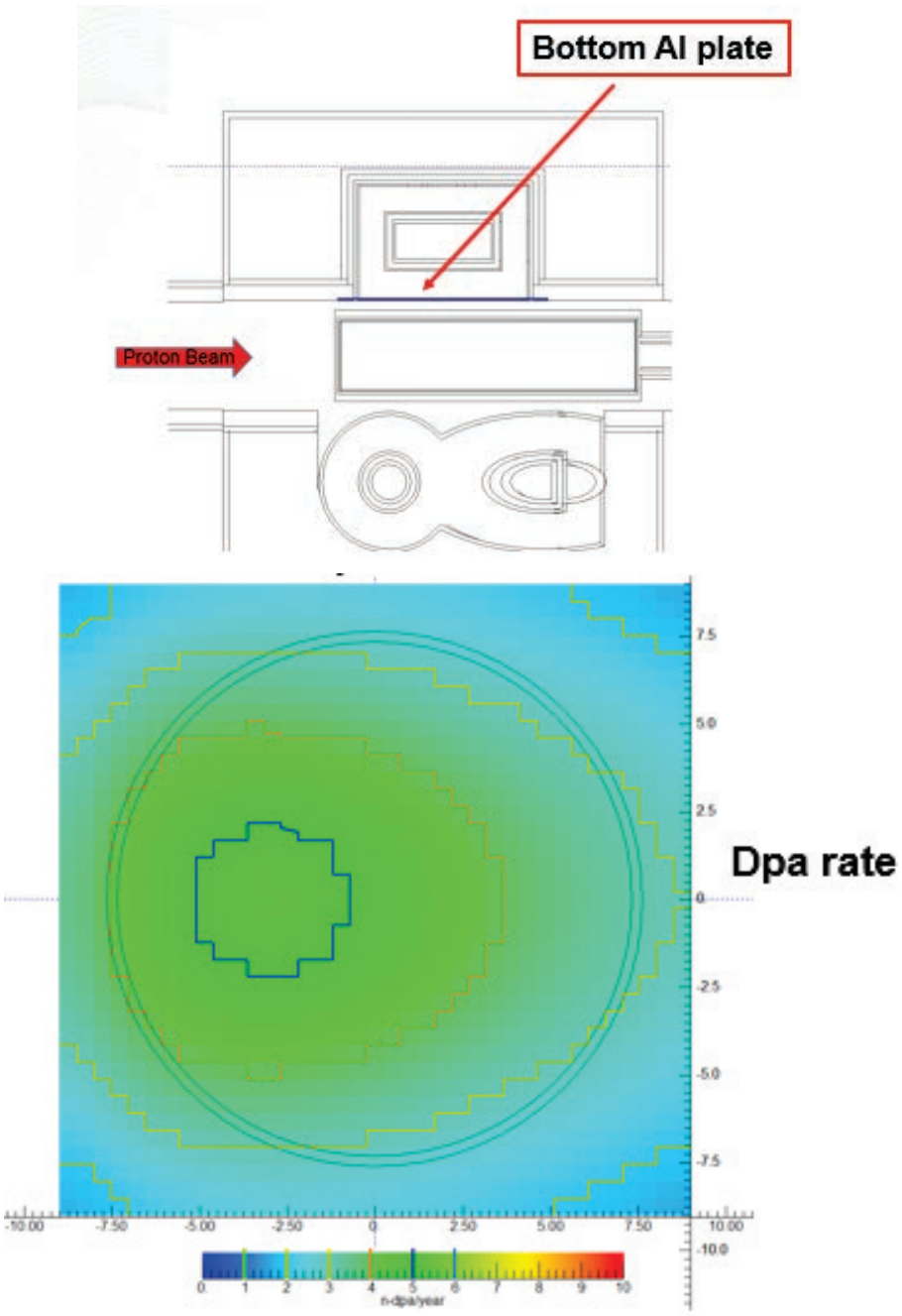

Figure 4.19. Radiation damage in the aluminum shell of the cylindrical moderator. Top: the location of the mesh tally is shown; bottom: map of the total neutron dpa rate. The scales on the side of the dpa rate map are dimensions in centimeter.

Steel shielding surrounding the target, moderators, and reflector also accumulates radiation damage. A map of the dpa rate in steel is shown in Figure 4.20. The dpa values shown are valid only in the steel stationary structures. The blue contour line bounds the volume within which the radiation damage in steel exceeds 12 dpa in 27 years of operation. The two red arrows point to the relatively small volumes of steel shielding that may need to be replaced before the facility end of life.

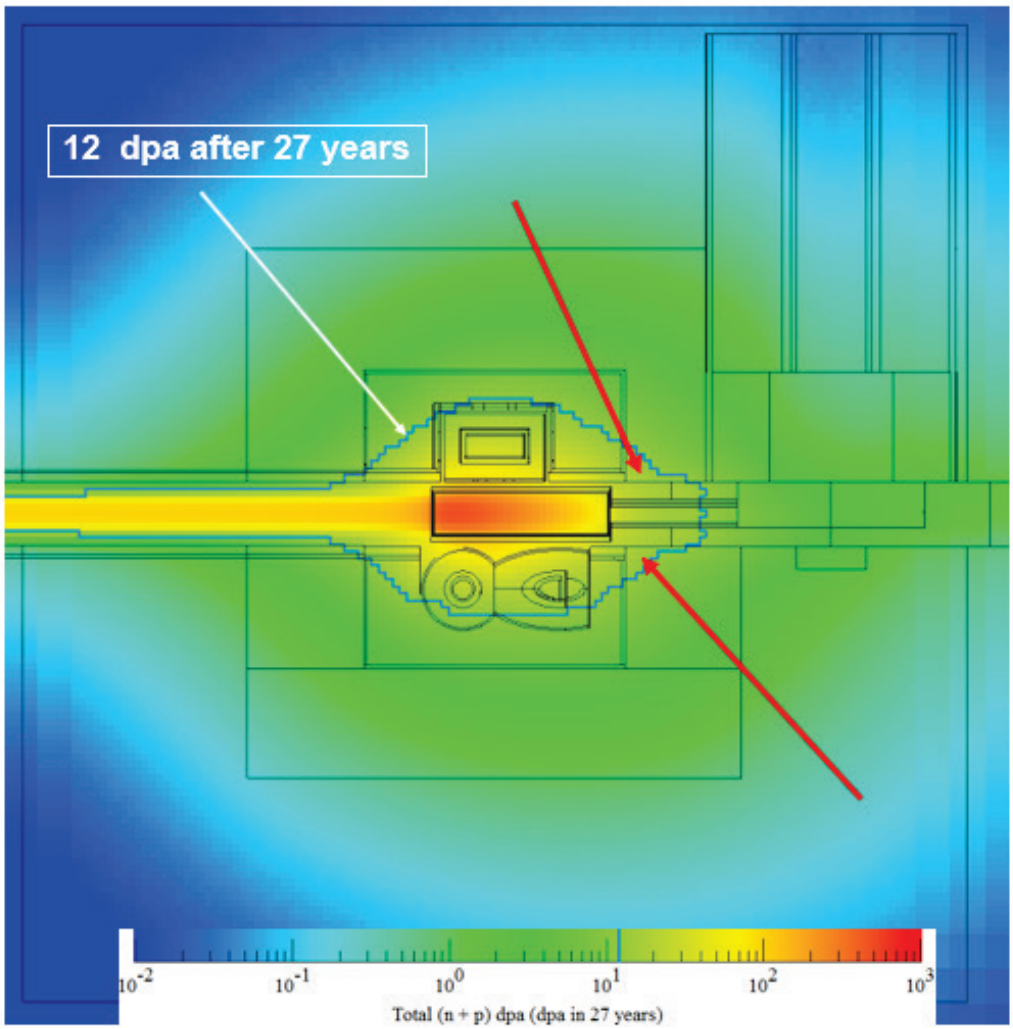

Figure 4.20. A map of the dpa in steel around the target. The dpa values shown are valid only in the steel stationary structures. The blue contour line bounds the volume within which the radiation damage exceeds 12 dpa in 27 years of operation. The two red arrows point to the parts of the steel shielding that may need to be replaced before the facility end of life is reached.

The map of the dpa in tungsten plate is shown in Figure 4.21. The highest dpa rate in tungsten is ~0.750 dpa/year. In 27 years of operation, the highest dpa in tungsten plate reaches 20.2 dpa. The regions that exceed 5, 10, 15, and 20 dpa in 27 years are shown in Figure 4.21. While there is no established lifetime dpa limit for tungsten, this information may be used to estimate the decrease in thermal conductivity in tungsten and may affect the cooling requirements for the target.

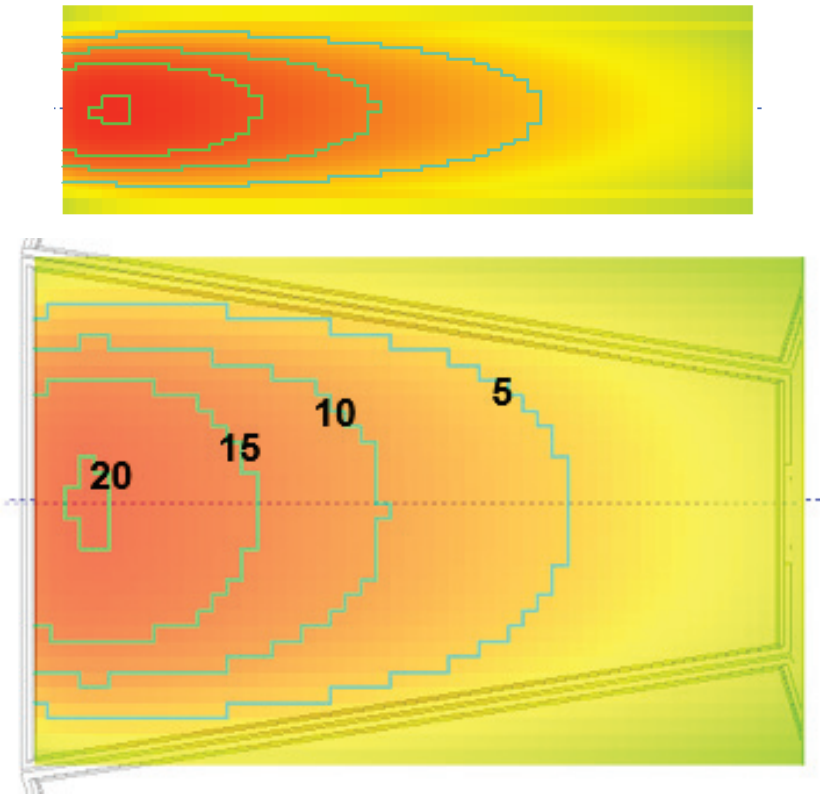

Figure 4.21. Distribution of the dpa in tungsten plate after 27 years of operation at 700 kW for 500 h per year. Vertical (top) and horizontal (bottom) cuts through the tungsten plate centerline are shown. The contours bound the volumes that exceed 5, 10, 15, and 20 dpa in 27 years of operation at 700 kW, for 5000 h/year.

A summary of the radiation damage rates and estimated lifetimes for selected STS components is given in Table 4.4. For comparison, the values are also listed for the stationary target and asynchronous rotating target. Two proton beam footprints are also considered: "small" refers to a ~30 cm^2 and "large" denotes a ~60 cm^2 proton beam footprint area. The component with the shortest lifetime is the PBW, at 3.2 years.

Table 4.4. Radiation damage and predicted lifetime for selected STS components.

Component	Material	Dpa limit (dpa)	Helium limit (appm)	Target type/ proton beam footprint	Dpa rate (dpa/ year)	Helium rate (appm/ year)	Lifetime (dpa limit) (years)	Lifetime (helium limit) (years)
Target window	SS	12		Stationary/ small	16.7		0.7	
				Asynchronous rotation/small	0.35		51	
				Synchronous rotation / large	0.444		**27**	
Proton beam window	Al	40	2000	Stationary or asynchronous/ small	2.3	1335	17	1.5
				Synchronous rotation / large	1.07	616.3	37	**3.2**
Moderator vessels	Al	40	2000	Stationary or asynchronous/ small	7.8	116	5.1	17
				Synchronous rotation / large	5.24	68.2	**7.6**	29

4.1.7 Operations

The Target Systems are a single failure point for the overall STS system. Therefore, availability, robustness, and maintainability are central values to the design. Where possible, the design incorporates redundancy and fail-safe modes to allow continued neutron production in the event that a portion of the system is operating in an off-normal mode.

The Target Systems have two distinctly different operating modes: beam-on operation and beam-off operation.

4.1.7.1 Beam-on Operation

When beam is on, the following systems require active operation, which is defined as operation under control of Target Systems operators or under the automated control system (EPICS):

- Proton beam diagnostics, harp, halo monitor, and target viewing periscope (TVP) (Section 4.2.2)
- Target technical component utility systems (Section 4.8)
- Target drive system (Section 4.3.3.3)
- CMS

These systems perform the three functions of cooling, monitoring, and positioning (in the case of the target drive system) the critical components of the Target Systems. The remaining target hardware is stationary during operation and does not necessitate active control. Because of the high levels of radiation, personnel will not be able to enter the utility vault, beamline access pits, or service cell while the proton beam is on. Consequently, high reliability, redundancy and remote monitoring are key elements in the design of these systems.

4.1.7.2 Beam-off Operation

Regular outages will be incorporated into the STS operating schedule to allow personnel to upgrade and maintain equipment. Two types of outages are common; weekly 8 hour shutdowns designated for modest fixes and 1–2 month biannual maintenance periods designed to allow for significant equipment maintenance.

8 Hour Shutdown Operations

Certain equipment has been identified as requiring maintenance or change-out during an 8 hour shutdown. This includes the target drive system, the TVP, and the valves, pumps, and sensors of the technical utilities system. Most of this work will be performed manually with limited special tooling

Access to the utility vaults is limited by the half-life of the radiation in the activated water. Experience at SNS with beam at ~1MW has shown that personnel can enter the target utility vaults 2–3 hours after the beam is off. Local radiation areas are roped off as required to control exposures (e.g., shielded ion exchange columns).

Extended Shutdown Operation

Maintenance or upgrade of large target system components will have to be performed during extended outages inside the service cell or using special handling equipment because of high levels of activation.

Targets will be changed and maintained in the shielded service cell. All target handling operations will be performed remotely because of the high level of residual radiation. When targets are not exposed in the cell, and the target cart is positioned in the monolith, personnel will be able to enter the cell to perform many routine maintenance functions.

Other target system components such as the PBW, beamline inserts, operational shutters, and inner reflector plug (IRP) will require dedicated, shielded handling tools. With the goal of simplifying operations and reducing costs, much of this work will be based on existing SNS tooling. However, new tooling will be required for the neutron beamline inserts and operating shutters.

4.2 PROTON BEAM INTERFACE COMPONENTS

Five proton beam interface components will be contained in the roughly 3.3 m long zone between the last quadrupole magnet and the target, as shown in Figure 4.22. The PBW assembly will separate the rough vacuum environment of the vessel from the high-vacuum accelerator. The harp, halo, and TVP assemblies will monitor the proton beam alignment and condition. A beam collimator will be located upstream of the PBW to prevent a misaligned beam from damaging the target, moderators, or alignment monitors. All these assemblies are designed to be compatible with the high bay remote handling system described in Section 4.9. The proton beam tube sections between the components are integral to the overall assembly. The tube sections are planned for life-of-facility operation; however, special replacement procedures can be implemented to restore operations.

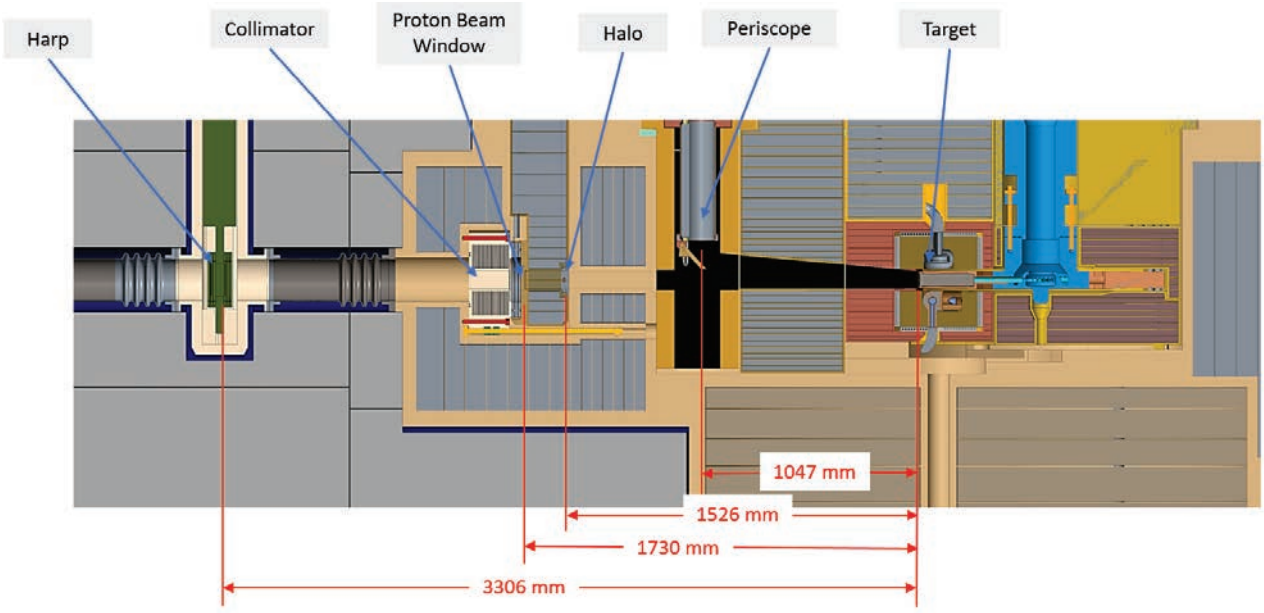

Figure 4.22. Section view of core vessel showing location of primary components.

4.2.1 Proton Beam Interface

4.2.1.1 Baseline Proton Beam

Target Systems and the STS Neutronics Group developed a proton beam profile at the PBW based on neutron production efficiency and target material thermal stress limits. The profile was expressed as a super-gaussian formula amenable to analysis by both groups. The accepted profile was then used by the Accelerator Group to design a magnet configuration. Figure 4.23 shows both the original super-gaussian

approximation and the accelerator design basis profiles expressed at integrals (protons/pulse/m) in each plane. The nominal maximum beam density is approximately 4.8×10^{16} protons/pulse/m^2. The figure identifies the ideally centered nominal 90% beam area as 62.3 cm^2 (4.8 by 13.0 cm). Also identified are the outside edges of the tantalum-clad tungsten blocks (6.0 cm tall by roughly15.0 cm wide). Neutronic analysis calculates 60% of the total beam energy is deposited in the target with the remaining 40% or 280 kW being deposited in the surrounding structure. Using data from the accelerator study, the additional heating outside the target due to misaligned beams was determined (see Table 4.5). For deviations of less than about 10 mm, the change is within the design margin for most of the target system components. However, off-center beams will increase stress in the target blocks and shroud, increase heating in the moderators, and change neutron production rates.

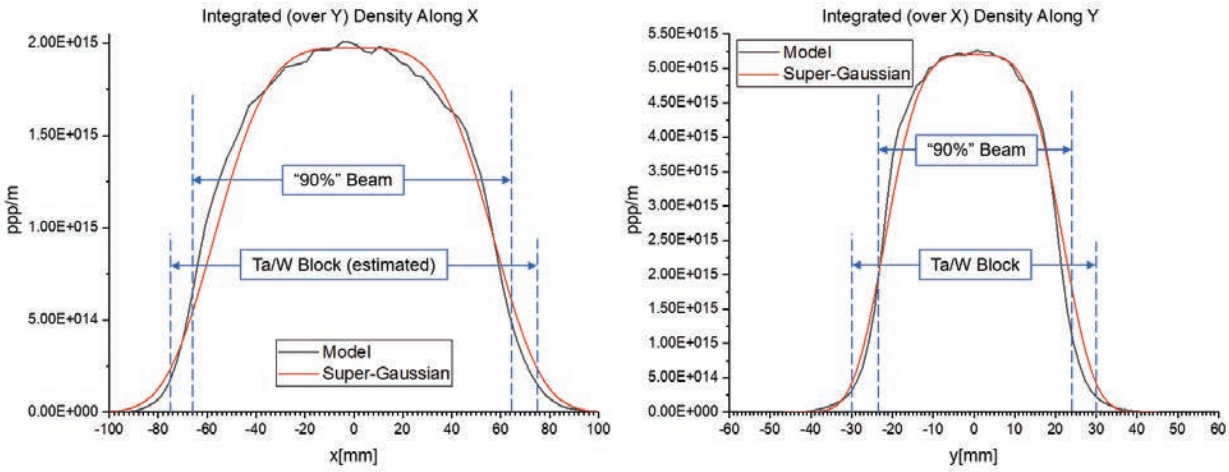

Figure 4.23. Mathematical approximation of theoretical proton beam-on-target configuration.

Table 4.5. Additional heating due to various beam offsets.

Beam offset (mm)	Fraction on target block	Additional heat outside target block (kW)	Total heat outside target block (kW)	Increase
0.00	98.4%	6.75	286.75	0%
3.00	97.7%	9.63	289.63	1%
6.00	96.1%	16.20	296.20	3%
9.00	94.7%	22.18	302.18	5%
12.00	90.2%	41.00	321.00	12%

The proton beam study also produced the beam profile along the flight path of the interface region, as shown in Figure 4.24. The profile provides both sizing and energy density information for use in the design of the interface components.

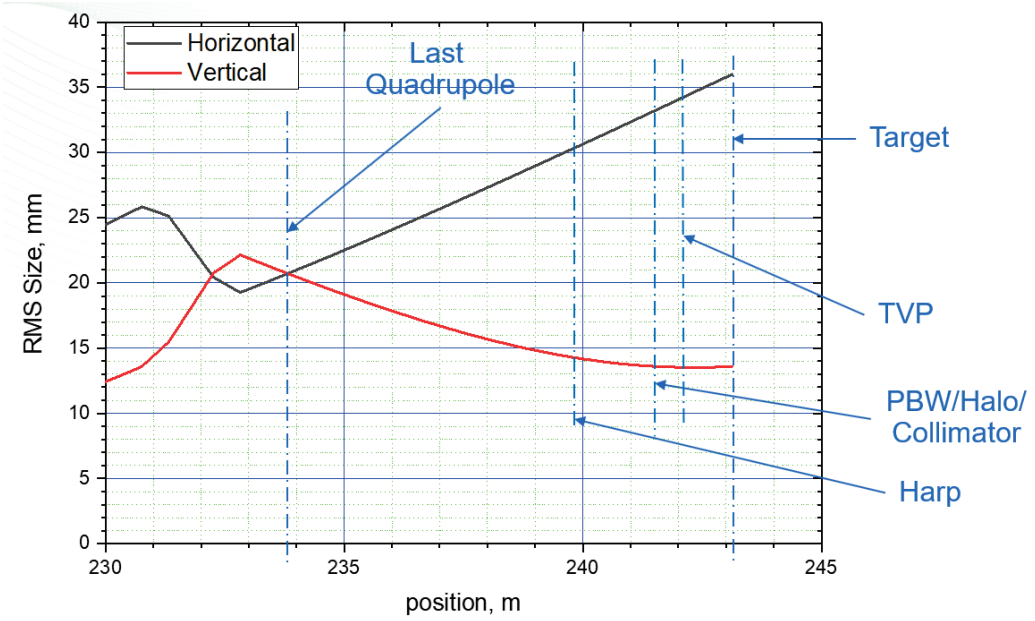

Figure 4.24. Proton beam profile between last quadrupole and target.

4.2.1.2 Beam-on-Target Baseline Configuration

As noted earlier, the baseline proton beam is designed to match the proposed rotating target. Figures 5.25 and 5.26 show the boundaries of the ideal 90% beam (95% vertical and horizontal beam energies) incident on the target. A vertical margin of ±6 mm is provided to account for beam misalignments, off-normal spread, and tails. Horizontal beam deviations are more easily accommodated by the configuration of the target assembly that includes a nominal margin of ±16 mm.

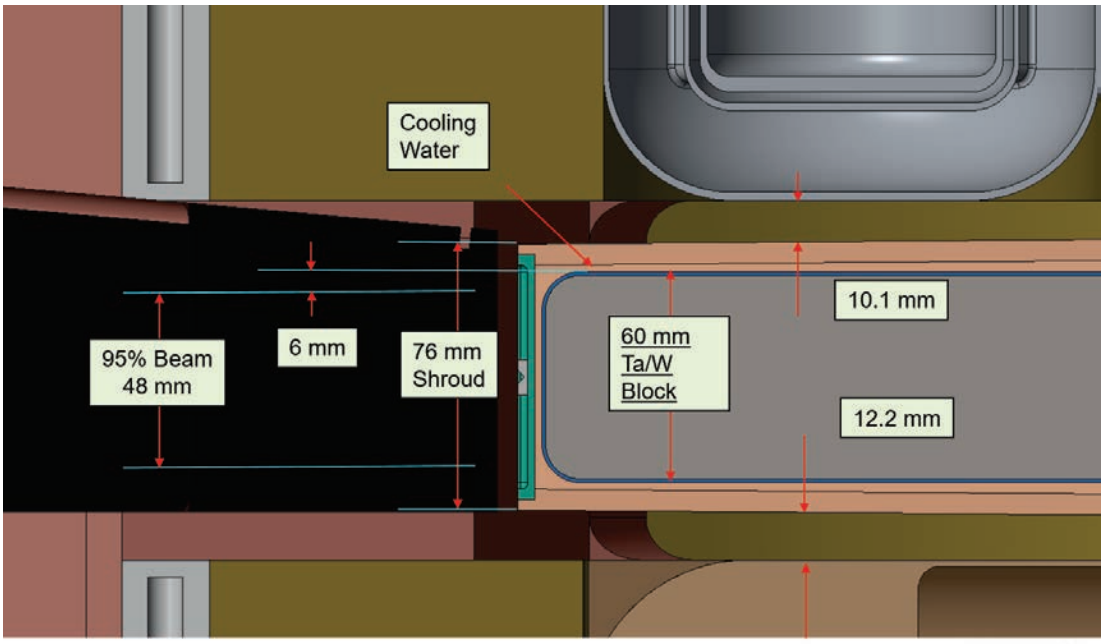

Figure 4.25. Vertical section of ideal beam-on-target configuration.

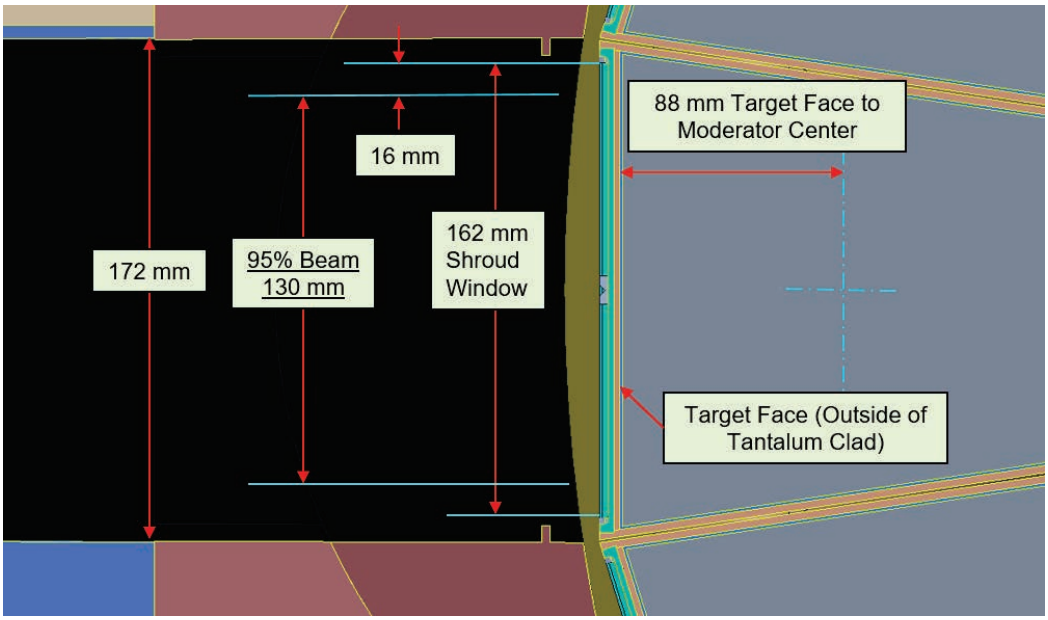

Figure 4.26. Horizontal section of ideal beam-on-target configuration.

4.2.1.3 Beam Position Monitoring Components

The proposed STS scheme for monitoring and controlling the position of the proton beam on the target is based on the FTS system. Mechanical descriptions for each of the STS monitoring components are provided in Section 4.2.2. The performance capabilities for these components are based on operational experience in FTS and, in the case of the TVP, full-scale mock-up testing. These are summarized in Table 4.6.

Table 4.6. Proton beam alignment capability of monitoring components.

	Alignment relative to ideal		
Alignment monitor	**TVP**	**BPM**	**Harp and halo**
Beam centroid (point)	<± 0.5 mm	± 1.0 mm	<± 4.0 mm
Beam spread	<+ 5%	NA	<+ 5%
Beam peaking normal	–	NA	+ 5%
Beam peaking limit	–	NA	<+ 10%
Beam operational drift (pulse-to-pulse)	<± 0.5mm	<± 0.5 mm	<± 0.5 mm
Total beam center to target center	**<± 1**	**<± 1.5 mm**	**<± 4.5 mm**

4.2.1.4 Beam-on-Target Baseline Operating Parameters

Preliminary proton beam, target, and neutronics studies combined with FTS experience provide a reasonable basis for establishing the initial beam-on-target operating parameters.

Normal, ideal operation will position the proton beam within ±1.5 mm of the ideal target center using the beam position monitor (BPM) and harp/halo combination. Both systems are based on proven FTS designs that have operated reliably for over 12 years. Optical feedback has proved to be accurate in FTS; however, functional and target coating lifetime issues make the TVP useful only for backup monitoring.

Individually, both the harp/halo and BPM systems will support non-ideal but acceptable beam operation. The harp/halo combination alone will be less accurate and, without calibration with the other monitors, BPM accuracy could change as a result of adjustments in proton beam operating parameters. With consideration given to these limitations, neutron production can continue. No time limit is applied for the non-ideal monitoring cases in order to provide time to institute repairs without halting neutron production.

Beam shutoff will occur if the monitoring components experience anomalies or failures, or if the beam is misdirected, peaks, or spreads outside specified operating limits. Note that FTS has demonstrated that these anomalies are extremely rare, and that the proton beam can be turned off in as little as one pulse. If necessary, STS also plans to include a beam collimator designed to contain misdirected or spread beams. Beam studies will be performed in the next design phase to establish beam operating limits and collimator design parameters.

4.2.2 Beam Interface Components

The mechanical configuration of the proton beam interface components is described below. Also included are comments on the fabrication and installation tolerances for the components, since both factors will ultimately bear on the quality of the alignment scheme. The BPMs are part of the accelerator and are therefore not described here.

4.2.2.1 Beam Collimator

Beam collimation will be required to protect the TVP mirror and PBW seal. As currently conceived, the collimator will be located upstream of the PBW and will be independently replaceable, as shown in Figure 4.27. The collimator aperture will be approximately 65 by 127 mm, including a fabrication and installation tolerance of ±1.5 mm. It will be attached to the interior vessel flange with remotely accessible bolts and sealed with double metal O-rings. It will be mounted on horizontal rails for retraction into the PBW cavity for vertical replacement. A secondary function of the collimator will be to provide a replaceable seal face for the PBW inflatable seal.

The materials used and the depth of the collimator will be developed based on future accelerator fault studies. For example, the maximum beam misalignment and duration remains to be determined. Maximum beam spread is another factor that will be instrumental in the design of the collimator.

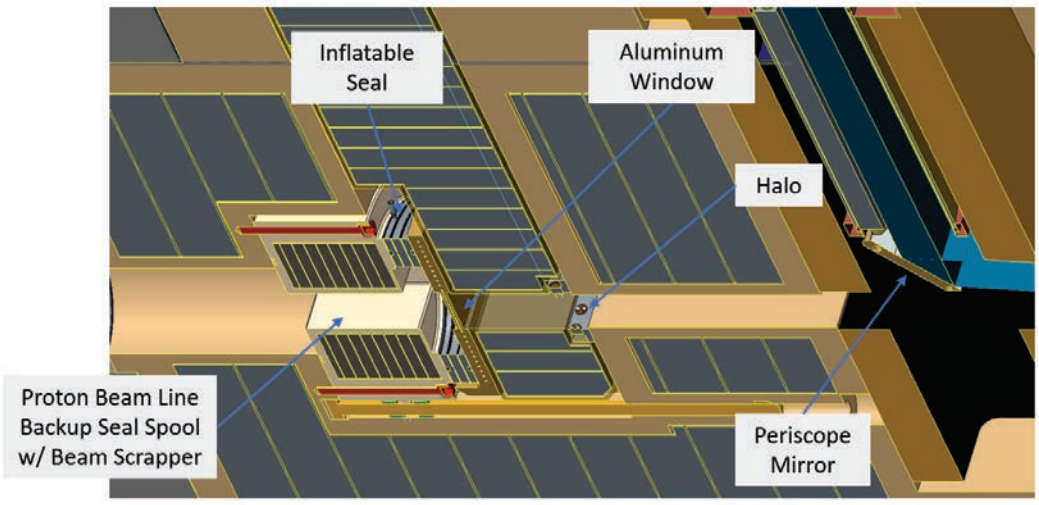

Figure 4.27. Proton beam window configuration.

4.2.2.2 Proton Beam Window

STS requires an atmospheric barrier between the core vessel, which will operate at sub-atmospheric pressure with the possible presence of water vapor, and the high vacuum in the accelerator. The PBW is based on a configuration proven in many accelerator-based neutron-scattering facilities, including the FTS (Figure 4.28). The window itself will be a thin, water-cooled plate mounted at the bottom of a vertical plug and sealed to the proton beam tube with an inflatable metal bellows seal. The window will be aluminum 6061, based on successful implementation in the FTS PBW assembly. Its limited beam scatter and longer life currently make aluminum the favored option. The PBW assembly will include a thermocouple-based halo monitor downstream of the window (see Section 4.2.2.4). Even though the halo is expected to have a long operating life, it will be mounted with the PBW to reduce the number of modular assemblies.

The PBW will be located inside the core vessel for several reasons. The in-vessel location will position the window as close as practical to the target, thus minimizing proton beam scatter. A seal between the PBW assembly and the vessel atmosphere will be eliminated. Alignment to the beamline will be optimized by positioning the assembly on surveyed positioning guides in the vessel. The PBW assembly will have a three-piece plug arrangement that conforms to the requirements of the STS remote handling system. All the active and cooled components will be grouped in a single module with upper two shield blocks that are passive and reusable. The utility stem to the lower module will be fully assembled at installation, thus eliminating inaccessible electrical connectors and tube joints in the shielding. During removal, the utility stem will be cut in situ to reduce the size of a spent assembly to simplify handling and packaging. An activated PBW assembly cannot be repaired and returned to service.

A vacuum seal will be located between the PBW and the collimator as shown in Figure 4.27. The seal will be a single-sided, all-metallic, inflatable assembly based on a design reliably employed at several accelerator facilities, including FTS. Because the seal can be retracted during handling, it will provide the clearance necessary for remote replacement operations. The inflatable metal seal has the disadvantage that it requires unblemished seal faces. The beam collimator can be replaced to correct for a seal face defect.

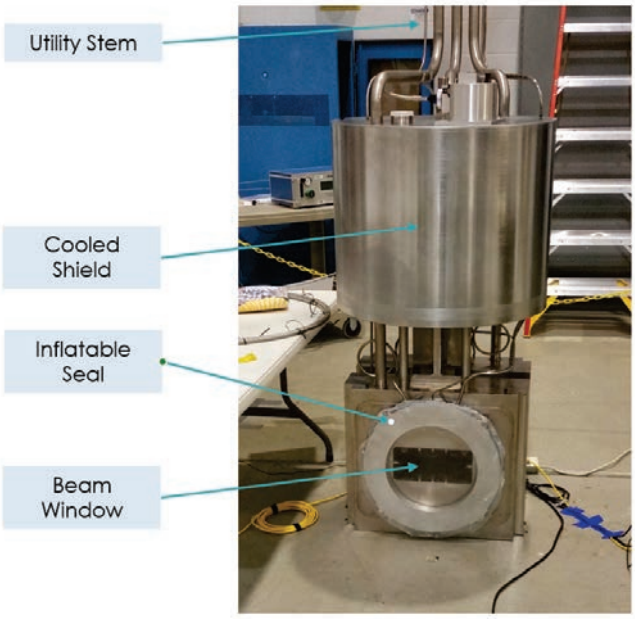

Figure 4.28. The FTS proton beam window assembly.

The neutronic analysis of an aluminum 6061 PBW estimates a damage rate of approximately 0.93 dpa/year, which would yield a lifetime of 37 years if a damage limit of 40+ dpa is used (Figure 4.29). On the other hand, if the more conservative lifetime limit of 2000 appm helium is used, then the calculated production rate of 616 appm/year will limit the life of the window to 3.2 years. Given this relatively short life, STS is evaluating two options. If water entering the accelerator is considered an acceptable risk, then the window could be operated to failure. Although this would introduce schedule uncertainty for the first windows, eventually a predictable mean time between failures could be developed to support a realistic change-out schedule. Another alternative would incorporate multiple window positions in the assembly with an in situ ability to shift between each without significant disassembly effort or time. If all three windows were cooled with one water loop, then in the case of a single window failure, the assembly would have to be changed. Cooling all three windows independently would complicate the assembly and reduce the system reliability. Note that halo monitor assemblies have proved to be highly reliable; however, a very long-lived PBW could challenge this limit. Additional analysis of this subject is required to ensure the two systems could be compatibly packaged in the same module.

The PBW is cooled by process loop 1, along with the target. Both components are directly heated by the proton beam, have similar cooling water activation products, and can use the same delay tank and gas/liquid separator. Having a common loop also has a potential safety benefit for target loss-of-cooling accidents. If the PBW cooling also were lost, the window would fail and the loss of high vacuum in the accelerator would provide a passive beam shutdown, even if the active safety systems designed to trip the proton beam were not functioning. Note that the accelerator will be equipped with fast-acting valves designed to contain the gas and water inflow in the event of a PBW failure.

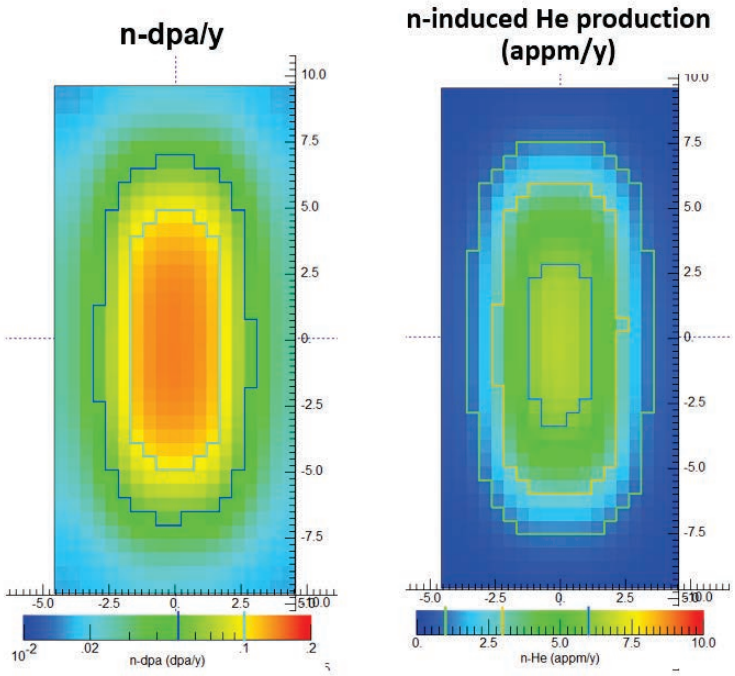

Figure 4.29. Proton beam dpa and helium in aluminum PBW based on a 15 Hz beam (windows shown rotated by 90°).

4.2.2.3 Proton Beam Wire Harp

STS will have a wire harp similar to the system used in FTS (Figure 4.30) and other similar accelerator facilities. The wire grid assembly based on the FTS design is expected to provide beam centroid positioning feedback to the control system within ± 4.5 mm of ideal vertical and ± 4.5 mm of ideal horizontal.

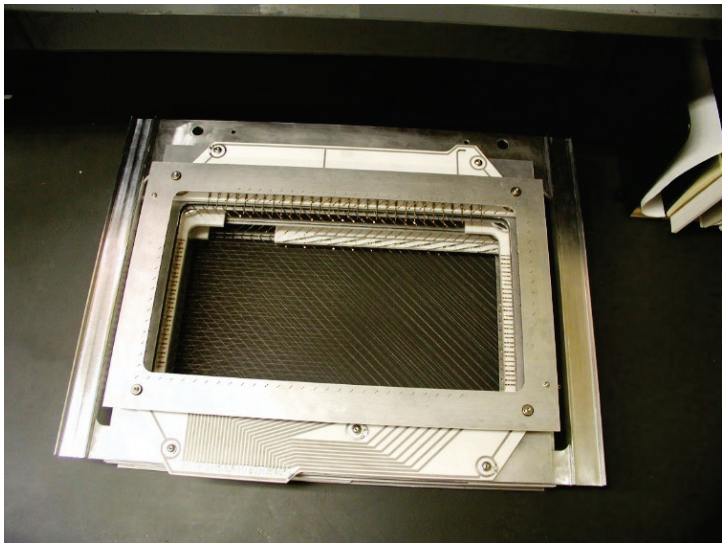

Figure 4.30. Current SNS proton beam harp module.

The harp will be installed upstream of the vessel as shown in Figure 4.31. It will be located in the high-vacuum proton beam tube at a tee, which will locate the seal above the activation zone and thus make the use of conventional sealing materials possible. The harp itself will be flexibly attached to the seal plate so that it can be positioned on vessel-mounted fiducials near the proton beam line at an accuracy of ±1.0 mm (vertically and horizontally).

The FTS harp has proved to be highly reliable, having remained continuously in the proton beam for 11 years to date. However, the STS proton beam flux density will be approximately 200% higher, so the operating life of the same basic system could be significantly shorter. Consequently, the proposed STS harp may incorporate a retraction mechanism to reduce beam exposure to ensure extended life. That could significantly reduce its effectiveness as a beam monitoring element. Regardless of the actual assembly operating life (assumed to be 5 years for planning purposes), the harp assembly is designed to be changed using the proven vertical shielded container arrangement described in Section 4.9.

The proposed harp mounting location in a vertical pipe tee will complicate the maintenance of the proton beam tube sections in the monolith. Fortunately, the FTS has demonstrated that there is a very low probability of damage to the beam tubes; nevertheless, STS will include features to enable replacement. Replacement will be a difficult operation because of the length, position, and activation of the assembly. The design of disassembly features will be undertaken in the next design phase. Alternatives such as installing the harp in the accelerator tunnel have been considered and eliminated either because they do not simplify the assembly or because they reduce the usefulness of the harp by placing it too far from the target.

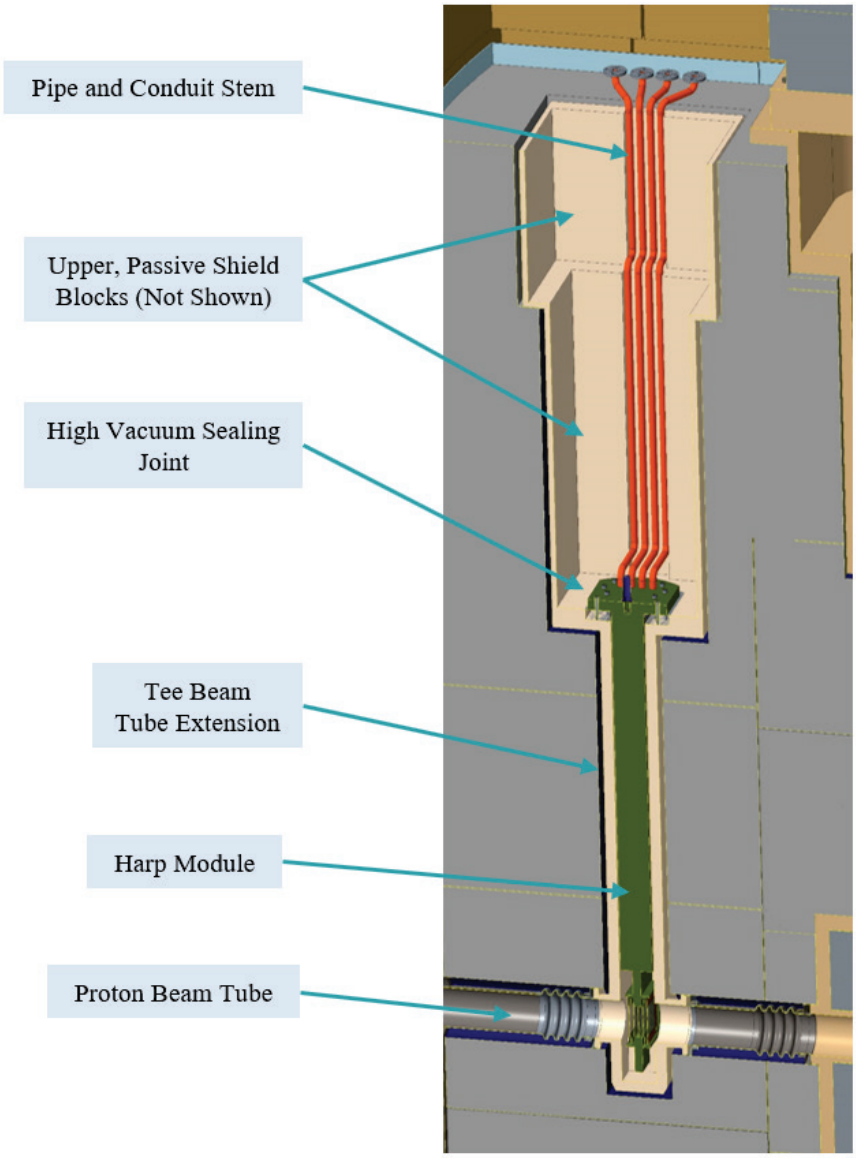

Figure 4.31. Harp configuration.

4.2.2.4 Beam Halo

As noted in Section 4.2.1 the PBW assembly will include a thermocouple halo as shown in Figure 4.32. The system will be like that used in FTS (Figure 4.33) and other similar accelerator facilities. This system has proved to be highly reliable because the thermocouples are exposed only to the relatively low-power perimeter beam. The halo and halo control system will be designed by the Accelerator Group. The mechanical installation will be designed and provided by Target Systems.

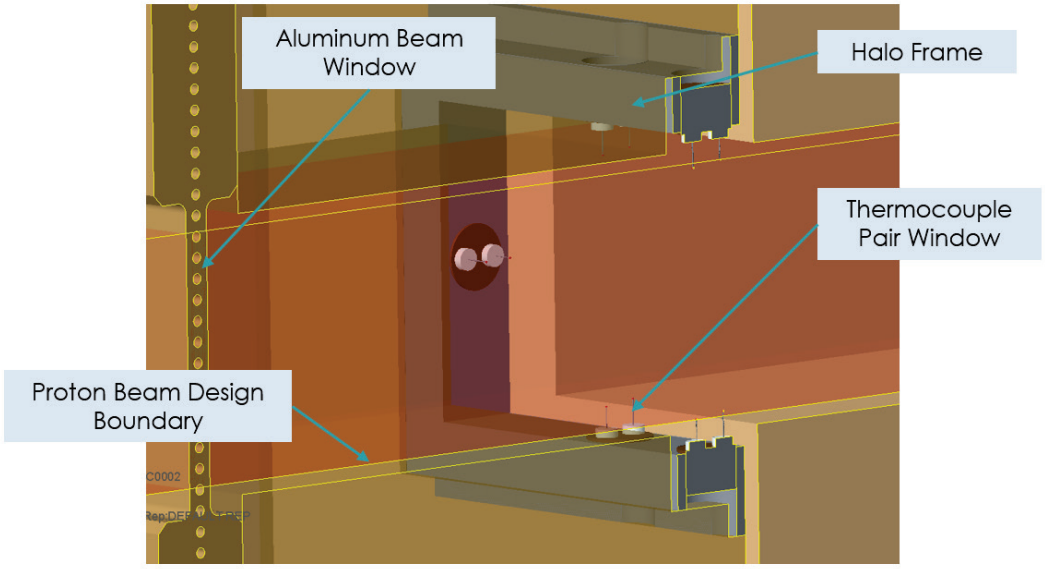

Figure 4.32. Beam halo monitor as mounted in the PBW assembly.

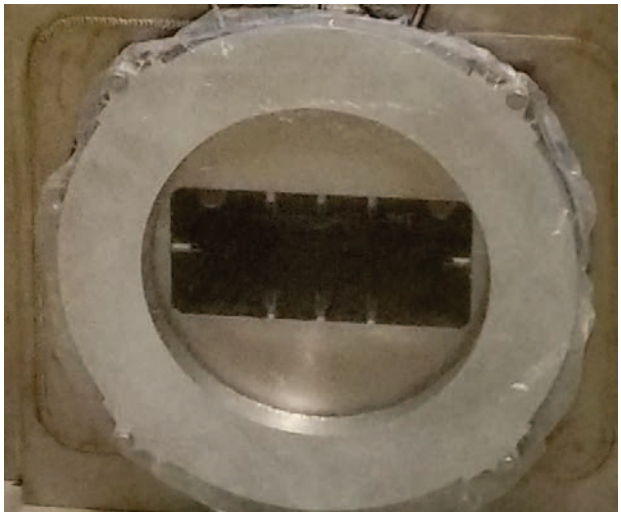

Figure 4.33. FTS halo monitor as mounted in PBW assembly.

4.2.2.5 Target Viewing Periscope

A Target Imaging System was retrofitted into the FTS PBW assembly. Despite the mechanical challenges that required the use of optic fiber, the system proved to be useful. STS provides the opportunity to install an optimized system based on direct viewing using mirror optics. The FTS target viewing team was enlisted to design and develop a robust periscope capable of providing continuous beam-on viewing of the target. This team determined the best approach to be a simple arrangement based on two flat mirrors and commercial optics positioned outside the target drive room to facilitate maintenance during beam-on operation. The resulting configuration (Figure 5.34) effectively means the camera has a telescopic view from approximately 10 m.

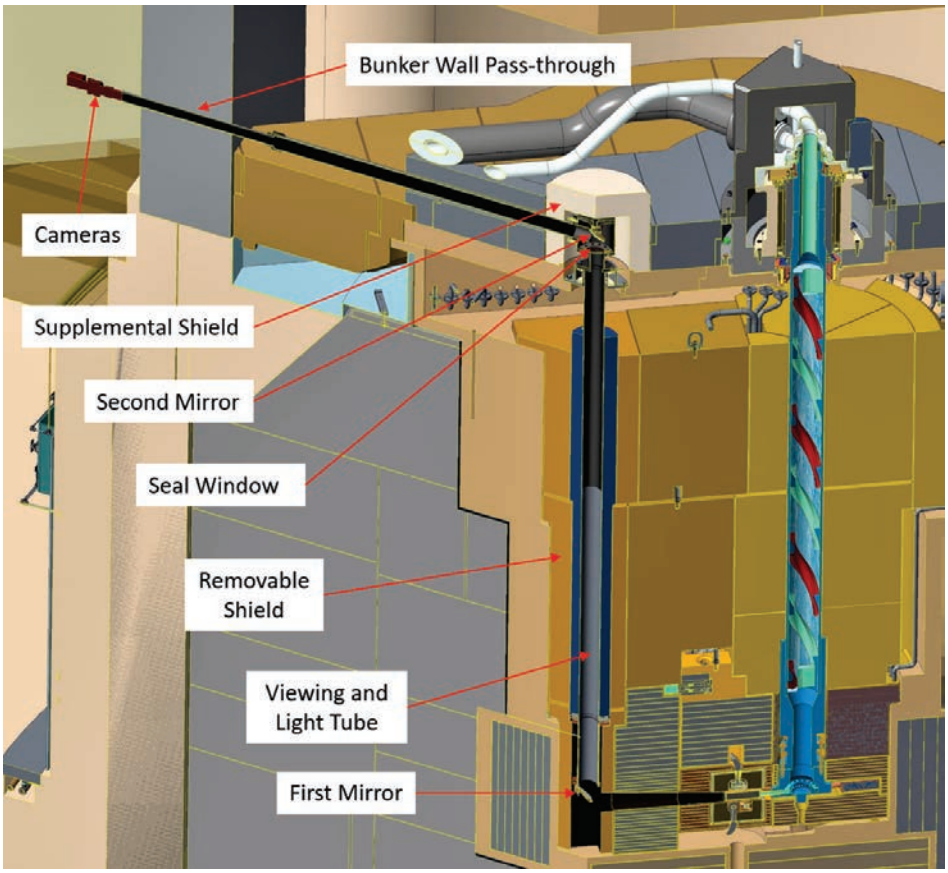

Figure 4.34. Section target monolith along periscope sightline.

The system will have a visible light mode and one infrared (IR) spectrum mode. During alignment and inspection (beam on or off), the target area, including certain critical moderator-reflector and vessel interfaces, will be illuminated by lights located in the target drive room. Two polished pipes will transmit the light to a reflective surface above the optic mirror that will illuminate the target area (Figure 4.35) and fixed fiducials along the beam line. This viewing mode will be particularly useful during the final alignment of the target disk relative to the moderator reflector assembly (MRA) aperture.

During beam-on operation, the proton beam incident spot on the target will be made visible by a luminescent coating with embedded fiducials (Figure 4.36). Thermal imaging will be made possible with a dichroic beam splitter, IR optics, and an IR camera. This simultaneous imaging will allow monitoring of the uniformity and consistency of the target nose temperature, which is an indicator of possible water distribution problems inside the target. Note that the target drive will have an operating range that will result in a horizontal drift of ±2.5 mm (see Section 4.3). This motion will be monitored with the TVP optics using fixed cross-hairs centered during start-up.

The TVP will be mounted in the monolith through the lid of the core vessel to provide clearance for the horizontal viewing tube and to facilitate rapid change-out. The replacement will be fully tested in the MUTS to ensure that the mirror is correctly positioned before installation. The second mirror can be manually adjusted during the reassembly process using the visual optics system. The vertical assembly will be positioned on vessel fiducials to within ±0.5 mm of ideal vertical and horizontal

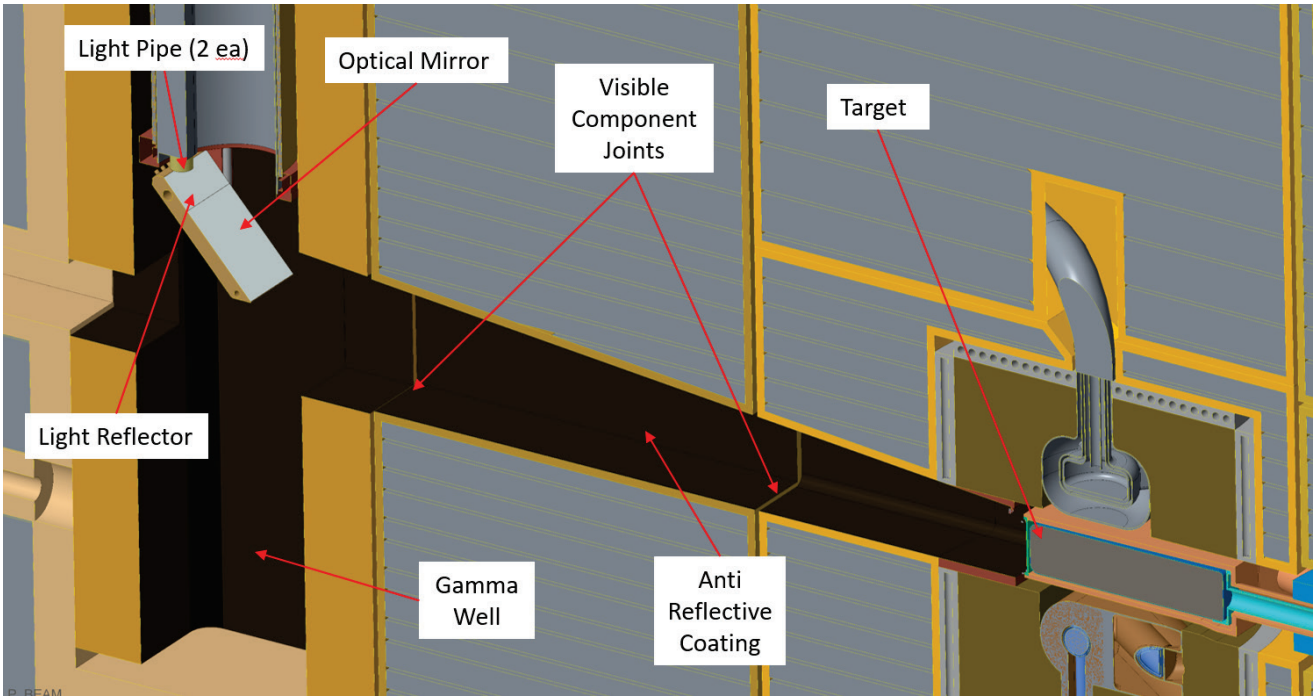

Figure 4.35. Detail of lower periscope configuration.

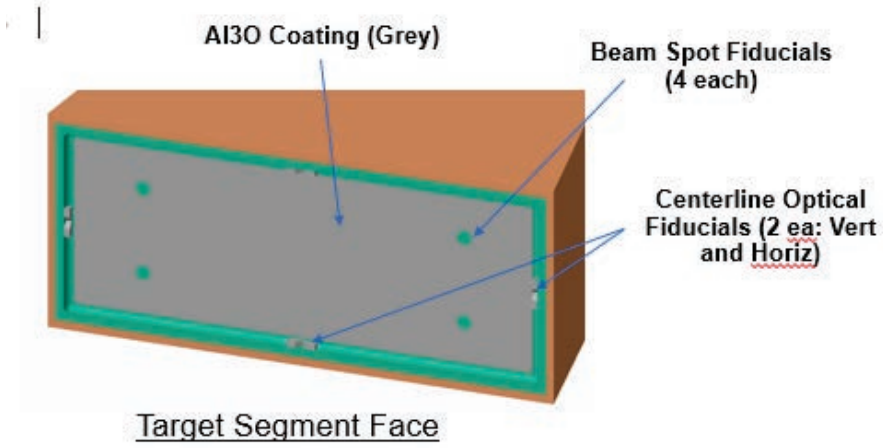

Figure 4.36. Fiducials on a typical target disk segment.

A full-scale mock-up of the proposed optical system was constructed at ORNL (Figure 4.37) in 2017. The mock-up demonstrated that the desired capabilities can be achieved; most important, tests showed that target area features can be discerned with <1 mm resolution (Figure 4.38). This level of precision allows the periscope to monitor the position of the target and to assist with proper alignment of replacement moderator/reflector and target assemblies. It was also demonstrated that atmospheric distortions will be minimal if the vessel must be operated with a sub-atmospheric helium environment rather than vacuum. Note that the IR thermal imaging and IR spectroscopy capabilities have not been tested in the mock-up system because they are well established, using commercially available products. Also, the current baseline calls for the use of the FTS luminescent coating even though improved coatings may become available through the ongoing development program under way in conjunction with the ESS project.

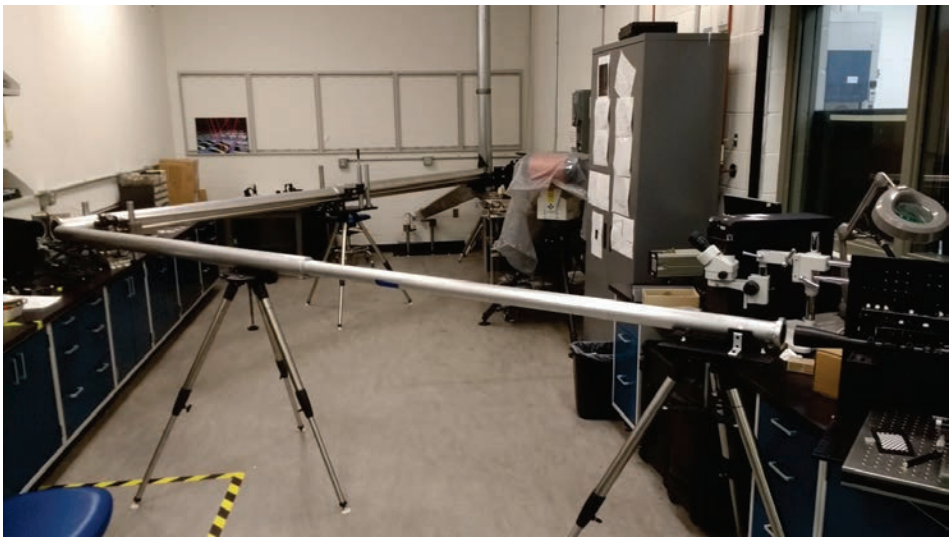

Figure 4.37. Periscope mock-up facility.

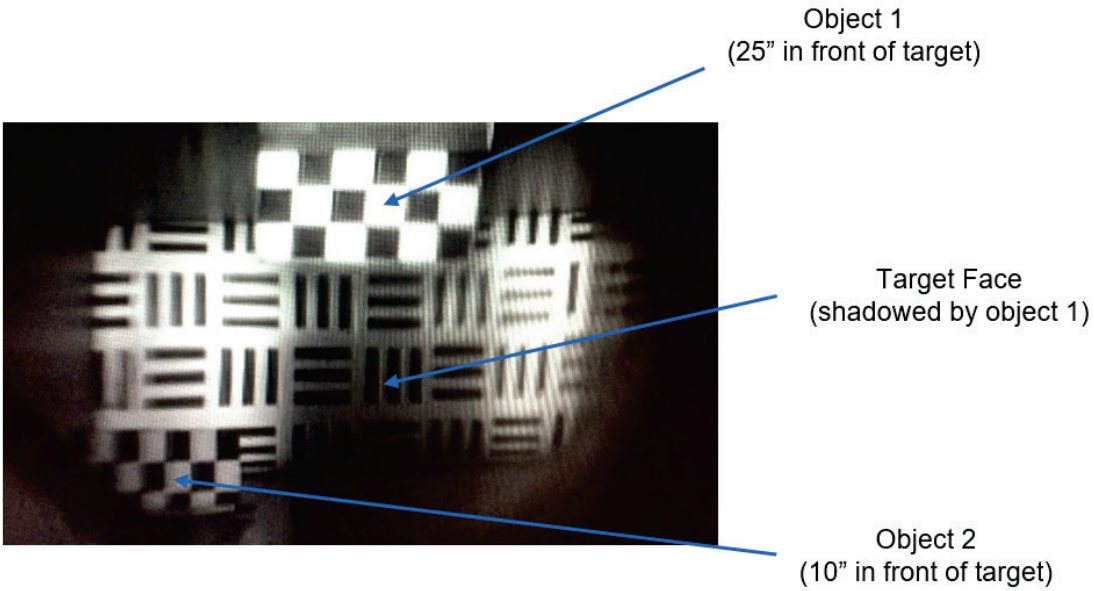

Figure 4.38. Mock-up periscope target image showing resolution and depth of field.

The water-cooled first mirror is the only uniquely new element of the proposed periscope. While all other components in the system are commercially available and can be maintained and aligned manually, the first mirror must be accurately aligned in the core vessel MUTS before assembly. The reflective surfaces of the first mirror must be protected against corrosion in the event of a small water leak inside the vessel by gold plating the critical surfaces. This will result in a different attenuation and optical spectrum, which might need to be considered along with adjustments to improve IR temperature measurements. The mirror must also be uniformly cooled to maintain reflective surface flatness and thus the quality of the image. Analysis of a smaller mirror indicated that it will be heated at a rate low enough that thermal distortion of the mirror face should be achievable. Note also that the design includes additional thermal control by holding the cooling water inlet temperature to a band of ±1°C.

Because the TVP offers direct access to the proton beamline, alternative viewing options may be implemented in the future. For example, it may be possible to develop a beam spot readout based on temperature (IR light) rather than luminescence. The readout may be required if it is determined that the luminescent coating on the target sections is not able to perform as expected over the full life of the target for reasons such as corrosion due to environmental contamination resulting from a water leak. It is also assumed that a special, temporary viewing system may be built for use during installation and maintenance to provide a full view of the proton beam passage. This system could include mirror tilting and rotation features not feasible for the beam-on TVP assembly.

4.2.2.6 Interface Component Fabrication and Installation Tolerances

The core vessel is the essential target system alignment feature. It will be installed as accurately as possible, grounded for minimal displacement over the life of the facility, and internally machined to provide reliable and precise placement of all the key target system components. The details of the vessel fabrication and installation are discussed in Section 4.6. However, based on the performance of FTS, the locations of the proton beam monitoring component positioning guides in the core vessel are conservatively assumed to be accurate to less than ±1.0 mm over the life of the facility. This level of accuracy will be accomplished by careful placement of the vessel with compensation for compression of the foundation piles as shielding is added around the vessel. Additionally, the component positioning guides will be installed with shimming and adjustments to provide maximum, surveyed alignment. Including these factors with internal tolerances, it is assumed that all the components in the proton beam path, except for the periscope and target, will be placed without in-place adjustment to within ±1.0 mm of the ideal beam line both vertically and horizontally. The suspended target disk will be positioned in situ at the drive mounting frame on the core vessel lid. This will provide for inevitable internal and assembly tolerance stack-up differences in replacement components. Similarly, the elevation and tilt of the TVP will also be adjustable in-place using fixed, visual fiducials in the beam tube.

4.2.3 Proton Beam Interface Development

Accelerator fault analyses will be performed in the next design phase to quantify the extent and duration of various off-normal events that can occur in the target interface region. Study results will be used to develop the proposed features to absorb these events, notably the configuration of the beam collimator.

4.3 TARGET ASSEMBLIES

A rotating solid target was selected for STS as the result of an evaluation of all known target options (see Section 4.3.2). The proposed configuration is based on a combination of solid target designs proved at other spallation facilities and a successful full-scale mock-up rotating drive test. The target is composed of 21 stainless steel–shrouded tantalum-clad tungsten blocks 6 cm high by 25 cm deep. The blocks are arranged in a multi-section, light-water–cooled, disk mounted on an axle supported and driven from above the monolith shielding. The target assembly is shown in Figure 4.39.

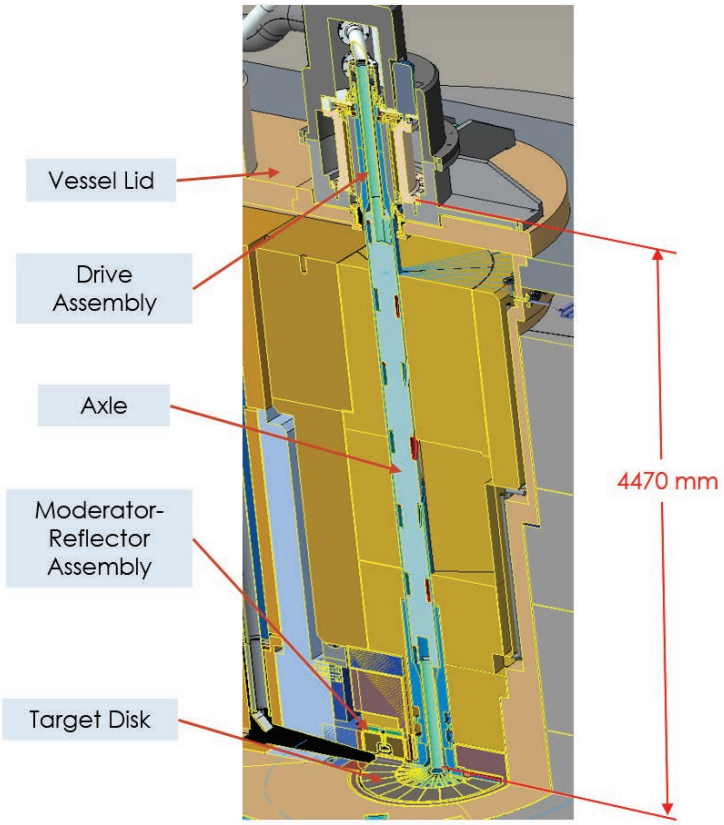

Figure 4.39. Vertical section view of rotating target assembly in the STS monolith.

4.3.1 Design Requirements

The high-level design requirements for the target assemblies are in the following subsections. Additional, more detailed, requirements are included in subsections for the three main subassemblies that make up the target assemblies.

4.3.1.1 Safely Accept the Proton Beam

The conceptual target design is evaluated for safety impacts in the STS Preliminary Hazards Analysis Report [McManamy 2019]. As the design matures, so too will the hazards analysis. The design must meet the facility goals for personal safety consequences and probabilities.

4.3.1.2 Allow Heat Removal of Deposited Energy (~60% of 700 KW)

Approximately 60% of the proton beam energy is directly converted to heat in the target region. This heat must be removed via the water-cooling system.

4.3.1.3 Optimize Design for High-brightness Neutronic Performance

High peak brightness is a key feature of STS. The target design shall be optimized to support high brightness. Key requirements that support optimization for high brightness include these:

- Minimizing the beam profile size that can be tolerated
- Minimizing target and shroud material outside the beam profile, allowing moderators to be positioned as close as possible to the target
- Maximizing the average material density in the neutron generation volume.
- Minimizing manufacturing and installation tolerances of the target disk
- Minimizing runout of the target disk

4.3.1.4 Maximize Design Lifetime

Target replacements cause facility downtime. The planned lifetime shall be maximized in order to limit facility downtime and reduce operating costs. Target shroud embrittlement due to radiation damage is one lifetime consideration. At present, target lifetime is more than 20 years if limited by shroud embrittlement. Other failure modes that lead to end of target life are loss of cooling due to a change in a coolant passage, leakage from the shroud, and breach of the tungsten casing, leading to tungsten erosion. The design must balance the trade-offs between optimized performance and robustness that supports extended and predictable lifetime.

4.3.1.5 Maintain/Exchange Target Drive System without Changing Target Assembly

The target drive system includes several components with expected lifetimes shorter than that of the target disk, such as water seals, gas seals, drive motors, and sensors.

4.3.1.6 Tolerate Off-nominal and Off-normal Beam

Conceptual proton beam alignment capabilities are outlined in Section 4.2.1. Ultimately, a set of allowable, off-nominal, normal operating variances will be developed. These will include vertical and horizontal offsets as well as peaked and divergent beam profiles. The target will be designed to accept all these cases without limitation.

In addition, off-normal cases, such as beam pulses when the target loses rotation or is not properly synched with the beam pulses must be considered. In these cases, the minimum design requirement is to comply with the facility safety requirements to minimize consequences to workers and the public. If possible, the design should accommodate off-normal operation without leading to end of target lifetime.

4.3.2 Target Type Selection

This section provides a summary of the target design and material choices that are considered in this conceptual design. It also provides the rational for proceeding with the solid tungsten rotating target.

Spallation neutron sources have used a variety of different target materials and cooling. Typically, high-Z target materials have been chosen since the production ratio of neutrons to protons increases with higher Z and density. Solid target materials that have been used include tungsten, tantalum, lead, and uranium. Uranium targets were used at the Intense Pulsed Neutron Source facility at Argonne National Laboratory [Boringer et al. 1991] and at the ISIS facility at Rutherford Appleton Laboratory in the UK [Finney 1990] but have had problems with swelling that caused failures in the cladding materials. Uranium also is undesirable for short-pulse operation because of delayed neutron production. Lead targets within tubes have been used at the Swiss Spallation Neutron Source, which operates at steady state. There have been

problems with lead leaking from the tubes [Dementjevs 2018]. Lead is lower in density than tantalum or tungsten and therefore has lower neutron production per proton. Tantalum was used at the ISIS facility and delivered good neutron production and reliability; however, it has very high levels of activation and long-lived decay heat. Because of handling difficulties with tantalum, tungsten was selected for later ISIS targets. Operation at Los Alamos National Laboratory of bare tungsten with water cooling in a 1 MW beam showed high rates of corrosion for sections within the beam profile. Recently, facilities with water-cooled solid targets have selected tungsten with tantalum cladding, including the Luan Center, ISIS target stations 1 and 2, and the Chinese Spallation Neutron Source (CSNS).

The ESS facility plans to use tungsten plates with helium cooling so that a separate cladding for corrosion protection is not needed. It will also use a large rotating target that allows for passive decay heat removal and low average power density in the target material.

Mercury is the other major target option that has been used at the SNS FTS and Japan Research Accelerator Research Complex facilities.

At STS, the target material and configuration choice must be consistent with the facility goals, including

- High brightness, intense, short pulses of neutrons
- High reliability and availability
- Acceptable accident safety consequences that are comparable (or improved) relative to FTS
- Minimized overall facility capital and operating costs

Given the experience to date with SNS, the major options considered for STS were

- Mercury target
- Compact stationary tungsten target with tantalum clad and water cooling
- Rotating tungsten target
  - Water cooled
  - Helium cooled

4.3.2.1 Option Comparison

It is likely that any of the major target options could be made to work for STS to some extent. A qualitative evaluation of some the principal advantages and disadvantages for each option are given in the following tables.

Mercury target	
Advantages	**Disadvantages**
Developed and used for SNS First Target Station	Additional water-cooled shroud needed, reducing moderator performance
Operators experienced with system operation	Cavitation damage potential is likely to be higher for STS than FTS because the peak proton pulse intensity is approximately 2 times higher than for the proton power upgrade design at 2 MW
Mercury process system has operated reliably for over 10 years	Average density and neutronic performance would be lower than for a solid rotating target
Possible similar system components with FTS for spares	Complex process cell for mercury system needed with full remote maintenance, which adds risks to availability
	Mercury containment adds complexity to primary confinement exhaust system and process cell construction

Compact stationary tungsten target with tantalum clad and water cooling	
Advantages	**Disadvantages**
Technology developed and used for ISIS TS1 and TS2, the Lujan Center at Los Alamos National Laboratory, and the Chinese Spallation Neutron Source	High decay heat within small target envelope for 700 kW beam operation
Separate water-cooled shroud not needed	Active cooling required after beam shutdown to prevent target damage
Compact target gives good neutronic performance	Decay heat with total loss of cooling would lead to tungsten vaporization and target collapse with long-term facility shutdown
SNS experienced with water cooling system design and operation in First Target Station	Target lifetime ~5% of comparable rotating target based on dpa damage
	Target carriage and process cell needed for target replacement

Rotating tungsten target—water cooled	
Advantages	**Disadvantages**
Good neutronic performance—low time-averaged heat generation requires less water in the beam for cooling compared with compact target and no separate shroud needed	Moderator replacement much more complex with target in place
Decay heat passively cooled, so total loss of cooling does not lead to tungsten vaporization	Mechanical complexity added for drive and shaft seals for water and vacuum
Very long target life for 1.2 m diameter target >20 years based on dpa damage	Additional initial target cost compared with a compact target
Proof of principle for drive and shaft demonstrated in 2010	Spent target handling is more complex and may require segmentation and/or procurement of a dedicated shipping cask
No connected process cell or horizontal carriage assembly required	Decay heat may require active cooling to prevent target damage during handling or loss of primary cooling

Rotating target—helium cooled	
Advantages	**Disadvantages**
Technology is being developed by ESS project	No operating experience in a spallation source
Reduces water/steam available for tungsten vaporization with loss of cooling and continued beam operation	Higher temperatures and pressures needed compared with water cooling
Does not require clad, thus reducing decay heat and production of ^{182}Ta, which is a primary contributor to offsite dose for a clad target	Very high helium purity must be maintained to prevent oxidation
Long target life compared with compact stationary target	Potentially lower average density if additional surface area is needed for helium cooling
No connected process cell or horizontal carriage assembly required	No quantitative evaluation has been done for the STS

4.3.2.2 Target Evaluations

The rotating water-cooled tungsten target was selected for STS based on good neutronic performance, extensive operating experience with water cooling, and the recommendations of a safety, operation, and reliability review comparing the compact stationary tungsten target and the rotating target. Mercury was not the first choice because of the expected lower neutronic performance caused by having a water-cooled shroud and lower-density material compared with a rotating target with tungsten.

The STS Technical Design Report issued in January 2105 was based on a compact stationary water-cooled tungsten target with a 470 kW, 10 Hz beam. That report identified the potential for high tungsten temperatures due to decay heat after a loss of cooling, with temperatures above the threshold for tungsten vaporization in steam. A review of target design alternatives for safety, operation, and reliability was conducted September 22–23, 2015, to examine compact and rotating target design options, including accident analysis. Reviewers included two engineers who were responsible for the safety evaluations of the tungsten target at the Los Alamos National Laboratory's Luan Center and two safety specialists who helped to develop the safety documentation for SNS.

The compact target design had 13 tantalum-clad tungsten plates of varying thickness, which were water cooled within a stainless steel shell. Two cryogenic moderators were located above and below the target. Decay heat from 470 kW operation was calculated by MCNP for each plate. Analysis showed that with a loss of target cooling, the decay heat would raise temperatures above the tungsten–steam vaporization threshold of 800°C; and simultaneous loss of pre-moderator cooling would lead to structural failures. Designs for a 1.2 m diameter rotating target were also presented, which showed that the decay heat could be passively removed by thermal radiation to the surrounding shielding at well below 800°C. The neutronic performance was expected to be similar for both concepts.

The rotating target concept was initially developed at ORNL in 2008–2009, and a full-scale mock-up was fabricated and tested. This was done in collaboration with the ESS-Bilbao team. They delivered a 4 m long shaft and a 1.2 m diameter target, which was assembled with a drive system designed and procured by ORNL in 2009. Figure 4.40 shows this assembly.

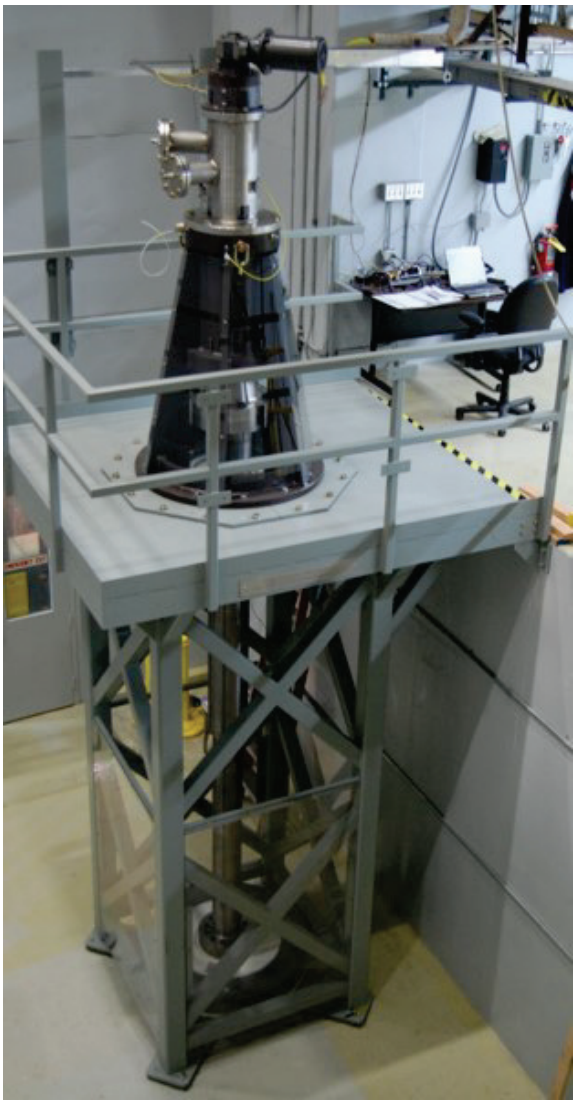

Figure 4.40. ORNL rotating target mock-up testing.

Mechanical testing of the assembly at 30 to 60 rpm showed very good alignment, with low run-out at the target outside radius (nominal ~0.2 mm and maximum ~0 .5 mm @ 34 Hz). The drive module was tested for 5400 h at 30–60 rpm with no water seal leakage [Rennich et al. 2010].

The review conclusions were given by letter on December 21, 2015, recommending the rotating target. The following is an excerpt from the letter:

> The committee recommended the rotating tungsten target as the STS target design option. As presented, the target delivered the desired brightness, possessed tolerable worst-case accident consequences, eliminated decay heat as an accident initiator, and possessed a multi-year lifetime. At this stage of the design, the rotating design also required the least amount of supporting infrastructure. The drive mechanism concept had been partially validated through successful operation of a full-scale mock-up at 60 rpm for 5,400 hours. The stationary target was not recommended due to irrecoverable facility impacts during loss of coolant accidents, unacceptable on-site consequence to workers during worst-case accident scenarios, and the likely extent of infrastructure required to address these risks.

4.3.2.3 Target Type Selection Summary

The water-cooled rotating target design concept was selected as the baseline in 2016 because of the safety review and internal project evaluations. The tantalum clad was selected based on the extensive operating experience at other facilities with this approach. It was recognized that the tantalum clad was the dominant source of decay heat after several hours and that the ^{182}Ta nuclide was potentially the largest contributor to off-site dose exposures. An R&D program was started to develop an alternative method to protect against water corrosion of the tungsten in beam. Options of "canning" with stainless steel or zircaloy will be evaluated. This would reduce the decay heat and radiological inventory. Adequate heat transfer and acceptable thermal stresses will need to be shown.

4.3.3 Target Design

The description of the target design is broken into the three subassemblies, which are the target disk, the target drive shaft, and the target drive system.

4.3.3.1 Target Disk

Target Disk Functional Requirements

The following are the functional requirements for the target disk:

- Maximize high-Z, high-density material in the neutron production volume to increase brightness.
- Minimize the size of the neutron production volume to increase brightness.
- Minimize the thickness of water-cooling gaps and water shroud material to limit neutron losses and allow the moderators to be as close as possible to the target material.
- Be water-cooled with a temperature difference of approximately 10°C.
- Prevent loss of target material to the water system, which is accomplished by encasing the tungsten target material in another material that is not subject to corrosion in the presence of high radiation levels and water.
- Maximize the operating life of the target by spreading dpa damage.
- Support the beam interface described in Section 4.2.1.
- Allow rotation at a speed that permits each 15 Hz beam pulse to impact the center of the next target segment.
- Operate continuously for time periods greater than 500 h.
- Survive ~100,000 beam trips, or thermal cycles, during performance lifetime.
- Maintain tungsten stress levels below thresholds so that dpa damage to the target shroud is the expected end-of-life mechanism.
- Use a stainless-steel shroud designed in accordance with ASME Boiler and Pressure Vessel Code (BPVC) stress limits.

- Minimize run-out, to less than 1 mm, to allow close positioning of the moderators to the target.
- Ensure the complete target assembly shall have a calculated, minimum natural frequency of 30 Hz.
- Include a “keeper” designed to prevent the disk from deviating from vertical by more than the drive system can accommodate without damage. A seismic event or the deterioration of a single tungsten block are possible causes of a significant out-of-balance condition.

Target Disk Design Description

The target disk is essentially 21 individual targets. The targets are welded to a central hub, from which cooling water is supplied and to which it returns. Synchronous operation will center the proton beam pulses on each of the segments, ensuring uniform thermal loading of the tungsten blocks. The diameter of the disk was optimized to avoid interference with the forward beam lines and to make room for the moderators and reflector in front of the axle. Table 4.7 summarizes the essential target parameters.

Table 4.7. General target parameters

Parameter	Value
Target diameter	1.16 m
Tantalum clad thickness	1 mm
Tungsten/Ta plate thickness	7.0 cm
Plate radial depth	25 cm
Rotation speed	42.9 rpm
Discrete target sections	21
Timing	Synchronous
Shell material	316L
Coolant	H_2O

The complete target disk and an exploded view of an individual target disk segment are shown in Figure 4.41. Each target segment is separated by 1 mm.

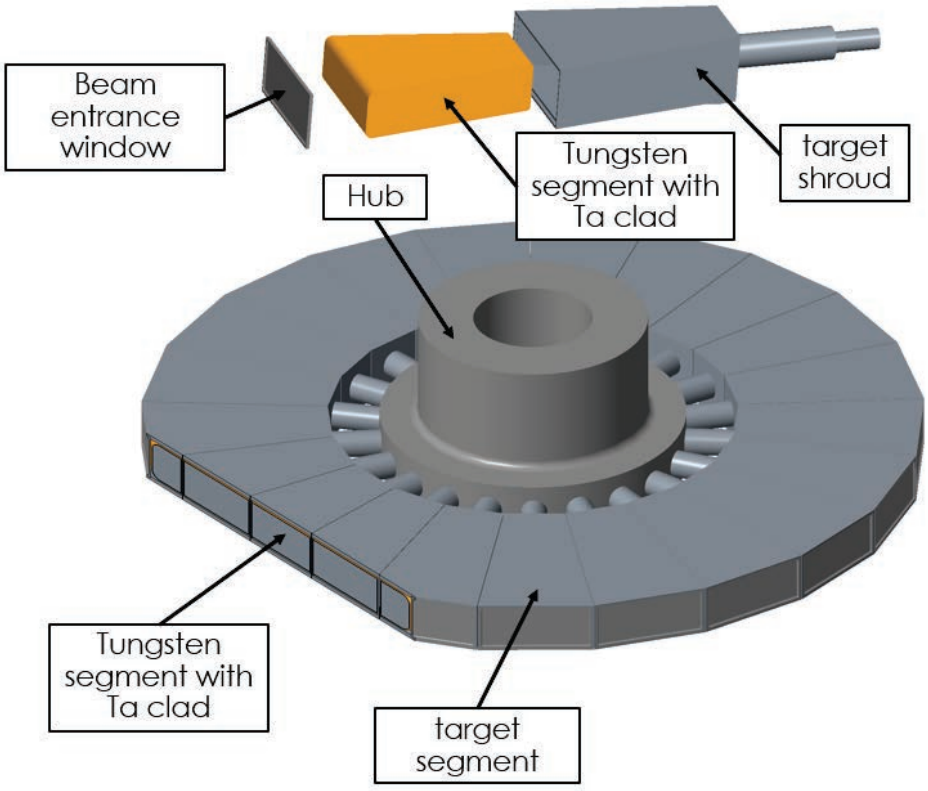

Figure 4.41. Complete target disk with exploded view of an individual target segment.

4.3.3.2 Target Drive Shaft

Target Drive Shaft Functional Requirements

Axle rigidity, alignment, and balance shall be compatible with the operating speed and disk runout requirements of the target system.

Cooling water supply and return shall be routed through the axle with a pressure drop of less than 0.03 MPa. Shielding will be provided in both the water cooling channels and along the outside of the axle.

The target disk and axle shall be replaceable using established remote handling techniques. Features should be included to facilitate disassembly and disposal. Notably, the axle shall be joined to the disk in a manner that facilitates disassembly, rather than with a welded connection.

Spent axles will be shipped in custom containers and disposed of whole.

Target Drive Shaft Design Description

The 4.5 m long, 1700 kg target drive shaft will be a machined and welded unit that will precisely align the target disk to the drive. It is currently envisioned to be a heavy-walled, gun-drilled cylinder with transition sections on either end. A parallel, double helix, water-routing insert will be closely fitted to the inside of the cylinder. The helix will provide both shielding and water passages. It is likely that the insert will be assembled in coupled sections to facilitate easier machining and handling. Drive shaft rigidity, alignment and balance must be compatible with the operating speed and disk runout requirements of the target system.

The target disk and drive shaft will be replaceable using established remote handling techniques. A precision taper-fit joint will connect the axle to the drive unit. The split locking ring will have two sets of bolts. One set will be used to pull the axle securely into the tapered drive collar. A second set of jack bolts in the collar will be used to separate the two assemblies. To ensure repeatable fit-up, a pair of precision manufacturing gages will be maintained by STS for use by manufacturers of replacement drives and axles. This configuration will allow

- Repair/replacement of the target drive system components without replacement of the drive shaft and disk
- Replacement of the shaft and disk with re-use of the target drive system.

Cooling water supply and return will be conveyed through the axle with a pressure drop of less than 0.03 MPa. Shielding is to be provided in both the water-cooling channels and along the outside of the axle.

Differences in the total lengths of replacement drive/axle assemblies due to machining accuracy will be addressed with in situ adjustment of the drive elevation at the interface between the drive frame and vessel lid.

4.3.3.3 Target Drive System

Target Drive System Functional Requirements

The drive shall contain all the target system active components such as control sensors, seals, motors, and bearings. It is expected to have a shorter life than is expected for the passive target disk and axle. Thus, the target drive unit shall be an independent assembly that can be maintained or replaced without requiring removal of the axle or disk.

Cooling water shall be contained with a dynamic seal with a normal leak rate of less than 1 l per 1000 h. Escaping water vapor shall be vented to the target drive room primary confinement exhaust system. Provisions shall be made to route liquid water leaks to the hot process vaults (HPVs) and away from the bearings.

A dynamic vessel gas seal shall be provided with a leak rate of less than 0.05 l/min at a differential pressure of 1 bar.

Provisions for vertical and radial alignment of the target assembly shall be incorporated into the drive unit. Dedicated installation tooling will be provided as needed.

The drive shall be designed in conjunction with the STS controls group to ensure precise synchronization and adequate feedback to prevent damage to the target. Positional tolerance at the perimeter of the target disk shall be less than ±0.25 radians. Momentum matching will also be considered in the design of the drive to ensure smooth operation.

Target Drive System Design Description

The design of the rotating target drive and axle arrangement is based on lessons learned during the design, fabrication, and testing of a full-scale prototypical assembly (Figure 4.42 [Rennich et al. 2010]. The prototype includes an independent overhead drive, water seals, and suspended disk similar in design to that proposed for STS. The still-functional test facility has now been operated for over 6000 h without significant maintenance intervention, leaking, or operating difficulty. Notably, neither the drive motor nor

the primary support bearings were relubricated, based on temperature and vibration monitoring. The low, constant operating speed, uniform torque, and a clean environment ensure minimum wear.

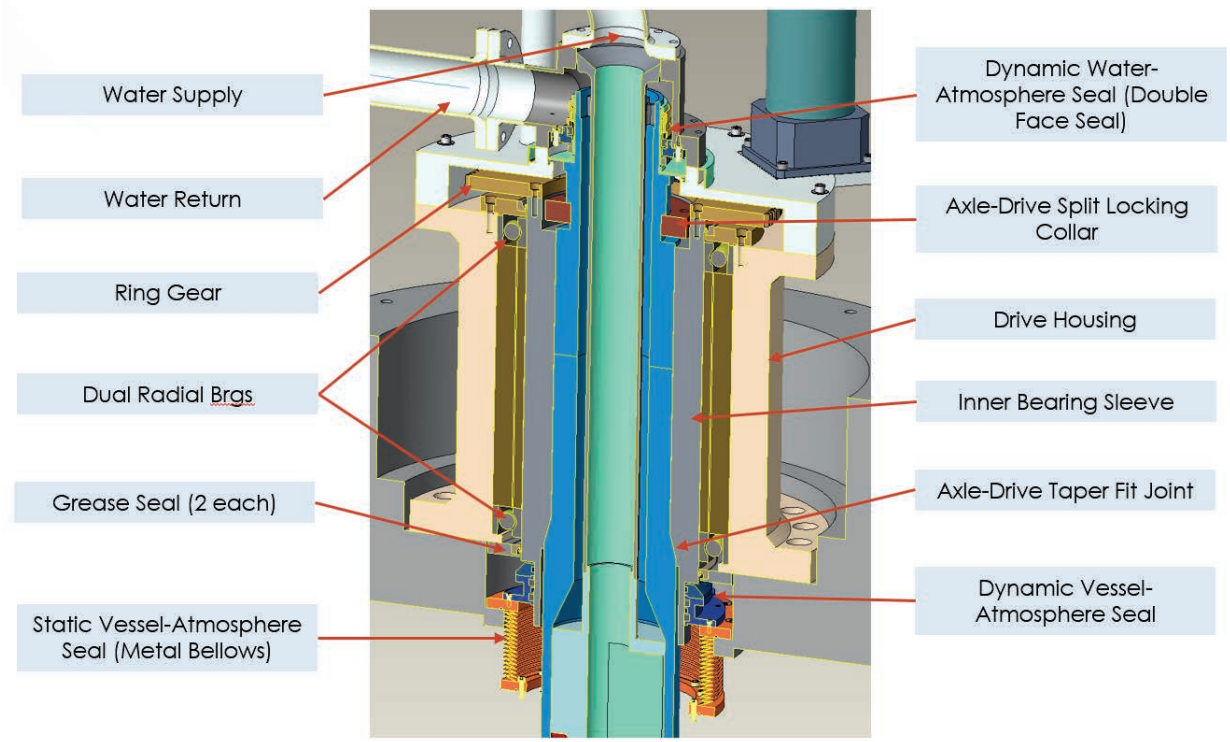

Figure 4.42. STS target drive section view.

There are three noteworthy differences between the mock-up and the proposed STS drive. The radial bearing assembly includes an inner sleeve with a taper fit connection to the axle rather than the flanged connection used in the mock-up. At 4.5 m, the cantilevered length of the STS axle is roughly 1 m longer. And the STS drive motor is coupled via a ring gear rather than directly connected to the axle.

Many observations from the testing program have been applied to the STS target design. The mock-up was operated between 30 and 60 rpm. Initial run-out, as measured with dial indicators positioned on the rim of the disk, was approximately 0.20 mm with an unpredicted peak of 0.55 mm at 34 rpm. After 5400 hours, the overall run-out was the same, whereas the peak at 34 rpm had decreased to 0.30 mm. Although this was not significant, it points to the importance of constructing and testing the STS drive system with enough lead time to make compensating adjustments for real-world factors.

By design, dynamic face seals require a small amount of leakage; this was indicated in the mock-up by the loss of an estimated 1–2 l of water during approximately 4000 h of testing. Forced-air ventilation of the drive shroud will both remove the water vapor and provide cooling. The ventilation air will be contained in the STS target room and hot offgas system. The proposed drive includes a drain to channel significant liquid leaks to the low-level liquid waste (LLLW) system. In general, the drive assembly water containment system must be designed to fit into the facility containment system and allow for continued operation in the event of nuisance water leaks. The mock-up seals were cooled with a fan but experienced temperature differences from the ambient varying around 4°C and spikes up to 12°C. Note that the normal operating seal temperatures were between 30 and 40°C. This is well below the seals' temperature rating of 200°C. To minimize the accumulation of contamination in the dynamic seal cavity, the water discharge

pipe will be mounted below the level of the seal. Features designed to promote turbulent flow in the seal cavity will also be added to the rotating axle interface.

The measured amperage, applied at a constant 460 V, decreased constantly throughout the test period. The initial measurement of roughly 1.76 A corresponds to 810 W, while the final amperage of about 1.72 required 791 W, a 2% decrease. Virtually all friction occurs in the face seals; the mock-up has two seals whereas STS will have only one, so it is assumed that the drive torque will be less. The drive/reducer was protected with a unidirectional clutch that allowed the axle to coast freely, preventing back-driving during a power or control failure. With this unit in place, the time for the target disk to coast from 50 rpm to zero after motor power was intentionally removed was initially measured at 26 seconds. The time at the end of the testing cycle was 29 seconds.

Restart after an extended shutdown is a normal target operating function. It was demonstrated in the mock-up 5 months after the conclusion of the long-duration test run and repeatedly over the life of the facility. System performance consistently returned to normal with only minimal change in the measured parameters.

A conservative neutronic analysis calculated that the unshielded radiation level of the target cooling water flowing through the drive unit is 10 Gy/h. Figure 4.43 shows the radiation levels inside the drive unit mapped from this analysis.

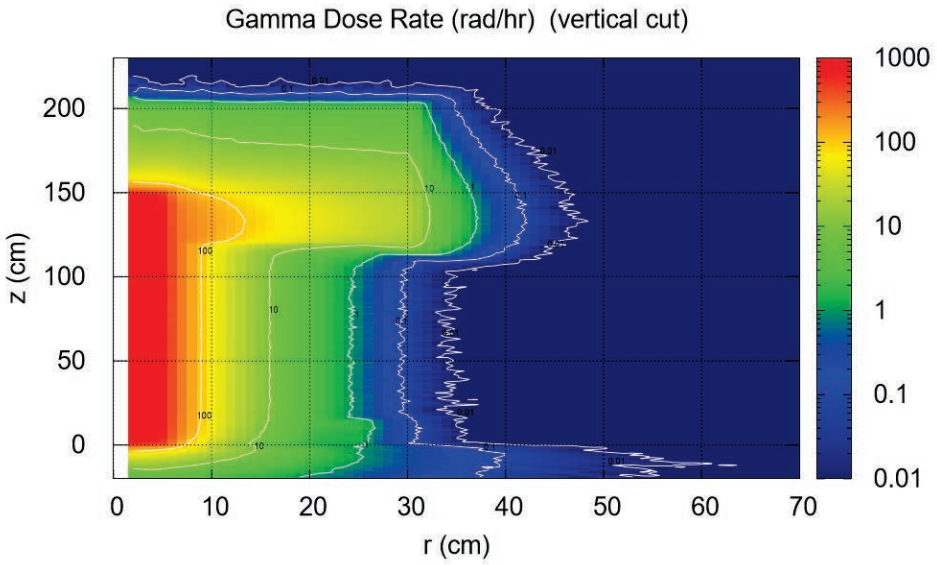

Figure 4.43. Radiation doses inside the drive unit due to activated target cooling water.

A local shielding shroud surrounding the drive unit and the return water pipe will reduce the radiation to the target drive room to less than 0.01 Gy/h. This will protect sensors, lights, and other components required inside the bunker. It will also help to minimize the thickness of the target drive room shield walls (currently about 100 cm of HDC).

The drive will be segmented into modules to enable replacement of individual components without removing the entire assembly (see Figure 4.44). The motor/reducer and the water seal are assumed to have lifetimes that are shortened by failures unrelated to radiation; therefore, they will be mounted on top of the drive assembly. The motor will be a conventional servo drive with an integral gear reducer with a ring and pinon gear interface to the axle. Provisions such as bevel gears and anti-backlash features will be used to limit slack in this connection. Based on the torque requirement for the full-scale mock-up and the

addition of an environmental seal, a minimum 2 horsepower, continuous-rated motor will be required, although motor sizing will also be dependent on momentum matching requirements. A servo drive with on-board encoder and electronics is required to match the target rotation with the accelerator. Because the servo is susceptible to radiation damage, it will be located outside the local shielding shroud. A backup, independent target rotation feedback sensor will also be located in the same shielded location. Based on experience with the FTS chopper drives, the control range of an encoder feedback control system will result in a positional accuracy at the perimeter of the target of approximately ±2.5 mm. Slack in the gear coupling could add to this but is currently assumed to be less than ±1.0 mm. The target disk segments will be wide enough to accommodate ±5.0 mm of horizontal deviation. A more sophisticated drive unit could be employed to reduce the radial deviation of the drive if necessary. The proposed full-scale target mock-up will provide the necessary design validation.

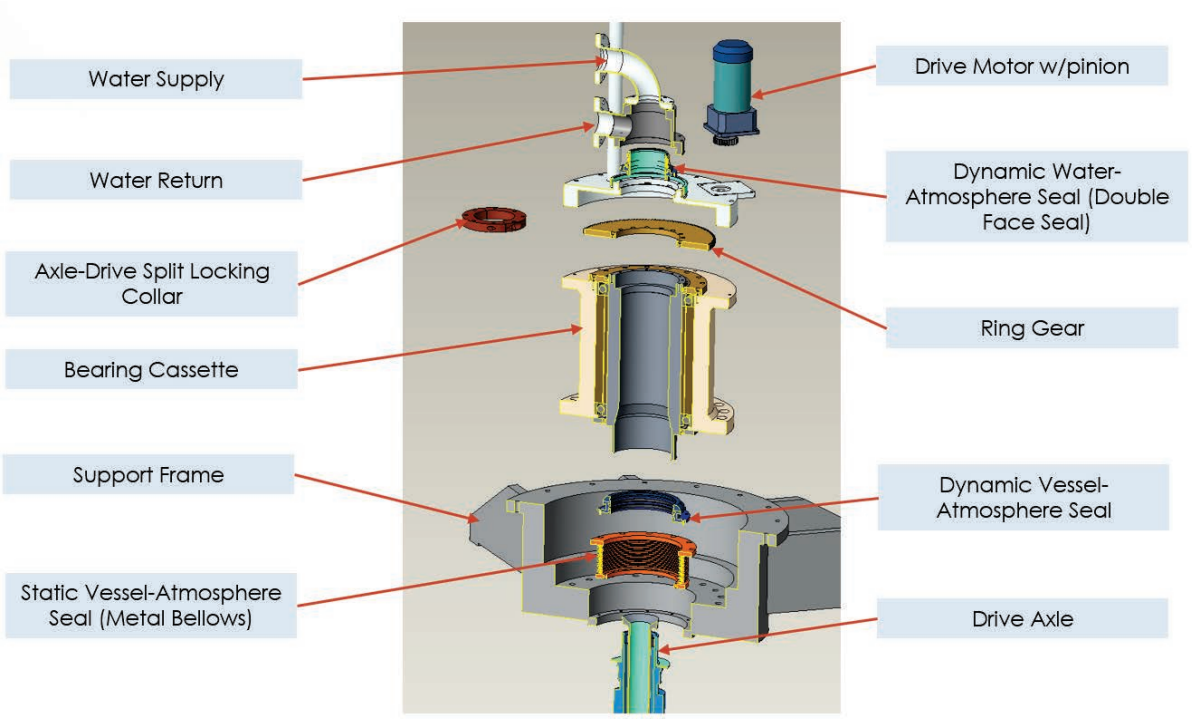

Figure 4.44. Target drive exploded view.

A single commercial graphite-on-stellite face seal will contain the cooling water in the target axle assembly. The John Crane 676 used in the mock-up is rated for a pressure of 0.83 MPa, well above the dead head pump pressure of 0.35 MPa. The proposed seal assembly will have several static, elastomeric O-rings with a radiation tolerance of 104 to 105 Gy. The calculated dose to the seals will be roughly 5 Gy/h, giving the seals a life of 4 years. In reality, a longer life is expected because experience has shown that static seals have significantly longer lives than predicted. The water return line will be positioned at the low point of the seal to promote flushing of entrained contaminates. Additional features may be added to ensure turbulent flow in the vicinity of the seal to further limit accumulation of contamination. A second water seal will be eliminated by separating the supply and discharge flows with a small gap with an acceptable bypass flow rate, currently estimated to be less than 5% of the total.

A pair of radial/thrust bearings mounted between the rigid structure and a heavy walled inner sleeve will support the axle and disk. The bearing and integral ring gear will be lubricated with a radiation-tolerant grease rated for 106 Gr. The grease will be contained in the bearings with two conventional nitrile rubber

seals with a radiation tolerance of roughly 105 Gy, giving them a predicted life of greater than 10 years based on the calculated exposure of approximately 1 Gy/h. The radiation-tolerant grease will be subject to normal decomposition; therefore, a manual regreasing capability will be built into the drive.

Sealing the vessel environment is considered the most significant target drive design challenge. In addition to the relatively high radiation dose of roughly 5 Gy/h, dynamic gas seals are inherently difficult. Installation and maintenance will be complicated by the close tolerances required. The lifetimes of contacting sealing faces will be limited by the poor cooling and lubricating capabilities of gas. And the sealing materials are necessarily delicate (e.g., carbon rings or elastomers). Considering these limitations, three basic options are available:

- Close-fitting, packing rings that have not proved successful for vacuum sealing. Radiation-tolerant graphite packing rings could be used. However, packing rings produce significant frictional heating and are subject to wear.

- Ferrofluidic seals that are delicate and complex, possibly making them inappropriate for the large, difficult-to-handle target drive. Tests performed at Brookhaven National Laboratory with gamma energies in the range of 2 to 9 MeV indicated ferrofluidic seals have a radiation tolerance of greater than 2×10^4 Gy, giving an STS vessel seal a predicted life of less than 1 year [Simos 2017].

- Close-fitting non-contact rings with intermediate vacuum pumping.

The latter option is currently considered the best choice for the STS drive. Two sets of graphite rings with sufficient intermediate vacuum pumping could be developed in the proposed mock-up drive unit. Graphite rings have a proven high radiation tolerance but would require precision machining and fit-up.

A static metal bellows will be required to minimize alignment forces in the dynamic seal. In the current drive configuration, the bellows and dynamic seal would be installed and aligned before the drive unit was installed. If a dedicated drive installation tool were used, the seal subassembly should not receive excessive loads.

Location of the vessel seal under the drive significantly complicates maintenance. The option of positioning the seal above the bearings will be considered in the next phase of design. In the latter arrangement, the bearing grease and grease cavity would become part of the vessel environment. This configuration may be acceptable for low-differential-pressure operation.

A set of sensors will monitor inlet and discharge water temperatures, bearing temperatures and vibration, coolant flow, leak detection, and rotation speed. Each of the sensors will be mounted for independent replacement. Thermocouples and “spark plug” leak detectors normally have long lives in radiation environments ($>10^6$ Gy). Nevertheless, all the thermocouples and leak detectors will be individually replaceable during a weekly 1 day shutdown. Vibration sensors are vulnerable to radiation and therefore must be located on extension rods outside the local shielding, even though this arrangement will reduce their sensitivity.

4.3.4 Target Analysis

4.3.4.1 Introduction

Pre-conceptual designs for a solid rotating target were developed for STS and reviewed in 2017. At the time, most of the target structural analysis was for quasi-steady state operation. It was recognized that short-pulse dynamic loading could be important, but design analysis was terminated at a very preliminary

stage because of a lack of funding. The design as of the end of 2017 included a set of thin plates near the front and a solid wedge in the rear for each of 30 wedge elements. The objective of the plates was to reduce the peak dynamic stress, but detailed analysis had not been done. The current effort evaluated this design and found significantly higher stresses than desired. Design options were then developed to reduce the stresses. It was found that a design with 21 solid wedges with a larger beam could reduce the stresses to acceptable levels with minor impact (<5%) on the moderator performance.

4.3.4.2 2017 Design Evaluation

Design Configuration

The 2017 target design was based on a compact beam with an area of approximately 30 cm^2. The mechanical design included 30 tungsten segments contained within 15 subassemblies (Figure 4.45).

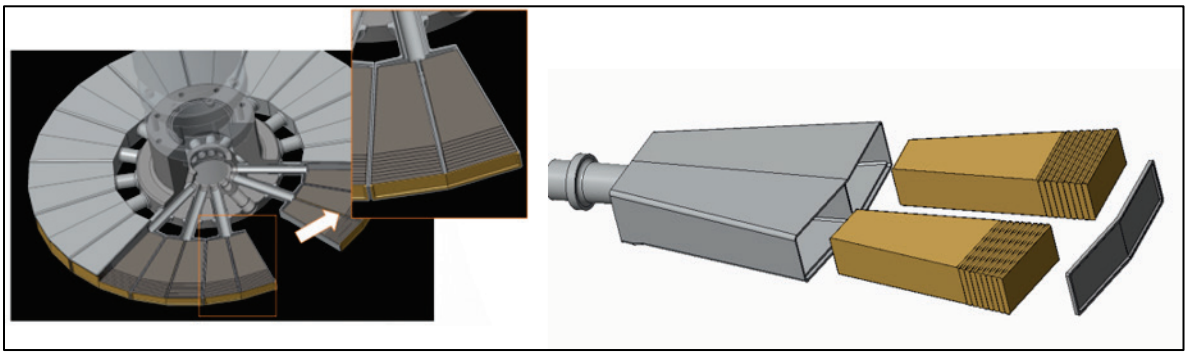

Figure 4.45. 2017 segmented target layout.

The vertical height of all tungsten pieces with tantalum clad was 5 cm. Each segment contained eight 6.35 mm thick tungsten plates with 0.5 mm tantalum clad on facing surfaces at the top, 2 mm clad on the side, and one thicker wedge in the rear with the same clad thickness. There was also a 1 mm gap for water between the plates. The proton was to be synchronized to hit the middle of each segment with a nominal size of 4 by 7.5 cm.

Preliminary 2017 Design Evaluation

An initial Abaqus model was made using linear tetrahedral mesh elements. Energy deposition profiles and the corresponding temperature rise from a pulse were generated by MCNP calculations for a similar geometry [Habainy 2018] and mapped onto this model. The mesh and the peak temperature rise of approximately 32°C in the tungsten after a pulse are shown in Figure 4.46.

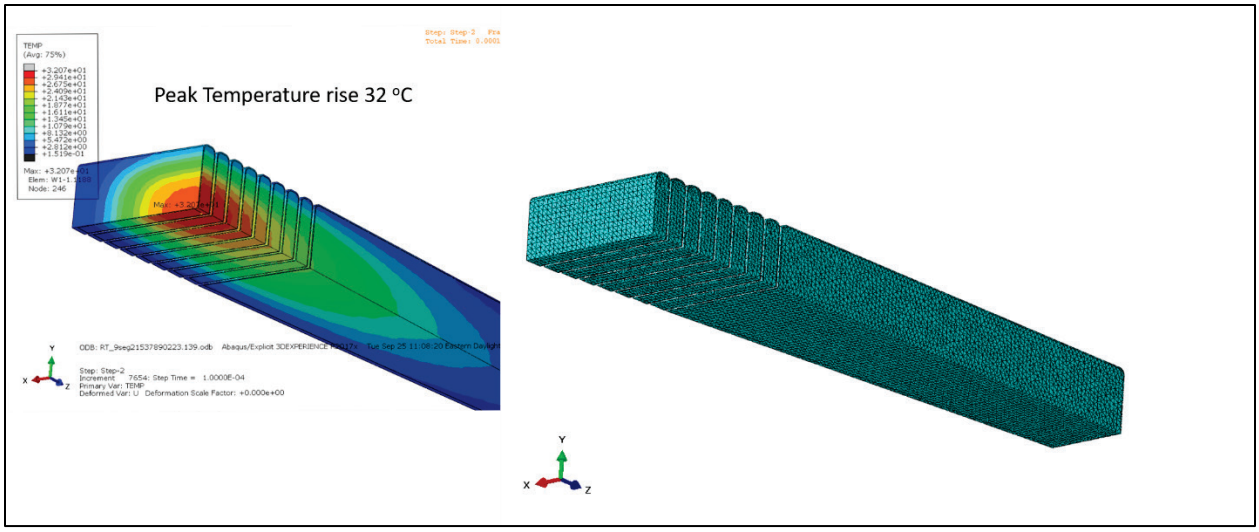

Figure 4.46. Tetrahedral mesh and temperature rise in quarter symmetric model.

The dynamic von Mises stress was evaluated by applying the temperature rise linearly over 10^{-6}s and evaluating the response over 120 μs. The peak stress was approximately 250 MPa at 93 μs (Figure 4.47).

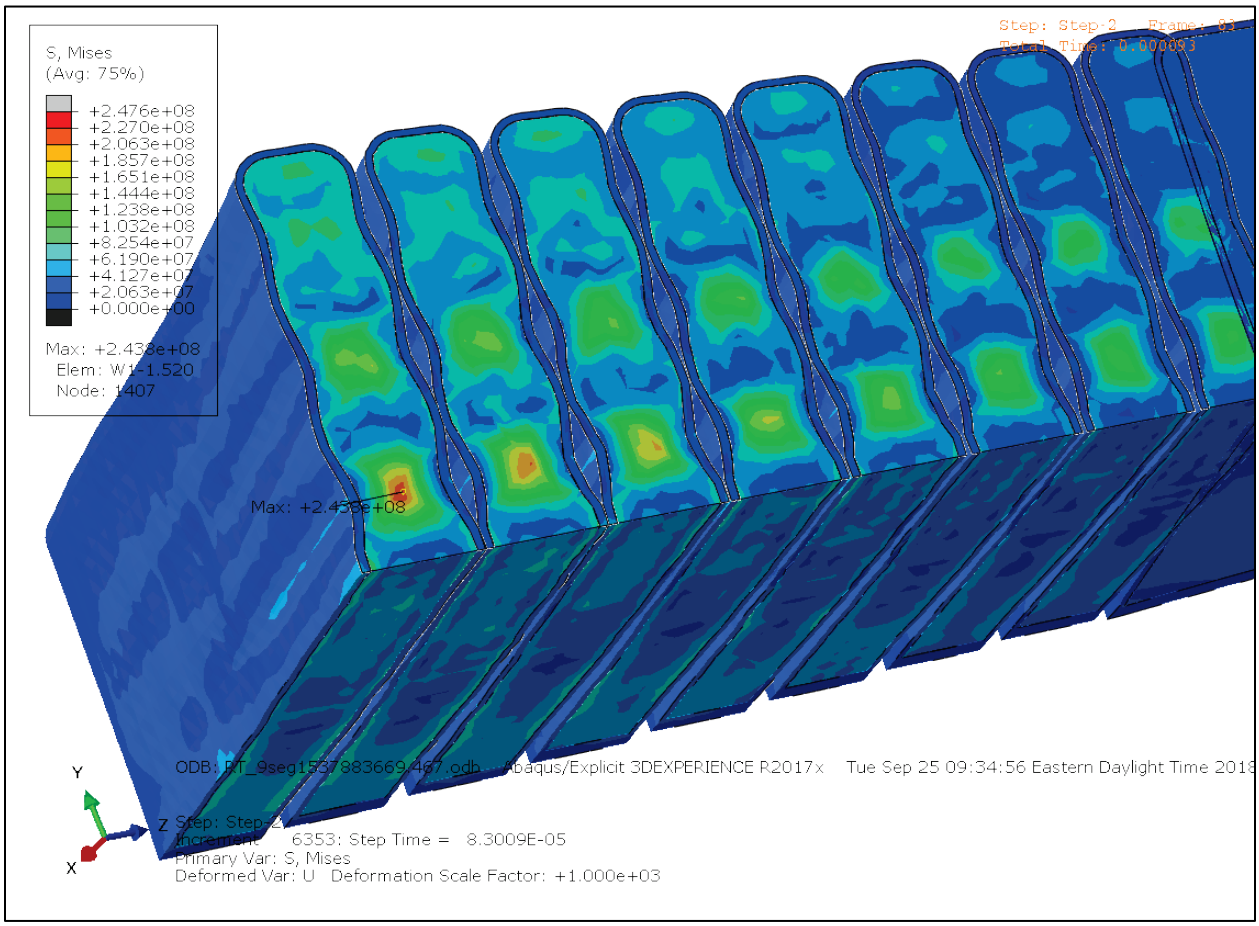

Figure 4.47. Peak stress of 248 MPa at 93 ms.

This peak was over two times what was expected and seemed to result from a constructive interference of different modes. To confirm the results, a more refined model of the first plate was made using linear hexagon elements (Figure 4.48).

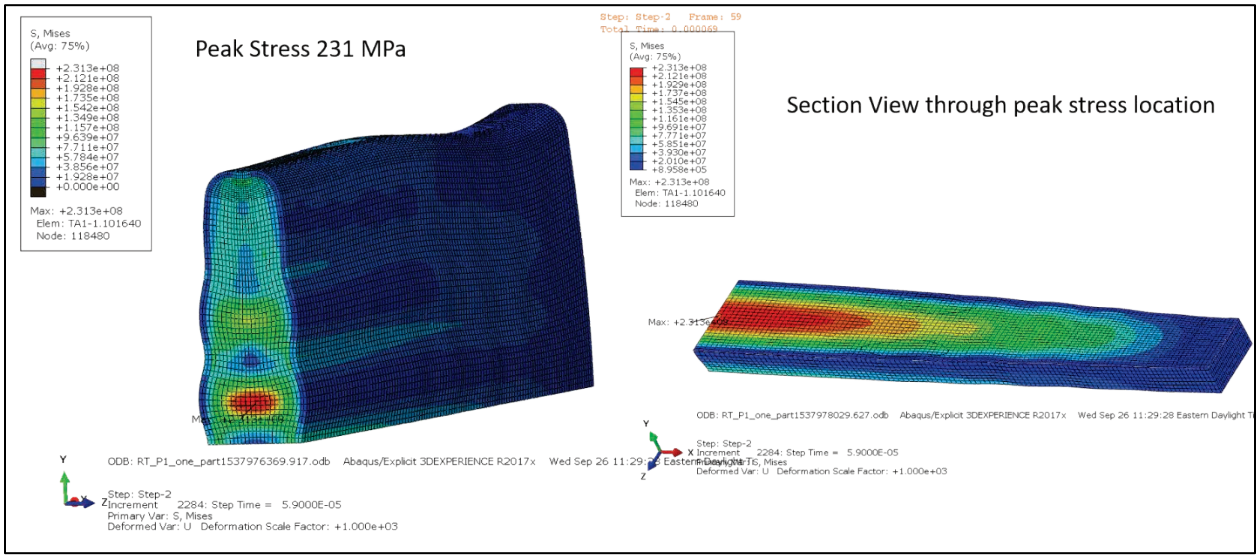

Figure 4.48. Peak von Mises stress for first plate of 231 MPa at 69 μs with hex mesh.

Although the more refined hex mesh produced a lower stress, the stress was still well above a desired maximum of 100 MPa. A thinner 4 mm thick plate was also evaluated; but it showed a peak stress of 154 MPa, still well above the desired limit (Figure 4.49).

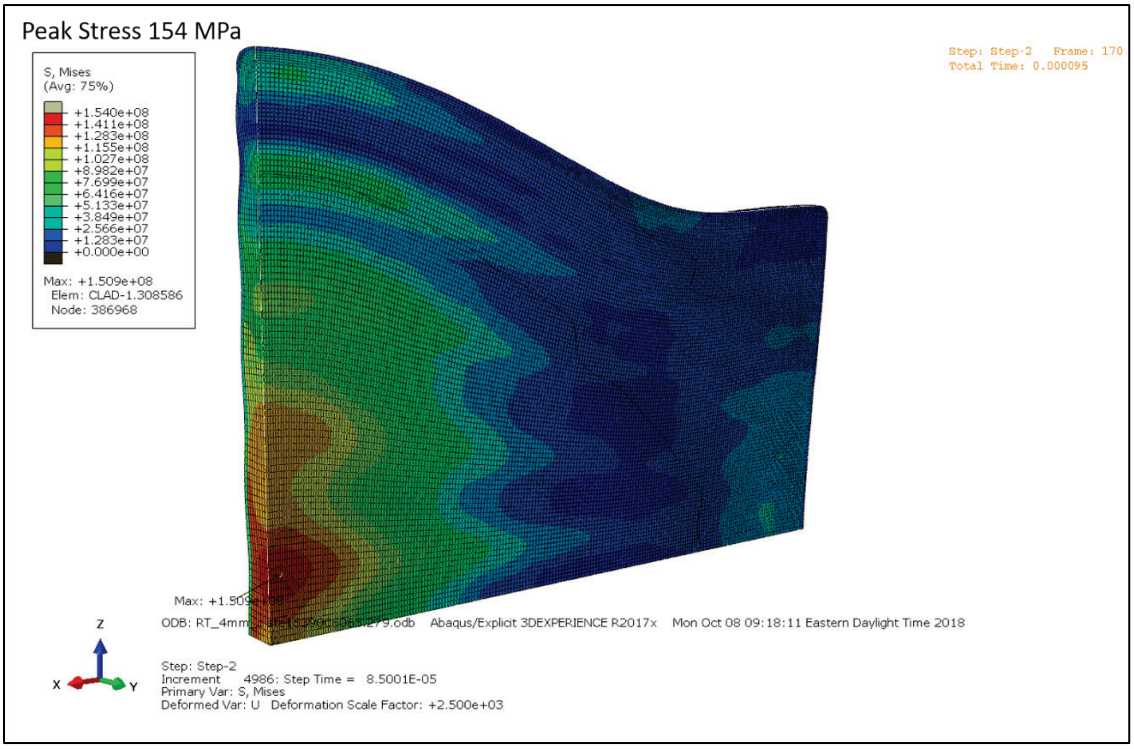

Figure 4.49. Mid-plane cut of 4 mm thick tungsten plate with .5 mm tantalum clad showing peak von Mises stress of 154 MPa at 95 ms.

Going to thinner plates was not considered because the tantalum fraction would become very high, increasing the radiological inventory of ^{182}Ta, increasing the decay heat, and reducing the neutron production.

4.3.4.3 Solid Wedge Model

Solid Wedge Abaqus Model

The dynamic stress for a single pulse for a solid wedge based on the 2017 segment design was evaluated. For this model, the tungsten was 48 mm thick with 0.5 mm tantalum clad on the front surface and 2 mm on the top and sides. Figure 4.50 shows the initial model.

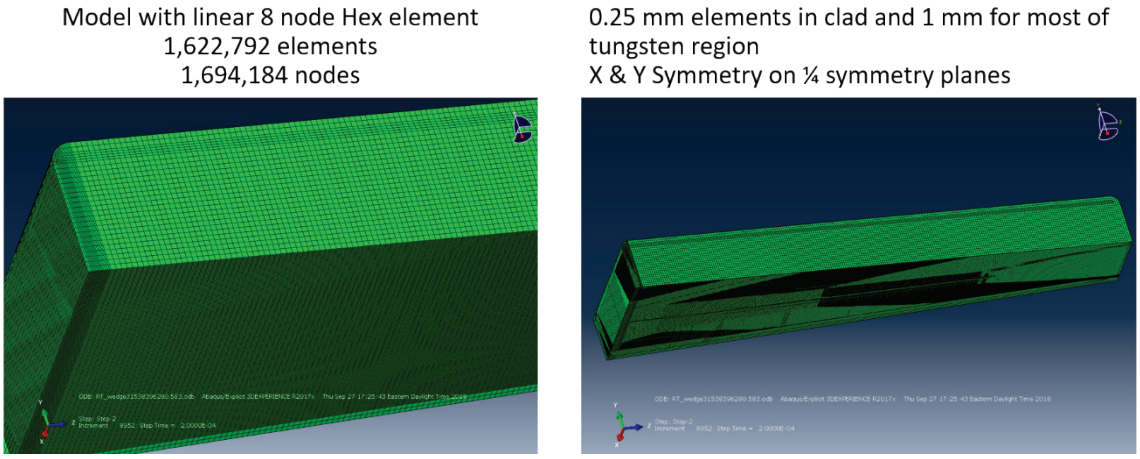

Figure 4.50. One-fourth wedge model based on 2017 layout.

The temperature rise distribution was applied linearly over the first μs and held constant after that. The tantalum heating as scaled as 83% of the tungsten heating. The initial temperature and the pressure at 1 μs are shown in Figure 4.51. Some relaxation during the pulse can be seen in the tungsten near the front wall.

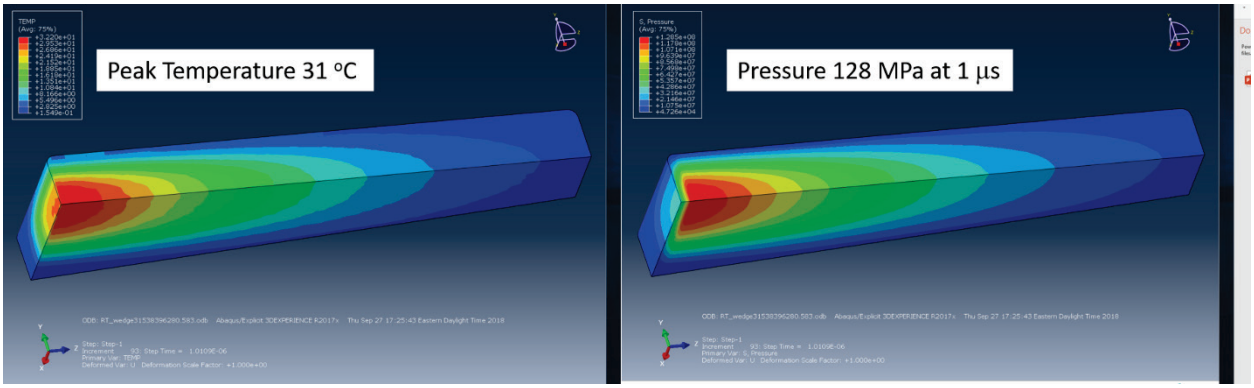

Figure 4.51. Target temperature rise and pressure at 1 μs.

Wedge von Mises Stress Results

The stress and deformation were calculated for 220 μs. The peak von Mises stress overall and the peak on the midplane are shown in Figure 4.52 with displacements magnified.

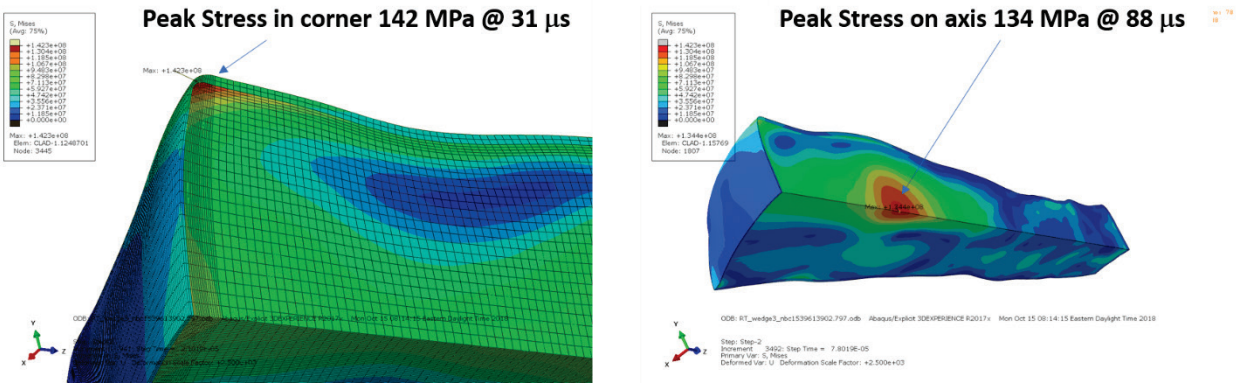

Figure 4.52. Target peak von Mises stress in corner and on mid-plane.

Because the peak stresses were well above the desired 100 MPa for the alternating stress range, several options for a broader beam with a lower peak intensity and a larger target were investigated.

4.3.4.4 Beam Profile Investigation

An initial scoping study was done for three larger beam profiles and for the original profile with new target models [Habainy et al. 2018]. The energy deposition in the target and the moderator performance used a previous target model, which had two radial tungsten zones with a stainless steel ring between them for support of the top and bottom disks. The beam profiles were defined by super-Gaussian functions with the sigma and n values as shown. The cases are given below.

CASE	Solid model	Max. dT (°C)	0.95 extent vertical (cm)	0.95 extent horizontal (cm)	Sigma vertical (cm)	Sigma horizontal (cm)	n vertical	n horizontal
1	Baseline	30.12	4	7.6	1.65	3.04	4	3.9
2	1 cm taller	25.17	4.8	7.6	1.98	3.04	4	3.9
3	1 cm+ 20% wider	21.06	4.8	9.2	1.98	3.648	4	3.9
4	1 cm+70% wider	15	4.8	13	1.98	5.168	4	3.9

The target model used and neutronic mesh area on the vertical midplane are shown in Figure 4.53. Energy deposition was evaluated over the darker mesh region shown.

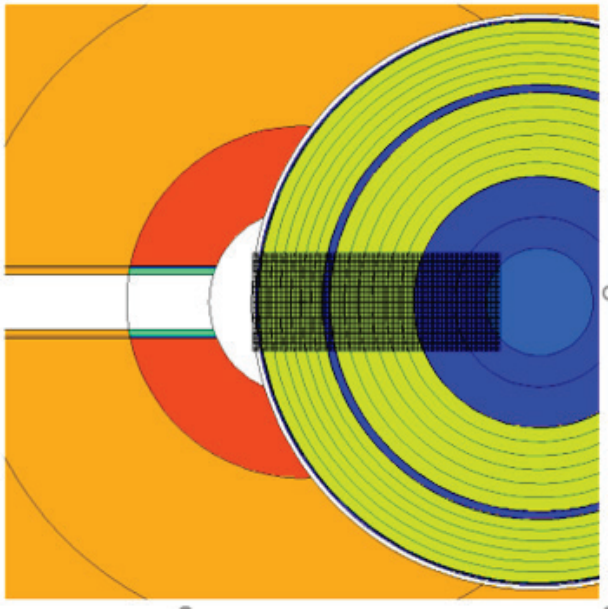

Figure 4.53. Target neutronic model—steel regions shown in blue and tungsten in yellow.

Mapping the temperature rise from the new neutronic model on the target shows a slightly lower peak and a lower rise where the steel ring is located; but the resulting peak stress on the axis is very close to previous results (Figure 4.54).

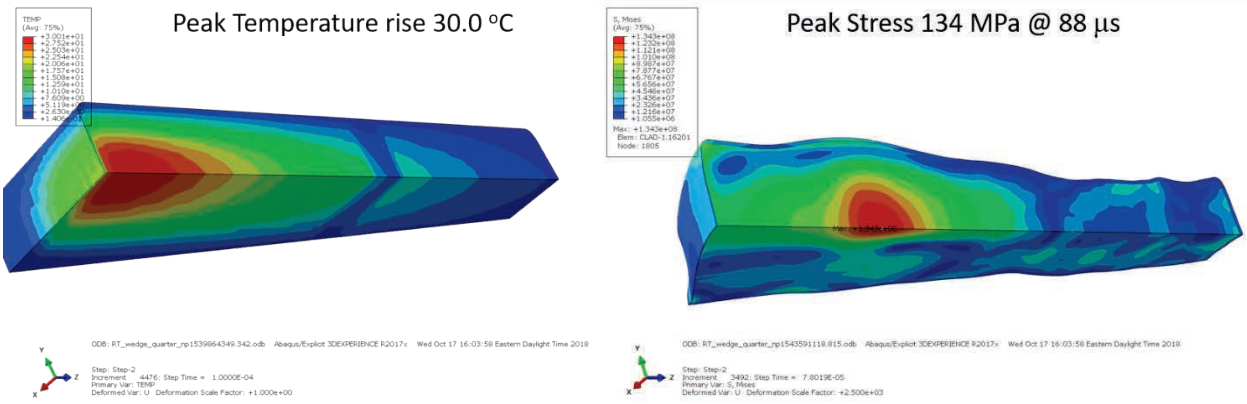

Figure 4.54. Temperature rise and peak von Mises stress with new neutronic model.

Abaqus models for cases 2, 3, and 4 were made using linear hex elements with a nominal mesh size of 0.75 mm for most elements. All models included 0.5 mm tantalum clad on the front surface and 2 mm on the remaining sides. The dynamic response was calculated over 110 µs and the peak von Mises stress identified. The results are summarized below.

CASE	Solid Model	Max. dT (deg. C)	Max. Von Mises (MPa)
1	Baseline	30.12	**134**
2	1cm taller	25.17	**106**
3	1cm+ 20% wider	21.06	**101**
4	1cm+70 % wider	15	**69**

The last case with half the initial current density and a peak temperature rise of 15°C gave the lowest stress level. Figure 4.55 shows the temperature distribution and the von Mises stress distribution at 84 μs which is when the peak stress of 69 MPa occurred.

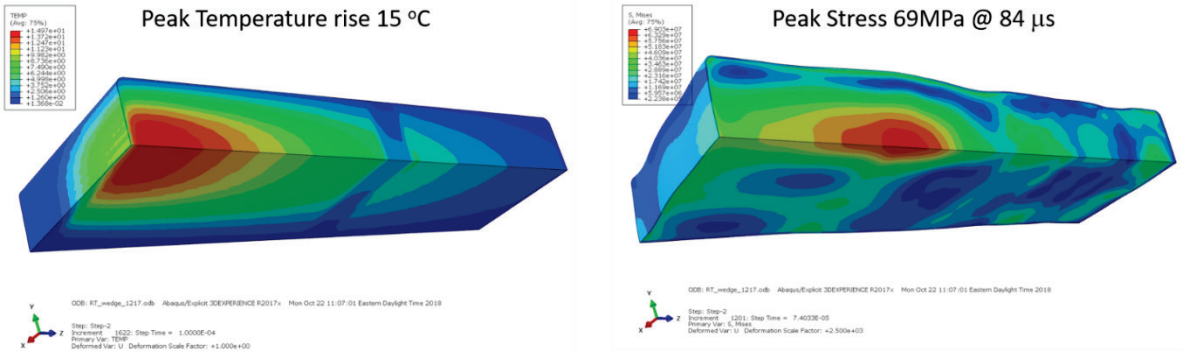

Figure 4.55. Temperature rise and stress distribution for the case 4 target.

The larger beam profile for case 4 was chosen for use for the baseline to give margin for additional thermal stresses and irradiated material properties.

4.3.4.5 Baseline Target Analysis

Target Geometry

The target model used for case 4 was wider than needed for the beam and would have required a larger target overall diameter. A new model was made assuming there would be 21 segments with nominally the same overall target diameter. Each tungsten wedge had a 1 mm tantalum clad on all external surfaces. The radius at the top front edge was increased to reduce stresses in that area. The wedge would be surrounded by a stainless steel shell and water cooled. Figure 4.56 shows a segment including the steel shell and water flow path.

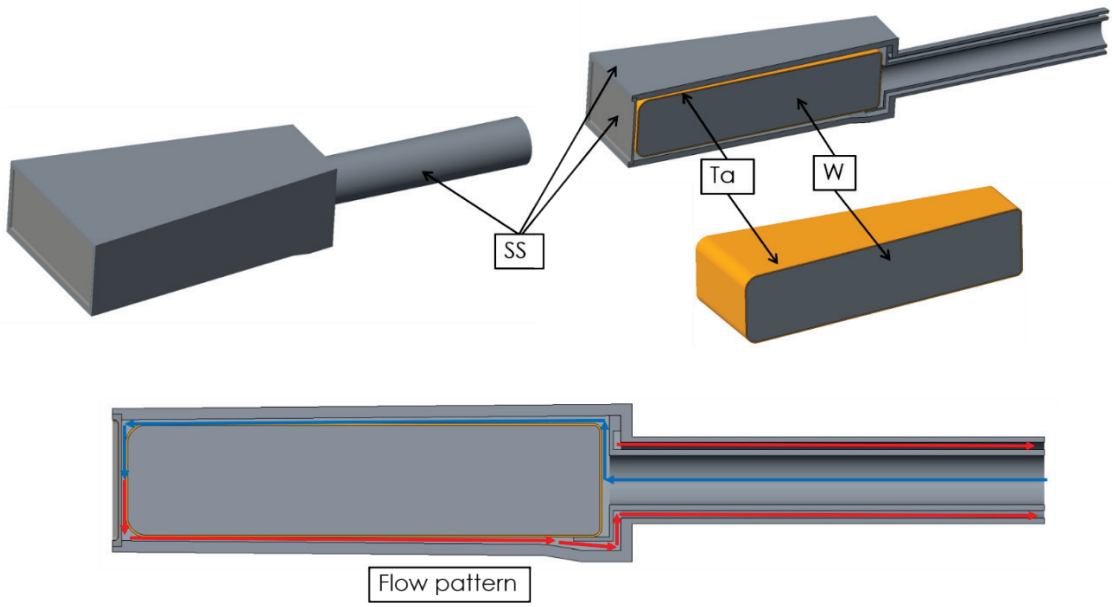

Figure 4.56. Target segment and water flow path.

The 21 target segments are arranged as shown in Figure 4.57. The radius from the center of the shaft to the center of the front tantalum surface is 0.57 m. Also shown is the location of the moderators above and below the target and representative neutron beam lines.

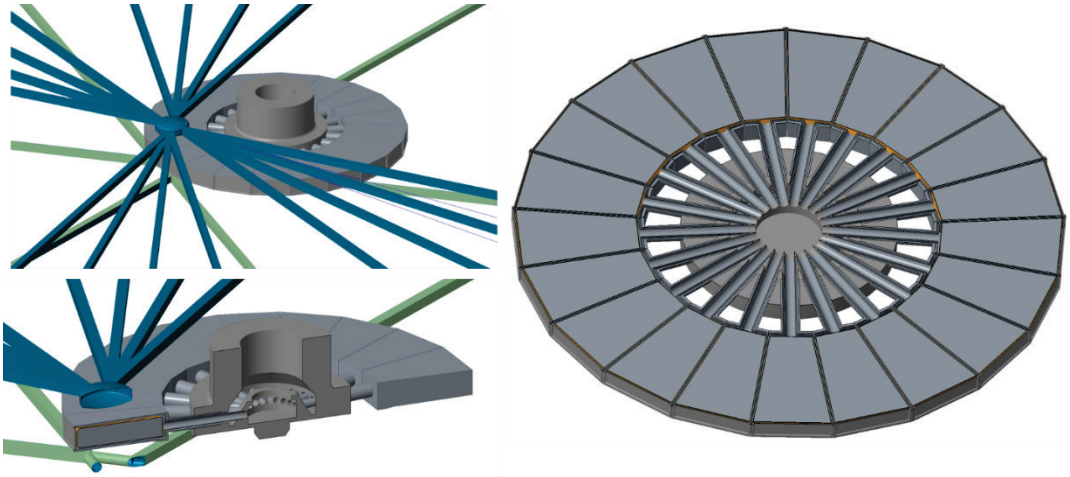

Figure 4.57. Target disk assembly with 21 segments and moderator relative location.

The 21-segment design with a 15 Hz beam pulse frequency gives a pulse repetition rate on a segment of 1.4 s or 0.714 Hz and 42.8 rpm for the disk. The beam pulses are to be synchronized to hit the center of each segment.

Material Properties and Design Limits

Room-temperature Unirradiated Properties

The unirradiated room-temperature material properties used for tungsten and tantalum, given in Table 4.8, follow what was used for the ISIS clad target analysis [Wilcox 2016].

Table 4.8. Tungsten and tantalum room-temperature properties

Property	Tungsten	Tantalum
Density (kg/m^3)	19250	16600
Young's modulus (GPa)	398	188
Poisson's ratio	0.28	0.35
Instantaneous coefficient of thermal expansion (/K)	4.5×10^{-6}	6.3×10^{-6}
Specific heat capacity (J/kg·K)	128.3	139
Thermal conductivity (W/m·K)	174.9	57.2

Irradiation Effects on Tungsten Properties

A study of material properties was done for the ESS project and included the effects of irradiation on tungsten thermal conductivity and stiffness [Habainy 2018]. Figure 4.58 shows available data on thermal conductivity with irradiation.

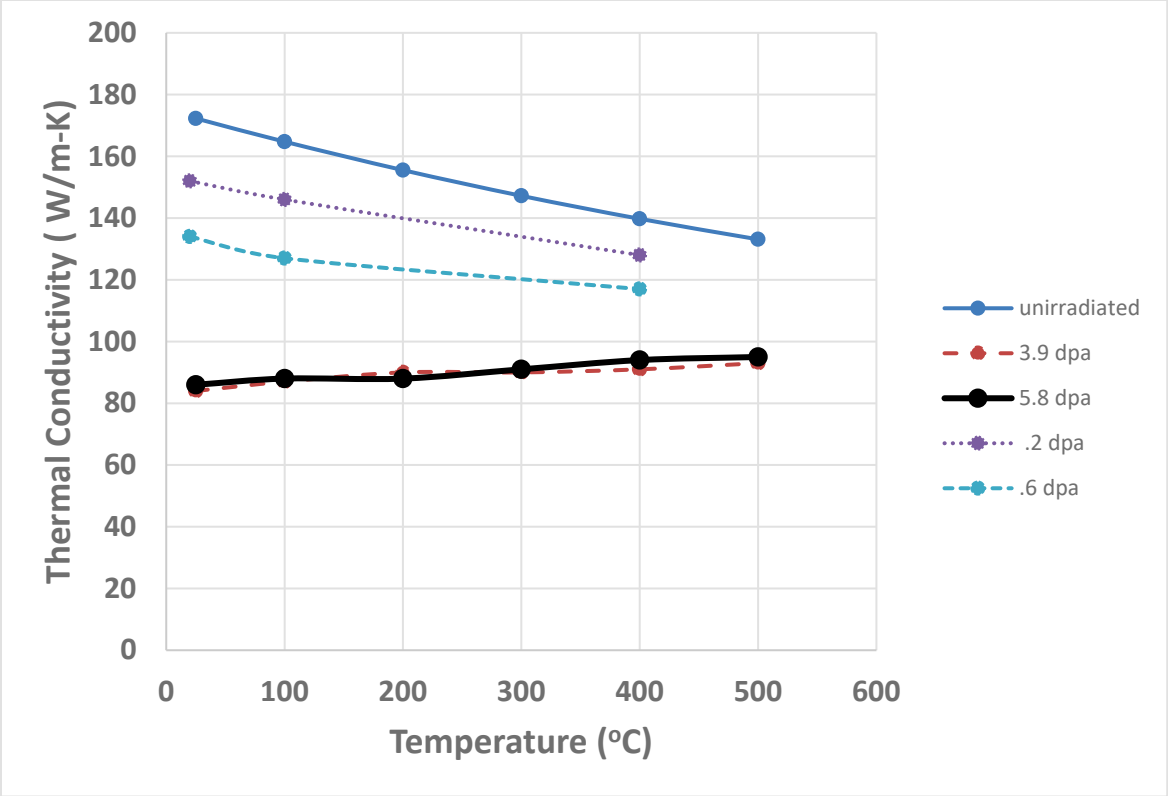

Figure 4.58. Thermal conductivity versus temperature with irradiation effects.

The Abaqus analysis of temperature and displacement for irradiation used the value of 87 W/m·K corresponding to the 100°C data with approximately 3.9 dpa or above. Reference [Habainy 2018] also found that hardness data after ion beam irradiation of small samples showed an increase of approximately 15%. For an estimate of the effect in ESS, an increase of 20% in stiffness was assumed. For STS, a 20% increase was also assumed giving a Young's modulus of 4.776×10^{11} Pa.

Design Limits

Some considerations to be considered in setting tungsten design limits are

- Tungsten has been shown to become brittle after irradiation (ductile-to-brittle-transition temperature shift).
- Limited mechanical fatigue data after irradiation are available.
- ESS testing of unirradiated fatigue life typically had minimum S_a for $10^5 - 10^6$ cycles of about 200 MPa[1].
- Three-point bend tests on irradiated samples at 25°C had an average failure strength of 304 MPa[2] .
- Ultimate strength is typically ~500 MPa but varies with fabrication methods, and at least one test on irradiated material failed at 60 MPa.
- ISIS has operated a target successfully with estimated stresses on the order of 200 MPa.

Another consideration is the experience and limits set at the ISIS facility with tantalum-clad tungsten targets, as summarized below [Wilcox 2017].

	TS1	TS2	TS1 Upgrade	Design Limit
Peak Temperature (deg C)	184	249	189	N/A
Peak Heat Flux (MW/m^2)	1.98	2.43	2.02	3
Tungsten Stress [Beam Only] (MPa)	89	157	98	275
Tantalum Stress [Beam Only] (MPa)	114	90	106	75
Tungsten Stress [HIP+Beam] (MPa)	207	191	165	275
Tantalum Stress [HIP+Beam] (MPa)	200*	200*	200*	75

Notes:
- Tantalum will yield at 200MPa
- TS1 and TS1 upgrade were modelled with MCNPX+CFX+ANSYS, 200μA
- TS2 was modelled with FLUKA+CFX+ANSYS, 40μA
- HIP pre-stress modelled assuming 500°C 'lock-in' temperature

The ESS project has been evaluating unclad helium-cooled tungsten. The limits it has set for tungsten are 100 MPa for mean stress and 50 MPa for alternating stress (Sa) [Habainy 2018].

The STS limit for peak stress will be 275 MPa based on the ISIS operating experience. The allowable alternating stress limit has not been set. It will be between the 50 MPa limit ESS is using and the 200 MPa seen for failure in fatigue testing.

Baseline Abaqus Model

A quarter symmetry model was made, as shown in Figure 4.59, including the tungsten and 1 mm thick tantalum clad. The overall width (x direction) at the front is 82.88 mm with a tungsten radius of 10 mm at the top front edge and 4 mm at the rear top edge. The tungsten radial length on the axis is 250 mm. The tantalum outside radius on the front center is 570 mm. The mesh is nominally 1.0 mm in the tungsten. The tantalum mesh had two elements through the thickness for all regions. Linear hex elements were used with a total of 529,815 elements in the model.

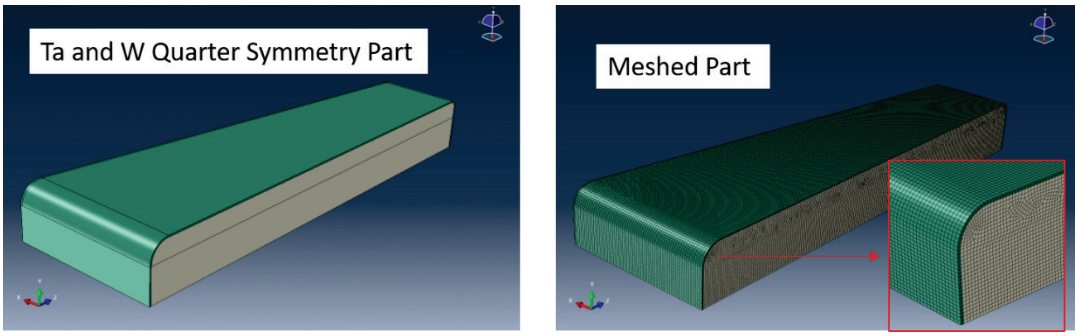

Figure 4.59. Baseline quarter symmetry part model and Abaqus hex mesh.

The same part and mesh model were used for two types of analysis. First a coupled thermal-displacement model with C3D8T elements was used to obtain the quasi-static temperature and stress distribution after multiple pulses. The stress distribution from this model just before a pulse was then used as an initial condition for a dynamic stress analysis with C3D8R elements for up to 310 μs.

Multiple Pulse Coupled Temperature-displacement Model

The energy deposition profile for case 4 was assumed to be deposited over 10^{-3} seconds to give a heating rate during a pulse. The Abaqus analysis used 30 steps to model 15 pulses. Heating was assumed for one step over 10^{-3}s with the next step lasting 1.399 seconds with no heating. This sequence was repeated 15 times. The initial part temperature was assumed to be 30°C. Water cooling was modeled with a surface heat transfer coefficient of 8×10^{3} W/m^2·K on the top and front surfaces with a bulk fluid temperature of 30°C. The assumed heat transfer coefficient corresponds to about a 1.2 m/s flow velocity in a 2 mm flow channel at r = 0.55 m and a total flow for all 21 segments of about 120 gpm. Figure 4.60 shows the assumed heat transfer model. The flat rear outer tantalum surface was assumed to be restrained in the axial direction for the thermal analysis. Displacement symmetry was assumed on the horizontal and vertical midplanes.

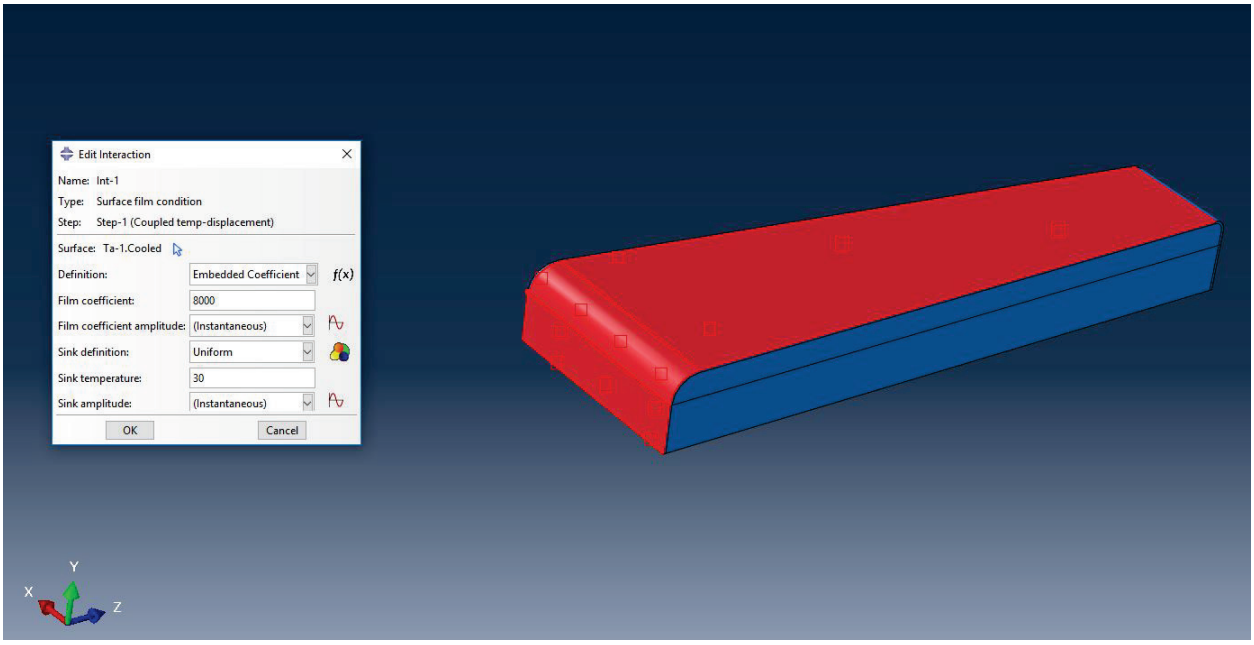

Figure 4.60. Heat transfer coefficient on top and front surfaces.

Multiple Pulse Coupled Temperature-displacement Results—Unirradiated

The temperature distribution after 1 pulse is shown in Figure 4.61 and shows a 15.6°C rise above the initial 30°C temperature.

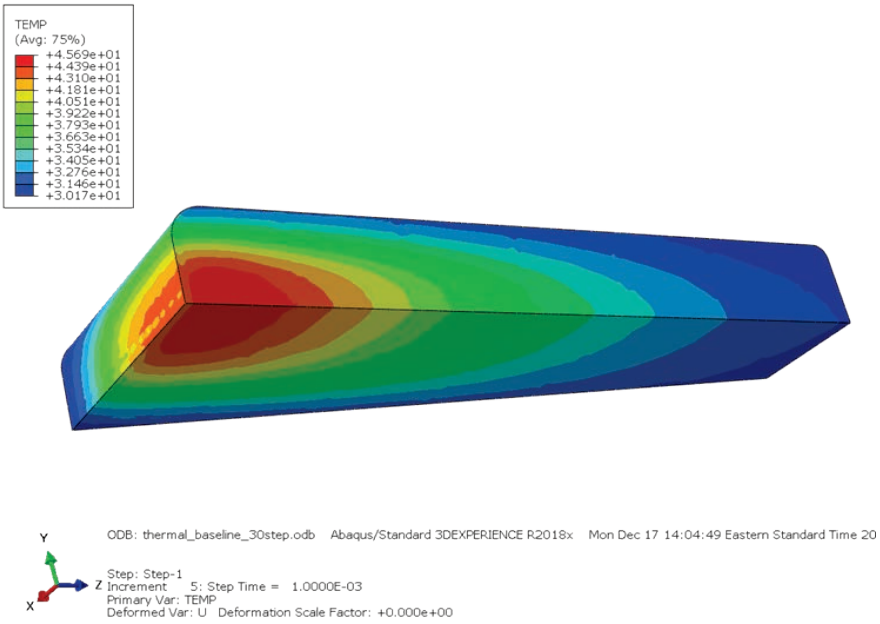

Figure 4.61. Temperature just after first pulse.

Figure 4.62 shows the temperature profiles just after the 15th pulse finishes.

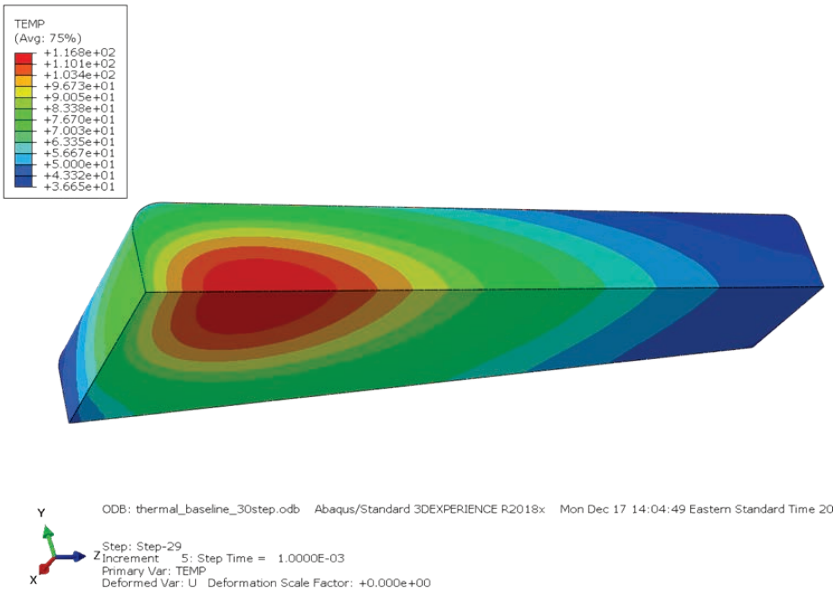

Figure 4.62. Temperature after 15th pulse with 116.8°C peak.

The temperature versus time for the element with the peak temperature after 15 pulses is shown in Figure 4.63, along with the steady state Abaqus temperature profile for the equivalent steady state heating profile.

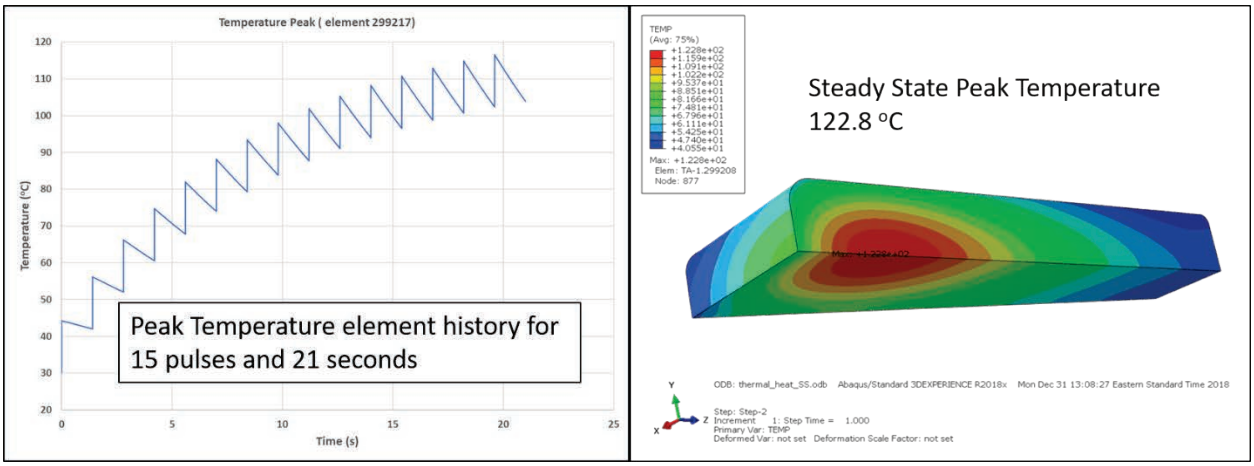

Figure 4.63. Peak temperature element time history for 15 pulses and steady state temperatures.

As shown in Figure 4.63, the temperatures are approaching quasi-steady-state but have not quite reached it after 15 pulses. The peak water-cooled surface temperature is approximately 76°C and is on the front face just after a pulse.

The von Mises stress distribution in the tungsten and the tantalum at 1.4 s after the 15th pulse is shown in Figure 4.64.

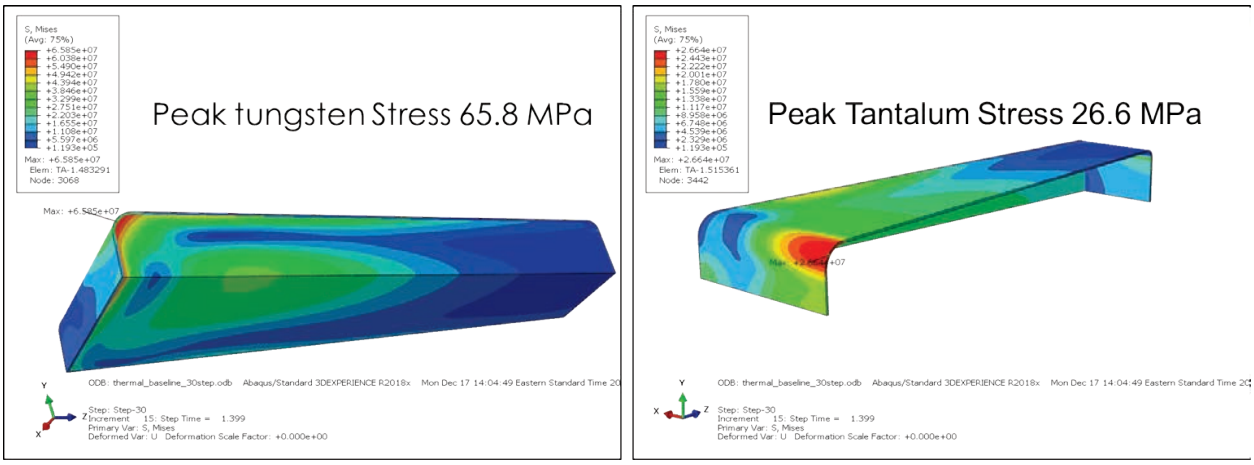

Figure 4.64. Tungsten and tantalum von Mises stress at 21 s just before the next pulse.

Dynamic Explicit Pulse Analysis

Input for the Model

An Abaqus dynamic explicit model was used with the same geometry and mesh as used for the coupled temperature displacement model. The stress distribution at the end of the 15 pulse analysis at 21 seconds just before the next pulse was input as an initial condition. Energy deposition was input as a linear temperature rise distribution over 10^{-6} s, and then the distribution was held constant. This produced the initial pressure distribution. The peak temperature rise in the distribution was 15°C. The transient response was calculated for up to 320 μs. The input distribution is shown in Figure 4.65.

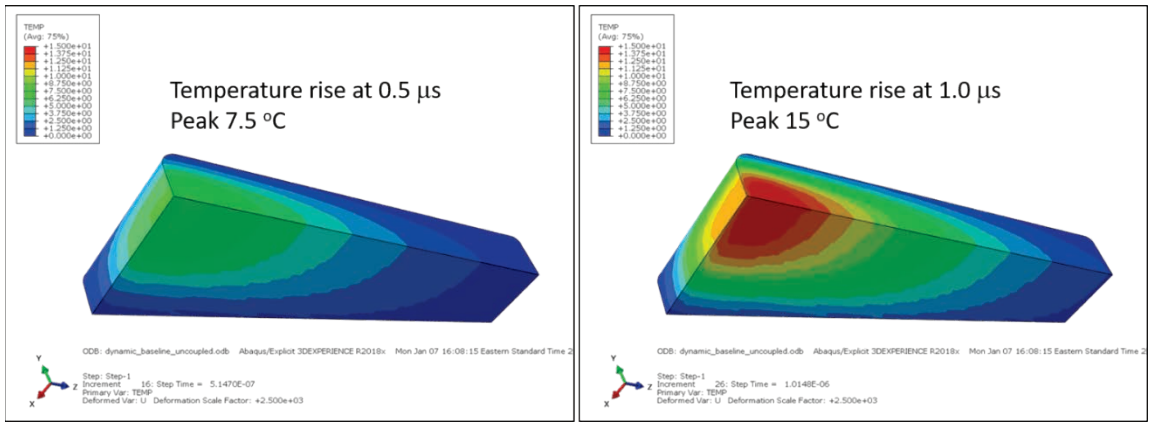

Figure 4.65. Imposed temperature distribution for dynamic analysis.

The pressure resulting from this profile alone and combined with the initial stress distribution is shown in Figure 4.66.

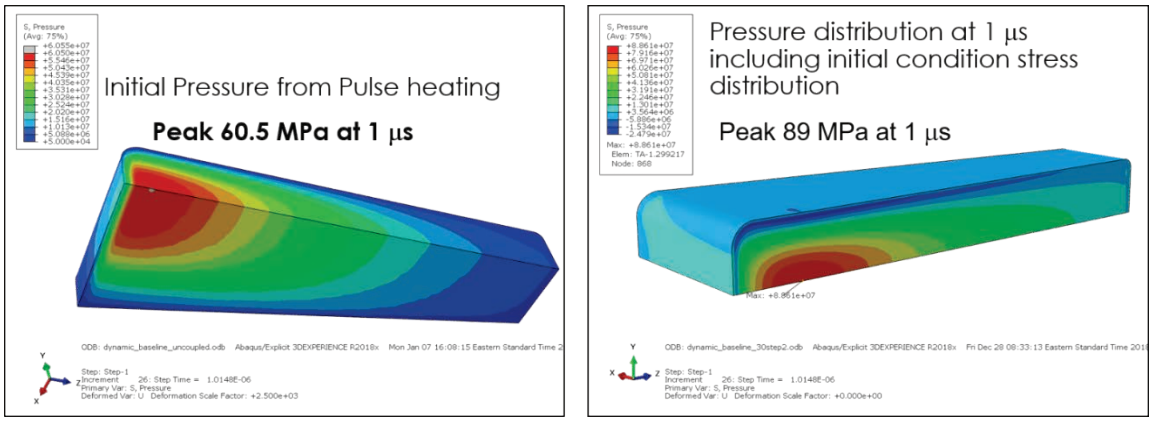

Figure 4.66. Pressure distribution from pulse heating and with initial condition.

The dynamic response shows many different modes of vibration, with the location of the peak stress varying between the front upper corner, along the axis, and other locations as a function of time. Figure 4.67 shows the von Mises stress and magnified displacements at 39 μs and 59 μs. The scale peak is 121 MPa.

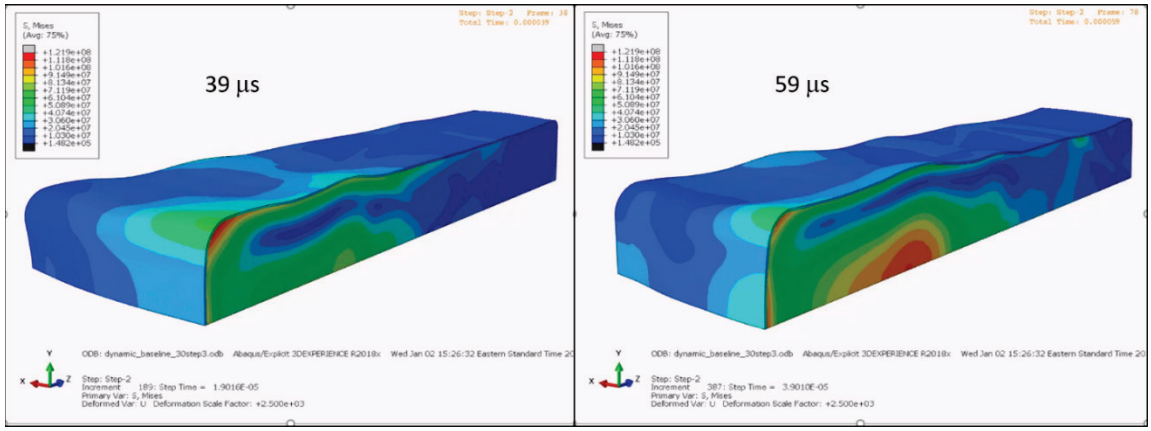

Figure 4.67. Dynamic response of target at 39 μs and 59 μs showing different peak stress locations.

The peak stress in the tungsten and the tantalum occurred at 41 ms and is shown in Figure 4.68 for each.

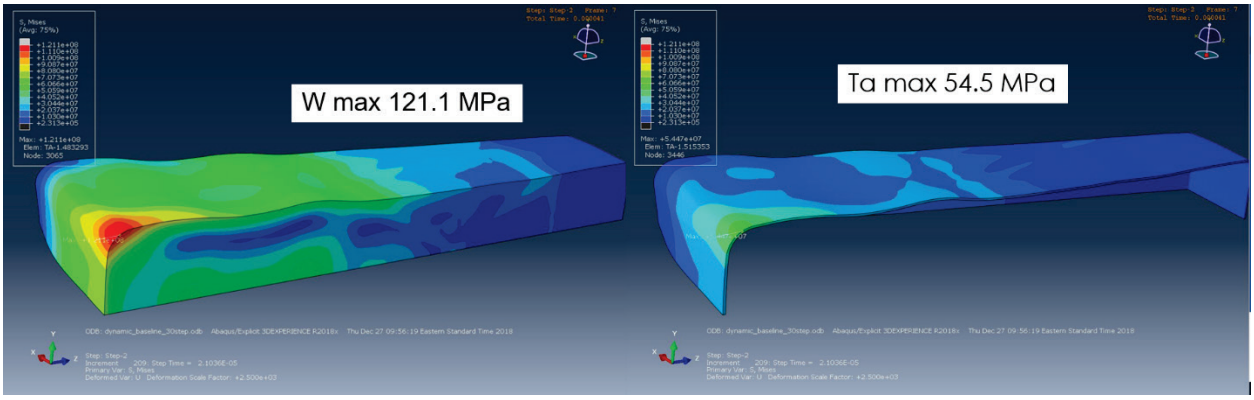

Figure 4.68. Peak stress in the tungsten and tantalum between 0 and 320 μs.

To show the time dependence of the von Mises stress, three representative elements were selected as shown in Figure 4.69.

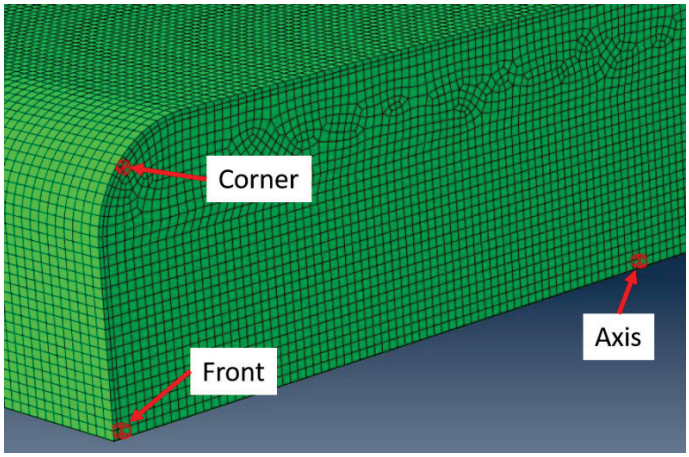

Figure 4.69. Selected elements for dynamic response over 320 μs.

The von Mises stress for these elements for 320 ms is shown in Figure 4.70.

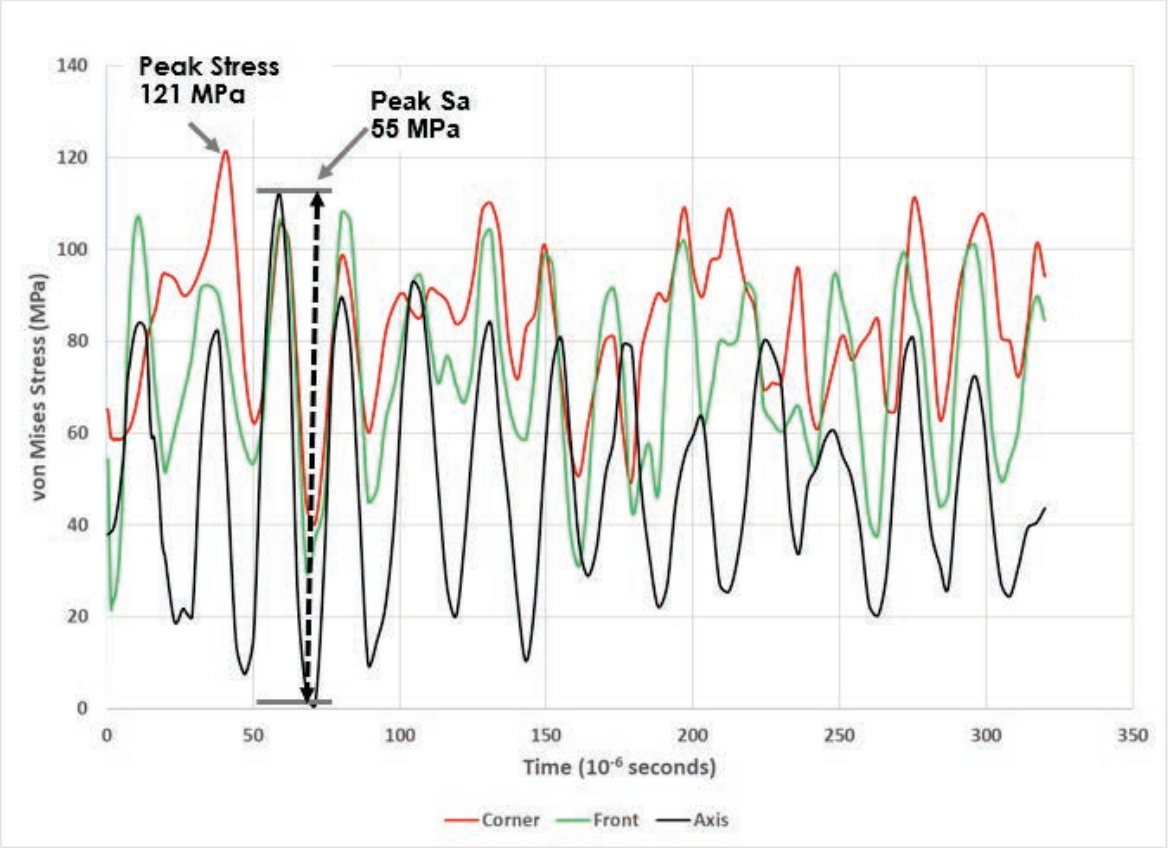

Figure 4.70. Corner, front, and axis elements von Mises stress vs. time.

The corner element starts at 66 MPa, as shown in Figure 4.70 and has a peak of 121 MPa at 41 μs. The highest alternating stress of 55 MPa is in the axis element at approximately 70 μs. As discussed previously, the effect of irradiation is to reduce the thermal conductivity and increase the stiffness. The coupled temperature and displacement model was run with the conductivity decreased to 87 W/m·K and then with both the conductivity decreased and the stiffness increased by 20%. The stress distributions for these two cases were then used as the input conditions for two more dynamic stress calculations. Figure 4.71 shows the results for the corner element for the unirradiated case, with just the conductivity decreased, and with the conductivity decreased and the stiffness increased.

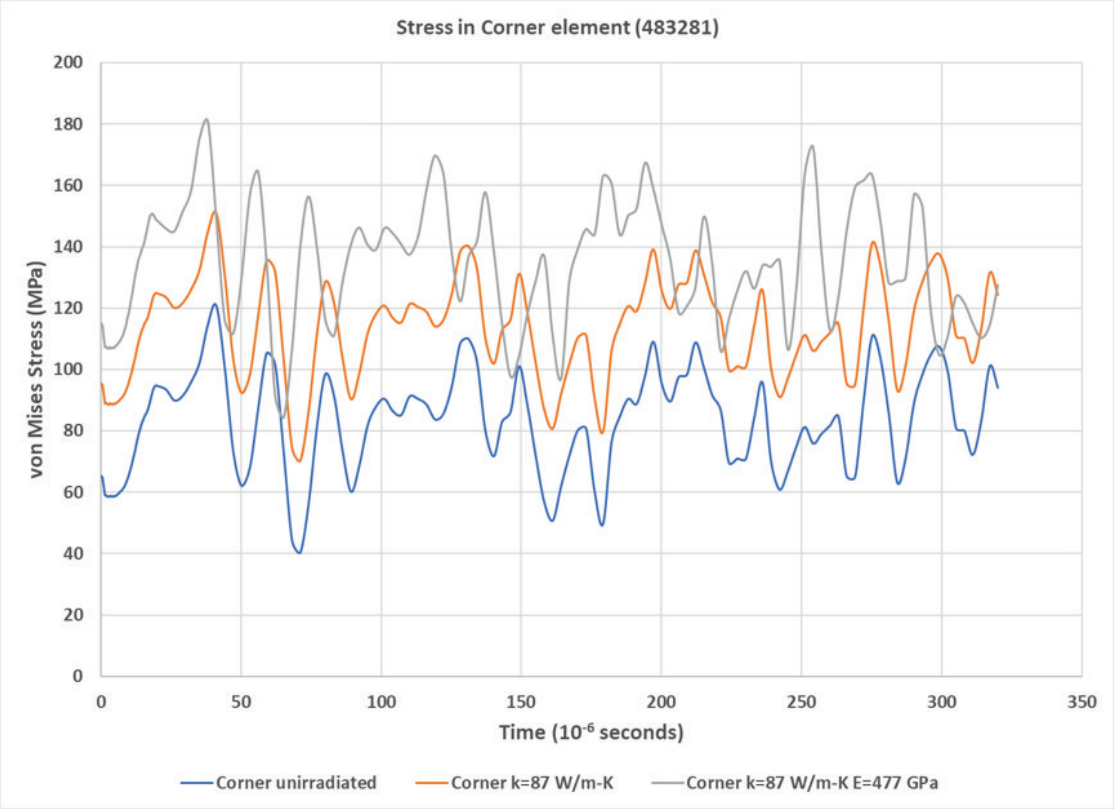

Figure 4.71. Corner element von Mises stress including irradiation effects.

The effect of the conductivity decrease is higher stresses. Increasing stiffness also decreases the time between peaks. The overall peak stress is in the corner at 181 MPa. The results for the axis element are shown in Figure 4.72. The peak alternating stress is 69 MPa.

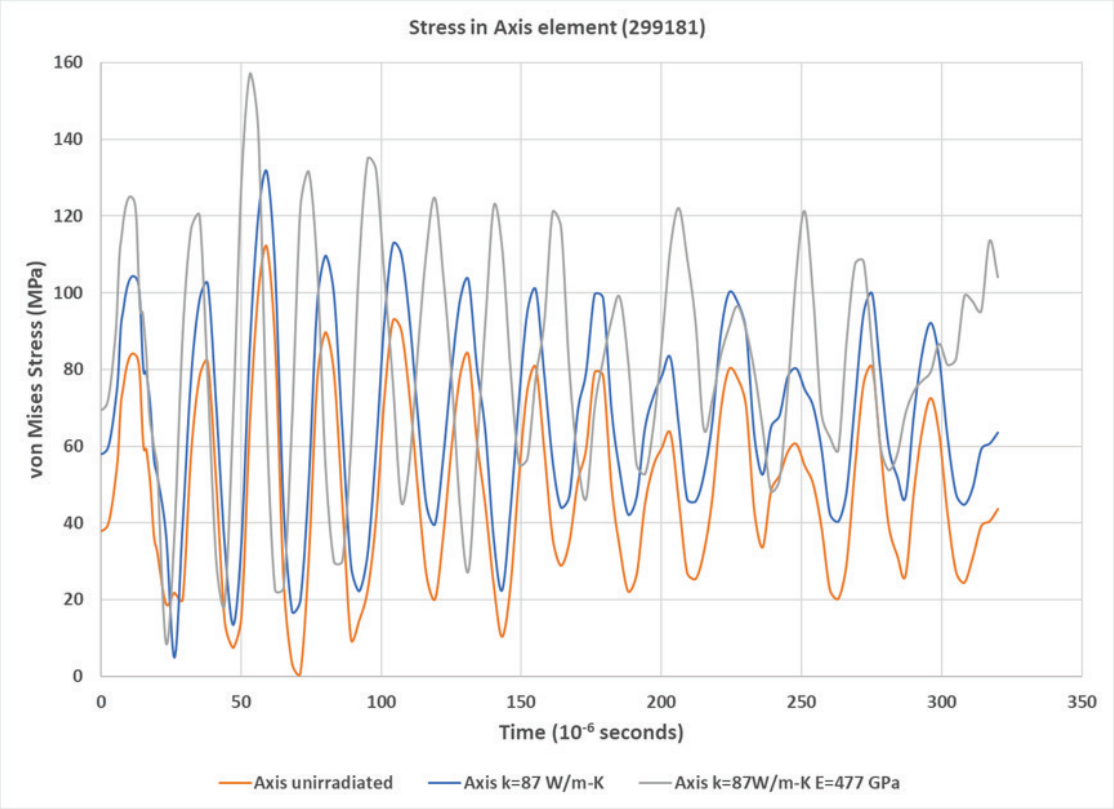

Figure 4.72. Axis element von Mises stress including irradiation effects.

The following is a summary of the results.

Location	Material properties		von Mises peak (MPa)	Sa (MPa)
	k (W/m·K)	E (GPa)		
Front	174.9	398	107	43
Top corner	174.9	398	121	31
Axis	174.9	398	112	55.5
Front	87	398	138	42
Top corner	87	398	151	31
Axis	87	398	132	59
Front	87	477	166	51
Top corner	87	477	**181**	37.5
Axis	87	477	157	**69**

The highest peak stress and alternating stress in the tantalum occur adjacent to the tungsten corner element. Figure 4.73 shows the dynamic response for the most highly stressed element. The peak stress is 69 MPa and the peak alternating stress is 21 MPa. This is below the 75 MPa limit used by ISIS. It does not include residual stress from the hot isostatic pressing process.

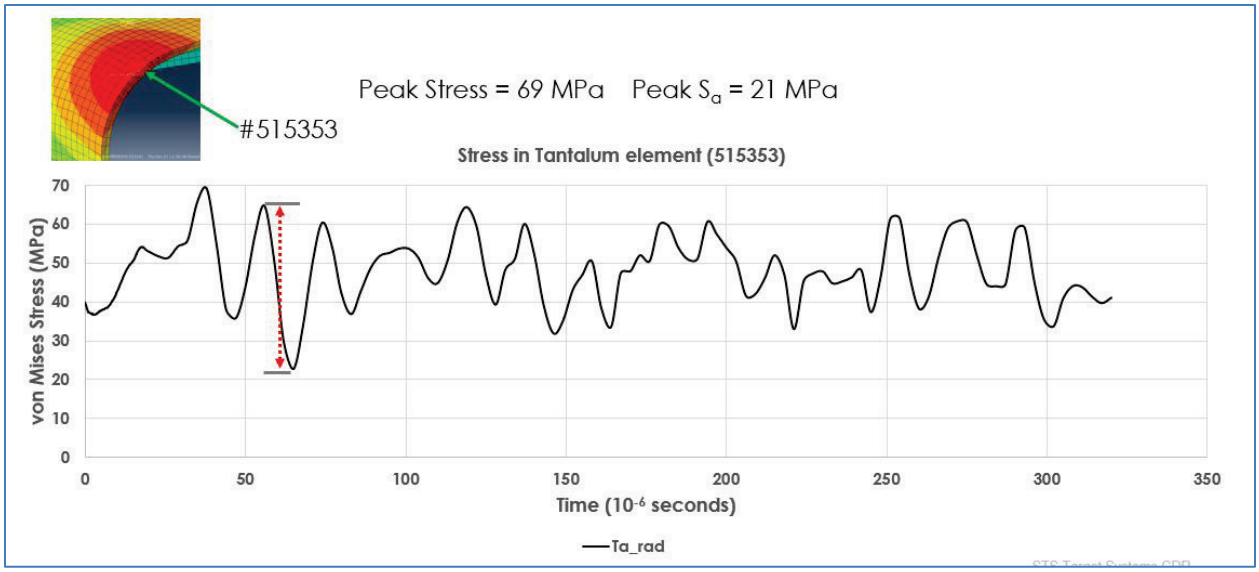

Figure 4.73. Tantalum peak stress vs. time for irradiated tungsten properties.

Computational Fluid Dynamics Analysis

Computational fluid dynamics (CFD) analysis for the baseline design (Figure 4.56) was done using two different codes, STARCCM+ and COMSOL. The inlet water velocity was 0.45 kg/s with an inlet temperature of 33°C. The shroud is designed with a 4 mm flow gap at the rear, which tapers down to 2 mm at the front. The intent was to produce a more uniform velocity by compensating for the change in width. The side surfaces of the tantalum are in contact with the stainless steel in this model, so there is no water cooling on those surfaces. Cooling requirements and the cooling design for the sides will be developed in preliminary design. The velocity distribution in the water channel from the STARCCM+ with a Realizable k-ε model is shown in Figure 4.74.

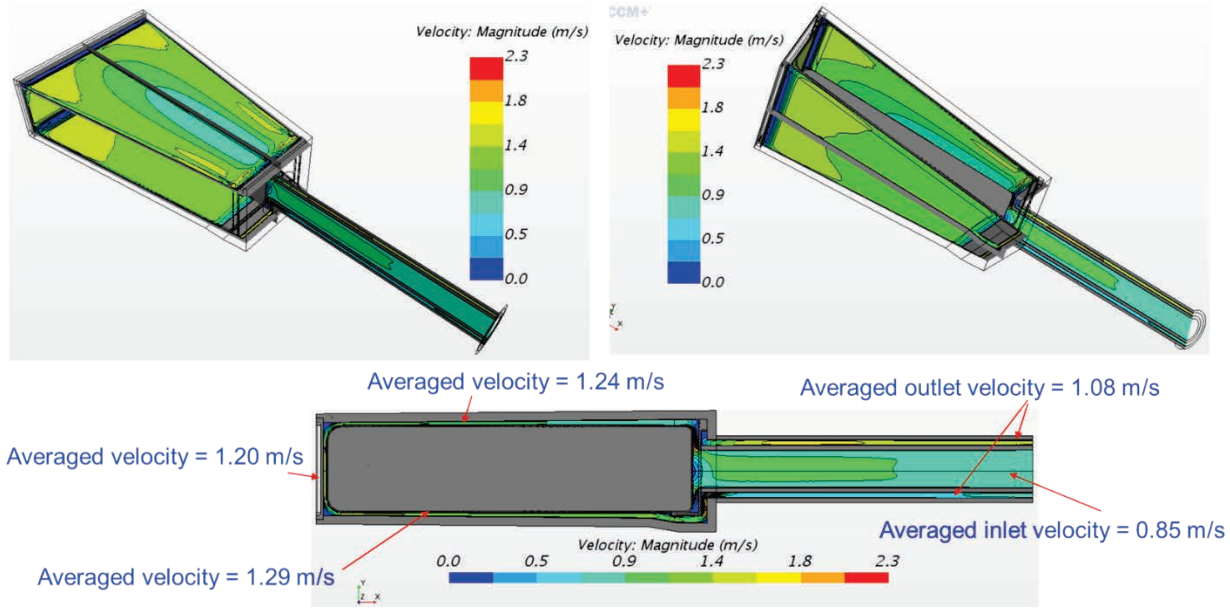

Figure 4.74. Velocity distribution within target segment water channel (STARCCM+: Realizable k-ε).

The flow from the inlet on the back surface produces a distribution on the top surface with higher velocities near the sides and a more uniform distribution on the bottom surface. The average velocity around the segment is approximately 1.2 m/s. The pressure drop for the region shown is 7.8 kPa (1 psi). The temperature distribution is shown in Figure 4.75.

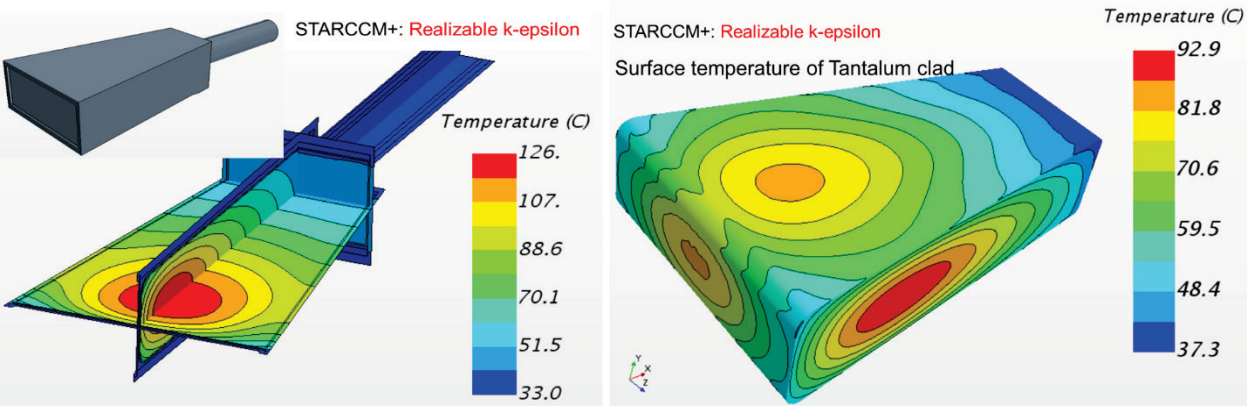

Figure 4.75. Temperature distribution within the tungsten and on the tantalum outer surface (top view).

The peak tungsten temperature of 126°C and distribution are very similar to what was obtained in the ABAQUS model. For that case, with an inlet temperature of 30°C, the steady state peak was 122.8°C. The peak water-cooled surface temperature on the tantalum from the CFD STARCCM+ calculation was 83°C, which gives adequate margin to boiling for water at 2–3 bar pressure. The bulk water temperature rise was approximately 8°C. A summary of the results with a comparison of STARCCM+ with COMSOL is given in Table 4.9.

Table 4.9. CFD summary for STARCCM+ and COMSOL results

Turbulence model	STARCCM+	COMSOL
	Realizable k–ε	Realizable k-ε
No. of mesh	3.0 million	3.0 million
Inlet temperature (C)	33	33
Mass flow (kg/s)	0.45	0.45
Pressure drop (inlet–outlet) (kPa)	7.8	7.7
Maximum temperature inside tungsten (°C)	126	131.7
Maximum temperature on tungsten surface (°C)	92.9	97.9
Minimum temperature on tungsten surface (°C)	38.3	39.1
Maximum temperature on tantalum surface (°C)	92.9	97.8
Minimum temperature on tantalum surface (°C)	37.3	35.7
Maximum water temperature (°C)	83.4	67.6
Outlet water temperature (°C)	40.94	41.27
Average velocity at top surface (m/s)	1.24	1.21
Average velocity at front surface (m/s)	1.20	1.17
Average velocity at bottom surface (m/s)	1.29	1.16
Average velocity at inlet (m/s)	0.85	0.86
Average velocity at outlet (m/s)	1.08	1.00

The CFD results show that the conceptual cooling system design is acceptable, with modest temperature rises, low pressure drop, and good margin to boiling. The results also show that the simplified heat transfer model used in ABAQUS for the structural response gave very similar temperature profiles. Plans are to add more cooling to the side walls during preliminary design, along with some modifications to obtain a more uniform velocity distribution on the top surface. In addition, the simplified heat transfer model will be modified to better incorporate the CFD results.

4.3.5 Target Development and Manufacturing

The overarching goal for design and development of the target assembly is that the lifetime be limited only by radiation damage to the target shroud.

There are two development and manufacturing challenges that will be addressed during the project:

1. Canned vs. clad casing of the individual tungsten segments
2. Integration of the target drive system with the drive shaft and target disk

4.3.5.1 Canned vs. Clad Tungsten Target Casing

As discussed in Section 4.3.2, bare tungsten in a spallation field cannot be directly cooled by water without experiencing corrosion. Therefore, the tungsten target block needs to be cased in another material. Tantalum cladding has been used at Los Alamos National Laboratory and at the ISIS spallation neutron source. As such, tantalum cladding is a primary alternative for STS.

STS will develop the tantalum cladding approach with a series of mockup and prototype target blocks. These blocks will be leak tested and destructively tested to understand the quality of the tantalum-tantalum and tantalum-tungsten bonds. STS needs this development work because the target blocks are significantly larger than those used at the other facilities.

In addition to the tantalum clad option, STS will develop a canned target option. In this design, the tungsten will be cased in a thin can, which would be made of stainless steel or zircaloy. The difference between this approach and the tantalum clad approach, other than casing material, is that the can would not be bonded to the tungsten. This eliminates this bi-metal interface from being a source of target failure. In addition, the use of stainless steel or zircaloy would reduce the radionuclide inventory and afterheat in the target. However, the lack of bonding increases the heat transfer resistance. Therefore, the tungsten block will operate at higher temperatures. Therefore, development efforts will characterize the contact heat transfer resistance between the can and the tungsten block.

4.3.5.2 Target Drive System Integration

A full-scale mock-up of the proposed target system is required to provide validation of manufacturability and operability beyond the scope of engineering analysis. This test apparatus will be built and tested early in the design process to provide time to incorporate results and observations into the final target system design. The mock-up will include all key features of the proposed system, including a replica of the drive and axle. The initial mock-up disk will have the same mass as the disk in the earlier mock-up. A fully prototypical disk could be added when it becomes available. A water-cooling loop will operate at representative temperatures and pressures. Like the earlier mock-up system, it will be subjected to a long-term test run to verify reliability. The long-term testing program will also include a program of shutdowns and restarts to confirm real-world operability. Stability of the disk and the functionality of the drive train are known issues expected to be resolved with the mock-up.

Although the target theoretically requires a low-torque drive, momentum matching will be a significant consideration because of the large rotational momentum of the target disk. Drive control, slack reduction, anti-backlash capability, freewheeling, and radiation tolerance will also be considered in the overall design. A drive specialist will be consulted to perform the necessary analysis.

4.4 MODERATOR REFLECTOR ASSEMBLY

4.4.1 Design Requirements

The MRA has been designed in conjunction with the STS instrument scientists and neutronics analysis team. The physics defining the characteristics and configuration of the MRA is documented in Section 4.1.6 (Physics Overview). Two coupled hydrogen moderators will be located at the peak neutron production point of the target, as shown in Figures 4.76 and 4.77. Each moderator will contain 0.35 to 0.5 l of supercritical para-hydrogen nominally operating at a pressure of 15 bar and a temperature of 20 K.

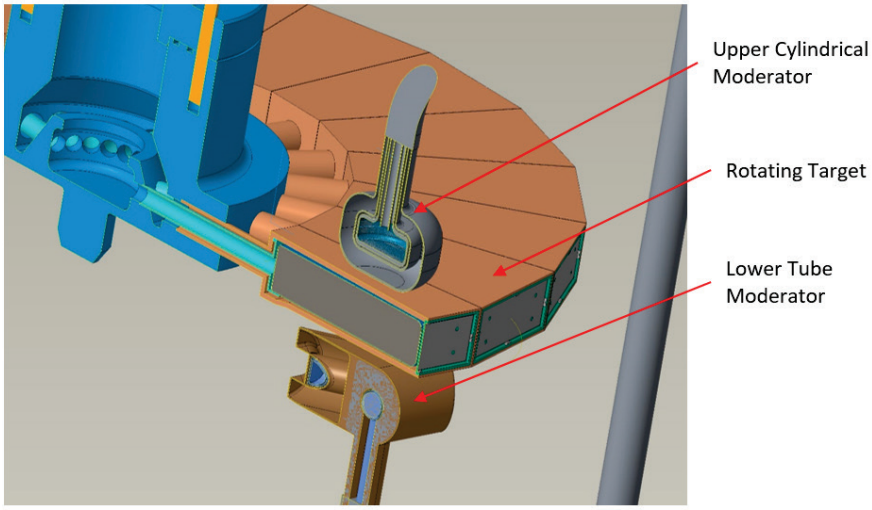

Figure 4.76. Moderator configuration.

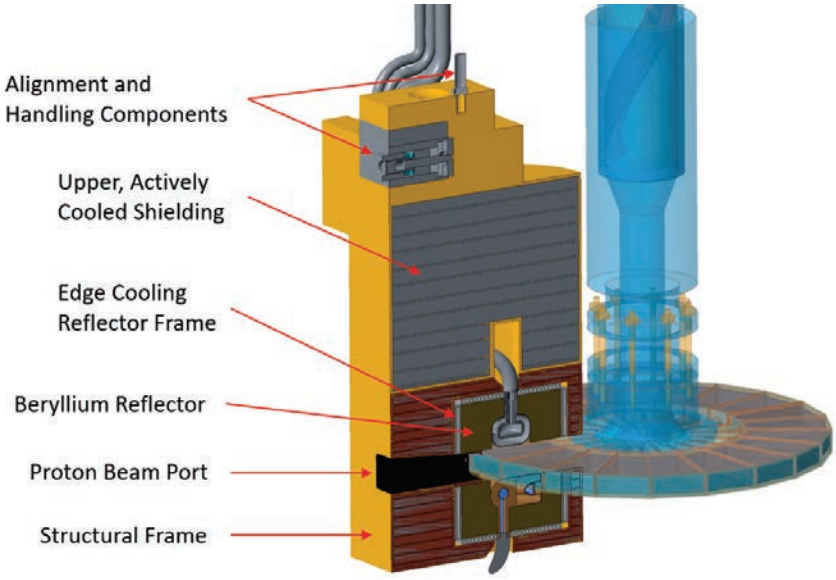

Figure 4.77. Section view of MRA along vertical proton beam centerline.

The upper moderator will be an 8.2 cm inner diameter cylindrical vessel viewed by 16 beamlines. The bottom moderator will have a delta configuration of three 14–16 cm long tubes viewed by six beamlines. Both moderators will be backed by reflectors of roughly 37 cm diameter. Beryllium was selected for the reflectors based on neutronic performance, successful operation in numerous facilities, high radiation tolerance, and good heat transfer characteristics.

The moderators will have a conventional cryogenic arrangement in which the hydrogen vessel will be surrounded by a vacuum vessel, which will be surrounded by a water vessel. The light water will cool the vacuum shell and act as a pre-moderator on all unviewed faces. A notable difference between the FTS and STS moderators will be the absence of a helium blanket separating water from vacuum within the core vessel. This layer is intended to provide a safe path for water leaks that might otherwise freeze and block the hydrogen vessel leak detection path. However, testing by ESS demonstrated that helium penetrates ice formations, thus enabling leak detection through the vacuum layer alone [Besler 2014].

Aluminum 6061-T6 will be used for the moderator vessels based on successful implementation at many facilities (including FTS) and a proven tolerance for radiation. Neutronic analysis indicates that radiation damage to the 6061 Al structure will occur at a rate of roughly 5.9 dpa/year, giving the moderators a lifetime of 7.6 years based on a total radiation tolerance of 40 dpa. The moderator vessels, including the surrounding vacuum vessel, will be designed and fabricated according to Section VIII of the ASME BPVC although, depending on the requirements of the STS safety analysis, the vessels may not be code stamped.

Each moderator will be served by an independent transfer line from the hydrogen utility room (HUR). To maintain the cryogenic operating temperature in the lines, the supply and return tubes will be surrounded by a vacuum pipe. The cryogenic hydrogen system, dedicated to the cold moderators, is defined in Section 4.7.

Alignment of the moderators with respect to the neutron beamlines is critical to the physics performance of STS. Specifically, the 3 cm tall neutron beamlines must have an unobstructed view of the hydrogen vessels. Section 4.2 describes the overall alignment scheme for the target station, of which the MRA will be an important part. The moderators are specified to have a vertical positional accuracy of ±1.5 mm of the ideal neutron beamline centers, accounting for manufacturing, assembly, and installation misalignments. The tube moderators will be further constrained by a requirement to be axially oriented to provide a full moderator face view to the neutron beam guide front opening.

STS does not have the capability to repair an MRA module; therefore, the modules are designed to be replaced individually while the remaining passive shielding blocks above the module are reused (see Section 4.5, Vessel Systems). Section 4.9, Remote Handling Systems, describes the replacement operation using the standard STS remote handling techniques. Uniquely, the assembly must be moved horizontally approximately 40 cm to clear the target disk and enable vertical removal.

4.4.2 Moderator Design and Manufacturing

MRAs are complicated by the need to combine many disparate manufacturing techniques in a single assembly. The FTS moderators have proved to be particularly challenging because the overlapping, thin-walled shells are difficult to inspect and must be welded together without damaging inner layers. The small size of the moderators and the need for precise alignment has led to a design that mechanically anchors the hydrogen moderator vessel inside the vacuum vessel. Consequently, manufacturing will be further complicated by the need for installation of thermally insulting spacers during assembly welding. Mechanically coupling the two vessels requires that the hydrogen supply piping include compliance for thermal contraction. Selection of the insulting materials and the configuration of the spacers to minimize

heat transfer will be part of the manufacturing development program. In addition, lessons learned in the manufacturing of the FTS moderators are being applied to the design of the STS moderators to improve manufacturability. The primary design goal is to minimize and simplify the number of welds.

The assembly of the cylindrical moderator is shown in Figure 4.78. The manufacturing will be based on welding six machined aluminum forgings using four electron beam (EB) welds. The hydrogen vessel will be fabricated from two aluminum forgings joined with a single circumferential weld. This will be a relatively high-pressure (19 bar) vessel; therefore, it will be easy to fully inspect it using x-ray techniques. The vacuum vessel, including the beam ports and part of the water vessel, will also be fabricated from two aluminum forgings and a single EB weld. Ceramic spacers will be used to separate the vacuum vessel (approximately 30°C) from the −253°C hydrogen vessel. The moderator will be completed by EB welding the two water (premoderator) caps to the vacuum vessel. To the extent possible, ultrasonic, radiograph, and visual inspection will be employed. Since the vessels have low cycle lives, pressure and cold shock testing will also be used.

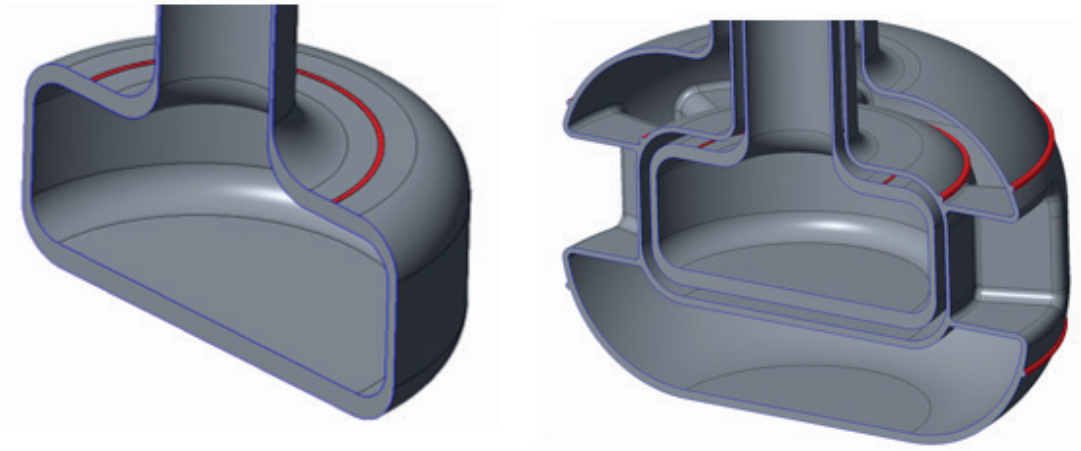

Figure 4.78. Manufacturing assembly of the STS cylindrical moderator.

The tube moderator will be more difficult to manufacture. An extensive development activity, similar to that used for the FTS moderators, is planned. Currently, the proposed manufacturing procedure involves 7 machined forgings and 18 gas tungsten arc and EB welds. The assembly is shown in Figure 4.79.

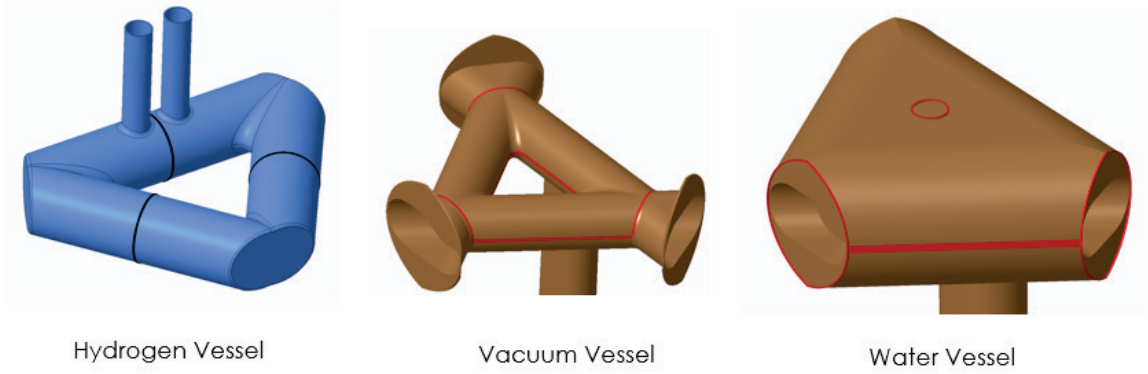

Figure 4.79. Manufacturing assembly of STS tube moderator.

Two independent multi-layer cryogenic lines will be used to circulate the cryogenic hydrogen between the CMS located in the HUR and the moderators. The transfer lines are nominally 46 m long but are sized to maintain a maximum pressure drop compatible with the hydrogen processing system. A helium heat shield may be incorporated into the tube moderator lines to reduce heat transfer between the return and supply lines. To eliminate the possibility of a bellows failure in an inaccessible area, Invar 36 will be used in the fabrication of the hydrogen supply and return layers of the transfer lines to minimize thermal stresses resulting from the cool-down contraction of hydrogen lines inside the warmer surrounding pipes. Friction-welded joints will be used between the Invar and the aluminum moderator vessel.

4.4.3 Moderator Analysis

The moderators were analyzed using heating data p based on a 700 kW, 15 Hz proton beam. The nominal 20 K hydrogen supply was determined to be 0.35 l/s at 14.5 bar and the water was set at 0.5 l/s at 30°C.

A CFD analysis was used to determine the flow and thermal performance of the hydrogen and water flow in both moderators. Figure 4.80 shows the hydrogen temperature pattern in the upper moderator assuming an inlet temperature of 18 K. With a boiling point of approximately 33 K, the maximum hydrogen temperature of 29.4 K ensures uniform, liquid density throughout the moderator, as required for optimal neutron production. The same CFD analysis shows a maximum vessel temperature of 48°C, which is significantly below the design limit of 120°C (Figure 4.81). The CFD analysis of the tube moderator showed similarly conservative results.

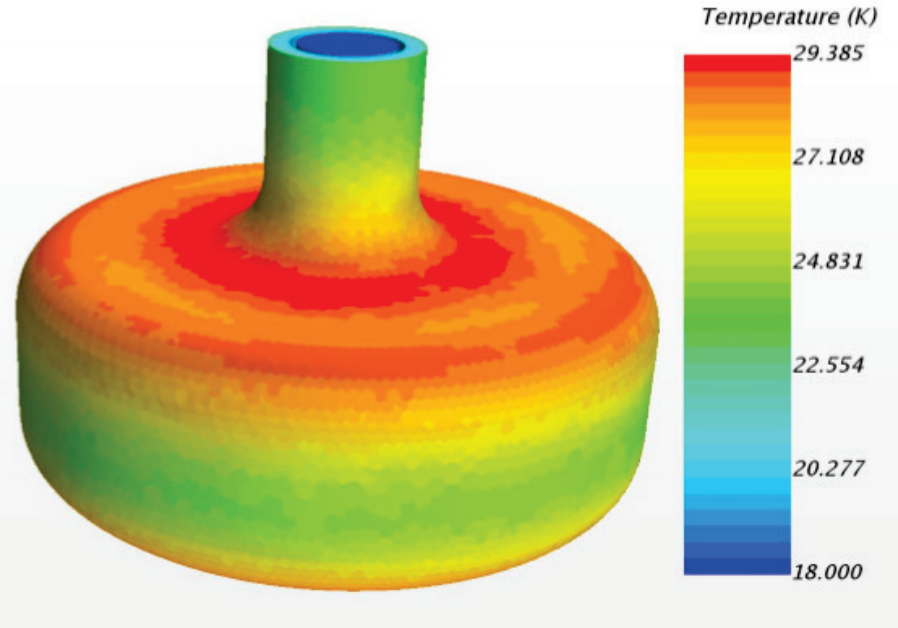

Figure 4.80. CFD analysis results showing the hydrogen temperature inside the cylindrical moderator.

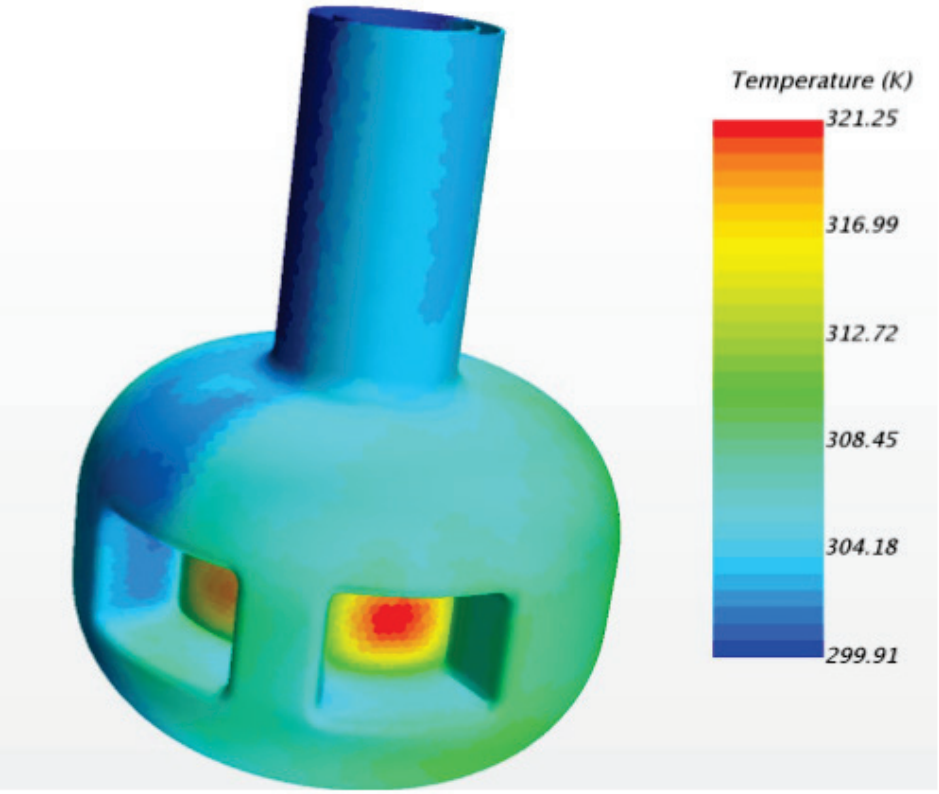

Figure 4.81. CFD analysis results showing temperature distribution in cylindrical water/vacuum vessel.

A maximum allowable working pressure (MAWP) of 19 bar provides a 24% operational margin over the 15 bar operating pressure of the hydrogen vessels. Using this input, an ANSYS finite element structural analysis of the vessels showed that the stresses meet the design requirements of the ASME BPVC Section VIII, Div. 2 for 6061-T6 aluminum:

- General membrane stresses below 81 MPa
- General membrane plus bending stresses below 121 MPa
- Localized stresses below 242 MPa
- Weld zone stresses below 83 MPa

Figure 4.82 provides the result for the upper cylindrical moderator showing a maximum von Mises stress of 113 MPa. Figure 4.83 shows a maximum von Mises stress of 120 MPa in the lower tube moderator. Maximum displacement will be 0.5 mm in the cylinder and 0.4 mm in the tube moderator.

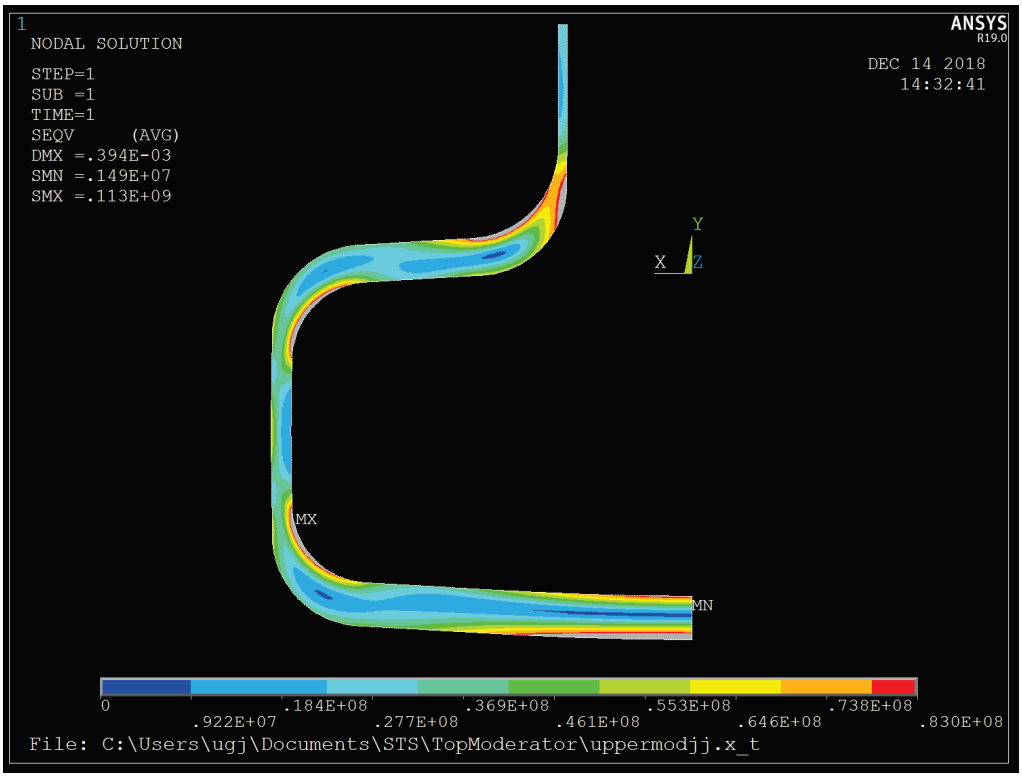

Figure 4.82. ANSYS stress plot of the cylindrical hydrogen vessel at 19 bar.

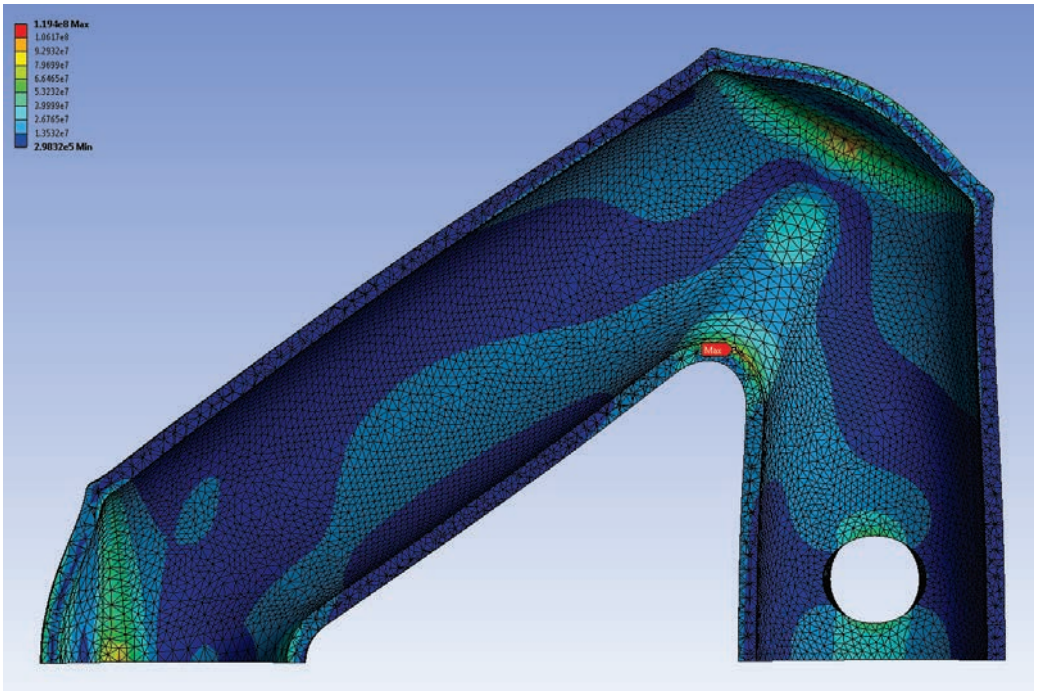

Figure 4.83. Example of tube moderator von Mises stress contour plot (maximum stress 119 MPa).

4.4.4 Reflector Design, Manufacturing, and Analysis

Neutronic analysis (see Section 4.1.6) was used to determine the sizes of the reflectors. The top reflector will be 37 cm in diameter by 15.5 cm high. It will include four, 33° cut-outs for the neutron beams. The bottom reflector will be 37 cm in diameter by 17 cm high with six conical cut-outs in line with the tube moderators.

Beryllium has a high thermal conductivity (200 W/m·K) that enables the top and bottom reflectors to be edge-cooled by heavy water–cooled aluminum plates. Currently, it is assumed the plates will be brazed to the reflectors to provide ideal thermal contact. A program will be required to develop a reliable bonding technique and quantify a realistic thermal contact resistance.

The aluminum plates will be manufactured in two layers approximately 20 mm thick with machined water passages 10 mm tall. The 30°C cooling water will have a velocity of 3 m/s. The plates may need to be segmented to reduce stress and assist with assembly. Beryllium is a hazardous material with a limited number of qualified fabricators. STS will work directly with these vendors to develop a feasible design and manufacturing schedule.

The reflectors were analyzed using thermal data provided by the neutronics analysis. Key inputs to the analysis include the assumption that the aluminum-to-beryllium joint has no thermal contact resistance, and the water convective heat transfer coefficient was ~12,600 W/m^2·K based on a Dittus-Boelter correlation.

Figure 4.84 is a thermal plot for the upper reflector showing a maximum temperature of 90°C. A similar analysis of the lower reflector shows a maximum temperature of 70°C. These temperatures are well below the 1287°C melting point of beryllium but must ultimately be considered in the thermal design of the moderators. Figure 4.85 is an ANSYS stress plot for the lower reflector showing a maximum von Mises stress of 104 MPa. The upper reflector has a calculated stress of 137 MPa. Both values are well below the 2/3 yield allowable for 167 MPa based on a given maximum yield strength of 250 MPa.

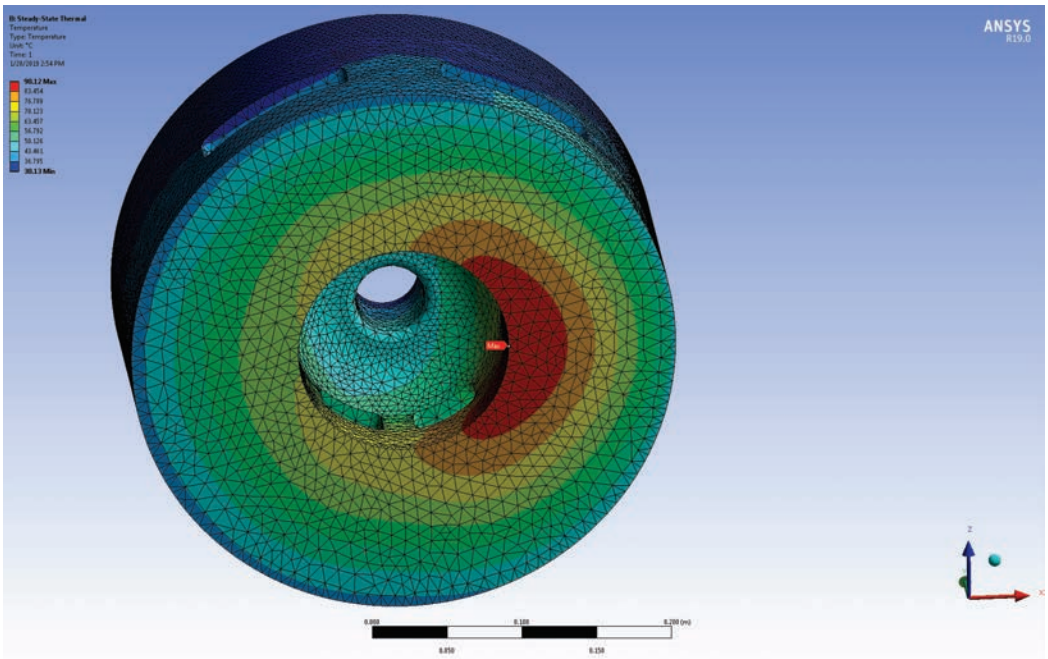

Figure 4.84. Temperature plot for upper reflector (maximum 30°C).

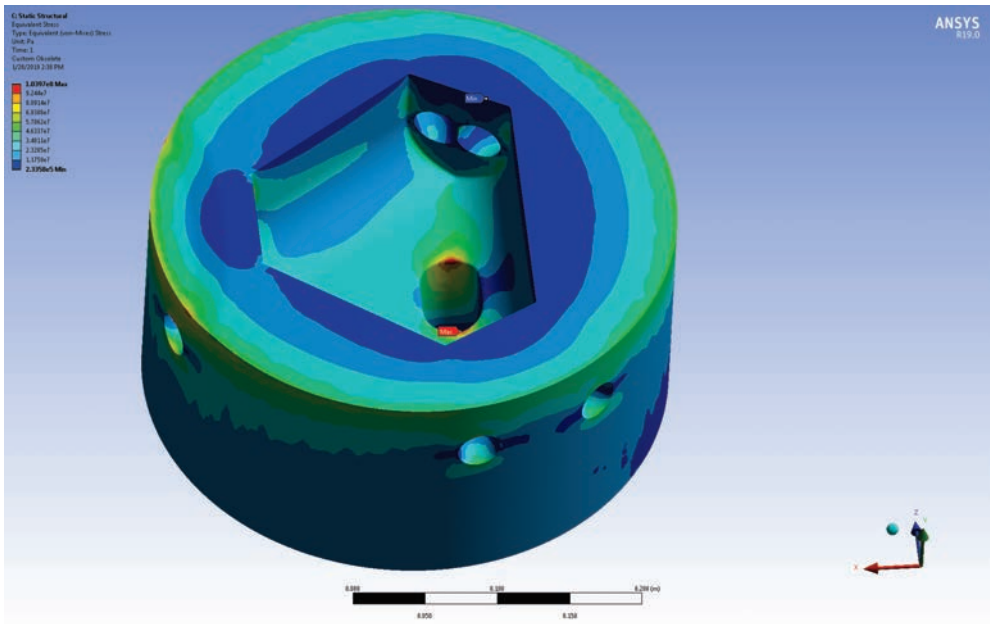

Figure 4.85. Von Mises stress plot for lower reflector (maximum: 233 MPa).

4.4.5 MRA Assembly and Handling

The clearance between the rotating target disk and the moderators must account for a significant number of factors, such as manufacturing tolerances, installation tolerances, and target and reflector thermal expansion. Conservative estimates of the total required nominal clearances are for a minimum of 10 mm between the top moderator and target disk and 12 mm below the disk.

Approximately, 70 kW of power will be removed from the MRA by several discrete water cooling channels with a total flow rate of approximately 1.9 l/s. The intermediate and upper IRPs will be stainless steel, as required for compatibly with the vessel environment. The complete MRA assembly will weigh approximately 29 tons.

Only five or six MRAs will be required during the 40 year STS operating life. The STS mock-up facility will provide on-site storage for replacements. The mock-up will also provide the capability for the maintenance technicians to practice the relatively rare replacement operation.

4.4.6 MRA Alternative Configuration

An alternative MRA design configuration based on individual moderator replacement was considered. The obvious advantage of this arrangement is that it would allow for the reuse of large portions of the MRA, thus potentially saving fabrication cost and reducing waste. However, the special tooling required to change the individual moderators with integrated piping inside the service cell would more than offset those savings. As proposed, the unified MRA design is based on the same segmentation as the FTS assembly, so established procedures can be used.

4.5 VESSEL SYSTEMS

Vessel systems include the core vessel and adjoining components as shown in Figure 4.86. The perimeter of the vessel will be determined by the active, water cooling boundary. Neutron guide port extensions from the perimeter to the outside of the monolith shielding (approximately 5 m) will provide access for beam guides

provided by Instrument Systems. The vessel will extend to the top of the monolith to provide access for vertical replacement of the active target system components (see Section 4.9). A stand under the vessel will elevate the centerline approximately 2.7 m above the liner base plate to provide space for iron shielding to protect the concrete foundation. Removable, passive shield blocks located above each of the remotely replaceable proton beam line components will be included in the vessel system with which they share primary interfaces. An HDC bunker, the target drive room, will enclose the region above the vessel to supplement the monolith and process water shielding. The STS core vessel configuration and design are based on the successful FTS vessel (Figure 4.87). Manufacturing tolerances, placement accuracy, operational reliability, and maintenance interfaces are derived from experience with this assembly.

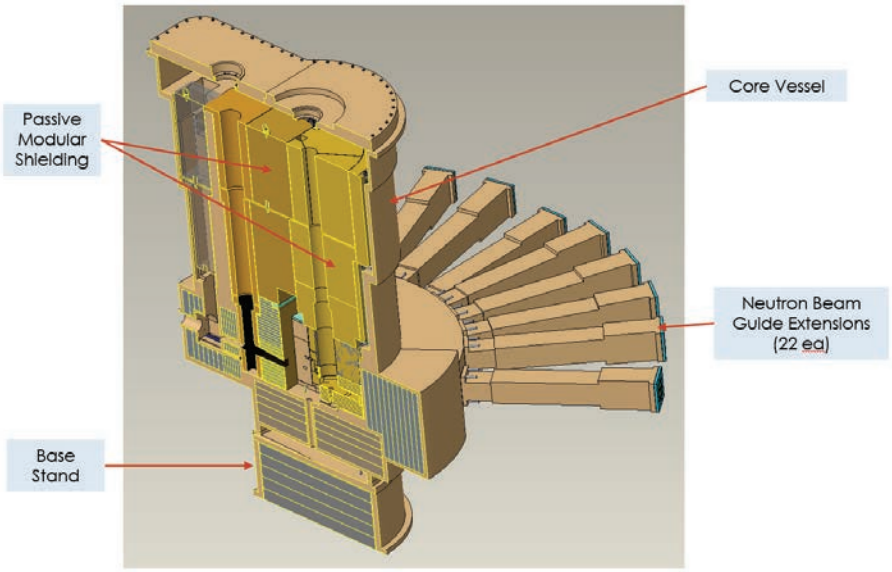

Figure 4.86. Vessel systems components.

Figure 4.87. FTS core vessel assembly.

4.5.1 Design Requirements

The vessel will include unique features that are not explicitly addressed by the ASME BPVC. Therefore, in keeping with 10 CFR 851.45.4, "Worker Safety and Health Program-Direction to NNSA contractors-Pressure Safety," the vessel will be fabricated in accordance with the intent of the BPVC to ensure a level of safety greater than or equal to the level of protection afforded by the ASME code.

4.5.1.1 Pressure Vessel Specifications

The STS core vessel will, to the extent possible, be designed, fabricated, and tested in accordance with "Section VIII, Division 2, Design and Fabrication of Pressure Vessels" of the ASME BPVC. It will not be code stamped.

Basic design specifications are as follows:

- Design pressure range: Vacuum to 0.2 MPa
- Cooling water pressure: 0.6 MPa
- Design factor of safety: 3.5
- Temperature: 20 to 50°C
- Corrosion allowance: 0.5 mm
- Load cycles: 2000
- Factory leak rate at vacuum (without internal shielding): 1×10^{-3} torr·l/s

The vessel and its support and anchorage shall be designed for seismic loads in accordance with the International Building Code (IBC) [ICC n.d.]. The vessel and its support shall be designed for a horizontal load using the load factors determined in accordance the STS Final Safety Analysis Report and the requirements of DOE-STD-1020-2016, *Natural Phenomena Hazards Analysis and Design Criteria for DOE Facilities* [DOE 2016].

4.5.1.2 Nozzles

Nozzles will be provided for the following vessel ports (see Figure 4.88):

- Twenty-two neutron beam guide nozzle extensions axially aligned with the moderators. The nozzles will be designed for installation of instrument-specific inserts (provided by Instrument Systems) after the completion of the Target Systems installation.

- Numerous water-cooling ports will be located near the top of the vessel. The ports will be based on a "spool" design with flanges designed for hands-on make-up inside and outside the vessel.

- A single port near the top of the vessel will provide a sealed pass-through for two, concentric pipe, transfer lines that circulate supercritical hydrogen between the moderators and the pump module in the HUR.

- The proton beam entry port will connect to the proton beam line with a remotely replaceable connection.

- The lid will have ports for the vacuum pump-down, rupture disk vent, TVP, and target drive.

- A drain port will be located at the low point in the bottom of the vessel

- Ports near the top of the vessel will be provided for the helium supply, thermocouple conduits, drain syphon, and other lines required for operational support.

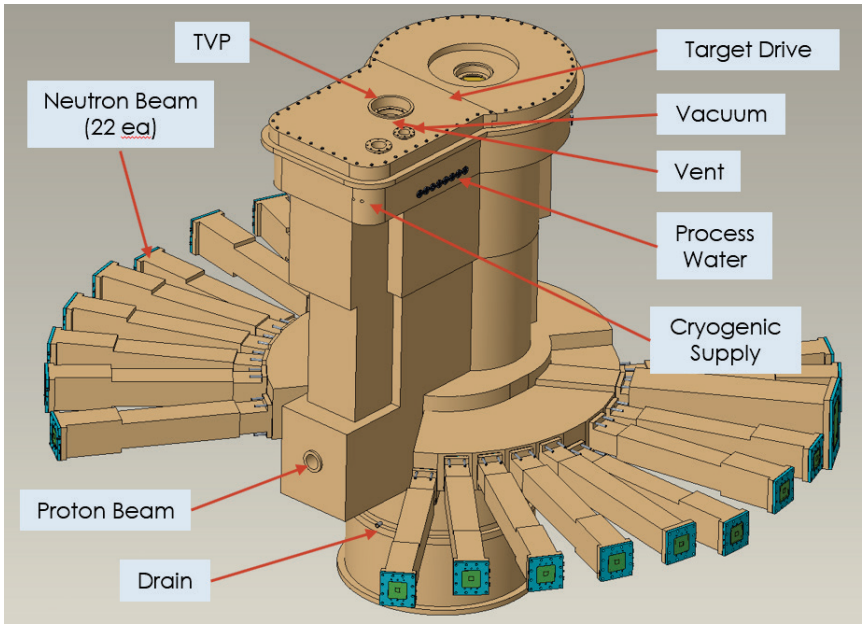

Figure 4.88. Select core vessel port locations.

4.5.1.3 Lifetime

The design lifetime of the vessel is 40 years. All components subject to radiation damage during the lifetime of the vessel will be replaceable.

4.5.1.4 Base Stand

The vessel will be installed on a cylindrical stand mounted on a base plate included in the monolith liner (see Section 4.6.3). It will be the interface between the monolith structure and the vessel. The stand will include features such as jacking stops and fiducials to aid with alignment during field installation. The elevation, level, and orientation of the vessel will be established by conventional grouting of the base plate combined with shimming between the base stand and base plate. Anchoring of the base plate, base stand, and vessel to the foundation structure shall be in accordance with seismic requirements.

4.5.1.5 Passive Internal Shielding

The vessel assembly will include significant portions of the STS shielding system as described in Section 4.6. Passive shield blocks located above each of the active modules will provide a majority of the vertical target system shielding. The blocks will be designed to be temporarily removed during module change-outs for reuse. The blocks will include handling features compatible with the STS remote handling system. Shielding containers required for personnel protection when the blocks are removed will be provided by Remote Handling (see Section 4.9).

4.5.1.6 Thermal Control

The vessel and interior shield assembly will be designed to contain over 99% of the total beam heating in either the target or water-cooled shield blocks. The goal is to enable all the shielding outside the vessel to

be passively cooled by natural convection and conduction. Air cooling paths through the shield stack and between the vessel and passive shielding will discharge this heat to the target drive room and primary containment environmental control system.

4.5.1.7 Atmospheric Control

Safety and operating requirements dictate a controlled atmosphere inside the vessel—ideally, pure helium at a sub-atmospheric pressure, (FTS operates at about 650 torr) or a vacuum mode in the rough vacuum regime. In certain circumstances, operation will continue with water leaks inside the vessel. Beam interaction with the vapor and other in-leakage could result in the generation of acids; therefore, the vessel and all exposed interior components will be fabricated from stainless steel.

4.5.1.8 Safety

Potential accidents, preventive features, and mitigation methods for the vessel system are identified by the Preliminary Hazards Analysis Report. Loss-of-cooling accident events can result in target failure with releases of water and hydrogen into the vessel. The inert helium or vacuum atmosphere is needed to prevent a hydrogen fire or detonation within the vessel. A rupture disk venting to a hydrogen safe stack is required to prevent vessel overpressures and failure of neutron beam windows. Ullage is required to limit pressure rises resulting from a large water leak and to contain water leaks below the level of the neutron beam ports. Seismic events beyond SDC-2 levels can be expected to cause the core vessel boundaries and the hydrogen lines within the vessel to fail, with potential hydrogen detonation within the vessel. Consequences will be limited by keeping the free volume adjacent to the target to a minimum, on the order of 0.2 m^3.

Personnel will be protected from radiation at 0.25 mrem/h outside the target drive room during beam-on operation. During maintenance outages, personnel will be able to safely enter the target drive room and perform maintenance on systems above the monolith shield.

4.5.1.9 Alignment Requirements

The core vessel will be the central target system alignment feature, as discussed in Section 4.2. Alignment fiducials and other positioning features shall be provided for the PBW, TVP, MRA, and target, as well as all accompanying shielding, piping, and sensors. These features will be particularly important because these components will generally be installed without in situ adjustment. The final alignment of these features relative to the ideal will be approximately as follows:

- Radial: ± 0.0002 radians (±1.0 mm at 5 m)
- Elevation: ± 0.5 mm
- Axial center: ± 0.5 mm
- Planner: ± 0.0002 radians

4.5.2 Vessel Systems Design

4.5.2.1 Vessel Fabrication and Installation

Accurate alignment of the 22 neutron beam guide ports, the proton beam port, and 5 active target components relative to the ideal target station center will be the primary vessel system design challenge. The design addresses this issue at each phase of fabrication and installation to achieve the final alignment specifications.

Fabrication precision requires the core vessel be machined as a unit with a minimum number of set-ups. The FTS experience demonstrated that this can be accomplish using a large multi-axis mill. Shipping and on-site handling of the assembly has also been demonstrated with the similarly sized FTS vessel.

Installation will be performed early in the overall construction of the STS facility when the vessel will not be enclosed. Even though survey and alignment personnel have the ability to locate the vessel accurately, real-world limitations, such as weather and non-uniform solar heating, result in the following vessel placement accuracies:

- Radial: ± 0.0004 radians (±2.0 mm at 5 m)
- Elevation: ± 2.0 mm
- Axial center: ± 2.0 mm
- Planner: ± 0.0004 radians

To achieve this positional accuracy, final alignment of component mounting positions will take place after all the monolith shielding has been installed. This schedule will compensate for environmental stability and foundation compression. With access to the vessel interior, survey and alignment personnel will precisely locate each component guide and alignment feature (see Figure 4.89). Using this information, corresponding module guides and fiducials will be fabricated and installed as needed. In addition, thermal and dimensional deviations will be compensated for by locating the positioning fiducials as close as practical to the proton beam line elevation.

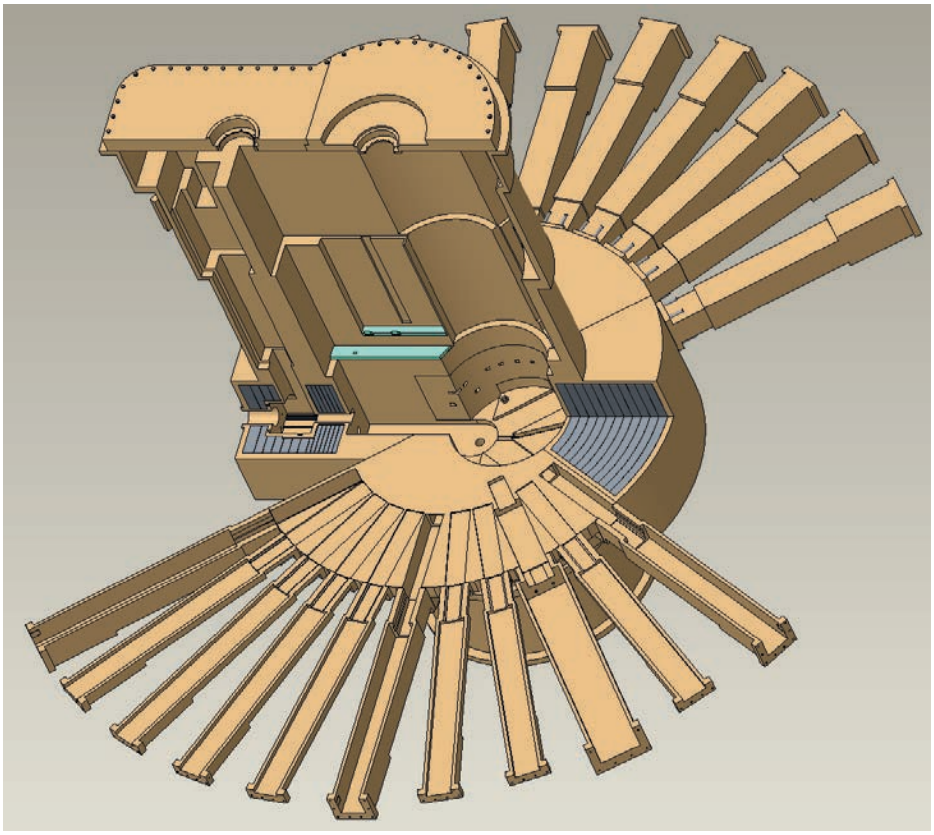

Figure 4.89. Interior features of core vessel.

4.5.2.2 Vessel Nozzles

There are two types of nozzles in the vessel: permanent and hands-on accessible. Permanent joints include the bottom drain and possibly some lower vessel cooling pipe connections. More significantly, joints between the vessel body and the neutron beam insert extension nozzles will be made during installation and then covered with monolith shielding. The vessel environment extends to the end of the neutron beam extensions because of the requirement that the beam guides, including the inner window, be replaceable. Consequently, reliable leak tightness and the structural integrity of the joints will be critical. These will be permanent bolted connections with double metal O-ring seals similar to those successfully employed in FTS.

Hands-on accessible nozzles are identified in Figure 4.90. These connections are either located in the lid with direct access inside the target drive room or under removable local shielding. Cooling water pipes will be connected with double, metal O-ring flanges. The two hydrogen transfer lines will be constructed of concentric tubes facilitating hydrogen supply, hydrogen return, the optional helium inert gas blanket, and the associated insulation vacuum. The lines will be of all-welded design. The transfer line sections at the top of the vessel will be cut and re-welded to facilitate removal and reinstallation of the MRA.

The rotating target will be supported on the lid of the vessel. Target stability will be ensured by the rigidity of the vessel structure. Sealing the rotating target shaft feedthrough at the lid is a known challenge. This issue is discussed in Section 4.5.5. The TVP also seals at the lid but requires only conventional static seals.

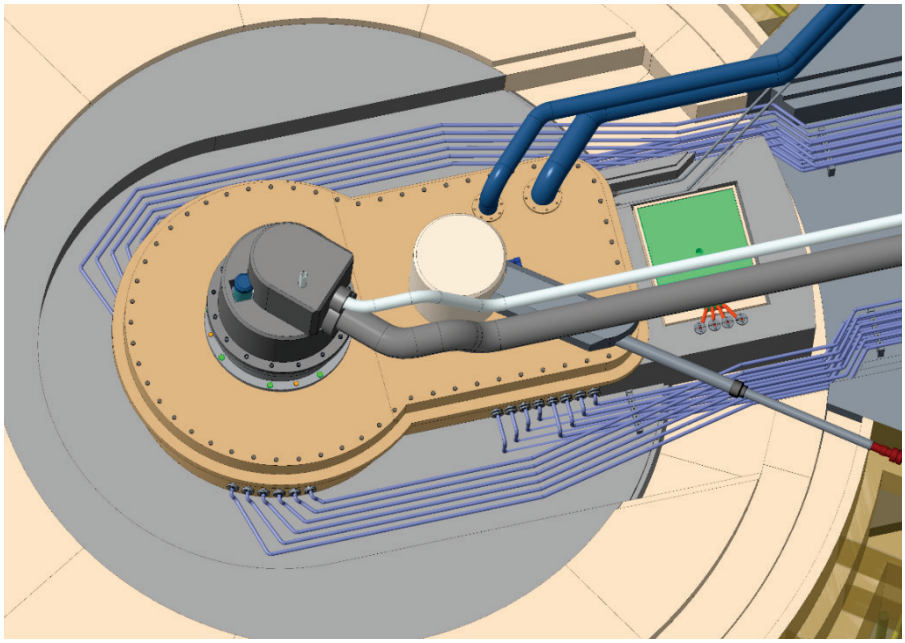

Figure 4.90. View of hands-on accessible nozzles and ports with local shielding removed.

4.5.2.3 Atmospheric Control Features

Sub-atmospheric pressure will be maintained with an inductor or vacuum pump venting to the hot offgas system. Because of the large number of surfaces and virtual leaks inside the vessel, it is assumed that contamination and water vapor will accumulate inside the vessel during maintenance operations. The dynamic rotating target axle seal is also a concern because of the limited maintenance access and material limitations due to high levels of radiation. Experience at numerous neutron facilities, including FTS,

shows that eventually internal water leaks will occur. A continuous flow of helium (less than 1 l/m) will be used to sweep these impurities from the vessel. Large water leaks will require vacuum pumping and possibly removal via the syphon or drain.

4.5.2.4 Thermal Control Features

Containment of beam heat inside the vessel will be achieved by establishing the actively cooled limit outside the heat deposition zone at 0.001 W/cc. The thermal distribution results from the preliminary neutronics analysis illustrated in Figure 4.91 show this boundary relative to the vessel perimeter. This configuration results in an estimated 4000 W being deposited in the external, bulk shielding. Note that the vessel has an actively cooled extended waist at the neutron beam nozzles to account for uncalculated losses along the relatively open guides and in the downstream beam direction.

Internal water-cooling channels will be designed to ensure the vessel assembly is uniformly cooled to limit temperature variations to no more than 30°C, thus eliminating thermal shifts that could reduce the component alignment. Internal shielding heated at a rate greater than 0.001 W/cc will be independently water cooled. Water-cooling pipes to these components will be welded below the level of the shielding. Jumpers in the vessel space above the shielding will route the cooling water to the vessel ports.

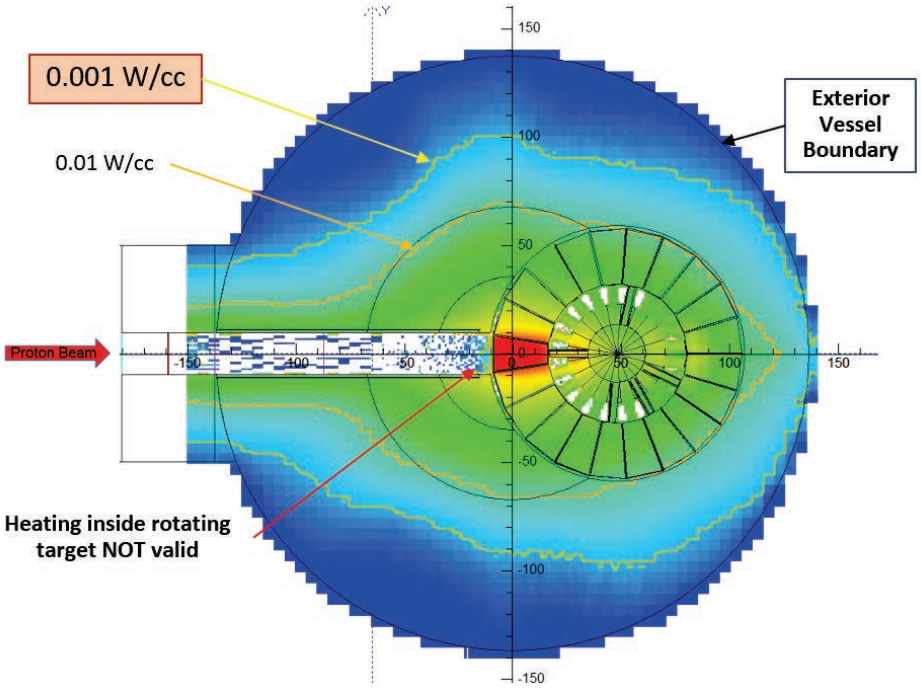

Figure 4.91. Nuclear heating (idealized) inside vessel interior at horizontal target center.

4.5.2.5 Safety Features

A safety relief device (rupture disk) will limit overpressures to 0.15 MPa. This pressure is lower than the 0.2 MPa design pressure for all other vessel components, specifically the neutron beam port windows. The safety vent will be designed to discharge to a dedicated, nitrogen-purged stack that vents outside the Target Building to minimize personnel exposure. The vent will be located at the top of the vessel in the open space between the shielding and lid to ensure full flow venting and to prevent water intake. The disk will be hands-on accessible to facilitate normal maintenance change-outs. The disk and vent size will be based on the requirements determined by the facility safety analysis in the next phase of design.

An ullage volume of approximately 0.75 m^3 will be located at the bottom of the vessel. An additional 0.25 m^3 will be provided by open volume below the neutron and proton beam ports for a total spill accumulation volume of 1.0 m^3. Accidental water releases, such as from a target shroud failure, can be contained within the ullage space. The ullage would be drained to the shielded cooling water drain tanks in the basement in a controlled manner. Backflow valves outside the vessel will prevent the decay and gas-liquid separator tanks fills from flowing back into the vessel when pumps are not operating.

Radiation protection will be provided by three layers of shielding (Section 4.6). The monolith shield will reduce the dose level from the neutron production zone to the target drive room to less than 10 rad/h during beam-on operation. Process cooling water will be activated to up to approximately 1000 rad/h (based on FTS measurements). To reduce background inside the target bunker during beam-on operation, the piping will be routed in channels with steel shield covers or in the vessel lid, which is roughly 61 cm thick. This will reduce the radiation background in the target drive room to less than 10 rad/h during beam-on operation. The target drive room enclosure will have HDC walls and a removable roof sufficient to reduce the personnel exposure radiation background outside the room to less than 0.25 mrem/h.

4.5.3 Interior Shield Assembly

Active components (PBW, TVP, target, and MRA) located inside the core vessel assembly will be configured for vertical remote handling. In all cases, the components themselves will include the actively cooled shielding associated with the component. The passive shielding blocks above the active components will be temporarily removed to allow access to the components for replacement, and then reused. The shield blocks will be solid steel and will be either solid stainless steel or stainless steel clad. Each will include a lifting eye designed to mate with remote handling tools. The blocks will be designed in conjunction with both the active components and vessel to incorporate pipe and conduit passages as well as mounting features. As currently configured, the vessel shield assembly will include approximately 20 significant shield blocks plus several smaller filler pieces.

4.6 TARGET STATION SHIELDING

Bulk shielding between the target vessel and conventional facilities will be provided by Target Systems. Included are the permanent iron shield surrounding the vessel and the steel liner between this shield and the HDC monolith enclosure. Also included are the removable shield blocks above the vessel and process water pipes (Figure 4.92). Although they are not included in Target Systems, the target drive room shield, monolith enclosure, and monolith foundation are important shielding elements. Therefore, they are included in the facility shielding analysis.

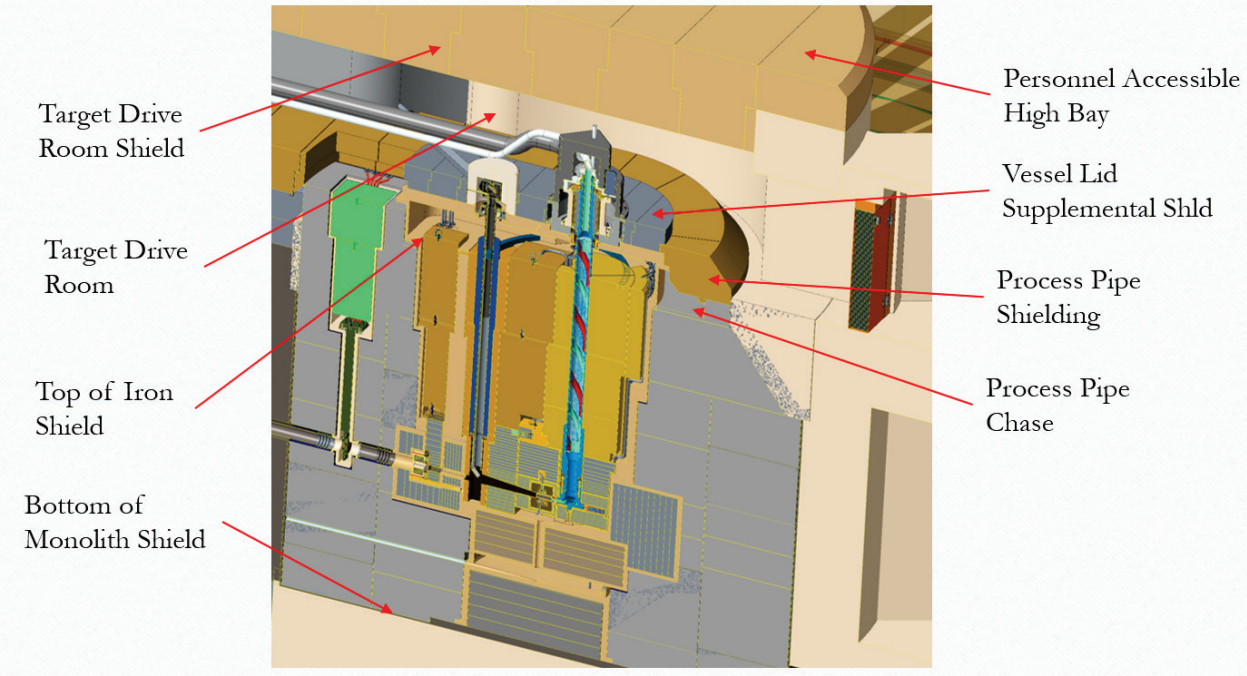

Figure 4.92. Section view of target monolith showing reference radiation exposure zones.

4.6.1 Shielding Requirements

Specific zones in and around the target monolith have radiation dose level or heat removal requirements as defined in Table 4.10.

Table 4.10. Target monolith radiation dose design criteria.

Location	Design criteria
Beam-on requirements	
Bulk shield interior	<001 W/cc
Top of monolith shield	0.25 mrem/h
Personnel accessible high bay	0.25 mrem/h
Target drive room	<10 rad/h
Bunker electronics room	1 n/cm^2·s (~0.25 mrem/h)
Bottom of monolith shield	<<0.001 W/cc
Beam-off requirements	
Target drive room	0.25 mrem/h
Top of iron shield	1.0 mrem/h
Neutron beam guide bunkers	0.25 mrem/h
Bunker electronics room	0.25 mrem/h

4.6.1.1 Neutronics Analysis

A preliminary STS shielding analysis is presented in Section 4.1.6. The neutronic model shown in Figure 4.16 was analyzed using radiation transport simulated with MCNPX calculation, starting with the proton beam. While the bulk shielding model has been simplified, the core target area is accurately modeled;

thus, the analysis provides a reasonable basis for determining the amount of shielding required in specific key areas of the current shielding configuration. The radiation dose maps resulting from the analysis are shown in Figures 4.93 and 4.94. The bulk shielding is conservatively designed; therefore, it is assumed that detailed neutronic shielding analyses performed in the preliminary design phase will not result in increased shielding requirements.

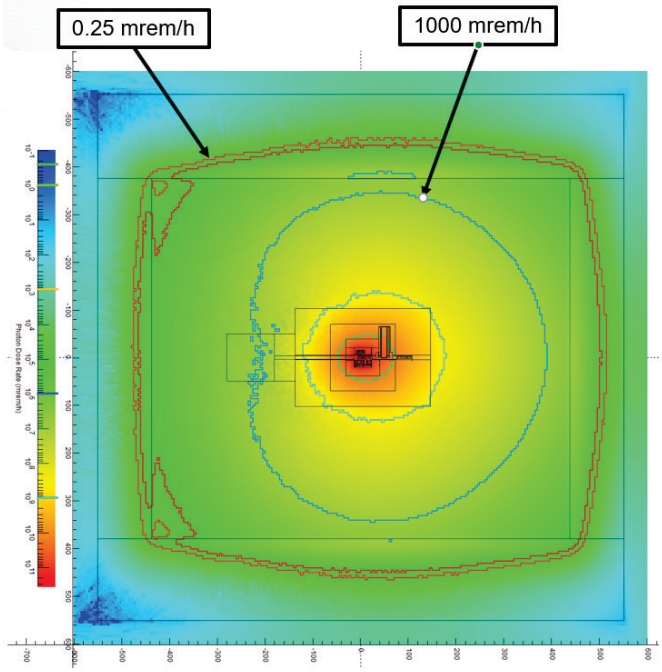

Figure 4.93. Vertical section of MCNPX model monolith showing calculated gamma radiation dose levels.

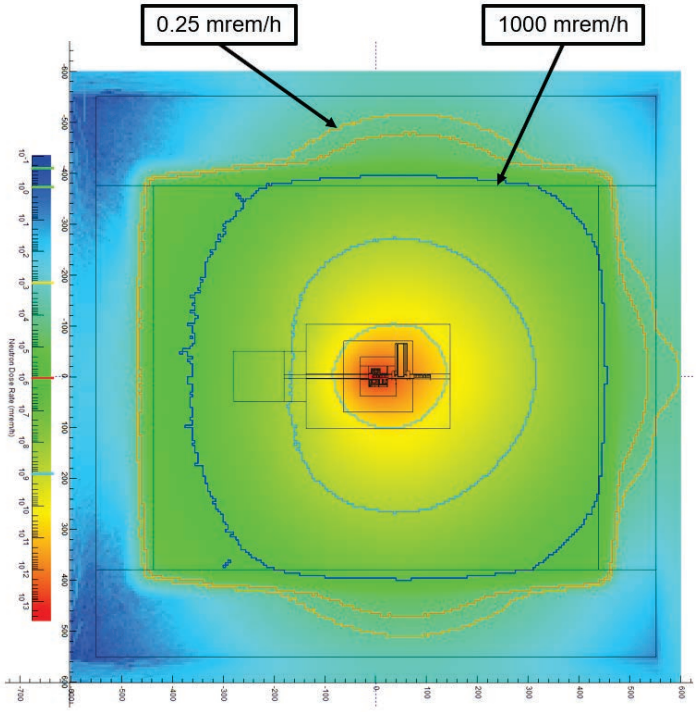

Figure 4.94. Vertical section of MCNPX model monolith showing neutron radiation dose levels.

Heating in the near-target area is a detailed output of the neutronics study used to determine the boundary between the vessel and the inside of the bulk shield. This output is shown in Figure 4.95. Note that heating shown in the target is not accurate since it was not modeled as rotating.

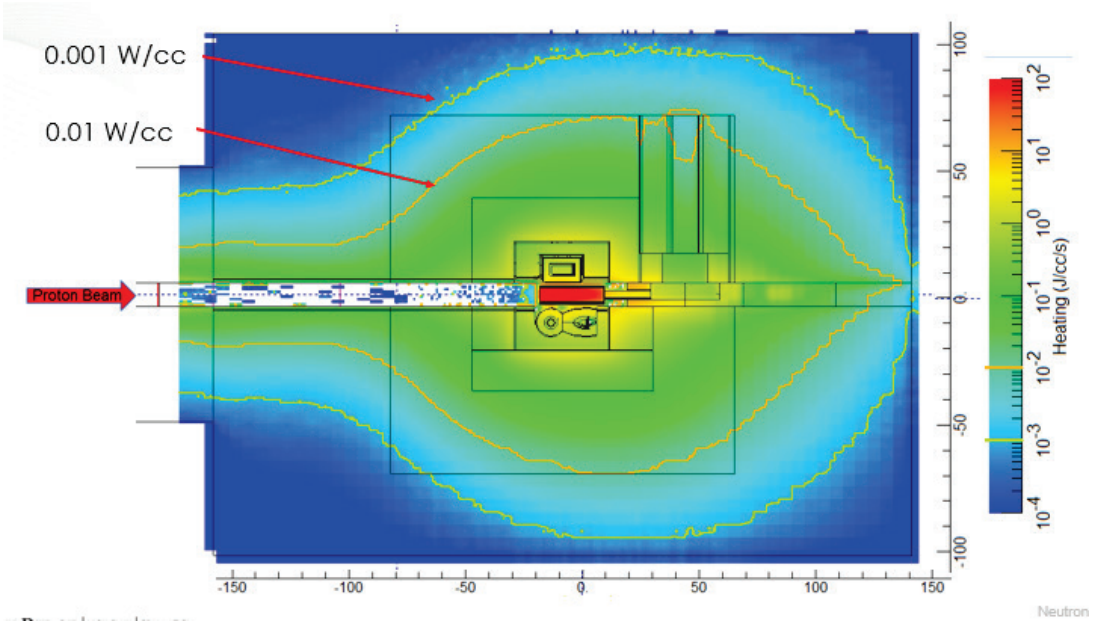

Figure 4.95. Vertical section through monolith showing beam heating near the STS target.

4.6.1.2 FTS Comparison

The FTS monolith has an arrangement (Figure 4.96) that approximates STS and has been proved to effectively shield radiation from the same source as STS. Thus, the real-world shield densities of FTS are compared with those of the current STS design.

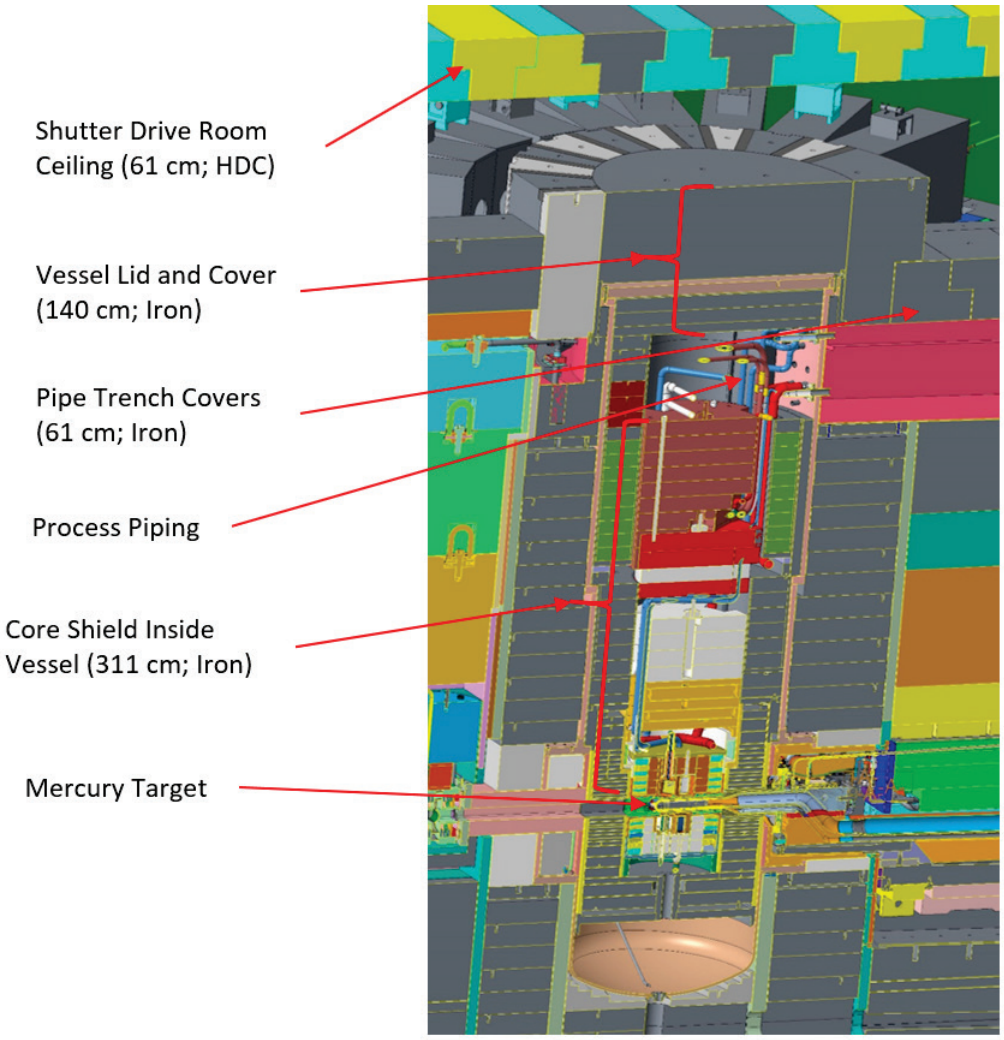

Figure 4.96. Vertical section view of FTS bulk shielding arrangement.

4.6.2 Shielding Design

The STS bulk shielding design was evaluated by comparing the density along key vectors with the FTS and neutronics densities (see Figure 4.97). Note that a minimum of 50 cm of HDC outside the iron shield is required to remove certain iron-penetrating gammas in shielding personnel. Further, since this is a conceptual design, the shielding design assumes additional material is required to account for unmodeled gaps and calculation inaccuracies. The result of the density analysis will be combined with operational and structural requirements to determine the overall size and configuration of the monolith and the monolith bulk shield. The following subsections detail the analysis for each vector.

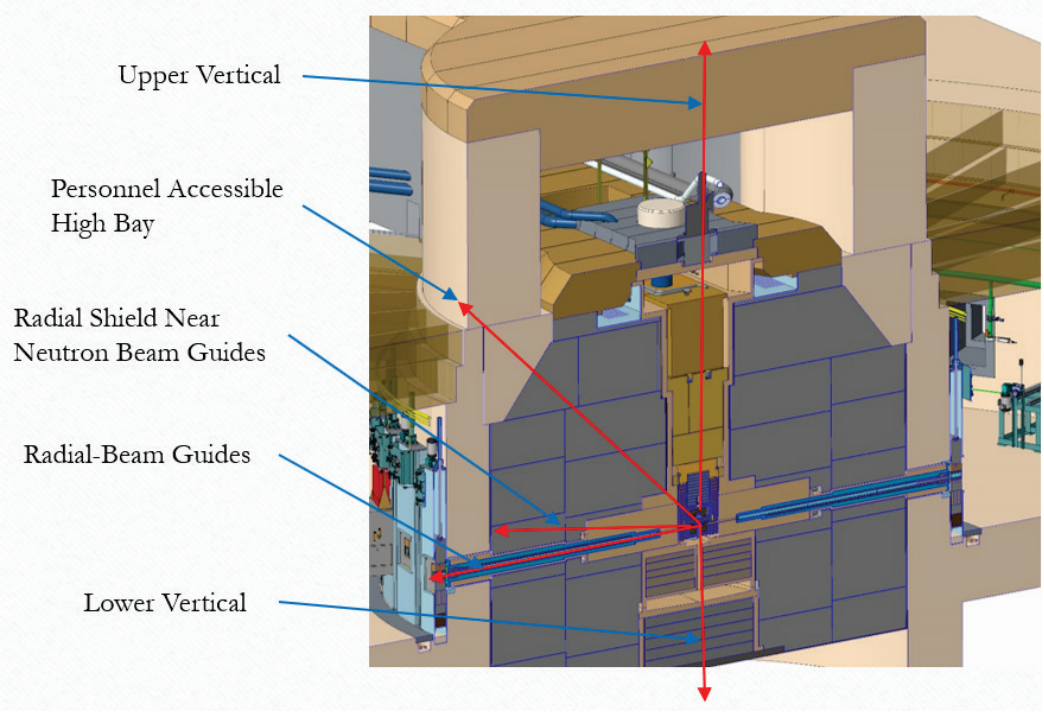

Figure 4.97. Vertical section of STS monolith, transverse to proton beam, showing shielding analysis vectors.

4.6.2.1 Radial Shield Near Neutron Beam Guides

The guide bunkers are designed for high-energy radiation emanating from the neutron guides with direct views of the moderators. Consequently, the bunkers have HDC walls and ceiling panels ranging in thickness from 1.5 to 2 m.

The diameter of the bulk shield is determined by the circumferential space required for shutters in the neutron beam guide bunkers. The combination of ~424 cm of iron and ~100 cm of HDC will reduce beam-on radiation doses to less than 0.25 mrem/h. This is significantly lower than is required for the unoccupied bunkers.

The neutron guide inserts will include significant streaming paths interrupted with steps. Design experience provides confidence that the current insert design will provide shielding comparable to the neighboring bulk shielding. The beam-off dose in the bunkers will be shielded by the shutters, which are sized based on FTS beam guide dose measurements.

4.6.2.2 Personnel-Accessible Portions of High Bay

As noted earlier, the circumference of the monolith is determined by the space requirements of the neutron beam line shutters. For structural and vertical access to the bunkers, this perimeter is projected vertically to also define the outside of the target drive room shielding. The outside of this shield will be the nearest a person can regularly approach to the target during beam-on operation. Because of the monolith configuration, the resulting shielding for this area will be roughly 40% greater than that required to reduce the dose to 0.25 mrem/h.

4.6.2.3 Lower, Vertical Bulk Shield

Preventing beam heating of the monolith foundation is required for the long-term stability of the target system. The amount of bulk shielding used in FTS has proved to be adequate; therefore, the same amount of shielding is proposed for STS (approximately 250 cm of iron).

4.6.2.4 Upper, Vertical Bulk Shield

Activated process water, pipe chases, and the requirements of the target drive room complicate the upper shield configuration. The basic height of the bulk shielding is fixed by the high bay personnel access level 427 cm above the target center. The activated process piping must be locally shielded with removable steel covers designed to reduce the drive room beam-on background to less than 10 rad/h. Based on the FTS system, the covers are currently designed to be 61 cm thick. The drive room HDC shielding will be designed to further reduce the dose level in the surrounding high bay for personnel access (0.25 mrem/h). For the purpose of the analysis, the shielding above the target and moderators is assumed to have the same density as the FTS vertical modules, to account for realistic vertical pipe chases and gaps between the modular shield blocks. As currently configured, the upper, vertical STS shielding will be over 40% greater than is required, and the drive room shielding thickness will be currently 250% thicker than in the FTS.

4.6.2.5 Downstream Bulk Shield

The neutronics analysis indicates that the bunker electronics room located downstream of the monolith will receive more radiation than is acceptable for reliable electronic performance or personnel entry during beam-on operation. Additional shielding will be added as determined by the detailed preliminary design phase neutronics analysis.

4.6.2.6 Bulk Shield Inner Configuration

Limiting bulk shield heating to less than the specified 0.001 W/cc defines the boundary between the core vessel and the bulk shielding. In general, the vessel will be much larger than necessary as a result of functional constraints. For example, vertical access extends the vessel beyond the heating zone. Similarly, the neutron beam nozzles also extend beyond the heating zone to provide adequate circumferential separation to attach the beam guide port extensions. Currently, the downstream area of the vessel has a local extension to contain the beam heating to 2 m or 25 cm beyond the calculated requirement.

4.6.3 Monolith Liner Design

A welded metal assembly will be located between the STS bulk shielding and conventional facilities monolith structure and foundation. The liner will have vertical sides and an open top to provide access for installation of the bulk shield. The roughly 2.5 cm thick assembly must be watertight up to the top of the iron bulk shield. It will be field assembled and structurally integrated with the monolith structure, serving as a form for some portions of the concrete placement.

The base of the liner will be the structural interface between the concrete foundation and the lower bulk shield assembly. Anchors to both sides of the base will be designed in accordance with the seismic criteria established for the STS monolith. The base will also include a plate designed to precisely align the core vessel relative to the ideal beam center during installation. This base will be sloped to a low-point drain that will direct leaks or spills to the LLLW process in the HPVs.

Openings for each of the 22 neutron beam lines and the proton beam will be integrated into the liner (see Figure 4.98). The maintenance shutter housings (provided by Instrument Systems) will be installed during the liner and concrete structure installation. These shutter housings will incorporate horizontal channels that will extend to the liner and be seal-welded to it. When the monolith wall is poured, these channels will provide openings through the shield wall into which beamline optical components can be inserted. These openings will have enough clearance to allow for independent alignment of the neutron beam port extensions that will be installed with the core vessel.

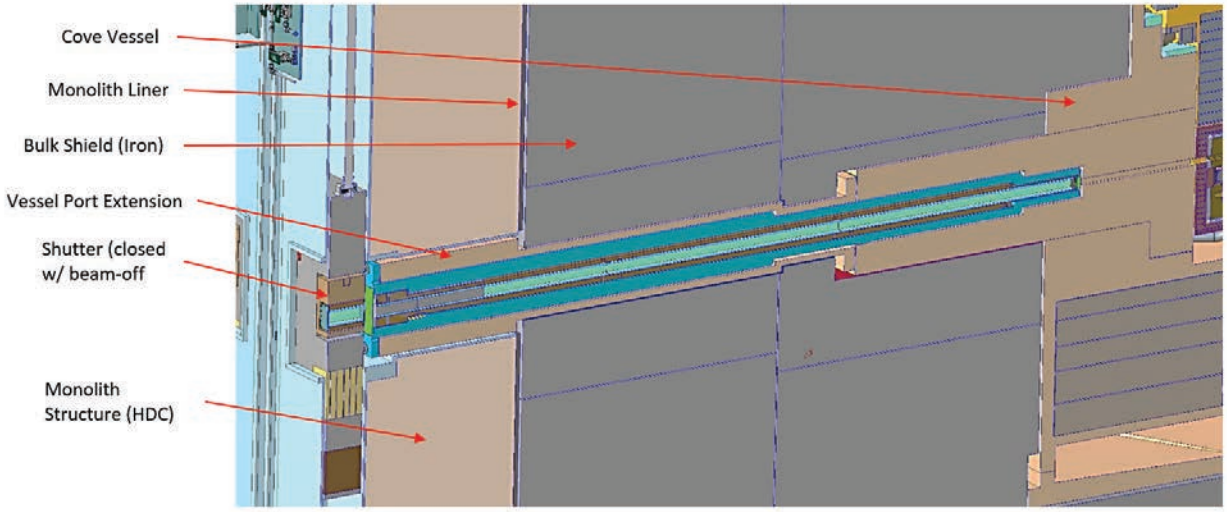

Figure 4.98. Neutron beam guide port interface with monolith liner.

4.7 CRYOGENIC MODERATOR SYSTEMS

The CMS will provide cryogenic hydrogen to the target moderators. Forced-flow circulation will be required to maintain the temperature of the moderators at a nominal 20 K with a small temperature variation (approximately 11 K) within the moderators. Based on the neutronics analysis of the STS system, the moderators will experience less than 1 kW of nuclear heating. A refrigeration capacity of approximately 2 kW will be installed to accommodate additional system heat leaks and provide adequate capacity contingency. Ortho-to-para-hydrogen converters will provide a para-hydrogen concentration of 99%.

The CMS will be physically and functionally similar to the existing SNS FTS hydrogen system. This system was fundamentally based upon designs successfully used for many years at other spallation neutron sources, namely LANL's Lujan Center and Rutherford Appleton's ISIS. Consequently, key components of that system will be used as the basis for the proposed STS system. While the STS heat load will be less than 25% that of the FTS system, the new system includes more margin for future upgrades and to reduce the hydrogen temperature variation from an average of approximately 3.3 K to 1.5 K.

The CMS will be located in the HUR outside the Target Building high bay. Two transfer lines will connect the system to the moderators. The HUR has its own ventilation system, including redundant active exhaust paths. The normal exhaust path and blower operate continuously during normal beamline operation. The two emergency vent paths remain in standby for actuation on detection of excessive hydrogen in the HUR. Loss of exhaust air flow will be indicated in the target control rooms. Hydrogen gas vented from relief valves and rupture disks will be directed to an inert gas-filled emergency vent stack.

The CMS will consist of two primary subsystems: a hydrogen circulation system and a helium refrigeration system. The helium refrigeration system will include a helium refrigerator, helium compressors, oil removal systems, helium gas management system, helium buffer tank storage, helium purifier, and associated interconnecting cryogenic piping. Both the hydrogen circulation system and helium refrigeration system will be supported by insulation vacuum systems.

4.7.1 Hydrogen Circulation System

The hydrogen circulating system will be a forced-flow, closed-loop system filled from pressurized cylinders of research-grade hydrogen. It will have two independent cryogenic loops, each containing a circulator, an accumulator, a heat exchanger, and an ortho-para-hydrogen convertor. Figure 4.99 illustrates one of these loops.

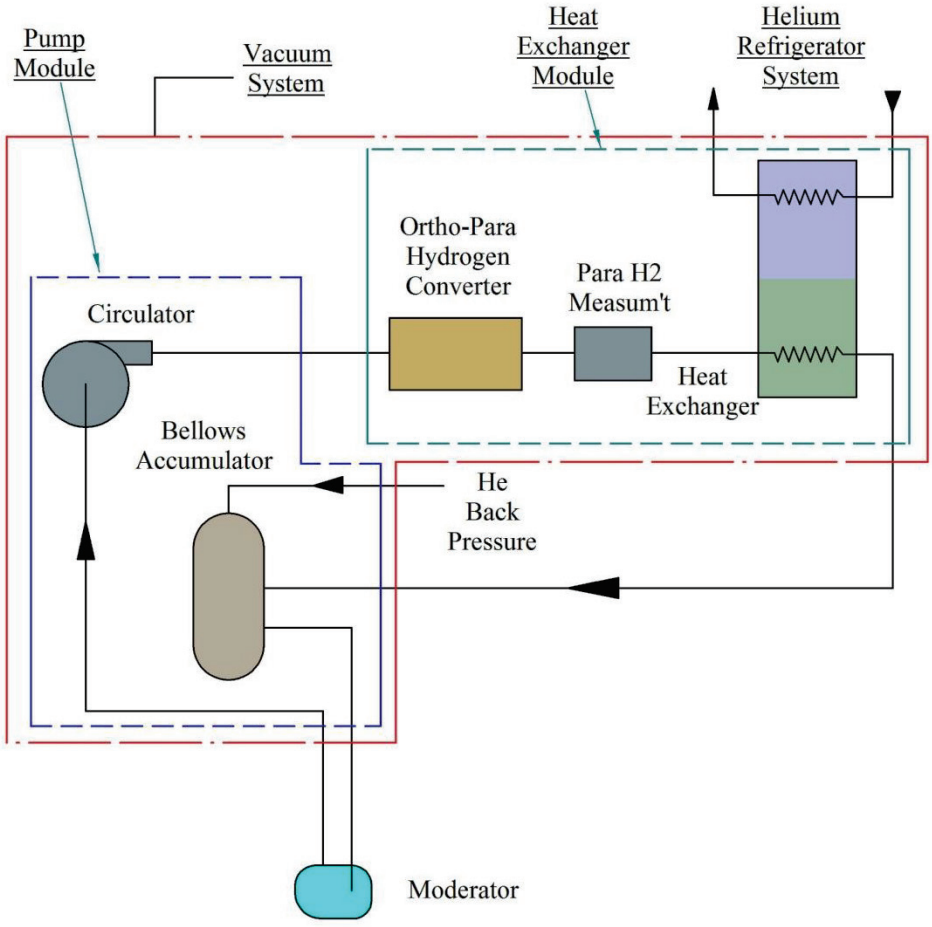

Figure 4.99. Simplified hydrogen loop diagram for STS.

The cryogenic hydrogen equipment will be packaged in two units—the heat exchanger module and the pump module (see Figure 4.100). The system also will include a hydrogen gas management system, pressure safety relief system, and associated interconnecting cryogenic piping. Since hydrogen will be maintained above the critical pressure at approximately 20 K, it is technically correct to refer to it as "supercritical" rather than liquid hydrogen. The system will always operate in this condition to eliminate phase change effects. The base pressure of the system will be maintained at 15 bar, providing a 1 bar

margin above the critical pressure and a 4 bar margin below the MAWP of the moderator vessels. The system will have a hydrogen inventory of approximately 5 Kg.

Figure 4.100. FTS cryogenic heat exchanger and pump modules.

The pump module and heat exchanger module vacuum systems will be separate from the vacuum for the transfer line and moderator vessel. Thus, a hydrogen leak inside the pump or heat exchanger module cannot flow through the vacuum layer down into the core vessel.

4.7.1.1 Heat Exchanger Module

The heat exchanger module will be a vacuum vessel housing two helium-to-hydrogen heat exchangers and two ortho-para-hydrogen converters, along with flow control and isolation valves on the associated helium piping. The heat exchanger module will also contain two para-hydrogen concentration measurement instruments. The heat exchangers will be brazed plate-fin heat exchangers like those used at FTS. Ortho-para-hydrogen converters will be vessels containing iron oxide. Increases in the hydrogen system volume and pressure drop resulting from this component have been incorporated in the system design. An in-line Raman spectroscopy probe is currently considered to be the primary ortho-para-hydrogen diagnostic. However, a thermal conductivity probe is a potential alternative. The STS design will benefit from ongoing development work included in the Proton Power Upgrade project.

4.7.1.2 Pump Module

The pump module will be a vacuum vessel containing two variable-speed circulators, two cryogenic accumulators, and various flow, temperature, and pressure sensors.

The circulators will pump the supercritical hydrogen around the loop between the heat exchanger and the moderator vessel. Cryogenic helium circulated through the heat exchanger will remove heat that the cryogenic hydrogen absorbs from neutron heating as well as static heat loads from the related cryogenic equipment.

The basic cryogenic circulator pumps will be like those that have operated reliably for over 10 years in FTS (Figure 4.100). However, the lower STS flow rates may require some differences. The project will work with the manufacturer to acquire the required configuration.

The accumulators will accommodate volume changes resulting from operational swings in temperature without the need to add hydrogen to or subtract it from the system. This will allow the system to passively accommodate the pressure fluctuations that accompany beam power variations or beam-trip–induced temperature transients. The hydrogen pressure control ranges are14–15 bar with the beam off and 15–16 bar with the beam on. The accumulator will work by balancing the hydrogen volume against a fixed helium volume with a metal bellows. The STS accumulator will be based on the units used in the FTS cryogenic system.

Metal bellows have historically been implemented in various systems as accumulators for not only thermal expansion but also pulsation damping. Edge-welded bellows have enough convolutions to theoretically have a virtually infinite cycle life because the bellows movement will be kept well within the elastic range. The bellows assembly will be contained in a double-walled, stainless steel vessel. The accumulator vessel will be surrounded by flowing hydrogen to ensure adequate cooling and isothermal expansion and compression of the helium gas. The expansion bellows will be designed with additional margin to provide enough stroke to accommodate pressure variations of 13 and 18 bar, thus addressing both overheating and over cooling conditions.

Although not used in operation, the cryogenic accumulator will be equipped with a laser-based measuring system to indicate the relative position of the bellows. The actual position of the bellows will not be used for any control inputs, as the system will be completely passive. However, knowing the actual bellows position and trending this data over time assists with monitoring the health of the system. In a constant-mass system, the pressure cannot be maintained if inventory is lost. A decrease in the loop base pressure would be the result of either a helium leak on the backside of the expansion bellows or a hydrogen leak. Monitoring the bellows position, however, will make it very clear which system is leaking. A loss of helium in the accumulator would result in bellows expansion and thus pressure decay at constant temperature. A loss of hydrogen would result in bellows compression and thus pressure decay at constant temperature.

4.7.1.3 Hydrogen Gas Management System

The hydrogen gas management system (see Figure 4.101) will consist of sensors and various remotely actuated isolation and pressure regulating valves to control the warm gas distribution and venting operations. To minimize the potential for hydrogen leaks, the system piping will generally be welded. Mechanical couplings will be used only where necessary for operational or maintenance reasons (e.g., in control valves). All interconnecting piping that contains the supercritical hydrogen will be vacuum jacketed to maintain cryogenic temperature and to contain the hydrogen in the event of a leak. All vacuum-jacketed piping will be evacuated with a portable dry vacuum pumping station and then sealed.

Figure 4.101. FTS Hydrogen gas management system.

The pressure safety relief system will use spring-loaded relief valves and rupture discs welded into the hydrogen fluid lines. Figure 4.102 illustrates the rupture disc assemblies welded into their associated manifolds. The discharge from these rupture discs will be plumbed to a common manifold so the lost hydrogen can be exhausted to the hydrogen safe vent stack.

Figure 4.102. FTS welded pressure relief rupture discs and manifold.

4.7.2 Helium Refrigerator System

The helium refrigeration system will provide active cryogenic cooling to the hydrogen circulation system by directing a closed-loop stream of cryogenic helium gas to the helium-to-hydrogen heat exchangers in the heat exchanger module described in Section 4.7.1.2.

4.7.2.1 Helium Refrigerator

The primary component of the helium refrigeration system will be the helium refrigerator (see Figure 4.103). The refrigerator will have a capacity of approximately 2 kW at 17 K to accommodate the calculated 1 kW moderator heat load plus normal operating loads. The refrigerator will expand and cool gas from the helium compressors to approximately 16 K. Discharged helium will be distributed to the two helium-to-hydrogen heat exchangers, where heat from the moderators and hydrogen system equipment will be absorbed. The returning gas stream will flow back through the low-pressure side of the refrigerator to the suction side of the helium compressors.

Lessons learned in the design and operation of the FTS and new High Flux Isotope Reactor helium systems will be incorporated into the STS helium refrigerator design. Liquid nitrogen precooling will not be used, in order to reduce complexity and cost as well as improve reliability. A vertical heat exchanger will be used, since this arrangement has proved to be more efficient and reliable because it reduces maldistribution problems. Other features shown to improve reliability are a single expansion turbine, redundant helium compressors and a full-flow helium purification system.

Figure 4.103. FTS Helium refrigerator.

4.7.2.2 Helium Compressors

STS will employ three water-cooled screw compressors, each capable of providing 50% of the required flow (see Figure 4.104). Each compressor will be skid-mounted with heat exchangers, relief valves, and an integral bulk oil removal system. Normally, two of the three compressors will operate, with the third compressor on standby. If a compressor fails and the beam trips off, the single operating compressor can maintain a cold system under passive loads while the third compressor is brought online, minimizing downtime.

Figure 4.104. FTS helium compressor.

4.7.2.3 Helium Purification System

An oil removal system will maintain the purity of the helium gas by reducing the entrained oil to less than 5 ppb. The system will use a series of coalescing filtration units in line with a regenerable charcoal absorber (see Figure 4.105). The helium refrigeration system will have two identical oil removal systems for redundancy. In addition, a liquid nitrogen–cooled helium purifier sized at 150% of total compressor capacity will be used to further improve helium purity (see Figure 4.106). The purifier will be capable of accepting the entire gas flow from the compressors, and its associated piping will be designed to allow the purifier to be isolated from the helium system while it is operating. A pyrolizing multi-component impurity detection system will continuously monitor helium gas purity.

Figure 4.105. FTS oil removal system.

Figure 4.106. FTS helium gas purifier.

4.7.2.4 Helium Gas Management System

The helium gas management system will continuously adjust the amount of helium gas in the system to account for load changes by withdrawing or discharging gas to the helium buffer tanks. Thermal stability

for the helium refrigeration system will be provided by an integral control heater capable of generating control heat equivalent to the total moderator system load.

4.7.3 Vacuum System

A major key to reliable operation of the cryogenic system will be the ability to maintain a high-vacuum envelope to provide effective thermal insulation around all parts of the system that contain cryogenic hydrogen and helium. The capability to hold an ~20 K hydrogen temperature will be very sensitive to the heat input and, therefore, to leakage of gases into the vacuum insulating layer. The vacuum utilities are designed to provide pump-down to the required (~10^{-6} torr) vacuum range. Engineered barriers with all-welded connections will minimize the chance of leakage. Any significant leakage of hydrogen or helium into the vacuum barrier would allow greater than normal heat transfer and cause the hydrogen temperature to increase. If enough leakage should bring the vacuum into the range of 10^{-2} torr or greater, rapid temperature and pressure increases would occur, requiring venting to control the pressure. System pressure will be controlled without operator intervention by the 18 bar spring-loaded relief valves and/or the 19 bar rupture discs, which will discharge into the inert-gas-purged vent line.

The CMS evacuated volumes will be separated to reduce the impact of a single leak and the potential for mixing of hydrogen. For example, the pump module and heat exchanger module vacuum systems will be separate from the vacuum for the transfer line and moderator vessel. Thus, a hydrogen leak inside the pump or heat exchanger module cannot flow through the vacuum layer down into the core vessel. In addition, the system will be of fully welded construction with no active vacuum pumping. This will enable pressure and temperature changes to act as a passive leak detection system.

4.8 TARGET TECHNICAL COMPONENT UTILITIES

The Target Systems technical component utilities scope includes three primary activated cooling-water loops, an LLLW system, leak collection systems, and helium and nitrogen gas distribution systems.

4.8.1 Target Cooling Water Systems

There will be three primary activated cooling-water loops servicing target components—two light water loops and one heavy water loop. Included in these systems will be components such as drain tanks, delay and gas/liquid separator tanks, piping assemblies, pumps, control and on/off isolation valves, ion exchangers, filters, gas analyzers, and samplers.

The conceptual design basis activated cooling-water heat loads are summarized in Table 4.11.

Table 4.11. Second Target Station design basis cooling water heat loads.

Activated cooling water loop	Design basis heat load, KW w/ safety factor	Water type	Ultimate heat sink
Loop 1	479	H_2O	TW
Loop 2	30	D_2O	TW
Loop 3	251	H_2O	TW

The design basis heat loads for the STS design are based on the preliminary neutronics analysis. Design safety factors were applied to all the heat loads based on engineering judgment.

4.8.1.1 Primary Cooling Water Loops

Figure 4.107 depicts a simplified block flow diagram, representing the primary components in the activated target station primary cooling water loops. Features unique to individual loops are highlighted in the figure and are described in the following paragraphs.

Light water-cooling loop 1 will remove heat from the rotating tungsten target, the target axle, and the aluminum PBW. Water in loop 1 will be significantly activated by the direct exposure to both the proton beam and neutron radiation. Combining the target and PBW on the same loop serves a safety function wherein a flow failure will result in a mechanical failure of the window, which ensures a proton beam shutdown. This feature will act as a backup to the normal target protection system. Full-flow filtration will be provided upstream of the delay tank for loop 1 to capture tungsten corrosion products that may be released in the event of a target cladding failure. The dual delay/filtration functionality may be provided in a set of parallel, combined delay/filter tanks. A means for early detection of a cladding failure will be pursued (e.g., pressure differential across filters, gamma radiation) to minimize the potential spread of activated particulates beyond the full flow filters. A bypass around the full-flow filters will be provided for operational flexibility and may be used to avoid excessive backpressure on the target. Loop 1 water flow will be maintained (with emergency power backup) for a to-be-determined time period to ensure the target is protected from structural damage due to decay heat during maintenance periods.

Heavy water-cooling loop 2 will remove heat from the beryllium reflectors, aluminum shells, and inner stainless-steel shielding. Water in loop 2 will be directly exposed to the proton beam and neutron radiation and will be significantly activated. To minimize losses of heavy water to the hot-offgas system, a gas recombination system will be employed in loop 2 to recombine the deuterium and oxygen for recycling to the loop.

Light water-cooling loop 3 will remove heat from the shielding, vessel, plugs, PBW shield, periscope mirror, pre-moderators, and neutron beamline monolith inserts. The loop 3 water will be primarily exposed to a neutron radiation environment.

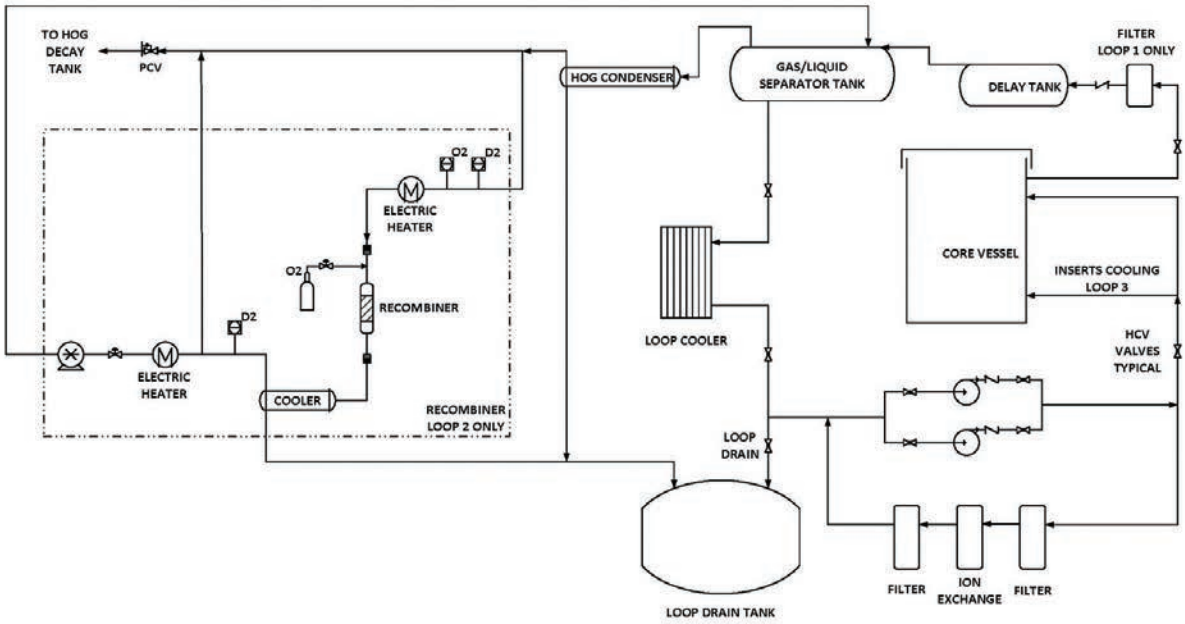

Figure 4.107. Primary cooling loop block flow diagram.

During normal operation of the water loops, water will circulate in a closed loop independent of the storage/drain tank. It is expected that discharge to the drain tank will be performed only if required (e.g., in response to an abnormal occurrence or to facilitate maintenance on loop equipment). Each of the primary target cooling water loops will reject heat to a secondary cooling water system. Delay tanks will be employed in the return line of each activated water loop to facilitate localized decay of some of the short-lived gamma and beta activity. The delay will also reduce the potential for neutron activation of components located in areas to which access must be provided for maintenance. Localized shielding will be provided as required to address the anticipated deposition of the longer-lived activation product radionuclides such as ^{7}Be in system components (e.g., heat exchangers, ion exchange units, and filters). Separation of gases generated in the water loops as a result of spallation and/or the radiolytic decomposition of water will be achieved in a gas/liquid separation tank to be located at the high point in the cooling loop. The radiolysis and activation gases will be vented to the hot offgas system provided as part of the conventional facilities.

To minimize heavy water losses to the hot offgas system, a recombination system will be provided to recombine the deuterium and oxygen formed by radiolysis in heavy water loop 2. An inert gas recycling system will also be employed to further reduce losses to the stack. As in the FTS, gas will be vented from the loop to maintain the loop pressure within an acceptable operating range. Recycling the purge gas has a side benefit of reducing the total gas flow through the hot offgas decay tank, thereby increasing residence time and lowering stack emissions. A bypass of the recombination system will be provided for operational flexibility (e.g., if the recombination effectiveness is compromised) and reliability, allowing direct venting of the loop 2 offgas to the hot offgas system. Refer to the Conventional Facilities Section 8.3.1 for details on the hot offgas decay system.

Components successfully used in the FTS water loops will be considered for applicability in the STS to reduce the spare parts inventory and required maintenance diversity (e.g., ion exchange columns, filters, valves, pumps, instruments).

4.8.1.2 Secondary Cooling Water Loops

Primary cooling loops 1, 2, and 3 will reject heat to a secondary 87°F deionized (DI) water cooling loop, which in turn will reject heat to the 82°F tower water system. If neutronics calculations indicate a significant benefit can be realized, the water flow to the pre-moderators may be further cooled using a chilled 70°F DI water flow to a water-water heat exchanger. The 70°F DI water will in turn reject heat to the 45°F chilled water system. These secondary loops will be provided by Conventional Facilities.

4.8.2 Target Utility System Layout

The primary cooling loop pumps, drain tanks, polishing loops, and valve manifolds will be in the shielded HPV in the basement of the Target Building as shown in Figure 4.108.

Drain tanks will be provided in pits in the Target Building basement to facilitate draining of the corresponding water loops for technical component removal or maintenance. The mezzanine levels in the HPV will house the loop 2 recombination system and the hot offgas condensers for all three loops as shown in Figure 4.109.

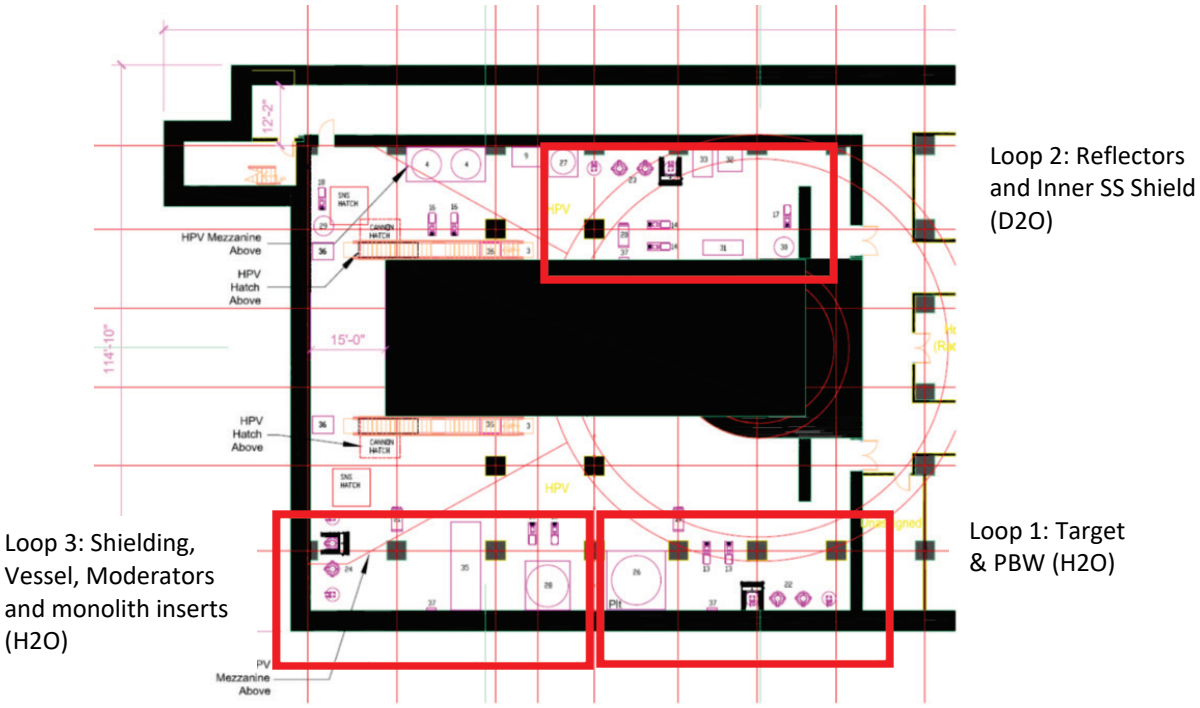

Figure 4.108. Utility systems in the hot process vault in the Target Building basement.

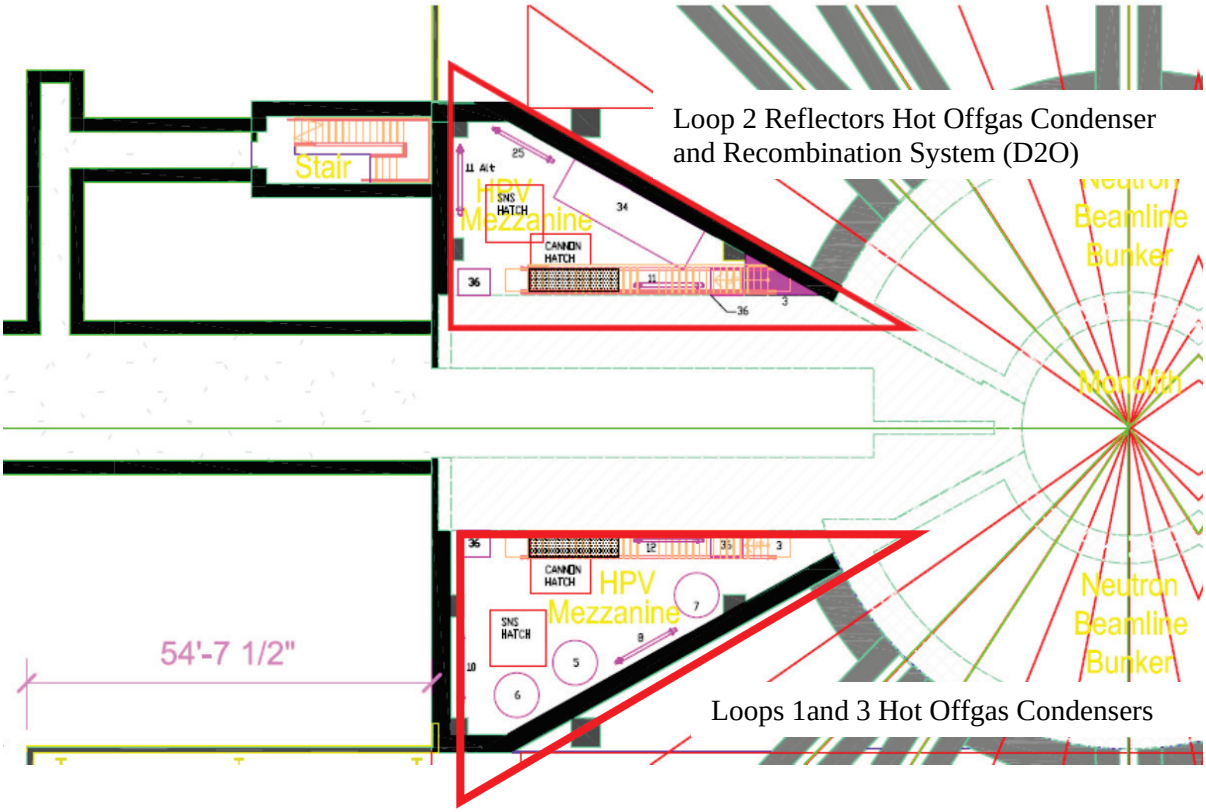

Figure 4.109. Mezzanine levels of the hot process vault.

The filter/delay tank and gas/liquid separator tank cavities will be in the high bay adjacent to the top of the shield stack as shown in Figure 4.110.

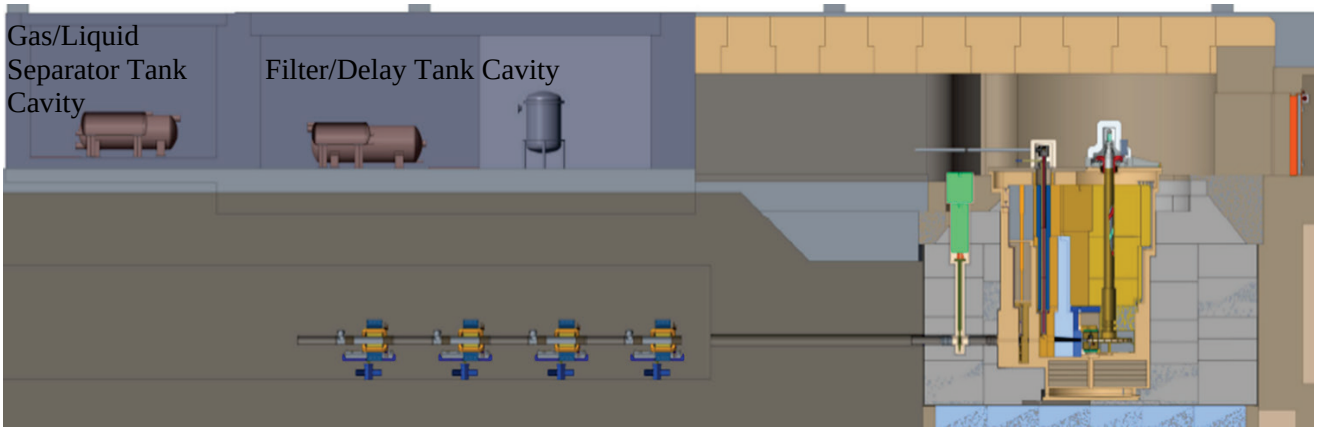

Figure 4.110. Filter/delay and gas/liquid separator tank cavities in the Target Building high bay.

Prefabricated vertical pipe chases will be provided to accommodate the routing of utilities from the HPV basement to the tank cavities located in the high bay, with service to the mezzanine levels as required. Horizontal pipe chases will be required to route piping between the mezzanine levels and the monolith bunkers, between the tank cavities, and to/from the top of the shield stack and vessel. Because of the high levels of short-lived radioisotopes in the water, the return cooling water lines and delay tanks require approximately 1.25 m of HDC shielding.

4.8.3 Low-Level Liquid Waste System

An LLLW system will be provided to facilitate the collection and disposition of the waste water from the light water loops. A simplified block flow diagram representing the primary components in the LLLW system is depicted in Figure 4.111.

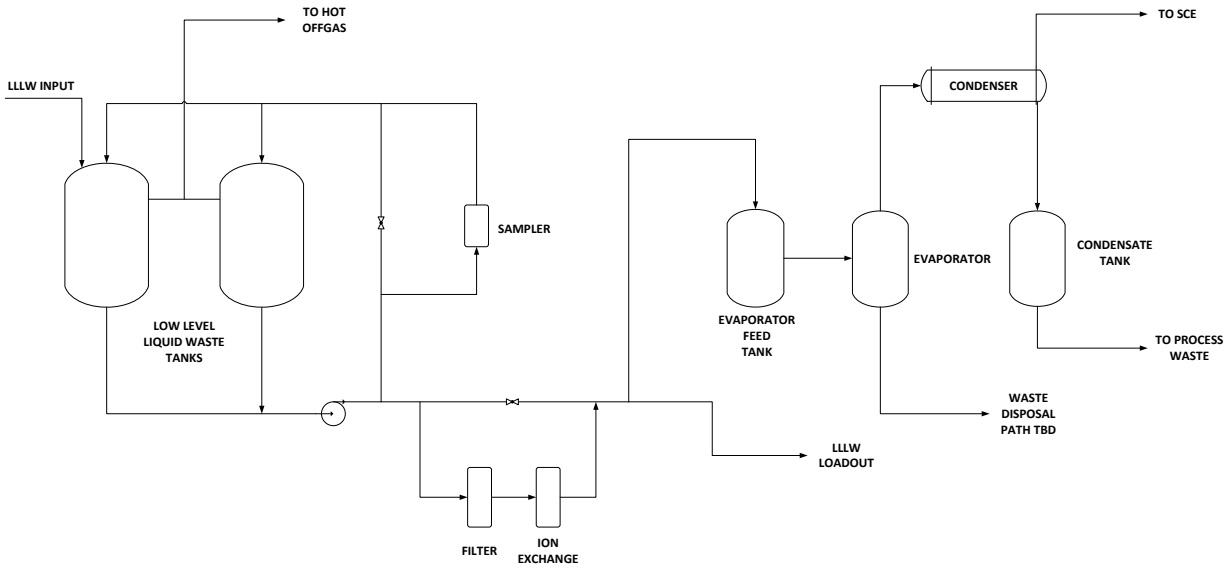

Figure 4.111. Low-level liquid waste block flow diagram.

The LLLW collection system will consist of two collection tanks, pumps, a sampler system, an evaporator feed tank, an evaporator, a condenser, and a condensate tank. A bypass cleanup system will also be provided with filtration and ion exchange columns to facilitate the removal of particulate and ions from water collected.

The LLLW system components will be located in the Target Building HPV on both the basement and mezzanine levels. For disposition of evaporated water vapor, the plan is to discharge offgas from the evaporator into the secondary confinement exhaust system. This would be done at a location that would ensure the secondary confinement exhaust system flow would be sufficient to carry the water vapor out without its condensing in the exhaust line to the stack.

The LLLW system flowsheet development will be based on the activation in the water and the anticipated source terms associated with recovering from a target cladding failure that results in water corrosion of the tungsten target material.

4.8.4 Leak Collection Systems

The leak collection systems provided in STS will allow for the detection and recovery of heavy or light water leaks in the various regions through which the water lines are routed, or where components containing residual water may be handled.

4.8.4.1 Core Vessel Drain Leak Collection System

The core vessel drain leak collection system will interface with the double-walled drain line provided by the core vessel WBS 5.6 and will collect any water that leaks into the core vessel from any of the three water loops for detection and disposition. The system will be housed in the HPV and will consist of a collection tank, a level indication instrument, a sampler, and a transfer pump system. The system will also interface with the hot offgas, nitrogen, LLW, and process waste systems.

4.8.4.2 Bulk Shielding Drain Collection System

The bulk shielding drain leak collection system will interface with the double-walled bulk shielding drain line provided by WBS 5.7. It will collect any water that leaks from water lines outside the core vessel into the bulk shielding from any of the three water loops for detection and disposition. Leaks may be at the top of the shield stack or in the bunker area outside the collection pan. The system will be housed in the HPV and will consist of a collection tank, a level indication device, a sampler, and a transfer pump system. The system will also interface with the hot offgas, nitrogen, LLW, and process waste systems.

4.8.4.3 Hot Process Vault Tank Pit Collection System

The leak collection system in the HPV will collect any water leaking from piping, from flanged joints in the HPV, or in the vertical chases that collects in any of the tank pits in the HPV floor. The system will consist of multiple-level detection instruments, suction lines down to the pits from the main floor level, and a transfer pump system that allows recovery, sampling, and recycling either to the appropriate water loop drain tank, the LLLW, or process waste system.

4.8.4.4 Mezzanine and Tank Cavity Leak Collection System

The mezzanine and tank cavity leak collection system will collect any water that leaks into the following areas for detection and disposition.

- Gas/liquid separator (GLS) tank cavity catch pan: This pan will collect leaks into the pipe pan between the delay tank cavity and the core vessel, which will leak back to the lined delay tank cavity, any leaks in the delay tank cavity that will drain back to the lined GLS cavity, and any leaks directly into the GLS cavity.

- Bunker catch pan: Leaks into the bunker catch pan will be detected in the monolith or on the corresponding mezzanine level to which the bunker pan drains. They will be collected and routed to the HPV basement via the vertical chases that pass through the mezzanine levels.

- Mezzanine-level catch pans: Any water that leaks from the water loop hot offgas condensers, chilled water to the condensers, waste water in the LLLW system, or recombined heavy water from the recombination system will be collected in a manifolded and monitored drain line collection system in the HPV.

The system will consist of multiple level detection instruments, a sampling system, a gravity drain system, and a collection tank and a transfer pump system that allows for recovery, sampling, and recycling either to the appropriate water loop drain tank, to the LLLW, or to process waste.

4.8.4.5 Service Bay Leak Collection System

The service bay leak collection system will interface with the service bay pit liner provided by Conventional Facilities and will collect any water that leaks into the service bay pit during handing of target components that may contain water. The system may be housed in the service bay and will consist of a level indication instrument and a transfer pump system. The system will interface with the hot offgas, nitrogen, LLW, and process waste systems.

4.8.5 Helium/Nitrogen Gas Distribution Systems

Helium and nitrogen gas will be supplied to STS by Conventional Facilities.

The core vessel will normally operate at a slightly sub-atmospheric pressure using a core vessel helium inerting system. Alternatively, the core vessel may be operated with a vacuum atmosphere to limit interference with neutron beams while providing a limited ability to eliminate or remove harmful gases or liquids that can be generated by small water leaks. If the normal operating mode is the helium mode, a helium recycling system may be considered.

4.8.5.1 Helium Distribution

Helium gas will be supplied to STS by Conventional Facilities. Conventional Facilities will provide the regulation/metering and the main helium gas supply line into the Target Building and the main distribution headers within the Target Building. The gaseous helium supply from the tube trailers will have a minimum purity of 99.995%.

Distribution in Target Building

Target utility systems will distribute the helium from the target basement gas panels to various end users within the Target Building, e.g., the core vessel, inflatable seal(s), and monolith inserts, and to water loops as a backup to the nitrogen used for atmospheric purging of flammable constituents.

4.8.5.2 Core Vessel Inerting System

The normal operating environment of the core vessel will range from full vacuum (~10^{-3} torr) to a helium environment at slightly below atmospheric pressure (approximately –30 in. water gauge). The core vessel inerting system will consist of a regulated helium supply and an air ejector controlled to maintain a slight vacuum within the core vessel during the helium mode of operation. If the primary operating mode is the helium mode, a helium recycling system may be considered.

The core vessel vacuum pumps (provided by a separate target vacuum WBS) will be used before transitioning to the helium mode of operation to remove air and to make a general assessment of seal integrity.

The exhaust from the vacuum pumps and the ejector will be routed to the secondary confinement exhaust system provided by Conventional Facilities.

A residual gas analyzer (provided by a separate target vacuum WBS) will be provided in the core vessel vent line to monitor the composition of the gas leaving the core vessel in either vacuum or helium mode. If water is detected in the core vessel, the core vessel will be isolated and, in some cases, the vessel offgas will be redirected to the hydrogen safe vent stack. A rupture disk will also be provided on the core vessel by to protect the vessel against overpressurization.

4.8.5.3 Nitrogen Distribution

Nitrogen gas will be supplied to STS by Conventional Facilities. Conventional Facilities will provide the liquid nitrogen tank and regulation, vaporizer, vacuum-jacketed supply lines, gas flowmeter, main supply lines, and main distribution headers within the Target Building. The gaseous nitrogen supply from the liquid nitrogen storage tank and vaporizer will have a minimum purity of 99.998%. The capability to refill liquid dewars at an outdoor refill station adjacent to the liquid nitrogen storage tank also will also be provided by Conventional Facilities.

Target utility systems will distribute the nitrogen to various target group end-users within the Target Building (e.g., gas/liquid separation tanks). Nitrogen will be used as a purge and cover gas in areas exposed to high-energy radiation to minimize the production of activated and corrosive gases and to prevent flammable gas mixtures from reaching the lower explosive limit concentration. Nitrogen will also be used to purge and backfill process systems before the cooling water loops are drained and filled with water, purge trapped volumes of cooling water from target components, and purge hydrogen safe vent stacks to minimize the potential for air ingress.

4.9 REMOTE HANDLING SYSTEMS

Operation of STS will require periodic maintenance or replacement of many components by remote handling as a result of activation and other radiological hazards. These remote handling operations include the replacement of activated components due to nominal end of life, installation of new components in radiologically hazardous areas, and the disposal of spent components as waste following replacement. Disposal of activated components as waste will use a shielded service cell to aid in size reduction and packaging of waste items and to provide infrastructure to perform post-irradiation examination. One aspect of the preparation for these activities includes full-scale mock-up testing activities. The scope of work for these activities is delineated as follows:

- Service Cell Systems

  - This work package consists of the processes and remote handling tooling required to support all service cell operations

- Component Replacement Systems
  - This work package consists of the processes and remote handling tooling required to support all planned component remote replacement operations

- Waste Disposal Systems
  - This work package consists of the processes and remote handling tooling required to support all component waste disposal operations

- Mock-up Facility
  - This work package consists of the infrastructure and tooling required to enable a variety of full-scale mock-up testing activities.

The following sections examine each of these WBS elements in further detail.

4.9.1 Service Cell Systems

A shielded “service cell” has been introduced into the STS Conceptual Design. All of the tooling and infrastructure associated with the service cell is included in WBS S.3.10.1. The primary reasons for inclusion of this feature were to enable size reduction and/or packaging of activated components in support of waste disposal operations and to provide the means to perform critical post-irradiation examination. A shielded service cell resolves challenging process and tooling issues associated with these activities.

Disposal of highly-activated components as waste will be accomplished via remote handling. The basic elements of the disposal process involve transfer of the waste item from a cask design for remote handling operations into a cask suitable for transport. This simple process will be complicated by the need to control the radiological hazards inherent in the handling operation and the need to conform to existing shipping cask capabilities. Often, conforming to the size and capacity requirements for existing casks will require some amount of size reduction. A service cell not only provides a means to control the radiological hazards but provides flexibility in the processes and tooling needed to perform this size reduction. Additionally, most highly activated waste must be handled remotely at the disposal site. This handling requirement drives the need for an interface compatible with the infrastructure at the disposal site. The SNS FTS routinely ships waste of this description in shipping casks that use an internal liner to provide this handling interface. The service cell will provide the means to load the waste item into the liner for subsequent loading into the disposal cask. These operations would be difficult and hazardous outside a cell environment.

For STS, it is envisioned that the disposal of the target wheel, the MRA, and the PBW, as a minimum, will use the service cell for disposal. Specifically, the cell will provide the means to transfer these items from the remote handling cask to the disposal cask. To inform the conceptual design of the service cell and its needed infrastructure, the following process was used:

1. Define the handling requirements to be accommodated in the cell
2. Develop a basic process that meets these handling requirements
3. Determine the cell interfaces and features needed to support this basic process
4. Develop floor space requirements needed to accommodate these interfaces and features

The basic process of target handling in the cell was viewed as the primary driver for cell design and was used to define the parameters and requirements. This process follows the process used successfully for more than 23 shipments from the FTS. The basic process is as follows:

1. Mate the target cask to the top loading port (TLP)
2. Lower the target assembly into the cell
3. Separate the target shaft from the wheel
4. Withdraw the shaft back up into the target cask
5. Load the target disposal liner in the cell via the TLP
6. Load the target wheel into the liner
7. Mate the disposal cask to the bottom loading port (BLP)
8. Load the target wheel liner into the disposal cask
9. De-mate the disposal cask and load onto transport truck for disposal

From this process, the following cell interfaces and features were identified to support the process:

- TLP to transfer items from high bay into the cell
- BLP to transfer items from the cell to a mated transport cask
- Personnel access/equipment loading door
- In-cell crane to enable movement of items within the cell
- Crane maintenance alcove to enable shielded access to the crane
- Activated component storage pit(s) to enable shielded storage of components
- Two window workstations to support size reduction/post-irradiation examination activities
- Primary confinement exhaust/LLLW infrastructure
- Camera/lighting system

Given the basic process and the interfaces and features needed to support the process, floor space requirements were used to develop the necessary operational footprints and tooling logistics. These footprints are

- TLP lay-down space
- Target wheel storage pit space
- MRA/PBW storage pit space
- Liner loading/ post-irradiation examination work area
- BLP space
- BLP plug laydown area/equipment access area

The conceptual layout derived from this process is shown in Figure 4.112. Given the conceptual layout and an estimation on the floor space requirements associated with these features, a dimensional layout can be created. This dimensional layout is shown in Figure 4.113.

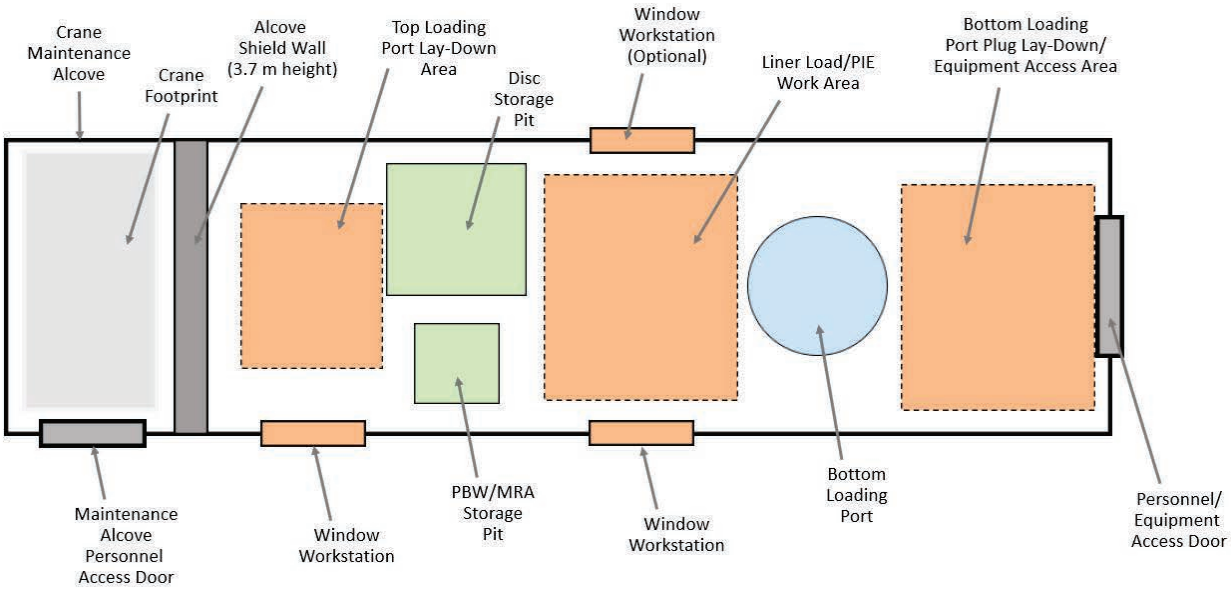

Figure 4.112. Conceptual service cell layout.

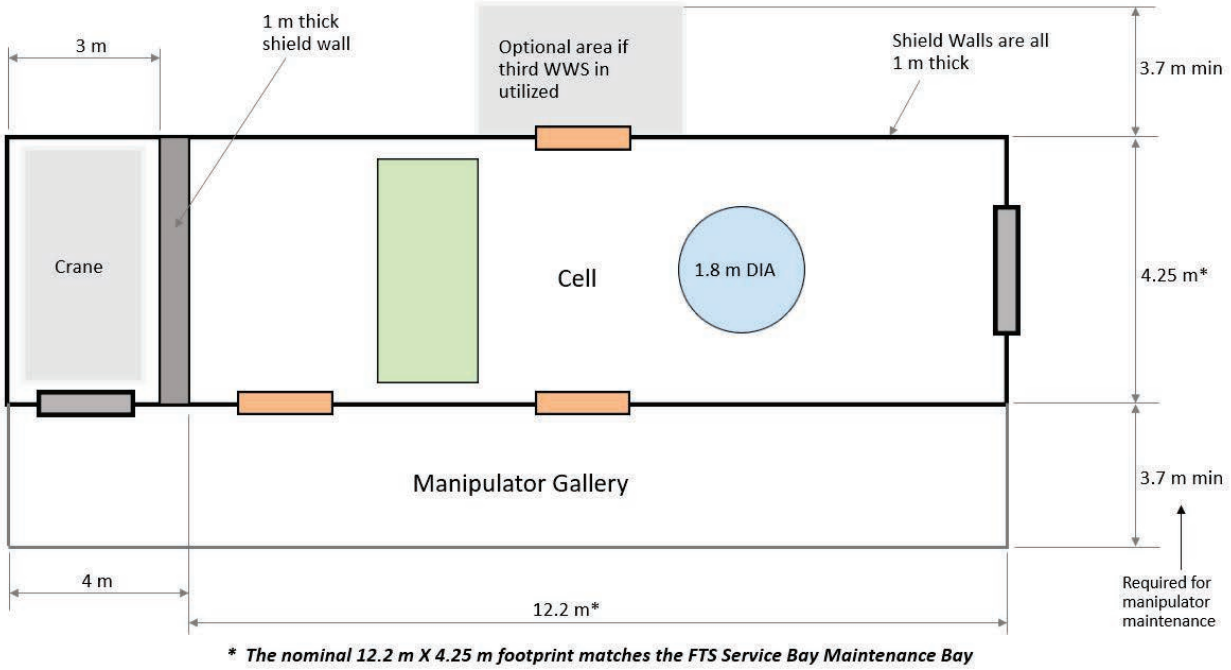

Figure 4.113. Service cell dimensional layout.

To support the handling operations anticipated, it is assumed that each window workstation will build off the experience gained in the operation of the FTS service bay and include two CRL Model F master-slave manipulators, along with the services needed to operate electric and pneumatic tools. Each window workstation will also include monitors with the requisite controls to use the in-cell cameras to support remote activities.

Finally, to support this basic process and other in-cell activities, a bridge crane with a capacity of at least 7.5 tons will be included. The in-cell crane will be used to move activated components, lift and move the

BLP shielded plug, and perform general crane operations. Based on estimated sizes of support stands, lifting fixtures, the clearances required for handling, and the items to be handled, a crane hook height requirement of 4.2 m has been defined.

The FTS service bay uses a complex dual-arm master slave servomanipulator to support all operations from target replacements to maintenance of in-cell equipment like lights and cameras. The FTS servomanipulator will be required as a result of the radiological hazards associated with the mercury process system. These unique hazards of the FTS cell will not be present in STS, so the need for a servomanipulator will be greatly reduced. The assumption for STS cell operations is that personnel access will be possible. Personnel access will be required to support and maintain in-cell infrastructure and to aid in the setup and configuration of tooling and equipment. As a result of this need for personnel access, contingency operations and recovery scenarios are being carefully considered.

4.9.2 Component Replacement Systems

Several STS components will require periodic replacement via remote handling. All tooling and infrastructure used to support these remote component replacements is included in WBS S.3.10.2. These components can be grouped into two subsets:

- Core Vessel Components
  - Target assembly
  - MRA
  - PBW
  - Beam imaging system

- High Bay Components
  - Monolith inserts
  - Primary cooling loop filters
  - Harp

The core vessel components are integral to the vessel and will require removal of the vessel lid(s) and specialized casks and tooling to enable replacement. Each of these components must be removed and reinstalled vertically. This constraint drives the remote handling operations and the tooling design to support these operations. The primary cooling loop filters and harp are located outside the core vessel but will require replacement by remote handling because of the anticipated dose rates; however, their replacement process will be similar in philosophy to that for the core vessel components. Each of the twenty monolith inserts will be installed during construction; but there will be a need to replace the optical guide modules integral to the monolith inserts as the facility matures, so remote handling processes and tooling will be required to support these replacements.

The core vessel component remote handling philosophy is informed by the expected replacement intervals. Neutronics analyses have been performed to estimate the radiation damage–driven replacement intervals for the target, PBW, and MRA. Note that other off normal factors such as leakage or corrosion may shorten the lifetimes of components and increase replacement frequency. The radiation damage based replacement intervals and expected replacement shutdown durations are as follows:

- Target: 27 years between replacements, 5–6 month shutdown to replace
- PBW: 3.2 years between replacements, 1–2 week shutdown to replace
- MRA: 7.6 years between replacements, 4 month shutdown to replace

Replacement of the PBW is anticipated to occur most often, indicating that the remote handling activities associated with this replacement should be possible with limited impact to other core vessel components. Additionally, the target will have a long lifetime. Therefore, replacement of the other core vessel components should have minimal impact on the target, if possible.

Trade studies have been performed to evaluate the various options for core vessel component replacement. Because of the design of the MRA, with the top and bottom moderators encasing and capturing the target wheel, horizontal translation of components will be required to enable clearance for the vertical travel needed to remove components from the vessel. These trade studies evaluated several replacement scenarios to converge on the most efficient philosophy. The result of this study was a remote handling philosophy that involves translation of the MRA.

To further develop the conceptual design solutions for replacement of the core vessel components, the following process was employed:

1. Define the unique requirements associated with the replacement of each specific core vessel component.

2. Develop a conceptual outline procedure for the replacement of each component.

3. Develop conceptual designs for shielding, casks, adapters, and other tooling as needed to fully support the outline procedure.

Replacement of the MRA was viewed as the most complex of the core vessel remote operations because of the translation requirement. As a result, a detailed conceptual solution was developed to ensure a workable solution for this operation. The basic steps of the MRA replacement process are as follows:

1. Remove monolith T-beams
2. Access monolith and disconnect periscope and MRA utilities (hands-on)
3. Remove upstream core vessel lid
4. Remove periscope assembly (optical equipment and shielding)
5. Remove upper MRA shield block
6. Remove the lower MRA shield block
7. Remove the preload that maintains the MRA in the installed “operational” position
8. Install the MRA drive tool and translate MRA upstream
9. Perform MRA pipe cutting
10. Install MRA cask over cavity
11. Remove the MRA
12. Install new MRA
13. Install the MRA drive tool and translate MRA into operational position
14. Preload MRA into alignment features
15. Install lower MRA shield block
16. Install upper MRA shield block
17. Install periscope assembly
18. Connect utilities, and so on
19. Install upstream core vessel lid and T-beams

The following tooling and casks are required to support the above operations:

- Shielded adapter plate
- Lower MRA shield block cask

- Pipe cutting tools
- MRA Translation tool
- MRA cask

This replacement process leverages the process and tooling concepts currently used in FTS operations. Following removal of the beam imaging system, a shielded adapter plate will be installed over the core vessel. This shielded adapter plate will align to the top flange of the core vessel at installation and will provide a stable platform for remote handling operations, technician shielding, and cask alignment for shield block/MRA removal operations. It is anticipated that the upper MRA shield block will be removable without the need for a dedicated cask. This philosophy of not using a cask unless required because of the radiological conditions is employed in FTS operations to mitigate operational risk. Figure 4.114 shows the removal of an upper PBW shield block during the FTS replacement operation.

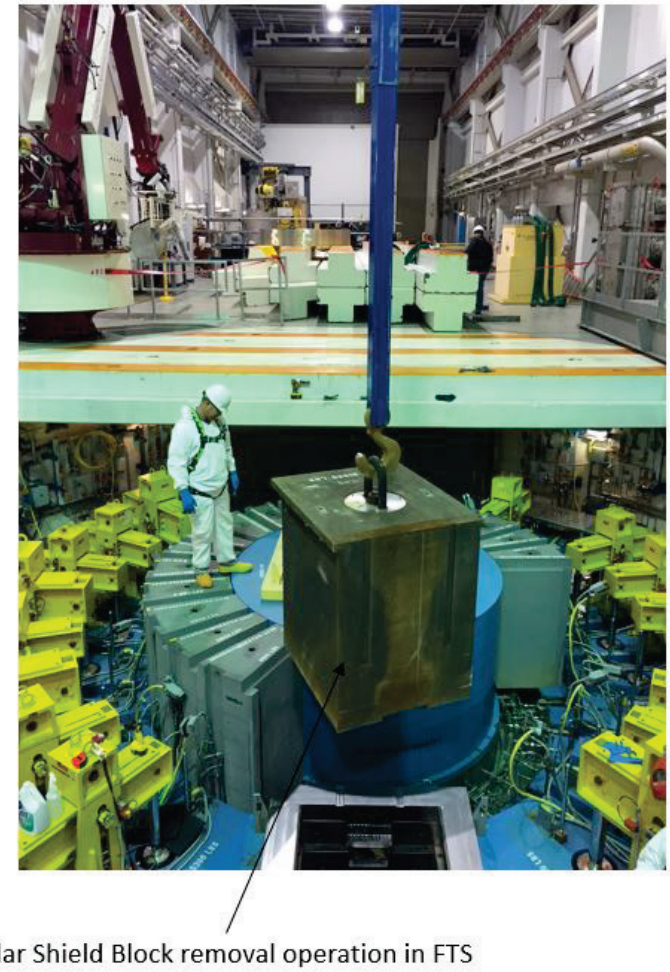

Figure 4.114. First Target Station shield block removal.

It is anticipated that the lower MRS shield block will require the use of a shielded cask. Using the alignment features of the shielded adapter plate, the cask for this block will be installed into position over the core vessel. The alignment features will position the cask to enable vertical crane movement to pull the shield block directly into the cask using a hook extender. The Ziplift grapple fixture will be used extensively in these operations. The Ziplift is a remotely-actuated grapple fixture that can engage and disengage a load with pure vertical movement—no translation is needed. The lifting interface on the

shield block to accommodate the Ziplift is a 1–8 UNC threaded stud. The shielded cask to be used for the lower block removal will also borrow from the designs employed in FTS. These casks consist of a base plate and removal shielded cask body. The cask assembly will be positioned near the monolith, where the cask body will be unbolted from the base plate and set in position on the shielded adapter plate. The cask body and shielded adapter plate will contain alignment features to ensure the cask body (and lifting interface opening) is positioned directly over the Ziplift stud on the shield block. Once the cask body is in place, the Ziplift (on the end of a hook extender) will be lowered through the opening in the cask body down to the block, where it will engage the Ziplift stud. The shield block will be then raised up and into the cask body. At this point in the operation, pins will be inserted into the cask body to retain the shield block. The Ziplift will be disengaged and withdrawn from the cask. Standard rigging will then be used to transfer the cask body/lower shield block back onto the base plate, where the cask body will be re-attached via bolts. The entire shielded cask assembly with the shield block can then be transferred to a storage location.

To optimize the size of the MRA cask, all piping will be cut and removed from the MRA itself before it is installed in its cask. This cutting operation will be performed before translation of the MRA. Cutting of the piping will be accomplished using long-handled hydraulic cutting tools. These tools have been developed and used extensively for FTS component replacement operations. Several tools are currently used that cover a wide range of cutting requirements, from thermocouple wires and fiber optic cable to multi-layer hydrogen transfer lines. These same tools will be adapted to the specific requirements of the STS applications.

Following the cutting and removal of the piping, the MRA will be ready to be translated into the “maintenance” position for removal. This translation will be required to enable the MRA to clear the target wheel before vertical movement out of the core vessel. The translation process itself will consist of

1. Removal of the preload that maintains the MRA in its alignment features
2. Installation of the MRA translation tool
3. Translation of the MRA from the operational to maintenance position
4. Removal of the MRA translation tool

The MRA will be aligned with the core vessel using a pair of kinematic alignment features. When in the operational position, the MRA will be preloaded into these features to ensure the moderators in the MRA remain properly positioned relative to the target wheel and beam ports. The MRA translation will be enabled by three ball transfer rollers integrated into the upper portion of the assembly. These rollers will allow the MRA to translate on specially machined and aligned plates integral to the core vessel. Before translation, the preload will be removed. The design of the preload mechanism is not complete, but it is expected that the preload mechanism will be a part of the MRA itself and will be actuated by a long-handle tool from above. Once the preload is removed, the MRA translation tool will be installed. This tool will consist of an upper plate that interfaces with the shielded adapter plate. The mechanism for translation will be suspended below this plate and will interface with both the MRA and the core vessel via features in both components. These features will react the forces needed to translate the MRA. The translation tool will include a lead-screw–driven mechanism to drive the MRA between the operational and maintenance positions. The nominal loads required for translation will be low as a result of the ball transfer roller design, but the tool will be designed for contingencies (such as a seized roller) to ensure successful translation.

Once the MRA is translated into the maintenance position, the translation tool will be removed and the MRA cask will be placed into position on the shielded adapter plate. Again, the shielded adapter plate features will align the cask precisely over the retracted MRA. The MRA cask will require significant shielding and must include features for personnel protection beyond those employed on the shield block

cask(s). The MRA cask design will mimic the design philosophy used for the FTS PBW cask. It will be a bell-jar style cask with an integral shielded door. When the cask is in position over the cavity, the cask will be positioned directly above the MRA. Again, the Ziplift grapple will be used as the lifting interface. Because of the longer reach required to access the MRA, the FTS PBW hoist will be used in lieu of a hook extender. The PBW hoist will be an air-operated chain hoist used for these operations in FTS. The MRA cask will include interfaces to mount the PBW hoist in the correct position to place the Ziplift grapple directly over the MRA. Figure 4.115 shows the nominal MRA cask design and Figure 4.116 shows the cask in position over the core vessel with the PBW hoist attached.

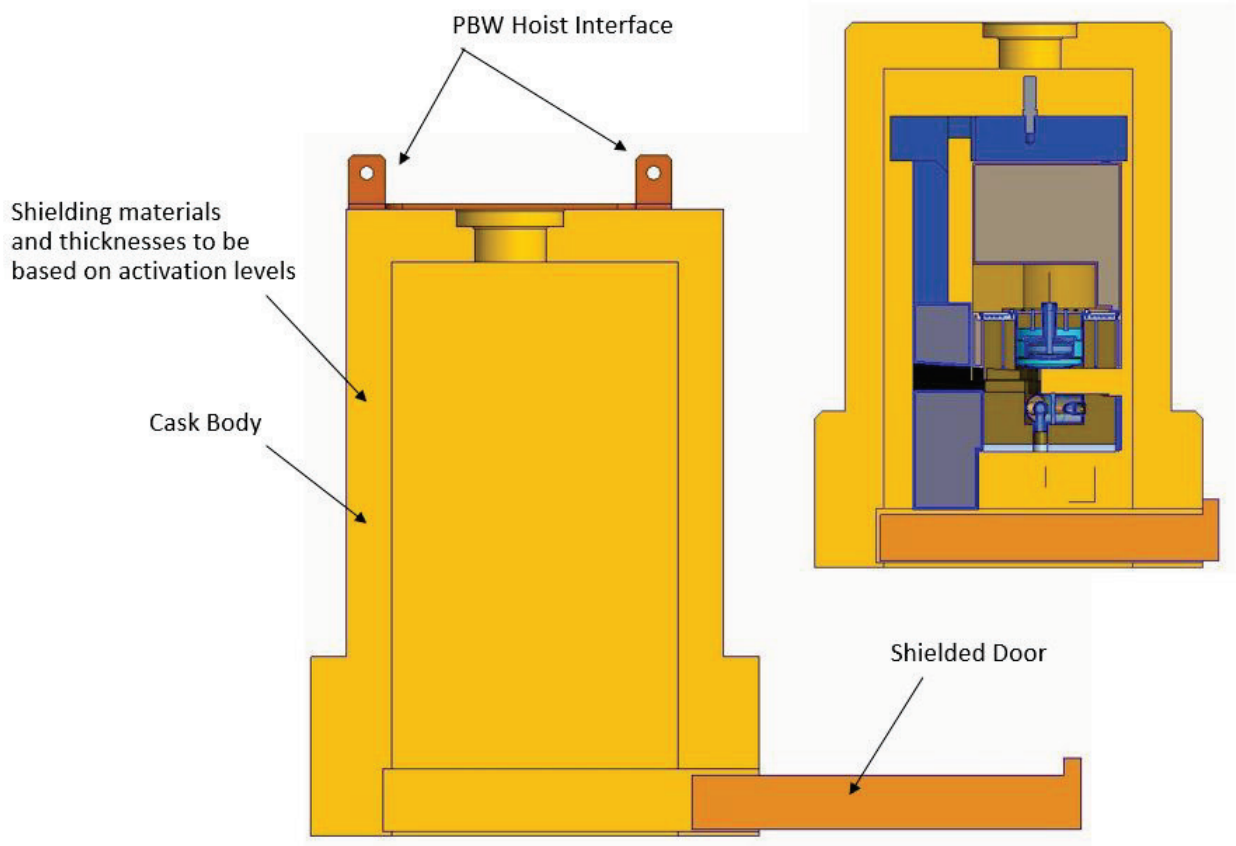

Figure 4.115. MRA cask design details.

The new MRA will be installed into the core vessel using the 50 T crane and hook extender with the Ziplift grapple. The MRA will be lowered into rough position and guided into position by coarse alignment guides. Once fully seated, the MRA must be translated into the operational position. Proper alignment of the MRA will occur during translation. See Section 4.4 for a discussion of the features and alignment plan for the MRA. The MRA translation tool will be used again to perform this translation. Once the MRA is driven into the operational position and into the alignment features, it must be preloaded in this position. To perform this preloading, the MRA translation tool will be removed. The preloading operation will be accomplished via a spring-loaded feature internal to the MRA itself. Actuation of this preload feature will be done remotely using a long-handled tool. The preload feature must have a surface to react the preload force, however, so a reaction block will be lowered into position upstream of the MRA. The reaction block will engage features in the core vessel to position the block relative to the MRA and to react the preload forces. Once the reaction block is in position, the long-handled tool will be used to preload the MRA.

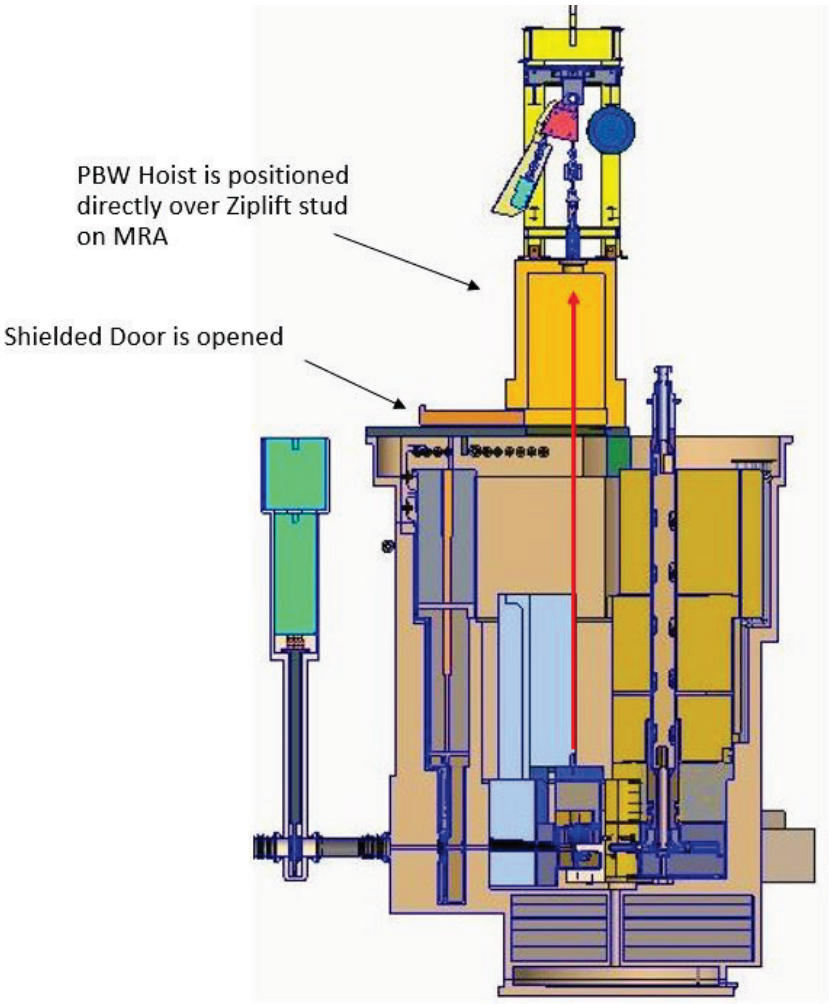

Figure 4.116. MRA cask installed on core vessel.

Following installation and alignment/preloading of the MRA, the lower shield block will be placed back into position. This will be accomplished by moving the cask assembly near the monolith, unbolting the cask body from the base plate, lifting the cask body/lower shield block into position on the shielded adapter plate, and then lowering the shield block out of the cask and back into position in the core vessel. This activity will be the same as that performed during PBW replacement in the FTS. Once the lower shield block is in place, the upper shield block will be also placed into position with the high bay crane.

In addition to the MRA, the PBW and beam imaging system will be maintained and/or replaced using the same remote handling philosophy. Utilization of casks for specific shield blocks and the sizing of these casks will be dependent on the results of more detailed neutronics analyses.

Replacement of the STS target module also represents a complex remote handling operation. Because of the physical envelope of the target assembly, the size and weight of the remote handling cask were evaluated to ensure compatibility with high bay crane capacity and hook height constraints. The cask design replicates the FTS remote handling philosophy used in both the PBW and IRP casks used in many successful operations. The cask will be a bell jar design with an integral shielded door. To accommodate the size of the target assembly, the resulting cask will be approximately 5.75 m tall and weigh approximately 32,000 kg. Preliminary neutronics analyses have indicated the need for approximately

28 cm of lead for the areas of the cask requiring maximum shielding. Figure 4.117 shows the conceptual cask design with lead shielding thicknesses.

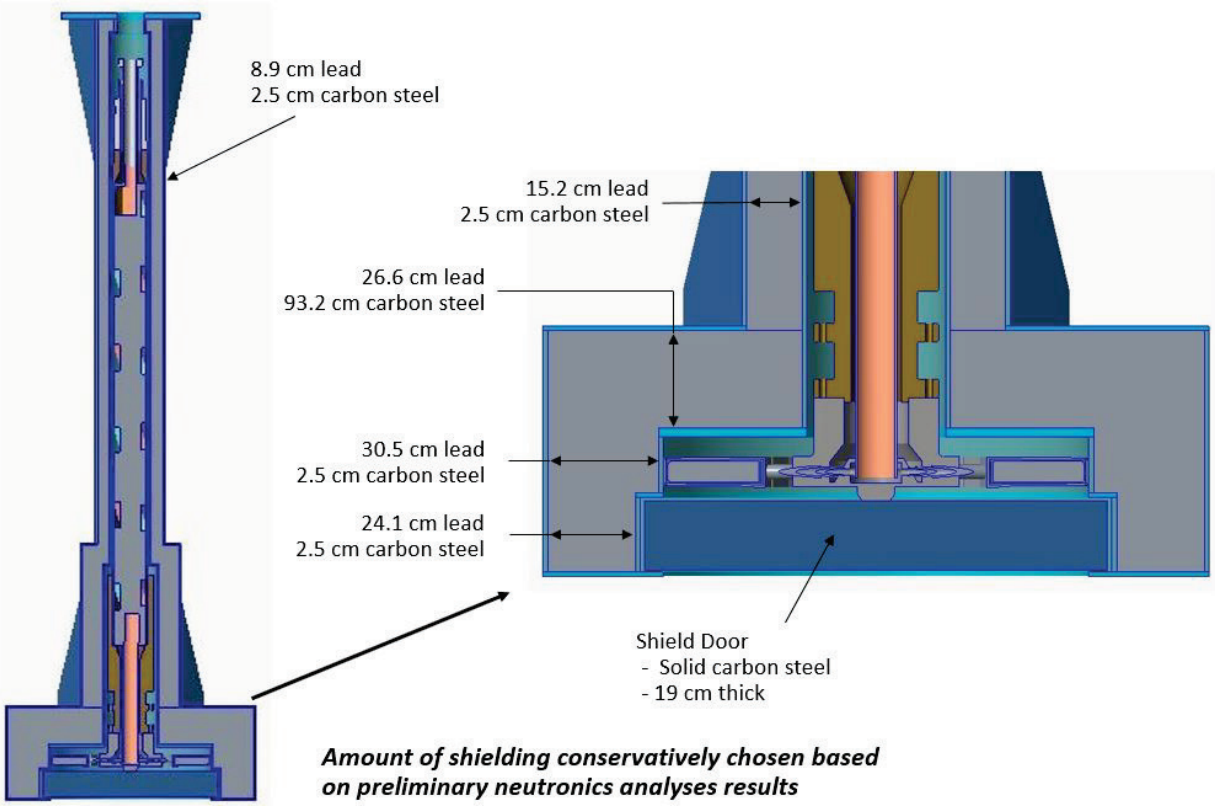

Figure 4.117. Target cask design and shielding details.

Given the nominal cask size needed to accommodate the size of the target and the conservative shielding requirements, the maximum high bay hook height requirements could be evaluated. Because of the nature of the target replacement operation and the crane hook travel requirements needed, the PBW hoist with the Ziplift grapple will again be used in this operation. The target cask will include an interface for the PBW hoist, as shown in Figure 4.118. Given this installation, a total hook height required will be revealed.

During the target replacement operation, the PBW hoist will not be attached to the target cask when the cask is moved into position over the core vessel. From Figure 4.119, it can then be seen that the maximum hook height needed for the target cask and nominal rigging will be approximately 7.4 m.

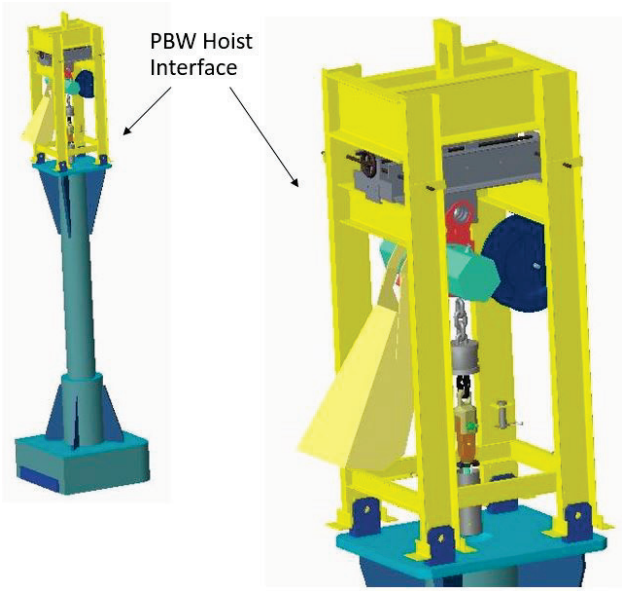

Figure 4.118. Target cask with PBW hoist installed.

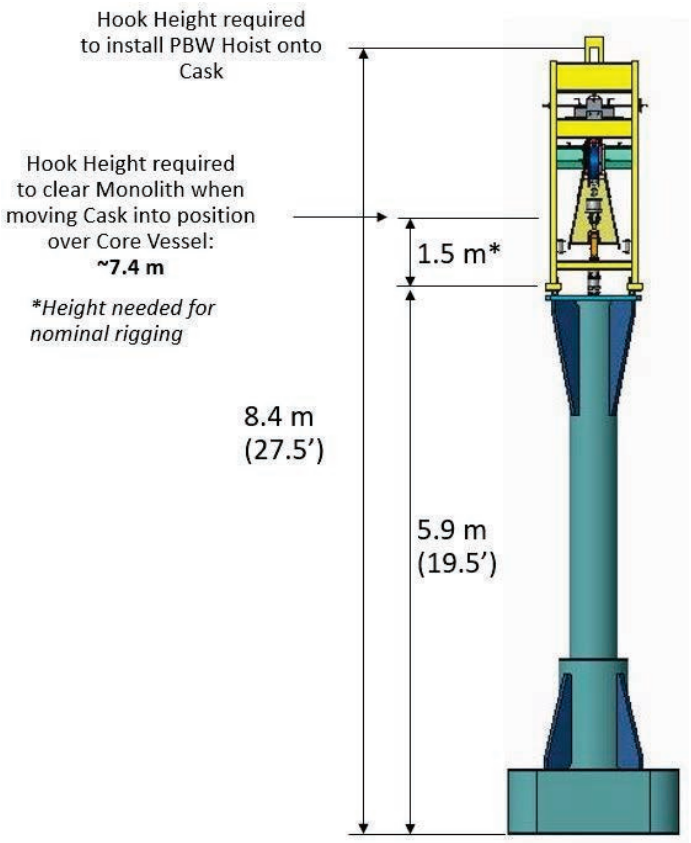

Figure 4.119. Target cask hook height requirements.

Target cask handling during remote operation will require lifting the cask into position over the core vessel inside the monolith/target drive room. The design of this room will be such that the walls extend

3.4 m above the nominal high bay floor. Given the 7.4 m of hook height required for handling the cask and the height needed to clear the target drive room wall, the total high bay crane hook height needed will be approximately 10.8 m. The actual high bay crane hook height is expected to be about 11.48 m, so there will be adequate clearance available for these target cask operations.

While the remote handling operations associated with the target replacement are straightforward and share the same philosophy with FTS operations, target disc decay heat necessitates an understanding of the potential need for active cooling during and after remote handling operations.

These needs for active cooling can be segregated into two scenarios:

- Cooling needs during nominal core vessel remote handling operations (not target replacement)
- Cooling needs during short term storage in the remote handling cask following removal

Preliminary thermal analyses indicate that leaving the target drive installed (and, as a result, maintaining nominal cooling) during core vessel operation ensures adequate cooling. Removal of the target drive (and loss of cooling) during target replacement does not represent an operational issue. The resulting temperature increases in the target disc structure will not be an issue for a spent target that will not be placed back into operation. The need to remove the target drive (and therefore the cooling) on an operational target does challenge the ability to maintain the target at an acceptable temperature. Several options are being considered for this cooling scenario, including using pre-installed ducts routed down through pipe chases in the shielding. The ducts can then be used to direct cooling air to the target. Finally, in the event cooling of the spent target is required after removal, the design of the target cask can include cooling tubes embedded in the lead shielding. This embedded tubing would allow the circulation of facility chilled water as needed to maintain temperatures.

The shutter cavities, nozzle extensions, and monolith inserts will be installed during facility construction. Figure 4.120 shows the installed configuration of these components.

Unpopulated beam lines will receive insert “plugs” as shown in Figure 4.20. These plugs will provide shielding to allow bunker access. Installation of a new beam line will require removal of the insert plug and installation of the beamline-specific optical guide cavity. Plans are to use a monolith insert tool for the initial installation of the monolith inserts. The goal is to design this insert tooling so that it can be also used during the optical guide installation process. The basic process for insert plug removal and optical guide installation is as follows:

1. Install the maintenance shutter.
2. Maintain shutter in the raised “maintenance” position.
3. Position insert handling tool and engage the insert plug.
4. Extract the insert plug into the shielded insert handling tool.
5. Lower maintenance shutter into the gamma blocking mode.
6. Remove insert handling tool and transfer plug into a storage cask.
7. Load the optical guide into the insert handling tool.
8. Position insert handling tool with guide at monolith insert.
9. Open maintenance shutter.
10. Insert optical guide into monolith insert.
11. Close maintenance shutter.

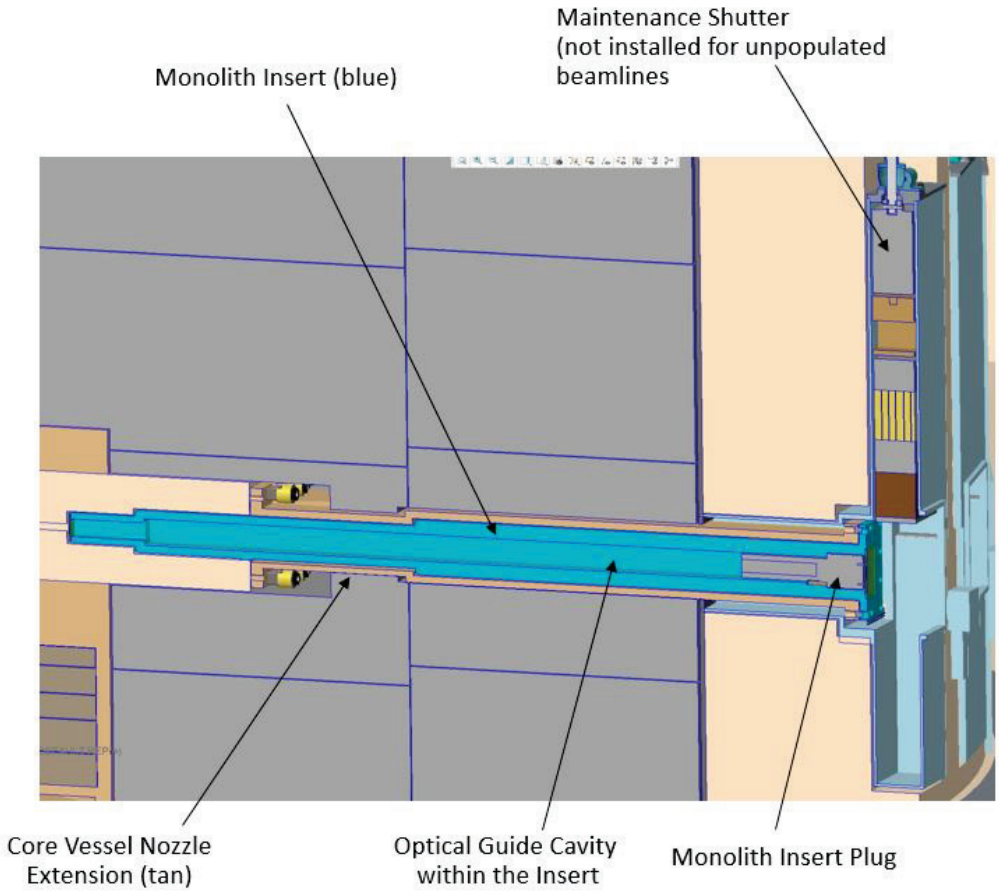

Figure 4.120. Monolith insert component installation.

Installation of the optical components for a new beamline will begin with the installation of a maintenance shutter. Unlike at FTS, these shutters will be used only during maintenance operations. Each shutter contains an optical component of the beamline, a gamma blocker, and a neutron absorber.

During optical guide installation, the shutter will either be raised in the “maintenance” position or be lowered to use the gamma blocker. Figure 4.121 shows the configuration of a maintenance shutter.

Following installation of the maintenance shutter, the fasteners securing the insert plug will be removed in preparation for removal of the plug itself. The insert handling tool will then be positioned in front of the monolith insert and the shielded door on the handling tool raised. At this point, the tower internal to the insert handling tool will be driven into position to enable latching of the insert plug. Figure 4.122 depicts this portion of the operation.

Once the insert plug is engaged, it will be withdrawn into the insert handling tool and the shielded door closed. See Figure 4.123.

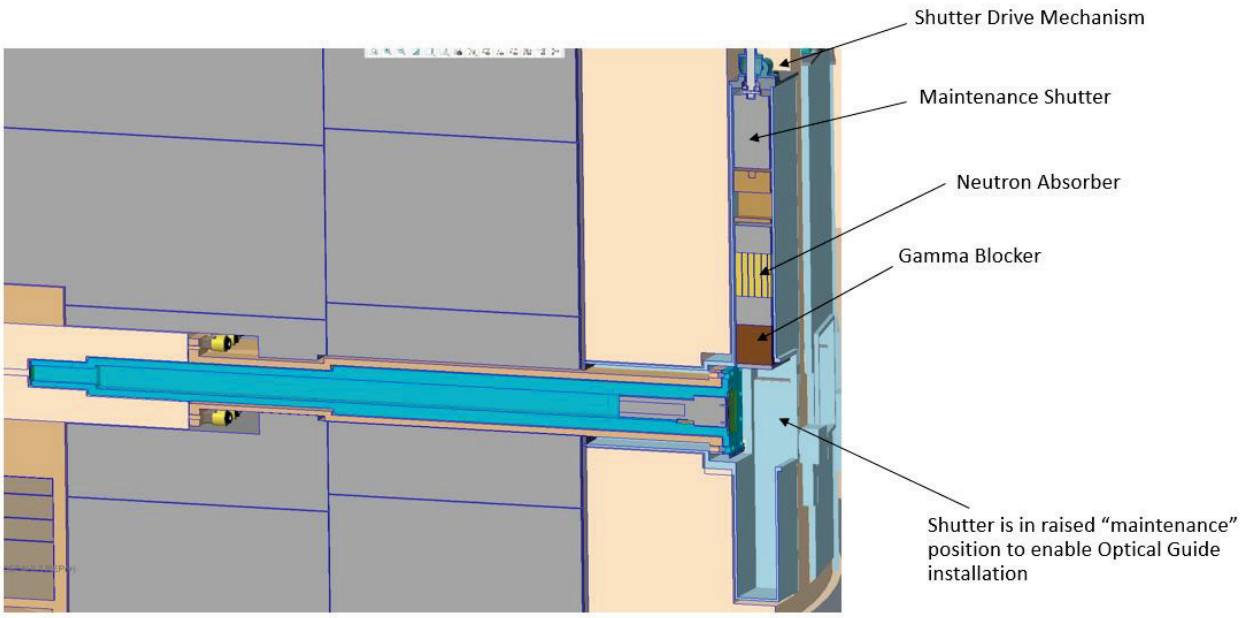

Figure 4.121. Maintenance shutter configuration.

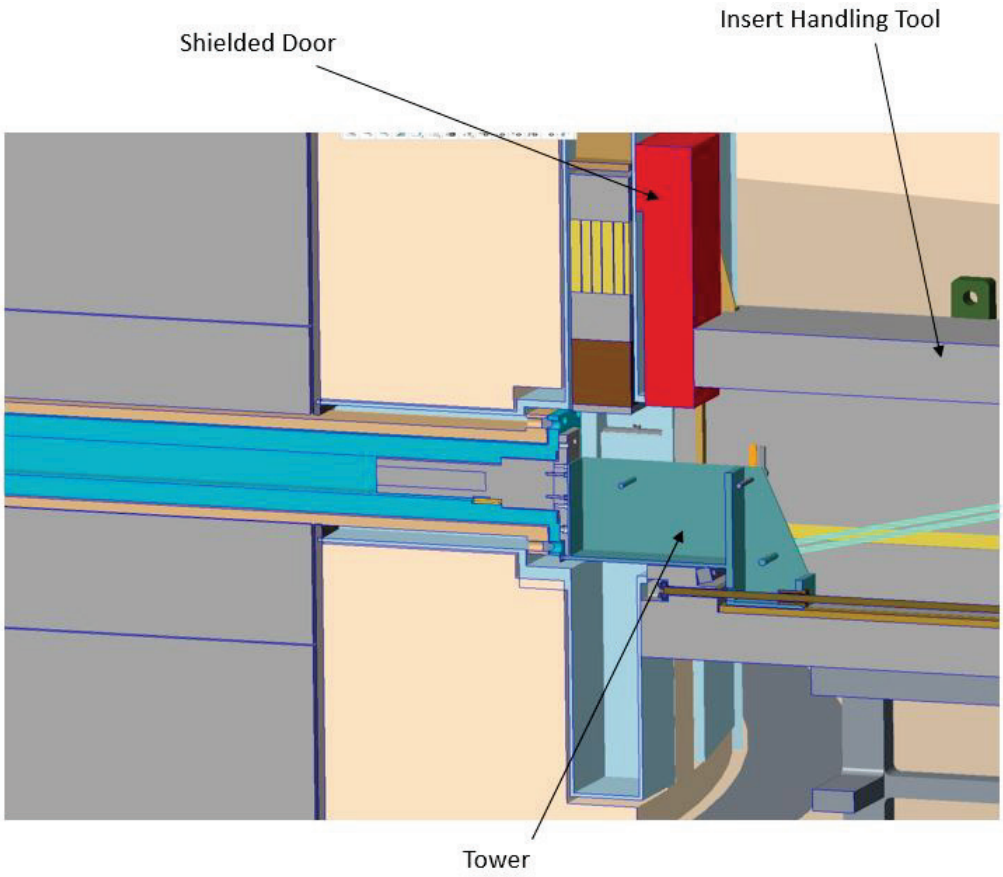

Figure 4.122. Insert handling tool in position to engage plug.

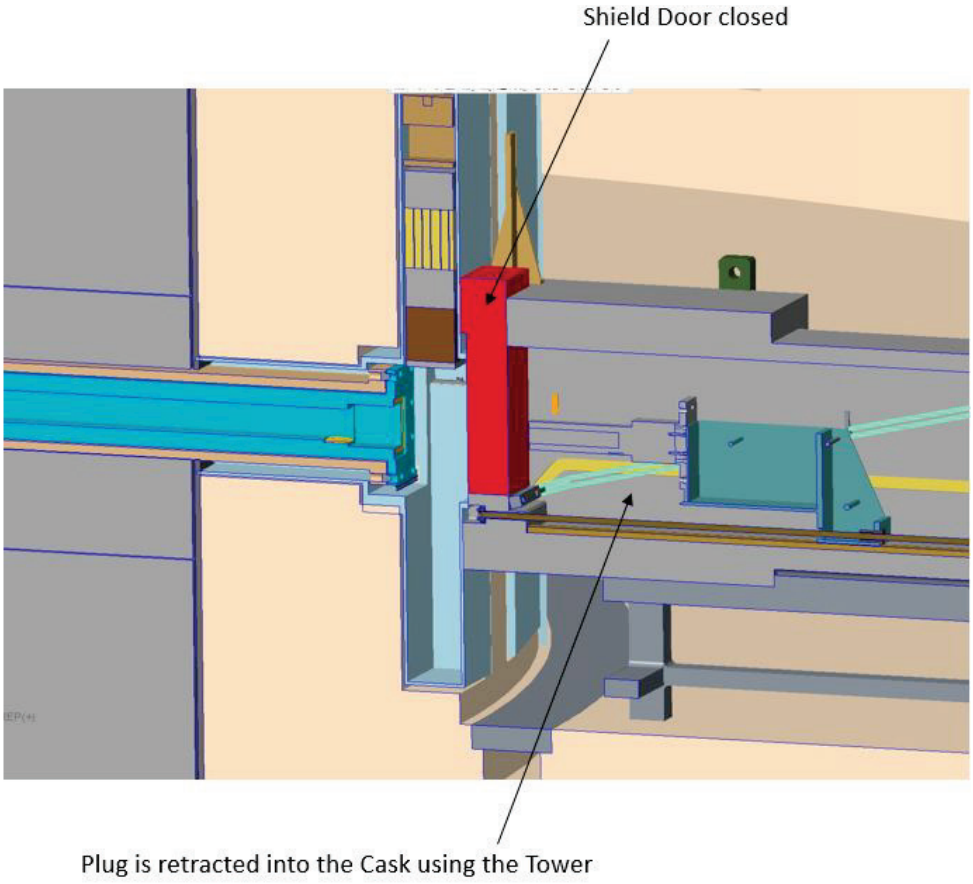

Figure 4.123. plug extracted into insert handling tool.

Removing the plug opens a direct view to the moderator, so the maintenance shutter and the handling tool must provide adequate shielding. Figure 4.124 shows this configuration.

Once the maintenance shutter has been lowered to the gamma blocker position, the insert handling tool can be removed. The insert handling tool will then be mated to an insert plug storage cask for insertion and temporary storage of the insert plug prior to disposal. At this point, the new optical guide can be loaded into the insert handling tool. Once the optical guide is installed, the insert tool will be positioned again at the beamline monolith insert. Figure 4.125 shows the handling tool in position with the optical guide installed.

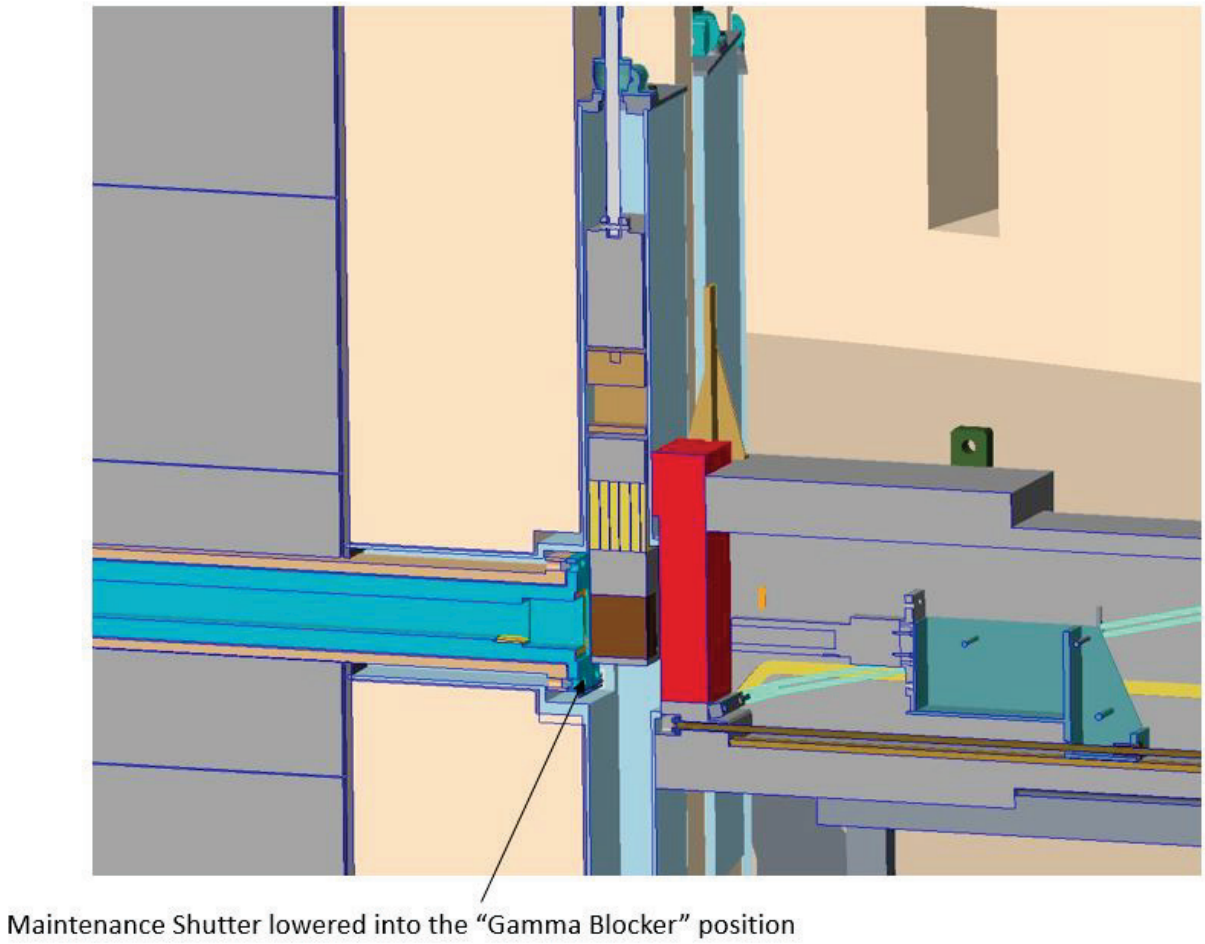

Figure 4.124. Maintenance shutter lowered to gamma blocker position.

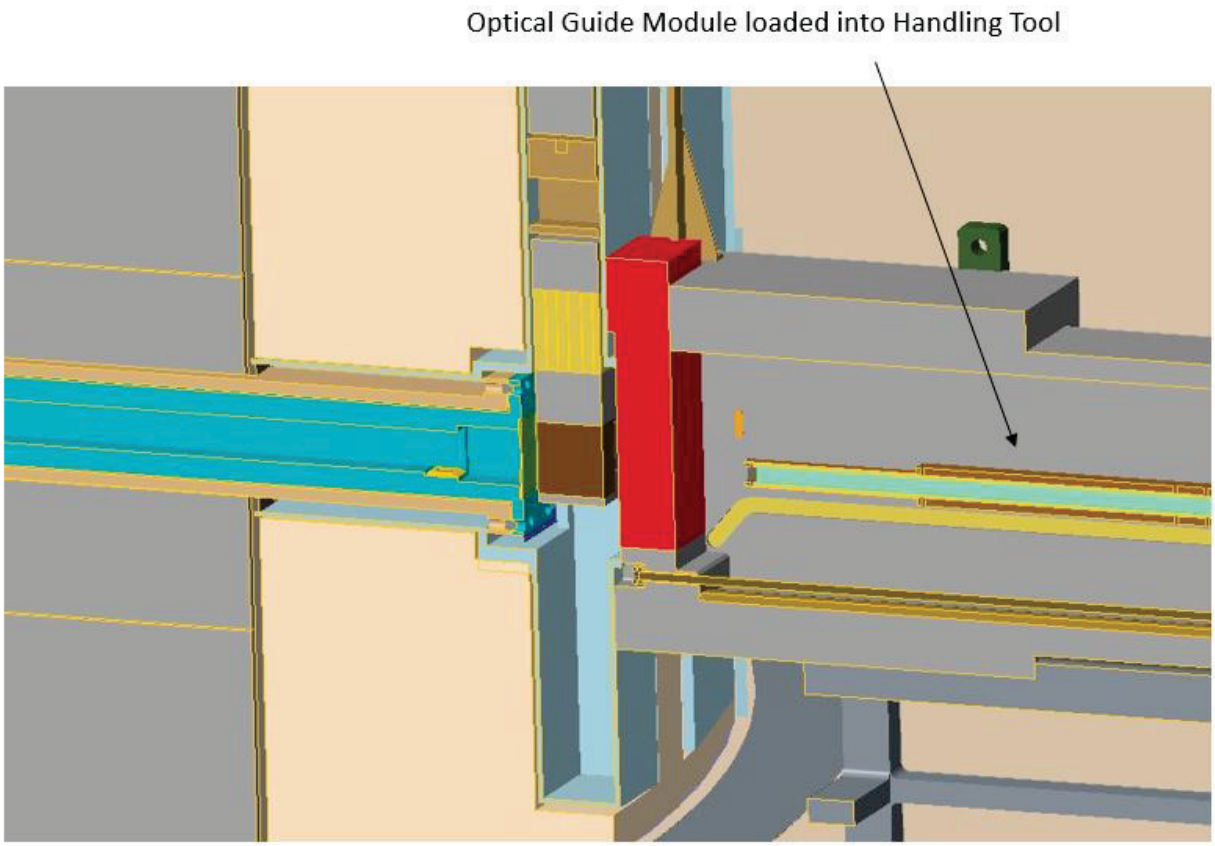

Figure 4.125. Optical guide in position for installation.

The maintenance shutter and the shielded door of the handling tool can now be raised to allow insertion of the optical guide. Figure 4.126 shows this optical guide insertion.

Once the optical guide is inserted into the monolith insert and the handling tool removed, the guide will be secured and utilities connected. The maintenance shutter will be then lowered into the gamma blocker position to allow hands-on installation of the remainder of the beamline bunker components.

The primary cooling loop for STS has the potential for tungsten contamination in the event of cladding failures. This potential drives the need to be able to replace the loop filters remotely. The location of these filters (in a cavity accessible from the high bay) drives the remote handling operation for replacement. Replacement of the filters will require

- An adapter structure to place over the cavity following shield block removal
- The ability to remotely remove the filter housing lids
- The ability to remotely remove and reinstall filter cartridges into shielded containers

This remote operation will be very similar to the process designed for harp replacement in FTS. The development of the process and the design of the tooling will use the concepts devised for the harp replacement.

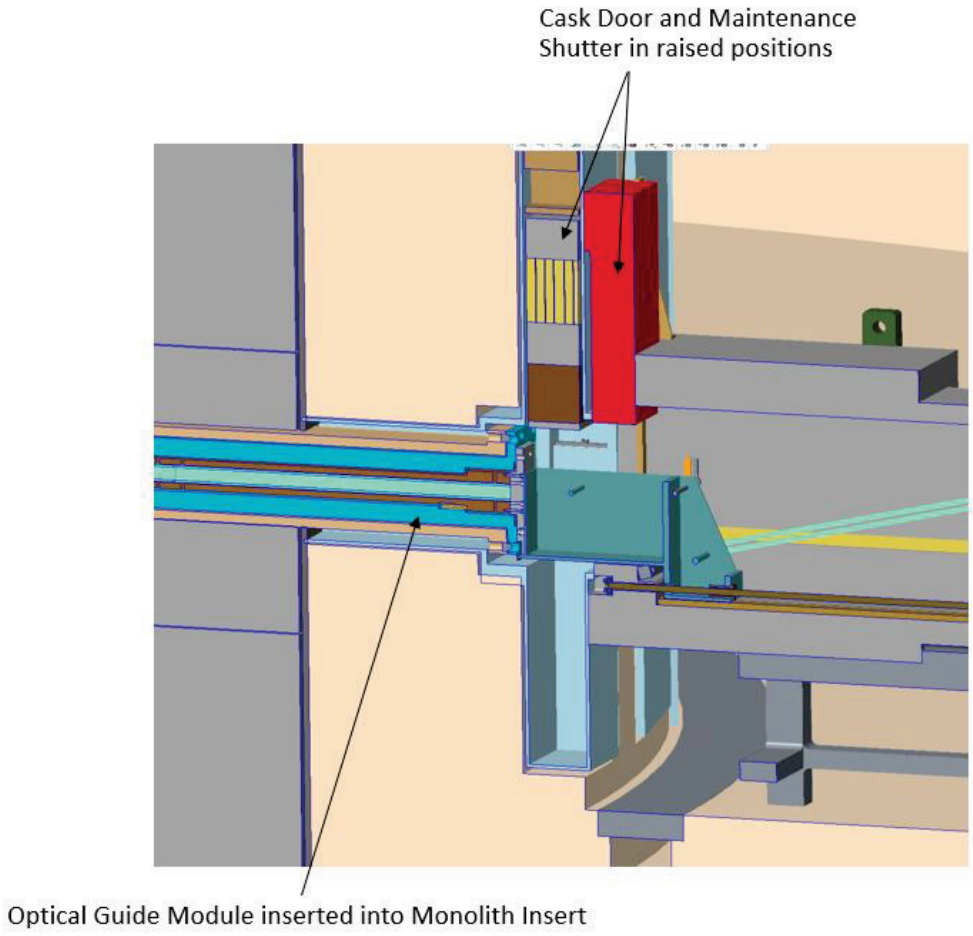

Figure 4.126. Optical guide installation.

4.9.3 Waste Disposal Systems

Remote handling will be required to support the disposal of many STS components as waste. All tooling and infrastructure associated with waste disposal are included in WBS S.3.10.3. Operational experience gained through the successful completion of 23 TN-RAM cask shipments has been leveraged to develop a conceptual waste disposal process and infrastructure/tooling required to support this operation. For highly activated components, the service cell will provide the infrastructure needed for successful waste handling while ensuring ALARA principles are maintained. Waste disposal of the target assembly represents the most challenging operation, so it will be the focus of the conceptual design.

Because of its size and activation, disposal of the target wheel will be challenging. Both the size and activation preclude the use of any existing over-the-road (OTR) waste disposal casks. Three potential options exist:

- **Option 1:** Size reduction and multiple shipments using an existing OTR cask (e.g., TN-RAM)
- **Option 2:** Use of an existing rail cask for shipment
- **Option 3:** Design and licensing of a new OTR cask specifically for target shipments

Each option has technical and economic factors to consider. Option 1 involves the size reduction of the target wheel into pieces small enough to permit shipment in existing casks. The advantages to this option include the following:

- Existing casks could be used.
- Disposal process is well understood.
- Disposal sites exist and are easily accessible.
- Post-irradiation examination activities could be folded into size reduction
- It avoids the costs associated with designing and licensing a new cask (likely $3–5 million) and the costs associated with maintaining the license

This option also has several disadvantages:

- Size reduction requires significant tooling and infrastructure.
- Current service cell concept would likely need to be enlarged to accommodate size reduction tooling and storage/ handling of target pieces prior to shipment.
- Radiological hazards are associated with size reduction.
- Multiple shipments per target would be required.
- There likely would be 3–4 TN-RAM shipments per target @ $300K each for a cost of >$1 million.

Option 2 resolves the OTR cask size issue and involves using an existing rail cask for shipment. These casks are typically used for the shipment of spent nuclear fuel and have both the capacity for an item the size of a target wheel and the shielding necessary. In fact, the size and shielding are the only advantages of this option. The disadvantages are many:

- Cask would be needlessly oversize for something as small as a target.
- There is no rail access at ORNL.
- There is no rail access at Nevada National Security Site—disposal site access is limited
- Cost is unknown but would likely be $1 million+ per shipment.
- Current service cell/conventional facilities concepts do not support spent fuel/rail cask infrastructure and operations.

This leaves Option 3, which involves the design and licensing of a new OTR cask specifically designed to accommodate the target wheel. The following are advantages associated with this option:

- Enables shipment of target disc without size reduction.
- Facility infrastructure (e.g., service cell) design can ensure compatibility.
- Process is well understood.
- Disposal sites exist and are easily accessible.
- Single shipment would mitigate costs (likely ~$300K per shipment).
- SNS would own the cask and control its use.

The disadvantages are few, but significant:

- Package size and shielding requirements push the limit of what is possible for an OTR cask (this is a significant unknown and investigation is needed).
- Nonrecurring costs up front would be high (likely $3–5 million).

For the purposes of the conceptual design, Option 3 was selected. To better define the technical challenges associated with Option 3, a waste disposal cask concept was created to

- Devise a nominal packaging plan
- Estimate the approximate weight of a conceptual package to understand transport options
  - Will size reduction be required?
  - Can a cask be designed that meets OTR weight limits?
  - Will a rail cask be required?
- Add fidelity to target disc disposal concepts to better define service cell configurations relative to cask handling and loading

The basic packaging plan replicates the FTS system in which a cask liner is loaded into the cell before waste disposal. This liner serves as the handling interface for the target disc both in the service cell and at the disposal site. The target disc is then installed into the liner. The disposal cask arrives at SNS and is mated to the service cell, and the liner is then loaded into the cask. The loaded cask is then placed back onto the transport vehicle for shipment. This process requires a new liner and new cask design.

To support the Option 3 disposal, a conceptual design of a liner was required. This liner design uses the same philosophy as current FTS TN-RAM liners. The liner is essentially a carbon steel shell with a lead-filled lid. The shell is sized and has features to securely hold the target wheel and includes a Ziplift stud for handling within the service cell. Figure 4.127 depicts the conceptual design.

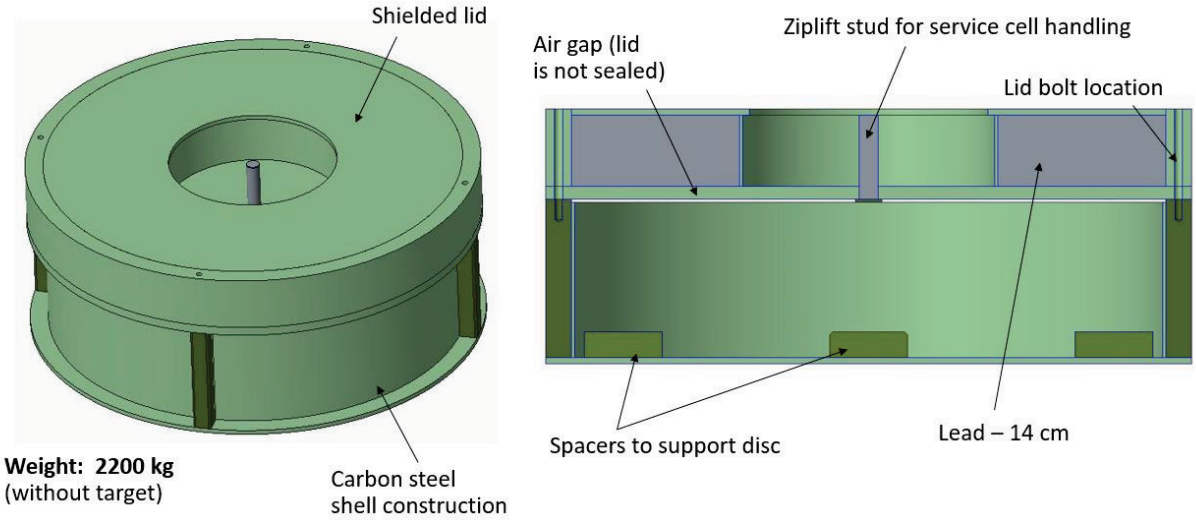

Figure 4.127. Target wheel liner design details.

The weight of the liner with the target wheel installed will be approximately 3070 kg. Given this liner design, the conceptual design of a cask could follow. A cask concept was devised primarily to understand the sizing needed to accommodate the liner and to understand the weights associated with this sizing. A nominal lead thickness of 28 cm was conservatively assumed, and an attempt was made to make the cask as compact as possible. Figure 4.128 shows the design details for the cask.

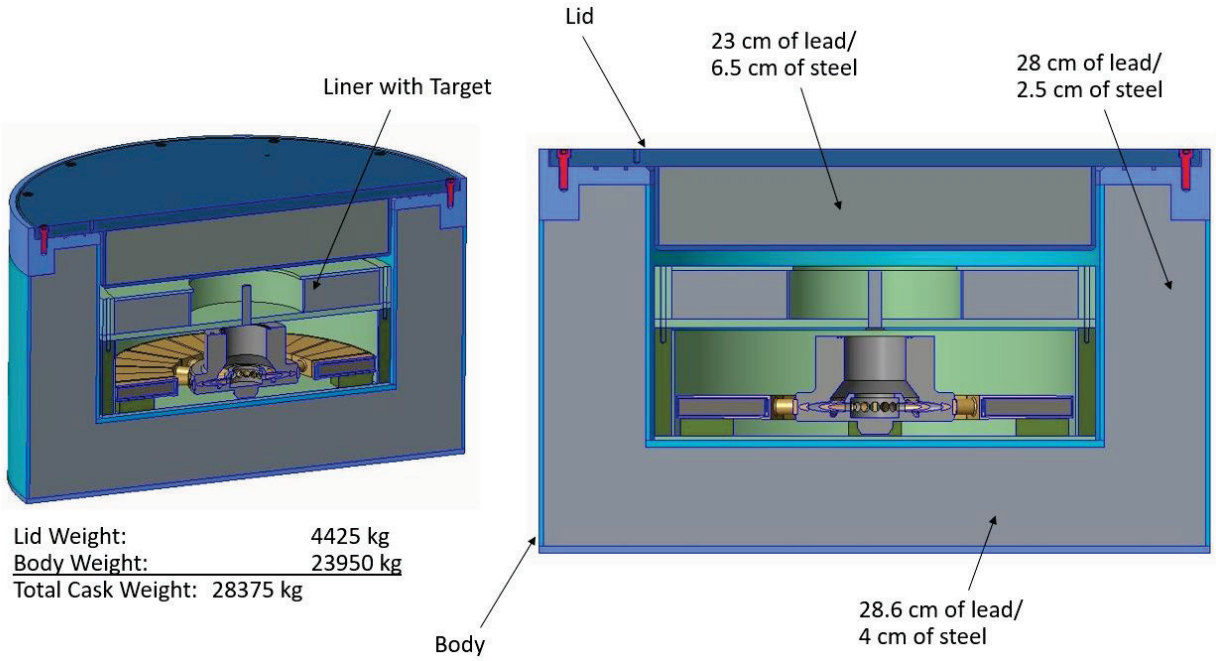

Figure 4.128. Cask design details.

To assess the overall size of the resulting cask to evaluate its suitability for OTR transport, nominal impact limiters were added. The conceptual assembly is shown in Figure 4.129.

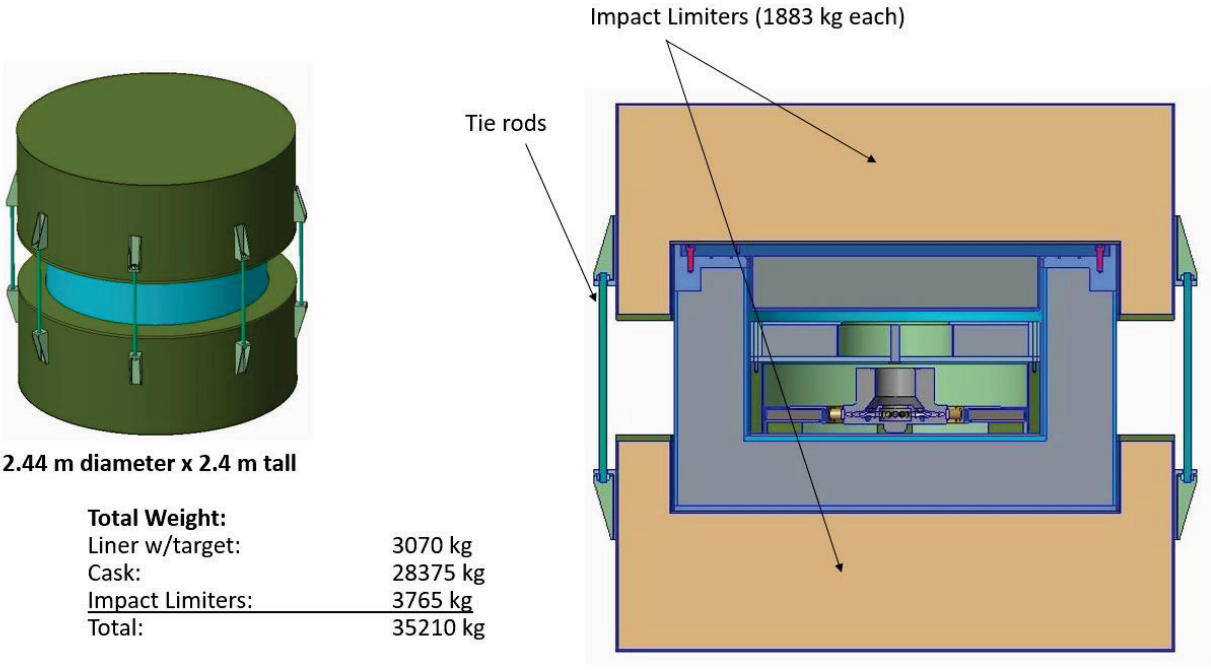

Figure 4.129. Disposal cask assembly.

The finding of this assessment is that the packaging of the STS target wheel seems reasonable. The wheel size permits packaging in a size that meets OTR requirements. An assumed lead thickness of roughly 28 cm yields a total package weight of less than 80,000 lb (35,210 kg/77,625 lb). This weight is

comparable to a fully loaded TN-RAM cask weight of 78,250 lb. The cask concept used many assumptions that will need to be verified moving forward with regard to shielding thicknesses and impact limiter design, but the conceptual design demonstrates that Option 3 is viable.

The Option 3 disposal process addresses the disposal of the target wheel, but the target shaft is also an issue. Disposal of the target assembly as waste requires separation of the shaft from the wheel. This separation will be easily performed in the service cell with the access and tools provided by the window workstation infrastructure. Once the shaft is mechanically separated from the disc, the shaft will be drawn back up into the target remote handling cask to await its disposal. Because of the relatively low activation of the target assembly shaft, its disposal path will be more straightforward. The plan is to dispose of the shaft as activated steel (much like the current effort to dispose of the FTS IRP upper shielding segments). Because of the size and shape of the shaft, it is expected that a custom, strong-tight container will be designed to house and transport the shaft.

Disposal of the remaining components (e.g., MRA or PBW) can be accomplished using existing casks (e.g., the TN-RAM). These components are compatible with the size/activation capabilities of the TN-RAM. The disposal process for these components mimics that used currently for FTS components and can be accommodated for STS with the following options:

- Use the existing FTS TN-RAM infrastructure.
- Modularize the STS infrastructure to accommodate multiple casks (BLP and cask cart adapters/flexibility).
- Transfer waste items into casks independent of service cell infrastructure (possibly building a transfer station to load casks).

4.9.4 Mock-up Facility

FTS has an MUTS that contains full-scale mock-ups of a PBW cavity, a shutter cavity, and a mock-up vessel that replicates the FTS core vessel. The MUTS has proved to be invaluable to the success of FTS remote handling operations. A Mock-up Facility is planned for STS. The STS Mock-up Facility will build on this legacy and be used extensively for

- Full-scale cold testing of remote handling tooling and processes
- Tooling prototyping and design development
- Fit and functional testing of casks and tooling
- Technician training
- Process and procedure development

All tooling and infrastructure associated with mock-up testing activities is included in WBS S.3.10.4. The STS Mock-up Facility will contain a full-scale mock-up of the core vessel. This mock-up will contain incorporate the features needed for high-fidelity testing of STS remote operations. For example, the mock-up vessel will contain the MRA alignment and interface features. This will allow full-scale validation of the installation and alignment process, including the tooling needed for translation and preloading of the MRA. For target replacements, the mock-up will include dimensionally accurate core vessel shielding blocks to enable testing of removal and installation handling operations, pipe cutting and removal operations, and target installation and handling.

A mock-up of the monolith insert handling operation will also be included. This mock-up will be stand-alone (not integral to the Mock-up Facility) and will allow testing of all phases of the monolith insert installation and maintenance process.

4.10 REFERENCES

ANSYS 2017. SpaceClaim 2017.2 (18.2), http://files.spaceclaim.com/SpaceClaim2017.2_SP0_ReleaseNotes.pdf.

Besler, Y. 2014. "Helium-Leak Detection, ESS design update phase," Central Institute for Engineering, Electronics and Analytics, Jülich, Germany, September 26, 2014

Bohringer, D., D. S. Kupperman J. L. Bailey, et al. 1991. "In situ ultrasonic examination of the Intense Pulsed Neutron Source (IPNS) enriched uranium target assembly," *J. Test. Eval*. 19(6), 6. DOI: 10.1520/JTE12610

Broom, T. A. 1005."Prospects for target and methane moderators at ISIS," *Proceedings of the Meetings ICANS-XIII and ESS-PM4*, Villigen PSI, Switzerland, October 11–14, 1995, PSI Proceedings 95-2, ISSN 1019-6447.

Carpenter, J. M., and T. E. Mason 2002. *Technical Concepts for a Long Wavelength Target Station for the Spallation Neutron Source*, ANL-02/16/ORNL/SNS-TM-2001/163, Argonne National Laboratory and Oak Ridge National Laboratory.

Chadwick, M. B. P. Oblozinsky, M. Herman, et al. 2006. *ENDF/B-VII.0: Next Generation Evaluated Nuclear Data Library for Nuclear Science and Technology*, UCRL-JRNL-225066, Lawrence Livermore National Laboratory, *Nuclear Data Sheets* 107(12), 2931–3060 (2006).

Dementjevs, S. 2018. "In-situ studies of phase transition related Pb transport in the SINQ target rods with use of the NEUTRA imaging instrument at PSI," *7th High Power Targetry Workshop*, Michigan State University, June 4–8 2018.

DOE (Department of Energy) 2016. *Natural Phenomena Hazards Analysis and Design Criteria for DOE Facilities*, DOE-STD-1020-2016, US Department of Energy, Washington DC.

Finney, J. L. 1990. "ISIS status report," *ICANS-XI International Collaboration on Advanced Neutron Sources KEK*, Tsukuba, Japan, October 22–26, 1990.

Galambos, J., ed. 2015. *Technical Design Report Second Target Station*, ORNL/TM-2015/24, Oak Ridge National Laboratory.

Gallmeier, F. 2018. *A Liquid Hydrogen Tube Moderator Arrangement for STS*, SNS-106100200-TRxxxx-R00, Oak Ridge National Laboratory.

Gallmeier, F. X., E. B. Iverson, W. Lu, et al. 2010b. "The CINDER'90 Transmutation code package for use in accelerator applications in combination with MCNPX," *Proceedings of ICANS XIX, 19th Meeting on Collaboration of Advanced Neutron Sources*, Grindelwald, Switzerland, March 8–12, 2010.

Gallmeier, F. X., E. B. Iverson, W. Lu, et al. 2010a. "SNS second target station moderator performance update," in *19th meeting on Collaboration of Advanced Neutron Sources*, Grindelwald, Switzerland, March 8–12, 2010.

Gallmeier, F. X., M. Wohlmuther, U. Filges, D. Kiselev, and G. Muhrer 2009. "Implementation of neutron mirror modeling capability into MCNPX and its demonstration in first applications," *Nucl. Technol.* 168(3), 768–772. DOI: 10.13182/NT09-A9304.

Gallmeier, F. X., W. Lu, B. W. Riemer, et al. 2016. "Conceptual moderator studies for the Spallation Neutron Source short-pulse second target station," *Rev. Sci. Instrum*. 87, 063304. DOI.org/10.1063/1.4953612

Habainy, J. 2018. *Characterisation of Mechanical and Thermal Properties of Tungsten for High Power Spallation Target Applications*, Department of Mechanical Engineering, Lund University.

Habainy, J., A. Lövberg, S. Ivengar, et al. 2018. “Fatigue properties of tungsten from two different processing routes,” *J. Nucl. Mater*. 506, 83–91.

Harada, M., N. Watanabe, M. Teshigawara, et al. 2007. “Neutronics of a poisoned para-hydrogen moderator for a pulsed spallation source,” *Nucl. Instrum. Methods Phys. Res., Sect. A* 574, 407–419.

Herwig, K. W., and M. J. Rennich, eds. 2017. *Spallation Neutron Source Second Target Station Integrated Systems Update*, ORNL/TM-2017/490, Oak Ridge National Laboratory.

ICC (International Code Council) n.d. *International Building Code: A Member of the International Code Family*, International Code Council, 500 New Jersey Avenue, NW, Washington, DC.

Kai, T., M. Harada, M. Teshigawara, et al. 2006. “Neutronic performance of rectangular and cylindrical coupled hydrogen moderators in wide-angle beam extraction of low-energy neutrons,” *Nucl. Instrum. Methods Phys. Res., Sect. A* 550, 329–342.

Kiyanagi, Y. 2006. “Experimental studies on neutronic performance of various cold-neutron moderators for pulsed neutron sources,” *Nucl. Instrum. Methods Phys. Res., Sect. A* 562, 561–564. DOI.org/10.1016/j.nima.2007.01.184

Lu, W., et al. 2011. “Improved moderator performance calculations at SNS,” in *Tenth International Topical Meeting on Nuclear Applications of Accelerators (AccApp11)*, Knoxville, TN, April 3–7, 2011, American Nuclear Society, LaGrange Park, IL.

McLane, V. 1996. *ENDF/B-VI Summary Documentation Supplement I, ENDF/He-VI Summary Documentation, ENDF-201*, BNL-NCS-17541, Brookhaven National Laboratory, Upton, NY.

McManamy, T., et al. 2019. “Rotating target development for SNS second target station,” in *Proceedings of ICANS XIX, 19th Meeting on Collaboration of Advanced Neutron Sources*, Grindelwald, Switzerland, March 8–12, 2010.

McManamy, T., et al. 2010. *Second Target Station Preliminary Hazard Analysis Report*, STS-S01030000-ES0002, R00. April 30, 2019.

Mosher, S. W., A. M. Bevil, S. R. Johnson, et al. 2015. *ADVANTG—An Automated Variance Reduction Parameter Generator*, ORNL/TM-2013/416, Rev. 1, Oak Ridge National Laboratory.

Ooi, M., H. Ogawa, H. Iwasa, et al. 2003. “Experimental studies of neutronic performance of a hydrogen moderator depending on para-hydrogen concentration,” in *Proceedings of ICANS XIV*, Neuss, Germany, May 12–15, 2003, pp. 791–800.

ORNL (Oak Ridge National Laboratory) 2007. “SNS Second Target Station white paper,” SNS-10000000-TR0029-R00, Oak Ridge National Laboratory, August.

Pelowitz, D. B., ed. 2008. *MCNPX User’s Manual Version 2.6.0*, LA-CP-07-1473, Los Alamos National Laboratory.

Pelowitz, D. B., ed. 2011. *MCNPX User’s Manual Version 2.7.0*, LA-CP-11-00438, Los Alamos National Laboratory.

Pelowitz, D. B., ed. 2013. *MCNP6 User’s Manual: Version 1.0*, LA-CP-13-00634, Los Alamos National Laboratory..

Popova, I. I., ed. 2018. *An Updated Manual for CINDER2008 Codes and Data in the AARE Package*, ORNL/TM-2018/926, Oak Ridge National Laboratory.

Remec, I., et al. 2015. “Neutronics analyses for the SNS Second Target Station,” *ANS MC2015—Joint International Conference on Mathematics and Computation (M&C), Supercomputing in Nuclear Applications (SNA) and the Monte Carlo (MC) Method*, Nashville, TN, April 19–23. Available on CD-ROM, American Nuclear Society, LaGrange Park, IL.

Remec, I., F. X. Gallmeier, and M. J. Rennich 2018. “Neutronics Analyses for the ORNL’s Spallation Neutron Source Second Target Station,” in *J. Phys.: Conf. Ser*.1021, 012084. DOI: 10.1088/1742-6596/1021/1/012084

Remec, I., F. X. Gallmeier, M. J. Rennich, et al. 2015. “Second Target Station moderator performance with a rotating target,” *Proc. AccApp ’15*, Washington DC, November 10–13, 2015, pp. 266–271.

Rennich, M., T. McManamy, V. Graves, et al. 2010. “Design and testing of a prototype Spallation Neutron Source rotating target assembly,” *Nineteeth International Collaboration on Advanced Neutron Sources Meeting (ICANS XIX)*, March 2010.

Riemer, B. W., Janney, J. G., S. Kaminskas, et al. 2013 “Target operational experience at the spallation neutron source,” *Eleventh International Topical Meeting on Nuclear Applications of Accelerators*, Bruges, Belgium, August 5–8, 2013. http://fullpapers.flexmax.eu/accapp2013/protected/THZTA02.pdf.

Russell, G. J., E. Pitcher, G. Muhrer, et al. 2003. “Changes in neutron spectra with ortho-hydrogen fraction for Lujan center flux-trap hydrogen moderator,” in *Proceedings of ICANS XIV*, Neuss, Germany, May 12–15, 2003, pp. 809–832.

Simos, N., S. Fernandez, W. Mittig, et al. 2017. “Performance Degradation of Ferrofluidic Feedthroughs in a Mixed Irradiation Field,” *Nuclear Instruments and Methods Physics Research A*, BNL-113600-2017-JA, February 16, 2017. https://www.bnl.gov/isd/documents/94555.pdf.

SNL (Sandia National Laboratories) 2017. *CUBIT Geometry and Mesh Generation Toolkit15.3 User Documentation*, SAND2017-6895 W, August. https://cubit.sandia.gov/,

Tautges, T. J., P.P.H. Wilson, J. A. Kraftcheck, et al. 2009 “Acceleration techniques for direct use of CAD-based geometries in Monte Carlo radiation transport,” in *International Conference on Mathematics, Computational Methods & Reactor Physics (M&C 2009)*, Saratoga Springs, NY, American Nuclear Society.

Wei, J., H. Chen, Y. Chen, et al. 2009. “China Spallation Neutron Source: Design, R&D, and outlook,” *Nucl. Instrum. Methods Phys. Res., Sect. A* 600, 10–13.

Wilcox, D. 2016. “Design and optimisation of the ISIS TS1 upgrade target,” *6th High Power Targetry Workshop*, Rutherford Appleton Laboratory, December 4, 2016.

Wilson, W. B., S. T. Cowell, T. R. England, et al. 2008. *A Manual for CINDER’90 Version 07.4, Codes and Data*, LA-UR-07-8412, Version 07.4.2 Update: March 2008.

Wohlmuther. M., and F. X. Gallmeier 2008. *User Guide for the Gamma Source Perl Script 1.0*, TM-85-08-02, Paul Scherrer Institut.

5. INSTRUMENT SYSTEMS

5.1 INTRODUCTION

The STS is designed to deliver the world's highest peak brightness of cold (long-wavelength) neutron beams. It will use one out of every four proton pulses produced by the upgraded SNS accelerator, which operates at 60 Hz, to deliver 700 kW (46.7 kJ/pulse) of proton beam power to the STS rotating solid tungsten target at 15 Hz. On average, 35 neutrons will be produced for each 1.3 GeV proton striking the tungsten target. The energy of these neutrons will be reduced in cryogenic moderators located above and below the target. Neutrons will be distributed to 22 experimental beamlines with high efficiency by neutron optical components located as close as 70 cm from the moderators. Instruments built on these beamlines will take advantage of state-of-the-art advances in neutron instrument design, methods, and technologies to multiply the greater than 20× increase in STS cold neutron brightness relative to the FTS to provide wholly new capabilities far beyond the reach of today's best instruments.

The 22 STS beamlines will support a suite of neutron scattering instruments that provide entirely new capabilities to the US research community (Figure 5.1). The STS project will build five neutron scattering instruments, each of which will include (1) the infrastructure to transport the neutrons from the moderators to the sample position and to shape, manipulate, and shield the neutron beam as required along the incident flight path; (2) the instrument end station and its associated shielding, mechanical components, neutron detectors, initial suite of sample environment equipment; and (3) the data management infrastructure and scientific software required to reduce and analyze data. *The objective of Instrument Systems is to deliver five instruments ready to begin commissioning with neutron beam during early STS operation, along with the key infrastructure required to ensure the early scientific success of the new facility.* The research community will be engaged in an instrument selection process early in the project preliminary design phase to select the instruments that will be built as part of the STS Project.

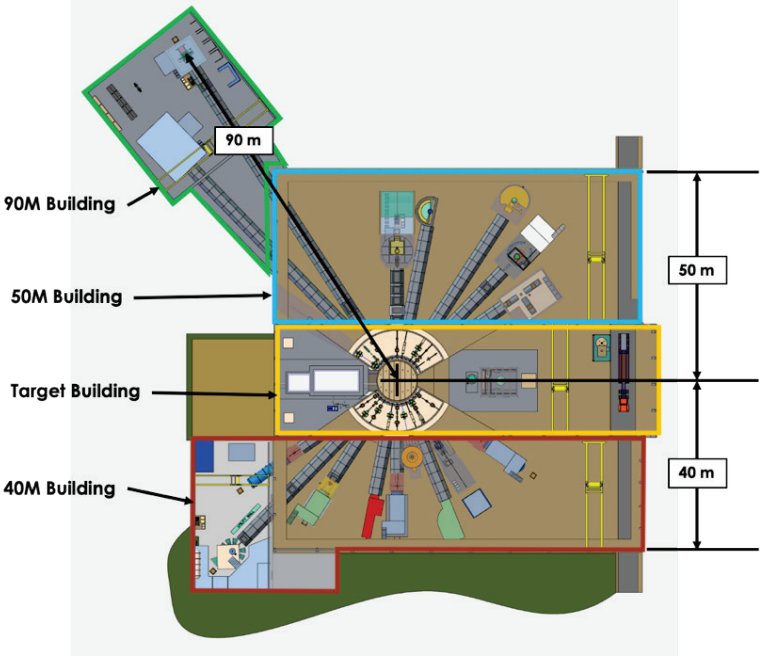

Figure 5.1. Schematic view of the target and experiment halls with 16 notional instrument concepts illustrated. STS beamlines are numbered from ST01 to ST22 counterclockwise from the lower left corner. Some beamlines have been left unoccupied. The 40M, 50M, and 90M instrument halls are indicated in the image.

5.1.1 Instrument Concepts

The capabilities of many instrument concepts were discussed at a user community workshop. [ORNL 2015] These are illustrated in Figure 5.1, which shows their possible distribution about the STS target monolith (the round structure in the left center of the Target Building). Five of these instruments were

identified for concept development to support project planning and are described in the following sections. These five instruments illustrate some of the science capabilities enabled by STS. They also represent the range of physical parameters and technical requirements anticipated for STS instruments; they are listed in Table 5.1. They include one inelastic spectrometer, two diffractometers, a small-angle/wide-angle neutron scattering (SANS/WANS) instrument, and a reflectometer. These concepts are described in later subsections of this section. Their locations in the instrument buildings are shown in Figure 5.2. While each of these five instrument concepts would deliver extraordinary new capabilities to the user community, changes to this initial set of instrument concepts can be anticipated based on future community input during the instrument selection process. Changes could extend to replacement of one or more of these planning instruments with higher priority instruments.

Table 5.1. List of five neutron scattering instruments developed as concepts that are representative of instruments that could be built at STS. These instruments demonstrate science capabilities that can be enabled at STS and have been used for project planning purposes. Moderator types are described in Section 5.2.

Beamline	Name	Description	Nominal length (m)[a]	Moderator type
ST03	CYGNUS	Small/wide-angle neutron scattering optimized to measure structures simultaneously at length scales from atomic to 100s of nanometers	30.25	Cylinder
ST09	QIKR	Kinetics reflectometer—horizontal sample reflectometer optimized for real-time studies of interfaces, enabling “cinematic” mode of operation	18	Cylinder
ST13	VERDI	Versatile diffractometer for magnetic structure studies of powder and single crystals featuring a full neutron polarization capability	40	Cylinder
ST17	CHESS	Cold neutron chopper spectrometer optimized to measure weak signals intrinsic to small neutron cross-sections or limited sample sizes with a wide range of incident neutron energies	30	Tube
ST20	EWALD	Single crystal diffractometer optimized for sample volumes below 0.01 mm^3 with unit cell edges from 10 to 300 Å (small molecule and macromolecular)	90	Cylinder

[a]Moderator-to-sample distance.

The beamlines number counterclockwise from 1 to 22 beginning at lower left (ST01 to ST11 left to right in the lower, 40M building, and ST12 to ST22 right to left in the upper 50M and 90M buildings). Space has been reserved on beamlines ST18 and ST19 adjacent to the 90M building for future long instruments. Figure 5.2 indicates the locations of the five concept instruments.

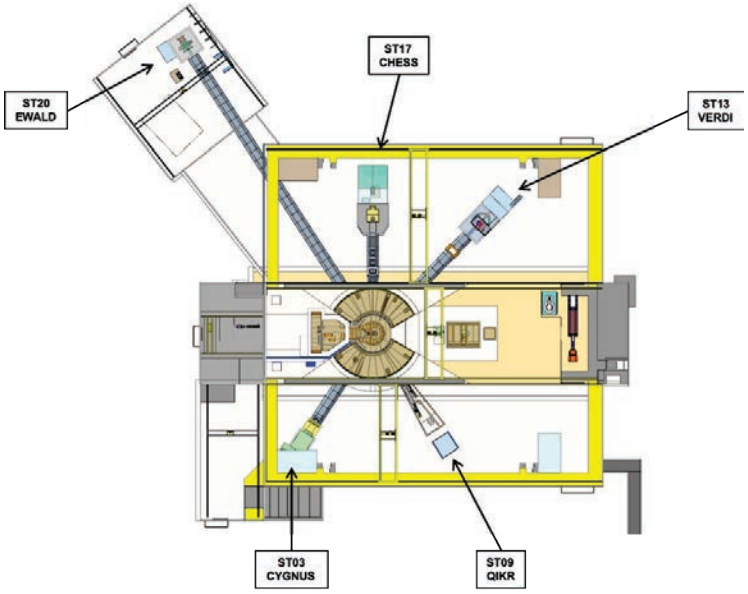

Figure 5.2. Locations of the five concept instruments being used for project planning.

5.1.2 Moderators

The primary interface between the neutron source and the instrument beamlines occurs at the faces of the neutron moderators that slow down the spallation-produced neutrons to energies that are useful for neutron scattering. Neutrons emitted from these moderator surfaces illuminate the beamlines that approach as close as 70 cm. Concepts for two high-brightness moderators have been developed based on instrument input as described in Section 5.2. The 3 cm tall cylinder moderator illuminates 16 STS beamlines, and the triangular tube moderator illuminates the remaining 6 beamlines. Both moderators are cold, coupled para-hydrogen, providing approximately the same peak brightness in the cold neutron range. The 3 cm diameter tube moderator has broader pulse widths that provide more neutrons to those instruments that can use lower-wavelength resolution. The geometry of this moderator type limits the number of beamlines it can support to six as illustrated in Figure 5.3. A final round of moderator optimization, including the sizes of the viewed faces and moderator diameters, will occur during preliminary design.

Instrument location around the facility and on specific beamlines was the result of considering a number of factors, including matching instruments to the appropriate moderator, grouping longer instruments on one side of the target, and avoiding geometric and magnetic interference. In particular, instruments deemed to have a high sensitivity to varying magnetic fields have been placed far away from the location identified for an extreme–magnetic field instrument (ZEEMANS) on ST02. This instrument poses particular challenges in minimizing its interference with neighboring instruments and providing the additional space for its high-field magnet support systems. The instrument was strategically placed to address these concerns.

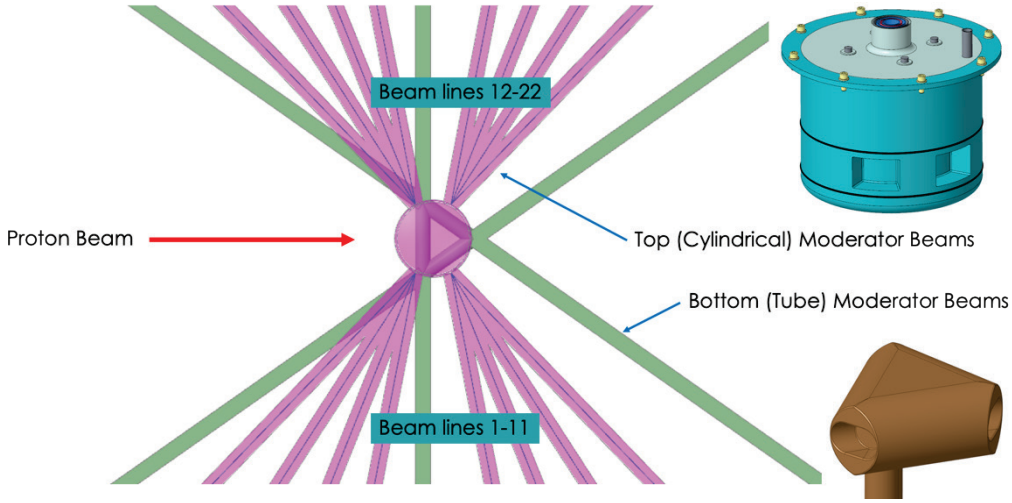

Figure 5.3. Beamline arrangement showing the six unique beamlines (green) illuminated by the triangular-shape tube moderator.

5.1.3 Instrument-supporting Infrastructure

In addition to the descriptions of instrument concepts in Sections 5.4 to 5.8, Section 5.9 describes key supporting infrastructure required by the neutron scattering instruments and provided by Instrument Systems, including scientific software, neutron technologies, biological shielding, and sample environments.

5.1.4 Instrument Systems Project Interfaces

Instrument Systems relies on a number of other STS Level 2 systems for certain areas of support and has several key interfaces across the STS Project:

- Conventional Facilities: Instrument Systems relies on Conventional Facilities to provide the buildings that house the instrument end stations and transport lines, as well as to provide standard utilities routed to designated locations inside the buildings. Routing utilities from these locations to the instrument end stations as required will be the responsibility of Instrument Systems. Requirements for floor loading and stability have been developed. Transport of equipment and personnel (staff and users) has been incorporated into the building requirements. Conventional Facilities will provide the poured-in-place bunker shield wall (Instrument Systems will provide the removable shield blocks that form the top of the bunker shielding. See Section 5.3)

- Target Systems: Instrument Systems interfaces with Target Systems both within and external to the target monolith. Instrument Systems has provided the optimization requirements for the moderator suite. Section 5.3 describes the interfaces between instruments and the target monolith and the equipment that is provided as part of the Instrument Systems scope.

- Integrated Controls: Instrument Systems relies on Integrated Controls Systems for the instrument data acquisition, experiment control, and computing infrastructure (see Section 6.4). Instrument Controls also provides the instrument personnel protection systems (see Section 6.2.3).

5.2 MODERATOR AND SOURCE CHARACTERISTICS

At the heart of the STS concept are advances in target and moderator technology that provide greater than 20× gains in the peak brightness of cold neutrons, with a corresponding gain in neutron flux at the sample position, for the STS compared with the current 1.4 MW FTS. At a pulsed spallation neutron source, neutrons are produced by impinging a high-energy proton pulse onto a heavy metal target. The resulting neutrons are slowed down to energies useful for neutron scattering experiments in moderators containing hydrogen located above and below the target. Neutrons leaving the faces of the moderators enter the neutron optics systems that direct neutrons to the neutron scattering instrument sample positions. Brighter moderators illuminate the neutron optics with more neutrons in the wavelength range and solid angle that the optics can accept and allow better optimization of the neutron optics system, especially in illuminating small areas. High brightness directly translates into higher neutron flux on the sample, which is the foundation for delivering the multiple order-of-magnitude gains in instrument performance required to address the science challenges envisioned for STS.

Figure 5.4 shows the neutron brightness emitted from the STS coupled moderator compared with its counterpart on FTS at the indicated operating conditions, which are those anticipated when STS is fully operational. The height of the pulse shapes is the peak brightness produced at the moderator face. The integral under the curve multiplied by the number of proton pulses per second (15 and 45 for STS and FTS, respectively) is the time-averaged brightness. Instrument performance scales with peak brightness if the intrinsic width of the pulse is broad enough to deliver the wavelength resolution desired, which is true for most of the instruments envisioned for STS. In the remaining cases, the wavelength resolution determined by the width of the moderator pulse divided by the neutron time-of-flight (TOF) may be better than typically required, but still useful for some measurements. Moderator geometries have been identified that provide the highest brightness of cold neutrons to the neutron scattering instruments, which is a core strength of STS. High-brightness moderators were identified early as the key to high-performance neutron scattering instruments. [Zhao et al. 2013, Gallmeier et al. 2016].

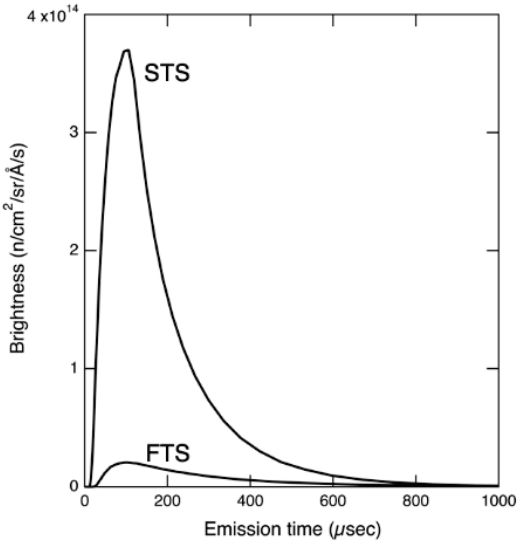

Figure 5.4. Pulse shapes emitted from FTS and STS cold, coupled moderators at a wavelength of 5 Å. Calculations are for STS operating at 15 Hz with 700 kW and FTS operating at 45 proton pulses per second and 2 MW.

Moderator performance is impacted by the choice of moderator materials; moderator size and temperature; position with regard to the neutron production zone; moderator environment, including pre-moderator and reflector material choices; and sizing. The neutron production zone is defined by proton beam characteristics such as beam energy, beam area and profile, beam power and pulse length, and target characteristics such as element charge number, material density, target dimensions, and cooling medium choice and volume fraction [Watanabe 2003, Carpenter and Yelon 1986]. Many choices are constrained by engineering considerations, such as for temperature, stress, material fatigue requirements, the need for heat removal, radiation-induced material degradation, and the requirements for safely containing the high radionuclide activity at all times in any operational and off-normal scenarios. Considering all options and constraints, STS is best served by liquid para-hydrogen moderators pre-moderated with ambient-temperature light water and placed in a wing arrangement relative to a solid

tungsten rotating disk target and surrounded by a beryllium reflector. Two moderators, one located above and one located below the target disk, will illuminate the 22 neutron beamlines. An opportunity for a final round of moderator geometric optimization is anticipated during the preliminary engineering design phase of the project. Responsibility for designing and providing STS moderators is part of the Target Systems WBS Level 2 and is described in Section 4.4. This current section describes the performance and optimization of the moderator physics design to meet the requirements of the neutron scattering instruments.

A proton beam of 1.3 GeV energy and 0.7 MW power pulsed at 15 Hz with sub-microsecond pulses generates a compact high-energy neutron production zone in the target volume of about 13×6×10 cm^3 (width × height × depth) feeding into the close-by moderator assemblies. Hydrogen or a hydrogenous material is the preferred moderator material because of its fast neutron slowing-down and moderating abilities that are needed to establish neutron pulses with reasonable characteristics, including high peak brightness and pulse widths matched to the instrument requirements. Liquid hydrogen is the best compromise, considering its high hydrogen density, radiation hardness, and temperature. The para-hydrogen flavor, the energetic ground state of the hydrogen molecule, is especially suitable because of its low neutron interaction probability below a neutron energy of 10 meV, enabling efficient extraction of cold, low-energy neutrons from 10–20 cm deep in the moderator volume. Hydrogen is condensed from its room-temperature normal gaseous state at 75% ortho and 25% para fractions into the liquid state as the moderator is initially filled, and radiation-induced conversion of para- to ortho-hydrogen occurs during operation. The natural relaxation to the thermodynamic equilibrium of 99.8% para at 20 K temperature takes many days. As a consequence, the STS hydrogen loop will be equipped with a sufficiently sized catalytic converter consisting of magnetic material such as iron or chromium oxide to speed up the relaxation process and promote conversion of ortho to para-hydrogen. The Japan Proton Accelerator Research Complex (J-PARC) Material and Life Science Experimental Facility has demonstrated that liquid hydrogen loops that include a catalytic convertor can operate at a 99.8% para fraction at a high-power spallation source [Kai et al. 2005, Teshigawara et al. 2016]. Based on this success, it is assumed that similar performance can be achieved for STS. Installation of a catalytic convertor is planned for FTS as part of the Proton Power Upgrade. All analysis work presented in this section assumes 100% para-hydrogen as the moderator material.

As cold neutrons are generated in para-hydrogen by a one-time down-scatter event from neutrons with energies above 10 meV, the moderator zones of 1–2 cm proximity to the pre-moderator interface are the most productive for cold neutron generation. Additionally, para-hydrogen has a mean free path for cold neutrons of 100–300 mm and hence is fairly transparent for cold neutrons. Neutrons can easily be extracted from moderator depths of the order of one mean free path. These two characteristics can be exploited by moderator configurations with a depth of the order of one mean free path but with reduced sizes in one or both of the other dimensions, with neutron extraction from the side(s) with reduced dimensions.

Two representative moderator concepts were adopted for the target station: a 30-mm-high cylindrical moderator [Gallmeier et al. 2016], called the cylinder moderator, and the triangular moderator comprising 30-mm-diameter tubes [Gallmeier 2018], called the tube moderator. Both will be pre-moderated by ambient-temperature light water and reflected by beryllium metal. The cylinder moderator was optimized to deliver the highest peak brightness (highest pulse peaks) with a resulting diameter of approximately 80 mm. It will have four 30 by 30 mm view ports with each view port illuminating four beamlines. The tube moderator composed of 3 connected 30 mm diameter hydrogen-filled tubes is optimized toward the highest pulse integrated brightness, resulting in a base length along the tube of approximately 160 mm. Neutrons will be emitted from this assembly along the tube axes at six locations to illuminate six beamlines. The two moderator configurations are depicted in Figure 5.5. The performance of the STS moderators is presented in Figures 5.6 to 5.9 and compared with the FTS coupled moderator as viewed by

beamline 5 at January 2019 conditions (1.4 MW power, 1 GeV proton energy, heavy water–cooled inner reflector plug, aluminum proton beam window, hydrogen at 30% ortho and 70% para state, performing at 80% of theoretical maximum because of power-induced degradation of neutron production). In time-averaged brightness, the STS tube and cylinder moderator show gains of a factor of 5-9 and 4-6, respectively, over the FTS coupled moderator. The STS moderators show gains of ≈20 in peak brightness relative to the FTS moderator.

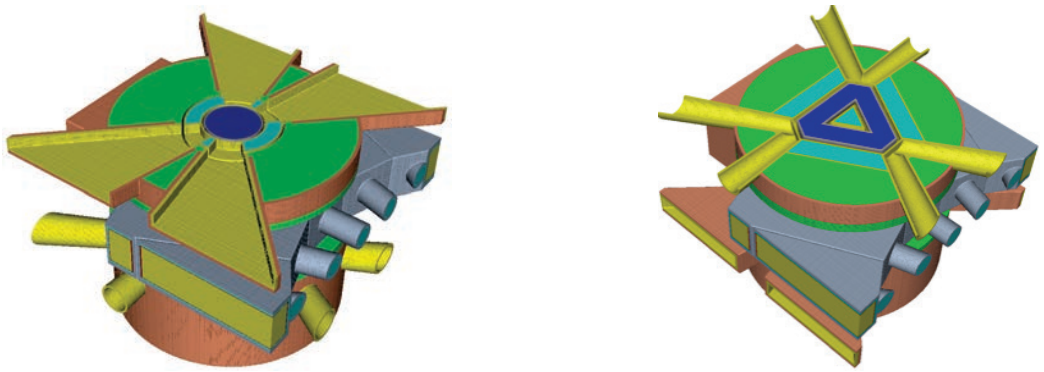

Figure 5.5. Horizontal cuts through the vertical center of the STS moderators: cylindrical moderator (left) viewed from above and tube moderator as viewed from below (right). Dark blue represents the para-hydrogen moderating material, light blue is the water pre-moderator, and green is the beryllium reflector located above and below the target wheel (grey assembly). The views of the moderators by the instrument beamlines is indicated in yellow.

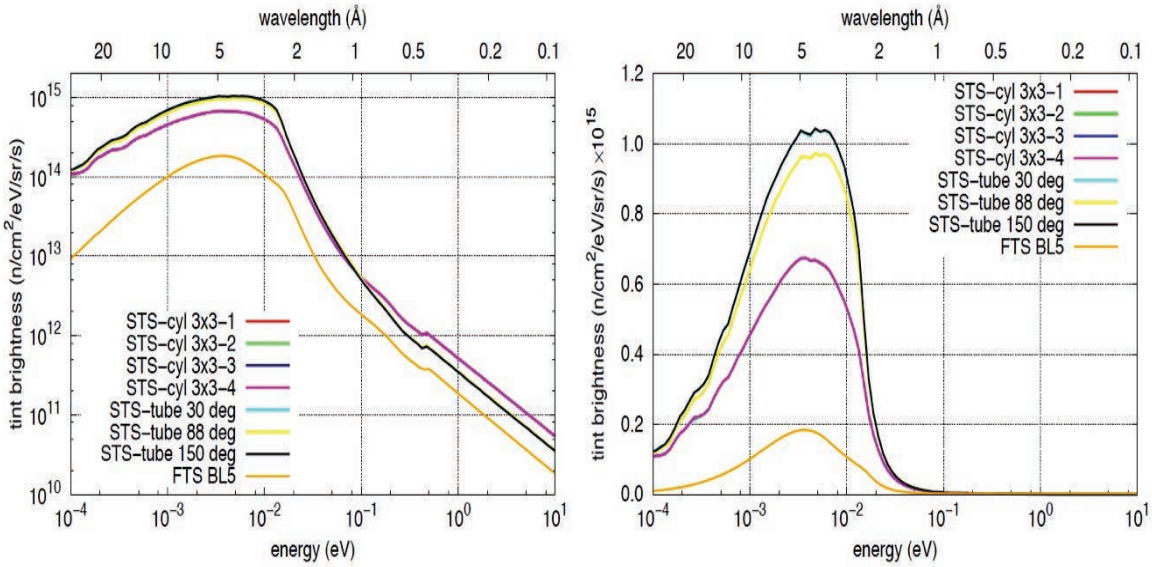

Figure 5.6. Time-averaged brightness of STS moderators. Numbers after the moderator indicate which view port is accessed.

The full-width-at-half-maximum (FWHM) pulse widths of the STS tube moderator are about 80% wider for thermal and cold neutrons compared with those of the STS cylinder moderator, whereas the FTS moderator exhibits a different energy dependence, bracketed by the two STS moderators, due to its ortho-hydrogen content. The STS cylinder moderator exhibits considerably shorter pulse rise times compared

with the STS tube moderator, as it has lower hydrogen depth. Both STS moderators result in faster pulse decay (long-time tails) than the FTS coupled moderator, an additional advantage over FTS resulting from the smaller STS moderator size as shown in Figure 5.9.

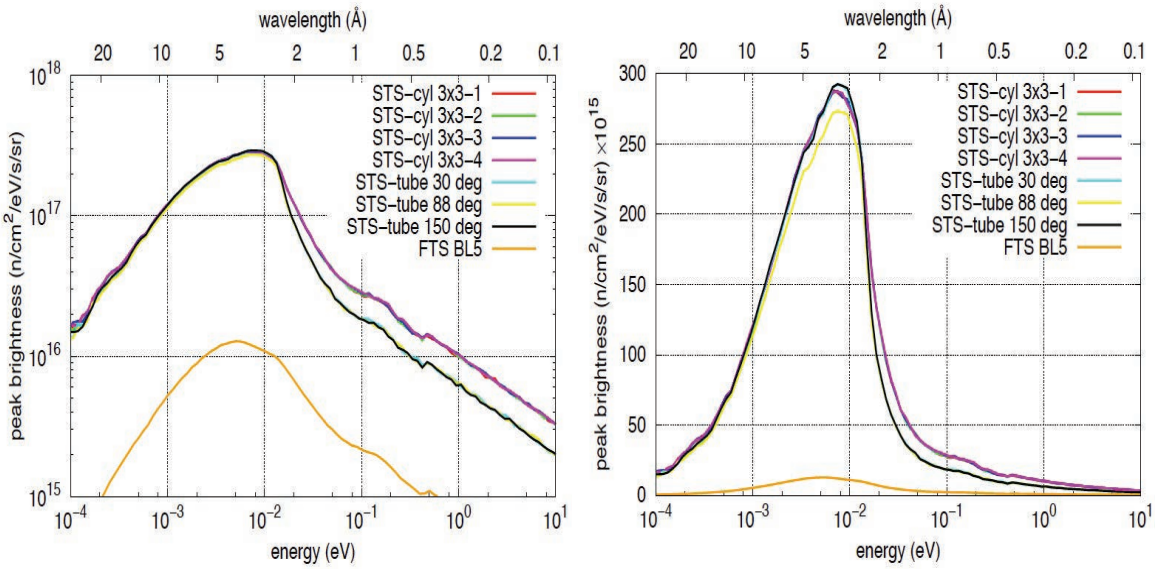

Figure 5.7. Pulse-peak brightness of STS moderators. Numbers after the moderator indicate which view port is accessed.

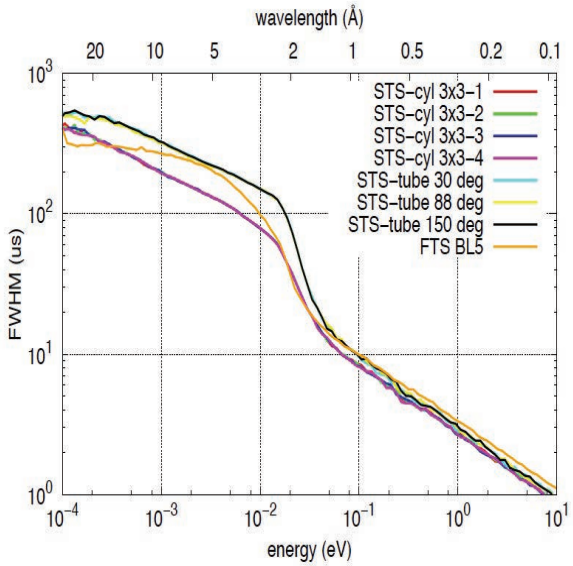

Figure 5.8. FWHM neutron pulse width of STS moderators compared to the coupled FTS moderator.

The geometric optimization was performed with an idealized fixed-area flat-profile proton beam footprint on the target of 3000 mm^2. This was later revised to the current super-Gaussian profile of 6200 mm^2 as proton beam simulation data became available and the pulse stress issues in the target needed to be reduced. The larger proton beam size also required an increase of the target disk height from 50 to 60 mm. The moderator performance simulation results shown in Figures 5.6–5.9 include all of these changes, reflecting the current concept; but the geometric optimization was not repeated with the changed

constraints. As the instrument concepts mature, plans are to reoptimize the moderator concepts to deliver neutron beams that best serve the requirements of the instruments.

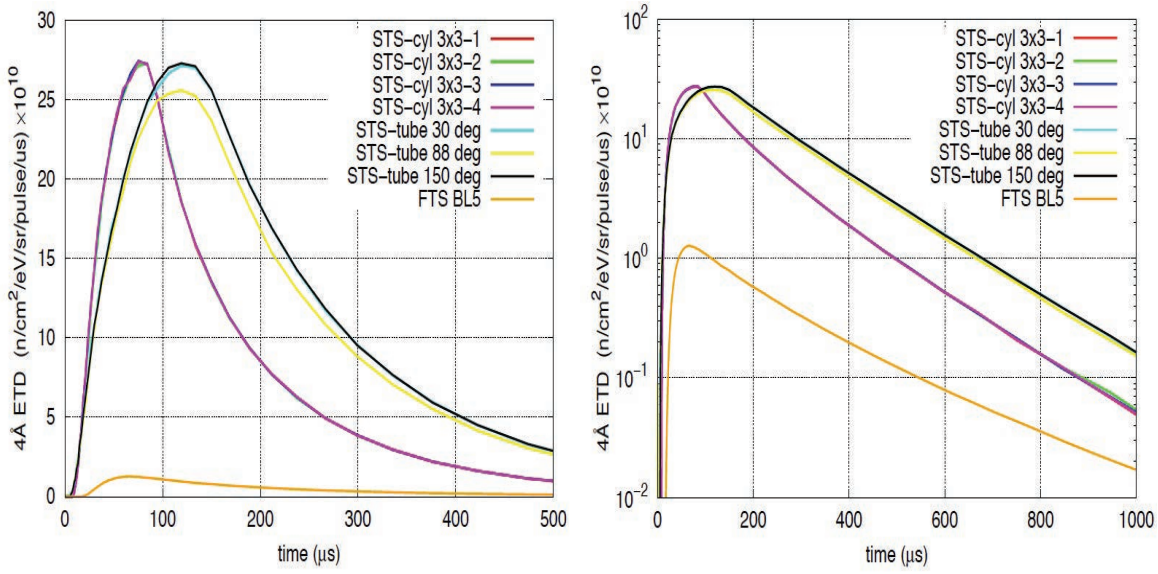

Figure 5.9. Emission-time distributions of STS moderators at 4 Å wavelength on linear scale to the left and log scale to the right.

5.3 NEUTRON BEAMLINE BUNKERS

STS will incorporate neutron beamline bunkers (Figure 5.10) on the north and south sides of the target monolith. In the context of STS, bunkers are heavily shielded rooms near the monolith where choppers and other beamline components are located; personnel can access them without unstacking significant amounts of local shielding. The use of bunkers was motivated by several factors:

- The desire to reduce background radiation by providing an integrated shielding design near the target monolith. On the SNS FTS, each instrument designed its shielding in this area, providing many additional interfaces and possible radiation leakage paths.

- The high-brightness STS moderators are smaller than their FTS counterparts, requiring greater precision in aligning the in-monolith optics packages. The bunker facilitates installation of high-precision, individual beamline single integrated assemblies into the target monolith.

- The desire for straightforward and flexible installation of the near-monolith beamline components and required services (vacuum, cooling water, and electrical).

The bunkers and many of their constituent components are described in this section. The geometries and sizes described in these concepts are based on preliminary neutronics estimates performed to provide initial shielding and shutter composition and thicknesses.

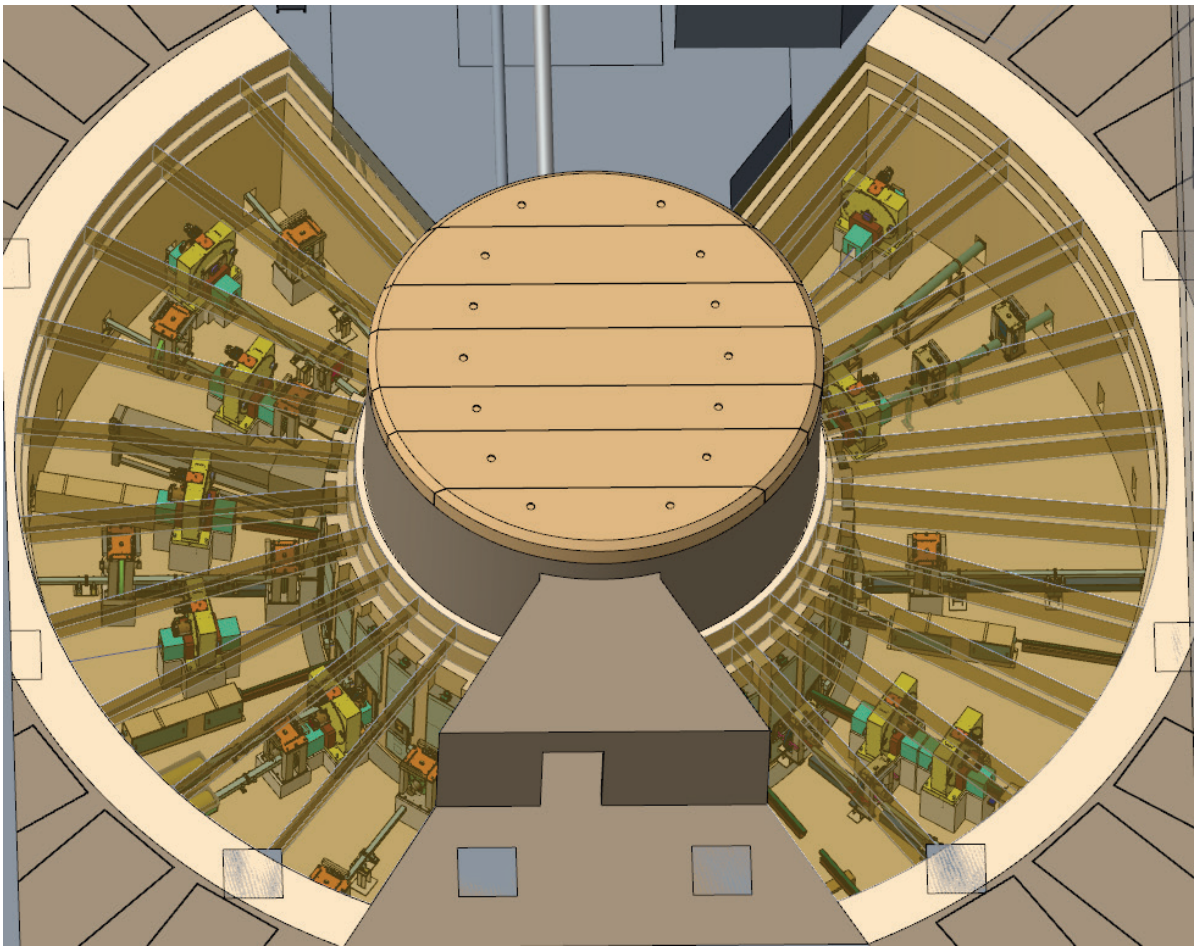

Figure 5.10. STS bunkers surrounding target monolith.

In the development of the bunker concept, the following performance and/or operational considerations drove the design.

Characteristic	Design Drivers
Facility performance	• 20–24 beamlines • Minimize moderator approach distances • Minimize optical windows • Eliminate optics breaks within monolith • Enable high-precision optical alignment within monolith
Facility operation	• Straightforward personnel access to near-monolith components • Integrated near-monolith shielding design rather than “leaky” local shielding • Adequate beamline separation near monolith • Straightforward installation of near-monolith components for initial and future beamlines • Simplified distribution of central utilities (cooling water, helium, vacuum) for near-monolith components

5.3.1 Bunker Description

In horizontally arrayed beamline configurations (Figure 5.11), personnel access to beamline components is limited by shielding and angular spacing between adjacent beamlines. While typically only passive optical components are located between the shutters and moderators, there is a desire to place choppers and other beamline components that require maintenance as close to the source as possible. Open bunkers (with local shielding of specific components) offer much better access to these components than is possible with individually shielded beamlines. Finally, the installation of future beamlines is significantly improved by better physical access to this area and a more open geometry to better align components.

In addition to the improved access characteristics, a bunker arrangement contributes to the performance of a high-brightness source by combining the separate FTS core vessel and shutter insert neutron guides into a single, integrated, in-monolith optical system with minimal windows. This integration results in better alignment between guide segments located near the source, since they are contained within a single module, and minimal attenuation of cold neutron beams from vacuum windows.

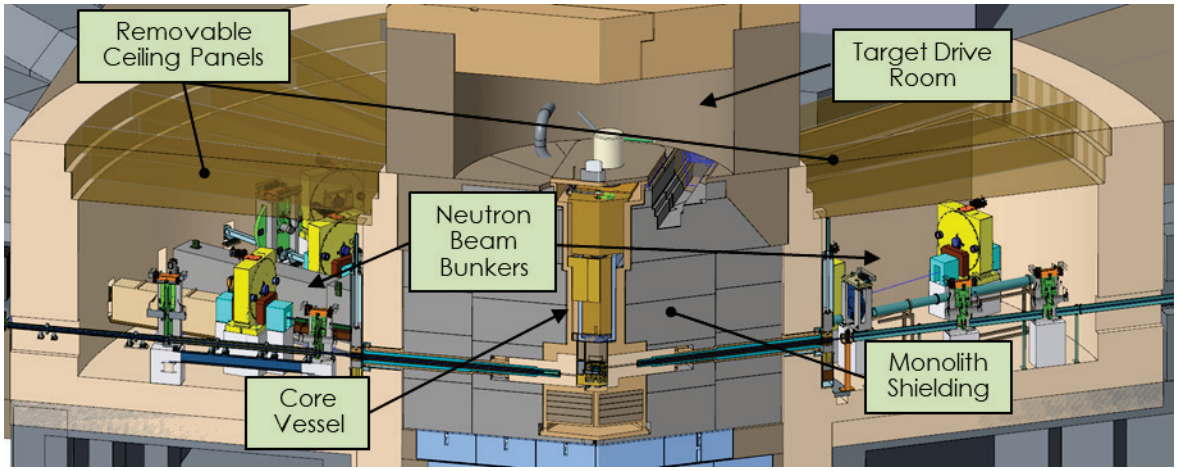

Figure 5.11. Target building section view showing neutron beamline bunkers.

The accessible space within the neutron bunkers is between radial distances of 6 and 11.5 m from the moderators. The radial width is driven by the length of the equipment required to handle the monolith inserts that are installed into the monolith structure. As the Target Building high bay walls are tangent to the bunker walls, the Target Building width is directly impacted by the bunker diameter, and vice versa. The tangency constraint is imposed to eliminate any building support columns between the beamlines on the instrument floor outside the bunker. But since it affects the Target Building width, it also imposes space constraints for high bay operations and utility support in the basement. Removable roof panels and a floor-level personnel entrance will provide beam-off crane and personnel access to the bunkers.

During construction, personnel access to the bunkers will primarily be through walk-in openings in the angular end walls of the bunkers or via temporary stairs from the high bay floor. Before facility operation begins, the walk-in openings will be filled with shielding blocks, and bunker access will be available only from the high bay using purpose-built ladders or steps after local roof panel removal. This access mode is required because the bunkers will contain significant amounts of beamline equipment and local shielding, and there is not adequate vertical clearance between the beamline equipment and the roof panels to allow walkways. Personnel access to the bunkers when the source is not operating and after some reasonable cooldown period (less than 24 h) is the assumption that drives the design and operating philosophy of the bunkers. This assumption is based on the experience at FTS, in which the activation levels of the T0

choppers have been much less than originally estimated and are low enough to permit hands-on maintenance.

Activation calculations were completed for the SNS SNAP instrument T0 chopper and are documented in SNS document 106100200-TR0147-R00. Induced radioactivity calculations were completed using Inconel 718 as the neutron absorber. Assuming 2 years of irradiation at 2 MW beam power, the Inconel 718 absorber had a calculated dose rate of ~1–2 rem/h on contact and a calculated dose rate of ~40 mrem/h @ 1 ft after 3 days of decay. After 180 days of decay, the calculated dose rate dropped by approximately another factor of 2. Although activation analyses were completed on Inconel 718, the final chopper design used Inconel X-750, which has a similar elemental composition. Actual activation levels of the T0 chopper have been significantly less than calculated. A SNAP T0 chopper was removed from service in December 2018. After 2.6 years of irradiation at >1 MW beam power, the Inconel X-750 absorber had a dose rate of 20 mrem/h on contact (25–50 times less than calculated) and a dose rate of 3.5 mrem/h @ 1 ft (5–6 times less than calculated) after 35 days of decay.

Even the USANS instrument T0 chopper, with the highest-to-date measured activation level (also removed from the instrument in December 2018 after 2 years of irradiation at >1 MW beam power, but in a different beamline), had a dose rate of 100 mrem/h on contact (approximately 10 times less than calculated for the SNAP T0 chopper) and a dose rate of 20 mrem/h @ 1 ft (approximately equal to the calculated level for the SNAP T0 chopper) after 14 days of decay. The higher activation and dose rates can be attributed to the USANS neutron beam being more than four times larger than the SNAP neutron beam.

5.3.2 Bunker Construction Scope and Design

The neutron beam bunkers and the equipment within them will be provided by Conventional Facilities and Instrument Systems. Figure 5.12 shows a typical section through the monolith and bunker area. The primary delineation between these two entities is that Conventional Facilities will provide the pour-in-place, permanent building concrete and shielding, while Instrument Systems will provide the removable roof shielding panels plus any local shielding and shielding within bunker wall penetrations. In addition, Instrument Systems will provide all technical equipment described in Section 5.3.3.

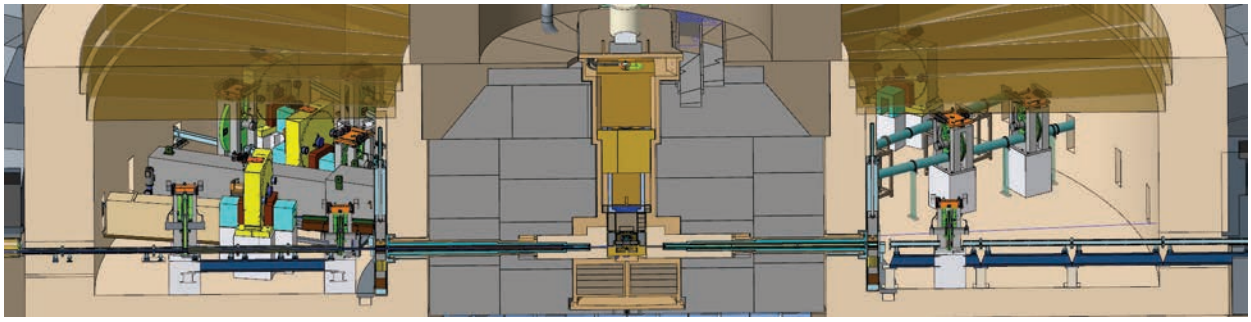

Figure 5.12. Bunker section view.

The bunker walls provide shielding protection to equipment and personnel in the instrument halls, and they also will delineate the ventilation boundary between secondary confinement within the bunker and normal building ventilation in the instrument halls. Penetrations through the bunker wall will allow neutron beam optics to bridge the two spaces, but provisions to locally shield within the penetrations and to provide ventilation separation will be required; Instrument Systems will be responsible for such provisions.

In addition to serving as shielding, the monolith and bunker walls support the weight of the removable bunker ceiling panels, so their thickness and composition will be driven by a combination of those requirements. Preliminary neutronics estimates indicate that the bunker walls and ceiling will need to be 1.5-m-thick, high-density (HD) concrete with provisions for special features such as frameworks for holding neutron-absorbing panels on the bottoms of the roof panels, built-in mechanical guides to aid in roof panel installation, and window frames designed to accommodate bunker wall shield inserts and future neutron optical equipment. Floor loading within the bunkers will not be particularly high since the equipment weight is not expected to be excessive; but since the bunker floors are over the basement of the Target Building, they must also provide shielding above the rooms located beneath them.

5.3.3 Bunker Technical Equipment

5.3.3.1 Monolith Inserts

Neutronic performance improvements in STS rely on the use of relatively small, high-brightness moderators, focusing optics, long imaging mirrors, precision alignment of guide components, and a minimal number of windows in the guides. All these requirements argue for long, purpose-built, continuous guides/optics in the monolith. Maximizing the acceptance angle by locating the initial beam guides as close as possible to the moderators, well inside the monolith shielding radius, is a primary instrument and target station design requirement. The primary factor determining the moderator approach distance is geometry: the width of each monolith insert and the angle between adjacent beamlines defines the physical separation between neighboring inserts and how close they can extend toward the moderators. A complicating requirement resulting from this proximity of the guides to the target is beam heating. Neutronic analyses will define the cooling requirements of the inserts, but the FTS insert cooling system is being used as the conceptual design basis.

To address these requirements and provide flexibility for future installations, STS will have a three-layer guide assembly (Figure 5.13). The inner layer will consist of the optical guide pieces (metallic or glass). They will be contained within a structural housing for handling. This two-layer module will then be located within the monolith insert housing which separates the target and bunker environments. Because the core vessel is not easily repairable, and since locating beam windows on close radius flanges is not feasible, nozzle extensions will be permanently attached to the core vessel and will extend the vessel environment to an accessible location outside the monolith shielding. This arrangement will provide for remotely replaceable structural monolith inserts to be installed inside the nozzles and sealed to the outside flanges of the nozzles. The active monolith inserts will be water cooled and will have aluminum windows at each end to provide an appropriate atmosphere boundary. The upstream window mounted to the monolith insert, insert housing, and downstream mounting flange will combine to form the barrier between the inner core vessel atmosphere and the secondary confinement.

Because of their estimated size (~4.5 m) and weight (~2 tons), it is preferred to install the monolith insert shells during facility construction rather than when beamlines are installed. Their reentrant design accommodates the installation and removal of optical guide modules or shielding modules without breaking their vacuum seals to the nozzles. Upstream windows pre-installed on each monolith insert are expected to be life-of-facility components and are not replaceable since they would be highly activated; however, if a failure occurs, the entire insert can be replaced.

Instrument-specific guide modules will be inserted into the monolith inserts. Although the monolith insert shells will be water-cooled via internal cooling channels, guide cooling will be provided by a convective helium environment within the monolith insert cavity confined between the permanently installed upstream monolith window and the outer window sealed to the monolith insert mounting flange. Monolith insert and guide module lengths are driven by the monolith shielding radius and are

approximately 4.5 m. Additional neutronic analysis is required to determine the ideal configuration of monolith shielding; although the shielding monolith diameter can increase, it cannot be significantly reduced because enough perimeter must be available to fit the maintenance shutters into the structure.

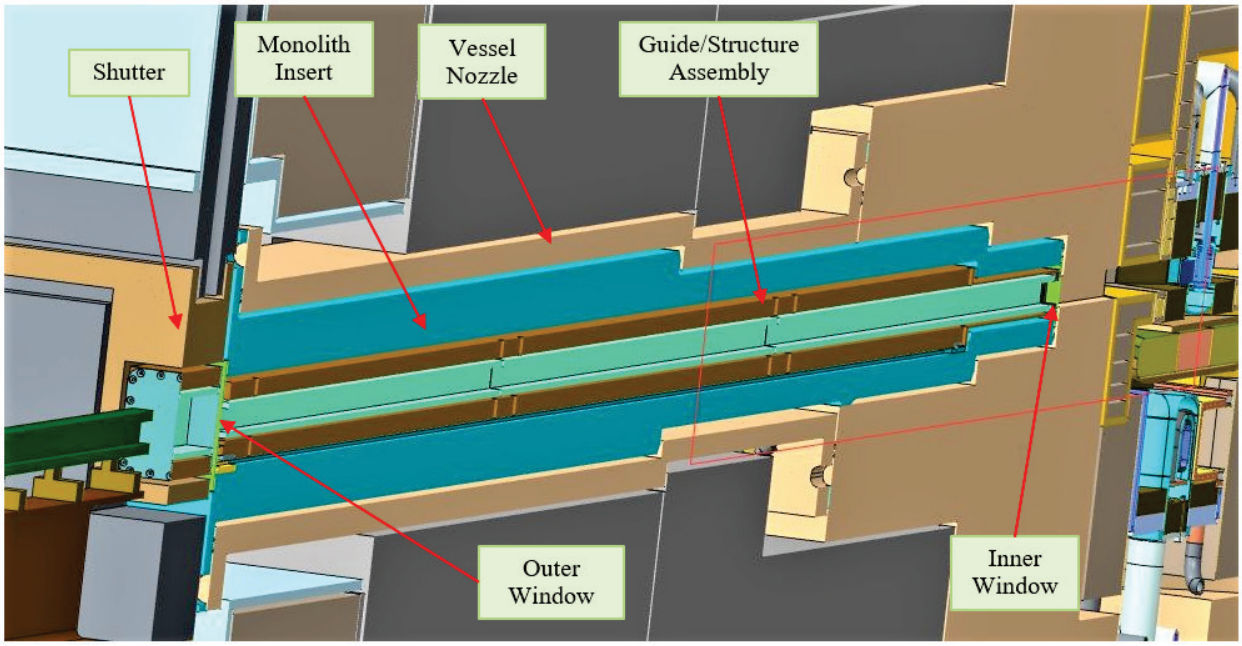

Figure 5.13. Typical neutron beamline monolith insert with guide module.

The use of monolith inserts within the monolith shielding will allow beam guides to come within 70 to 100 cm of their respective moderators, depending on their proximity to neighboring inserts or the rotating target disk (see Figure 5.14 and Table 5.2). Insert width significantly impacts the beam guide approach distance to the moderators, and the shape of the insert walls has been considered in some detail to minimize their overall width while still providing adequate thickness to accommodate internal water-cooling channels in the most upstream portion of the inserts. The current moderator view size is standardized as 3 by 3 cm, but the standard insert provides a 5 by 5 cm opening for those instruments that require a diverging guide. As beamline designs evolve, it is anticipated that some customization may be required for specialized optical requirements. Currently, however, all inserts are identical, except for QIKR, which incorporates two inclined viewing channels of the same moderator. Descriptions of this unique concept are provided in Section 5.5.

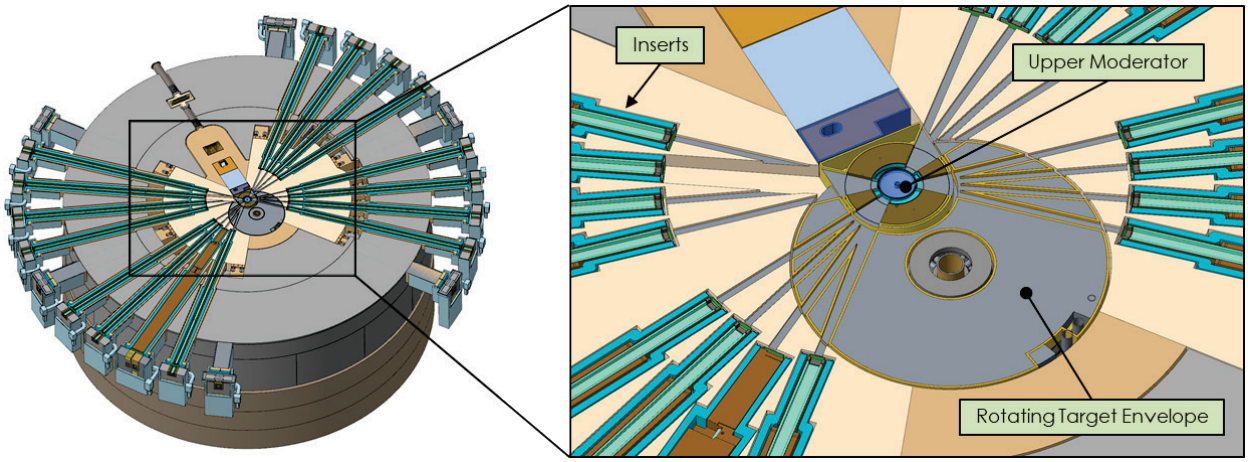

Figure 5.14. Monolith inserts viewing the upper moderator.

Table 5.2. Moderator approach distances by beamline.

Beamline	Moderator	Moderator approach distance to first window (cm)	Beamline	Moderator	Moderator approach distance to first window (cm)
1	Tube	90	22	Tube	90
2	Cylinder	90	21	Cylinder	90
3	Cylinder	90	20	Cylinder	90
4	Cylinder	90	19	Cylinder	90
5	Cylinder	90	18	Cylinder	90
6	Tube	73	17	Tube	73
7	Cylinder	90	16	Cylinder	90
8	Cylinder	90	15	Cylinder	90
9	Cylinder	95	14	Cylinder	90
10	Cylinder	90	13	Cylinder	90
11	Tube	103	12	Tube	103

Note: Listed beamline order matches physical beamline port locations.

Figure 5.14 shows the geometric layout of the monolith inserts viewing the upper moderator and how their widths determine the approach distance. These widths were developed based on information and assumptions provided by neutron guide vendors in creating a concept from the inside to the outside. Figure 5.15 shows the geometric assumptions made for the wall thicknesses and clearance gaps between various components of the monolith inserts and the optical guide modules that are inserted within them. An additional step was inserted into the monolith insert and optical module housings to further reduce the moderator approach distances; Figure 5.15 shows the dimensions before and after this step. In summary, the assumed 50 by 50 mm neutron flight path allowance ends up requiring a 140 mm-wide monolith insert at the upstream end; this insert width drives the moderator approach distances given in Table 5.2.

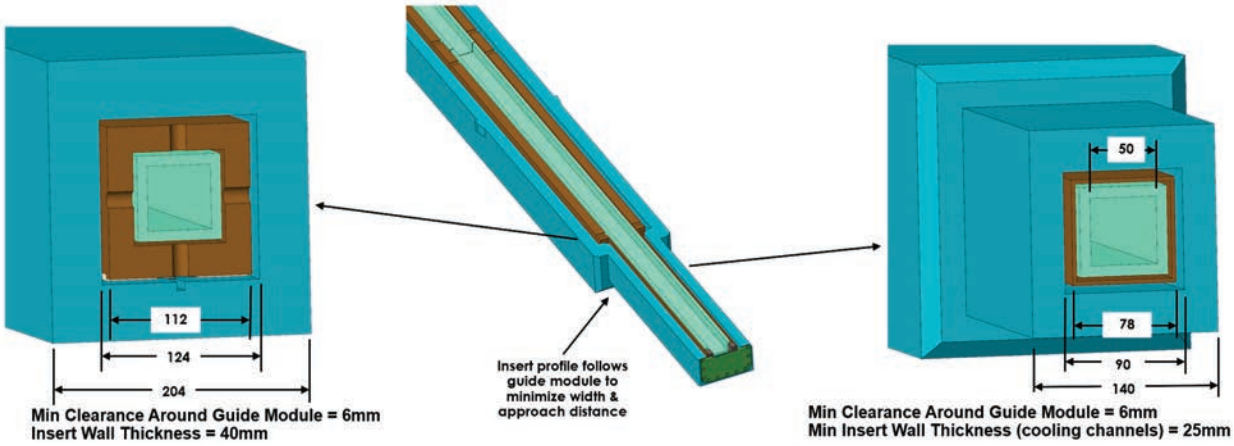

Figure 5.15. Monolith insert and optics module assumed dimensions.

Because all the inserts are installed during initial construction, the sizing of the reentrant openings must rely on assumptions and limits regarding the optical requirements of future instruments. A goal will be to provide reasonable additional space for larger future optics; but because the array of inserts is width-constrained, providing additional vertical space within the inserts will be simpler than providing horizontal space. During facility construction, each insert will be filled with either an operational guide module or a shielding plug, with the environment within the insert being controlled in either case. As future beamlines are installed, the shield plugs will be replaced with purpose-built guide modules by removing the downstream insert windows. Figure 5.16 shows an optical guide module being installed within a monolith insert. This operation must be performed at least semi-remotely because the moderators and target will remain in place as future beamlines are installed. The guide modules will have kinematic locating features that will engage matching internal insert features using a simple pushing motion during guide installation; gravity will hold the guide modules in position once the kinematic features have engaged. These features are described in more detail in Section 5.9.7.1.

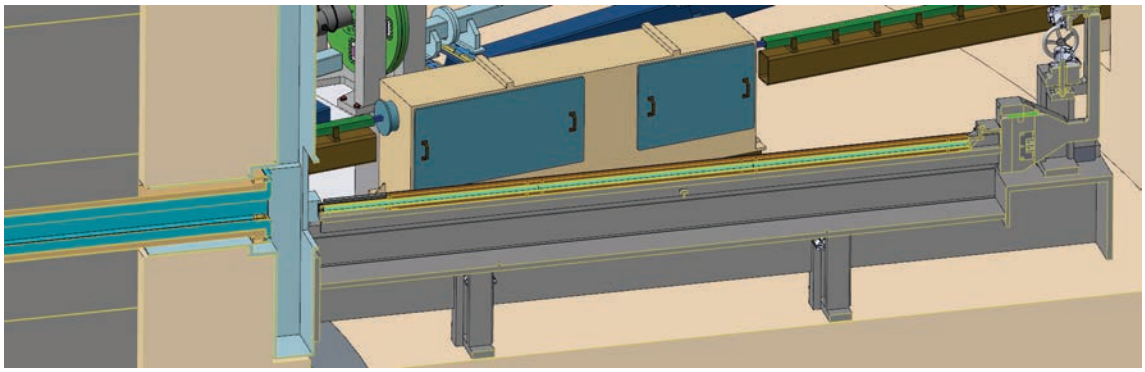

Figure 5.16. Guide module being inserted into a monolith insert. Top shielding not shown.

5.3.3.2 Monolith Optics Installation Tooling

Monolith inserts will be changed using the same basic procedure used for the vertical assemblies; however, the tooling will be designed to pull spent inserts and push new inserts into position (Figure 5.17). All 22 inserts will be installed during facility construction. Only the inserts that support the initial instrument suite will contain optical guide modules; shield plugs will be installed in the inserts of unpopulated beamlines. While the inserts themselves will be installed by hand and are expected to be life-of-facility components, the capability for replacing activated inserts and swapping shield plugs with new

optic modules is required. Such operations will require the use of shielded containers and mechanisms that are capable of at least semi-remote control. In fact, the tooling for these operations drives the radial width of the bunkers. The tooling will also be used to perform the same operation to place inserts inside a commercial shipping container while it is positioned on the high bay floor.

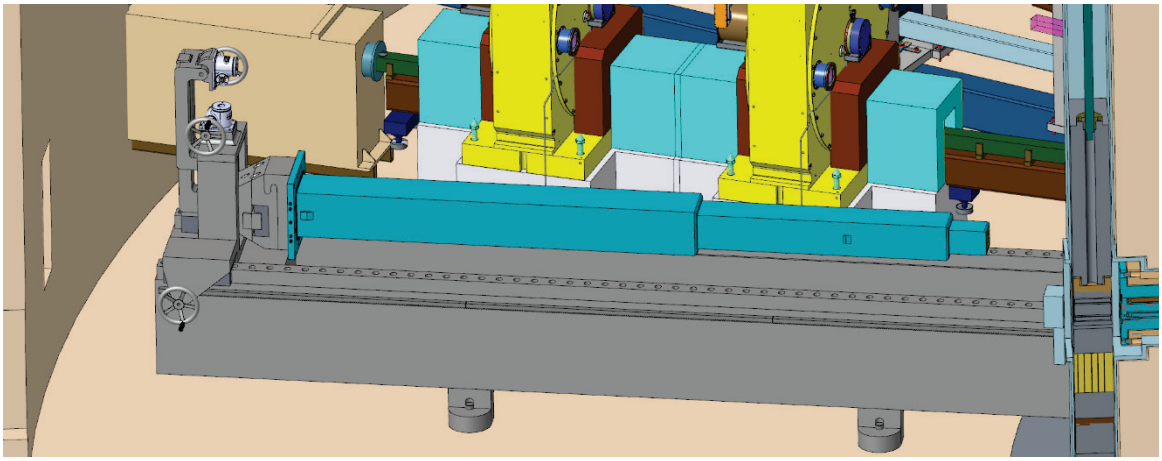

Figure 5.17. Monolith insert handling machine located in the bunker. Top shielding not shown.

5.3.3.3 Shutters

Neutron beam shutters have historically served as neutron gates or valves, stopping all neutron and gamma radiation and allowing downstream beamline access for sample access and/or maintenance operations. In doing so, they reach activation levels that restrict human access; so, in most facilities such as FTS, these shutters are located within inaccessible, shielded structures. Providing personnel access to the bunker during beam-off maintenance periods, even after years of facility operation, is a fundamental requirement for the facility; it requires a different shutter philosophy. Instead of neutron gate shutters, STS will incorporate maintenance shutters located at the inner bunker radius that minimally activate, thus allowing personnel access to the bunkers for beam-off maintenance and installation activities. These maintenance shutters are provided to isolate the bunkers only during beam-off maintenance operations; and they cannot be used to provide downstream access to the beamline during operation, as even relatively short exposure to neutrons will activate the tungsten shielding to levels that will preclude bunker access. Instead, each beamline will provide its own operations shutter to support daily experimental operations. The FTS experience supports this shutter philosophy since, as Table 5.3 shows, only a few FTS beamlines use their near-target primary shutters for experimental operations; and most use the primary shutters for weekly or run-cycle-shutdowns only. Most of the FTS beamlines that do not rely on their primary shutters have relatively small secondary shutters to support daily operations.

Table 5.3. FTS shutter use during beam-on operations between Jan 21 and Apr 21, 2015 (~13 weeks).

FTS beamline	Primary shutter operations	Ops/week
3	347	26.9
18	133	10.3
12	94	7.3
17	57	4.4
5	37	2.9
14	13	1.0

Table 5.3. FTS shutter use during beam-on operations between Jan 21 and Apr 21, 2015 (~13 weeks) (continued)

FTS beamline	Primary shutter operations	Ops/week
13	11	0.9
1	7	0.5
2	6	0.5
4	6	0.5
16	3	0.2
6	1	0.1
7	1	0.1
11	1	0.1
15	1	0.1

Maintenance Shutters

Since they are shielding personnel only from gamma radiation (and not neutrons) emanating from the target area and passing through the monolith along the neutron beamlines, the maintenance shutters are estimated to be relatively short (~20 cm tungsten). As shown in Figure 5.18, the maintenance shutters will have three separate regions that can be positioned within the beamline: a beam-open position that may contain an optional optical guide with kinematic locating features used during normal beam operations; a neutron absorber to be used for reducing the activation of a failed downstream component (such as a chopper), and a gamma blocker to be used only during facility maintenance periods when neutrons are not being produced. Before personnel access the bunker, all maintenance shutters will be placed into gamma-blocking mode.

It is also assumed that maintenance shutters will not be installed in unused beam ports but will be included as a part of new neutron beamline installations. This approach assumes shield plugs will be installed within the monolith insert housings and that those plugs will provide adequate shielding to allow personnel access into the bunker during maintenance periods. These plugs are the responsibility of Instrument Systems to provide.

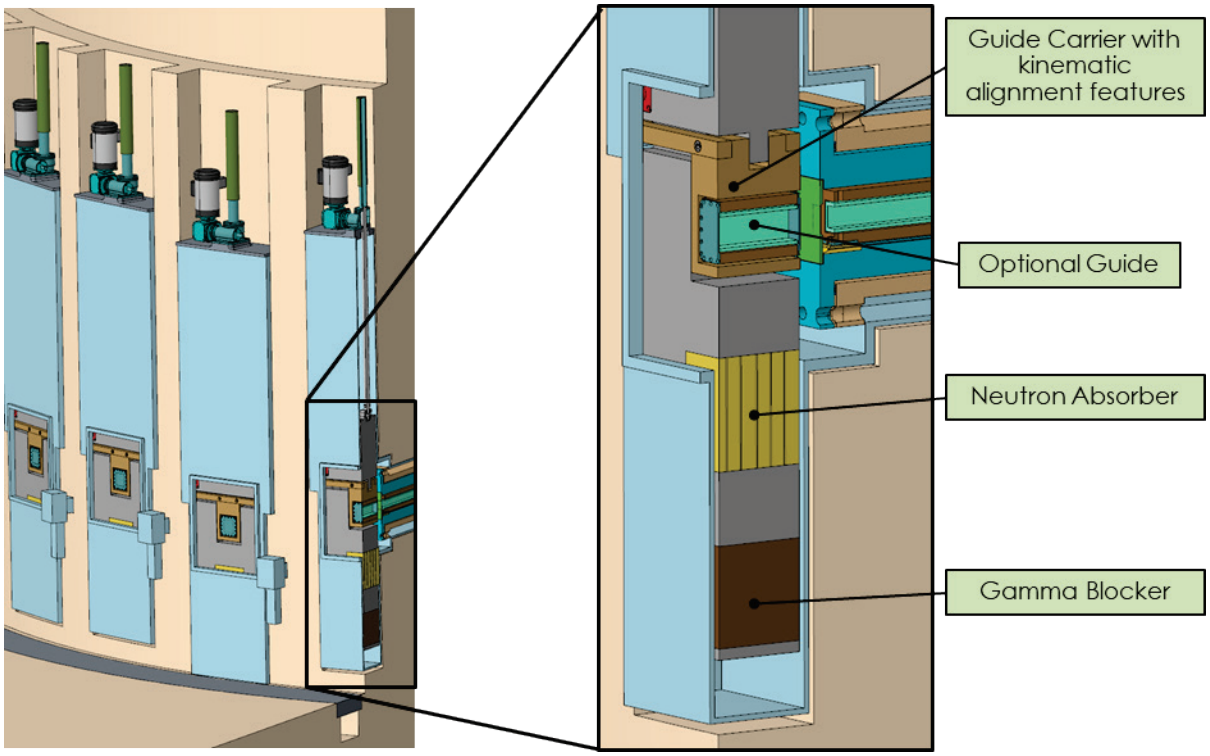

Figure 5.18. Maintenance shutters.

Operations Shutters

For beamline operation, each instrument will provide an operations shutter. Figure 5.19 shows conceptual operations shutter designs based on existing FTS implementations; these concepts are currently assumed to be the STS standards and are incorporated universally throughout the beamline concepts. For those beamlines with adequate curvature or deflected beams, a relatively thin, guillotine-style, neutron absorber shutter will suffice for stopping low-energy neutrons, since the high-energy neutrons and gammas will enter the bulk shielding along the beamline. For straight beamlines that have direct moderator views, a heavy shutter will be required. Based on FTS experience, an estimated length of such a high-energy, neutron-stopping shutter is 1 m of tungsten. During preliminary and detailed design, the heavy shutter material composition and its surrounding shielding will be optimized to minimize activation and provide for better local access to equipment in its near vicinity. Personnel access to the sample area and to any failed beamline components during proton beam-on will be provided only by the operations shutter; access to failed components upstream of the operations shutter will be possible only during facility shutdowns.

Since they are not space-constrained, long beamlines can generally locate high-energy, neutron-stopping shutters in a convenient location, as the shutters do not typically affect instrument performance. However, some of the shorter instruments may have difficulty in allocating space for such shutters, especially since the operations shutters should be in locations allowing vertical access for maintenance purposes. While not preferred, for these short instruments, it may be necessary that their operations shutters be located in the bunker. Heavy local shielding may be required to shield personnel from activated shutter components during maintenance periods requiring local access in such instances. Detailed design will rely heavily on neutronics activation and dose analyses.

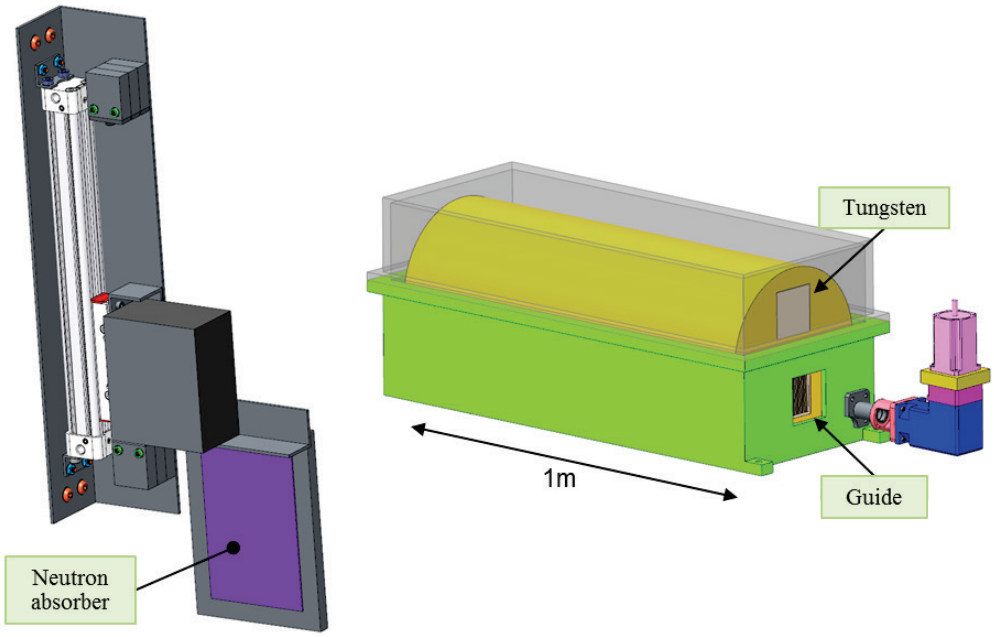

Figure 5.19. STS Operations shutter concepts for low- and high-energy neutrons.

5.3.3.4 Bunker Utilities

Because of the tight confines and the fact that the bunkers will house the confluence of equipment from multiple STS design groups, the design of bunker systems will necessarily require well-defined interfaces and design coordination. Conventional Facilities will provide the standard industrial utilities to the bunker; Instrument Systems will provide the neutron beamline components (both in the bunker and within the monolith), the removable bunker ceiling panels, and the maintenance shutters; and Target Systems will provide the monolith insert cooling water and cover gases. Those utilities associated with the monolith optics and shutters will be distributed around the monolith wall, while the utilities associated with the beamline components will be distributed around the bunker wall, with many instrumentation and control cables feeding through the bunker wall penetrations. Because of the neutron irradiation concerns, electronics within the bunker will likely not be allowed or will be minimized. Electronics associated with the maintenance shutters will be located as close as possible but outside the bunkers.

One difference planned for STS vs. FTS is the incorporation of a central neutron guide vacuum system at STS. FTS beamlines provide their own guide vacuum, with individual roughing pumps distributed throughout the facility. STS intends to provide guide vacuum to all the beamlines as a utility, and the bunker will house the distribution system, which will likely be located on the bunker wall. A room in the Target Building basement near the bunker will house primary and backup roughing pumps. Vacuum pipes will penetrate the bunker walls and will follow the beamlines to provide connections as needed for individual guide sections. Such a scheme requires implementation of a guide vacuum specification and a standard vacuum housing design to ensure all beam guides meet the required level of vacuum capacity. Each beamline will be required to undergo a leak check before tying into the central vacuum system. When problems occur, the offending beamline will be isolated from the system and will use local pumping so that other beamlines can continue operating normally. At this time, it is unclear whether STS choppers will be part of the guide vacuum system, since their vacuum requirements are generally tighter than is required for beam guides. That question will be addressed during preliminary design.

Finally, the neutron bunkers will be part of the secondary confinement exhaust (SCE) system because they have the potential to produce airborne contamination and may also contain activated water leaks from the monolith insert cooling system. The bunker wall will be the outer SCE boundary, and the wall penetrations will require some sort of air barrier from the instrument bays. The current plan is to fill the bunker wall penetrations with steel shot around the beamline optics, then incorporate a flexible sheet material over the openings. This approach would separate the bunker environment from the instrument bay environment so that the bunkers could be held at a slightly negative pressure so that flow is always into the bunker from the instrument bays. It is noted that the Target Building high bay air space communicates with the bunker and is also part of the SCE.

5.4 CHESS

5.4.1 Summary

CHESS is a direct geometry, inelastic spectrometer designed to probe the weak signals intrinsic to small cross-sections (e.g., small magnetic moments) or the limited sample sizes often available for new materials or associated with extreme sample environments such as high pressure. It will be optimized for the study of quantum and functional materials, but its broad dynamic range is also well-matched to measuring diffusion and excitations in soft and biological matter. It will have the ability to simultaneously measure dynamic processes over a wide energy range, making it the spectrometer of choice for first measurements of new materials. This instrument will support the option for polarized neutron beam and polarization analysis to separate nuclear from magnetic scattering and coherent from incoherent scattering processes in hydrogenous materials. This section presents a science case for the instrument; reviews the basic design concept, technical solutions, and performance estimates; and lists some R&D that is needed. CHESS will be a flagship spectrometer for the facility, a world-leading instrument in its class, and is technically feasible to construct and operate.

5.4.2 Science Case

Inelastic neutron scattering is an essential experimental probe for the dynamical properties of materials, because energy and momentum transfer are simultaneously accessible in a scattering experiment. Unlike a local probe such as μSR or Mössbauer spectroscopy, neutron scattering provides both spatial and dynamical information in a coupled manner. The measured scattering function $S(\mathbf{Q},\omega)$ is directly proportional to the imaginary part of a generalized, momentum- and energy-dependent susceptibility, and thus it is straightforward to make the connection between measured data and theoretical modeling.

The most important practical limitation for the technique, in particular with hard condensed matter and with biological materials, is the sample size needed to obtain a statistically significant inelastic signal over the period of time (~days) typically allocated for experiments in user facilities. Pushing down the feasibility limit for sample size in realistic experiments is therefore considered the highest priority for the design of a new inelastic spectrometer at STS. The basic design choices for CHESS—the beam size at the sample position, the targeted energy resolution range (3–5%), and the detector array covering ~2π sr —all aim to maximize the scattering signal for small samples. Figure 5.20 compares thresholds in sample sizes with typical sample growth and preparation techniques. The most interesting new materials are often available either in limited quantities or as small crystals. Lowering the limits for measuring weakly scattering (or highly absorbing) samples opens the door to early, highly impactful studies of novel, new materials.

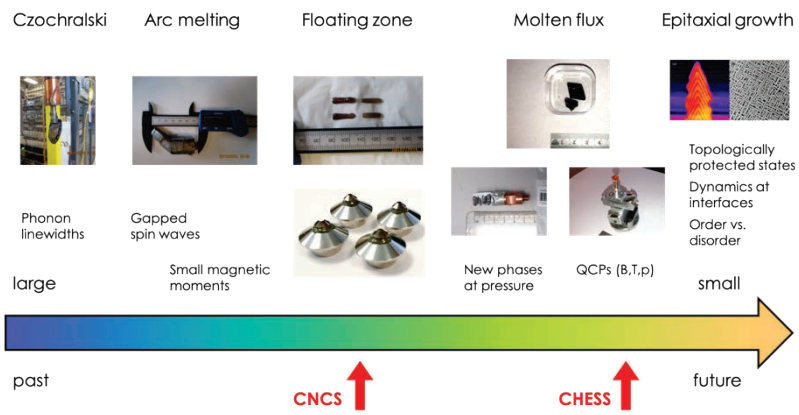

Figure 5.20. Illustration of the thresholds in sample volumes that can be successfully studied on cold neutron chopper spectrometers. The SNS first target station Cold Neutron Chopper Spectrometer has already established new thresholds in its ability to measure small samples. CHESS will push the threshold further to the right.

CHESS is a direct geometry spectrometer. Instruments of this class are known for their flexibility in choosing the energy and (independently) the energy resolution, for their excellent signal-to-noise ratio, and for the wide range of science areas to which they contribute. Indirect geometry spectrometers are more efficient in obtaining scattered intensity in the horizontal scattering plane and do therefore allow spectroscopy with potentially smaller samples. However, the reduced flexibility of indirect geometry spectrometers in terms of resolution means that they tend to have a narrower, more focused science case, and that a direct geometry instrument is better suited to be a workhorse, multi-purpose, general spectrometer. Another possible STS instrument concept, ZEEMANS, is of the indirect geometry type, as it seeks to maximize the data that can be collected in the scattering plane for samples in extreme magnetic fields.

The wide wavelength bandwidth employed by CHESS (see Section 5.4.3) means that it will naturally lend itself to performing survey-type experiments in which dynamic processes in a material are simultaneously studied over a wide energy range. Therefore, in many cases, a study at CHESS may be the first dynamics investigation for a new material (which is often only available in a small amount) by means of scattering. This puts CHESS in a leading position to enable first experiments on new materials with high scientific impact.

The scientific and technological environment at ORNL, in which CHESS will be embedded, will be relevant for all science areas discussed. Combining state-of-the-art cold neutron spectroscopy at CHESS with the world-class computing capabilities at the Oak Ridge Leadership Computing Facility (OLCF) will be key to solving complex problems in condensed matter for decades to come. The materials studied with neutron spectroscopy—quantum magnets and soft materials alike—are becoming more and more complex. The key signatures in the scattering that need to be resolved will be weaker, more diffuse, and hidden by other processes or correlations of less interest that are also present in the materials. It will be increasingly necessary to integrate neutron scattering experiments with advanced computational methods for data analysis and theoretical modeling. OLCF, currently home to the fastest civilian supercomputer in the United States, and ORNL have the capabilities and people skills to develop a synergistic program, in which theory and experiment go hand in hand, to address the grand challenges of contemporary condensed matter research.

The following subsections expand on a few scientific areas of current interest for which inelastic neutron scattering experiments at CHESS are expected to make a major impact.

5.4.2.1 Quantum Magnets

In a textbook magnet, one will observe long-range order of the magnetic moments (often ferro- or antiferromagnetic) if the material is cooled to sufficiently low temperature. In a quantum magnet,

quantum fluctuations will prevent the formation of conventional magnetic order, and the resulting ground state will host quasiparticle excitations that can be characterized with inelastic neutron scattering and are key to understanding the ground state. The excitations reveal the symmetry, the energy scale and type (e.g., exchange, anisotropy) of the underlying correlations. These excitations are often of low energy, which makes cold neutron spectroscopy a suitable probe to study them.

CHESS will transform the ability to probe excitations in quantum magnets; it will detect weaker and more diffuse signals than existing instruments in its class and offer neutron polarization analysis when it is advantageous. CHESS will provide essential information about the fundamental interactions and processes in quantum materials that give rise to their unique properties. CHESS will have sufficient energy resolution to measure small gaps in an excitation spectrum, which in many cases is crucial to confirm the ground state of a material.

The quantum spin liquid (QSL) is a prominent example for the ground state in a material that is dominated by quantum fluctuations. Defining characteristics of such a state are the absence of magnetic order in the zero-temperature limit; a high degree of quantum entanglement; and the presence of continuous, non-local excitations. It is difficult to *directly* confirm these characteristics experimentally and, in particular, to measure the degree of quantum entanglement. A few materials are presently known which appear to realize a QSL ground state [Balz et al. 2016, Paddison et al. 2017], but the community agrees that definite positive experimental evidence for it is still lacking.

Topological quantum materials offer great potential for dissipation-less electronic transport and topologically protected quasiparticles. This is an area of intense current research activity. The discovery of a skyrmion lattice in MnSi is perhaps the best-known example [Mühlbauer et al. 2009]. Topological spin structures of potential interest are known to exist at zero magnetic field but may also be stabilized in a magnetic field [Martin and Batista 2008, Kamiya and Batista 2014, Leonov and Mostovoy2015].

For all of these systems, high-quality single crystals and the ability to simultaneously reach mK temperatures and high magnetic fields are needed to exploit the unique insight derived from inelastic neutron scattering. Available high-quality crystals are frequently small (for example, when they are grown from flux), and their study requires the leap in capability that CHESS will provide. CHESS will provide a competitive edge for the early characterization of new materials exhibiting-low temperature magnetism. The need for this capability was explicitly identified in a recent DOE Basic Research Needs workshop: “However, neutron scattering instrumentation able to probe all relevant aspects of quantum materials with greater efficiency and a broader range of thermodynamic parameters is needed: Broadband high efficiency inelastic neutron scattering that can provide detailed and comprehensive mapping of spin-resolved electronic correlations in small single crystalline samples (<1 mm^3) from mK to 1000 K … .” [DOE 2016].

5.4.2.2 Systems at Pressure, Quantum Criticality

The optimization of CHESS for a small beam, ~1 cm^2, will be highly beneficial for studying samples at pressure or under other extreme conditions that tend to require small sample volumes. Progress in the synthesis of large diamonds via chemical vapor deposition will enable the design of new diamond anvil cells to reach ~10 GPa pressure in a volume large enough for inelastic scattering at CHESS. Pressure is a relevant and clean thermodynamic variable for many materials and physical phenomena, for example, superconductivity and quantum criticality. As an alternative to hydrostatic pressure, chemical doping is also routinely used to introduce chemical pressure in a material. This avoids the restriction on the sample size imposed by high-pressure cells and thus often produces profound results. For example, high-temperature superconductivity is found only when parent copper-oxide insulators are chemically doped

[Orenstein and Millis 2000, Lee et al. 2006]. However, chemical substitution necessarily introduces disorder, which may obscure the underlying physics.

Phases like unconventional superconductivity often emerge upon suppression of a competing magnetic phase. In the zero-temperature limit, a material enters a quantum critical regime; and the associated fluctuations are of interest for a range of phenomena in correlated materials. In f-electron metals, for example, the interactions are mediated via the conduction electrons that simultaneously screen magnetic 4f moments, a process known as the Kondo effect. The competing interactions give rise to large effective masses for the conduction electrons, leading to an overall low-energy scale for spin fluctuations. In these materials, hydrostatic pressure tends to be a much cleaner tuning parameter than chemical pressure, and the highest T_C values are found in undoped materials or in undoped materials under pressure [Pfleiderer 2009].

Quantum critical systems are intrinsically weak scatterers as a result of the small magnetic moments, and the increased brightness at STS will enable measurements previously not possible. As quantum critical fluctuations occur over a wide range of energies, repetition rate multiplication at CHESS will offer the flexibility to collect data at all relevant incident energies simultaneously. Previous neutron work on quantum critical points in materials such as $YbAlB_4$ [Okawa et al. 2010], CePdAl [Fritsch et al. 2014], and $CeRhIn_5$ [Yashima et al. 2007] identified the pressure-induced phase transitions. Attempts to probe the spin fluctuations at pressure were largely unsuccessful because of the resolution limits of the instruments and the low signal-to-noise ratio achieved with the available pressure cells. The combination of the various technological advances (higher brightness beam, repetition rate multiplication, larger detector solid angle, and better pressure cells) will enable significant improvements for such studies at CHESS to reveal the underlying critical scattering.

Temperature and magnetic field are other thermodynamic variables important in this context. Today, our ability to measure an inelastic neutron scattering spectrum under simultaneous application of extreme conditions in all three variables has been demonstrated (T=250 mK, B=8 T, P=2 GPa) at ORNL [private communication from Andrey Podlesnyak, ORNL, to Georg Ehlers, ORNL, 2018]. In an era when CHESS is operational, this capability will be applicable to a far wider range of materials than it is today.

5.4.2.3 Thermoelectric Materials

Thermoelectric materials are at the heart of waste-heat recovery devices and find use, for example, in the automotive sector, electrically driven refrigeration, and thermometry. If the conversion efficiency can be further improved, new fields of applications will become viable. For example, replacing classical batteries by thermoelectric generators would be desirable in many places. Such devices have high reliability, no moving parts, and therefore long maintenance intervals, all of which are attractive features.

The thermoelectric figure-of-merit of a material is good when the electrical conductivity is high while the thermal conductivity is low. The latter has two main contributing terms: from band electrons and from phonons (collective lattice vibrations). The thermal conductivity will be low when the free propagation of phonons is in some way perturbed, for example, through scattering by other phonons or lattice defects.

Inelastic neutron scattering research on the role of phonons in the heat transport properties of thermoelectric materials is an area of great recent success at ORNL [Delaire et al. 2015, Li et al. 2015]. The key factors for this success are the comprehensiveness of the scattering data, $S(\mathbf{Q},\omega)$ in four dimensions and the combination with first principles calculations. A future possible direction for this research, which would make full use of the enhanced capabilities provided by CHESS, would be to move toward nano-structured materials with larger unit cells, which may feature a broader and more complex spectrum of low-energy modes [Minnich et al. 2009].

5.4.2.4 Battery Materials

Storage systems for electrical energy are advancing rapidly. This advance has huge impacts on modern society, including personal computers, smartphones, cars, home security systems, and many other applications. Achieving better performance from a battery in terms of storage capacity, the number of recharging-discharging cycles, and reliability requires a more detailed understanding of the underlying electrochemical processes at the molecular level.

Fundamental research on battery materials to improve their performance is of vital importance. For example, some members of the lithium-orthophosphate family of materials ($LiMPO_4$, M=Mn, Fe) are attractive candidates for electrodes in lithium-based rechargeable batteries because of their high Li-ion conductivity through channels in the olivine crystal structure. These materials are complex and by no means well understood. This is particularly true for the "operational mode" when a current is flowing. The ability to predict battery lifetime and capacity, and to design materials with improved properties, is limited. Obviously, a huge body of work is being done in this area of research; and neutron scattering has a role, as it directly reveals the structure and dynamics on the atomic level.

5.4.2.5 Soft Matter

Neutron scattering is an invaluable tool for studying the structure and dynamics in soft matter because soft matter is typically rich in hydrogen, and the neutron scattering lengths for protons and deuterons are vastly different. It is thus possible, by selective deuteration, to highlight particular parts in a molecule without significantly changing its nature chemically and to tune the contrast in a scattering experiment to preferentially reveal certain aspects of a soft material.

Quasi-elastic neutron scattering is a widely used tool for measuring self-motion and collective dynamics, respectively, in soft materials. Many soft materials exhibit dynamics across a wide energy/time range, often over many decades (from ps to ms and slower). Today, it is often necessary to combine data from two or more instruments operating in different energy windows to gain a complete picture of a material. An instrument like CHESS, which operates in a wide energy window, is thus particularly well suited to studying the dynamics in soft materials, as it can probe a broader, more significant fraction of these processes simultaneously. The increased cold neutron flux and the high brightness at CHESS will not only enable neutron spectroscopic experiments on samples of small volumes and low concentrations, but also experiments with a high throughput of samples in a series where compositional parameters are being changed. It may also be possible to look at kinetic phenomena, for example, a small volume under shear, to see how these materials respond dynamically to real-life situations.

Many soft materials, such as melts of polymers, but also simpler molecules that are liquid at ambient conditions are known to undergo a glass transition on cooling. This is an old but still current topic, and neutron scattering has provided some insights [Doster et al. 1989, Frick and Richter 1995]. Again, the wide energy range in which CHESS simultaneously collects data, and the increased sensitivity to small signals, may provide new momentum for this research area.

5.4.2.6 Life Sciences

The dynamical properties of biomolecules are essential to their function. The past decade has seen enormous progress in the use of neutron scattering in biology. Today, it is possible to study the dynamics of a protein [Nickels et al. 2012] and its hydration water [Perticaroli et al. 2017] in isolation, distinguishing their mutual roles in the dynamics of protein function. Beyond this, neutrons have been used to study the structure of biomembranes [Nickels et al. 2017] and dynamics of proteins [Anunciado et al. 2017] within living cells. However, biological systems are extremely complex; and isolating scattering

features from individual components within crowded and diverse biological systems requires extensive bio-deuteration efforts, along with sample mass requirements that are prohibitive for most of the biological community.

The new capabilities of CHESS will enable the next generation of scattering experiments in biological systems with increased flux to reduce sample mass requirements and polarized beam capabilities that will allow the separation of coherent and incoherent scattering processes in hydrogenous materials. The latter correspond to collective and single-molecule dynamics, respectively [Gaspar et al. 2010, Burankova et al. 2014]. One example of how coherent neutron scattering might be extended is the demonstrated sensitivity of neutrons to low-frequency vibrations in proteins. The low-frequency vibrations of proteins reflect the global rigidity of the folded protein's secondary structure [Nickels et al. 2013, Perticaroli et al. 2013]. Recently, other forms of vibrational spectroscopy (optical Kerr-effect spectroscopy) have identified changes in protein low-frequency vibrations upon binding to substrates [Turton et al. 2014].

5.4.3 High-level Capability Requirements

The main requirement for studying small samples implies that a relatively low resolution range of ~3–5% will be used most often to achieve sufficient neutron flux (for cold neutron spectroscopy this can be considered coarse resolution). Occasionally, it will be necessary to select better resolution with the chopper system, down to ~2% of the incident energy. This implies that the overall length of the instrument must be of the order of ~30 m to match the contribution of the neutron pulse width with the other terms contributing to the resolution. Given the source frequency of f=15 Hz, it follows that a wide bandwidth of ~7–8 Å will be available at this instrument length. A longer instrument would reduce the bandwidth, and the neutron pulse would not fully illuminate the P-chopper opening time window (see Section 5.4.4 for definitions of neutron chopper types), resulting in an intensity loss with only marginal resolution gain.

The moderator neutron pulse width should be about Δt [s]~0.25 [m]/v [m/s], where *v* is the velocity of the neutron (for a wavelength of 5 Å, this would be about a 0.3 ms neutron pulse width) [Ehlers et al. 2018].

The wide bandwidth then requires that the instrument be able to operate in repetition rate multiplication (RRM) mode with typically 5–10 energies arriving in sequence at the sample within a single frame, the time between subsequent proton pulses striking the neutron generating target (1/15 Hz = 66.667 ms). For a single proton pulse reaching the target, 5–10 mini-pulses of neutrons, each having a different energy, E_i, will be selected to reach the sample. A flexible scheme will be needed to adjust the time window in which energy loss is observed for each incident neutron energy. For example, measuring to 90% energy loss requires more time between mini-pulses than measuring to 80%. The amount of time needed to measure to a particular energy loss also depends on the incident energy. In the extreme, observing quasi-elastic scattering that requires measuring only to ~50% energy loss would allow many more mini-pulses to be used than when measuring to higher energy losses. The suppression scheme must be flexible enough to allow any number of mini-pulses between 1 and 20. At the maximum number of mini-pulses, the instrument is effectively operating at 300 Hz.

The scientific design that exploits high solid-angle detector coverage with high out-of-plane scattering angles and full in-plane angular coverage places a premium on symmetric horizontal and vertical beam angular divergence. The guide has to be straight for optimized neutron transport achieving symmetric beam profiles. Bending the beam out of the line-of-sight over a short distance (~30 m to the sample) would result in too much asymmetry between the right and left sides of the instrument. Therefore, a T_0 chopper will be needed to block the flash pulse of high-energy particles (neutrons and photons) from the target.

The P chopper and M chopper will operate in a double-blind configuration [Vickery and Deen 2014]. This will ensure that the time width of neutron mini-pulses on the sample will increase with wavelength and will help to make the energy resolution more even between pulses.

It is important that CHESS offer polarization analysis from day 1 of operation. This is a crucial requirement for much of the science case.

The instrument must be located on the STS east side, away from the background generated at the FTS. CHESS will produce short monochromatic pulses incident on the sample. The objective is to measure inelastic scattering, which will be observed at the neutron TOF between such pulses. Because inelastic scattering is much weaker than elastic scattering, the ambient background between pulses needs to be as low as possible. The FTS will operate at a higher repetition rate than STS and receive pulses between those directed to STS during the time that CHESS is measuring weak inelastic signals. The high-energy component of the pulses directed to FTS cannot be well shielded. Therefore, it is essential to maximize the distance between CHESS and the FTS target. To a lesser extent, it is also important to maximize the distance to the possible extreme–magnetic field instrument, ZEEMANS—which may be located on STS beamline ST02—and its high magnetic field, which might interfere with the operation of polarized ^{3}He cells proposed for neutron polarization analysis at CHESS.

The key capabilities of CHESS that are required by the science case in Section 5.4.2 are summarized in Table 5.4. These capabilities are the drivers for the physics and technical instrument concepts described in Section 5.4.4.

Table 5.4. Key capability requirements for CHESS.

Parameter	Description
Beam size at sample	1 cm^2
Detector solid angle	$\Omega \sim 2\pi$ sr
Incident energy range	0.5 meV $\leq E_i \leq$ 25 meV; with repetition rate multiplication, the source pulse will be typically subdivided to 5–10 (up to 20) incident energies across a bandwidth of 7–8 Å
Energy transfer resolution	2–5% E_i at the elastic line, flexible
Bandwidth ($\Delta\lambda$)	7–8 Å
Q-range	0.03 $Å^{-1} \leq Q \leq 10$ $Å^{-1}$
Q-resolution	$\Delta Q/Q \sim 0.02 - 0.05$
Polarization	Polarized beam and polarization analysis
Ambient conditions	Low changing magnetic field interference

5.4.4 Physics Design and Engineering Concept

Figure 5.21 is a time-distance diagram that illustrates the functional conceptual design of CHESS. The main part of the figure is a time-distance diagram of CHESS operating with six mini-pulses on the sample (per source pulse) with the highest-energy pulse at 5.11 meV. Note that the times between pulses are not equal. In the settings shown, the time between pulses is enough to observe an 80% neutron energy loss for each pulse. On the left, the diagram shows the locations of the choppers, the transmission polarizer (W), and the profile of the neutron guide width. The vertical shaded bars indicate the time range to be blocked by the T_0 chopper (once per source pulse).

The neutron optical beam transport system is a ballistic guide that consists of two main sections (Figure 5.21, left). The guide has two pinch points at the locations of the high-speed choppers (P and M). Such a system will achieve a neutron brilliance transfer of ~0.4 and at the same time allow the choppers to generate the very short pulses needed for the scientific mission.

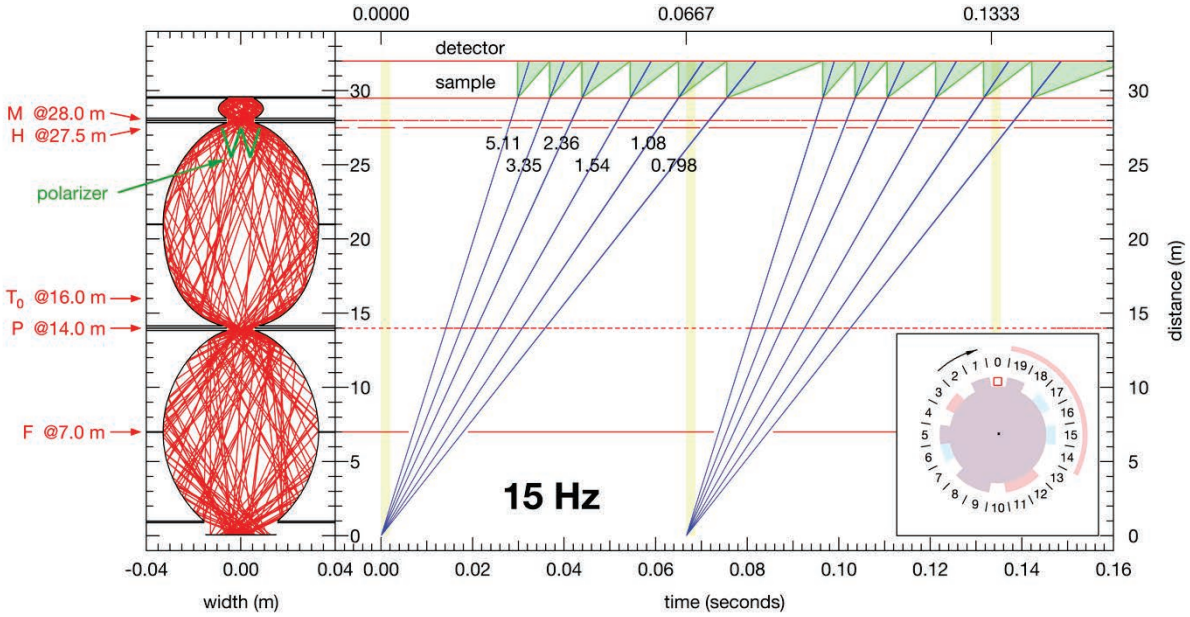

Figure 5.21. Functional layout of CHESS. *Source: G. Sala et al. J. Appl. Crystallogr. 51, 282–293, 2018.*

The four disk choppers are labeled, in sequence from the source to the sample, F, P, H and M. Each of these is a double-disk chopper. P and M are high-speed choppers (300 Hz) and define the working wavelengths in each incident mini-pulse through their relative phase. At 300 Hz, such a pair of double-disk choppers would generate 20 mini-pulses per source pulse (assuming that each M chopper disk has one slit and each P chopper disk has two slits). The F and H choppers run at source frequency (15 Hz) and serve to take care of frame overlap and pulse suppression. The H chopper is depicted in the bottom right corner of Figure 5.21. Each of its two disks has six slits, and the relative phase between the two disks determines which and how many pulses are suppressed.

Figure 5.22 shows a 3D rendering of the engineering concept. The detector array will be mounted in a vacuum vessel, as it is standard for this type of spectrometer. The detectors will be position-sensitive 1 in. diameter ^{3}He tubes that are 1.5 m long, at a mean distance of 2.5 m from the sample. They will be arranged in ~160 8-packs, which is a standard ORNL design. The scaffold with the detectors will also hold eight coils in place, which are needed to produce a homogeneous magnetic field around the sample position for polarized beam operation.

The design concept (with detector tubes arranged as much around the sample as possible) will result in a rather long distance from the sample location to the top flange from which the sample environment equipment is mounted. At the same time, the sample and the beam will be small, which means that the correct placement of the sample in the beam may become an engineering challenge. This issue will require some attention during the instrument design. There will be no space for a gate valve to separate the main vacuum from the sample environment. This implies design requirements for the vacuum system to keep changeover times between different equipment configurations to a minimum. A further complication is that the detector electronics and the magnetic field coils will be sources of heat that must be removed from the vacuum vessel.

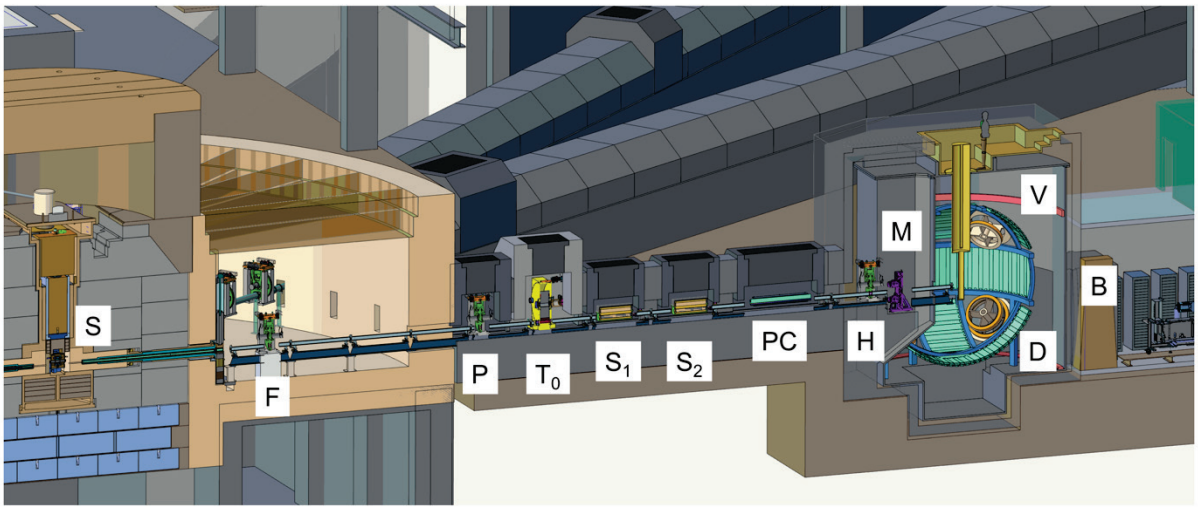

Figure 5.22. Engineering concept of CHESS. The main components**,** labeled in sequence from left to right**, are** S–source, F–F chopper, P–P chopper, T_0–T_0 chopper, $S_{1,2}$–operations shutters, PC–polarizer cavity, H–H chopper, M–M chopper, D–detector array, V–vacuum tank, B–beam stop.

A few critical choices made with this design have not yet been verified to be optimum by considering alternatives. This work is left for the detailed design of the instrument at a later time. The options include a different distance ratio to the source of the P and M-choppers (1:2); the requirement for RRM is that this be a commensurate ratio. Further, other slit configurations should be considered in the choppers; currently the M-chopper has one slit and the P-chopper has two slits. Alternate placement options for the transmission polarizer should be considered, as it is currently placed at a point of large beam divergence. Table 5.5 lists the key components and their locations along the beamline.

Table 5.5. A list of key CHESS instrument components and their locations.

Component	Description	Location from moderator
Beam delivery		
Neutron guides	Straight, ballistic guide with pinch points at the P and M choppers	Z = 0.7 – 28 m
F-chopper	2 disks @ 15 Hz, frame-overlap	Z = 7 m (in bunker)
P-chopper	2 disks @ 300 Hz, pulse-shaping	Z = 14 m
T_0-chopper	1 rotor @ 15 Hz	Z = 16 m
Operations shutters	Primary and secondary shutters for daily operations	Z=18 m and 20.5 m
Transmission polarizer	Polarize the beam, located on translation table	Z = 23 m
RF spin flipper	Flip the spin state	Z = 26 m
H-chopper	2 disks @ 15 Hz	Z = 27 m
End station		
M-chopper	2 disks @ 300 Hz, monochromator	Z = 28 m
P- and M-chopper translation system	Change this disk separation between 1 cm and ~5 cm (M chopper) or ~20 cm (P chopper)	At chopper position
Aperture system	Tailors beam size and divergence	Various locations TBD

Table 5.5. A list of key CHESS instrument components and their locations (continued).

Component	Description	Location from moderator
Beamline shielding	Bunker to cave	Z = 13.2 – 26 m
Sample location		Z = 30 m
Shield cave		Z = -4/+4 m
Guide carousel	Last section of guide in the detector tank	Z = -1.8 m
Detector array	~160 8-packs of linear PSD ^{3}He tubes	R = 2.5 m

5.4.5 Performance Estimate

The neutronic performance of CHESS has been modeled with McStas and compared with that of the Cold Neutron Chopper Spectrometer (CNCS) at the FTS [Sala et al. 2018]. Overall, the high-level expectations in terms of intensity on sample per pulse and instrument resolution have been confirmed, even though the functional design has not been fully optimized in many details. For example, the guide coating was set to m=3, constant along the entire length of the guide. Another critical parameter for neutron transport, the ratio of the guide widths between the widest and narrowest points, has not been optimized against the chopper performance (a wider guide at the choppers would negatively affect the chopper performance and the time-profile of the beam but would have a positive effect on the brilliance transfer). Figure 5.23 shows some key results for the beam at the sample position.

From top to bottom, left to right, the figure shows the intensity profile on the sample, the wavelength-dependent intensity across the width, the divergence profile (with color profiles normalized to the wavelength spectrum), the wavelength spectrum per pulse and unit area, the brilliance transfer (1 cm^2 beam with 2° divergence, FWHM) and the intensity gain over CNCS at equal resolution.

For the instrument setting depicted in Figure 5.23, and medium resolution, the neutron flux on the sample and the energy resolution at the elastic line have been simulated. The data are summarized in Table 5.6. The flux Φ on the sample is given in neutrons per pulse (STS at 700 kW and 15 Hz, 1 cm^2 beam with 2° divergence, FWHM). These numbers confirm the design intent of reaching 3–4% energy resolution in the cold range as “medium” resolution.

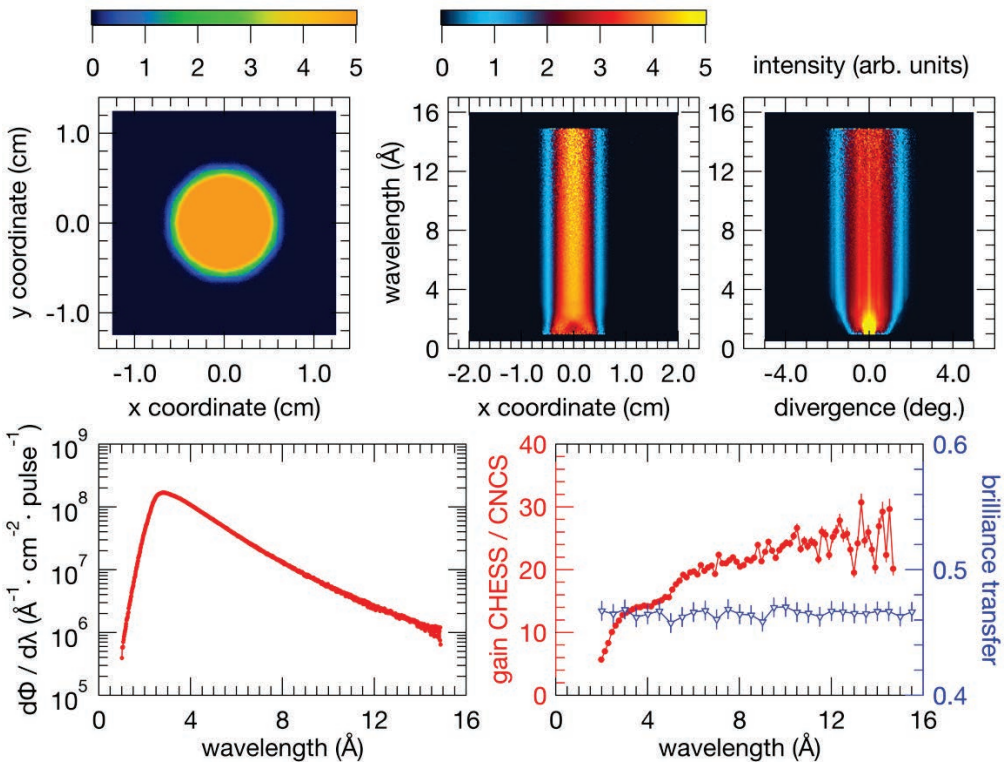

Figure 5.23. Key results describing the beam transport to the sample. *Source: G. Sala et al. J. Appl. Crystallogr. 51, 282–293, 2018.*

Table 5.6. Neutrons per pulse on sample for a medium resolution setting and 6 pulses with RRM.

E_i, meV	Δt_M, ms	Φ, n/pulse	$\Delta E/E_i$
5.11	0.033	1.93×10^5	0.040
3.35	0.035	1.53×10^5	0.036
2.36	0.037	1.16×10^5	0.033
1.54	0.041	7.50×10^4	0.030
1.08	0.046	4.76×10^4	0.029
0.80	0.053	3.18×10^4	0.028

The scattering from a particular sample, 1 gram of $K_2V_3O_8$, has been simulated and compared with CNCS (Figure 5.24). The main purpose of this simulation was to estimate the Q-resolution at CHESS and to show that it is adequate for the science mission. Since the tubes are closer to the sample than at CNCS, but have the same diameter, the Q-resolution is expected to be somewhat coarser (in particular in the forward direction). Going for thinner tubes is possible but would come at a price (more electronics parts and more complex mounting). The simulation showed that it is not necessary to use thinner tubes.

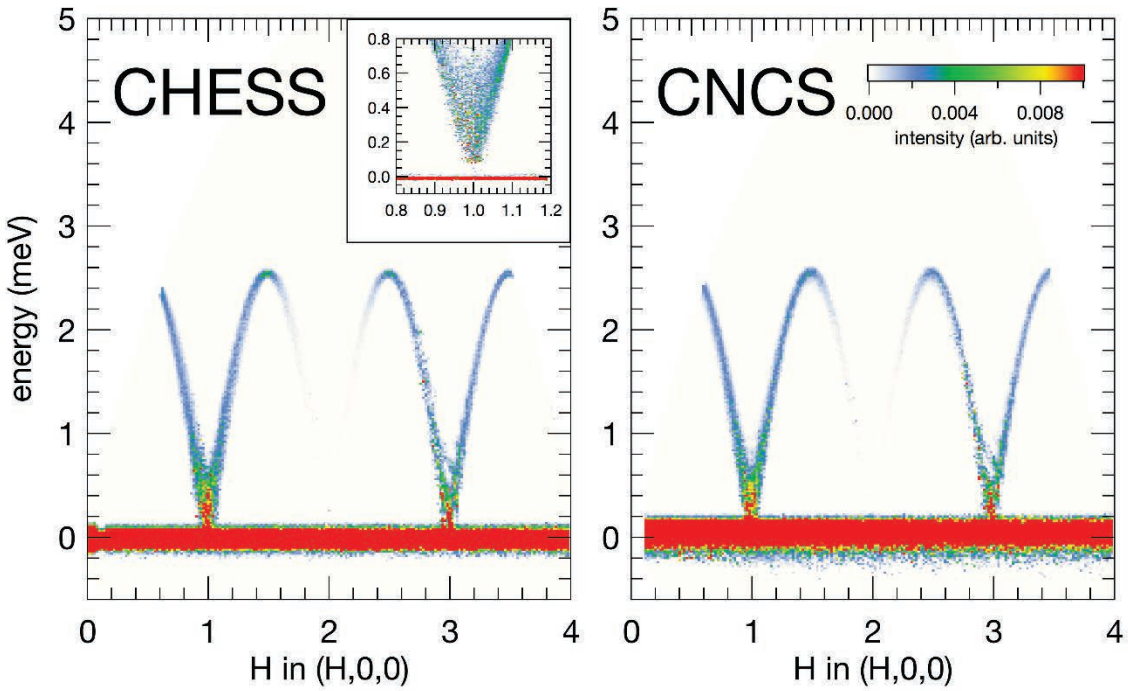

Figure 5.24. Simulation of scattering from spin waves in $K_2V_3O_8$. *Source: G. Sala et al. J. Appl. Crystallogr. 51, 282–293, 2018.*

5.4.6 Feasibility, Research and Development

The key technical requirements for CHESS can be met with current technology. They include the following main technical requirements:

- Disk choppers (diameter ~50 cm) spinning at 300 Hz. The scientific value of operating at 330 Hz or 360 Hz will be studied.
- Cryogenic vacuum in a large tank that houses the secondary spectrometer.
- Accurate control of the magnetic guide fields around the sample position to avoid polarization loss in the ^{3}He polarization analyzer.
- Position-sensitive detectors (PSDs) coping with an instantaneous rate (on a Bragg peak) in excess of 10 kHz.
- Ambient detector background between pulses as low as possible, below 0.1 counts per minute per meter of tube.
- Detector electronics with 100-ns timing resolution and 2-cm position resolution.

However, a few areas have been identified in which technical development and further R&D may be needed:

- Neutron guide alignment system. It will be necessary to align long sections of neutron guide to greater precision than at the FTS. This concerns deviations from the ideal location and direction of the guide sections. This is a need for many instruments at the STS.

- Collimation system in the scattered beam. These collimators will likely be 3D printed. Requirements for these collimators regarding length, thickness, surface roughness, neutron stopping power, and alignment precision in front of the detectors need to be studied.

- New technical solutions for low-efficiency neutron beam monitors will be needed.

- Fast and efficient software will be needed to reduce data collected at multiple incident energies and to convert the data to physically meaningful quantities such as $S(\mathbf{Q},\omega)$.

- CHESS will see the use of cryomagnets, operating at 8T or more, and at other times ^{3}He cells for polarization analysis. The latter are very sensitive to inhomogeneous magnetic stray fields. The utmost care in the design of the instrument and the choice of particular materials will be needed to prevent a cryomagnet from generating residual magnetization in the secondary spectrometer.

5.5 QIKR—THE QUITE INTENSE KINETICS REFLECTOMETER

5.5.1 Summary

The Quite Intense Kinetics Reflectometer (QIKR) will enable real-time studies of interfaces, including free liquids and the transport of atoms, molecules or charge across interfaces. Many advanced properties sought through materials by design will be realized only in new materials having at least one nanoscale dimension, where new functionality can arise from surface-dominated forces and interactions. New insights unlocked by QIKR will be key to enabling the creation of next-generation batteries, magnetic films, environmentally responsive coatings, drug delivery systems, and sensors. Exploiting the increased peak neutron brilliance of the STS, it will become possible to collect specular and off-specular reflectivity data much faster than at the best such existing machines. Of perhaps greater import, the large wavelength bandwidth enabled by the STS 15 Hz repetition rate will greatly simplify data collection. Using frame-suppression to operate at effectively 7.5 Hz, it will often be possible to collect complete specular reflectivity curves using a single instrument setting, enabling “cinematic” operation, wherein the user simply turns on the instrument and starts observing the sample. Samples in time-dependent environments (e.g., undergoing temperature, electrochemical, magnetic, or chemical alteration) will be observed in real time, with frame rates as fast as 1 Hz in favorable cases. When data are collected in a single setting, the time resolution can be specified during post-experiment analysis of the data time stream. Sections 5.5.2–5.5.6 present the science case for the instrument, the design concept, technical solutions, performance estimates, and needed R&D.

5.5.2 Science Case

Interfaces are ubiquitous, and the transport of atoms, molecules, or charge across interfaces is fundamentally important to the properties and function of materials. Interfacial potential energy gradients drive a host of thermodynamic processes. Many advanced properties sought through materials by design will be realized only in new materials having at least one nanoscale dimension. In these systems, new functionality can arise from surface-dominated forces and interactions, rather than from the less-specific interactions that span the bulk. Neutron reflectometry specifically probes air/solid, solid/liquid, air/liquid, and liquid/liquid interfaces. QIKR is designed to shine the unprecedented brightness of the STS onto these problems.

The ability to perform time-resolved studies with the unique capabilities that neutron beams offer is one of the most important advances enabled by the STS. Structural alterations that follow changes in temperature, shear, pressure, and other environmental conditions are vital to the performance and/or processing of materials. Many of these interesting structural processes occur over seconds to minutes after

the stimulus, making them good matches for the new capabilities afforded by the STS. In favorable cases, the potential for resolving materials changes with each neutron pulse may exist; hence, time-resolved experiments (~100 milliseconds) become feasible. The following selected vignettes illustrate the wide range of topics addressable by a high-intensity reflectometer like QIKR.

5.5.2.1 Soft Matter

Soft matter encompasses materials that are at least 1000 times mechanically weaker than conventional solids. Soft matter is typically composed of large molecules, polymers, membranes, colloidal suspensions, or foams. Common examples are plastics, detergents, oils, gels, toothpaste, paint, and mayonnaise. There is strong overlap and synergy between soft matter and biological materials.

Polymer molecules at solid or fluid interfaces have an enormous spectrum of technological applications. For example, they provide a mechanism for imparting colloidal stabilization; and they are used as protective coatings, including the mechanical protection of solids against friction and wear. They govern the interactions of biological cells with surfaces, and through judicious design they are used to modulate dispersion properties (e.g., rheology) under a variety of processing conditions [Stockton and Rubner 1997]. Knowledge of the conformations that adsorbed or terminally anchored chain molecules adopt when subjected to confinement and/or solvent flow is essential for predicting the interaction forces and tribological and rheological properties in materials using thin-film technologies [Sanchez 2013].

Processes occurring at liquid-liquid interfaces are relevant across a broad range of scientific disciplines, from chemical extraction to metabolic processes at biological and synthetic membranes. These interfaces are difficult to interrogate, but the penetrating power of neutrons and their sensitivity to light elements provide a unique capability. QIKR will provide new tools for studying liquid-liquid interfaces.

Solvent extraction plays a major role in the hydrometallurgical separation of base and precious metals, such as rare earth metals [Tasker et al. 2004], as well as in the reprocessing of spent nuclear fuel and the separation and isolation of long-lived radionuclides from high-level nuclear waste [Nash et al. 2006]. Solvent extraction is a flexible and scalable technique based on the distribution of chemical species between two immiscible liquids, usually an aqueous phase in contact with an organic phase. Although the interaction of metal ions with aqueous complexants and organic extractants at the aqueous-organic interface determines the efficiency and kinetics of extraction processes, little is known about the molecular complexes that form at the interface or the ion transfer mechanisms that underlie the process of solvent extraction. Neutron reflectometry provides a unique ability to view this interface by traversing a liquid phase as the incident medium. Depending on the problem, the transmitting medium may be either above or below the interface, so QIKR is designed to operate in both geometries.

5.5.2.2 Energy Materials

For rechargeable batteries, the reaction between the liquid electrolyte and the lithium-ion battery anode material is arguably the most important chemical process. This reaction occurs when an aprotic electrolyte, such as a 1.2 M $LiPF_6$-ethylene carbonate / dimethyl carbonate (3:7 wt %) mixture, is reduced on the anode surface at a potential typically less than 1.0 V, forming a solid-electrolyte interphase (SEI). This reduction reaction forms a passivating layer, which has been shown to be a mixture of inorganic (e.g., LiF, POF) and organic/polymeric (e.g., C−O−C, Li-*R*OCO_2) species that build up on the surface. If properly formed, this layer inhibits additional electrolyte degradation and enables long-term cycling. A poorly formed SEI layer leads to safety issues, such as fires and gassing, as well as lifetime and power limitations due to the consumption of electrolyte and increased resistivity. Most of our understanding of the SEI layer comes from ex situ chemical analysis of already formed films using methods such as infrared spectroscopy and x-ray photoelectron spectroscopy (XPS).

Typically, SEI layers are formed during charge/discharge cycles and the cells are disassembled and washed for analysis. The limitation of these methods is the removal of soluble or highly volatile species in vacuum, effectively removing part of the SEI layer. Furthermore, these methods generally lack depth sensitivity, unless recently developed synchrotron-based XPS instruments are used. Given the importance of the SEI, several recent studies have focused on following layer growth and chemistry in situ. For example, extensive efforts have been made to study the SEI layer on various anode materials using in situ electrochemical cells coupled with an electron microscope [Gu et al. 2013]. These efforts provide exquisite views of local structure, but it is often difficult to match the results with macroscopic quantities—such as the number of Coulombs of charge passed through the cells—and that difficulty impedes quantitative analysis. In addition, numerous groups have worked with nuclear magnetic resonance spectroscopy, which enables chemical specificity but lacks depth resolution. Finally, there have been interesting studies using atomic force microscopy, but unfortunately they are limited by the need to use an open cell design that may result in solvent loss [Lu et al. 2017].

Neutron reflectivity, with its sensitivity to light elements like Li and H, is an ideal approach to in situ tracking of electrode structural changes under different electrochemical conditions [Hüger et al. 2015, Browning et al. 2014, Veith et al. 2015]. Current practice has a potentiostat run through a sequence of steps in I-V space to prepare a stable film and then collect a reflectivity curve in this stable state. Performing these measurements on QIKR cinematically, in real-time, will enable tracking and resolution of intermediate structures during the formation of these layers, potentially yielding new insights into formation mechanisms and thermodynamics.

The chemical interaction of heat transfer fluids with the materials used to contain them is an area of great current interest. The extreme corrosivity of many heat transfer fluids, such as the Li-containing reactive species in heat exchangers or the coolants in molten-salt nuclear reactors, constitutes the dominant technological barrier that must be retired for widespread implementation of third-generation concentrating solar power systems and nuclear reactors. Ion transport across the salt/alloy interface is the defining physical process that enables corrosion in molten chlorides, yet there is no definitive understanding of the interfacial corrosion mechanism, the interplay with alloy structure, or the commensurate performance of proposed protecting layers. Direct investigations of the structure of the molten salt/alloy interface will provide the critical information needed to mitigate alloy corrosion in molten chloride salts. While interfacial corrosion species can be identified by grazing incidence (GI) x-ray absorption spectroscopy, the effect of structure on corrosion can best be determined by GI small angle x-ray/neutron scattering and x-ray/neutron reflectometry.

5.5.2.3 Biology

Bilayer membranes, composed of inner and outer amphiphilic leaflets, are a defining structural motif in biology. Lipid flip-flop is a biological process in which lipids traverse a bilayer membrane from one leaflet to the other. Polar head groups of the lipids must translocate across membranes not only to sustain membrane growth but also to support the function of certain biosynthetic pathways, to maintain membrane nonrandom asymmetry, to contribute to the mechanical stability of the cell, and to manage programmed cell death. Lipids are actively transported across a lipid bilayer by membrane proteins, or flippases, on second or minute timescales. Flippases also exist in forms that trigger non-bilayer rearrangement or induce transient defects in lipid bilayers. Much work has focused on the thermodynamics of lipid translocation, to establish the flipping mechanism and to identify intermediate structures. However, there are discrepancies in the timescale, occurrence, and features of the flip-flop mechanism, depending on the techniques used to characterize it. Sum-frequency vibrational spectroscopy (SFVS) and neutron reflectometry have fundamental advantages over other techniques that employ chemically modified/labeled lipids, which possibly have chemical and structural differences from the native lipids found in biological membranes. The SFVS technique relies on the cancellation of two

perpendicular transition dipole moments of the terminal methyl groups from two opposite lipid leaflets [Liu and Conboy 2005]. Therefore, any intrinsic features of the bilayer that might change this orientation to a state no longer perpendicular to the interface, may lead to errors in data interpretation, particularly the rate of transmembrane diffusion of lipids or lipid flip-flop. The more complex the membrane system, the harder it is to interpret SFVS. On the other hand, neutron reflectivity provides information on the composition of membrane leaflets in the direction normal to the interface, which overcomes the uncertainty of SFVS interpretation for complex biological membranes, and thus makes the technique essentially suited to studying lipid flip-flop systems [Gerelli et al. 2012]. QIKR, with wider bandwidth and greater flux, will be able to capture fast lipid translocation triggered by flippases and to identify the mechanisms of lipid flip-flop systems for the first time.

Medical devices, such as infusion tubes or prefilled syringes, typically either are made of hydrophobic polymeric materials or are coated with a layer of hydrophobic oil on a glass surface. Understanding the effects of interfacial rheological forces from these hydrophobic surfaces on the adsorption and possible conformational changes of proteins and surfactants is crucial for storage stability and delivery of pharmaceutical liquid formulations [Chi et al. 2003]. To mimic medical injection processes on a beamline, a rheometer is used to generate the flow of protein solution. The in situ interfacial interactions between the hydrophobic coated substrates and protein molecules can be tracked by neutron reflectivity techniques. QIKR at the STS, with flux and bandwidth advantages, will be able to better capture the assembly/disassembly of proteins under flow.

Intrinsically disordered proteins (IDPs) are highly dynamic and do not have well-defined shapes. Depending on the interaction between IDPs and surrounding materials, e.g., lipid membranes, IDPs quickly adapt into stable conformations, complexes, and networks [Dyson and Wright 2002]. Time-resolved measurements can elucidate the mechanisms for protein agglomeration, adding to the understanding of the molecular basis of neurodegenerative and other diseases.

5.5.2.4 Quantum Materials

Because interfaces break inversion symmetry, they are natural hosts of novel phenomena arising from Dzyaloshinskii-Moriya [Bertaina et al. 2008], biquadratic [Heinrich et al. 1993], and chiral [Pappas 2012] interactions that enable spin texture but are usually only marginally important in bulk matter [Hellman et al. 2017]. Electric currents in materials lacking inversion symmetry (an interface is one example) can induce non-uniform distributions of spin density. When these materials are combined with materials having larger spin-orbit coupling, unusual topological properties may emerge, e.g., topologically protected insulating or superconducting states [Qi et al. 2008]. Interfaces are particularly conducive to energetic stabilization of new spin phases and properties because interfaces are places where charge transfer, orbital ordering, atomic reconstruction, and intermixing occur. By breaking inversion symmetry, interfaces also enable relativistic spin-orbit torques. Such torques can induce nonequilibrium spin density, which can be harnessed to produce spin current for applications in spintronics—electronic materials that make use of the spin degree of freedom [Hoffmann and Badar 2015]. Many examples involve ferromagnets combined with Rashba spin-orbit coupling [Soumyanarayanan et al. 2016], although spin-currents can also exist in paramagnets and antiferromagnets. Comprehending non-uniform spin density and the correlation between spin density and electric current is necessary to develop certain architectures for quantum entanglement. With high flux and the availability of polarized neutron beams, QIKR offers opportunities to better understand quantum materials.

For more than a decade, much research has focused on spintronic ferromagnetic (FM) materials. An example is the use of spin torque to read and write information—a technology likely to be ported to devices in the near future. Looking beyond FM spintronics, many see even better options in the synthesis of superconducting and antiferromagnetic (AFM) spintronic heterostructures [Baltz et al. 2018]. The

planar interfaces in these or similar heterostructures are thought possibly to host topologically protected spin textures. One specific example is formation of a Majorana fermion at the interface between a superconductor and a skyrmion (one example of a topologically protected spin texture). Control of the skyrmion may enable control of a Majorana fermion, e.g., braiding. Equipping QIKR with a polarized beam and polarization analysis will allow detection of skyrimons and provide the opportunity to learn how spin texture can be controlled with time-dependent electric currents.

Current driven through materials that locally lack a center of inversion symmetry (within the unit cell) can produce a shift of the Fermi surface that depends on the electron's spin [Železný et al. 2014]. Examples of such materials include Mn_2Au [Barthem et al. 2013] and CuMnAs [Wadley et al. 2016]. By passing an electric current through these materials, spin accumulation is generated. The direction of the spin polarization is related to the direction of electric current, enabling control of magnetization via electric field. Alternatively, for systems containing interfaces (perhaps even topological systems [Mellnik et al. 2014]) and spin-orbit coupling that create nonequilibrium spin density/spin accumulation at the surface of a proximal magnet, the magnetism can be observed with polarized neutron reflectometry. For the latter case, the spin density arises from electron current; thus, the spin accumulation lacks a suitable x-ray resonance. With the increased brightness of QIKR, neutron reflectivity will be able to determine the spin density profile and to observe the quantized perturbation of the magnetic induction arising from modest surface currents on a topological insulator [Qi et al. 2008].

Also of interest is the observation of spin accumulation induced by electric current, and the complementary effect—the spin-galvanic effect—from which a nonequilibrium spin density, e.g., resulting from optical pumping, produces an electric current [Ganichev et al. 2002]. Applications of so-called Néel spin-orbit torque (NSOT) will use time-dependent electric fields to induce spin precession, similar to how magnetization in an FM spin torque is presently manipulated, albeit at much higher frequencies (the dynamics of AFM order is much faster than that of FM order—part of the attraction and challenge of AFM spintronics). We envision static and dynamic neutron scattering experiments (the latter will use optical pumps or microwave cavities) to provide insight into the mechanisms of NSOT. The accumulation of net spin density at surfaces and interfaces, topological magnetization current, or expulsion of magnetic induction as in topological superconductors will be observed with reflectometry using polarized neutron beams. These examples all share a common theme: the accumulation of spin, or creation of spin texture, is confined at or within a unit cell of an interface. These highly confined regions of spin are too difficult to detect with existing neutron reflectometers.

5.5.3 High-level Capability Requirements

The range of scientific fields served by QIKR is very large, requiring specialized sample environments to interrogate solid and free liquid surfaces, as well as solid-liquid, liquid-liquid and solid-solid internal interfaces. Free liquid and liquid-liquid experiments (and to a lesser extent rheology) are constrained in that the sample surface is defined by gravity and so cannot be tilted. The incident reflection angle in these cases must be defined by deflecting [Campbell et al. 2011] or sampling the angular divergence of the incident neutron beam [Ankner et al. 2002]. Free liquid surfaces and upper-subphase-transmitting liquid-liquid interfaces require a downward-directed incident beam, while lower-subphase-transmitting liquid-liquid interfaces and rheometers need an upward-directed incident beam. Solid and solid-liquid samples can be tilted and generally are not sensitive to incident-beam direction. Massive sample environments such as cryogenic magnets, however, may also benefit from a stationary sample. Therefore, to address the interests of the entire scientific community, QIKR features both downward- and upward-directed incident beams.

Collecting data rapidly and accurately is important for all experiments. Beyond rapid data acquisition, the neutron flux of the STS will enable experiments with unprecedented time resolution. True kinetic

measurements must be collected at a single instrument setting covering the full Q-range of interest. The 15 Hz STS repetition rate affords a much larger wavelength bandwidth than is available at the 60 Hz FTS; but to achieve true single-setting operation for most samples, QIKR will run in frame-skipping mode at 7.5 Hz. In addition, while optimizing transport of short-wavelength neutrons at peak moderator flux (λ = 2.5 Å) is essential to maximize Q bandwidth and minimize counting time, the instrument will also be capable of operating at 15 Hz and in different wavelength bands. In such modes, the full Q-range is covered with multiple incident beam settings.

As data acquisition time decreases, the proportion of time spent in setting up and waiting for sample environments to equilibrate and in aligning samples grows. To maximize time spent collecting data, it is worthwhile to consider how to configure the instrument and its enclosure to carry out these support tasks as efficiently as possible.

These considerations may be summarized in the following list of requirements and Table 5.7:

1. QIKR sample stage and environs must accommodate a wide range of sample environment equipment.

2. QIKR must have adaptable front-end optics (e.g. for neutron polarization).

3. QIKR must provide incident beams from above and below the horizon.

4. QIKR must be able to operate at both 15 and 7.5 Hz.

5. QIKR must effectively transport moderator brightness at the spectrum peak (λ = 2.5 Å).

6. QIKR should be placed as close to the moderator as possible to maximize bandwidth, with adequate shielding to achieve low background.

7. The QIKR instrument enclosure should be designed to minimize sample environment setup time and sample alignment time.

Table 5.7. Key capability requirements for QIKR.

Parameter	Description
Beam footprint at sample	Variable from 5×10 mm to 25×75 mm
Q-range	0.009 Å^{-1} < Q < 0.088 Å^{-1} at 1.0° incident angle 0.023 Å^{-1} < Q < 0.219 Å^{-1} at 2.5° incident angle 0.037 Å^{-1} < Q < 0.351 Å^{-1} at 4.0° incident angle
Q-resolution	$0.02 \leq \delta Q/Q \leq 0.10$
Bandwidth ($\Delta\lambda$)	21 Å (7.5 Hz); λ_{min}= 2.5 Å
Polarization	Incident-beam polarization and analysis

5.5.4 Physics Design and Engineering Concept

The kinetic performance of a TOF-based neutron reflectometer is straightforward to describe, and several of the design features dictated by the requirements list in Table 5.7 may be captured in a single equation. By manipulating $Q = 4\pi \sin\theta / \lambda$ and wave-particle duality, $h^2/2m\lambda^2 = mv^2/2$, the dynamic range of a specular reflectivity measurement at a single instrument setting can be described in terms of Planck's constant h, the neutron mass m, source-detector distance L, source repetition frequency f, and the minimum neutron wavelength, λ_{min}, in the band used for the measurement,

$$Q_{max} / Q_{min} = 1 + (h/m) \times L^{-1} \times f^{-1} \times \lambda_{min}^{-1} \equiv D.$$

The parameter D is the dynamic range of a measurement and is maximized for short-flight-path instruments viewing low-frequency neutron sources featuring peak flux at short wavelengths (h/m = 3956.0 m-Hz-Å). Table 5.8 lists the dynamic ranges of QIKR under different operating conditions. It will often be possible to span the entire useful Q-range at a single angle by operating QIKR at 7.5 Hz. In addition to simplifying data collection and reduction, single-shot measurement capability enables operating the instrument cinematically for kinetic studies.

Table 5.8. Single setting operating parameters and dynamic ranges, Q_{max}/Q_{min} = D, of QIKR lower and upper end stations.

Instrument	L (m)	λ_{min} (Å)	f (Hz)	D
QIKR (lower)	20.0	2.5	15	6.3
			7.5	11.5
QIKR (upper)	24.0	2.5	15	5.4
			7.5	9.8

Optimized neutron guides and a single disk chopper achieve the design goals of filtering out high-energy neutrons, providing beam angular divergence, and enabling pulse skipping to operate at 7.5 Hz. Figure 5.25 shows scaled vertical and horizontal schematics of the QIKR components. The small 3 by 3 cm STS moderator, unlike the larger FTS moderators, does not provide enough intrinsic angular divergence to cover the full required Q-range (0.009 Å^{-1} < Q < 0.35 Å^{-1}) for fixed-surface free liquid and liquid-liquid measurements, so we employ diverging/converging tapered guides in the vertical direction. The diverging section possesses the added virtue of reducing the average number of neutron impacts with the guide. A T_0 chopper cannot effectively be used for pulse-skipping, so we employ a 3-channel, 173 m radius-of-curvature bender in the horizontal plane to filter out high-energy neutrons. A single bandwidth chopper coupled with a frame-overlap mirror (not shown) defines the desired wavelength band.

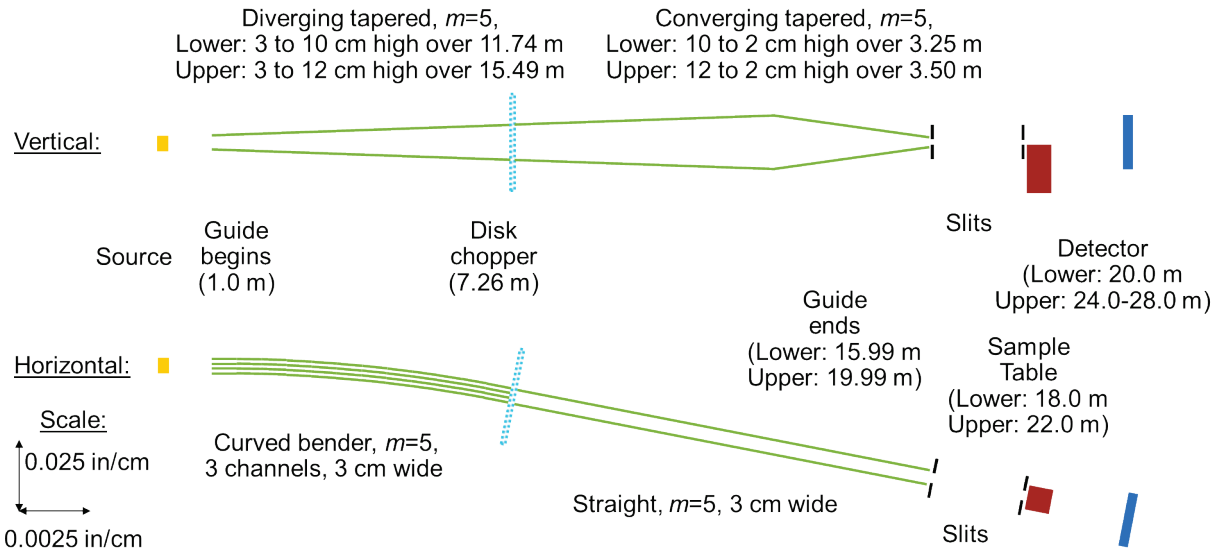

Figure 5.25. Schematic of QIKR neutron beam transport, consisting of a 3-channel horizontal curved guide, a single disk chopper, and a vertical diverging/converging guide.

The efficacy of the guide and chopper system in defining a frame-skipped wavelength band is depicted in Figure 5.26. The red circles show the simulated brightness of the cylindrical coupled-H_2 moderator. The 3-channel bender is designed to pass all neutrons with $\lambda > 2.5$ Å but to filter out the prompt flash of highly energetic neutrons. The blue diamonds show the moderator spectrum multiplied by the transmission function of the guide. The bender consists of 12 segments offset by 0.17° from one another, featuring a hard wavelength cutoff for $\lambda < 0.17$ Å and a horizontal displacement of the beam of 10.3 cm or 3.4 times its width. The chopper is run in pulse-skipping mode at 7.5 Hz to deliver 2.5 Å < λ < 23.5 Å, and its transmission function is applied to the bender flux (light green upward-pointed triangles). The chopper disk (transmission 10^{-5} at 1 Å) passes an attenuated flux of neutrons from the unwanted pulse (dark green downward-pointed triangles). This level of leakage is comparable to that of the First Target Station Liquids Reflectometer and should not pose a problem. The guide system transports the available brightness over the desired wavelength range.

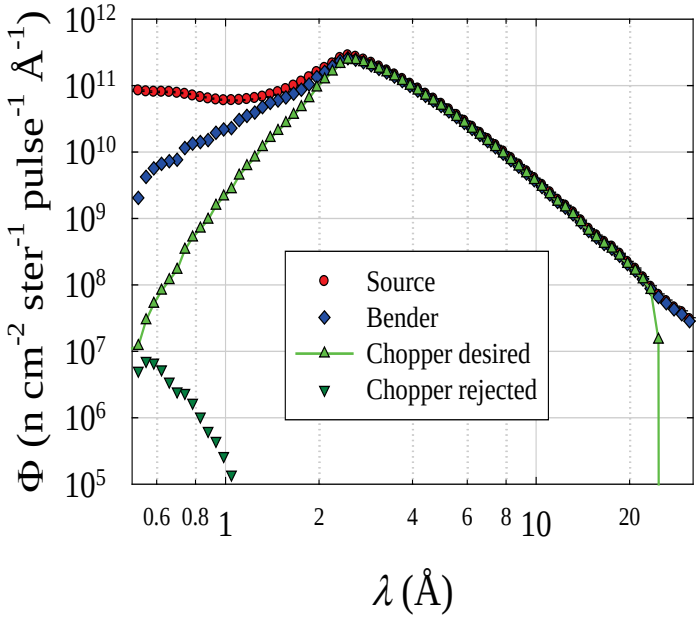

Figure 5.26. The filtering effect on the source flux (red circles) of the curved bender guide (blue diamonds) and disk chopper (green triangles). The chopper runs in frame-suppression mode at 7.5 Hz. The desired bandwidth of 2.5 Å < λ < 23.5 Å is shown by the light green upward-pointing triangles; neutrons from the rejected pulse are shown as downward-pointing dark green triangles.

Providing angular divergence for free liquid and liquid-liquid measurements is another crucial function of the guide system. A reasonable Q-range for such measurements is 0.009 Å^{-1} < Q < 0.35 Å^{-1}. Using a 7.5 Hz bandwidth, these requirements can be satisfied in two settings with incident beams at θ = 1° and 4° (Table 5.9). By employing a vertical guide that gently tapers outward from the 3 cm moderator to 10 cm over 11.74 m, and then more aggressively tapers back to a 2 cm height at the guide exit 3.25 m further on, we create satellite images of the moderator separated in angle from the center of the guide by ±1.5°.

The phase-space acceptance of the QIKR guides is plotted in Figure 5.27 against the angular displacement of 2.5 Å neutrons from the guide centerline, $\Delta\theta_{\text{cline}}$. The upper plot shows color-coded acceptance contributions from populations of neutrons that have undergone different numbers of bounces *b* traversing the guide. In the lower plot, these contributions are summed assuming perfect guide reflectivity (R=1) and by weighting the bounce contributions assuming an average reflectivity of 0.8 per bounce. The latter assumption is confirmed by Monte Carlo simulations using more realistic guide coating reflectivity profiles. By optimizing the guide taper dimensions and using m=5 supermirror coatings, we can place the

satellite reflections ±1.5° from the vertical guide centerline. Inclining this centerline 2.5° allows us to access the free-liquid and liquid/liquid Q-ranges specified in Table 5.9.

Table 5.9. Accessible Q-ranges for a free liquid surface or liquid-liquid interface for the three angles provided by the QIKR guide system using the pulse skipping 7.5 Hz wavelength band for the lower (2.5 Å < λ < 23.5 Å) and upper (2.5 Å < λ < 19.9 Å) end stations.

Station	θ (°)	Q_{min} (Å^{-1})	Q_{max} (Å^{-1})	$\delta\theta$ (°)
	–1.0	0.009	0.088	0.49
Lower	–2.5	0.023	0.219	0.49
	–4.0	0.037	0.351	0.49
	0.8	0.009	0.070	0.39
Upper	2.5	0.028	0.219	0.39
	4.2	0.046	0.368	0.39

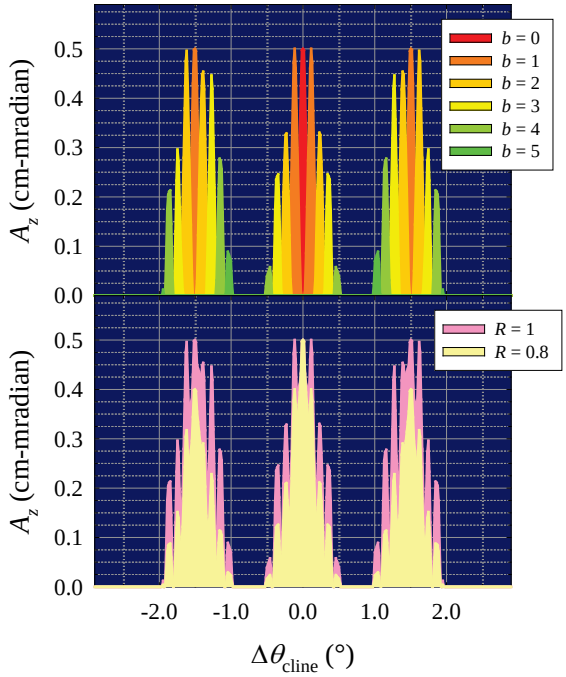

Figure 5.27. Phase-space vertical acceptance plots of 2.5 Å neutrons exiting from the QIKR guide plotted versus the guide centerline direction, θ_{cline}. The upper plot shows acceptance color coded by the number of bounces, *b*, that each population has undergone. The bottom plot sums these contributions assuming perfect guide reflection (*R*=1) and a more realistic *m*=5 average guide reflectivity of 0.8.

Providing a downward-directed beam for free liquid measurements and an upward-directed beam proves to be difficult if the aim is to preserve optimum transmission of 2.5 Å neutrons and deflect the nominal incident beam by 5º. The Figaro instrument at Institut Laue Langevin [Campbell et al. 2011] uses deflecting supermirrors to divert a softer-spectrum beam through shallower angles.

Instead of making this compromise, we propose a different solution. By extracting *two* beams from the monolith, directed ±2.5º vertically and separated by ~4.5º in the horizontal plane at the experiment stations, the moderator can supply neutrons to two separate instrument end stations. Figure 5.28 depicts a

layout featuring two replicas of the Liquids Reflectometer goniostat and detector arm. There is a fundamental tension between extracting two beams from the monolith upstream of the chopper (tight) and achieving maximum separation of the stations in the sample area. There remains substantial optimization work to configure the operating cave, but we feel this will be well worth the effort to address the breadth of the science case, enhance sample environment flexibility, and reduce beamline downtime. A single disk chopper placed symmetrically between the guides feeds one of these stations at 15 Hz or, in favorable circumstances, both stations at 7.5 Hz.

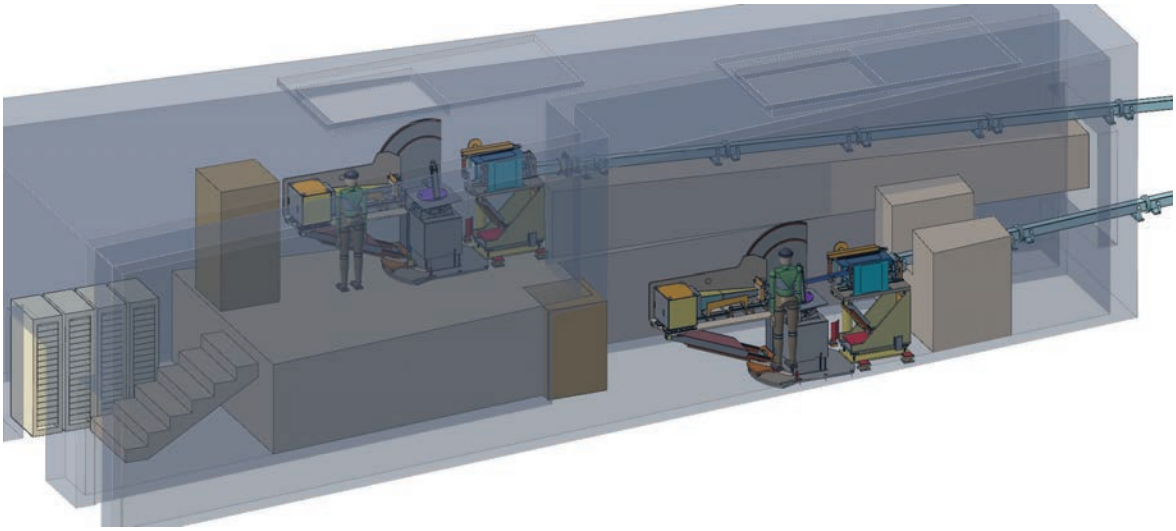

Figure 5.28. Neutrons from the cylindrical moderator (right) viewed by beamline 9 are transported by identical guides separated by ±2.5º vertically and −1.5°/+3.0° horizontally. The guides share a common double-disk chopper placed symmetrically between them and feed two independent experiment stations sharing a common cave (left).

Extracting two beams at different heights and horizontal separations will require a custom-designed monolith insert, handling gear, and beam shutter with associated increased cost and operational complexity. However, there are significant advantages to this concept:

1. Uncompromised spectrum and source brightness for environments viewing both downward- and upward-directed beams.

2. Configurational flexibility in optimizing the two stations, with, e.g., the upper being devoted to polarized-beam, liquid-liquid, and rheometry. and the lower to Langmuir-trough and liquid-liquid experiments. Solid and liquid-solid samples using a variety of sample environments can be measured at either station.

3. Scheduling flexibility: while one station is running, the other can be configured and prepped with a sample environment for an upcoming measurement. Samples in air could be initially assessed on one station and then placed in an environment on the other, with the assessing station operating in a subsidiary mode. In many instances, both stations can be operated simultaneously and independently.

A list of the primary components of QIKR is given in Table 5.10.

Table 5.10. Primary QIKR instrument components and the locations.

Component	Station	Description	Location *Z* (m)
Beam delivery			
Bender/diverging guide	Both	H: 3 cm wide; 3 channels; R_c = 173 m V: diverging 3–7 cm	1.0–7.22
Double disk chopper	Both		7.22–7.29
Straight/diverging guide	Lower	H: 3 cm wide straight V: diverging 7–10 cm	7.29–12.74
	Upper	H: 3 cm wide straight V: diverging 7–12 cm	7.29–16.49
Straight/converging guide	Lower	H: 3 cm wide straight V: converging 10–2 cm	12.74–15.99
	Upper	H: 3 cm wide straight V: converging 12–2 cm	16.49–19.99
Shield cave	Both	Houses both stations, separated by wall	13.2–29.8
End stations			
Incident table and sample goniostat	Lower	Similar to existing Liquids Reflectometer stages	16.0–18.0
	Upper		16.0–18.0
Detector arm	Lower	Similar to existing Liquids Reflectometer arm	18.0–20.0
	Upper	Variable length for GISANS	22.0–28.0
2D PSD	Lower	1–2 mm resolution, 20 by 20 cm area, high-count-rate capable	20.0
	Upper		24.0–28.0

5.5.5 Performance Estimate

We can estimate QIKR performance using the moderator source-brightness files describing the performance of the STS moderators. Multiply the guide-filtered, chopped neutron brightness in Figure 5.27 (upward-pointing green triangles) by a bandwidth that splits the difference between adjacent tabulated wavelength values [$\Delta\lambda_j = (\lambda_{j+1} - \lambda_{j-1})/2$], integrate over wavelength, and assess a penalty for imperfect guide transport to estimate an integrated brightness at the sample position:

$$\Phi(\text{n cm}^{-2}\ \text{sec}^{-1}\ \text{ster}^{-1}) = \varepsilon_{\text{guide}} \times \Sigma_j\ \Phi_j(\text{n cm}^{-2}\ \text{sec}^{-1}\ \text{ster}^{-1}\ \text{Å}^{-1}) \times \Delta\lambda_j$$

Acceptance-diagram transport calculations (verified by Monte Carlo), like those plotted in Figure 5.27 (yellow area plot on the bottom), indicate the brilliance transfer, $\varepsilon_{\text{guide}}$, varies between 0.4 and 1.0, depending on sampled beam divergence and wavelength. Table 5.11 lists the expected divergence-independent brightness for QIKR, assuming $\varepsilon_{\text{guide}} = 0.4$. The expanded wavelength range and resultant Q-bandwidth, coupled with this increased flux, can qualitatively alter how measurements are made.

Table 5.11. Brightness expected for QIKR.

Instrument	*f* (Hz)	$\Delta\lambda$ (Å)	$\varepsilon_{\text{guide}} \times \Phi$ (n cm^{-2} sec^{-1} ster^{-1})
QIKR	15	2.5 Å < λ < 13.0 Å	24.0×10^{11}
	7.5	2.5 Å < λ < 23.5 Å	12.0×10^{11}

The guide and chopper parameters and performance were calculated analytically to optimize the design, and the resulting instrument was implemented for Monte Carlo simulation using McStas. A McStas virtual source was created at the exit of the guide that was sampled by a slit system with the resulting beam illuminating a specularly reflecting sample using MCViNE [Lin et al. 2016]. The reflected beam passed onto a 2D PSD (MCViNE), from which were generated NeXus event data files, which were reduced using our current software. The virtual source illuminated an Ir calibration film under several different experimental conditions. These measurements are shown in Figure 5.29. The upper two curves (blue and red) were collected conventionally at 7.5 Hz, using two angles to span the required Q-range. These two simulated sets used the 1° and 4° settings in Table 2 to span 0.009 $Å^{-1}$ < Q < 0.35 $Å^{-1}$. For both, the 1º data were collected in a single pulse; the 4° sets were collected for 10 minutes (blue) and 1 minute (red). The third set was collected at a single setting at 2.5º for one minute. The base model for the Ir film was taken from an actual film used on the Liquids Reflectometer for calibration. Despite its being a (very) noble metal, the Ir sputter deposited on a Si substrate nonetheless exhibited a surface oxide layer as well as retaining an essentially intact native Si oxide layer on the substrate. Table 5.12 shows fits to reflectivity data with counting statistics generated from the McStas virtual source using slit settings that illuminate the sample in a 2.0 by 3.0 cm footprint on a 5.0 cm diameter substrate using a constant relative angular resolution $\delta\theta/\theta = 0.023$.

Each reflecting layer features a thickness d, a scattering length density Σ, and a root mean square (rms) interfacial mixing width, σ, with the overlying layer. Reducing the counting time of the higher angle to 1 min results in a notable decrease in fit quality, particularly for the interfacial widths. Interestingly, the single-setting 1-min data set model is intermediate in quality and superior in that it does not require a 60–90 s instrument adjustment between settings. QIKR can simply be turned on, collecting data as the sample evolves under environmental stimuli. What portion of the time stream is of value and what time resolution is required may be sorted out post-experiment from the event stream. In general, determining interfacial widths of thin layers requires data acquisition to large Q and relatively long counting times. Finally, Figure 5.29 and Table 5.12 show that a single selected Q-range will often provide excellent model determination, particularly when interfacial width is not a critical parameter. In such cases, it will be possible to push time resolution below 1 min.

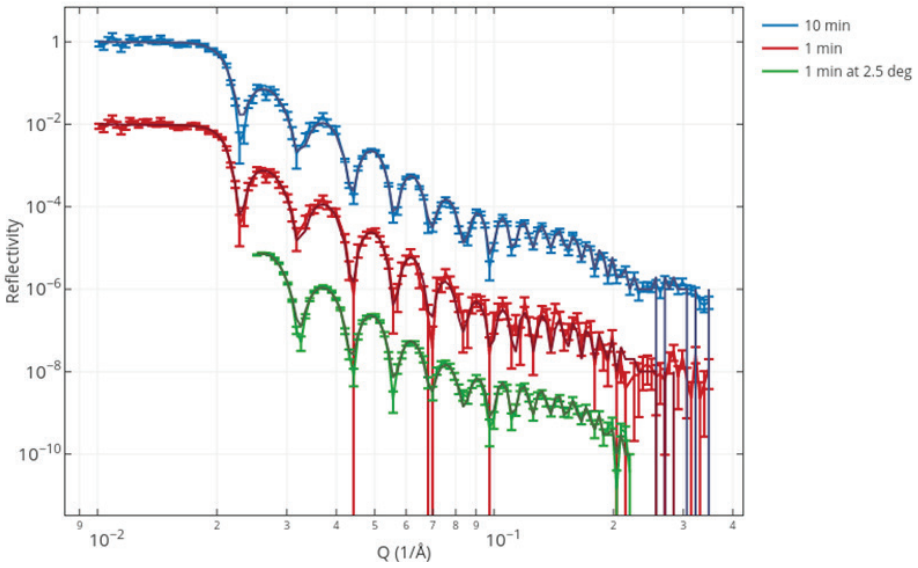

Figure 5.29. Simulated 7.5 Hz STS-QIKR reflectivity from an Ir calibration film collected under three different conditions: (top—blue) measurements at angles θ=1º and 4º for 0.133 and 600 s, respectively; (middle—red) those same angles collected for 0.133 and 60 s; and (bottom—green) a single measurement at 2.5º collected for 60 s.

Table 5.12. Fitted model parameters for the data sets shown in Figure 5.29, with the left column corresponding with the top blue data set, the middle column with the middle red data, and the right column with the bottom green set. Thickness (d), scattering-length density (Σ), and rms interfacial width (σ) were fitted for the Ir film, its oxide layers above and below, and the Si substrate.

Parameter	Two angles, 10 min	Two angles, 1 min	One angle, 1 min
d_{IrOx} (Å)	39.8±0.3	37.2±1.5	39.6±0.5
Σ_{irOx} (10^{-6} Å^{-2})	2.57±0.06	2.32±0.27	2.60±0.10
σ_{IrOx} (Å)	2.5±0.6	1.6±1.7	1.2±1.0
d_{Ir} (Å)	459.1±0.3	460.5±1.2	461.6±0.8
Σ_{ir} (10^{-6} Å^{-2})	6.97±0.02	7.04±0.03	7.00±0.03
σ_{Ir} (Å)	1.2±0.3	7.3±2.1	3.0±0.8
d_{SiOx} (Å)	23.2±0.6	28.6±7.2	27.0±5.0
Σ_{SiOx} (10^{-6} Å^{-2})	3.37±0.08	3.27±0.37	2.90±0.40
σ_{SiOx} (Å)	1.1±0.4	1.1±2.2	4.6±1.4
σ_{Si} (Å)	3.0±1.1	8.2±6.3	1.2±4.4

As a more relevant example, consider the kinetics of the crosslinking reaction of a polyelectrolyte hydrogel. We have shown in recent experiments on responsive hydrogels that multilayer films of polymethacrylic acid (PMAA) assembled through hydrogen bonded layer-by-layer adsorption with polyvinylpyrrolidone (PVPON) on surfaces can be crosslinked with ethylenediamine (EDA) and the PVPON subsequently released at high pH to leave a crosslinked PMAA hydrogel [Kozlovskaya et al. 2013]. However, the events that occur on small time scales during the crosslinking have yet to be fully characterized and therefore remain a fundamental inquiry in this type of assembly. Specifically, the addition of EDA to the network was shown to ionize the PMAA's acid groups that were not activated by the carbodiimide. Fourier transform infrared analysis showed that significant ionization had already occurred during the two minutes required for the measurement. Ionization of PMAA necessarily disrupts film stability, as ionized COO^- groups cannot participate in hydrogen bonding. However, using neutron reflectometry, we have shown that spin-coated multilayer films are highly organized after crosslinking and removal of the non-crosslinked component. This structural persistence implies that the transition between activated, non-crosslinked PMAA and crosslinked PMAA must happen on a time scale shorter than or very close to that of the induced ionization by the EDA. Therefore, we would like to study the time-resolved conversion of the hydrogen-bonded film with activated COOH groups to crosslinked PMAA with EDA-induced ionization by probing the film's structure with neutrons at sub-minute resolution.

Collapse of the film during EDA crosslinking and PVPON release implies that the reaction can be well tracked by measuring the spacing between deuterated PMAA marker layers. We can use the as-deposited fit to this data (Figure 2 in [Kozlovskaya et al. 2013]) and simulate reflectivity collected for varying lengths of time. Fitting this manufactured data demonstrates the sensitivity of QIKR to changes in marker-layer spacing as counting statistics improve. In Figure 5.30, simulated data are collected at a single incident angle (2.5°) at 7.5 Hz (2.5 Å < λ < 23.5 Å). The simulated data and fitted reflectivity curves for a range of collection times are shown at left and the dependence of χ^2 on the fitted bilayer spacing is shown at right. A fair measure of film thickness can be achieved in 1 s. As discussed earlier, counting statistics required to specify different model parameters will vary, but if the data are collected cinematically at a single instrument setting, what is needed can be decided post-experiment. Collected this way, in situ kinetic measurements of this process and others like it appear to be quite feasible.

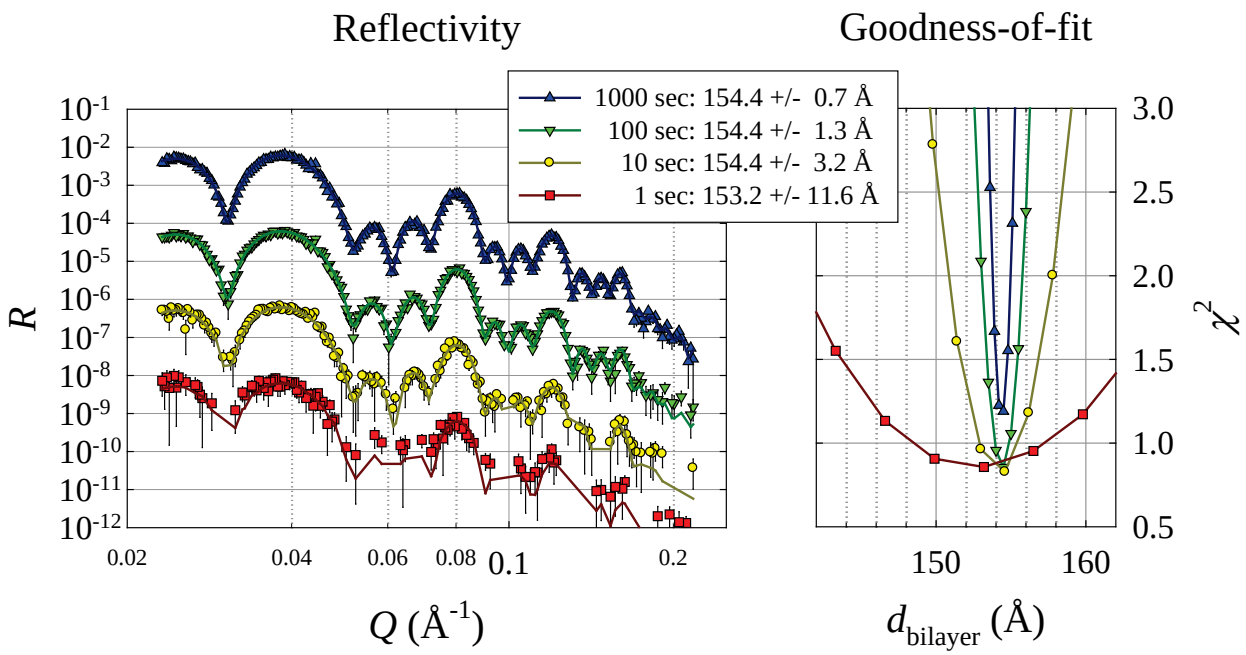

Figure 5.30. Simulated 7.5 Hz STS-QIKR reflectivity from polyelectrolyte multilayer (left) for several different data collection times. Plotted at right is the dependence of χ^2 for the fitted value of the marker-layer spacing.

5.5.6 Feasibility, Research and Development

The neutron guides and choppers are standard items available today. In terms of technology, only the detectors pose a challenge. QIKR requires mm-resolution detectors able to count at >10,000 cps in small areas (a typical area would be a 2 by 20 mm strip). A 2D detector with 1–2 mm pixels will enable a GISANS capability as well as specular and off-specular reflectivity. The higher the maximum count rate, the better. On the Liquids Reflectometer, the detector is operated at a low enough count rate (<1000 cps) so as not to require a dead-time correction because of a concern that such a correction would introduce artifacts into the reflectivity curves.

Extracting two beams through the target monolith will require custom penetrations that do not compromise the performance of adjacent beamlines.

To allow the installation of two end stations, the instrument cave must be carefully and cleverly designed, supporting a wide range of sample environments and enabling access to a tight space.

5.6 CYGNUS—SMALL-/WIDE-ANGLE NEUTRON SCATTERING INSTRUMENT FOR STS

5.6.1 Summary

Simultaneous SANS/ WANS will bridge the gap in length scales between those measured on conventional SANS and diffractometers to simultaneously study the evolution of structure from the sub angstrom scale to ≈300 nm. The CYGNUS SANS/WANS instrument exploits the wide bandwidth of the STS to provide continuous coverage over this range of length scales. The instrument will simultaneously measure structures across a dynamic range (Q_{max}/Q_{min}) approaching four orders of magnitude. The flux afforded by the STS will make it possible to perform in situ and operando studies inaccessible to any of the present neutron scattering instruments at ORNL.

5.6.2 Science Case

Materials characterization using neutrons leverages the unique features of the probe to gain insights that cannot be gained by other methods. The properties of the neutron—it is highly penetrating while producing minimal radiation damage, it is sensitive to isotopic composition and light elements, and it has s spin—make neutron scattering applicable to many scientific disciplines. The sub-angstrom to micron length scales of interest to materials science have traditionally been served by different kinds of instruments. Diffractometers probe high-resolution structural features in materials, whereas SANS instruments focus on length scales greater than 1 nm. A new instrument that can probe both regimes simultaneously is motivated by the appreciation that many naturally occurring materials, e.g., wood, and man-made ones, e.g., high-entropy alloys, possess complex hierarchical structures. Interactions across multiple length scales govern the properties and function of hierarchical materials; thus, characterization of the interplay among these interactions in response to the environment requires a paradigm shift in how to apply neutron scattering.

The main driver for simultaneous SANS/WANS scattering measurements is to study materials away from equilibrium. Performing time-resolved multiscale characterization of kinetic processes ensures that the response of the materials is captured at all length scales under precisely the same conditions. When the experiments are enhanced with additional online experimental techniques that provide complementary information, such as spectroscopic or thermodynamic measurements, a more complete picture results of how the sample is changing in response to the conditions to which it is subjected.

There is a renewed interest in performing SANS/WANS measurements. Presently, only the TAIKAN and iMATERIA instruments at J-PARC simultaneously probe length scales from the angstrom to 100 nm. The HEIMDAL instrument under development for the ESS will also have SANS/WANS capabilities. HEIMDAL is interesting in that two guides that view different moderators will be used to provide different intrinsic Q-resolutions for the SANS and WANS measurements of the same sample.

One can readily conclude that an opportunity exists for a dedicated SANS/WANS instrument at the STS of SNS to fill this specific scientific capability gap in the instrumentation suite at ORNL. Herein, a concept for a SANS/WANS instrument for STS, called CYGNUS, is presented. The potential applications of the unique capability afforded by the instrument span polymer science, chemistry, biology, condensed matter physics and materials science. Uniquely, CYGNUS will incorporate a statistical chopper, described later in this section, for discriminating between elastic and inelastic scattering. The addition will improve the utility of the instrument for studying hydrogen-rich samples.

5.6.2.1 Polymers, Biology and Self-Assembly

SANS has long been an important characterization tool in polymer science [Higgins and Benoit 1997, Hammouda 2010]. Studies of biological materials and large-scale self-assembled structures similarly benefit from SANS. In all of these cases, the shorter length scales accessible on WANS instruments are as important for understanding these systems. While small-/wide-angle X-ray scattering (SAXS/WAXS) instruments have been excellent tools for investigating both structural regimes simultaneously, SANS instruments have not traditionally included WANS capabilities. The strong incoherent background that hydrogen produces, which contains a significant amount of inelastic scattering, makes it very difficult to resolve relatively weak diffraction features from hydrogen-rich soft materials. The proposed inclusion of the statistical chopper [Rosenkranz and Osborn 2008] in CYGNUS will help distinguish the strong inelastic scattering signal of hydrogen from that due to elastic scattering.

One research area for which CYGNUS is well suited is polymer crystallization, which is of fundamental interest in polymer science and has been studied via SAXS/WAXS [Ryan et al. 1995, Rangarajan et al.

1995]. Crystallization in the presence of applied forces like shear or deformation is of considerable interest because it plays important roles during industrial processing [Di Lorenzo and Silvestre 1999]. For example, the process of extrusion, long employed in industrial preparation of polymers, is of equal or greater importance in additive manufacturing using polymers. Not only does the crystallization within a single, deposited layer determine the strength of the printed part, but also the interlayer diffusion and subsequent crystallization of the partially shear-oriented molecules must be better understood and controlled to truly realize the potential of additive manufacturing with polymers. Similar arguments can be made for block copolymer organic electronics, for which the production process has a large impact on the final performance of the material. By performing SANS/WANS measurements with judicious deuterium labeling, it is possible to study both crystallization and single chain conformation during crystallization.

Soft materials appropriate for examination with CYGNUS are not limited to neat polymers. Many materials having enhanced physical properties are blends and composites. Understanding how the components interact across a wider range of length scales will help improve means of controlling their formation to achieve the desired properties. Further, their response to strain and shear is best understood by performing time-resolved multiscale characterization. The flux provided to CYGNUS by the STS, as well as the detector arrangement, are useful for these experiments and can resolve the anisotropic scattering features that result when a force is applied to a sample.

The structures of polymers, proteins in solution are governed by their interactions with the surrounding solvent, as are self-assembly behaviors of macromolecules and small molecules. Studies of solvation are well suited to CYGNUS; they will enable large-scale structures to be correlated with the local interactions between the solvent molecules and the macromolecule, providing a unique capability at ORNL. Similarly, the structuring of solvents at the interface with large-scale self-assembled structures can be investigated. Examples include water structure around proteins and lipid bilayers, and investigation of the local interactions that give rise to changes in solubility with temperature. CYGNUS can be used to study changes that happen rapidly with time.

The length scales probed by CYGNUS are also useful for biological membranes, and time-dependent changes in samples that are important for function can be readily studied. The capability to resolve diffraction peaks in the WANS regime is important for understanding biological membranes [Groen et al. 2011], in which order blends with disorder to create functional barriers like those between the cell and its surrounding environment. By simultaneously probing the SANS regime, CYGNUS will also be able to resolve the large-scale structures that are formed in the bilayer, such as transmembrane pores [Qian and Rai 2018], simultaneously with the local structures that show whether or not the lipids have become more ordered.

When SANS/WANS is combined with selective deuterium labeling, truly unique information can be obtained. For example, the response of model membranes to the introduction of chemicals and therapeutic agents can be studied simultaneously with specific local interactions that take place. Structural changes that occur over time during transdermal drug delivery to lipid membranes mimicking the epidermis is of great interest to the pharmaceutical and cosmetics industries. Similarly, the interaction of various lipid species with amyloid-forming proteins can be followed during the aggregation process that gives rise to plaques. The local structure of the protein and the aggregates are revealed, while the large-scale structures are measured.

5.6.2.2 Chemistry and Materials Science

The Q-range probed by CYGNUS affords excellent opportunities to understand chemical processes and reactions. The process of crystallization can be followed from solution through nucleation and growth

without any of the x-ray radiation-induced chemistry that is nearly always present in synchrotron-based SAXS/WAXS experiments. The range of length scales that CYGNUS can simultaneously observe at a Q-resolution better than that of a traditional SANS instrument makes it excellent for understanding chemistry and materials science across a wide range of length scales. Several topics from solution chemistry can be investigated with unprecedented detail with CYGNUS.

Mixed solvents used in chemistry impart important characteristics that allow reactions to take place, but these systems can simultaneously display long-range and local ordering that can impact the reactions and may change as the process progresses. Deep eutectic solvents [Zhang et al. 2012] and ionic liquids [Welton 1999] differ greatly from traditional solvents and have attracted a great deal of research interest because of these differences. CYGNUS could provide a great deal of unique insight into these solvents and how they respond to solutes. Liquid-liquid extraction processes are also suitable for study by CYGNUS because of the wide range of length scales that are involved [Motokawa et al. 2019].

Any chemical process can be studied in situ by CYGNUS, although those that arise from or give rise to self-assembly are appropriate for the full range of capabilities of CYGNUS. For example, in situ polymer synthesis in supercritical CO_2 [Hermida-Merino et al. 2014, Jennings et al. 2016] can be investigated over a wide range of length scales without concerns about radiation-induced chemistry. Similarly, preparation of mesoporous materials and ceramics, which display structural evolution at both local and large length scales, can be followed in situ with the proposed instrument. Solution phase chemistry can also be studied. Solvent-solute interactions in mixed solvent systems would be well-served, as would supercritical CO_2 processing. Any system with interactions that give rise to local ordering, clusters and aggregates that can extend into the nanoscale would be suitable for investigation on CYGNUS.

Similarly, catalysts play an important role in chemistry and yet many questions remain that can be answered with CYGNUS. In situ studies of the deactivation and recycling of homogeneous catalysts can provide new insight into how local interactions change before large-scale changes, such as aggregation or phase separation, take place in the reaction vessel. In heterogeneous catalysts, such as palladium immobilized in mesoporous silica [Jana et al. 2008], in situ studies of chemical reactions will be possible. In cases where the catalyst deactivates through formation of a layer on its surface, its growth can be visualized in real time with CYGNUS, while changes in the framework supporting the catalyst can be observed.

Materials science can also make good use of time-resolved studies of structures that span the length scales served by CYGNUS. For example, structural changes in battery materials—prototypical hierarchical materials—resulting from materials preparation and cycling take place across the entire range of length scales accessible to CYGNUS, but to date they have been studied by SANS and neutron powder diffraction independently [Bridges et al. 2012, Kim et al. 2014]. The detector arrangement, described below, is optimized for the planar geometry normally employed by SANS. With CYGNUS, the changes that take place at atomic length scales within a functional half-coin cell can be measured simultaneously with those at the nanoscale. Hybrid nanostructures consisting of metal nanoparticle-biopolymer conjugates and the large-scale structures that can be assembled from them [Mirkin et al. 1996] can also be studied. Not only are the structures of the nanoparticles of interest to materials science, but also the manner in which the materials to which they are conjugated drive large-scale assembly into functional materials.

Investigations of metals, alloys, high-entropy alloys, and superalloys will also greatly benefit from time-resolved SANS/WANS studies. Structural changes that take place during annealing, such as precipitation, give rise to scattering features that span a wide range of length scales. Rather than performing diffraction and SANS measurements independently [Hany et al. 2018], both length scales can be probed simultaneously in situ on CYGNUS. Further, the response of these materials to deformation can be

tracked in situ with the instrument. Phase transitions in metals and alloys are also fitting for study. Better understanding of formation and processing, as well as damage development, will result from investigating the temporal behavior of alloys over the length scales sampled by CYGNUS.

Glasses have long been studied by scattering methods and are widely used materials. CYGNUS is ideally suited to studying glass formation in situ. In particular, the study of clustering during glass formation is relevant to the wide range of length scales available to CYGNUS, as is crystallization of materials from glassy matter. The evolution of local structure can be directly measured with large-scale structures that may form. Bulk metallic glasses have excellent properties to which both local and long-range structures are important, and investigating their formation in situ would provide unique insight not available from ex situ characterization of the final product. The vitrification of radioactive or toxic waste materials [Bingham and Hand 2006] is another process that could be studied in situ with CYGNUS. Local and large-scale structures, such as porosity, that result either during formation or as the material ages are important for the long-term function of glasses in these applications.

In situ studies of porous materials are also an excellent fit for experiments with CYGNUS. For example, gas or liquid loading into porous materials is of interest for technological applications, as well as in the geosciences. Questions that can be addressed include gas or liquid penetration and local structuring within rocks or man-made porous materials, such as membranes. Instead of correlating two experiments using different instruments (often with different sample geometries), the long-range and local structures can be determined simultaneously.

5.6.2.3 Condensed Matter Physics

The wider Q-range probed and the improved resolution provided by the CYGNUS enable simultaneous characterization of both local magnetic structure and large-scale structures, such as skyrmions [Mühlbauer et al. 2009]. Shape memory alloys would also benefit from the range of length scales sampled by CYGNUS; an improved understanding could be obtained of temperature-dependent, long-range ferromagnetic correlations that have been observed [Aksoy et al. 2009]. Similarly, the relationships between domain structures and local nuclear and magnetic structures in multiferroics, ferroelectrics, and piezoelectrics are suitable for study with CYGNUS. Of particular interest in all of these topics is the ability to simultaneously probe length scales, as the sample is subjected to changing conditions in situ, such as temperature, and applied electric or magnetic fields.

Interestingly, the statistical chopper on CORELLI at the SNS [Ye et al. 2018] enables the instrument to function as a spectrometer, although the higher energy scales that exist in hard condensed matter are better suited to spectroscopic measurements with a statistical chopper than the lower energy scales associated with soft matter. The expected energy resolution of CYGNUS, detailed in Section 5.6.3, has considerable potential for such measurements if the right wavelength range is used, even though CORELLI views a decoupled, poisoned moderator at the SNS FTS and therefore has better wavelength resolution [Ye et al. 2018].

5.6.3 High-level Capability Requirements

To address the science that the instrument is anticipated to serve, the following performance requirements discussed during the STS Workshop held October 2015 at ORNL [Eskildsen and Kayhovich 2015] were deemed important for the performance of a SANS/WANS instrument.

- 0.01 Å^{-1} < Q < 6.0 Å^{-1} (D-spacings > 1 Å) with the ability to cover this entire range at once
- $\Delta Q/Q$ < 1%

- Small samples (< 100 μL, < 0.001 cm^3, < 10 mg)
- An open, flexible sample area

These requirements are broad, largely because there is generally a dearth of SANS/WANS instruments that members of the user community at the workshop could refer to. Therefore, it is useful to consider the needs of each of the potential user communities mentioned earlier and approach the instrument from the perspective of compromising performance characteristics to meet their needs. The sample size is not considered in the discussion. In contrast, the open, flexible sample area is critical for enabling new science. Providing a versatile sample area makes it possible to study time-dependent processes in samples in complex environments while employing secondary probes, such as optical spectroscopies, thereby enabling novel studies that can provide unprecedented insight into materials.

5.6.3.1 Polymer Science and Biology

The lower end of the Q-range of CYGNUS provides a macromolecular structure useful in polymer science and therefore can benefit from having as low a minimum Q as possible. Crystalline polymers can give rise to multiple orders of diffraction peaks. However, even highly crystalline polymers lack the type of long-range order that is typical of small molecule crystals. The first-order peak resulting from chain-chain packing is on the order of 1.5 $Å^{-1}$. Given that the focus of the polymer research that requires simultaneous SANS and WANS is time-resolved studies of crystallization, three or four diffraction features are sufficient for tracking the process. Exceedingly high Q-resolution is not required, given the science driver and the structures being studied.

Biological structures, regardless of whether they are made of macromolecules (proteins, RNA, DNA), small molecules (e.g., lipids, sterols), or a combination thereof, are of similar length scales to those found in polymer science. The structures are large, and they will not give rise to long-range order that is suitable for high-resolution structural determination during investigations of how they change over time in response to conditions to which they are subjected. Therefore, the following performance parameters are suggested.

- 0.001 $Å^{-1} < Q <$ 6.0 $Å^{-1}$ (D-spacings > 1 Å)
- 2% < $\Delta Q/Q$ < 5%

5.6.3.2 Chemistry and Materials Science

In contrast to soft materials, much of the research in chemistry and materials science for which a SANS/WANS instrument would be used includes materials that will form highly crystalline structures with repeat spacings on the order of interatomic bond lengths. While knowing the crystal structure is very important, long length scales are also crucial for understanding the performance of many materials. For example, grain or precipitate formation in alloys can result in the growth of very large structures that could be seen only with an instrument capable of very low Q. The potential d-spacing of the diffraction features and the resulting density of peaks necessitates a relatively high Q-resolution to resolve sufficient peaks to understand the material being measured. However, identifying the onset of crystallization, identifying space groups, or estimating crystallite volume from Scherrer broadening of diffraction peaks would have less stringent demands. As a result, the following performance parameters are suggested.

- 0.001 $Å^{-1} < Q <$ 20.0 $Å^{-1}$ (D-spacings > 0.3 Å)
- $\Delta Q/Q \leq 1\%$

5.6.3.3 Condensed Matter Physics

The materials studied by condensed matter physicists are nearly always highly crystalline; yet the scattering features that arise from correlated electrons, such as skyrmions and flux lattices, or from magnetic diffraction peaks are unlike those found in other fields of research. While the former features are generally found at long length scales, and therefore in a Q-range that is typical of a SANS instrument, the magnetic diffraction peaks can manifest for Q > 0.50 Å^{-1}. For features that arise from magnetic structures with periodicities greater than typical bond lengths, the resulting pattern of magnetic diffraction peaks would be well spread out in reciprocal space and would not require a very high resolution in Q. Magnetic diffraction peaks arising from smaller structures could benefit from higher resolution. As a result, the following performance parameters are suggested.

- 0.001 Å^{-1} < Q < 20.0 Å^{-1} (D-spacings > 0.3 Å)
- 1% < $\Delta Q/Q$ < 3%

Table 5.13 summarizes the bounding key capabilities for CYGNUS from the requirements described. Collecting data across the full desired Q-range simultaneously is a key requirement for this instrument.

Table 5.13. Key capability requirements for CYGNUS.

Parameter	Description
Beam size at sample	2 by 2 cm maximum
Beam divergence	Variable ~±0.4º maximum, selected by source and sample apertures
Q-range	0.001 Å^{-1} ≤ Q ≤ 20 Å^{-1}, in a single instrument configuration
Q-resolution	ΔQ/Q ≤ 0.01
Ambient conditions	Open, versatile sample area Ability to use magnet up to 15 T

5.6.4 Physics Design and Engineering Concept

The CYGNUS instrument concept is discussed in this section and is shown in Figure 5.31. Throughout the instrument, the guides are 2 by 2 cm and have a coating that is m = 3. The justification for this value is provided in the performance estimate. For maximum compatibility between the instrument's diffraction and SANS capabilities, a flat sample geometry has been selected as the primary mode of operation This geometry has influenced the location and geometry of the neutron detectors, but other geometries can be supported depending on particular needs of a given experiment.

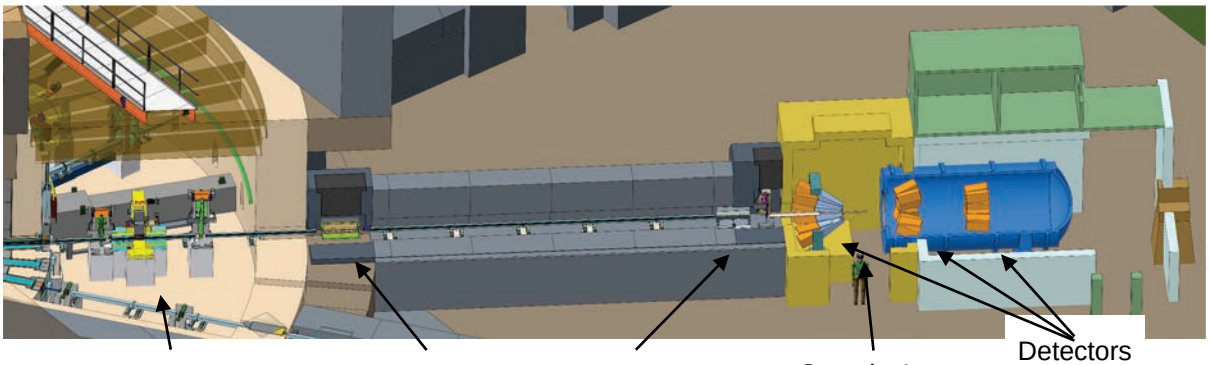

Figure 5.31. The CYGNUS instrument.

5.6.4.1 Description of the Instrument Components

- The instrument is in position ST03, which views the 3 by 3 cm upper cylinder moderator.
- A straight guide starts 0.900 m from the face of the moderator and extends to chopper 1. The maintenance shutter interrupts the continuity of the guide. The open position for the shutter will have a guide.
- Chopper 1, which is an STS medium double disk chopper, sits at 7.000 m. The opening in the chopper is 90°.
- Next, a straight section of guide extends from the outlet of chopper 1 to the T0 chopper.
- A T0 chopper of STS large T0 chopper type sits at 8.000 m.
- SA straight guide extends from the T0 chopper to chopper 2, which is an STS large double disk chopper and is located at 10.000 m. The opening in each disk is 120°.
- A straight guide in which a frame-overlap mirror is installed extends from chopper 2 to the outer wall of the bunker that is at 13.288 m.
- The operations shutter is just outside the bunker wall and extends to 14.463 m.
- From the operations shutter, a long section of straight guide extends to a correlation chopper.
- The correlation chopper, which is an STS high-speed disk chopper, sits at 27.000 m.
- Then, the source aperture is mounted at 27.250 m inside an evacuated volume having a translation stage to allow the source aperture to be varied, although it is assumed to be 20 mm in diameter in the simulations presented herein.
- After the source aperture, an evacuated flight tube extends to very close to the nominal sample position.

- Next, the sample aperture is positioned immediately before the nominal sample position. It is assumed to be 5 mm in diameter for the simulations described below.

- The nominal sample position is located at 30.250 m.

- The face of the vacuum tank for the two banks of forward scattering detectors starts at 30.500 m and has a 30 cm sapphire window.

- There are three detector banks, which are described in Section 5.6.4.3. The types of detectors are specified; they consist of modules having an active area of 30 by 30 cm. Two of the banks are inside the vacuum tank. The third bank, the backscattering bank, is described below.

    - The low angle bank is arranged on a 3 m radius sphere. The surfaces of the active areas are tangent to the sphere. There are 9 modules in the low angle bank arranged in a 3 by 3 square that is centered on the beam.

    - The high angle bank is arranged on a 1 m radius sphere. The surfaces of the active areas are tangent to the sphere. There are eight modules in the high angle bank, arranged in a 3 by 3 square that is missing the center module that would otherwise be centered on the beam.

    - The backscattering bank is arranged on a 1.25 m radius sphere. The surfaces of the active areas are tangent to the sphere. There are seven modules in the backscattering bank, arranged in a 3 by 3 square that is missing the center module that would otherwise be centered on the beam, as well as the one below it. Each module of the backscattering bank is mounted in a frame that allows it to move along the beam direction so that it can have the center of the sphere located at the sample position. Each module has its own evacuated flight path, which has a neutron transparent window, such as sapphire or silicon, on the upstream ends and aluminum or vanadium on the downstream ends.

5.6.4.2 A Statistical Chopper for Filtering Inelastic Scattering

Perhaps one of the greatest technical challenges faced by TOF SANS and neutron diffraction instruments is that they resolve changes in neutron energy, as this changes the neutron TOF [Do et al. 2014]. As a result, the data collected from most samples, but particularly those containing hydrogen, become distorted as a result of the changes in neutron energy that take place in the sample. These energy changes cause issues during data reduction and the subsequent interpretation because the TOF is altered, resulting in incorrect assignment of the neutron wavelength and therefore Q. Importantly for diffraction measurements, the changes in energy have the potential to diminish or wash out weak diffraction features, such as would exist in a hydrogenous material exhibiting a large incoherent scattering signal. Differentiating or removing the inelastic scattering portion of the signal, for example, by using a very narrow incident energy range (i.e., operating the instrument as a spectrometer) or by using neutron polarization methods, has considerable appeal. Unfortunately, operating the instrument as a spectrometer greatly reduces the flux on sample, which negatively impacts time-resolved studies and the scientific throughput of the instrument. Neutron polarization methods, such as dynamic nuclear polarization [Noda et al. 2016], reduce the flux to a lesser extent but require that the samples be studied at temperatures on the order of 1 K, which limits their utility for investigating time-dependent processes. Finding a better approach to address inelastic scattering on TOF SANS instruments would be highly valuable for the scientific community.

An alternative method for differentiating elastic and inelastic scattering events is through the use of a statistical chopper that has a much higher duty factor than conventional neutron choppers [Rosenkranz

and Osborn 2008]. A statistical chopper has a pseudo-random sequence of openings to provide a modulated incident beam intensity. This modulation can then be used to distinguish elastic from inelastic scattering. It is particularly advantageous for instruments employing a relatively broad bandwidth of incident energies. The method was implemented on the CORELLI instrument at the SNS FTS, which is used as a quasi-Laue diffractometer with elastic energy discrimination for studying diffuse scattering [Ye et al. 2018]. This approach has potential for use on a SANS instrument and merits future consideration for inclusion in the SANS-1 instrument after a detailed study has been performed.

The energy resolution of an instrument with a statistical chopper is given by the following equation [Windsor 1981]:

$$\frac{\Delta E}{E} = \left[\left(2\frac{\Delta t_{ch}}{t_{ch}}\left[1+\frac{L_{ms}}{L_{sd}}\right]\right)^2 + \left(2\frac{\Delta t_m}{t_{ch}}\left[1+\frac{L_{cs}}{L_{sd}}\right]\right)^2\right]^{1/2},$$

where t_{ch} is the TOF from the moderator to the statistical chopper, Δt_{ch} is the size and frequency-dependent time width of the chopper aperture, and Δt_m is the width of the emission of the moderator, which is wavelength-dependent. L_{ms} is the distance from the moderator to the sample, L_{cs} is the distance from the statistical chopper to the sample, and L_{sd} is the sample-to-detector distance. CYGNUS is appropriate for a statistical chopper of this nature because the sample-to-detector distance is relatively short. With the instrument layout described, the $\Delta E/E$ for CYGNUS with a statistical chopper of the type currently installed in CORELLI [Ye et al. 2018] is presented in Figure 5.32. Note that the energy resolution provided by the chopper is not good for the shortest wavelengths but improves quickly with increasing wavelength. A more thorough investigation of the potential for a statistical chopper is needed to understand how the Q and energy resolution of the instrument impact its scientific performance. In particular, detailed accurate physics simulations, such as with MCNP, are needed to evaluate the ability of the statistical chopper to discriminate between elastic and inelastic scattering events.

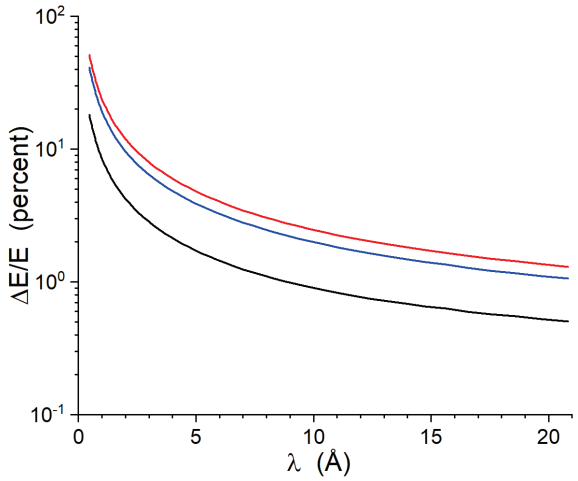

Figure 5.32. Energy resolution provided by the statistical chopper for the low angle bank (black), high angle bank (red) and backscattering bank (blue).

5.6.4.3 Specifications for Detectors

Experience gained on the SANS instruments at the SNS FTS and HFIR suggest that ^{3}He-based PSDs built around the 8-pack technology developed at SNS perform adequately under many circumstances. Unfortunately, the detectors can be driven out of their ideal response range at the high counting rates that result from the strong beams interacting with strongly scattering samples or sample environments. Therefore, the specific detector technology, while not strictly specified at present, must be capable of higher count rates than the existing ^{3}He technology can provide.

The arrangement of the detectors discussed is based around the assumption that the detector elements are modules based on silicon-PM Anger camera technology, which is the next-generation technology in development at the SNS. The modules in the CYGNUS concept, which have an active area of 30 by 30

cm divided into a 100 by 100 array of pixels, yielding 3 by 3 mm pixels, are individual units that can be readily arranged into the geometry shown above. In the performance estimate (Section 5.6.5), count rate estimates are provided that demonstrate some common data rates in modules in the various detector banks described previously. Based on these estimates, a minimum requirement is that each detector module be capable of handling 10^6 counts/second with linear performance, and that linear performance be maintained up to a per-pixel count rate of 100 counts/second in a single pixel. The performance estimates presented herein suggest that these values provide a sufficient margin of safety for linear performance for strongly scattering samples that display diffraction peaks.

5.6.4.4 Neutron Bandwidth Choppers

A time-distance diagram was developed using the chopper positions and parameters presented previously. The T0 chopper and the statistical chopper were omitted from the time-distance diagram. Both 15 Hz and 7.5 Hz operation were considered and provide bandwidths of ~7.9 Å and ~15.8 Å, respectively. Figure 5.33 shows both modes of operation assuming a minimum wavelength of 0.5 Å. The locations of the choppers appear to block neutrons from longer-wavelength bands from making it through later openings in the choppers. McStas simulations were performed to test for leakage in the 15 Hz mode of operation using minimum wavelength settings of 0.5 Å, 1.0 Å, and 2.0 Å. The results revealed a very weak and incredibly narrow band of neutrons near 83 Å regardless of the wavelength setting. The fact that it did not move with the minimum wavelength setting raises the possibility that it was an artifact of the simulation; in any case, the production and transmission of these neutron wavelengths is exceedingly small. No leakage was observed in the results of simulations performed at 7.5 Hz for wavelength settings of 0.5 Å, 1.0 Å, 2.0 Å, and 4.0 Å. The actual performance of the STS moderators will reduce, to a small extent, the actual wavelength bands that can be used, because of the neutron pulse width, thereby slightly changing the actual timing of the choppers shown in Figure 5.33. But the differences do not fundamentally alter the anticipated Q-range of the instrument that are presented herein and are not expected to change the leakage performance of the chopper system in the instrument.

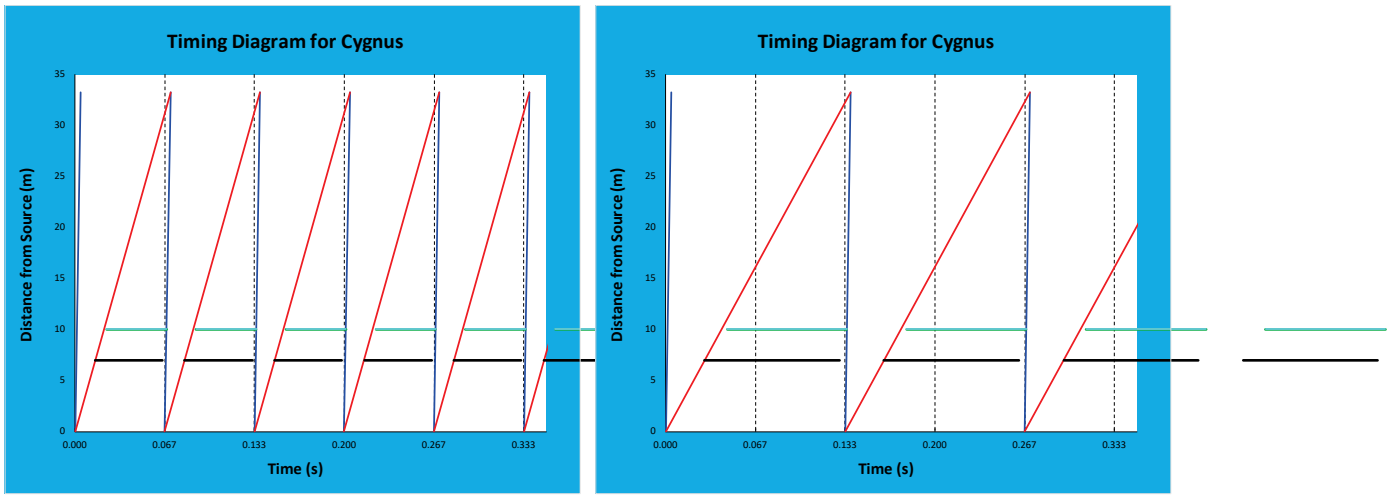

Figure 5.33. Time-distance diagram for CYGNUS for 15 Hz (left) and 7.5 Hz (right).

Table 5.14 lists the main components of CYGNUS and their locations along the beamline.

Table 5.14. List of CYGNUS instrument components.

Component	Description	Location
	Beam delivery	
Neutron guide	Straight guide	Z = 0.9 – 28 m
Chopper 1	Double disk	Z = 7.0 m (in bunker)
T0 chopper		Z = 8.0 m (in bunker)
Chopper 2	Double disk	Z = 10.0 m (in bunker)
Frame overlap mirror		Z = 10.8 m (in bunker)
Operations shutter	Shutter for daily operations	Z = 13.3 m
Correlation chopper	High-speed disk	Z = 27.0 m
Source aperture	Reconfigurable vacuum box with translation stage for inserting and removing different apertures	Z = 27.1 m
Flight tube	Evacuated tube ending close to sample position	Z = 27.1 – 30.0 m
Beamline shielding	Bunker to cave	Z = 13.2 – 27.5 m
Sample location	Variable	Z = 29.8 – 30.25 m
Component	**Description**	**Location from sample**
	End Station	
Shield cave		Z = -2.75/+8.5 m
Detector tank	Evacuated cylindrical tank	Z = +0.3/+5 m
Low-angle detectors	Fixed	Z = +3.0 m
High-angle detectors	Fixed	Z = +1.0 m
Backscattering detectors	Fixed relative to sample position	Z = -1.25 m

5.6.5 Performance Estimate

Simulations were performed using McStas version 2.4.1 [Willendrup et al. 2014]. The positions of the components were as described, using suitable gaps to represent spaces between the guides and other optical components. At present, no McStas component exists for the T0 choppers to be used at the STS. As a result, the position was left as an empty gap in the Monte Carlo model. Simulations to estimate brilliance transfer through the guide system did not include the detector array because only the transported beam was of interest. The samples used for certain performance estimate simulations are noted in Section 5.6.5.3.

5.6.5.1 Brilliance Transfer and Guide Coating

The maximum usable divergence of CYGNUS was determined assuming that the largest sample that could be reasonably measured on the instrument is the same size as the guides: 2 by 2 cm. As a result, the maximum usable divergence is ±0.382°. The typical sample will be smaller, and a formal optimization will be performed as the instrument design progresses. McStas simulations were performed as a function of the m-value of the guides in the instrument to determine the best value. The results are presented in Figure 5.34 and indicate that the guide system performs best over the desired wavelength range when m ≥3. However, no real gain in performance is realized when m > 3. As a result, the performance estimate simulations all use m = 3.

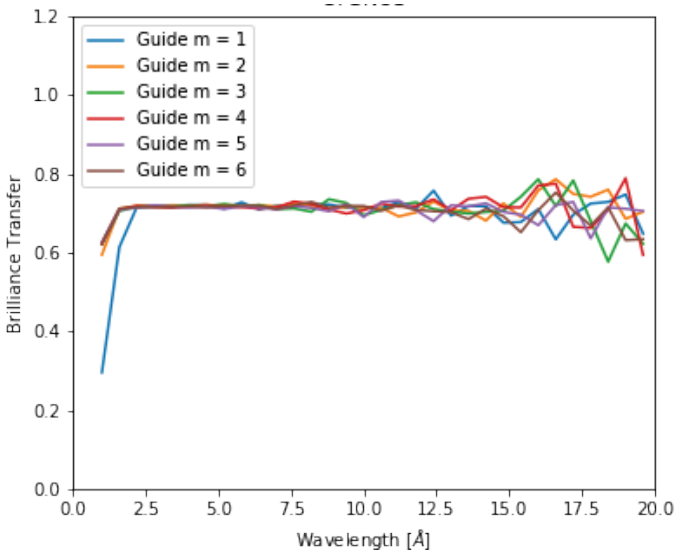

Figure 5.34. Brilliance transfer as a function of wavelength for the indicated guide coating m-values.

5.6.5.2 Q-range and Flux on Sample

The detector arrangement affords the ability to simultaneously measure a much wider Q-range than in a typical SANS instrument. However, the gap in angular coverage presents limitations on the wavelength bands that allow overlap in Q-space between the forward and backscattering banks, as can be seen in Table 5.15. In 15 Hz operation, there is insufficient overlap in Q between the high angle and backscattering banks of detectors when the minimum wavelength setting is greater than 2 Å. During operation at 7.5 Hz, overlap in Q-space is maintained out to a minimum wavelength setting of 4 Å. Flux estimates for representative configurations at both potential operating frequencies were also calculated and are presented in Table 5.16. The results demonstrate that the CYGNUS concept satisfies the desired Q_{max} specified in Section 5.6.3 and provides Q_{min} of 0.01 Å^{-1} or less. Further, the flux is very good, which ensures that the instrument is capable of time-resolved measurements of kinetic processes.

Table 5.15. Overlap in Q-space between high angle and backscattering banks as a function of minimum wavelength, λ_{min}. Only select λ_{min} are presented.

λ_{min} (Å)	Q_{max}, high angle (Å^{-1}), 15 Hz	Q_{min}, backscattering (Å^{-1}), 15 Hz	Q_{max}, high angle (Å^{-1}), 7.5 Hz	Q_{min}, backscattering (Å^{-1}), 7.5 Hz
0.5	5.225	1.440	5.225	0.742
2.0	1.306	1.222	1.306	0.679
4.0	*no overlap*	*no overlap*	0.653	0.611

Table 5.16. Q-range and neutron flux at the sample for select minimum wavelength settings (λ_{min}) and the indicated effective repetition rate.

λ_{min} (Å)	Q_{min} (Å^{-1})	Q_{max} (Å^{-1})	d_{min} (Å)	Φ (n/cm^2·s)
0.5, 15 Hz	0.00373	24.918	0.252	2.42E+8
1.0, 15 Hz	0.00352	12.459	0.504	2.33E+8
2.0, 15 Hz	0.00316	6.229	1.009	1.98E+8
0.5, 7.5 Hz	0.00192	24.918	0.252	1.24E+8
2.0, 7.5 Hz	0.00176	6.229	1.009	9.79E+7
4.0, 7.5 Hz	0.00158	3.115	2.017	3.03E+7

5.6.5.3 Count Rate in the Detector Array

The Sans_spheres component was employed as a sample to estimate the count rate in the instrument. Two different sets of parameters were assumed, 100 Å spheres at a 5% volume fraction and 1000 Å spheres at 1% volume fraction. The remainder of the parameters were set to the default values; the size of the sample was 2 by 2 cm and it had a pathlength of 1 mm. The minimum wavelength was set to 2 Å for the simulation, and the sample aperture was assumed to be round with a 5 mm diameter. The Sans_spheres component does not support incoherent scattering, which results in effective count rates that are almost entirely in the forward scattering array. For the 100 Å sphere test, the total count rate was 7.9E+4 cts/s, and the rate was 8.3e+3 cts/s for the 1000 Å spheres. A second test employed the PowderN McStas component with C60.lau downloaded from the McStas website (http://www.McStas.org/) providing the diffraction pattern information, which is more important for the backscattering bank of detectors. In this case, the total count rate was 1.20E+5 cts/s, primarily distributed over the high angle and backscattering banks of detectors. This count rate is comparable to measurements of C_{60} on the NOMAD instrument at the SNS FTS. NOMAD has a greater solid angle coverage (~4.0 ster compared with ~1.2 ster for CYGNUS), and this count rate is well within the capabilities of the NOMAD detectors and data acquisition system. Although these simulations cannot be representative of the full range of samples that can be studied on CYGNUS, the values confirm that the detectors specified for the instrument are reasonable.

To estimate the possible maximum global count rate to which the detector array could be exposed, we assume that a 1 by 1 cm sample scatters ~20 % of the incident beam isotropically, as a very thick volume of water might do. Table 5.17 provides an estimate of the count rate seen by the three different banks of detectors. The rate per pixel is also provided in the table. Again, the scattering signal in the SANS and diffraction regimes can vary considerably from sample to sample, which can result in very different local counting rates. However, the detector specifications provided earlier are anticipated to be adequate for most situations. The detector specifications are also suitable for samples showing diffraction peaks, which are smeared out in real space because of the TOF nature of the instrument.

Table 5.17. Count rates for a strongly isotropic scattering sample.

	Cts/sec per module, high angle	Cts/sec per module, low angle	Cts/sec per module, backscatter	Total cts/s	Maximum cts/s per pixel
λ_{min}=0.5 Å	272000	30234	174000	3.67E+6	27.2

5.6.5.4 Estimates of $\Delta Q/Q$ for Diffraction

The Q-resolution in the backscattering detector bank was estimated from a McStas simulation using a powder crystalline pseudo-sample that generated very narrow diffraction peaks at select values of Q. For simplicity, the detector was modeled as a vertical cylinder with a radius of 1.25 m centered on the sample location with 8 mm pixel size. The sample was 1by 1cm flat plate geometry. The simulation TOF data were converted to Q using standard algorithms in the Mantid software package [Taylor et al. 2012]. Figure 5.35 shows the reduced data, which exhibit excellent Q-resolution. The FWHM of the Q=2.5 Å-1 peak shown in the lower plot is approximately 0.016 $Å^{-1}$ for a $\Delta Q/Q = 0.0065$, which satisfies the science-driven requirement of better than 1%. At this distance from the moderator, the wavelength resolution $\Delta\lambda/\lambda$ is between 0.001 and 0.0035 for the range of neutron wavelengths CYGNUS is designed to use, $0.5 Å \leq \lambda \leq 15 Å$, which is adequate to ensure the required Q-resolution across the entire diffraction range.

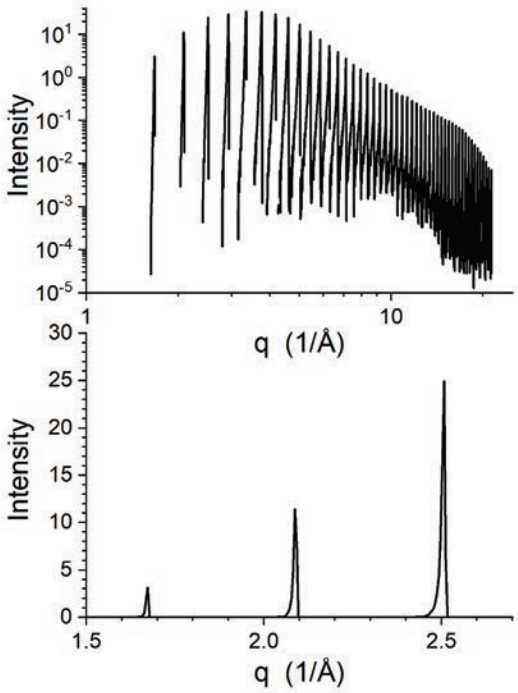

Figure 5.35. Diffraction Bragg peaks measured in the CYGNUS backscattering detector as modeled in McStas.

5.6.6 Feasibility, Research and Development

The CYGNUS instrument can largely be built with current technologies, apart from the detectors, which require some development that builds on the ORNL Si-PM based Anger camera technology (as discussed in Section 5.9.4 on neutron detectors.

5.7 EWALD—A SINGLE CRYSTAL DIFFRACTOMETER FOR SMALL SAMPLES

5.7.1 Summary

EWALD is a single crystal diffractometer optimized for collecting Bragg diffraction data from crystal volumes below $0.01mm^3$ with unit cell edges between 10 to 300 Å. The compact high-brightness coupled moderator at the STS coupled with the deployment of a Montel (nested) Kirkpatrick–Baez (KB) neutron supermirror system will deliver small, intense neutron beams to the sample position [Coates and Robertson 2017][Coates et al. 2018]. This will enable EWALD to collect data from crystals orders of magnitude smaller than those that can currently be studied using existing neutron instrumentation. That ability will enable studies of most of the macromolecular systems for which crystals of the volume required by current instrumentation cannot be grown. The broad wavelength range available in a single STS pulse coupled with the high detector angular coverage of this instrument will enable complete data sets to be collected rapidly, in as few as a single orientation of the crystal. This section outlines a science case for the instrument, reviews the basic design concept, and gives detailed performance estimates.

5.7.2 Science Case

Single crystal diffraction has provided a wealth of information on structure in studies ranging from small molecules composed of less than ten atoms to large macromolecular complexes consisting of many

thousands of atoms. Over the past 50 years, single crystal diffraction has become the dominant method of choice for obtaining high-resolution data on the structure of molecules (Figure 5.36). To date, the Cambridge Structural Database [Groom et al. 2016] contains more than 900,000 small molecule structures and the Protein Data Bank [Berman et al. 2000] includes the structures of more than 140,000 macromolecules.

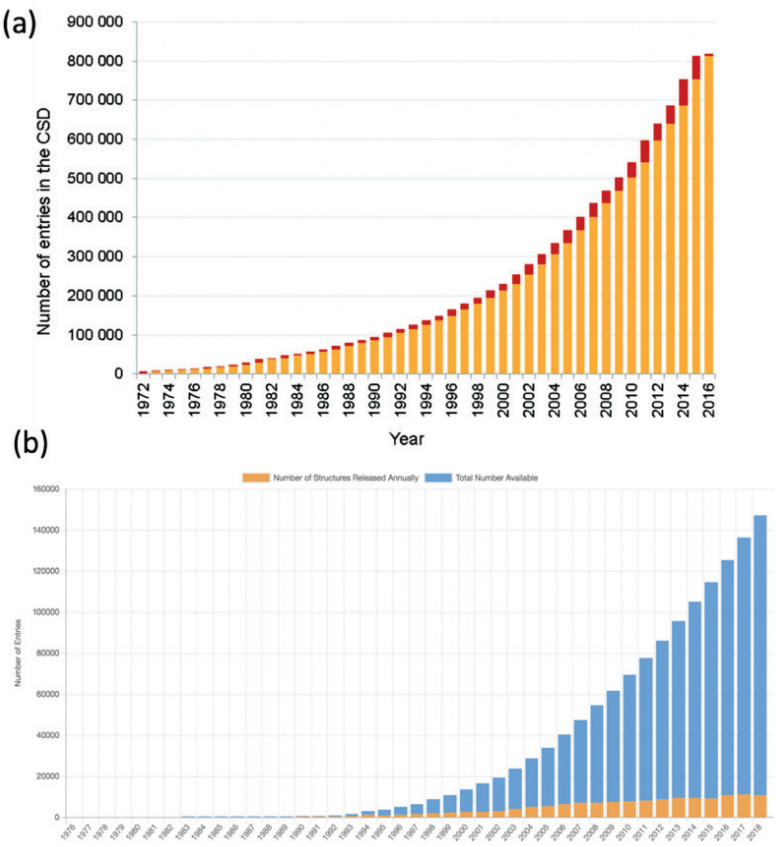

Figure 5.36. Yearly increase in the number of crystal structures deposited. (a) Growth of the Cambridge Structural Database since 1972; the red bar shows the number of structures added annually. (b) Growth of the Protein Data Bank since 1976; the orange bar indicates the number of structures added per year.

X-rays and electrons interact with an atom's electrons. As a result, they are relatively insensitive to hydrogen, which is abundant in biomolecules and plays essential catalytic and structural roles, but has only one electron. Neutrons, on the other hand, interact directly with an atom's nucleus and are highly sensitive to hydrogen; so they can locate important hydrogen atoms not detectable with x-rays or electrons, even in atomically resolved structures. Neutrons are a unique non-ionizing probe that can be used to study protein structures free from the artifacts of radiation damage that rapidly occur when x-rays or electrons are used as probes.

However, single crystal neutron diffraction has been limited in its use by the low flux of current instruments, which is typically offset by requiring a large volume crystal. The majority of protein crystals can be grown only to small volumes below 0.5 mm^3, a severe limitation on the systems that can be studied with neutrons. In particular, the larger the volume of the unit cell of a crystal, the more difficult an experiment becomes (Figure 5.37)—as unit cell size increases, so does the crystal size requirement.

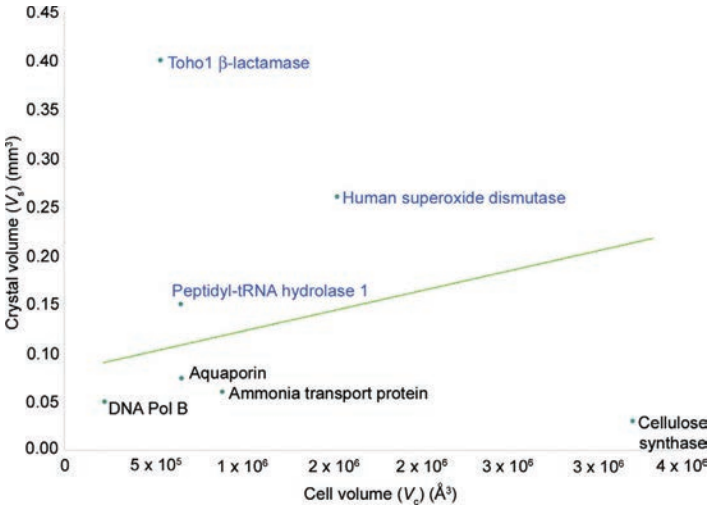

Figure 5.37. A scatter plot of examples of challenging protein crystals collected on MaNDi (blue text) and several examples of protein crystals that the EWALD instrument can bring into range for neutron crystallography (black text). The green line shows an empirical limit that has been observed on the MaNDi instrument. *Source: Coates and Robertson. J. Appl. Crystallogr. 50, 1174–1178, 2017.*

The following sections detail selected scientific areas in which experiments on EWALD will make a major impact.

5.7.2.1 Life Sciences

Biological research and its resultant applications provide a wide range of benefits to the nation. The benefits are especially conspicuous in human health and medicine but also pervade society in areas such as agriculture, food, consumer products, biofuels, materials, environmental protection, national security, and industrial processes. This research is vital for the long term because it is the key to new technologies and sustainable prosperity. Natural systems reflect a mastery of physical laws and engineering principles against which the best artificial systems look primitive. This mastery spans catalysis, energy conversion, materials synthesis, sensing, communications, and computation, among other areas. In addition to performing these functions, biological systems are self-organizing, self-assembling, adaptive, and robust, while operating far from equilibrium.

Most of the oxygen in the atmosphere is generated by plants, algae, and cyanobacteria through the photo-induced oxidation of water to oxygen gas (O_2). This reaction also lies at the heart of efforts to create artificial photosynthetic systems for converting solar energy to fuels. In photosynthetic organisms (Figure 5.38), the reaction is catalyzed by the multi-subunit membrane protein photosystem II (PS-II). The oxygen-evolving complex (OEC) of PS-II contains a metal cluster (Mn_4CaO_5) that catalyzes the oxidation of H_2O to O_2 [Kern et al. 2014]; that cluster is known to be damaged by radiation during x-ray diffraction [Yano et al. 2005].

While x-ray structures have begun to unveil details of the mechanism of this reaction [Kern et al. 2014, Young et al. 2016], the underlying chemistry is complex, and many key questions remain unanswered. In particular, the role of protonation patterns of waters in the vicinity of the active site and the networks for the entry of substrate (water) and exit of products (protons and oxygen) are still not well understood. To obtain a detailed picture of the water environment of the catalytic site and elucidate the important role of light-induced changes in the hydrogen bonding network around the active site, the new capabilities of the STS and EWALD will be vital. When H_2O is oxidized, it produces O_2 and protons and sequentially releases four electrons in an oxygen atom. This light-induced reaction involves a five-state kinetic model for photosynthetic oxygen evolution. That consists of four (meta)stable intermediates, a transient state, which precedes the formation of dioxygen.

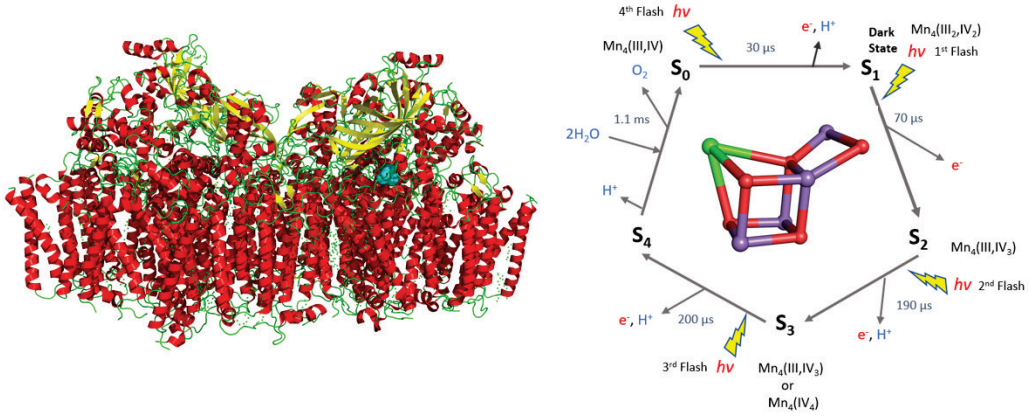

Figure 5.38. Photosynthesis is a central metabolic pathway found in plants, cyanobacteria, and algae that captures solar energy for downstream carbon dioxide fixation and produces the oxygen that supports life on Earth. The photosynthetic PS-II complex (left) is a multicomponent, hierarchical assembly tuned to optimize capture of available light and maximize the efficiency of energy conversion. The first step in photosynthesis is light capture by antennae complexes within the thylakoid membranes that absorb and transfer solar energy to PS-II, where water-splitting at the OEC within PS-II occurs via the Kok cycle (right).

The oxidation state of the manganese atoms within the OEC cluster alters during the reaction, which illustrates the importance of using a probe that does not influence the oxidation states [Yano et al. 2015]. Neutrons are thus ideally suited to follow oxygen evolution, as PS-II crystals can be moved among the four (meta)stable intermediates using laser pumping, enabling data to be collected in a pump-probe approach. The large neutron bandwidth of EWALD ($\Delta\lambda$=3Å) coupled with a detector coverage of 5.1sr means that up to 70% of the unique Bragg reflections required to collect a complete data set can be collected from a single orientation of a PS-II crystal. The high resolution of EWALD (see Section 5.7.4) ensures that Bragg peaks can be resolved to a d_{min} value of 2 Å even from a PS-II crystal which has a maximum unit cell dimension of 308 Å. Recent progress has been made in the growth of larger crystals up to 0.5mm^3 of PS-II for neutron diffraction studies by the Yano group [Hussein et al. 2018]. As PS-II crystals contain a large macromolecular complex consisting of several subunits, coupled with a high solvent content (70%), data collection has not been feasible on MaNDi. Crystals of this volume would be suitable for neutron diffraction experiments on EWALD.

Membrane proteins (MPs) are core components of biological membranes and play a key role in the communication between cells, the transfer of information between the cell's inner and outer environments, and the transport of molecules and ions across the membrane. More than 30% of a cell's proteins are either embedded integrally into the membrane or associated with its periphery. Moreover, it is well recognized that MPs are the targets for over 50% of current drug formulations.

Many MPs are involved in the transport of molecules across cellular membranes; these mechanisms of transport are not well understood because x-rays cannot distinguish among different chemical species. However, these proteins and their complexes have proved difficult to crystallize into samples large enough for neutron diffraction studies. Ammonia transport channels (AMT) are MPs that serve as channels for the conductance of ammonia from the periplasm into the cytoplasm for archaea, eubacteria, fungi, and plants; in animals, they are closely related to the Rhesus family (Figure 5.39).

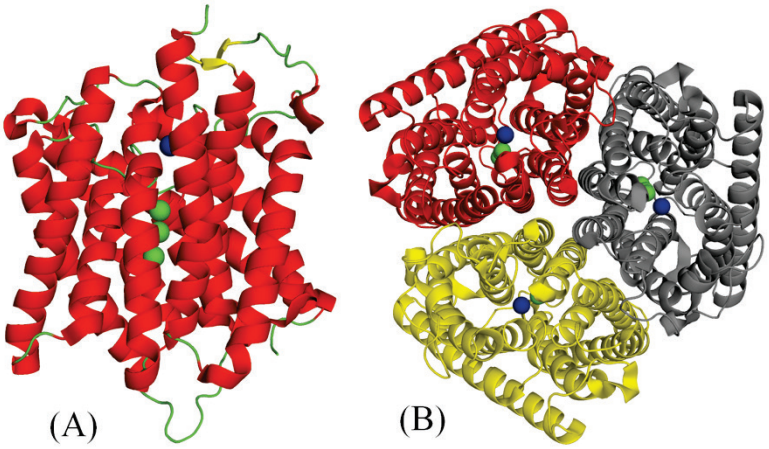

Figure 5.39. (A) The structure of a monomer of the *E.coli* ammonium transport protein (AMTb).

Three putative ammonia molecules are shown as green spheres, with a putative ammonium ion shown as a blue sphere. (B) The structure of the trimer formed by the ammonium transport protein within the cytoplasmic membrane.

For a bacterium, ammonia (NH_3) is an important nutrient that must be taken up from the surroundings to provide a source of nitrogen required for the synthesis of amino acids. The ammonium transfer (AMT) proteins are alpha helical bundles that span the membrane between the periplasm and the cytoplasm (the cell interior). They reside within the cell membrane and serve as entry and exit portals by which ammonia can be transported across biological membranes. In the membrane, they form a trimer, with each monomer containing an ammonia conducting channel. A key finding of the original x-ray structure determination at a resolution of 1.35 Å [Khademi et al. 2004] was the presence of three ammonia molecules within a membrane-spanning hydrophobic channel in the protein structure. The residues lining this pore and its entry sites are predominantly hydrophobic. It has been proposed that the soluble ammonium ions (NH_4^+) are converted into ammonia gas for transport across the membrane via this hydrophobic channel within the protein.

This conversion process is thought to take place in two vestibules present at either end of the hydrophobic channel. Ammonia is stabilized within the hydrophobic channel by two conserved histidine residues present within the channel and again becomes an ammonium ion when deposited into the vestibule in the cell interior. From x-ray diffraction data, even at 1.35 Å resolution, it is difficult to distinguish ammonia molecules from water molecules, as nitrogen and oxygen differ by only a single electron. The scattering power of hydrogen, with its single electron, is low in x-ray studies; thus, the electron density for H_2O and NH_3 is indistinguishable. This situation, coupled with the high thermal motion of the atoms in the hydrophobic channel (30–50 $Å^2$), makes it virtually impossible to discriminate between water molecules and ammonia molecules. With neutron diffraction, the situation is different: D_2O and ND_3 can easily be distinguished even at modest resolutions of around 2.0 Å. The neutron density for D_2O molecules is typically planar and banana-shaped, while the neutron density for ND_3 is larger triangular and nonplanar. The identification of the molecules in question would help to resolve conflict within the field, as some of the conclusions derived from the original structure are not in agreement with previous biophysical studies [Nakhoul and Hamm 2004]. The nature of the substrate for AMT proteins and their mode of action is still a highly contentious issue [Thornton et al. 2006].

5.7.2.2 Small Molecules

In addition to its ability to resolve large unit cells associated with macromolecules, EWALD is well suited to determining atomic positions and displacement parameters of light elements (such as hydrogen) next to heavy metals in small molecule. Moreover, the high detector coverage makes EWALD suitable for the study of magnetic structures, disordered structures, and phase transitions. Examples include catalytic and dihydrogen activation or exchange materials for the study of metal-hydrogen bonding in electrocatalysts and nanosize copper clusters. EWALD will enable accurate atomic position and atomic displacement

parameters for charge density studies of organic crystals, which contain a high percentage of hydrogen atoms. The small, highly focused neutron beam on EWALD also makes the instrument useful for extreme high-pressure studies, which intrinsically require the use of smaller samples. EWALD enables the use of smaller sample volumes, which correlate to higher pressures, and its optics design and distance from the source will reduce background levels and improve the signal-to-noise.

5.7.3 High-level Capability Requirements

The science case articulated for EWALD identifies the need for a single crystal diffractometer optimized for the study of small crystal volumes below 0.01 mm^3 with unit cell edges between 10 and 300 Å. EWALD has been designed to transport neutrons with wavelengths between 1 and 4 Å with a maximum beam size of 1mm^2 at the sample position, which provides the flexibility to study larger crystals when they are available. The detector solid angle coverage of 5.1 sr enables Bragg reflections to be measured up to 2θ angles of 160º; thus, data can be recorded up to a maximum resolution of d_{min}=0.6 Å, facilitating the collection of high-resolution data from small molecules. The high-solid-angle detector coverage coupled with the wide wavelength band enabled at STS enables simultaneous measurement of large volumes of reciprocal space, minimizing the number of crystal rotations required to collect a complete data set. Table 5.18 lists the key science requirements for the instrument. These key characteristics will allow EWALD to collect high-resolution single crystal diffraction data on both small and large molecules using crystal volumes as low as 0.1mm^3 to 0.001mm^3.

Table 5.18. Key capability requirements for EWALD.

Parameter	Description
Beam size at sample	1 to 0.001 mm^2 — variable
Detector solid angle	$\Omega > 5.1$ sr
d-spacing range	0.6 Å ≤ 20 Å
d-spacing resolution	$\delta d/d \leq 0.006$
Bandwidth (Δλ)	3 Å

5.7.4 Physics Design and Engineering Concept

The neutron optics system for EWALD (Figure 5.40) is based on a pair of nested elliptical KB focusing neutron supermirrors located at 54 m and 84 m from the moderator. These neutron supermirrors are 3m in length and 15 cm in height and image a neutron slit that will be positioned 5 m from the moderator. The opening of this slit will be demagnified (focused) by a factor of 30× (in area) at the sample position. By varying the size of the slit opening, we will be able to adjust the dimensions of the neutron beam at the sample position down to 0.001 mm^2. Using this mechanism, we will be able to closely match the beam size at the sample position to match the dimensions of the crystal to reduce background and increase the signal-to-noise ratio. Using this arrangement, we also will have no line of sight from the moderator to the sample position, further reducing background while preventing any fast neutrons and gammas produced during neutron production from reaching the sample position even in the event of a chopper failure. The horizontal and vertical divergence of the neutron beam at the sample is fixed by the KB mirror system at up to 0.38° FWHM across the wavelength band. This value was chosen because it matches the expected mosaic spread of crystals typically used for neutron experiments (Table 5.19).

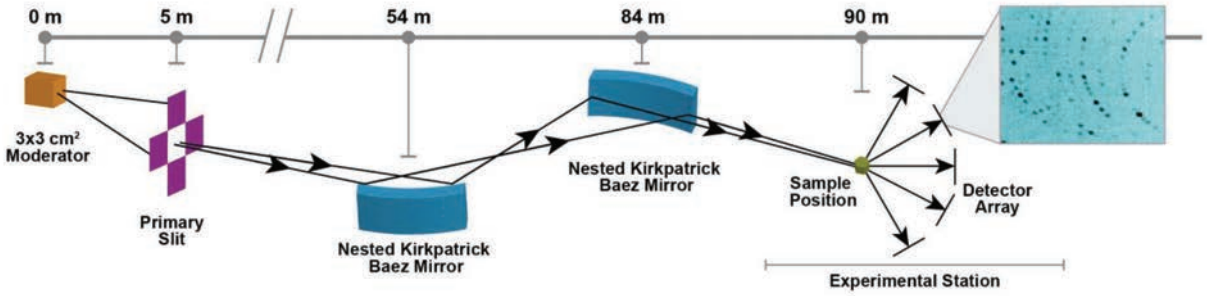

Figure 5.40. A schematic overview of the neutron optics on EWALD showing the location of the moderator, primary slit, Kirkpatrick-Baez (KB) neutron supermirrors, sample position, detector array, and diffraction pattern from a single detector module. *Source: Coates and Robertson. J. Appl. Crystallogr. 50, 1174–1178, 2017.*

Table 5.19. A list of the primary components of the EWALD beamline and their locations.

Component	Description	Location
	Beam delivery	
Flight tube	Evacuated flight tube	0.9 – 89.8 m
Slit	Defines beam size at sample position	Z = 5.8 m (in bunker)
First bandwidth chopper	2 disks @ 15 Hz, defines bandwidth	Z = 8.5 m (in bunker)
Second bandwidth chopper	2 disks @ 15 Hz, defines bandwidth	Z = 10.5 m (in bunker)
First mirror	Steerable KB mirror	Z = 54 m
Second mirror	Steerable KB mirror	Z = 84 m
Operations shutter	Primary shutter for daily operations	Z = 81.3 m
Flight tube	Evacuated flight tube	Z = 5.9 – 89.9 m
Beamline shielding	Bunker to cave	Z = 13.2 – 86.4 m
Sample location		Z = 90 m
Component	**Description**	**Location from sample**
	End station	
Shield cave		Z = –3.6/+3.0 m
Detector array	37 silicon photo-multiplier detectors providing 5.3 sr coverage	R = 0.34 m
Goniometer	Sample positioning for crystals	Z = 0 m
Pressure cell	Pressure device	Z = 0 m

Two bandwidth choppers positioned at 8 m and 10 m from the moderator will remove fast neutrons and gammas and select the neutron wavelengths to be used for each experiment. A secondary shutter located at 84.6m will allow easy change-out of samples. At the sample position (90 m), a high-precision goniometer will align and position the crystal into the neutron beam. Neutrons scattered from the sample will be detected by a semi-spherical array of next-generation high-resolution SNS Anger camera detectors based on silicon photo-multiplier technology. MaNDi [Schultz et al. 2005] views a poisoned, decoupled hydrogen moderator at the SNS FTS that gives sharp neutron pulses with short emission times (17.4 μsec FWHM at 2 Å), enabling the study of both small and large unit cell axes up to 300 Å. To ensure the same or better wavelength resolution for EWALD [Coates and Robertson 2017] as at the STS, which views a 3×3×3 cm high-brightness coupled moderator, requires an instrument around three times longer to account for the moderator pulse width difference (43.3 μsec FWHM at 2 Å). Thus, EWALD has a flight path length (moderator–sample) of 90 m, three times that of MaNDi. At this length and with the 15 Hz

repetition rate of the STS, EWALD will have a bandwidth ($\Delta\lambda$) of 3 Å, which is perfect for neutron crystallography as all useful wavelengths (1.0–4.0 Å) can be used in a single frame.

Resolution in macromolecular crystallography is defined by the minimum d-spacing (d_{min}) to which observed data are obtained (equivalently, Q_{max}), which is related to features within the structure in real space. It has been shown that for a TOF diffractometer to be able to resolve two Bragg peaks at a given d_{min}, the following equation must be satisfied [Schultz et al 2005]:

$$\Delta t_{pulse} \leq 505 L (d_{min}^2/a) sin\theta \,,$$

where Δt_{pulse} is the uncertainty in neutron emission time from the moderator in milliseconds, L is the beamline length in meters, and the maximum unit cell dimension, a, and d_{min} are in units of Å. Using this equation, we calculated maximum values for Δt_{pulse} at the EWALD instrument length for a d_{min} value of 2.0 Å and a maximum unit cell dimension of 300 Å at select wavelengths and scattering angles. Table 5.20 compares those values with the emission times of the STS cylinder moderator that EWALD uses.

Table 5.20. Calculated maximum allowable pulse widths and the corresponding pulse widths of the 3 by 3 cm coupled moderator at the STS, which EWALD views.

Theta θ (°)	Wavelength (Å)	d_{min} (Å)	Unit cell edge (Å)	L (m)	Δt_{pulse} (μs)	STS pulse (90% of full width) (μs)
31.5	2.12	2.0	300	90	317	266
41	2.60	2.0	300	90	398	299
47	2.90	2.0	300	90	443	299

As can be seen from Table 5.20, the emission times at each of the neutron wavelengths we evaluated are well below the maximum allowable pulse width required to resolve Bragg peaks at a d_{min} of 2 Å. That indicates that EWALD will easily be able to resolve Bragg reflections from unit cell sizes of 300 Å to d_{min} values of 2.0 Å and beyond. Thus, it will be able to identify proton and water molecule locations in real space even on large macromolecular complexes such as PS-II, which has a maximum unit cell edge of 308 Å.

The end station of the EWALD instrument (Figure 5.41) has been optimized to accommodate a range of single crystal experiments and sample environments. A sample goniostat is available at the sample position for standard single crystal data collections along with an optional nitrogen cryostream (100 K) or helium cryostream (15 K). A standard Arinax sample automounter will facilitate automated sample change-outs using crystal pins housed within the community standard universal puck system, and an on-axis video microscope will be used for sample alignment.

The detector array frame translates parallel to the neutron beam to allow unobstructed access to the sample position. A hexapod system will be able to translate into the sample position (Figure 5.42) to enable the use of diamond anvil cells for high-pressure studies of single crystal systems. Other sample hardware that may be translated into the neutron beam includes a dynamic nuclear polarization device, as described in Section 5.7.6.

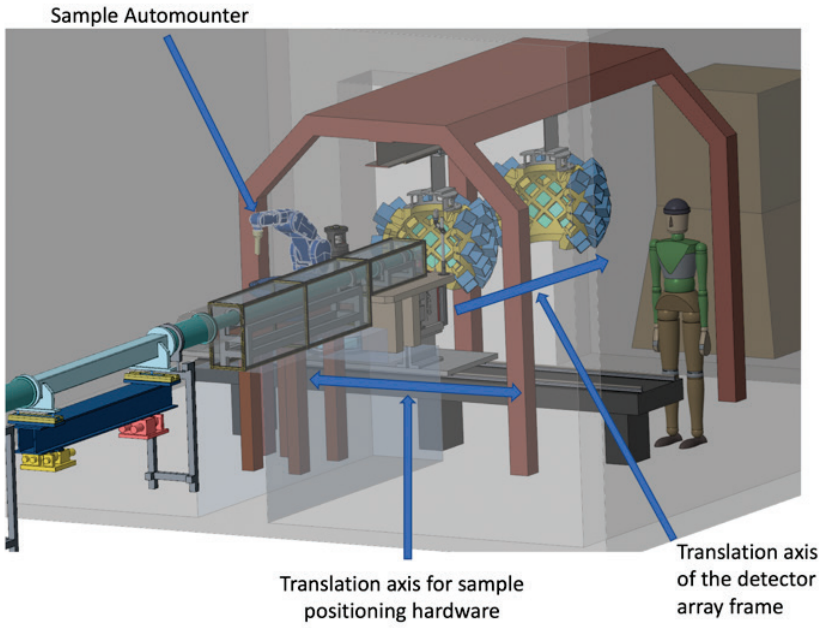

Figure 5.41. The end station of the EWALD instrument.

A standard sample automounting robotic arm will enable sample changes with crystals mounted using standard pins positioned in the beam with a goniostat. The detector array can translate downstream, parallel to the neutron beam, to provide access to the sample area. Sample hardware can be translated transverse to the neutron beam to switch between the goniostat and other hardware, including a hexapod for high-pressure studies.

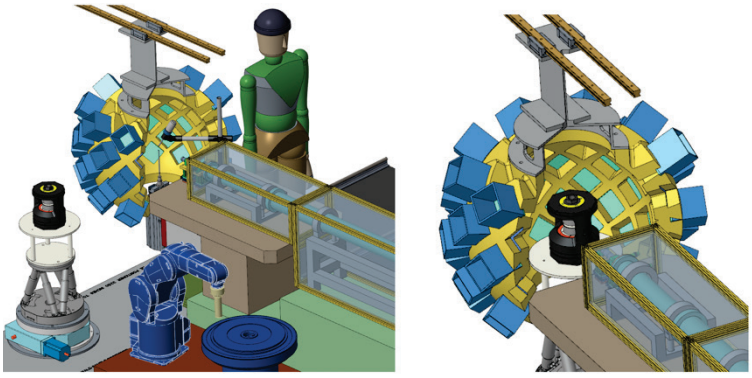

Figure 5.42. A closeup view of the sample position of the EWALD instrument. (a) A commercially available goniostat coupled with a nitrogen cryostream is shown at the sample position. In this setup, EWALD will be able to collect data from single crystals of small and macromolecular compounds. (b) A hexapod and a diamond anvil pressure cell are shown at the sample position; they will enable high-pressure studies on EWALD.

Using the McStas program, we were able to simulate the shapes of Bragg reflections using different crystal sizes, beam divergence values, sample-to detector-distances, and detector pixel sizes to ensure that the 3D profile fitting of Bragg reflections is possible. Profile fitting enables better estimations of the intensity of each Bragg peak, leading to more consistent and accurate data. To achieve valid profiles, each Bragg reflection should cover a grid of at least 5 by 5 detector pixels. For a given beam divergence the number of detector pixels a Bragg reflection covers can be increased by lengthening the sample-to-detector distance. However, for a set number of detectors, the solid angle coverage decreases when the sample-to-detector distance is lengthened. Therefore, it is more cost effective to place more highly pixelated detectors closer to the sample position to maximize detector solid angle coverage. After a series of iterations and optimizations, optimal Bragg reflection shapes were generated using a beam divergence of 0.38°, a detector pixel size of 0.3 mm, and a sample-to-detector distance of 0.3 m when a nominal crystal size of $0.01 mm^3$ is used (Figure 5.43).

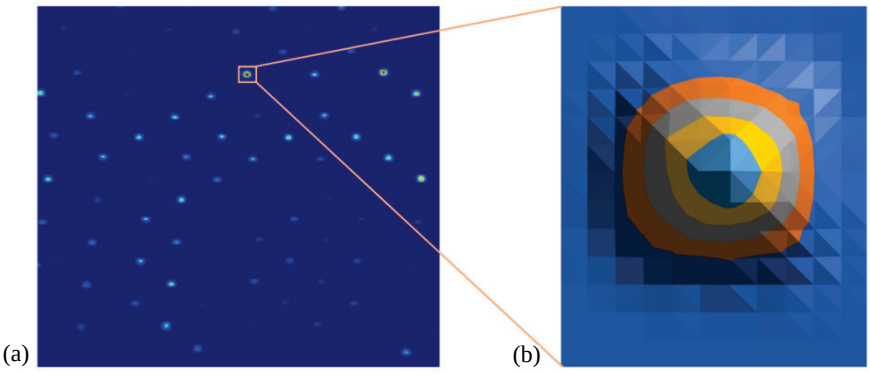

Figure 5.43. Simulated Bragg reflection data from a high-resolution SNS Anger camera module with a pixel size of 0.3 mm positioned 0.3 m from a macromolecular crystal with a volume of 0.01mm^3. (b) A close-up of a single Bragg reflection, which is spread over 81 detector pixels in a 9 by 9 array.

The EWALD end station is initially designed with 37 high-resolution-SNS Anger cameras (114 by144 mm), which are mounted on a semi-spherical movable detector array frame that can easily be retracted to allow for the installation of sample environments for data collection at low temperature or high pressure. The high-resolution-SNS Anger cameras will be placed 300 mm from the sample position with a pixel size of 300 by 300 micron. A list of the primary components in the EWALD beamline is given in Table 5.19.

5.7.5 Performance Estimate

The McStas program [Willendrup et al. 2014] was used to conduct several initial Monte Carlo simulations of EWALD to assess its performance relative to that of MaNDi [Coates et al. 2015] at the SNS FTS (Figure 5.44). On MaNDi, with a fixed beam divergence of 0.38° at the sample position, the flux on the sample is 1.3×10^5 n s^{-1} mm^{-2} for all neutrons between 2 and 4.16 Å. The higher-brightness coupled moderator available at the STS, coupled with a KB neutron optics system, allows the flux on sample at EWALD to be increased to 7.64×10^6 n s^{-1}mm^{-2} for all neutrons between 1.5 and 4.5 Å with a fixed beam divergence of 0.38° at the sample position; this gives a simulated gain factor in flux of 59×. For comparison with the mirror system illustrated in Figure 5.40, a more traditional elliptical guide was simulated. The flux on sample was 3×10^6 n s^{-1}mm^{-2}, a little less than half as efficient as the KB optics system. However, in the latter case, the beam size at the sample was far larger than the 1 mm^2 required, and the elliptical guide delivered approximately 1000× more neutrons outside the desired beam spot than inside the 1 mm^2. These neutrons will not contribute to the desired signal, since they will not intercept the sample; but they represent a significant source of background that would require shielding. The KB mirror system is far more efficient than a conventional elliptical guide.

The single crystal module of McStas was used to simulate peak shapes from a crystal 0.0156 mm^3 with parameters (mosaic spread, cell dimensions Δd/d), closely matched to those of real samples experimentally determined from experiments conducted at the Advanced Photon Source from macromolecular data (Table 5.21) [Langan et al. 2018]. The mosaic spread of the crystal, coupled with the divergence of the neutron beam and the variance in crystal lattice dimensions, defines the shape of the Bragg reflection at the detector position.

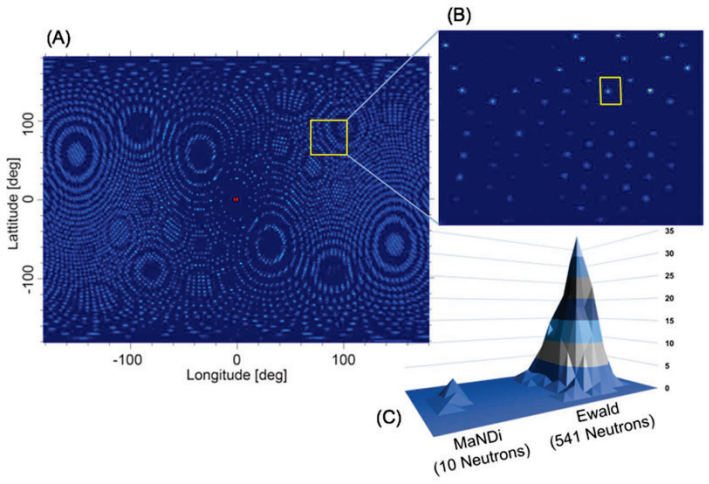

Figure 5.44. Monte Carlo simulated diffraction patterns from a protein crystal 0.01 mm^3 in volume on the EWALD instrument. (A) The complete set of Bragg diffraction peaks produced by the protein crystal at a hypothetical spherical detector located 300 mm from the sample. (B) A subset of diffraction peaks as observed by a single high-resolution SNS Anger camera at a 2θ angle of 90° is shown for EWALD. (C) Close-ups of a simulated Bragg peak corresponding to a resolution of 2.0 Å are shown for both EWALD and the current instrument, MaNDi. The simulated Bragg peak produced from EWALD is composed of 541 neutron counts, compared with just 10 from MaNDi, showing the ability of EWALD to collect meaningful data on protein crystal volumes of 0.01 mm^3 and less. *Source: Coates and Robertson. J. Appl. Crystallogr. 50, 1174–1178, 2017.*

Table 5.21. Single crystal parameters used for the Monte Carlo simulations shown in Figures 5.43 and 5.44.

Parameter	Value
Crystal size (mm)	0.25×0.25×0.25
Crystal volume (mm^3)	0.0156
Full-width mosaic spread (°)	0.3
Cell dimensions Δd/d	0.006
Sample-to-detector distance (mm)	300
FWHM beam divergence at sample (°)	0.38
Detector pixel size (mm)	0.3 x 0.3

5.7.6 Feasibility, Research and Development

Dynamic neutron polarization (DNP) uses a combination of high magnetic fields and low temperature to enhance and manipulate the nuclear polarization in macromolecular crystals, giving the ability to control the neutron cross section [Pierce et al. 2009, Pierce et al. 2010]. In situ control of the neutron cross-section will significantly enhance the contribution of hydrogen—which accounts for over half the atoms in a typical protein crystal—to the measured signal while simultaneously minimizing the incoherent scattering background. This will potentially further reduce the crystal size required for EWALD by a further order of magnitude (10×). EWALD has been flexibly designed to accommodate DNP equipment and sample environments.

Further work on the instrument design will include modeling of the effects of gravity on the neutron optics system, improving detector coverage, and ensuring that a range of sample environments can be accommodated at the sample position.

5.8 VERDI—VERSATILE DIFFRACTOMETER FOR MAGNETIC STRUCTURE STUDIES ON POWDER AND SINGLE CRYSTALS

5.8.1 Summary

VERDI will excel at diffraction studies of magnetism in powders and single crystals, allowing routine measurements of milligram-size samples, small-moment compounds, and diffuse signals. The instrument will probe magnetic local and long-range ordering in quantum materials that exhibit emergent properties arising from collective behavior. These insights will help reveal fundamental behavior in quantum magnets that will help drive development and understanding of the next generation of quantum materials with the potential to transform computers and data storage and raise the efficiency of energy storage and transmission. This diffractometer will be equipped with full polarization capability and will be optimized for studies under extreme conditions of temperature, pressure and magnetic field. Its unique use of polarized neutrons to isolate the magnetic signature in the measured data will enable detailed insight into local magnetic ordering.

This section presents a science case for the instrument; reviews the basic design concept, technical solutions, and performance estimates; and lists some R&D that is needed. VERDI will be a flagship diffractometer for the facility by offering world-leading capabilities for magnetic studies and is technically feasible to construct and operate.

5.8.2 Science Case

The overriding science driver for VERDI is the need for an instrument to probe ever more complex magnetic ordering, with neutron diffraction being the premier technique to extract the magnetic moment direction and magnitude and the short- or long-range periodicity. A major science focus will be quantum materials that exhibit emergent properties arising from collective effects in condensed matter. This will directly support the “Predict, Realize, and Probe New States of Quantum Magnets” thrust area identified in the recent DOE Basic Research Needs Workshop on quantum materials [DOE 2016]. Having an instrument capable of revealing fundamental behavior in quantum magnets will in turn offer ground-breaking technological opportunities, as stressed in the report: “Just as the discovery of semiconductors revolutionized computation and information storage, and ushered in today’s hundred-billion dollar electronics industry, quantum materials have the potential to revolutionize energy and energy-related technologies.”

The science case for VERDI echoes the findings from both the Basic Research Needs report and the Quantum Condensed Matter Workshop report [DOE 2014], which lists understanding “exotic ground states in quantum magnets” first in its list of Important Problem in Quantum Materials Research. Compelling research areas include exploration of small moment quantum magnets (including organic magnets and other S=1/2 materials); unconventional superconductors; quantum critical phenomena in magnetic insulators; itinerant magnets; spin glass materials; and diffuse scattering. To access these phenomena, the report says, “High efficiency diffraction, both powder and single crystal, is important to rapidly characterize both the crystal and magnetic structure of newly discovered materials.” [DOE 2014]. Additionally, it states, “Implementation of polarization analysis, particularly when combined with TOF instrumentation can provide critical information to understand the nature of exotic ground states including those with strong coupling between magnetic and lattice degrees of freedom.” [DOE 2014].

The following sections expand on a selection of scientific areas of current interest in quantum materials for which neutron diffraction experiments at VERDI are expected to make a major impact.

5.8.2.1 Spin-orbit Coupling and Correlated Electron Behavior in 5D Materials

5*d*-based compounds exhibit fundamentally new forms of spin-orbital intertwined, correlated, topological states, which offer avenues to quantum computing and spintronic applications (see Figure 5.45 for examples) [Pesin 2010, Witczak-Krempa et al. 2014]. The emergence of these new states is often characterized by unusual metal-insulator transitions (MITs) in which magnetic order evolves [Savary et al. 2014, Wang et al. 2017]. Consequently, neutron diffraction is essential to access the phase space; however, its use is severely limited by the small moment sizes, typically (~0.25 μ_B) in J_{eff}=1/2 iridates, and often by small sample sizes due to difficulties in sample synthesis as well as to the need to optimize the beam attenuation from highly absorbing isotopes. Therefore, no traditional neutron powder diffractometer in the United States has measured magnetic order in iridates.

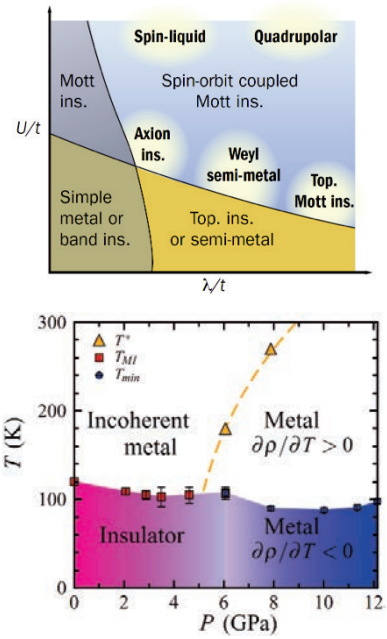

Figure 5.45 (Top) Generic phase diagram for electronic properties in terms of interaction strength, U/t, and spin-orbit coupling, λ/t. *Source: D. Pesin and L. Balants, Nat. Phys. 6, 376–381, 2010.* (Bottom) Pressure-temperature phase diagram for $Eu_2Ir_2O_7$.

The exotic behavior is exemplified in the pyrochlore iridates, $A_2Ir_2O_7$, where *A* is a rare earth. A series of magnetic and electronic phase transitions evolve by varying the *A*-site or applying pressure (<10 GPa) (Figure 5.45) to drive an MIT, which is concomitant with a magnetic phase transition [Tafti 2012, Matsuhira et al. 2007]. Some examples of proposed behavior are a chiral spin liquid and Weyl semimetal in $Pr_2Ir_2O_7$ [Machida et al. 2010] and $(Nd_{1-x}Pr_x)_2Ir_2O_7$ [Tian et al. 2016] and an anomalous pressure-driven MIT in $Eu_2Ir_2O_7$ [Tafti et al. 2012]. Little is understood, however, regarding the nature of these transitions and the novel emergent ground states. A principle hurdle is the inability to accurately characterize the nature of the magnetic ground state as it evolves from the insulating Mott state into anomalous regimes. This is an area where neutron scattering can have a tremendous impact.

There is a critical need for a high-flux and low background VERDI instrument that can probe small sample sizes (milligrams) with small ordered moments (<0.25μ_B). Such measurements should additionally be feasible in pressure cells, requiring tunable beam sizes. Accessing diffuse signals—which, for example, would reveal indications of a chiral spin liquid in the metallic state or the underlying physics at the critical point—would provide key insights in the novel topological behavior inherent to the MIT.

5.8.2.2 Determination of Complex Field- or Pressure-Induced Incommensurate Long-range Magnetic Order in Quantum Magnets

Quantum magnets are natural realizations of gases of interacting bosons whose relevant parameters such as dimensionality, lattice geometry, amount of disorder, nature of the interactions, and particle concentration can vary widely [Zapf et al. 2014]. The particle concentration can be tuned easily by applying an external magnetic field or pressure. These external stimuli play the role of a chemical potential, and the system can be driven from a state with no bosons to a state with a finite number of bosons, thereby creating a quantum phase transition [Giamarchi et al. 2008]. Neutron diffraction is uniquely sensitive to directly probe the static ordered magnetic moment in the induced ordered states. In some cases, the spin ordering becomes extremely complex, characterized by one or more incommensurate wave-vectors [Garlea et al. 2009]. For instance, there are rather unusual broken symmetry states that

could be stabilized in frustrated quantum magnets. $Ba_3Mn_2O_8$, Sul-Cu_2Cl_4, and Cs_2CuCl_4 are three examples in which frustration leads to spiral structures with incommensurate wave vectors (Figure 5.46).

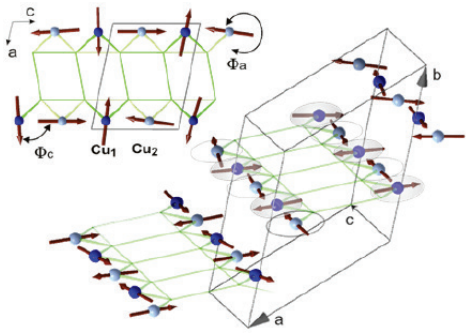

Figure 5.46. Incommensurate helical structure induced by magnetic fields in Sul-Cu_2Cl. *Source: V. O. Garlea et al. Phys. Rev. B. 79, 060404, 2009.*

Such systems are characterized by at least two different lowest-energy modes k = ±Q, and bosons condense into a multi-Q Bose-Einstein condensate state. It has recently been shown that a plethora of multi-Q condensates can also be stabilized in highly frustrated quantum spin systems with *p*-fold symmetric lattices where $p \geq 3$. These can lead to the emergence of novel magnetic vortex phases similar to the already known Skyrmion lattices [Kamiya and Batista 2014]. The possibility of stabilizing magnetic crystals of topological spin structures opens a new road for studying and exploiting magnetoelectric coupling in Mott insulators.

A VERDI instrument is needed to probe complex incommensurate and multi-Q magnetic structures as they evolve with magnetic field and/or pressure. This requires high resolution at low Q to precisely define the magnetic reflections. A magnet and instrument with sufficiently wide Q-coverage are needed to accurately determine the crystal lattice and subsequently the magnetic propagation vector.

5.8.2.3 Short-range Magnetic Order with Polarized Total Scattering (mPDF)

The total scattering method provides powerful real-space insights into systems with local disorder or distortions by determining the atomic pair distribution function (PDF) from the Fourier transform of a measurement that includes both Bragg and diffuse scattering. Recently PDF has been extended to include the magnetic spin (mPDF) to give access to local spin correlations [Frandsen et al. 2014]. This offers the potential for myriad new insights. Studies where mPDF is expected to have a strong impact include frustrated compounds where local disorder and short range correlations dominate, multiferroics where subtle structural and magnetic interactions couple to the ferroic phenomena, magnetic semiconductors where doping introduces local spin alterations as shown in Figure 5.47, spin glasses where structural disorder suppresses long-range order, understanding short-range correlations in magnetic systems from standard [Frandsen et al. 2016] to frustrated [Frandsen et al. 2017] magnetism, and distinguishing between single-k and multi-k structures in powders.

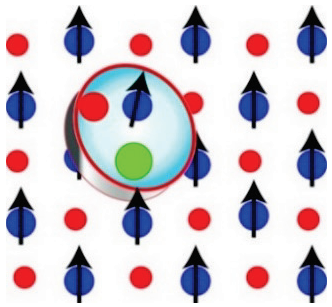

Figure 5.47. Changes in the local crystal structure, such as the substitution of a red atom for a green atom or the introduction of defects/vacancies, can lead to changes in the local magnetic structure.

Currently, mPDF analysis is typically done in conjunction with atomic PDF. This can lead to ambiguity because the magnetic scattering is typically much weaker than the nuclear scattering. Moreover, this route

necessitates a large Q_{max} >20 Å^{-1} to resolve the atomic PDF before accessing the mPDF information, which limits the available beamlines and therefore the sample environments.

VERDI can fill this void to become the world-leading mPDF instrument by allowing extraction of the magnetic signal with full polarization analysis. This will remove the need for traditional atomic PDF analysis, which consequently reduces the required Q_{max}. Considering 3*d*-based materials, the Fe or Cu magnetic form factor results in essentially no intensity at Q>8 Å^{-1}. For 4*d*/5*d* materials, the required Q_{max} is reduced further.

5.8.2.4 Measurements of Diffuse Features in Highly Frustrated Magnets with Polarized Neutrons

The two-in, two-out spin ice configuration is a highly degenerate ground state that exists on certain pyrochlore lattices and has been shown to host emergent magnetic monopoles [Castelnovo et al. 2008]. The magnetic state arises from the magnetic dipole-dipole interaction between the spins with local exchange interactions being of secondary importance. The "ice-rule" is not purely a local effect but is stabilized by both the near-neighbor and long-range part of the dipolar interaction, making it an emergent, many-body property [Fennell et al. 2009, Fennell et al. 2007, Sibille et al. 2018]. The key experimental signatures of either the "real" or "effective" dipolar correlations are expected to be pinch-point singularities, bow-tie–like diffuse features centered on nuclear Bragg positions, (Figure 5.48).

Polarized neutron experiments can be designed at VERDI to measure two independent components of the tensor $S^{\alpha\beta}(Q)$ that are typically labeled as spin flip and non–spin flip, making it possible to separate the contributions of the components of spin correlations in and out of the scattering plane, as was done to reveal pinch-points shown in Figure 5.48. To access further topologically constrained properties in frustrated systems requires a VERDI instrument with polarization, high flux, and low background.

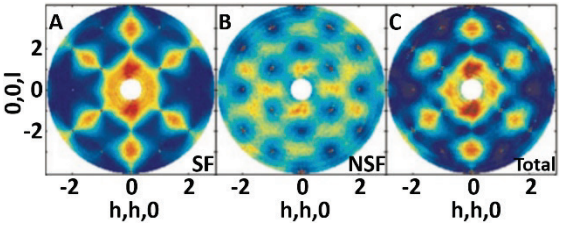

Figure 5.48. Diffuse scattering maps from spin ice, $Ho_2Ti_2O_7$. Experimental (a) spin-flip (SF), (b) non–spin flip (NSF), and (c) total.

5.8.2.5 Complex Quantum Organic Magnets and Spin-Density Plots

Magnetic organic compounds offer an unparalleled route to chemically design materials with tailored quantum phenomena. One promising class is hybrid compounds, metal-organic frameworks (MOFs), composed of distinct metal and organic building blocks on a regular crystalline framework, which offer a highly tunable motif and near- limitless combinations of the basic building blocks. MOFs have revolutionized diverse areas of science including drug delivery, gas storage, catalysis, and chemical separation. However, many properties and applications remain to be discovered, and investigations of magnetism are in their infancy. MOFs have been described as a gold mine for low-dimensional and frustrated magnetism [Kurmoo 2009]; and their future fundamental and applied scientific impact is undeniable, with promising routes to spintronic applicability [Talin et al. 2014, Sheberla et al. 2014].

A VERDI instrument would be able to uncover the potential of MOFs by accessing the following phenomena:

- The spin can be dispersed over organic linkers, requiring polarization measurements to reveal the spin interaction, direction and location through magnetization density plots. See Figure 5.49 for calculations on a quasi-low-dimensional quantum magnet MOF [Dos Santos et al. 2016].

- The dimensionality of the crystalline framework can be tuned to host 1D or 2D quantum behavior with diffuse short-range magnetic interactions [e.g., Harcombe et al. 2016] that require an instrument with excellent signal to noise and polarized capabilities.

- The large unit cell size and complex interaction pathways will result in low Q and incommensurate scattering [Fabelo et al. 2011], necessitating high resolution and large coverage to low Q to define the crystal and magnetic unit cells.

- The porosity of the materials will allow the physics to be readily tuned with pressure and applied field, and the weak interactions will require low temperatures.

- Strong magneto-coupling and the ability to combine magnetism with tailored properties from organic linkers require simultaneous understanding of the spin and lattice, requiring large Q coverage and high resolution.

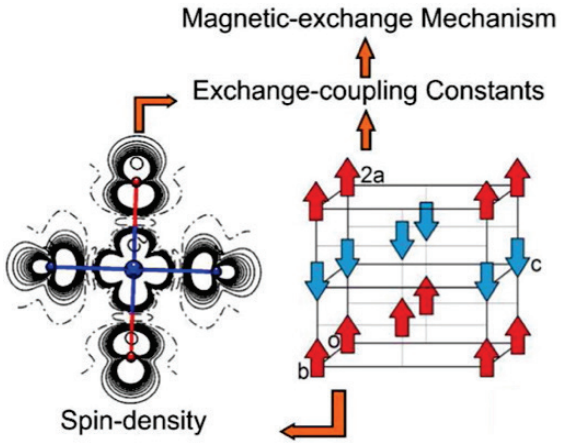

Figure 5.49. Spin density measurements with polarized neutrons in organic magnets to access spin interactions. *Source*: *Reprinted with permission from L.H.R. Dos Santos et al. 2016. "Experimental and theoretical electron density analysis of copper pyrazine nitrate quasi-low-dimensional quantum magnets," J. Am. Chem. Soc. 138(7), 2280−2291). Copyright (2016) American Chemical Society.* https://pubs.acs.org/doi/10.1021/jacs.5b12817

5.8.2.6 Multiferroics: Deeper Insights with Polarization

Multiferroics are materials that simultaneously exhibit multiple ferroic properties, including ferromagnetism, ferroelectricity, ferroelectricity and ferrotorodicity; polarized neutron measurements are required to uncover the latter [Ressouche et al. 2010, Baum et al. 2013]. The coupled properties offer both fundamental interest and appealing future applicability. Polarization analysis allows a unique tool to probe and distinguish between the intertwined interactions. One such example is found in the material $Ni_3V_2O_8$ (Figure 5.50). The ferroelectricity in this compound is of magnetic origin and emerges from a cycloidal spin order. An unresolved question that was answered by polarized neutron scattering was to show that the spin helicity, that is, the sense of rotation of the spins within the cycloids (clockwise or counterclockwise), was connected to the direction of the spontaneous electric polarization. This was then used to control this sense by an electric field applied on cooling the sample.

VERDI, with full polarization analysis, will be able to tackle complex forefront science problems not currently accessible. The combination of high flux, extreme sample environments, and resolution is crucial for unambiguous measurements of emergent magnetic phenomena in powders and single crystals.

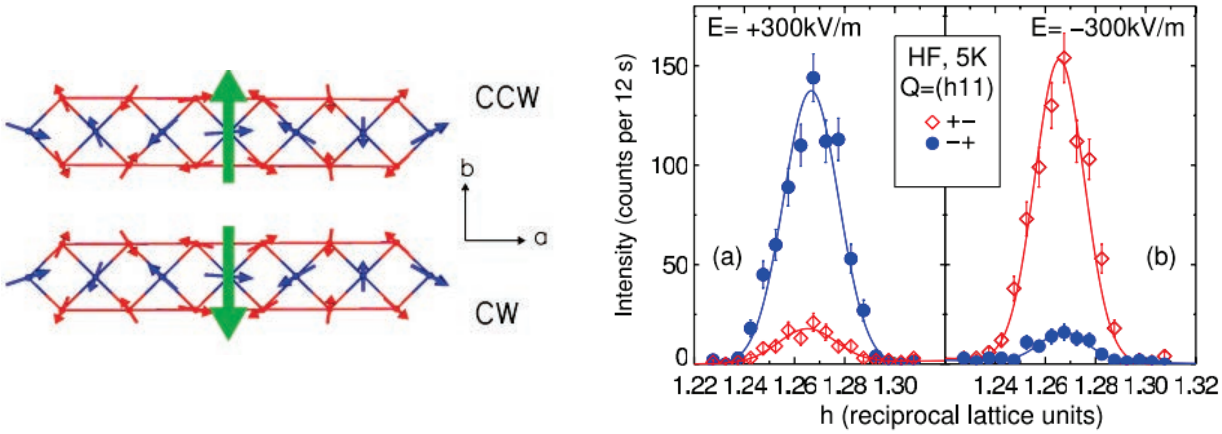

Figure 5.50. (Left): Spin cycloids propagating in $Ni_3V_2O_8$.

The green arrow indicates the electric polarization direction. (Right): full polarized magnetic diffraction in an electric field to reveal the magnetic ordering. *Source: Ressouche et al., Phys. Rev. B 82, 100408, 2010. Used courtesy of Creative Commons.*

5.8.2.7 Science Cases beyond Quantum Materials

The science focus will be primarily on magnetic materials, a broad and key area of material research that will continue for decades to come. However, there are great opportunities to expand the impact of VERDI into other areas. The implementation of polarization allows the isolation of not only magnetic scattering but also incoherent scattering. This offers clear advantages to the study of nonmagnetic hydrogen-based materials. Therefore, given the instrument characteristics, it is expected that large unit cell nonmagnetic organic materials will be well suited to study on VERDI.

5.8.3 High-level Capability Requirements

The overriding scientific driver for VERDI is to probe magnetic order in powders and single crystals. The emphasis, therefore, is on offering high resolution at low momentum transfers, which can be traded for higher flux as required, with a low background. Flexibility in beam divergence is required to allow measurements of both powder and single crystals, as well as different sample sizes.

Accessing low Q, $Q_{min} \approx 0.1$ Å^{-1} (d≈65 Å), is critical; however a large Q-range is still necessary for most of the anticipated science. For example, a large Q-coverage is required to accurately define incommensurate magnetic propagation vectors, since doing so relies on an accurate determination of the crystal unit cell. Moreover, magnetic PDF studies need access to both low Q as well as a $Q_{max} \approx 8$ Å^{-1}. To provide the necessary Q-range in a single wavelength band, a wide bandwidth is required, combined with wide detector coverage. The STS low source frequency of 15 Hz coupled with the appropriate instrument length near 40 m will naturally supply a large single-frame bandwidth of ~6 Å with a wavelength range of 1–7 Å to achieve these Q-range requirements. The option to access other wavelength frames or run at half frequency (7.5 Hz) to double the Q-range accessible for each diffraction angle will provide further flexibility in increasing Q coverage.

A resolution of $\Delta Q/Q \approx 0.3\%$ is required to investigate complex magnetism, such as incommensurate magnetic structures. The resolution will be variable to allow high resolution and high flux modes as required.

Low background (excellent signal-to-noise ratio) is crucial to investigate small magnetic signals and/or milligram-size samples and is a central consideration driving all aspects of the instrument design. This has led to the consideration of a curved guide layout to avoid a direct line of sight to the moderator and mitigate background from fast neutrons and gammas.

Full polarization is a key science-driven requirement. Automated changing between unpolarized, half-polarized, and fully polarized options will be required. This flexibility will allow unpolarized measurements to be performed without any loss of flux in the guides.

Both powders and single crystals will be measured. To accommodate the different sizes of powder/crystal samples, a variable beam size from 3 by 3 mm (crystals) to 10 by 10 mm (powders) will be needed. Therefore, the beam divergence will need to be variable: 0.2–1° horizontal and 2–3° vertical for powders and symmetric 1° horizontal and vertical for single crystals.

To measure both powders and single crystals, a large horizontal detector coverage, covering 320° (2 × 160°), is needed for the wide Q-range. For single crystal measurements, continuous detector coverage and sufficient out-of-plane coverage is required. The detectors must be able to operate in the presence of stray magnetic fields.

Dilution temperatures, magnetic fields, and pressure measurements are expected to be routine; therefore, the sample area should be able to accommodate them. Sample translation and centering capabilities should be incorporated. A dedicated magnet for fields >14 T is anticipated to satisfy the science cases for measuring magnetic structures in applied fields. The magnet will require customization to give full Q coverage and optimized out-of-plane coverage. The instrument construction materials will be chosen to allow such a magnet.

VERDI is located on ST13 and will face the cylinder coupled para-hydrogen moderator with a 3 by 3 cm viewed area. The position makes it one of the furthest instruments from the position identified for the extreme magnetic field instrument concept, ZEEMANS, which may be located on STS beamline ST02. This will mitigate any effects from stray fields from ZEEMANS on the polarized operation at VERDI.

In the context of the neutron suite at ORNL, VERDI will be unique in being a wide-wavelength bandwidth diffractometer optimized for magnetic studies. All the other current or planned SNS diffractometers with powder capabilities that are situated at the FTS make use of a narrow bandwidth at short wavelengths for their science focus. Instruments at HFIR (HB-2A/WAND^2) currently offer strong options for magnetic structure determinations; however, they have limited Q-range and resolution. Therefore, VERDI will greatly complement the current oversubscribed diffraction suite at ORNL by offering higher wavelengths (lower Q), lower background, and higher resolution at low Q to allow ORNL to lead the way in tackling ever more complex magnetic science problems not feasible on the current instrumentation. Presently, the WISH instrument located at ISIS-TS2 is the most analogous instrument in current operation worldwide and is widely considered the world-leading powder diffractometer for magnetic studies. The operating frequencies of ISIS-TS2 (10 Hz) and SNS-STS (15 Hz) are similar; however, the peak brightness at the STS will be over an order of magnitude larger. With the addition of full polarization and optimized guides, VERDI will set a new standard for a world-class magnetic diffractometer, with versatility for both powder and single crystal samples. Table 5.22 lists the key capability requirements for VERDI.

Table 5.22. Key capability requirements for VERDI.

Parameter	Description
Beam size at sample	3×3 mm to 10×10 mm — variable
Variable beam divergence	0.2° to 1° (H), 2° to 3° (V): powders 1°(H), 1° (V): single crystal
Q-range	0.1 $Å^{-1} \leq Q \leq \approx 8$ $Å^{-1}$
Q-resolution	$\Delta Q/Q \approx 0.3\%$
Bandwidth (Δλ)	6–7 Å (15 Hz)
Polarization	Polarized beam and wide-angle analyzer
Ambient conditions	Low changing magnetic field interference

5.8.4 Physics Design and Engineering Concept

The optimal moderator–sample instrument length is 40 m, based on McStas simulations (see Section 5.8.5). This distance is identical to that of the WISH instrument at ISIS-TS2, despite the different neutron moderator pulse widths, which would suggest a longer instrument length for VERDI to achieve the same wavelength resolution. Extending VERDI beyond 40 m, however, offered negligible improvement in resolution and would have raised the cost of the guide/shielding and reduced the flux on the sample by lowering the wavelength bandwidth.

A curved/deflected guide layout, shown in Figure 5.51, as opposed to a guide providing a direct view of the moderator, offers the lowest-background option and therefore fulfills a key science-driven requirement. This choice cuts off wavelengths below 1 Å; however, it will not compromise the science-driven $Q_{max} \approx 8$ $Å^{-1}$ or required bandwidth. The VERDI horizontal guide concept allows for both a high-resolution powder mode, a high-intensity single crystal mode, and a polarized beam option. It uses several elliptical guide pieces, some of which can be exchanged mechanically. The first guide is the same for all modes. It starts at 6.35 m at an initial displacement of 84 mm and ends at 26.9 m with a displacement of 75.5 mm off axis. The ellipse is defined by $y = 2b \cdot \mathrm{sqrt}(x/L \cdot (1 - x/L))$, where b is the semi minor axis (10.5 cm), x is the coordinate along the beam, and L (the major axis of the ellipse) is the distance between the moderator and the secondary source: 31.75 m. The second guide piece after the secondary source has two configurations to provide the high-resolution and high-intensity modes, which are identical to the polarized option up to an exchangeable guide option to switch between polarized and unpolarized beam. (1) For high-resolution mode, the second elliptical guide piece starts at 32.93 m with a displacement of −17.5 mm at the entrance. The exit is at 36.46 m, displaced by −24.74 mm (b=2.5 cm). (2) For high-intensity mode, the second guide piece starts at 35.05 m, displaced by –49 mm, and ends at 37.5 m with an exit displacement of −18.37 mm (b=5 cm). The major axis of the ellipse is 8.25 m for both cases. An interchangeable polarizing supermirror will follow the guide setting of the high-intensity mode. A supermirror ratio of m = 3.6 would be enough to secure reflection of neutrons over a 1 Å wavelength for polarized operation.

The overall shape of the vertical guide is an ellipse with a semi-minor axis of 19.78 cm and a semi-major axis of 18.06 m. Since the vertical guide attaches to the horizontal counterparts described above, it has several interruptions that cause gaps. The individual guide pieces are therefore slightly offset against each other to prevent holes in the sample illumination. The ellipse is coupled with a feeder guide (1.27 m long) starting at 6.18 m and tapering in width from 2.38 cm to 2.4 cm.

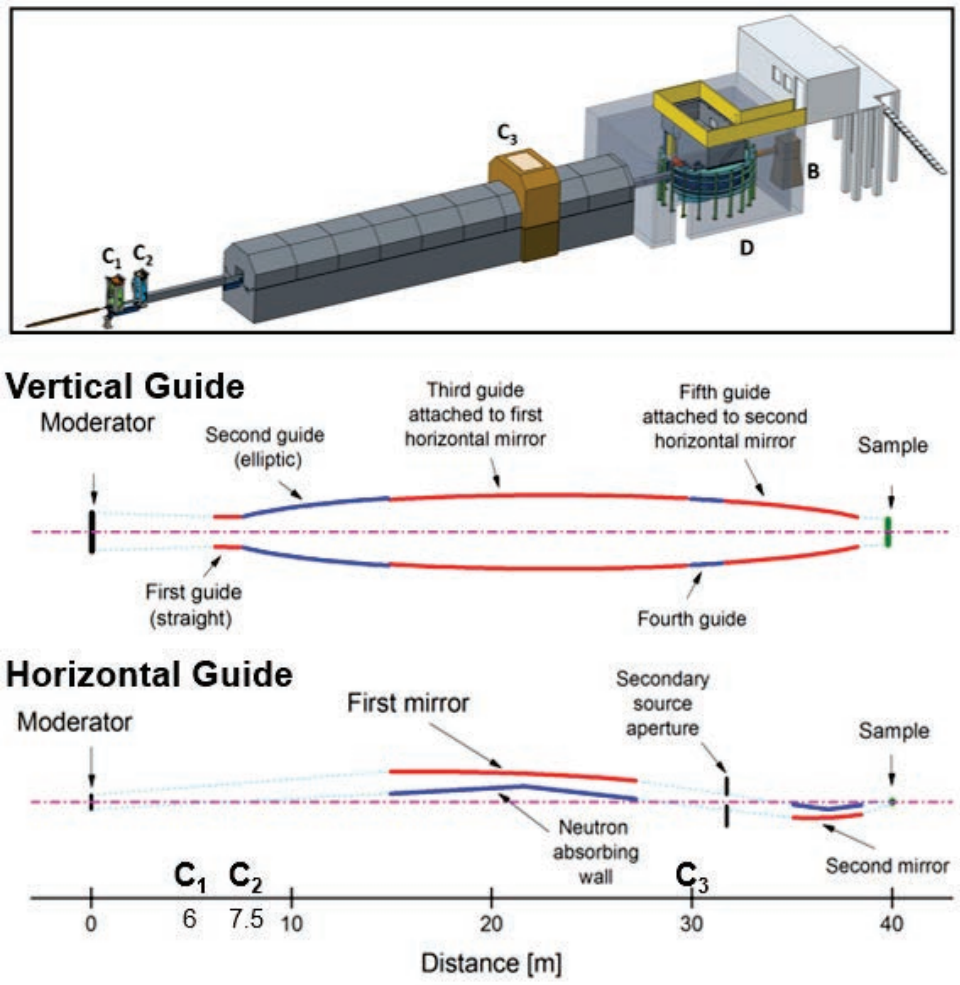

Figure 5.51. Engineering concept of VERDI (top, inset) and schematic of curved guide layout. The main components are labeled, with C corresponding to choppers, D to detectors, and B to beam stop.

Three choppers (Figure 5.51) will be located at 6 m (double disc, C_1), 7.5 m (single disc, C_2), and 30 m (double disc, C_3) to define the bandwidth and suppress band overlap, informed by McStas simulations (see Section 5.8.5). This combination will allow the instrument to run at the natural source frequency of 15 Hz, be phase-shifted to access other wavelength bands, or run at half frequency (7.5 Hz) to double the Q-range accessible for each diffraction angle.

The sample area will be composed of a top-loading vacuum tank. The dimensions will be similar to those of POWGEN and will support a full set of sample environments as well as Helmholtz coils around the sample position, which will be used during measurements with polarized neutron beam.

An oscillating radial collimator composed of Mylar blades will define a small sample volume, an ~ 20 mm radius cylinder that the detectors will view to minimize background from non-sample scattering. This will be interchangeable with a solid angle polarizing supermirror array on one side of the instrument. The other side will have a fixed oscillating radial collimator with high out-of-plane coverage. The curved analyzer will be located on an elevator, enabling easy user selection between it and the oscillating radial collimator during measurements. A curved supermirror analyzer with 60° in-plane and ±7° out-of-plane coverage is operational on HYSPEC at the SNS FTS. Consequently, it is anticipated that more than one analyzer will be required to achieve full angular coverage on VERDI. Ideally two 75–80° analyzers will

be used, if fabrication technology has progressed; otherwise, four 40° mirrors can be readily used. Out-of-plane coverage will be increased to ±13°.

To ensure reliability and ease of troubleshooting, the current concept has the collimator/analyzer in air between the vacuum tank and an argon-filled tank filling the remaining volume out to the detectors. Key considerations include the thickness of the windows on the argon tank. Additional options will be explored during preliminary engineering design. The detectors will be in air, allowing ease of access.

A logarithmic spiral detector design like that deployed on POWGEN, as opposed to a cylindrical design, best supports the science case of high resolution at low-Q. Distances from the sample will be 3.1 m at forward scattering (5°) and 1.2 m at backscattering (165°). It is anticipated that both sides of the instrument will have full detector coverage in the scattering plane (horizontal angular range of 5° to 165°). However, given the anticipated cost associated with the curved polarizing supermirror analyzer, only one side will offer full polarization analysis. In addition to full in-plane angular coverage, the other side of the instrument will add out-of-plane coverage over a horizontal angular range of 45–135° from a second row of ^{3}He detectors. This will give out-of-plane coverage of +35° in this region to enable more efficient single-crystal measurements.

Helium-3 detector tubes are the preferred detector technology because they can offer the required full gapless coverage, pixel size, compatibility with stray fields, and gamma discrimination. These are a proven technology and so represent minimal unknown risks; however, as technology advances, further options for detectors will be considered. Helium-3 tubes 1 m tall will give suitable out-of-plane coverage of ~ ±13°, which will increase to +34° upon the addition of an out-of-plane row, as discussed earlier. Tube diameters of 8 mm or 12.7 mm (0.5 in.) are under consideration. Final selection will be based on the results of detailed simulations and consideration of the increased cost associated with the smaller diameter. The inefficiencies at the edges of the tubes will potentially impact single crystal measurements; however, most measurements will be performed at several crystal rotations, which should mitigate the issue. Nevertheless, consideration will be given to a two-row staggered detector layout over the single-row detector layout currently in the VERDI concept.

Table 5.23 lists the key instrument components and their positions along the beamline.

Table 5.23. Major VERDI instrument components and their positions.

Component	Description	Location
	Beam delivery	
Neutron guide	Curved / deflected flight path	Z = 6.35 – 37.5 m
Chopper (C_1)	2 disks @ 15 Hz, defines bandwidth	Z = 6.06 m (in bunker)
Chopper (C_2)	1 disks @ 15 Hz, prevents frame overlap	Z = 7.5 m (in bunker)
Operations shutter	Shutter for daily operations	Z = 11.8 m
Chopper (C_3)	2 disks @ 15 Hz, defines bandwidth	Z = 30 m
Horizontal guide 1	Elliptical mirror	Z = 32.93 – 36.46 m (HR)
Horizontal guide 2	Elliptical mirror	Z = 35.05 – 37.5 m (HI/Polarized)
Guide sections	Vertical feeder guide	Z = 6.18 – 7.45 m
Slit system (AS)	Redefines secondary source size and dimensions	Z = 31.75 m
Beamline shielding	Bunker to cave	Z = 13.2 – 35.5 m
Sample location		Z = 40 m

Table 5.23. Major VERDI instrument components and their positions (continued).

Component	Description	Location from sample
	End station	
Shielded cave	Contains detectors	Z = –4.5/+4.5 m
Detector array	Logarithmic spiral detector layout. ~240 8-packs of 8 mm PSD ^{3}He tubes or ~150 8-packs of 0.5 in. ^{3}He tubes	R = 1.2 – 3.1 m
Sample vacuum tank	Houses sample environment	R = 0.5 m
Argon tank	Reduce scattered beam background	R = 1.2 – 2.9 m
Elevator with collimator/analyzer	Supermirror analyzer installed only on one side to cover 160° horizontal scattering plane (1 m tube).	R = 1.2 m
RF flipper and guide field for XYZ polarization	RF flipper for controlling direction of polarization of incident beam. Helmholtz coils for providing variable direction guide fields at the sample position	

5.8.5 Performance Estimate

Monte Carlo simulations using the McStas package have been performed to inform the VERDI concept and ensure that the instrument concept achieves the science-driven key instrument capabilities. Collectively, these simulations have guided development of the initial instrument concept described. The main results are described below.

Simulations were performed for a range of moderator to sample (L_1) lengths from 30 m to 60 m and neutron beam angular divergence of 0.1° to 1.0°. These simulations did not include the effects of neutron choppers or guides, which are required to define the neutron bandwidth and optimized to deliver the simulated neutron beam divergence. The results are illustrated in Figure 5.52 as “onion plots” that show instrument resolution as a function of detector radius in concentric rings around the sample from 1 to 4 m. One of the key VERDI performance parameters is to achieve the desired Q-resolution at the lowest Q, which is obtained at the lowest detector angles. Increasing the instrument length beyond 40 m had a negligible effect on improving the resolution at these low scattering angles. Therefore, the instrument length was set at 40 m.

The neutron optics system described previously and in Table 5.23 was modeled to generate an estimate of performance for two modes of operation, high-resolution powder samples and high-intensity single crystal samples. The beam size and angular divergence from these calculations are shown in Figure 5.53. For powder measurements, the beam is defined by slits of 11 by 11 mm and divergence of ~0.23° (FWHM). For single crystal measurements, the beam is 5 by 5 mm with a divergence of ~0.9° (FWHM). The peak flux for high-resolution powder mode is 4.77×10^7 n/s·cm^2·Å and for high-intensity single crystal mode is 4.35×10^8 n/s·cm^2·Å. These guides offer the required neutron beam sizes and angular divergences for both modes. Calculations were done of the brilliance transfer that reflects the efficiency of the guide at transporting the desired neutron phase space to the sample position. As shown in Figure 5.54, this guide system is highly efficient, although careful consideration and optimization of guide coatings will be required to deliver the desired lowest neutron wavelength of 1 Å to the sample location.

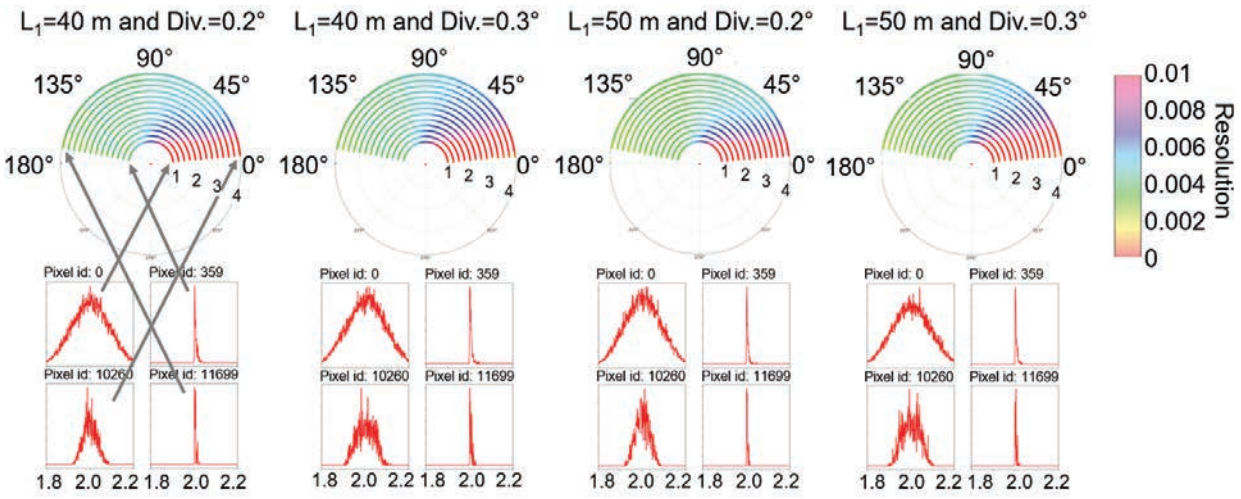

Figure 5.52. McStas simulation of resolution as a function of scattered angle (2θ) and distance from sample (m) of a 2Å peak. The simulations were done for selected moderator-to-detector distances (L1) and for different neutron beam angular divergence as indicated in the figure.

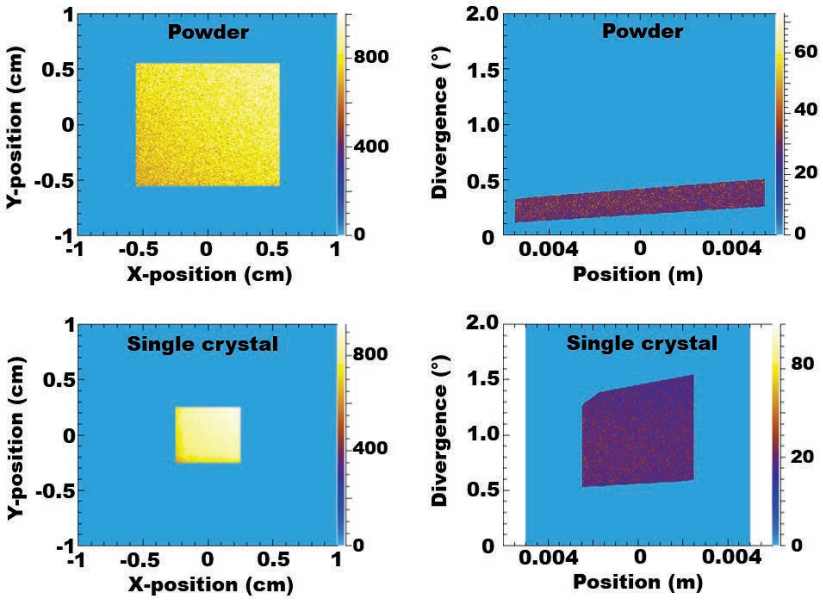

Figure 5.53. Simulated beam dimension and divergence resulting from the guide concept for high-resolution powder mode and high-intensity single crystal mode.

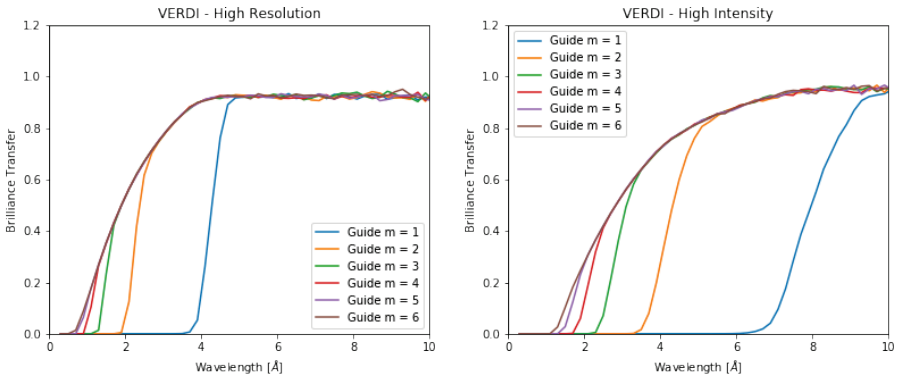

Figure 5.54. Brilliance transfer for two operating modes of VERDI, high-resolution powder (a) and high-intensity single-crystal (b). Beam conditions were as described in the text. Calculations were done for the indicated series of guide coatings. For simplicity, these coatings were used for the entire guide surface. Detailed optimization will use the highest index guide coatings only in the required locations.

Neutron choppers are required to define the neutron wavelength band at the detectors so that fast neutrons from subsequent source pulses do not overlap with the slowest desired neutrons from the previous pulse. Two neutron choppers located at 6 m and 7.5 m respectively from the moderator will combine to eliminate frame overlap (Figure 5.55) for both 15 Hz and 7.5 Hz frame-suppression modes of operation. An optional third chopper loctated near 30 m from the moderator will provide a sharper bandwidth definition, maximizing the range of neutron wavelengths that can be used. This effect is illustrated in Figure 5.56. With these chopper locations and a 40 m distance from the moderator to the sample, VERDI has an operating wavelength range of 1 to 6.75 Å with a central wavelength of 3.9 Å. This bandwidth could be shifted to longer wavelengths to provide a central wavelength of 9.4 Å and extend to a maximum wavelength of 12.3 Å (not shown). Operating in frame-suppression mode at 7.5 Hz would enable the instrument to collect data from neutron wavelengths of 1 Å to 12.3 Å in a single instrument configuration as indicated in Figure 5.56.

Instrument performance was compared for a logarithmic spiral detector geometry (–1.2 m to 3.1 m) with varying sample-to-detector distance to a cylindrical geometry (2.5 m radius) with detectors at a constant radius using a powder crystalline sample to yield a diffraction pattern (Figure 5.57). As expected, the spiral geometry with low-angle detectors further from the sample shows improved resolution compared with all the detectors at the same nominal 2.5 m from the sample. At high angles, the slightly closer distances for the detectors in the spiral geometry result in very slight degradation of the resolution compared with the 2.5 m cylindrical geometry. The spiral geometry enables optimal detector placement. Simulations were performed that compared the resolution obtained at 8 mm with that using 12.7 mm diameter detector tubes. The results in Figure 5.58a–b show small but observable resolution gain for 8 mm cylindrical layout detectors at 2.5 m. Detailed simulations with the optimal spiral geometry and single crystals will be required to make a final choice in the required detector tube diameter. Finally, Figure 5.59 shows the effect of neutron beam angular divergence on the instrument resolution, illustrating the possible trade-offs between higher count rate and Q-resolution enabled by the flexible VERDI neutron optics system.

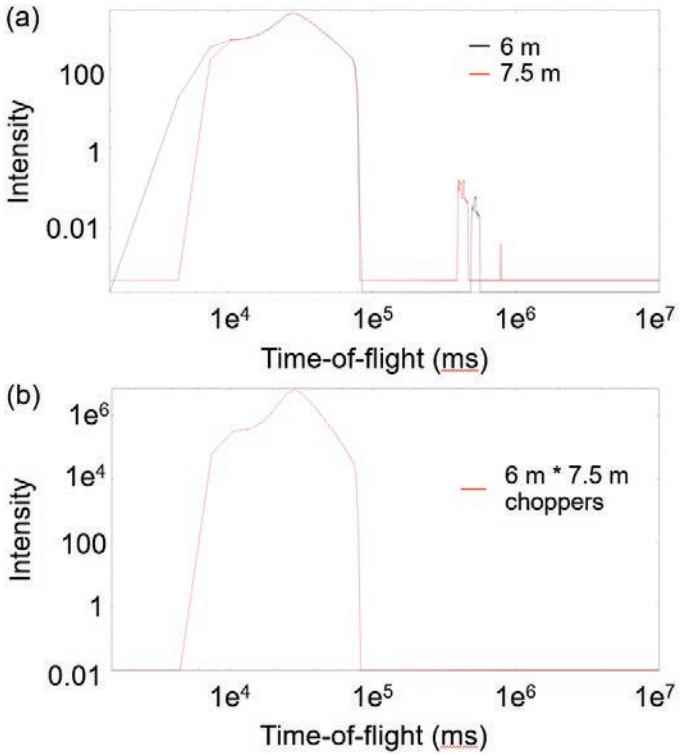

Figure 5.55. Neutron chopper transmission at 15 Hz. Individual chopper transmissions are shown for choppers at 6 and 7.5 m (a). Combining the 6 and 7.5 m choppers removes band overlap and better defines the bandwidth (b). Note that for all the chopper simulations, the blade opening angle is not finalized since the dimensions of the beam at chopper position are not finalized; therefore, nominal values were used.

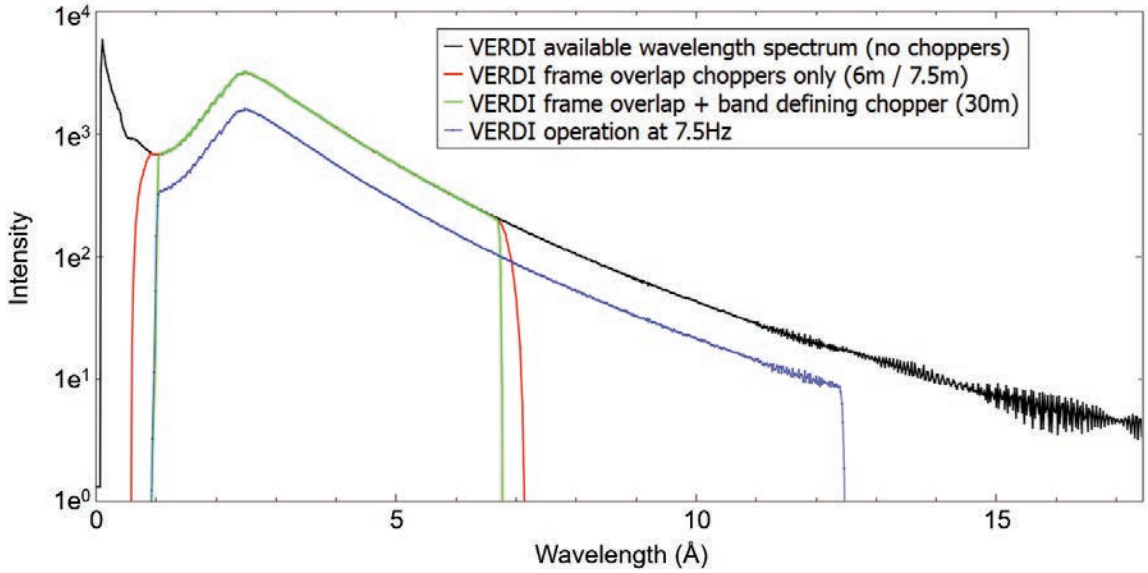

Figure 5.56. Simulations of the wavelength bandwidth defined by the neutron choppers.

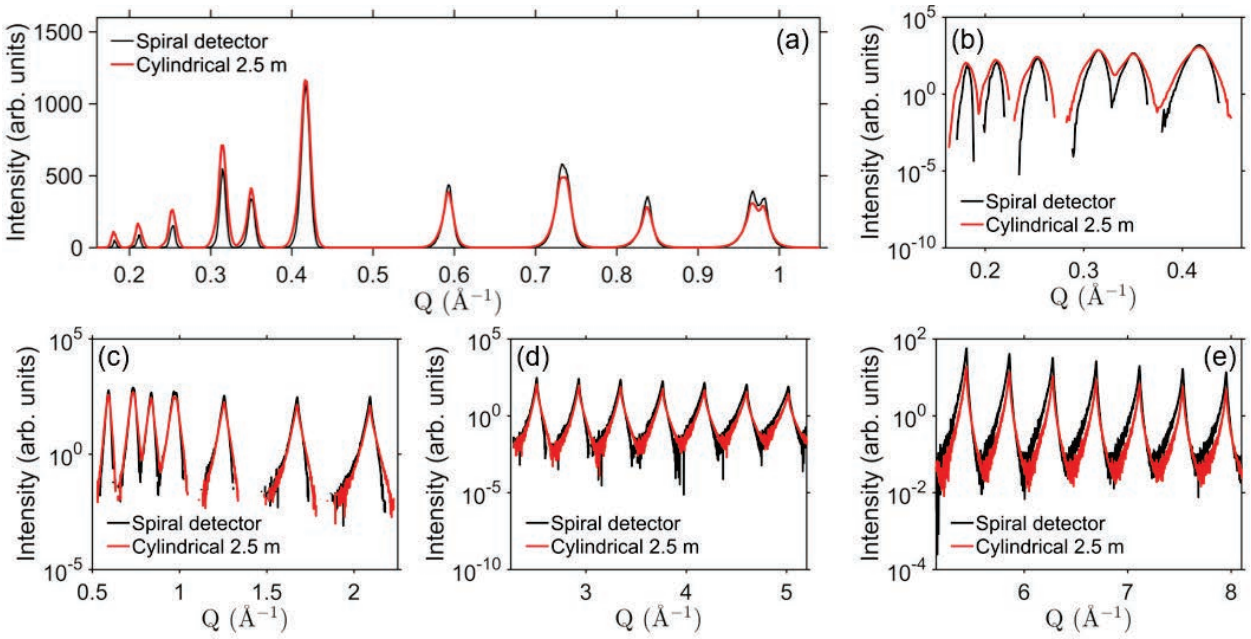

Figure 5.57. McStas simulations of diffraction patterns obtained for spiral detector and cylindrical detector. (a) Low-Q region. (b)–(e) Full Q-range shown with log intensity.

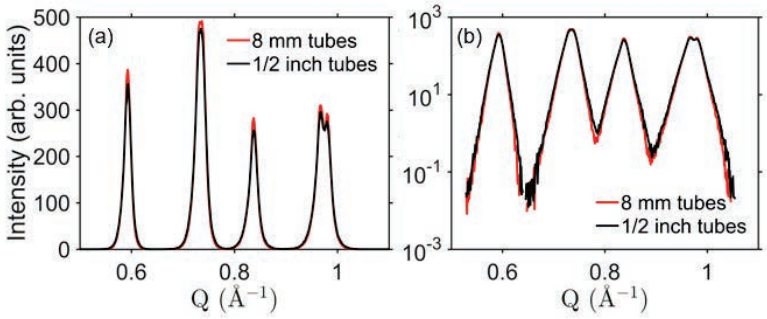

Figure 5.58. McStas simulation for different size detector tubes. The detector geometry was cylindrical at 2.5 m from sample for tube diameter of 8 mm (a) and 12.7 mm (b).

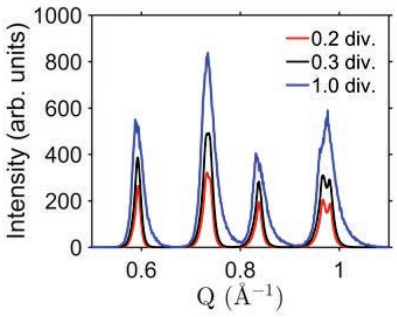

Figure 5.59. McStas simulation comparing different beam divergence (div.).

5.8.6 Feasibility, Research and Development

The key technical requirements for VERDI can be met with current technology. This includes the following main technical requirements:

- In-plane vacuum and argon tank for secondary flight paths are operational on similar instruments.
- Polarizing supermirrors are proven on other ORNL beamlines.
- Detector electronics with 8 mm position resolution in the horizontal and vertical direction are achievable with current ^{3}He detector technology and demonstrated on ORNL instruments.

Therefore, currently, a project to build VERDI at the STS is technically feasible. However, some areas are identified in which technical development and further research is needed.

- For the neutron optics alignment system, the use of higher-precision optics on VERDI will require higher alignment precision than was typically required for FTS instruments. This is a need for many instruments at the STS.

- The polarizing supermirror technology will require optimization if larger reflection m-values are required. This will be the subject of discussion with vendors.

- Data analysis optimization is required because there are currently no white beam fully polarized neutron instruments with a wide detector layout. ORNL is well positioned to develop this capability, based on the successful implementation and operation of HYSPEC, which is currently the only polarized inelastic spectrometer located at a spallation source.

- The large bandwidth at STS will generate data sets in which contributions from different detector angles and wavelengths will overlap in Q but at significantly different resolutions. Combining these data will lead to complicated resolution profiles (peak shapes) that may be impossible to fit with current empirical formulas. Detailed simulations will be undertaken to understand the instrument resolution function.

- Fast, efficient software will be needed to reduce single crystal data. This will benefit from ongoing efforts at SNS FTS instruments.

5.9 SUPPORTING INFRASTRUCTURE

5.9.1 Introduction

The following sections describe key neutron scattering instrument infrastructure. Scientific software is required to both reduce and analyze neutron scattering data, and STS instruments will require extensions to existing software tools (Section 5.9.2). Neutron choppers (Section 5.9.3) and neutron detectors (Section 5.9.4) are key technologies to define the incident neutron beams on instruments and to measure the position and time-of-arrival of neutrons scattered by the samples. An initial suite of sample environment equipment is envisioned to ensure that the neutron scattering instruments are equipped to address key questions from their individual science cases (Section 5.9.5). The neutron scattering instruments include large amounts of biological shielding along their length (Section 5.9.6), as well as more specialized shielding to control background levels at the instrument end stations. The high-brightness STS moderators with their relatively small viewed areas, combined with the, in many cases, advanced neutron optics designs, emphasize early consideration of alignment and stability requirements (Section 5.9.7). Finally, neutrons will be transported to the instruments in a vacuum environment, which will be provided to the instrument beamlines as a central service (Section 5.9.8). Many instruments require higher levels of vacuum environment at their sample locations, and this will be provided by standardized equipment and controls, benefiting from experience gained on FTS instruments.

5.9.2 Scientific Software—Data Reduction and Analysis

Although the initial instrument suite has not been selected, the planning instrument suite described imposes new requirements for scientific software. These requirements are sufficiently representative of general changes in workflow and the need for new software to provide guidance for planning purposes for the scope described in this section. SNS uses multiple tools including Mantid [Arnold et al. 2014] for reduction of event data from the neutron instruments at the FTS. There are multiple interfaces to the data

reduction algorithms provided at the FTS, including Python command line interfaces, interactive web notebooks, and graphical user interfaces. We expect that overall the infrastructure already in place at the FTS is adequate to address the needs of STS but that some work will be needed to address increased data rates. The input to FTS data reduction software is the output from the instrument data acquisition, specifically a NeXus event file [Konnecke et al. 2015]. STS reduction software, especially Mantid, can also read directly from the live stream of events coming from the instrument. This feature is used for monitoring purposes at the FTS.

For most of the STS instruments, minimal software work will be needed to take such a file and reduce it in the same workflow as at FTS. In fact, already in this early concept stage of the instruments, some simulated results have been reduced using simulated event files and the Mantid routines. Figure 5.60 shows reduced simulated data for QIKR and Figure 5.61 shows reduced data for CHESS [Sala et al. 2018, Lin et al. 2018].

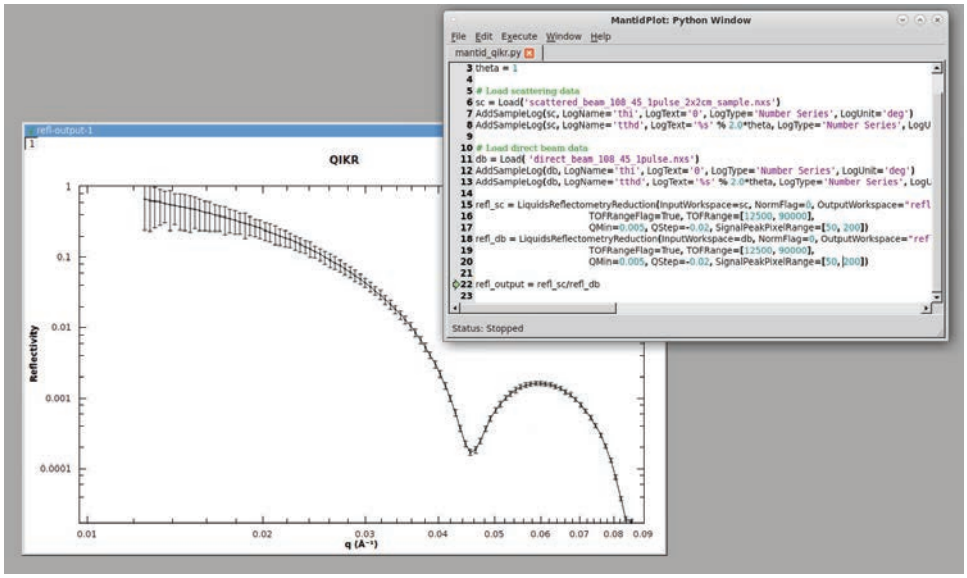

Figure 5.60. A view of a simulated reflectivity curve for QIKR reduced in MantidPlot. The script to reduce to the reflectivity curve (upper right) uses the same routines as the current Liquids Reflectometer reduction.

However, targeted areas where reduction and analysis software work will need to be performed have been identified. This work will be managed and integrated in the project as described in Section 5.9.2.1. The needs for working with polarized data are described in Section 5.9.2.2, taking fuller advantage of the live data stream is described in Section 5.9.2.3, describing new web based interfaces is described in Section 5.9.2.4, and working with multiscale data is described in Section 5.9.2.5.

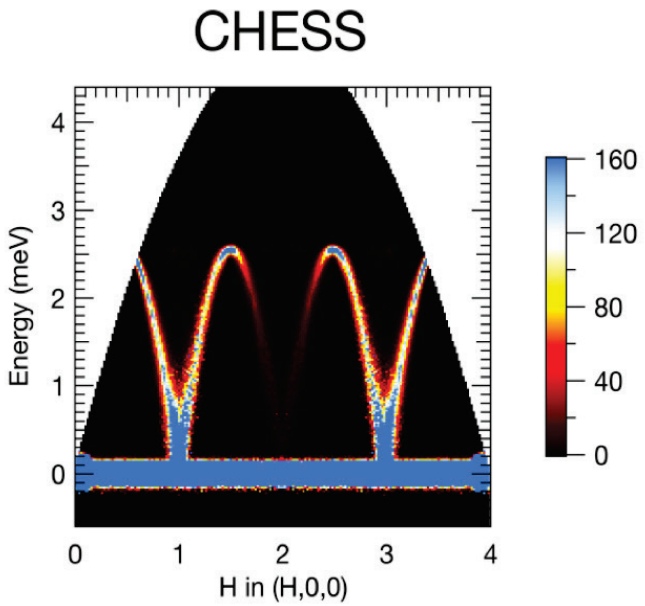

Figure 5.61. Simulated $K_2V_3O_8$ data from the conceptual CHESS instrument. The output from the MCViNE Monte Carlo Ray tracing simulation is reduced and visualized using the current Mantid reduction routines.

5.9.2.1 Management and Integration

Mantid provides a framework within the Python programming language to allow for custom workflows. This is especially important for the custom needs that will be encountered during instrument commissioning. Plans to accommodate these needs will be based on the descriptions of the commissioning activities in commissioning plans to be worked out on a per-instrument basis.

For both the traditional and the stream-based reduction, an instrument definition file (IDF) containing the location of the detectors will need to be developed and debugged for each instrument. As shown in Figure 5.60 and Figure 5.61, the proposed STS instruments are being modeled in more detail than ever before. Therefore, we expect these IDF files to be developed well before an instrument starts commissioning.

5.9.2.2 Polarized Data

The use of polarized neutron beams is one of the main methods of disentangling complex features in magnetic scattering. Polarized beams can also be used to better understand the structures of organic materials, if the hydrogen in the samples is polarized. Currently, SNS has a few instruments that can deal with polarized neutron beams, and we plan to use some of their software and data processing knowledge for instruments at STS.

From the software point of view, dealing with polarization involves two main aspects. In the reduction step, TOF recordings of neutron detection events are transformed into physical quantities familiar to users, such as scattering cross section as a function of momentum transfer. This step is mostly similar to the nonpolarized case. Additional transmission effects must be experimentally measured, and a wavelength-dependent correction is straightforward to implement. Measurements with different polarizations are then combined [Schweika 2010] into different magnetic and nonmagnetic cross sections. Modifications to the current reduction workflows will mostly have to deal with the wavelength dependence of the polarization [Willams 1988, Dalgliesh et al. 2007] which will depend on instrument

implementation. A correction for the angular dependent flipping ratio [Zaliznyak et al. 2017] has already been tested. Since the angle between the polarization and momentum transfer is wavelength- and detector-dependent (already present in the current reduction software), the wavelength dependence of the polarization magnitude can be implemented in a similar fashion.

The second step involves the analysis and modeling of the reduced data to extract insights about the structure and dynamics in the samples. This step needs significant development. In certain cases, there are some workarounds that can obtain additional information, but without using the full potential of the polarized neutron measurements.

Polarization for the proposed CHESS spectrometer is likely to come from a polarizing guide, with the polarization analysis provided by a ^{3}He cell. Data processing will be similar to that for the HYSPEC spectrometer at the FTS and to the LET spectrometer at ISIS. No further reduction software work is needed until the first polarized measurements are performed. Some analysis software, such as SpinW [Toth and Lake 2015], allows in principle the calculation of the polarization-dependent dynamic structure factors. Work is required to make these calculations user friendly and compatible with the measurement/analysis workflow at ORNL.

The QIKR reflectometer will probably use supermirrors for both polarizing the incident beam and analyzing the scattered beam. From the software point of view, polarization at QIKR will be comparable to polarization at the Magnetism Reflectometer at the FTS. Some issues will need to be clarified. One of them is the use of a wider wavelength band. The other is that the incident/scattered beams allow for fast changes in polarization. Currently, we filter neutron events by the state of the polarization flippers. For long time intervals between pulses, this change in polarization state might occur during the measurement of one frame. The polarization efficiency is effectively wavelength-dependent. There are two ways to deal with such occurrences. One is to “correct the data,” which is desirable for fast visualization but can introduce artifacts. Doing so can be relatively easy to implement in Mantid. However, a more exact approach is to apply these polarization efficiency corrections to the reflectivity model. This is more difficult to implement, since we do not have access to all possible data analysis programs for neutron reflectivity.

For the CYGNUS instrument, polarization is not planned as a day 1 capability. However, the design will support adding polarization capabilities at a later date.

The VERDI diffractometer will operate with a wider bandwidth of incident neutrons than any polarized instrument at the FTS. In the case of VERDI, a vertical dependence of the polarization efficiency must also be considered. As in the reflectometer case, two software solutions must be provided, one for visualization and one for analysis. The current structure refinement packages do not contain a full TOF-compatible polarization mode, especially for single crystal measurements. A full analysis workflow needs to be designed and implemented that accounts for different angles between the momentum transfer and polarization at different detectors and/or at different wavelengths.

5.9.2.3 On-stream Data for High Throughput

For some of the instruments the data rate is high enough that reloading the data from a file for routine reduction will be too slow. Instead, a method via which some amount of reduction is performed on the live event stream will be employed. The expanded work for this method of operation is described in the following subsection “Expanded live reduction.”

Correlation choppers have shown the ability to isolate truly static behavior from dynamic behavior on CORELLI. We expect several other instruments to implement this technology, especially the SANS-like

instruments, at STS. Work on this technique is described in the following subsection “Broader use of correlation choppers.”

Expanded Live Reduction/Event Filtering

As the data acquired at the SNS are time-stamped event data, they can be used very effectively with time varying metadata such as electric field, magnetic field, stress, strain, and temperature [Granroth et al. 2018]. The expanded bandwidth of QIKR will mean a sufficient amount of the reflectivity curve can be acquired simultaneously to allow for time-resolved surveys of materials. Event filtering will need to be added to the interfaces for reflectometry. We envision similar growth in this technique for SANS and SANS/WANS instruments, including the CYGNUS concept.

For high count-rate instruments, the events will be used in a different way. Here a final event file will be sufficiently large that waiting until it is completed to process the event filter will take too long for every reduction. Instead, we will strengthen and develop the live data facility in Mantid to start processing the data on the live stream. The current live data facilities have been tested to a state for qualitative analysis. The routines will need to be tested and strengthened to a quantitative level. The expanded use of the stream will also allow for more complex counting criteria, for example counting to a statistical measure of model fit or peak width. Such use is envisioned on all instruments.

EWALD is envisioned with an automated self-calibration mode of operation as the instrument collects data. This is crucial because the detectors will be moved to allow for different sample environments. Currently, the single crystal diffraction codes use calibration from a standard crystal to fix their geometry before reducing their data. For protein crystals, the unit cell is usually well-known information before the experiment. Given this information, the sample distance can be refined as the data are collected.

Clustering for Automated Phase Transition Detection

Clustering algorithms are a class of tools that allow data sets with similar features to be grouped. Such algorithms have recently been shown to reveal the presence of different phases of materials and can be used to alert the experiment team or facility staff of unexpected changing conditions during an experiment [Peterson et al. 2018]. We will implement these routines in the Mantid framework so they can be employed routinely on STS instruments.

5.9.2.4 Web-based Interfaces to Reduction

The current interfaces to the reduction and analysis scripts are implemented through Python scripting and Qt-based GUIs. By the time STS is coming online, a different method will likely be optimal for the GUIs. We expect this method will be web-based. We have worked on prototype tools in Javascript and will look at expanding those as the view in a Model View Controller design pattern that allows us to separate rapidly changing graphical interfaces from complex scientific-based code.

5.9.2.5 Working with Multiscale data

Multiscale data provide some analysis challenges. First the RRM technique can make instruments more efficient and allow measurement over multiple energy scales such as proposed for the CHESS instrument. Second the science case calls for instruments that bridge multiple length scales. Methods of working in these two modes need to be developed.

Repetition Rate Multiplication Data Analysis

The CHESS instrument will use the RRM [Russina and Mezei 2009] mode of operation to enhance its throughput. In RRM, multiple energies are incident on the sample during a source frame, rather than a single energy. This mode of operation has been demonstrated on SEQUOIA [Granroth 2011] at the FTS and is in regular use on LET [Bewley et al. 2011] at ISIS and 4-Seasons [Nakamura et al. 2009] at J-PARC. In all of these cases, each incident energy is analyzed independently and the results are correlated. The ability to co-analyze data using the multiple incident energies together will be implemented. This implementation will cover both the quasielastic cases in which the resolution is measured with a V standard, and the inelastic case in which the resolution is calculated using MCViNE. The assumption for this scope is that the subframes will not overlap.

Multiple Length Scales

The science case for STS calls for the study of hierarchical materials. These materials have relevant length scales that bridge the SANS and traditional diffraction regimes. Analysis tools to facilitate exploring this overlap regime are needed and will be developed to assist in these studies. This may be one instance in which AI/machine learning could assist in determining an analysis approach.

Broader Use of Correlation Choppers

The correlation chopper in use on the FTS CORELLI instrument has been effective in removing inelastic features for diffuse scattering measurements and other time-disturbing background features [Ye et al. 2018, Liu et al. 2018]. It is expected that other white-beam instruments will find these enhancements helpful. The incorporation of correlation event filtering on CYGNUS will require integrating the current correlation routines into these techniques.

5.9.3 Neutron Choppers

Neutron choppers periodically interrupt the neutron beam being transmitted along a beamline with an absorbing material to (1) limit the range of the neutron wavelengths transmitted (bandwidth disk chopper), (2) define the neutron energy (high-speed disk or Fermi chopper), or (3) block the prompt flash of high-energy neutrons and gammas generated when the proton beam impinges on the tungsten target (T0 chopper). Years of experience gained in designing, producing, and operating neutron choppers in the FTS will be incorporated into the STS 15 Hz chopper designs. It is intended that the choppers will be standardized to the maximum extent possible, especially the commonly used T0 and disk choppers, to minimize design and fabrication costs and reduce the number of spare parts required.

5.9.3.1 STS Chopper Requirements

Aside from correlation choppers, neutron choppers operate at a frequency commensurate with or at a sub-harmonic of the source frequency. A key parameter in the performance of a neutron chopper is the time it takes to transition from fully open to fully closed. For a given neutron beam dimension and chopper rotating frequency, this transition occurs more rapidly with increasing chopper rotor diameter, which is desirable for neutron instrument performance. The STS chopper specification is defined as *the minimum diameter rotor that allows the edge of the neutron absorber to sweep through the entire width of the STS standard size neutron beam while operating at the source frequency and being equal in time to that same specification in the FTS at SNS*. Since STS operates at ¼ of the design frequency of FTS, this specification implies increasing the rotor diameter of the STS neutron choppers. A faster chopper transition from fully closed to fully open allows the chopper to be placed closer to the moderator,

produces cleaner edges on the neutron pulse, and reduces the possibility for leakage of undesired neutron energies through the chopper because it is open, or partially open, for less time.

For conceptual design purposes, a neutron beam dimension of 7 by 7 cm was used as the basis for developing concepts for the STS neutron chopper suite (final size requirements will be identified during instrument preliminary design). To achieve the specified performance requirements for this size beam, the chopper diameter is 1.24 m. The FTS chopper diameter is 0.64 m, so the STS choppers will be almost double the size of their FTS counterparts. Figure 5.62 illustrates the size of the 15 Hz STS choppers. Also shown is a smaller chopper with a diameter of 0.7 m. It meets the STS chopper requirement while operating at 15 Hz if there is a pair of neutron choppers in a counter-rotating double disk configuration so that the chopper disks close the neutron beam, beginning at either side and overlapping as they traverse the middle of the beam.

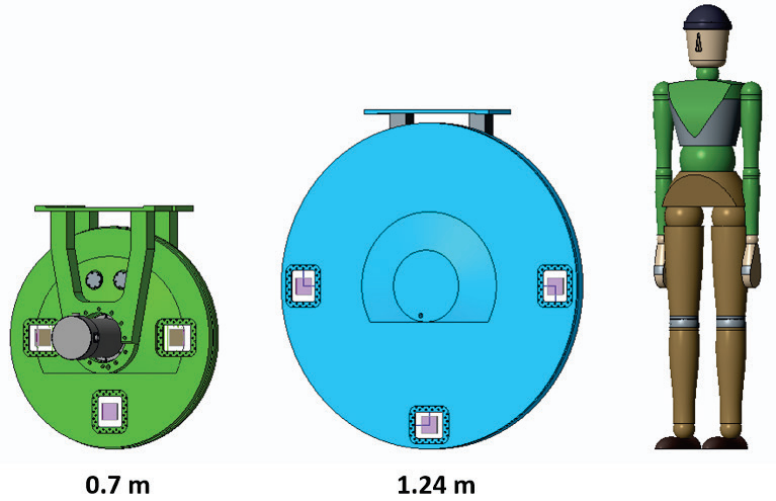

Figure 5.62. Comparison of 15 Hz chopper diameters.

Figures 5.63 and 5.64 depict potential 1.24 m T0 chopper placements within the bunker, illustrating that sufficient separation between the neutron beamlines exists for neutron choppers of this size.

In locations where space limitations exist, smaller-diameter choppers, both T0 choppers and disk choppers, will be available for use. But they are likely to be arranged in a counter-rotating double-rotor configuration to achieve the STS chopper requirement for time to open or close the neutron beam, as shown in Figure 5.65.

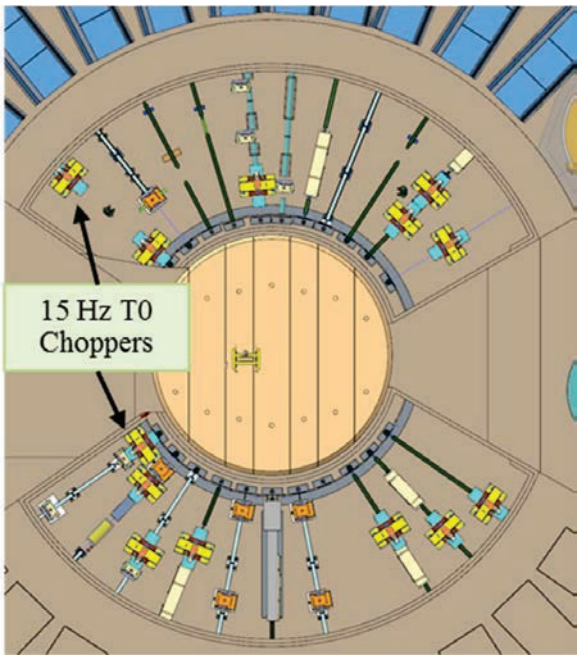

Figure 5.63. STS bunker view showing close fit of 1.24 m T0 choppers.

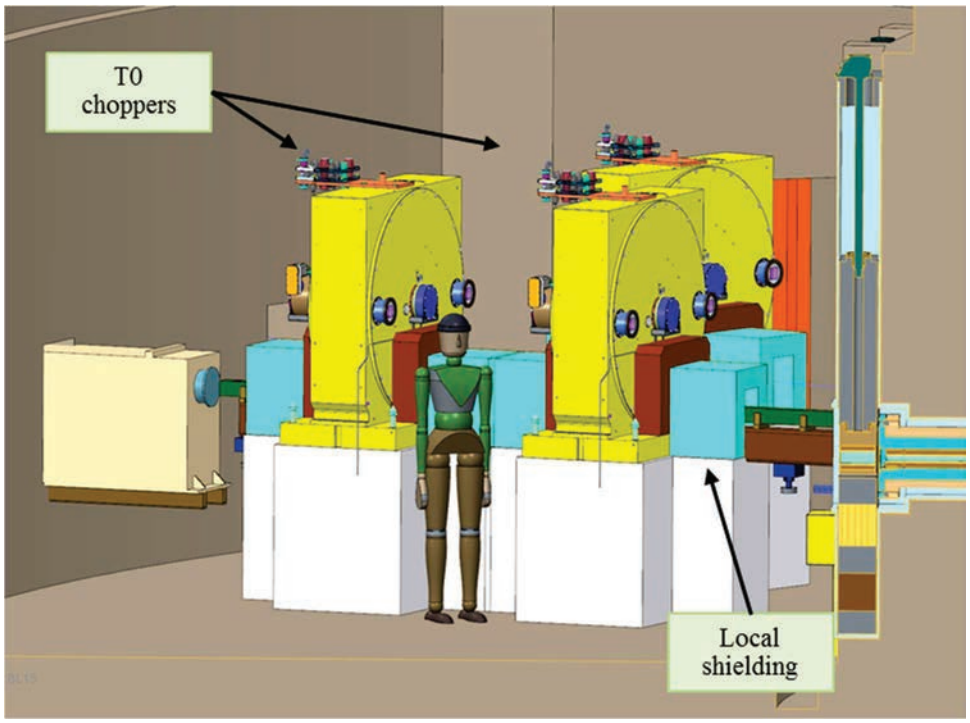

Figure 5.64. Close spacing of T0 choppers within the STS bunker.

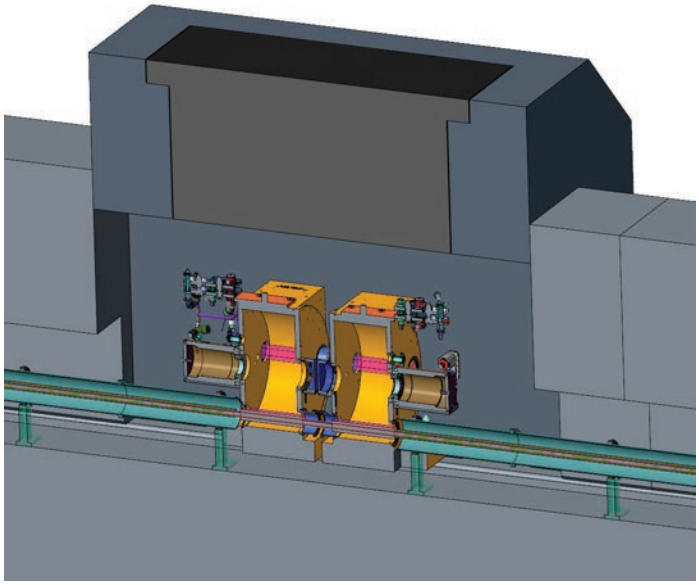

Figure 5.65. Downstream shield house with counter-rotating 0.7 m double-rotor choppers.

Design concepts for many types of choppers expected to be used in the STS have been developed based on existing FTS designs. To aid in understanding the different chopper concepts planned for the STS and to separate their different capabilities based on chopper characteristics, the chopper concepts were grouped into three categories:

- STS chopper specification compliant concepts.
- STS high-speed chopper concepts.
- STS chopper specification noncompliant concepts. Because of the smaller diameters of these choppers, when operated individually instead of in pairs, they do not have the linear velocity to sweep through the entire width of the STS standard-size neutron beam in the required time but may still provide acceptable instrument performance.

These concepts, shown in Figures 5.66, 5.67, and 5.68, have been developed primarily to represent the space required along the neutron beamlines and will be updated as STS concepts mature.

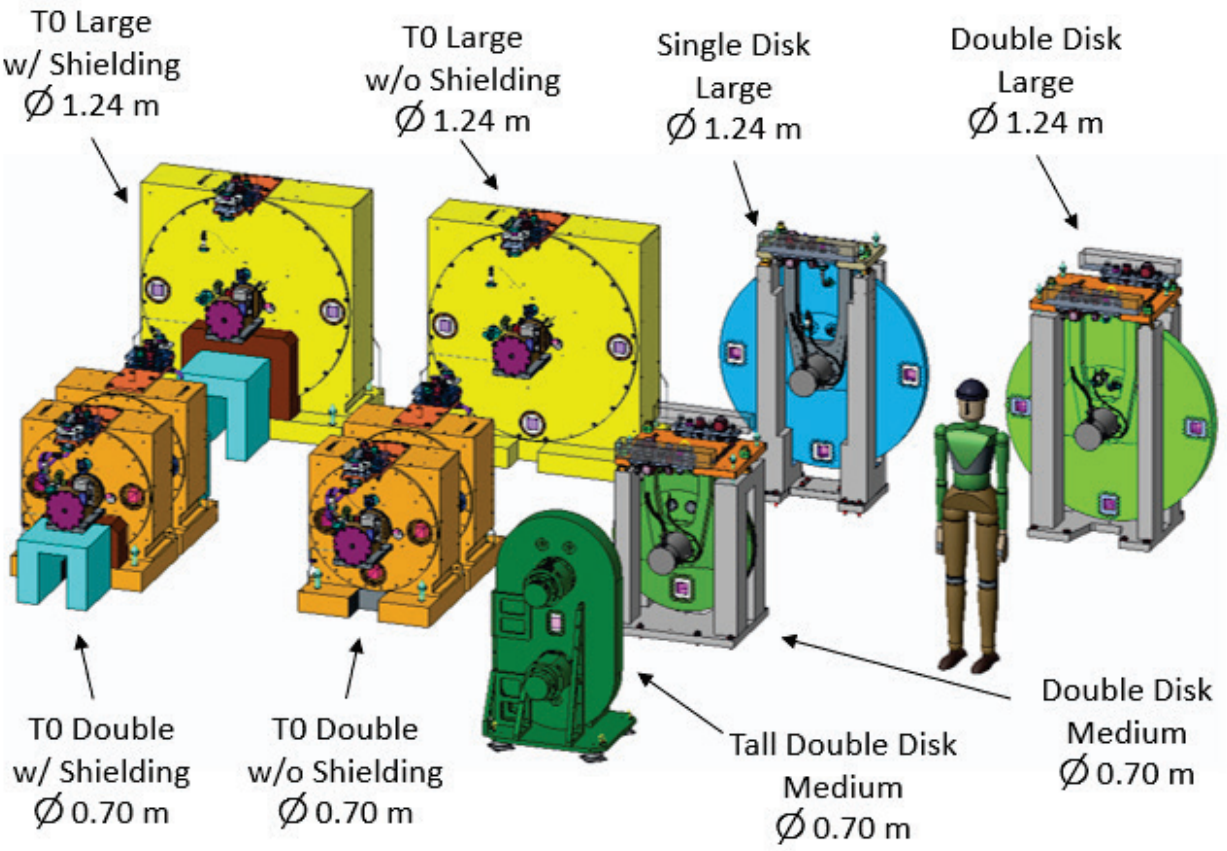

Figure 5.66. STS chopper specification compliant concepts.

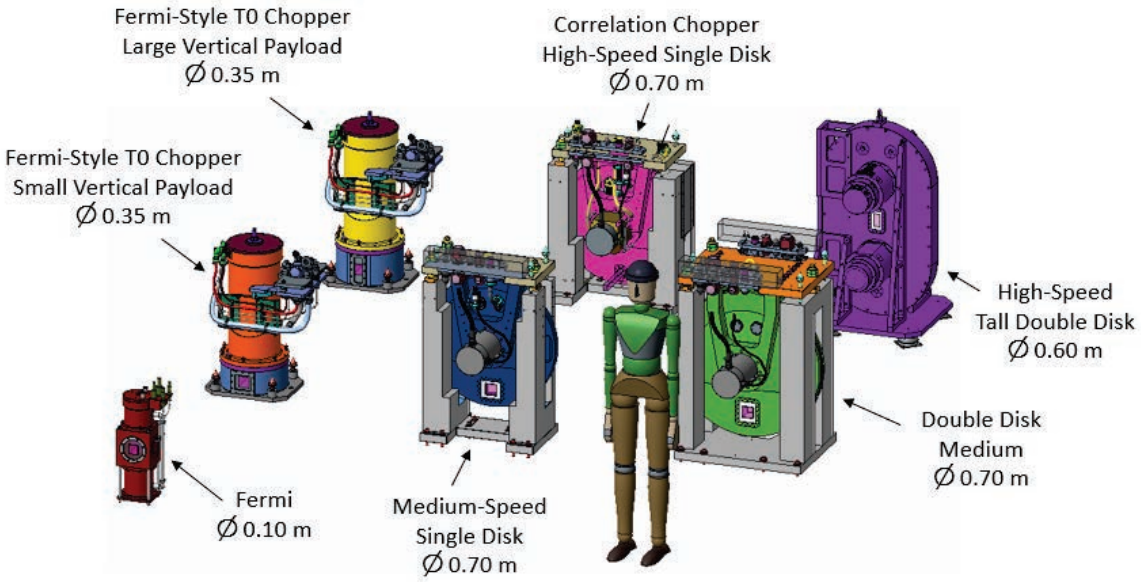

Figure 5.67. STS high-speed chopper concepts.

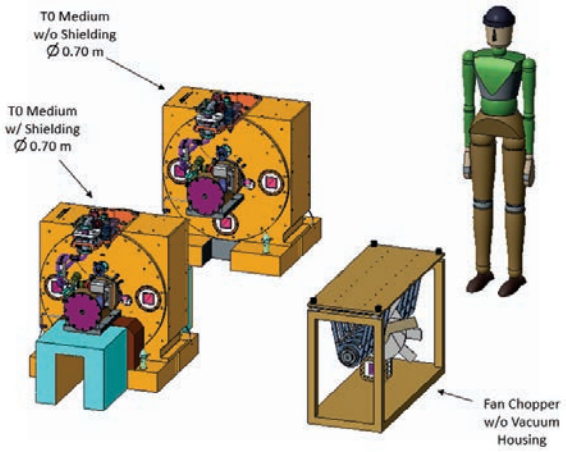

Figure 5.68. STS chopper specification noncompliant chopper concepts.

5.9.3.2 Chopper Technology Development

Many of the currently proposed STS instruments are expected to specify neutron optics that will require higher stability and tighter alignment than was required for FTS instruments. Some instruments will use elliptical guides, while others will rely upon sets of focusing mirrors. With some beamlines approaching 90 m in length, the stability of these optics will be critical to the performance of the instruments. Considering that, in many instances, rotating choppers will be installed near these sensitive optical components, chopper-induced vibration of these components is a concern. All equipment rotating on mechanical bearings develops some amount of vibration that is transferred to neighboring equipment. The transfer of vibrations from the source to the receiver can be reduced, but the most effective means of reducing vibration transfer is to isolate the source.

Chopper vibrations can be minimized by a combination of reducing design tolerances of parts, obtaining tighter fits during assembly, performing a higher-grade balance leveling of the rotating equipment, conducting a trim balance after assembly, and using vibration dampers. Although the first four methods can reduce vibration, some vibration still will be transferred to the mounting structure and other equipment. In the case of vibration dampers, less vibration is transferred to neighboring equipment; but the chopper assembly itself is left to vibrate, shortening its life expectancy significantly. The massive size of the STS T0 choppers multiplies the vibration problem because a heavier rotating mass equates to larger vibrations transferred into the mounting structure. There is no way to anticipate how much transferred vibrations from a T0 chopper will impact the neutron optics without characterizing an assembled system that accurately represents the intended installation structure. The use of magnetic bearing T0 choppers would eliminate the source of the problem, minimizing performance risk for STS instruments.

Magnetic bearings are already in use in over 80% of the FTS choppers (88% of the disk choppers, all of the Fermi choppers, and all of the Fermi-style T0 choppers.) They are also used in industry for equipment that is much larger than the STS T0 choppers. All the SNS FTS blade-style T0 choppers currently use mechanical bearings, and a magnetic bearing, blade-style T0 chopper meeting the STS requirements is currently not available. The path to developing STS magnetic bearing T0 choppers is straightforward, requiring (1) the design of correctly sized magnetic bearings, (2) specification of a motor to meet the chopper phasing requirements, and (3) integration of the rotor and housing design. Experience shows that the design, manufacture, tuning, testing, and delivery of a new magnetic bearing T0 chopper will take 2–4 years. (Manufacture, tuning, testing, and delivery of an FTS-style T0 chopper currently takes 9 months.)

Chopper manufacturers have already designed more powerful magnetic bearings to control the higher forces associated with large-disk choppers. The motors in the magnetic bearing spindles have been updated to provide the higher torque required to accelerate large-diameter, higher-mass disks to speed in a reasonable amount of time. In addition, the control systems have been modernized with (1) higher-speed processors to provide faster control of the system while also offering greater functionality with even more parameters, (2) hardware that uses current industry standard communication technology, and (3) a host of firmware and software upgrades to better diagnose and manage the control issues of the system. Preliminary study has determined that one of these new control systems has enough power to control an STS magnetic bearing T0 chopper. In addition, the manufacturers are implementing lessons learned from previous systems to provide faster, more repeatable tuning techniques; in one case, these allowed the tuned chopper system to satisfy the requirements in Parts 1–3 of ISO 14839, "Vibration of Rotating Machinery Equipped with Active Magnetic Bearing Systems."

The STS Project will invest in developing a first-article, magnetic bearing T0 chopper using existing technology that has already proved it can easily eliminate vibrations. This will provide a significant cost savings over the life of the facility, improving operational reliability and reducing maintenance needs.

5.9.4 Neutron Detectors

Neutron detector technology has advanced rapidly over the past 10 years but the smaller, brighter neutron beams at STS will require new detectors with higher spatial resolution (smaller pixels) that are capable of higher neutron count rates than current technologies can support. Instrument types that are particularly demanding include SANS, SANS/WANS, reflectometers and single-crystal diffractometers, most of which are represented in the instrument concepts (Sections 5.5–5.7).

Recent developments in scintillator-based technologies at ORNL are leading the way to meeting the requirements of these instrument types. Anger-logic technology use an array of sensors to measure the cone of light emitted from a scintillator upon neutron absorption and then triangulate to the spot where the event occurred. Recent advances in this technology using silicon photomultipliers (SiPM) as light sensors have demonstrated 0.7 mm FWHM spatial resolution (see Figure 5.69). That is adequate for use on FTS and HFIR neutron scattering instruments, but continued development will be needed to reach the 0.3 mm requirement of the STS single crystal diffractometer EWALD.

The QIKR reflectometer will require a detector with the highest linearity and highest small-area count rate, ~100 $n \cdot mm^{-1} \cdot s^{-1}$ (100 times the requirement for the SANS-like instruments) over a local area approaching 100 mm^2 within a total 400 cm^2 detection area to support its cinematic mode of operation. ORNL is in the early stages of developing a new pixelated, scintillator-based detector with the potential to meet these requirements, but further development is required. As recent developments in support of the ESS reflectometers mature [Mauri et al. 2018], they will also be considered for use on STS instruments.

The remaining instrument concepts (CHESS and VERDI) rely on large area arrays of detectors (up to 10s of square meters). Traditionally, these instruments often would have used large numbers of ^{3}He-filled tubes to measure the scattered neutrons. Helium-3–based detectors have desirable characteristics for many neutron scattering applications—including low gamma-sensitivity, high uniformity of response, and high neutron counting efficiency—and the technology is very mature and robust. These instrument concepts require relatively low spatial resolution (≥ 6 mm) and low per-pixel line count rates (generally ≤ 6000 $n \cdot s^{-1}$), which are well satisfied by current commercially available ^{3}He tube array technology.

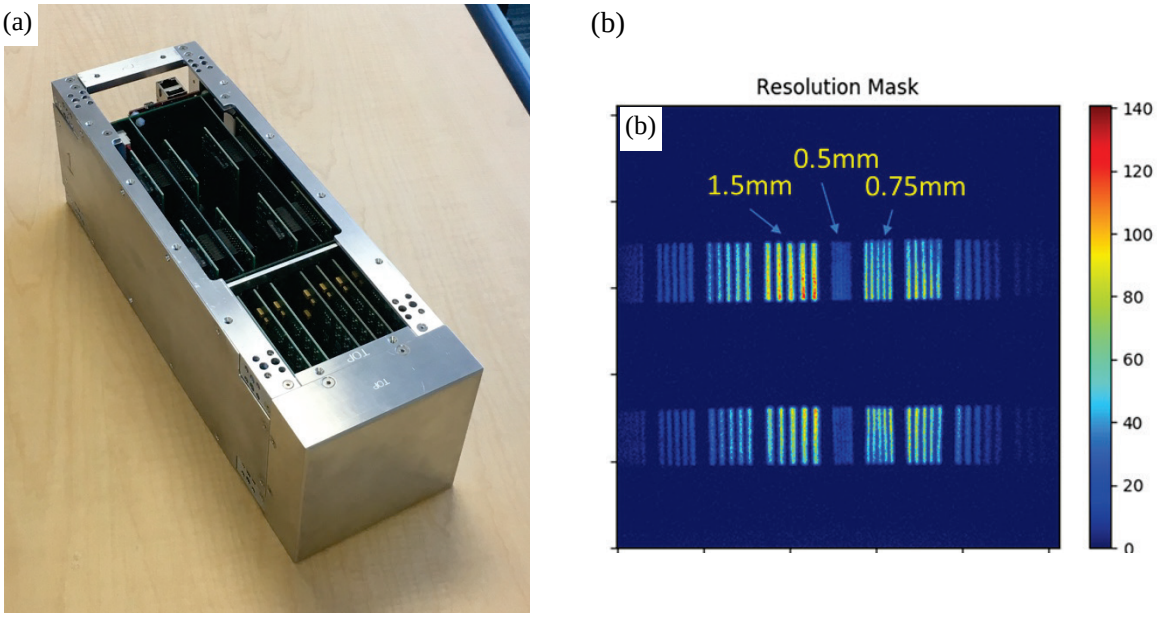

Figure 5.69. Scintillator Anger camera detector technology. (a) The first production SNS scintillator-SiPM Anger camera. Scale: The front face is 120 by 120 mm. (b) Resolution mask image collected on prototype SiPM Anger camera demonstrating 0.7 mm FWHM spatial resolution.

The highest anticipated per-tube count rate for an STS instrument is ~15,000 $n \cdot s^{-1}$ which is close to the acceptable limit for this technology when it is used for diffraction. Because of the high cost and recent limited availability of ^{3}He, alternative $^{10}B_4C$-based technologies have been developed, especially for use as large detector arrays on powder diffractometers and direct geometry inelastic spectrometers [Lacy et al. 2011, Anastasopoulos et al. 2017]. When ^{3}He detector technology meets the requirements (speed and pixel size) of a neutron scattering instrument, it is usually the detector technology of choice. However, as these alternate technologies continue to mature and their performance is demonstrated in large installations, they may become the detector of choice for some STS instruments. Particularly for large detector arrays, cost can become a significant consideration.

At SNS, the standard scintillator currently used on Anger cameras is a Ce-activated ^{6}Li GS20 neutron scintillator glass manufactured by Scintacor. This reference-like scintillator is suitable for the instruments proposed. However, evaluation of alternative scintillator–SiPM combinations could result in a performance increase with regard to gamma discrimination, yielding lower background rates. As currently envisioned, the ^{6}Li GS20 scintillator glass would have a thickness in the range 0.8–1.5 mm (to be optimized according to the wavelength range of each instrument), but alternative scintillator formulations based on ^{10}B as a neutron convertor, such as Ce-activated borosilicate glass—$^{10}B_2O_3$:ZnS:Ag, $^{10}B_2O_3$:ZnO, $^{6}Li_6Y(^{10}BO_3)_9$:Ce, and so on—could offer equal neutron counting performance with a relative thickness of < 25% of GS20 glass.

For the suite of the five representative STS instruments, Table 5.24 presents a summary of the most relevant instrument design parameters and consequential detector requirements, and selected detector technology with physical quantity/size parameters. The distribution of determined detector technologies is evenly split across the instruments, four being ^{3}He tube array and four being scintillator–SiPM based detectors.

Table 5.24. Summary of instrument and associated detector parameters for the five representative STS instruments.

											Detector requirements		Detector			
(a)	(b)	(c)	(d)	(e)	(f)	(g)	(h)	(i)	(j)	(k)	(l)	(m)	(n)	(o)	(p)	(q)
Moderator	**Instrument**	**Incident energy or wavelength**	**Operating frequency**	**Flight paths**	**Flux at sample**	**Intensity on sample**	**Sample size**	**Angle range**	**Solid angle**	**Purpose**	**Spatial resolution**	**Rate capability: total, individual**	**Type**	**Axis (if ^{3}He tubes)**	**Size**	**Quantity**
				L1, L2												
		(meV) or (Å)	(Hz)	(m)	(n/mm^2/s)	(n/s)	(mm)	(deg)	(sr)		(mm)	(n/s)			(mm)	
T	CHESS	0.8 – 5.1	15	29.5, 2.5	75 K	7.5 M	10	Complex	6.2	Spec.	20	1M, 6K	LPSD ^{3}He tubes (8 atm)	H	1500 × 25ϕ	160 × 8
C	CYGNUS	0.5 – 8	15	30.25, 1–3	2 M	200 M	10	±25	1.2	Diff.	3	3.7M, 270K	Scintillator-SiPM Anger cameras		300 × 300	24
C	QIKR	2.5 – 23	7.5	18, 1.9	2.4 M	100 M	20 × 2	0–6	0.03	Diff.	1 × 2	25K	Scintillator-SiPM pixelated camera		400 × 200	1
C	EWALD	1 – 5	15	90, 0.3	7.5 M	2 M	0.5	15–165	5.7	Diff.	0.3	200K, 10K	Scintillator-SiPM Anger cameras		116 × 116	37
C	VERDI	1 – 7	15	40, 1.5–3.5	1.2 M	150 M	11	5–165	2.9	Diff.	10	2.5M, 15K	LPSD ^{3}He tubes (12 atm)	V	1000 × 10ϕ	224 × 8

In addition to the detector technologies described above, rapid advances have been made in very high-spatial-resolution (50 micron) imaging detectors that might find application on some of the five instrument concepts described and would be essential for other possible STS instruments, such as a wavelength-resolved cold neutron imaging station. This detector requirement can be met by a ^{10}B/Gd-MCP Quad-Timepix detector technology, which was developed originally at Berkley University using commercially available subcomponents.[Tremsin 2011, Tremsin 2015] SNS has several years of operational experience with this type detector at both SNS and the higher–neutron flux HFIR imaging station. Advancing to the latest-generation silicon solid-state Timepix3 sensor, SNS is developing in-house design and production capabilities (Figure 5.70) to meet increasing demands for this type of detector across all three neutron sources at ORNL.

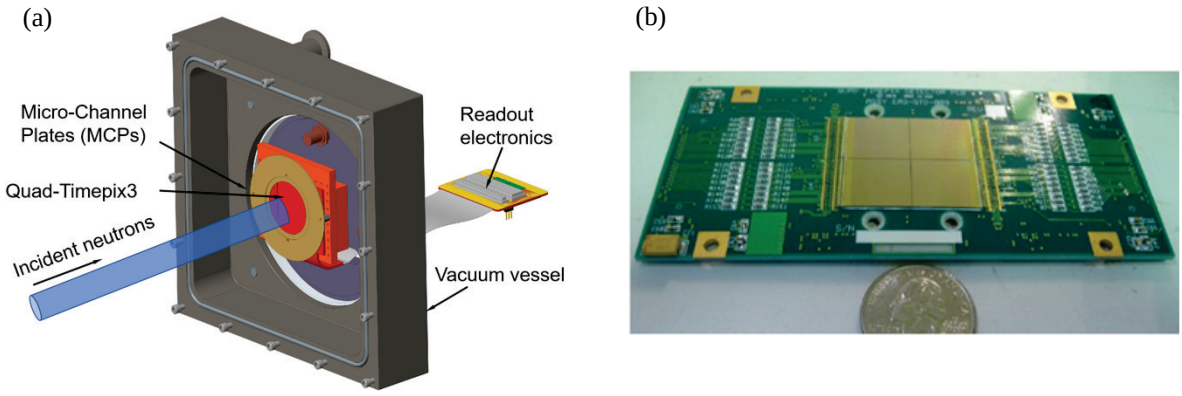

Figure 5.70. Imaging detector. (a) Engineering schematic of SNS 10B/Gd-MCP Timepix3 detector. (b) Prior-generation Timepix2 component module.

5.9.5 Sample Environment

Sample environments are essential to scientific experiments that use neutron scattering. A successful neutron scattering experiment depends on the ability to precisely and accurately control experimental parameters such as temperature, pressure, and magnetic fields. Reliable operation is essential to a successful user program, as defined by the sample environment equipment performing its required functions (control temperature, pressure, magnetic field) under stated conditions (vacuum, inert atmosphere) for a specified period (length of experiment) in routine and/or unexpected circumstances.

The focus is on providing an initial complement of sample environment equipment that is essential for the early scientific measurements envisioned at the instruments. The goal is to have the new STS instruments science-ready from the time they are commissioned. This goal can be achieved by integrating the design, procurement, installation, and testing of key sample environments into the instrument projects. The proposed sample environments are feasible without extensive research and development and can be readily provided through new procurements and the use of existing equipment.

Table 5.25 describes the essential sample environments that have been identified for each of the five representative instruments. As indicated in the table, some existing sample environments can be used to complement procurement of some additional key equipment.

Table 5.25. List of sample environment equipment identified as core needs to fulfill the science cases of the neutron scattering instruments.

Instrument	New equipment	Adapt existing equipment
EWALD	Cryo-stream system (80 K)	
CHESS	Superconducting cryomagnet (8–9 T, 1.5 K) Liquid helium bath cryostat (1.5 K) ^{3}He insert (0.30 K) Dilution refrigeration insert (0.030 K)	
CYGNUS	Multiple position sample changer with Peltier temperature control (–5 to 110°C) 4–800 K cryofurnace	Anton-Paar rheometer, McHugh pressure cells, humidity chamber, rotating tumbler, stopped flow cell
QIKR	Multiple-position robotic sample changer Langmuir trough Environmental chamber Custom cryofurnace (4–-800 K) Potentiostat and liquid/solid cells	Anton-Paar rheometer
VERDI	Superconducting cryomagnet (14 T, 1.5 K) Liquid helium bath cryostat (1.5 K) ^{3}He insert (0.30 K) Dilution refrigeration insert (0.030 K)	

The current sample environments for SANS at HFIR and FTS include an Anton-Paar rheometer, McHugh style pressure cells, controlled humidity chamber, rotating tumbler, stopped flow cell, liquid helium bath cryostat, various cryomagnets, and electromagnets. These have been identified as needed for CYGNUS. The equipment list for reflectivity also includes an Anton-Paar rheometer. To share these sample environments across HFIR, FTS, and STS, it is important to incorporate common sample mounting platforms/schemes in the instrument designs of CYGNUS and QIKR. New, high-throughput multiple sample changers are needed to take advantage of the higher flux at STS. Development of a high-throughput, robotic sample changer like those employed at synchrotrons will make CYGNUS more productive, and a robotic sample changer is already planned for QIKR. Low-temperature and magnet sample environments are proposed for EWALD, CHESS, and VERDI.

First-day experiments for the EWALD instrument will require moderately low sample temperatures. These temperatures can be achieved with standard cryo-stream-like equipment such as the Oxford Cryosystems Cobra®. Cryogen-free systems are preferred over liquid nitrogen systems. The nozzle should be placed as close to the sample as possible. Detector coverage will be blocked in the region where the nozzle is placed; therefore, careful consideration should be given to the placement of the nozzle. EWALD will use a micron-size neutron beam. Because of the relatively small beam size, future sample environments may resemble those found at synchrotrons. One challenge for EWALD, which is somewhat tied to sample environments, is sample alignment. A micron-size neutron beam coupled to micron-size samples presents challenges. Sample environments that use optically opaque heat shields for lower temperatures will be difficult to use where a user might want to view the sample during alignment.

The CHESS first-day sample environments will include one superconducting cryomagnet, one liquid helium bath cryostat, one dilution refrigeration insert, and one ^{3}He insert. The cryomagnet and liquid helium bath cryostat will be custom made and unique to the instrument because of the flange-to-beam center distance of 3 m. The estimated cost for the CHESS sample environments will be double that of typical neutron scattering spectrometers, since these will be custom made to some extent. It is preferable that all four environments be fabricated by the same vendor and built at the same time. This approach will ensure that the low-temperature inserts will be interchangeable and compatible with the cryomagnet and

liquid helium bath cryostat. It is also important that heat exchangers on the low-temperature inserts match the variable-temperature inserts on the cryomagnet and liquid helium bath cryostat. The cryomagnet should be built with a static variable-temperature insert and should not be dynamic in order to prevent scattering from rotons or recoil scattering from helium. The magnet design should incorporate support wedges instead of rings to reduce the amount of scattering from incident and scattered neutrons.

First-day sample environments for the VERDI instrument will include one superconducting cryomagnet, one liquid helium bath cryostat, one dilution refrigeration insert, one ^{3}He insert, and one high-temperature furnace. The cryomagnet will be custom made and unique to the instrument because of the large in-plane opening. The cryomagnet for VERDI should be comparable to the magnet on the WISH instrument at ISIS (14 T, 340° in-plane and –5°/+10° out-of-plane opening). It is preferable that all four magnet and low-temperature environments be fabricated by the same vendor and built at the same time; this will ensure that the low-temperature inserts are interchangeable and compatible with the cryomagnet and liquid helium bath cryostat.

5.9.6 Shielding

A preliminary analysis based on a 15 Hz operating frequency and 700 kW beam power has been performed to estimate the shielding thicknesses required for the STS beamlines. In this calculation, constant cross section guides of 5 by 5 cm area were assumed. Calculations were done both for straight guides with an unobstructed view of the moderator and for a curved beamline that loses line-of-sight of the moderator with a radius of curvature of 2000 m. Calculations were done for both regular and high-density concrete shielding sufficient to limit dose rates to 0.25 mrem/h, which is the design goal for STS (this is the same requirement as used by FTS neutron beamlines). Figure 5.71 shows the shielding thicknesses required to achieve this dose rate for instruments illuminated by both the STS tube and cylinder moderators. Forward-facing beamlines (relative to the proton beam direction) have significantly greater high-energy neutron components and thus require considerably more shielding along their lengths.

After curved beamlines lose line-of-sight at about 30 m from the moderator face, their shielding requirements drop abruptly and are reduced relative to those for straight beamlines that require considerable shielding along their entire length. For reference, the outer bunker wall (Section 5.3) is at approximately 13 m on these plots. These shielding thicknesses were used to guide initial estimates of neutron instrument and bunker shielding for planning purposes.

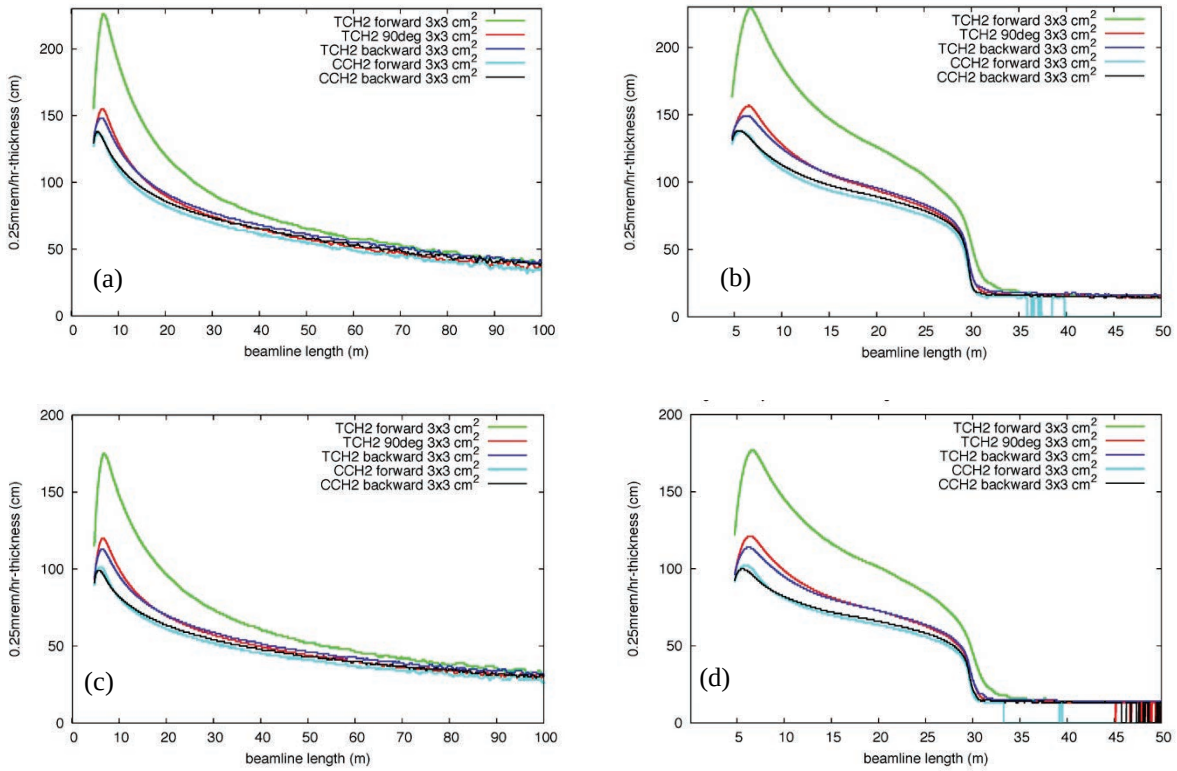

Figure 5.71. Estimated shielding thicknesses along the STS beamlines. The x-axis is the distance from the moderator face. (a) Straight beamline, regular-density concrete; (b) curved beamline, regular-density concrete; (c) straight, high-density concrete; and (d) curved, high-density concrete. TCH2 is the triangular tube moderator and CCH2 is the cylinder moderator at the indicated directions relative to the proton beam direction.

5.9.7 Optics and Alignment Systems

Accurate alignment and stability of all the target station and beamline components are fundamental requirements for a compact neutron source that supports long beamlines with advanced neutron optical systems. The literal foundation on which these optics are supported and which allows such performance is provided by Conventional Facilities. Instrument Systems has communicated the importance of the building construction to Conventional Facilities and has provided stability requirements of 1 mm allowable dead load deflection after the target monolith is installed, and 1 mm allowable live load deflection as local shielding is installed along the beamlines. Relative movements between the target monolith and the instrument floors are also critical and must be minimized. These requirements are being incorporated into the design of the target and instrument buildings as the result of such requirements.

Three separate alignments are involved in determining the necessary precision to provide optimum physics performance: proton beam to target, moderators to target, and neutron beamline optics to moderators. This section discusses the alignment of beamline optics to moderators and the conceptual features designed to accommodate them. In addition, it is expected that “steerable” optics along the beamline will be required in specific cases; they are discussed in this section as well.

5.9.7.1 Neutron Beamline Optics to Moderators

The 22 neutron beamlines will be distributed among 2 moderators, 16 of which will view the upper, cylindrical moderator and 6 the lower, triangular tube moderator. Each beam port can view only a single moderator, and so an appropriate port must be chosen for a beamline instrument during the design phase. In addition, the beam ports will not be oversized to accommodate significantly larger moderators in the future.

Defining the beamline misalignment tolerances requires an understanding of the effects of such misalignments on the performance of the STS instruments. Sensitivity analyses will be required to fully define such tolerances; but it assumed the cylindrical moderator, which supports multiple beamlines in each of its windows, will be more forgiving of beamline misalignments than the tube moderator, which is viewed by a single beamline on each end of the three tubes making up the moderator (see Figure 5.5 in Section 5.2). A preliminary study of the tube moderator [Gallmeier 2018] was performed that included information on the effects of misalignment (as would be the case if multiple beamlines viewed the face of the moderator). The results are shown in Figure 5.72, with the following explanation:

> Brightness changes with regard to the on-axis brightness are presented for 3-cm-diameter moderator, for the tube directed at 90° with regard to the incoming proton beam. It is not surprising that the brightness for off-axis extraction is seeing a reduction over the on-axis extraction as firstly the neutron emission area of the moderator is effectively reduced in size by the cosine of the angle, and secondly the volume of the moderator contributing to the emission is reduced as part of the moderator volume is in the shadow of the collimator. The brightness is reduced by as much as 15% for 3 degree off-angle emission for the 3-cm-diameter moderator. The cold neutron emission in the direction towards the outside of the triangular moderator shape (signed out as positive angle in the plots) is more severely affected compared to the view towards the triangle inside, but at slight gains at thermal energies. [Gallmeier 2018]

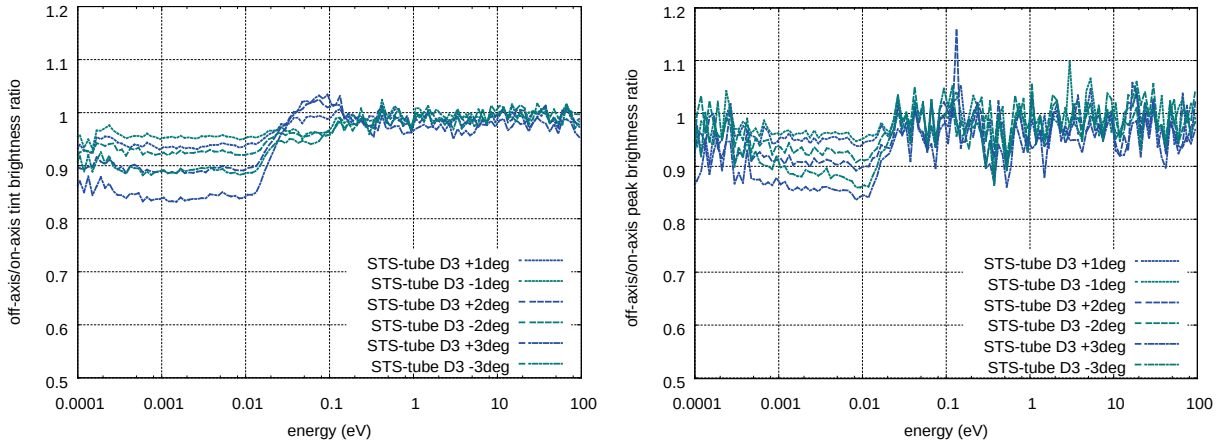

Figure 5.72. Brightness changes at neutron emission for off-axis angles for the brightness of a 3 cm diameter tube moderator. The effect on the time-integrated brightness is shown on the left plot, and peak brightness is on the right plot.

The initial conclusion from this study is that beamlines viewing these tube moderators should be aligned within 0.5° of the tube axis, but further alignment sensitivity analyses will be performed on both the cylindrical and tube moderators during preliminary design.

The STS vacuum vessel, along with its beam ports and their associated vacuum extension nozzles, are shown in Figure 5.73. The nozzles will be installed onsite during facility construction after the vacuum vessel is set in position and the lower bulk shielding has been added, with the upper bulk shielding assembled afterward so that the entire monolith weight will be in place before any beamline alignment operations commence. The neutron beam optics must interface with the core vessel beam port flanges and their associated nozzles in this configuration. These large components significantly influence the ultimate location of the neutron beam optics, both the initially installed instruments and those installed in the future; so accurate measurement and mapping during fabrication and installation are critical. Any fabrication and installation errors within these components must be accounted for in the final installation and alignment of the beamline optical systems. Input from a potential vendor of vessel and extensions has suggested that positional and angular manufacturing tolerances on the mating vessel and extension faces are ±0.1 mm and ±0.002°. In addition, installation tolerances on the extensions are ±0.2mm. This information leads to a requirement that the downstream ends of the monolith inserts must accommodate positional adjustability of ±0.9 mm to allow the inserted guide modules to be located on the nominal beam centerlines. This adjustability will come in the form of shims that are configured before installation of the monolith inserts.

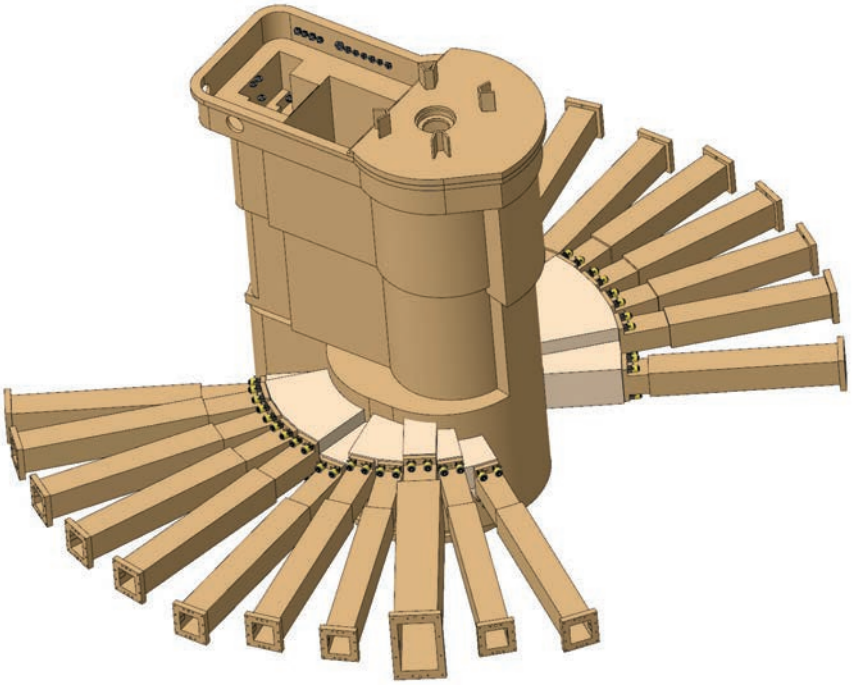

Figure 5.73. STS core vessel and nozzles.

As shown in Figure 5.74, the monolith inserts will incorporate external alignment features (shims) that will position them within the nozzles and port flanges. The portion of the inserts upstream of the front shims will be cantilevered about the bottom front shim and can pivot vertically and horizontally about that location as dictated by the rear shims.

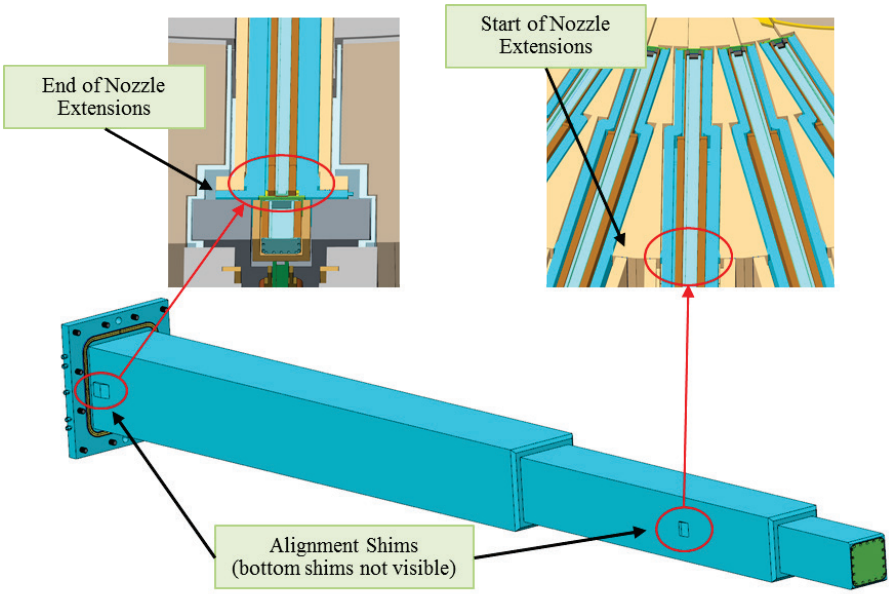

Figure 5.74. External alignment features of monolith inserts.

The inserts will also have internal alignment features that will interface with mating features on the guide modules that are installed later. These internal features are conceptually shown in Figure 5.75; adjustments to the alignment of the guide modules will be controlled with shims installed on the modules before installation. Because the guide modules may not be installed for several years after STS construction, the internal alignment surfaces of the inserts must be mapped and recorded before their installation. Note that because the monolith inserts and guide modules are designed for remote removal and installation, additional clearance of 6 mm around these components is assumed, so the internal adjustability features should not impose any additional space requirements within the nozzles or inserts.

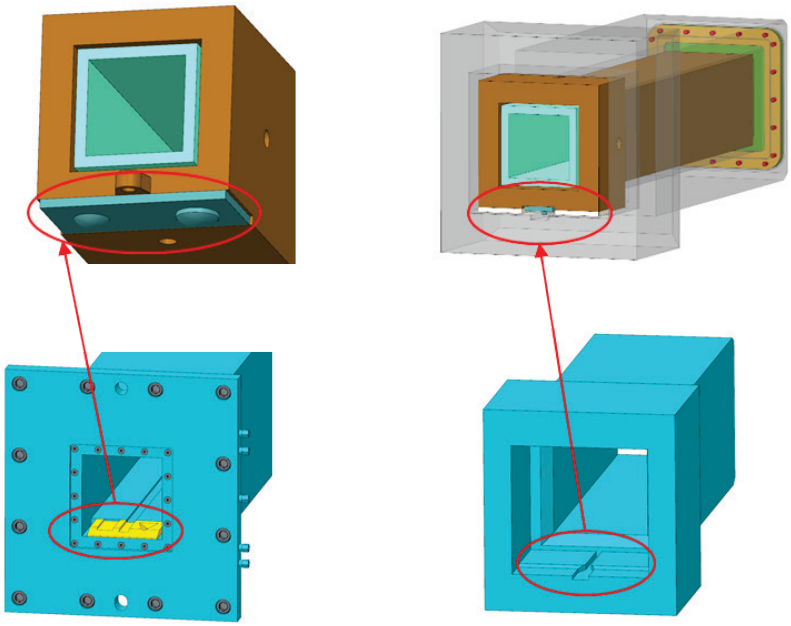

Figure 5.75. Internal kinematic alignment features of the monolith inserts. Left-side images show the downstream features, and the right-side images show the upstream features.

5.9.7.2 Neutron Beam Optics

The optical components used by STS instruments must be aligned to much greater precision than the neutron guide optics typically used by FTS instruments. There are several reasons for this. The primary reason is that the smaller size of the STS moderators is geometrically optimized for high brightness, and the use of more sophisticated optical components can achieve even higher instrument performance than would be expected from the additional brightness alone. The development follows the natural progression from neutron beam transport (neutron guide) to focusing optics (elliptical and converging guides) to imaging optics (elliptical, hyperbolic, parabolic, and logarithmic mirrors) and parallels a very similar development path in x-ray optics. The use of imaging optics on neutron scattering instruments entails large mirrors, several meters in length, separated by tens of meters. This poses some challenges:

- In many cases, a mirror is much too large to be fabricated as a single piece but must be a composite mirror assembled from several individual mirrors. The assembly must be aligned well enough to obtain the required figure of the composite mirror. The acceptable figure error in the composite mirror will depend on the particular demands of the optical system of which it is a part; but in nearly all cases, it will exceed what has been required for past installations.

- Once the mirror assemblies are aligned, they must be placed on the beamline at the correct orientation and location. The allowable tolerance for this alignment is also reduced from what has previously been required for neutron scattering beamlines.

At this point in the conceptual design, hard values for such tolerances that are based on neutronic simulations are not available. However, SNS has some experience on which to draw for both cases. The allowable figure error of a mirror assembly is not drastically different from what is required for the nested KB mirrors that have been constructed and tested in the past [Ice et al. 2009]. This work can be extended to produce mirror assemblies of the size required for STS beamlines. For the placement and orientation of the mirror assemblies on the beamline, the STS requirements can be estimated from experience in installing and aligning the mirrors on the IMAGINE beamline at HFIR. Here, two elliptical mirrors were used in series to image the entrance slit onto the sample. Each of the mirrors was about 70 cm in length, and the distance from the entrance slit to the first mirror was greater than 10 m. It was observed that translational adjustments less than 0.1 mm and rotational adjustments less than 0.01° had no measurable effect on the focal image at the sample position. These deviations simply scale with the length of the mirror and the distance between mirrors. So—for STS instruments on which the lengths of the mirrors and the distance between will not exceed a factor of 10—the alignment tolerances will scale to 0.01 mm for position and 0.001° for rotation. A system that can meet such alignment requirements is presented here.

For these imaging optics, some effort has been spent on developing a concept for the alignment and remote adjustability of these mirrors. Some of them will be several meters long and will be formed from glass segments on the order of 500 mm in length, as is currently done for curved guides. The current concept assumes these segments will be housed within vacuum housings and that the group of housings will be mounted onto a stable strongback such as a granite or steel beam using manually adjustable kinematic mounts, as shown in Figure 5.76, to account for deflections within the strongback.

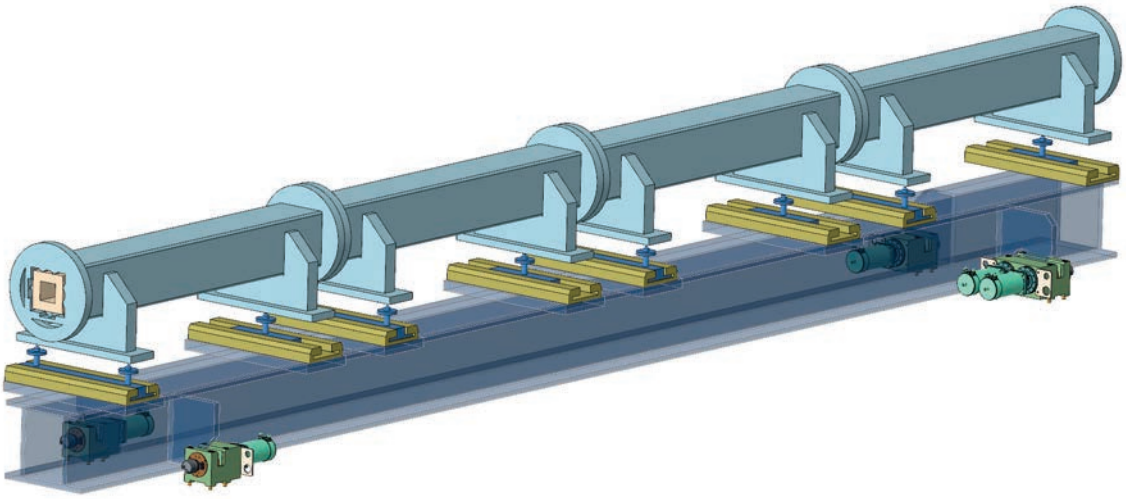

Figure 5.76. Focusing mirror assembly on remotely actuated precision movers.

The entire mirror shown in Figure 5.76 is 4 m in length with 1 m long segments. It is expected that several STS instruments will require such mirror systems, so a standard method of incorporating them is needed. Figure 5.77 shows the EWALD beamline concept near its detector and includes the second of two elliptical imaging mirrors on a remotely adjustable support system.

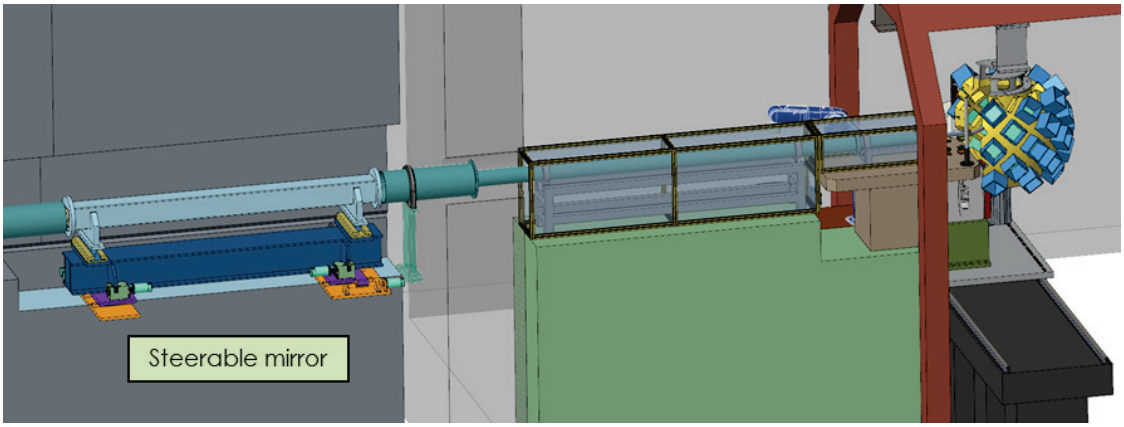

Figure 5.77. Final focusing mirror within STS EWALD instrument concept.

For external alignment of mirrors to the beamline, typical guide installation methods such as fixed supports and manual adjustment of mounts using standard survey and alignment techniques—which may be accurate to within 50–100 microns—are likely to be insufficient to ensure that neutrons are focused on the sample. This is the case particularly because some STS beamlines for which incorporation of these nested mirror systems is planned may be up to 90 m in length. Therefore, a method of remotely adjusting the entire mirror assembly is proposed. Such a system would need to stably support weights of a few tons over many years but still provide micron-level position and angle adjustability. The proposed method is illustrated conceptually in Figure 5.78 as a two-point support system with motorized actuators. This approach would enable final, remote adjustment of the optics system to tune the neutron beam at the sample position when required (i.e., as the beam optics support system responds to increased floor loading as additional instruments are installed).

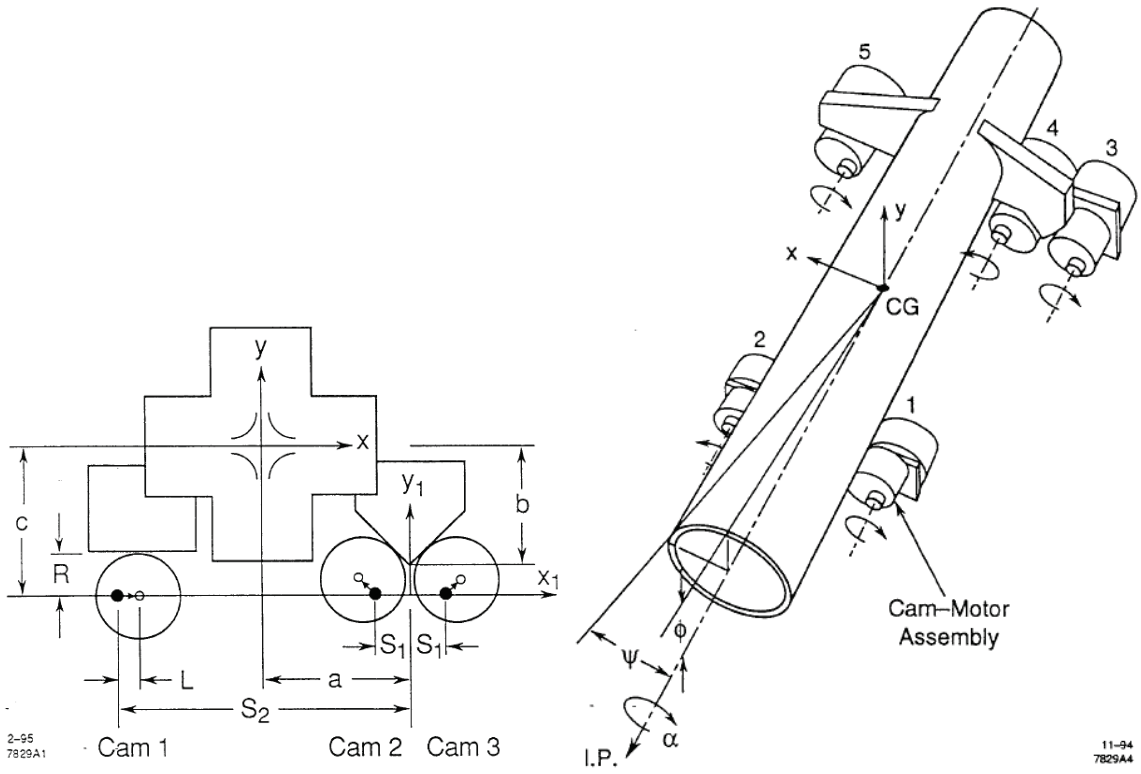

Figure 5.78. Images from SLAC-PUB-95-6132 showing the operating principle of 3- and 5-DOF eccentric roller movers.

Such a remote alignment concept is based on a magnet mover system developed for the Final Focus Test Beam at SLAC in the mid-1990s [Bowden et al. 1995]. This system used eccentric cam rollers driven by high-gear-reduction stepper motors to move 100 kg magnets over a range of a few millimeters with sub-micron precision. The basic mechanics of a 3 degrees-of-freedom (DOF) mover and a 5 DOF mover suitable for STS focusing optics are shown in Figure 5.78.

Since the initial deployment at SLAC, other facilities have successfully implemented this high-precision mover system to support heavy magnet systems. As shown in Figure 5.79, examples include the storage ring at the Swiss Light Source (SLS), the LCLS undulator magnet support system at SLAC, and the ATF2 final focus beamline at the KEK High Energy Accelerator. No implementations of such mover systems within neutron scattering facilities are known, however, so it is likely that STS may be the first to consider such a system for neutron beam focusing optics. While the engineering of such a system will require some development effort and testing, implementation at STS should be straightforward given that such systems are operational in other scientific facilities.

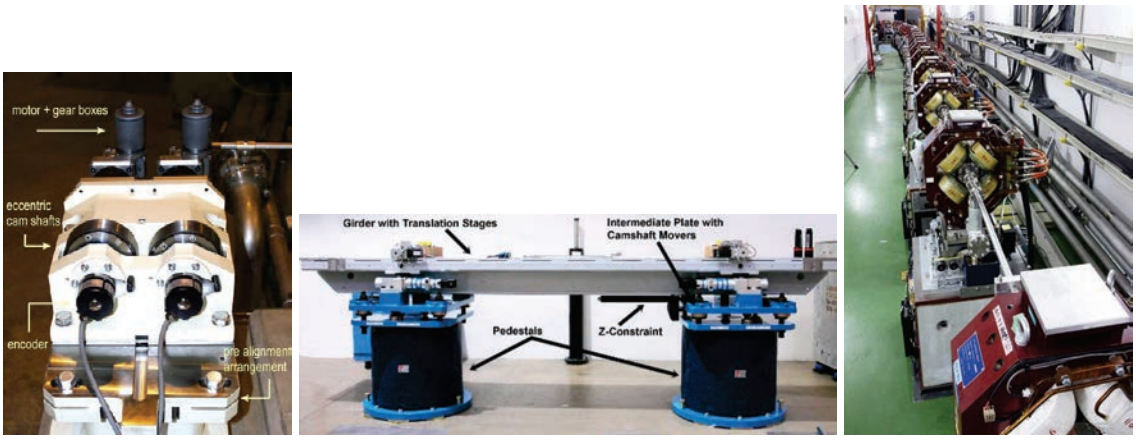

Figure 5.79. Examples of magnet mover implementations at SLS, SLAC, and KEK.

It is understood that rigidity and long-term stability of such structures is critical to their successful implementation and that environmental conditions must be tightly controlled. Experience with the HFIR IMAGINE beamline suggests the required rigidity and stability are possible; but as the mirrors grow larger, this issue will be investigated through mockups.

5.9.8 Instrument Vacuum Systems

Vacuum systems are an integral requirement for neutron beamlines. Incident flight paths are typically evacuated to minimize attenuation of the neutron beam due to scattering from air. Neutron choppers often require internal vacuum for the rotating components. Neutron instrument end stations almost always require vacuum around the sample location to enable operation of sample environment equipment like furnaces or cryostats and to minimize the amount of spurious scattering near the sample. Instruments that have a high requirement for measuring weak signals are particularly sensitive to background and may use evacuated final flight paths from the sample to the detectors to minimize air scattering.

5.9.8.1 Neutron Guides

Operating pressure in neutron guides is nominally 10–100 mTorr. Vacuum generation for the neutron guides on the various instruments will be accomplished with a central guide vacuum system. A manifold that runs around the inner bunker wall (Figure 5.79) will supply vacuum from an appropriately sized dry screw pump to each instrument, as indicated in Figure 5.80. The dry screw pump will be in the basement area of the Target Building for serviceability, along with a standby spare pump and appropriate valving and instrumentation. Each instrument's branch leg off the manifold will contain convection-enhanced Pirani pressure instrumentation, an electro-pneumatic isolation valve, and a safety valve to prevent damage to others in the event of a catastrophic failure on one instrument or the central vacuum system itself. A programmable logic controller (PLC) will be used to operate the central vacuum system and protect the guides in case of a component failure by closing one or more of the isolation valves servicing the guides.

Each individual guide section for each neutron instrument will be served by this central vacuum system. Stainless steel flex hoses will be used to serve guides that are downstream of one or more neutron choppers so that all the guide sections of a particular instrument will be daisy-chained together. The pressures in the guides will be monitored by the PLC-based controller for the instrument vacuum system.

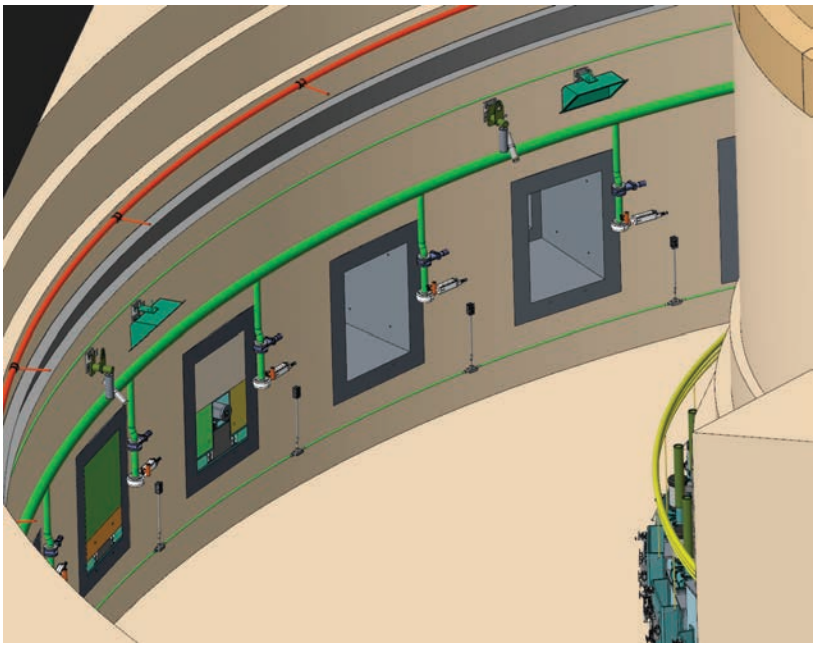

Figure 5.80. Mechanical model of STS central guide vacuum manifold. Each downward branch off the manifold includes manual and pneumatic valves that can isolate each beamline from the rest of the vacuum system.

5.9.8.2 Neutron Choppers

Operating pressure requirements in neutron choppers are dependent on the type of chopper. They range from as high as 1–10 mTorr to as low as below 0.1 mTorr. As mentioned earlier, vacuum for neutron choppers will be independent from guide vacuum. Vacuum for each chopper housing will be handled by a multi-stage roots pump or a hybrid bearing turbomolecular pump, depending on the pressure requirements of the specific chopper. In both cases, the vacuum pump will have an isolation valve that will protect the chopper in case of a pump failure, as determined by the PLC-based controller for the instrument vacuum system. Vacuum instrumentation will be selected based upon the nominal operating pressure of the chopper; it will be either a convection-enhanced Pirani or a cold cathode gauge.

5.9.8.3 Instruments

Vacuum system design for the neutron instruments will be handled on a case-by-case basis with the primary concerns being as follows:

- Pressure/time requirements from the instrument staff
- Geometry and expected gas loads for the instrument
- Commonality of equipment with the other instruments

Obviously, operational vacuum will need to be attained in a reasonable amount of time to maximize the use of neutron beam time as well as minimize recovery time after a maintenance period. For the four instrument concepts that require this system, the detector tanks will require pressures of 2E-5 Torr or lower and will be as large as 25 m^3. In each case, these specifications will be accomplished with a combination of the following:

- One or more dry screw pumps with roots-style blowers to attain rough vacuum

- One or more cryo-chillers with pumping speeds of up to 200,000 l/s to handle water vapor and other condensables

- One or more hybrid bearing turbomolecular pumps backed by multi-stage roots pumps to handle noncondensables

- Vacuum instrumentation selected based upon the nominal operating pressure—either a capacitance manometer, a convection-enhanced Pirani, or a cold cathode gauge

For example, the CHESS instrument has a requirement of reaching low E-5 Torr pressures in its 250 m^3 detector tank within 24 h. With the expected high gas loads within the vessel arising from internal neutron shielding and other sources, preliminary modeling indicates that this will require the following:

- Two 630 m^3/h dry screw pumps with 2000 m^3/h roots blowers
- Two 200,000 l/s cryo-chiller pumps
- Four 2300 l/s hybrid bearing turbomolecular pumps

Other instruments will use similar combinations of pumps based upon their specific pressure and time requirements, as well as their expected gas loads.

5.10 REFERENCES

Aksoy, S., M. Acet, P. P. Deen, et al. 2009. “Magnetic correlations in martensitic Ni-Mn-based Heusler shape-memory alloys: neutron polarization analysis,” *Phys. Rev. B* 79, 212401.

Anastasopoulos, M., R. Bebb, K. Berry, et al. 2017. “Multi-grid detector for neutron spectroscopy: Results obtained on time-of-flight spectrometer CNCS,” *J. Instrum.* 12, P04030.

Ankner, J. F., C. Rehm, E.D. Blakeman, et al. 2002., “Optical design of the SNS liquids reflectometer,” in *Advances in Neutron Scattering Information, Proceedings of SPIE*, Vol. 4785. DOI:10.1117/12.451684.

Anunciado, D. B., V. P. Nyugen, G. B. Hurst, et al. 2017. “In vivo protein dynamics on the nanometer length scale and nanosecond time scale,” *J. Phys. Chem. Lett.* 8(8), 1899–1904. DOI: 10.1021/acs.jpclett.7b00399.

Arnold, O., J. C. Bilheux, J. M. Borreguero, et al. 2014. "Mantid-Data analysis and visualization package for neutron scattering and mu SR experiments." *Nuclear Instruments & Methods in Physics Research Section a-Accelerators Spectrometers Detectors and Associated Equipment* **764**: 156-166.

Baltz, V., A. Manchon, M. Tsoi, et al. 2018. “Antiferromagnetic spintronics,” *Rev. Mod. Phys*. 90, 015005. DOI: 10.1103/RevModPhys.90.015005.

Balz, C., B. Lake, J. Reuther, et al. 2016. “Physical realization of a quantum spin liquid based on a complex frustration mechanism,” *Nat. Phys.* 12, 942–949. DOI: 10.1038/nphys3826.

Barthem, V.M.T.S., C.V. Colin, H. Mayaffre, et al. 2013. “Revealing the properties of Mn_2Au for antiferromagnetic spintronics,” *Nat. Commun*. 4, 2892. DOI: 10.1038/ncomms3892.

Baum, M., K. Schmalzl, P. Steffens, et al. 2013. “Controlling toroidal moments by crossed electric and magnetic fields,” *Phys. Rev. B* 88, 024414.

Berman, H. M., J. Westbrook, Z. Feng, et al. 2000. “The Protein Data Bank,” *Nucleic Acids Res.*, 28(1), 235–241. DOI: https://doi.org/10.1093/nar/28.1.235.

Bertaina, S., S. Gambarelli, T. Mitra, et al. 2008. “Quantum oscillations in a molecular magnet,” *Nature* 453(7192), 203. DOI: 10.1038/nature06962.

Betzig, E., G. H. Patterson, R. Sougrat, et al. 2006. “Imaging intracellular fluorescent proteins at nanometer resolution,” *Science* 313(5793), 1642–1645.

Bewley, R. I., J. W. Taylor and S. M. Bennington. 2011. “LET, a cold neutron multi-disk chopper spectrometer at ISIS,” *Nucl. Instrum. Methods Phys. Res A* 637(1), 128–134.

Bingham, P. A. and R. J. Hand. 2006. “Vitrification of toxic wastes: A brief review,” *Adv. Appl. Ceram.* 105, 21–3. DOI: 10.1179/174367606X81687.

Bowden, G., P. Holik, and S. R. Wagner. 1995. *Precision Magnet Movers for the Final Focus Test Beam*, SLAC-PUB-95-6132, Stanford Linear Accelerator Center, June 1995.

Bridges, C. A., X. G. Sun, J. Zhao, et al. 2012. “In situ observation of solid electrolyte interphase formation in ordered mesoporous hard carbon by small-angle neutron scattering,” *J. Phys. Chem. C* 116, 7701–7711. DOI: 10.1021/jp3012393.

Browning, J. F., L. Baggetto, K. L. Jungjohann, et al. 2014. “In situ determination of the liquid/solid interface thickness and composition for the Li ion cathode $LiMn_{1.5}Ni_{0.5}O_4$,” *ACS Appl. Mater. & Interf.* 6, 18569. DOI: 10.1021/am5032055.

Burankova, T., R. Hempelmann, A. Wildes, et al. 2014. “Collective ion diffusion and localized single particle dynamics in pyridinium-based ionic liquids,” *J. Phys. Chemistry B* 118(49), 14452-60. DOI: 10.1021/jp5092416.

Burle, J., C. D., J. M. Fisher, et al. 2018. “BornAgain—Software for simulating and fitting x-ray and neutron small-angle scattering at grazing incidence, version N.n,” .http://www.bornagainproject.org. Accessed July 2019.

Butler, K. T., D. W. Davies, H. Cartwright, et al. 2018. “Machine learning for molecular and materials science." *Nature* 559(7715), 547–555.

Cabrera, I., M. Kenzelmann, G. Lawes, et al. 2009. “Coupled magnetic and ferroelectric domains in multiferroic $Ni_3V_2O_8$,” *Phys. Rev. Let*t. 103, 087201.

Cai, L., K. An, Z. L. Feng, et al. 2013. “In-situ observation of inhomogeneous degradation in large format Li-ion cells by neutron diffraction,” *J. Power Sources* 236, 163–168.

CAMEA—Continuous Angle Multi-Energy Analysis—Spectrometer Concept Phase Report: ESS Instrument Construction Proposal, internal technical report, 2014.

Campbell, R. A., H. P. Wacklin, I. Sutton, et al. 2011. “FIGARO: The new horizontal neutron reflectometer at the ILL,” *Eur. Phys. J. Plus* 126, 107. DOI: 10.1140/epjp/i2011-11107-8.

Capel, D. 2004. *Image Mosaicing and Super-Resolution*, Springer–Verlag.

Carpenter, J. M., and W. B. Yelon. 1986. “Neutron sources,” *Methods in Exp. Phys*, 23 (part A), 99–196.

Castelnovo, C., R. Moessner, and S. L. Sondhi. 2008. “Magnetic monopoles in spin ice,” *Nature* 451, 42–45.

Chi, E. Y., S. Krishnan, T. W. Randolph, et al. 2003. “Physical stability of proteins in aqueous solution: Mechanism and driving forces in nonnative protein aggregation,” *Pharm. Res*. 20, 1325. DOI: 10.1023/A:1025771421906.

Chourou, S. T., A. Sarje, X. Y. S. Li, et al. 2013. “HipGISAXS: A high-performance computing code for simulating grazing-incidence X-ray scattering data,” *J. Appl. Crystallogr*. 46, 1781–1795.

Coates, L., and L. Robertson. 2017. “EWALD: an extended wide-angle Laue diffractometer for the second target station of the Spallation Neutron Source,” *J. Appl. Crystallogr.*, 50(4), 1174–1178.

Coates, L., H. B. Cao, B. C. Chakoumakos, et al. 2018. “A suite-level review of the neutron single-crystal diffraction instruments at Oak Ridge National Laboratory,” *Rev. Sci. Instrum.*, 89(9), 092802. DOI: 10.1063/1.5030896.

Coates, L., M. J. Cuneo, M. J. Frost, et al. 2015. “The macromolecular neutron diffractometer MaNDi at the Spallation Neutron Source,” *J. Appl. Crystallogr.*, 48, 1302–1306.

Dalgliesh, R. M., A. A. van Well, S. Boag, et al. 2007. “Broad bandpass spin polarizers for the ISIS second target station,” *Physica B–Condens. Matter* 397(1–2), 176–178.

Daniel, J. S., B. Lesage and P. Lacombe. 1971. “Influence of temperature on slip and twinning in uranium,” *Acta Metall.* 19(2), 163.

Delaire, O., J. Ma, K. Marty, et al. 2015. “Giant anharmonic phonon scattering in PbTe,” *Nat. Mater.* 10(8), 614.

Di Lorenzo, M. L., and C. Silvestre. 1999. “Non-isothermal crystallization of polymers,” *Prog. Polymer Sci*. 24, 917–950. DOI: 10.1016/S0079-6700(99)00019-2.

Diallo, S. O., J. Y. Y. Lin, D. L. Abernathy, et al. 2016. “Momentum and energy dependent resolution function of the ARCS neutron chopper spectrometer at high momentum transfer: Comparing simulation and experiment,” *Nucl. Instrum. Methods Phys. Res A* 835, 34–41.

Do, C., W. T. Heller, C. Stanley, et al. 2014. “Understanding inelastically scattered neutrons from water on a time-of-flight small-angle neutron scattering (SANS) instrument,” *Nucl. Inst. Meth. Phys. Res. A* 737, 42–46. DOI: 10.1016/j.nima.2013.11.030.

DOE (Department of Energy). 2014. *Quantum Condensed Matter*, Report of the Quantum Condensed Matter Workshop, Berkeley, CA, December 9–10, 2013, R. J. Birgenau, R. Ramesh, and S. E. Nagler, chairs. https://neutrons.ornl.gov/sites/default/files/Berkeley_workshop_report_2014_rev_10.pdf (2014).

DOE (US Department of Energy). 2016. *Basic Research Needs Workshop on Quantum Materials for Energy Relevant Technology*, February 8–10, 2016, BES Workshop Reports, Office of Basic Energy Sciences. https://science.osti.gov/-/media/bes/pdf/reports/2016/BRNQM_rpt_Final_12-09-2016.pdf?la=en&hash=E7760711641883FFC9F110D70385937D6A31C64F.

Dos Santos, L.H.R., A. Lanza, A. M. Barton, et al. 2016. “Experimental and theoretical electron density analysis of copper pyrazine nitrate quasi-low-dimensional quantum magnets,” *J. Am. Chem. Soc*. 138(7), 2280−2291.

Doster, W., S. Cusack, and W. Petry. 1989. “Dynamical transition of myoglobin revealed by inelastic neutron scattering,” *Nature* 337(6209), 754–56. DOI: 10.1038/337754a0.

Dyson, H. J., and P. E. Wright. 2002. “Coupling of folding and binding for unstructured proteins,” *Curr. Opin. Struc. Bio*. 12, 54. DOI: 10.1016/S0959-440X(02)00289-0.

Ehlers, G., G. Sala, F. Gallmeier, et al. 2018. “Figure-of-merit for a cold coupled moderator at the SNS Second Target Station suited for direct geometry inelastic spectrometers,” *J. Phys.: Conf. Ser.* 1021, 012032. DOI 10.1088/1742-6596/1021/1/012032.

Eskildsen, M. R., and B. Kayhovich, chairs. 2015. *Second Target Station Workshop Report*, Second Target Station Workshop held at Oak Ridge National Laboratory, October 27–29, 2015.

Fabelo, O., L. Cañadillas-Delgado, I. P. Orench, et al. 2011. “Low temperature neutron diffraction studies in [Mn3(suc)2(ina)2]n: an homometallic molecular 3D ferrimagnet,” *Inorg. Chem.* 50, 7129.

Fennell, T., P. P. Dean, A. R. Wildes, et al. 2009. “Magnetic Coulomb phase in the spin ice $Ho_2Ti_2O_7$,” Science 326, 415.

Fennell, T., S. T. Bramwell, D. F. McMorrow, et al. 2007. “Pinch points and Kasteleyn transitions in kagome ice,” *Nat. Phys.* 3, 566–572.

Fisher, E. S. 1966. “Temperature dependence of elastic moduli in alpha uranium single crystals. 4. (298 degrees to 923 degrees K),” *J. Nucl. Mater.* 18(1), 39.

Frandsen, B. A., K. A. Ross, J. W. Krizan, et al., 2017. “Real-space investigation of short-range magnetic correlations in fluoride pyrochlores $NaCaCo_2F_7$ and $NaSrCo_2F_7$ with magnetic pair distribution function analysis,” *Phys. Rev. Mater.* 1, 074412.

Frandsen, B. A., M. Brunelli, K. Page, et al. 2016. “Verification of Anderson superexchange in MnO via magnetic pair distribution function analysis and ab initio theory,” *Phys. Rev. Lett.* 116, 197204.

Frandsen, B. A., X. Yang, S.K.L. Billinge, et al. 2014. “Magnetic pair distribution function analysis of local magnetic correlations,” *Acta Crystallogr*. A70, 3–11.

Freeman, W. T., E. C. Pasztor, and O. T. Carmichael. 2000. “Learning low-level vision,” *Int. J. Comput. Vis.* 40(1), 25–47.

Freiman, Y., and H-J. Jodl. 2004. “Solid oxygen,” *Physics Reports* 401(1–4), 1–228.

Frick, B., and D. Richter. 1995. “Microscopic basis of the glass transition in polymers from neutron scattering studies,” *Science* 267(5206), 1939–45. DOI: 10.1126/science.267.5206.1939.

Fritsch, V. N. Bagrets, G. Goll, et al. 2014. “Approaching quantum criticality in a partially geometrically frustrated heavy-fermion metal,” *Phys. Rev. B* 89(5), 054416. DOI: 10.1103/PhysRevB.89.054416.

Fultz, B. 2010. “DANSE—Distributed Data Analysis for Neutron Scattering Experiments,” http://danse.us. Accessed July 2019

Gallmeier, F. X. 2018. *A Liquid Hydrogen Tube Moderator Arrangement for STS,* STS03-31-TR0005-R00, Oak Ridge National Laboratory.

Gallmeier, F. X., W. Lu, B. W. Riemer et al. 2016. “Conceptual moderator studies for the Spallation Neutron Source short-pulse Second Target Station,” *Rev. Sci. Instrum.* 87, 063304-1–13. DOI: 10.1063/1.4953612.

Ganichev, S, D., E. L. Ivchenko, V. V. Bel’kov, et al. 2002. “Spin-galvanic effect,” *Nature* 417(6885), 153. DOI: 10.1038/417153a.

Garlea, V. O., A. Zheludev, K. Habicht, et al. 2009. “Dimensional crossover in a spin-liquid-to-helimagnet quantum phase transition,” *Phys. Rev. B* 79(6), 060404.

Gaspar, A. M., S. Busch, M.-S. Appavou, et al. 2010 “Using polarization analysis to separate the coherent and incoherent scattering from protein samples,” *Biochim. Biophys. Acta* 1804(1), 76–82. DOI: 10.1016/j.bbapap.2009.06.024.

Gerelli, Y., L. Porcar, and G. Fragneto. 2012. “Lipid rearrangement in DSPC/DMPC bilayers: A neutron reflectometry study,” *Langmuir* 28, 15922. DOI: 10.1021/la303662e.

Giamarchi, T., C. Rüegg, and O. Tchernyshyov. 2008. “Bose–Einstein condensation in magnetic insulators,” *Nat. Phys*. 4, 198–204.

Glasner, D., S. Bagon, M. Irani. 2009. “Super-resolution from a single image,” in *International Conference on Computer Vision 2009*. http://www.wisdom.weizmann.ac.il/~vision/single_image_SR/files/single_image_SR.pdf. Accessed July 2019

Goncharenko, N., O. Makarova, and L. Ulivi. 2004. “Direct determination of the magnetic structure of the delta phase of oxygen,” *Phys. Rev. Lett*. 93, 055502.

Granroth, G. E. 2011. “Advances in neutron spectroscopy and high magnetic field instrumentation for studies of correlated electron systems,” *J. Phys. Soc. Jpn.* 80.

Granroth, G. E., K. An, H. L. Smith, et al. 2018. “Event-based processing of neutron scattering data at the Spallation Neutron Source,” *J. Appl. Crystallogr.* 51, 616–629.

Groen, D., G. S. Gooris, D. J. Barlow, et al. 2011. “Disposition of ceramide in model lipid membranes determined by neutron diffraction,” *Biophys. J*. 100, 1481–1489. DOI: 10.1016.j.bpj.2011.02.001.

Groom, C. R., I. J. Bruno, M. P. Lightfoot, et al. 2016. “The Cambridge Structural Database,” *Acta Crystallogr., Sect. B: Struct. Sci., Cryst. Eng. Mater.*, B72, 171–179. DOI: 10.1107/S2052520616003954

Gu, M., L. R. Parent, B. Layla Mehdi, et al. 2013. “Demonstration of an electrochemical liquid cell for operando transmission electron microscopy observation of the lithiation/delithiation behavior of Si nanowire battery anodes,” *ACS Nano Letters* 13, 6106. DOI: 10.1021/nl403402q.

Hahn, S. E., A. A. Podlesnyak, G. Ehlers, et al. 2014. “Inelastic neutron scattering studies of $YFeO_3$,” *Phys. Rev. B* 89(1).

Hammouda, B. 2010. “SANS from polymers—Review of recent literature,” *Polymer Reviews* 50, 14–39. DOI: 10.1080/15583720903503460.

Hany, S., M. Milochova, K. Littrell, et al. 2018. “Advanced characterization of cryogenic ^{9}Ni steel using synchrotron radiation, neutron scattering and ^{57}Fe Mössbauer spectroscopy,” *Mater. Des*. 146, 219–22. DOI: 10.1016/j.matdes.2018.03.024.

Harburn, G., C. A. Taylor, and T. R. Welberry. 1975. *Atlas of Optical Transforms*, G. Bell and Sons, London.

Harcombe, D. R., P. G. Welch, P. Manuel, et al. 2016. “One-dimensional magnetic order in the metal-organic framework $Tb(HCOO)_3$,” *Phys. Rev. B* 94, 174429.

Heinrich, B., Z. Celinski, J. F. Cochran, et al. 1993. “Bilinear and biquadratic exchange coupling in bcc Fe/Cu/Fe trilayers: Ferromagnetic-resonance and surface magneto-optical Kerr-effect studies,” *Phys. Rev. B* 47, 5077. DOI: 10.1103/PhysRevB.47.5077.

Hell, S. W., M. Dyba, and S. Jakobs. 2004. “Concepts for nanoscale resolution in fluorescence microscopy,” *Curr. Opin. Neurobiol.* 14(5), 599–609.

Hellenbrandt, M. 2004. “The Inorganic Crystal Structure Database (ICSD)—Present and future,” *Crystallogr. Rev.* 10(1), 17–22.

Heller, W. T. 2016. “An expert system for automated modeling of small-angle neutron scattering data,” presentation to *Laboratory Directors Research and Development Program*, Oak Ridge National Laboratory.

Hellman, F., A. Hoffmann, Y. Tserkovnyak, et al. 2017. “Interface-induced phenomena in magnetism,” *Rev. Mod. Phys*. 89, 25006. DOI: 10.1103/RevModPhys.89.025006.

Hermida-Merino, D., G. Portale, P. Fields, et al. 2014. “A high pressure cell for supercritical CO_2 on-line chemical reactions studied with X-ray techniques,” *Rev. Sci. Instrum*. 85, 093905. DOI: 10.1063/1.4895717.

Higgins, J. S. and H. C. Benoít. 1997. *Polymers and Neutron Scattering*, Clarendon Press, Oxford, UK. ISBN: 9780198500636.

Hoffmann, A., and S. D. Bader. 2015. “Opportunities at the frontiers of spintronics,” *Phys. Rev. Appl.* 4, 047001. DOI: 10.1103/PhysRevApplied.4.047001.

Huang, S. Y., K. An, Y. Gao, et al. 2018. “Determination of gamma/gamma ' lattice misfit in Ni-based single-crystal superalloys at high temperatures by neutron diffraction,” *Metall. Mater. Trans. A* 49a(3), 740–751.

Hüger, E., J. Stahn, and H. Schmidt. 2015. “Neutron reflectometry to measure in situ Li permeation through ultrathin silicon layers and interfaces,” *J. Electrochem. Soc.* 162, A7104. DOI: 10.1149/2.0131513jes.

Hussein, R., M. Ibrahim, R. Chatterjee, et al. 2018. “Optimizing crystal size of photosystem II by macroseeding: Toward neutron protein crystallography,” *Cryst. Growth Des.*, 18(1), 85–94.

Ice, G., R. Barabash, A. Khounsary. 2009. “Nested mirrors for x-rays and neutrons,” *Proc. SPIE 7448, Advances in X-Ray/EUV Optics and Components IV*, 74480B, September 4, 2009. https://doi.org/10.1117/12.831078

Irani, M., and S. Peleg. 1991. “Improving resolution by image registration,” *CVGIP—Graphical Models and Image Processing* 53(3), 231–239.

Jana, S., B. Dutta, R. Bera, et al. 2008. “Immobilization of palladium in mesoporous silica matrix: Preparation, characterization, and its catalytic efficacy in carbon-carbon coupling reactions,” *Inorg. Chem*. 47, 5512–5520. DOI: 10.1021/ic80004294.

Jennings, J., S. P. Bassett, D. Hermida-Merino, et al. 2016. “How does dense phase CO_2 influence the phase behavior of block copolymers synthesized by dispersion polymerisation?” *Polym. Chem*. 7, 905–916. DOI: 10.1039/c5py01823d.

J-PARC (Japan Proton Accelerator Research Complex) 2011. “Materials and Life Science Experimental Facility.” https://j-parc.jp/researcher/MatLife/en/instrumentation/ns.html

Kai, T., M. Harada, M. Teshigawara, et al. 2005. “Neutronic performance of rectangular and cylindrical coupled hydrogen moderators in wide-angle beam extraction of low-energy neutrons,” *Nucl. Instrum. Meth. Phys. Res. A*, 550, 329–342. DOI: 10.1016/j.nima.2005.04.082.

Kamiya, Y., and C. D. Batista. 2014. “Magnetic vortex crystals in frustrated Mott insulator,” *Phys. Rev. X* (4), 011023. DOI: 10.1103/PhysRevX.4.011023.

Kern, J., R. Tran, R. Alonso-Mori, et al. 2014. “Taking snapshots of photosynthetic water oxidation using femtosecond x-ray diffraction and spectroscopy,” *Nat. Commun.* 5, 4371.

Khademi, S., J. O’Connell, J. Remis, et al. 2004. “Mechanism of ammonia transport by Amt/MEP/Rh: Structure of AmtB at 1.35 A,” *Science*, 305(5690), 1587–1594. DOI: 10.1126/science.1101952.

Kim, J.-H., A. Huq, M. Chi, et al. 2014. “Integrated nano-domains of disordered and ordered spinel phases in $LiNi_{0.5}Mn_{1.5}O_4$ for Li-ion batteries,” *Chem. Mater*. 26, 4377–4386. DOI: 10.1021/cm501203r.

Kim, K. H., N. Harrison, H. Amitsuka, et al. 2004. “Nexus between quantum criticality and phase formation in $U(Ru_{1-x}Rh_x)_2Si_2$,” *Phys. Rev. Lett.* 93, 206402.

Kittelmann, T., E. Klinkby, E. B. Knudsen, et al. 2017. “Monte Carlo Particle Lists: MCPL.” *Comput. Phys. Commun.* 218, 17–42.

Klotz, S., Th. Strässle, A. L. Cornelius, et al., 2010. “Magnetic ordering in solid oxygen up to room temperature,” *Phys. Rev. Lett.* 104, 115501–4.

Klotz, S., Th. Strässle, and Th. Hansen. 2012. “Magnetism of solid oxygen under pressure by neutron scattering,” *Notic. Neutr. Luce Sinc.* 17, 1004, 10–15.

Konnecke, M., F. A. Akeroyd, H. J. Bernstein, et al. 2015. “The NeXus data format,” *J. Appl. Crystallogr.* 48(1), 301–305.

Kozlovskaya, V., O. Zavgorodnya, Y. Wang, et al. 2013. “Tailoring architecture of nanothin hydrogels: Effect of layering on pH-triggered swelling,” *ACS Macro Lett.* 2, 226. DOI: 10.1021/mz300661f.

Kurmoo, M., 2009. “Magnetic metal-organic frameworks,” *Chem. Soc. Rev*. 38(5), 1353–1379.

Lacy, J. L., A. Athanasiades, L. Sun, et al. 2011. “Boron-coated straws as a replacement for 3 He-based neutron detectors,” *Nucl. Instrum. Methods A* 652, 359–363.

Langan, P. S., V. G. Vandavasi, S. J. Cooper, et al. 2018. “Substrate binding induces conformational changes in a class A β-lactamase that prime it for catalysis,” *ACS Catal.* 8(3), 2428–2437. DOI: https://doi.org/10.1021/acscatal.7b04114.

Lee, P. A., N. Nagaosa, and X.-G. Wen. 2006. “Doping a Mott insulator: Physics of high-temperature superconductivity,” *Rev. Mod. Phys.* 78(1), 17–85. DOI: https://doi.org/10.1103/RevModPhys.78.17.

Leonov, A. O., and M. Mostovoy. 2015. “Multiply periodic states and isolated skyrmions in an anisotropic frustrated magnet,” *Nat. Commun*, 6, 8275. DOI: https://doi.org/10.1038/ncomms9275.

Li, C. W., J. Hong, A. F. May, et al. 2015. “Orbitally driven giant phonon anharmonicity in SnSe,” *Nat. Phys.* 11, 1063.

Lin, , J.Y.Y., H. L. Smith, G. E. Granroth, et al. 2016. “MCViNE—An object oriented Monte Carlo neutron ray tracing simulation package,” *Nucl. Instrum. and Meth. A* 810, 86. DOI: 10.1016/j.nima.2015.11.118.

Lin, J.Y.Y., A. A. Aczel, D. L. Abernathy, et al. 2014. “Using Monte Carlo ray tracing simulations to model the quantum harmonic oscillator modes observed in uranium nitride,” *Phys. Rev. B* 89(14).

Liu, H. D., H. Liu, I. D. Seymour, et al. 2018. “Identifying the chemical and structural irreversibility in $LiNi_{0.8}Co_{0.15}Al_{0.05}O_2$—A model compound for classical layered intercalation,” *J. Mater. Chem. A* 6(9), 4189–4198.

Liu, J., and J. C. Conboy. 2005. “1,2-diacyl-phosphatidylcholine flip-flop measured directly by sum-frequency vibrational spectroscopy,” *Biophys. J.* 89, 2522. DOI: 10.1529/biophysj.105.065672.

Lu, W., J. Zhang, J. Xu, et al. 2017. “In situ visualized cathode electrolyte interphase on $LiCoO_2$ in high voltage cycling,” *ACS Appl. Mater. & Interf.* 9, 19313. DOI: 10.1021/acsami.7b03024.

Machida, Y., S. Nakatsuji, S. Onoda, et al. 2010. “Time-reversal symmetry breaking and spontaneous Hall effect without magnetic dipole order,” *Nature* 463(7278), 201. DOI: 10.1038/nature08680

Mamontov, E., and K. W. Herwig. 2011. “A time-of-flight backscattering spectrometer at the Spallation Neutron Source, BASIS,” *Rev. Sci. Instrum.* 82, 085109.

Marchler-Bauer, A., Y. Bo, L. Han, et al. 2017. “CDD/SPARCLE: Functional classification of proteins via subfamily domain architectures,” *Nuc. Acids Res.* 45(D1): D200–D203.

Martin, I., and C. D. Batista. 2008. “Itinerant electron-driven chiral magnetic ordering and spontaneous quantum Hall effect in triangular lattice models,” *Phys. Rev. Lett.* 101(15), 156402. DOI: https://doi.org/10.1103/PhysRevLett.101.156402.

Matsuda, Y. H., N. Abe, S. Takeyama, et al. 2013. “Magnetization of $SrCu_2(BO_3)2$ in ultrahigh magnetic fields up to 118 T,” *Phys. Rev. Lett.* 111, 137204.

Matsuhira, K., M. Wakeshima, Y. Hinatsu, et al. 2007. “Crystalline electric field study in the pyrochlore $Nd_2Ir_2O_7$ with metal-insulator transition,” *J. Phys. Soc. Jpn*. 76, 043706.

Mauri, G., F. Messi, M. Anastasopolous, et al. 2018. “Neutron reflectometry with the multi-blade ^{10}B-based detector,” *Proc. R. Soc. A* 474, 20180266.

Mellnik, A. R., J. S. Lee, A. Richardella, et al. 2014. “Spin-transfer torque generated by a topological insulator,” *Nature* 511(7510), 449. DOI: 10.1038/nature13534.

Minnich, A. J., M. S. Dresselhaus, Z. F. Ren, et al. 2009. “Bulk nanostructured thermoelectric materials: Current research and future prospects,” *Energy Environ. Sci.* 2, 466.

Mirkin, C. A., R. L. Letsinger, R. C. Mucic, et al. 1996. “A DNA-based method for rationally assembling nanoparticles into macroscopic materials,” *Nature* 382, 607–609. DOI: 10.1038/382607a0.

Motokawa, R., T. Kobayashi, H. Endo, et al. 2019. “A telescoping view of solute architectures in a complex fluid system,” *ACS Cent. Sci*. 5, 85–96. DOI: 10.1021/acscensci.8b00669.

Mueller, T., A. G. Kusne, and R Ramprasad. 2016. “Machine Learning in Materials Science: Recent Progress and Emerging Applications,” Chapter 4 in *Reviews in Computational Chemistry*, vol. 29, 186–273, John Wiley and Sons.

Mühlbauer, S., B. Binz, F. Jonietz, et al. 2009. “Skyrmion lattice in a chiral magnet,” *Science* 323(5916), 915–919. DOI: 10.1126/science.1166767.

Nakamura, M., R. Kajimoto, Y. Inamura, et al. 2009. “First demonstration of novel method for inelastic neutron scattering measurement utilizing multiple incident energies.” *J. Phys. Soc. Jpn.* 78(9), 093002.

Nakhoul, N. L., and L. L. Hamm. 2004. “Non-erythroid Rh glycoproteins: A putative new family of mammalian ammonium transporters,” *Pflugers Arch*, 447(5), 807–812. DOI:10.1007/s00424-003-1142-8.

Nash, K. L. G. L. Jumetta, S. B. Clark, et al. 2006. “Significance of the nuclear fuel cycle in the 21st Century,” in *Separations for the Nuclear Fuel Cycle in the 21st Century, ACS Symposium Series* 933, eds. G. L. Lumetta, K. L. Nash, S. B. Clark, and J. Friese, American Chemical Society, Washington, DC, 2006, pp. 21-40. DOI: 10.1021/bk-2006-0933.ch001

Nickels, J. D., H. O’Neill, L. Hong, et al. 2012. “Dynamics of protein and its hydration water: Neutron scattering studies on fully deuterated GFP,” *Biophys. J*, 103, 1566.

Nickels, J. D., S. Chatterjee, C. B. Stanley, et al. 2017. “The in vivo structure of biological membranes and evidence for lipid domains,” *PLoS Biol*, 15, e2002214.

Nickels, J. D., S. Perticaroli, H. O’Neill, et al. 2013. “Coherent neutron scattering and collective dynamics in the protein, GFP,” *Biophys. J.* 105, 2182.

Noda, Y., S. Koizumi, T. Masui, et al. 2016. “Contrast variation by dynamic nuclear polarization and time-of-flight small-angle neutron scattering. I. Application to industrial multi-component nanocomposites,” *J. Appl. Crystallogr.* 49, 2036–2045. DOI: 10.1107/S1600576716016472.

Okawa, M., M. Matsunami, K. Ishizaka, et al. 2010. “Strong valence fluctuation in the quantum critical heavy fermion superconductor β-YbAlB4: A hard x-ray photoemission study,” *Phys. Rev. Lett.* 104, 247201.

Orenstein, J., and A. J. Millis. 2000. “Advances in the physics of high-temperature superconductivity,” *Science* 288(5465), 468.

ORNL (Oak Ridge National Laboratory) 2015. *Second Target Station Workshop Report*. workshop co-chairs M. R. Eskildsen and B. Khaykovich. https://neutrons.ornl.gov/sites/default/files/STS%20Workshop%20Report.pdf.

Paddison, J.A.M., M. Daum, Z. Dun, et al. 2017. “Continuous excitations of the triangular-lattice quantum spin liquid $YbMgGaO_4$,” *Nat. Phys*. 13, 117.

Pappas, C. 2012. “A new twist in chiral magnets,” *Physics—Uspekhi* 5(28). DOI: 10.1103/Physics.5.28.

Perticaroli, S., G. Ehlers, C. B. Stanley, et al. 2017. “Description of hydration water in protein (green fluorescent protein) solution,” *J. Am. Chem. Soc*, 139, 1098.

Perticaroli, S., J. D. Nickels, G. Ehlers, et al. 2013. “Secondary structure and rigidity in model proteins,” *Soft Matter* 9, 9548.)

Pesin, D., and L. Balants. 2010. “Mott physics and band topology in materials with strong spin–orbit interaction,” *Nat. Phys.* 6, 376–38.

Peterson, P. F., D. Olds, A. T. Savici, et al. 2018. “Advances in utilizing event based data structures for neutron scattering experiments,” *Rev. Sci. Instrum.* 89(9).

Petrovic, C., P. G. Pagliuso, M. F. Hundley, et al. 2001. “Heavy-fermion superconductivity in $CeCoIn_5$ at 2.3 K,” *J. Phys.: Condens. Matter 13*, L337.

Pfleiderer, C. 2009. “Superconducting phases of f-electron compounds,” *Rev. Mod. Phys.* 81(4), 1551. DOI: https://doi.org/10.1103/RevModPhys.81.1551.

Pierce, J., D. Crabb, and J. K. Zhao. 2009. “Dynamically polarized sample for neutron scattering at the Spallation Neutron Source,” *Spin Physics*, 1149, 872–875.

Pierce, J., D. G. Crabb, S. Tomanicek, et al. 2010. “Dynamically polarized sample at the Spallation Neutron Source,” *J. Phys.: Conf. Ser.*, 251(1), 012088. DOI: https://doi.org/10.1088/1742-6596/251/1/012088.

Prisk, T. R., M. S. Bryan, P. E. Sokol, et al. 2017. “The momentum distribution of liquid,” *J. Low Temp. Phys.* 189(3–4), 158–184.

Proffen, T. 2015. “Analysis and feature detection in large volumes of diffuse x-ray and neutron scattering from complex materials,” Supercomputing 2015, Austin, Texas, November 15–15, 2015.

Qi, X.-L., T. L. Hughes, and S.-C. Zhang. 2008. “Topological field theory of time-reversal invariant insulators,” *Phys. Rev. B* 78, 195424. DOI: 10.1103/PhysRevB.78.195424.

Qian, S., and D. K. Rai. 2018. “Grazing-angle neutron diffraction study of the water distribution in membrane hemifusion: from the lamellar to the rhombohedral phase,” *J. Phys. Chem. Lett*. 9, 5788–5784. DOI: 10.1021/acs.jpclett.8b01602.

Ragarajan, P., R. A. Register, L. J. Fetters, et al. 1995. “Crystallization in weakly segregated polyolefin diblock copolymer,” *Macromolecules* 28, 4932–4938. DOI: 10.1021/ma00118a021.

Ressouche, E., M. Loire, V. Simonet, et al. 2010. “Magnetoelectric $MnPS_3$ as a candidate for ferrotoroidicity,” *Phys. Rev. B* 82, 100408(R).

Rosenkranz, S., and Osborn, R. 2008. “CORELLI: Efficient single crystal diffraction with elastic discrimination,” *Pramana—J. Phys*. 71, 705–711. DOI: 10.1007/s12043-008-0259-x.

Russina, M., and F. Mezei. 2009. “First implementation of repetition rate multiplication in neutron spectroscopy,” *Nucl. Inst. Meth. Phys. Res. A* 604(3), 624–631.

Ryan, A. J., I. W. Hamley, and F. S. Bates. 1995. “Structure development in semicrystalline diblock copolymers crystallizing from the ordered melt,” *Macromolecules* 28, 3860–3868. DOI: 10.1021/ma.00115a016.

Sala, G., J.Y.Y. Lin, V. B. Graves, et al. 2018. “Conceptual design of CHESS, a new direct-geometry inelastic neutron spectrometer dedicated to studying small samples,” *J. Appl. Crystallogr*, 51, 282.

Sanchez, I. C. (ed.) 2013. *Physics of Polymer Surfaces and Interfaces*, Butterworth-Heinemann, Waltham, MA.

Savary, L., E.-G. Moon, and L. Balents. 2014. “New type of quantum criticality in the pyrochlore iridates,” *Phys. Rev. X* 4, 041027.

Schultz, A. J., P. Thiyagarajan, J. P. Hodges, et al. 2005. “Conceptual design of a macromolecular neutron diffractometer (MaNDi) for the SNS,” *J. Appl. Crystallogr.*, 38(6), 964–974. DOI: https://doi.org/10.1107/S0021889805030256.

Schweika, W. 2010. “XYZ-polarisation analysis of diffuse magnetic neutron scattering from single crystals,” *Polarized Neutrons and Synchrotron X-Rays for Magnetism Conference 2009*, 211.

Sheberla, D., L. Sun, M. A. Blood-Forsythe, et al. 2014. “High electrical conductivity in Ni_3(2,3,6,7,10,11–hexaiminotriphenylene) 2 , a semiconducting metal–organic graphene analogue,” *J. Am. Chem. Soc*., 136(25), 8859.

Sibille, R., N. Gauthier, H. Yan, et al. 2018. “Experimental signatures of emergent quantum electrodynamics in $Pr_2Hf_2O_7$,” *Nat. Phys*. 14, 711–715.

Soumyanarayanan, A., N. Reyren, A. Fert, et al. 2016. “Emergent phenomena induced by spin-orbit coupling at surfaces and interfaces,” *Nature* 539(7630), 509. DOI: 10.1038/nature19820.

Stockton, W. B., and M. F. Rubner. 1997. “Molecular-level processing of conjugated polymers. 4. Layer-by-layer manipulation of polyaniline via hydrogen-bonding interactions,” *Macromolecules* 30, 2717. DOI: 10.1021/ma9700486.

Sullivan, B., R. Archibald, P. S. Langan, et al. 2018. “Improving the accuracy and resolution of neutron crystallographic data by three-dimensional profile fitting of Bragg peaks in reciprocal space,” *Acta Crystallogr., Sect. D: Struct. Biol.*, 74(11), 1085–1095. DOI: 10.1107/S2059798318013347.

Tafti, F. F., J. J. Ishikawa, A. McCollam, et al. 2012. “Pressure-tuned insulator to metal transition in $Eu_2Ir_2O_7$,” *Phys. Rev. B*. 85, 205104.

Talin, A. A., A. Centrone, A. C. Ford, et al. 2014. “Tunable electrical conductivity in metal-organic framework thin-film devices,” *Science* 343(6166), 66.

Tasker, P. A., P. G. Plieger, and L. C. West. 2004. “Metal Complexes for Hydrometallurgy and Extraction,” in *Comprehensive Coordination Chemistry II: From Biology to Nanotechnology*, Vol. 9, eds. J. A. McCleverty and T. J. Meyer, Elsevier, Oxford, pp. 759–808.

Taylor, J., O. Arnold, J. Bilheux, et al. 2012. “Mantid, A high performance framework for reduction and analysis of neutron scattering data,” *Bulletin of the American Physical Society* 57.

Teshigawara, M., M. Harada, H. Tatsumoto, et al. 2016. “Experimental verification of equilibrium para-hydrogen levels in hydrogen moderators irradiated by spallation neutrons at J-PARC,” *Nucl. Instrum. Meth. Phys. Res. B*, 368, 66–70. DOI: 10.1016/j.nimb.2015.12.023.

Thornton, J., D. Blakey, E. Scanlon, et al. 2006. “The ammonia channel protein AmtB from *Escherichia coli* is a polytopic membrane protein with a cleavable signal peptide,” *FEMS Microbiol. Lett.*, 258(1), 114–120.

Tian, Z., Y. Kohama, T. Tomita, et al. 2016. “Field-induced quantum metal–insulator transition in the pyrochlore iridate $Nd_2Ir_2O_7$,” *Nat. Phys*. 12, 134.

Toth, S., and B. Lake. 2015. “Linear spin wave theory for single-Q incommensurate magnetic structures,” *J. Phys.–Condens. Matter* 27(16).

Tremsin, A. S., J. B. McPhate, J. V. Vallerga, et al. 2011. “Improved efficiency of high resolution thermal and cold neutron imaging,” *Nucl. Instrum. Methods A* 628(1), 415–418.

Tremsin, A. S., J. V. Vallerga, J. B. McPhate, et al. 2015. “Optimization of high count rate event counting detector with microchannel plates and quad Timepix readout,” W. *Nucl. Instrum. Methods A* 787, 20–25.

Turton, D. A., H. M. Senn, T. Harwood, et al. 2014. “Terahertz underdamped vibrational motion governs protein-ligand binding in solution,” *Nat. Commun.* 5, 3999.

Udby, L., P. K. Willendrup, E. Knudsen, et al. 2011. “Analysing neutron scattering data using McStas virtual experiments,” *Nucl. Instrum. and Meth. A* 634, S138–S143.

Veith, G. M., M. Doucet, J. K. Baldwin, et al. 2015. “Direct determination of solid-electrolyte interphase thickness and composition as a function of state of charge on a silicon anode,” *J. Phys. Chem. C* 119, 20339. DOI: 10.1021/acs.jpcc.5b06817.

Vickery, A., and P. P. Deen. 2014. “Choppers to optimise the repetition rate multiplication technique on a direct geometry neutron chopper spectrometer,” *Rev. Sci. Instrum.* 85, 115103.

Wadley, P., B. Howells, J. Železnýet al. 2016. “Electrical switching of an antiferromagnet,” *Science* 35(6273), 587. DOI: 10.1126/science.aab1031.

Wang, Y., H. Weng, L. Fu, et al. 2017. “Noncollinear magnetic structure and multipolar order in $Eu_2Ir_2O_7$,” *Phys. Rev. Lett*. 119, 187203.

Watanabe, N. 2003. “Neutronics of pulsed spallation neutron sources,” *Rep. Prog. Phys*, 66, 339–381.

Welton, T. 1999. “Room-temperature ionic liquids. Solvents for synthesis and catalysis,” *Chem. Rev*. 99, 2071–2083. DOI: 10.1021/cr980032t.

Willams, W. G. 1988. *Polarized Neutrons*, Oxford University Press.

Willendrup, P. K., E. B. Knudsen, E. Klinkby, et al. 2014. “New developments in the McStas neutron instrument simulation package,” *International Workshop on Neutron Optics and Detectors (Nop&D 2013), J. Phys.: Conf. Ser.*, 528(1), 012035. DOI: https://doi.org/10.1088/1742-6596/528/1/012035.

Willendrup, P., E. Fahri, E. Knudsen, et al. 2014. “McStas: Past, present and future,” *J. Neut. Res*. 17, 35–43. DOI: 10.3233/JNR-130004.

Willendrup, P., E. Farhi and K. Lefmann. 2004. “McStas 1.7—A new version of the flexible Monte Carlo neutron scattering package,” *Physica B–Condensed Matter* 350(1–3), E735–E737.

Willendrup, P., U. Filges, L. Keller, et al. 2006. “Validation of a realistic powder sample using data from DMC at PSI,” *Physica B–Condensed Matter* 385–386, 1032–1034.

Windsor, C. G. 1981. *Pulsed Neutron Scattering*, Taylor and Francis, London, UK. ISBN: 9780470271315.

Witczak-Krempa, W., G. Chen, Y. B. Kim, et al. 2014. “Correlated quantum phenomena in the strong spin-orbit regime,” *Annu. Rev. Condens. Matter Phys*. 5, 57.

Yablinsky, C. A., K. M. Flores, M. J. Mills, et al. 2008. “Fatigue behavior in monocrystalline Ni-based superalloys for blade applications,” *Superalloys 2008*, 535.

Yadav, R., N. A. Bogdanov, V. M. Katukuri, et al. 2016. “Kitaev exchange and field-induced quantum spin-liquid states in honeycomb α-RuCl3,” *Sci. Rep.* 6, 3792.

Yano, J., J. Kern, K. D. Irrgang, et al. 2005. “X-ray damage to the Mn_4Ca complex in single crystals of photosystem II: A case study for metalloprotein crystallography,” *Proc Natl. Acad. Sci.* 102(34), 12047–12052.

Yashima, M., S. Kawasaki, H. Mukuda, et al. 2007. “Quantum phase diagram of antiferromagnetism and superconductivity with a tetracritical point in $CeRhIn_5$ in zero magnetic field,” *Phys. Rev. B* 76, 020509.

Ye, F., Y. Liu, R. Whitfield, et al. 2018. “Implementation of cross correlation for energy discrimination on the time-of-flight spectrometer CORELLI,” *J. Appl. Crystallogr*. 51, 315–322. DOI: 10.1107/S160057671800403X.

Yoo, M. H. 1968. “Slip modes of alpha uranium,” *J. Nucl. Mater*. 26(3), 307.

Young, I. D., M. Ibrahim, R. Chatterjee, et al. 2016. “Structure of photosystem II and substrate binding at room temperature,” *Nature*, 540(7633), 453–457. DOI: 10.1038/nature20161.

Zaliznyak, I. A., A. T. Savici, V. O. Garlea, et al. 2017. “Polarized neutron scattering on HYSPEC: The HYbrid SPECtrometer at SNS,” *International Conference on Polarised Neutrons for Condensed Matter Investigations (Pncmi 2016)*, 862.

Zapf, V., M. Jaime, and C. D. Batista. 2014. “Bose-Einstein condensation in quantum magnets,” *Rev. Mod. Phys.* 86, 563.

Železný, J., H. Gao, K. Výborný, et al. 2014. “Relativistic Néel-order fields induced by electrical current in antiferromagnets,” *Phys. Rev. Lett*. 113, 157201. DOI: 10.1103/PhysRevLett.113.157201.

Zhang, Q. H., K. D. Vigier, S. Royer, et al. 2012. “Deep eutetic solvents: syntheses, properties and applications,” *Chem. Soc. Rev.* 41, 7108–7146. DOI: 10.1039/c2cs35178a.

Zhao, J. K., J. L. Robertson, K. W. Herwig, et al. 2013. “Optimizing moderator dimensions for neutron scattering at the Spallation Neutron Source,” *Rev. Sci. Instrum.* 84, 125104-1–8. D

6. INTEGRATED CONTROL SYSTEMS

6.1 ICS OVERVIEW

The Integrated Control Systems (ICS) scope for the SNS STS includes the control systems and computing infrastructure for all technical systems included in the STS Project. It includes the accelerator, neutron scattering instruments, and target, plus the control systems for the technical systems utilities for the conventional facilities. Also included are the data acquisition (DAQ) software and hardware for the neutron scattering instruments. Modifications and additions to the Personnel Protection System (PPS) required for the accelerator, target, and STS instruments are also included in this scope. Some existing SNS controls systems will require updates, extensions, or modifications to support the STS.

The ICS will provide supervisory control, automation, and operational tools for the upgraded facility. The control system includes hardware interfaces to technical systems, process control software, timing and communication networks, and user interfaces. Operational tools include system data archiving, alarm systems, and databases. The ICS has interfaces to technical systems across the project (Table 6.1).

Table 6.1. High-level interfaces for ICS systems.

S.6 Integrated Control Systems	S.2 Accelerator	S.3 Target	S.4 Instruments	S.5 Conventional Facilities
S.6.2 Accelerator Controls	Vacuum, power supplies, radio frequency, cooling, timing, machine protection systems			
S.6.3 Target Controls		Target utilities, target protection, cryogenic moderator, target assembly		
S.6.4 Instrument Controls and DAQ			All subsystem for instruments and shared common components across instruments	
S.6.5 Conventional Facility Controls				Utilities, technical building systems
S.6.6 Global Systems	Common database tools, personnel protection system	Common database tools, personnel protection system	Common database tools, personnel protection system	Common database tools

ICS functional requirements include the following:

- ICS shall provide remote control, monitoring, alarms, and data archiving to enable supervisory control, automation, and operational analysis from an appropriate control room (e.g. Central Control Room for machine systems, Instrument Hutch for neutron scattering instruments) for STS scope including accelerator, target, conventional facilities technical systems, and instruments.

- The ICS shall support interleaved operation of beam to FTS and STS, operation of beam to FTS only, and operation of beam to STS only.

- ICS shall provide the computing and network infrastructure to support the technical scope for the STS project, integrated with the existing networks.

- ICS shall maintain compatibility with the existing EPICS-based SNS control systems.

- The ICS shall provide protection systems for the machine to protect equipment from beam loss or damage from the beam.

- The Accelerator Control System shall provide interfaces to accelerator systems, including magnet power supplies, vacuum equipment, and radio frequency (RF) equipment and necessary computing and network equipment.

- The Accelerator Control System shall be integrated with the machine control system including accelerator, target, CF and related controls.

- The Accelerator Control System shall provide beam synchronous timing triggers and beam related metadata for accelerator, target and instrument systems, supporting independent operation of the two target stations.

- The PPS shall provide credited engineering controls as appropriate to ensure operations consistent with the constraints of the operational envelope and accelerator safety envelope.

- The PPS shall able to be monitored through the machine control system within the Central Control Room.

- The PPS shall include credited engineering controls, including access controls for the RTBT, second target area, and instrument beam lines; interface to radiation monitors; and oxygen deficiency monitoring.

- The PPS for the STS systems shall be integrated with the existing SNS PPS.

- The Target Control System shall provide interfaces to target systems including target assembly, cryogenic moderator, utilities, and vacuum systems.

- The Target Control System shall provide target protection systems.

- The Target Control System shall be integrated with the machine control system, including accelerator, target, conventional facilities (CF), and related controls.

- The Instruments DAQ and Control System shall provide DAQ hardware and DAQ software to collect data from the STS instruments, including neutron scattering data, beam monitor data, accelerator metadata, and instrument metadata sufficient for processing the experiment data.

- The Instruments DAQ and Control System shall provide software and user interfaces for beamline control, data collection, and experiment automation.

- The Instruments DAQ and Control System shall provide the computing, network, and data storage infrastructure for operating the instruments; collecting, managing and preserving data; and providing access to the data for post-processing.

- The CF Control System shall provide interfaces to technical CF systems, including water systems, building controls (heating, ventilation, and air conditioning), and compressed air systems for CUB-II, CEF-II, RTST, Target Building II/Instrument Buildings.

- The CF control system shall be integrated with the machine control system including accelerator, target, CF and related controls.

ICS development for the STS Project will build on the existing SNS control system infrastructure. The existing SNS machine control system integrates all aspects of the accelerator complex, including all accelerator subsystems, CF controls for technical building systems, and target systems for the SNS FTS. The existing neutron scattering instrument control systems provide a dedicated system for each beamline, integrating all aspects of operating the instrument, controlling and monitoring the experiment, and acquiring data. For the most part, extending and expanding the existing control systems will meet the needs of the STS Project. The resulting upgraded facility will retain the existing control systems, including the core infrastructure. Most of the existing software tools will be retained or upgraded as part of ongoing life cycle improvements through facility operations, with a few existing subsystems to be updated as a part of the STS Project.

The existing SNS control systems are built using the Experimental Physics and Industrial Control System (EPICS) [EPICS 2020] tool kit. EPICS provides a collection of software tools for building distributed control systems for large experimental physics projects. It includes a run-time database; robust network protocols; a rich collection of device drivers for interfacing to hardware; and a suite of client tools to provide operator control and monitoring, data archiving, and alarms. The modular design is extensible and can easily be used to satisfy the projected STS needs.

This integrated approach ensures consistency in tools and techniques for meeting the control systems needs across the project for all technical systems. Using a common tool kit foundation simplifies data exchange across the systems, thereby enhancing the operability of the facility. In addition, the standardization of control system tools simplifies long-term maintenance and support and leverages available technical expertise.

The EPICS software tool kit is supported by an active collaboration of experienced software developers. EPICS leverages development efforts from numerous DOE-funded laboratories and international partners to provide a software platform that can meet the needs of the STS Project. Recent and ongoing accelerator projects using EPICS for ICS include the National Synchrotron Light Source-II (NSLS-II) at Brookhaven National Laboratory, Advanced Photon Source-Upgrade (APS) at Argonne National Laboratory, Advanced Light Source-Upgrade at Lawrence Berkeley Laboratory, Linac Coherent Light Source-II (LCLS) at Stanford Linear Accelerator Center, and European Spallation Source (ESS) in Sweden. EPICS is also widely used for instrument controls and DAQ at current and future photon and neutron scattering beamlines, including NSLS-II, APS, LCLS, ISIS, and ESS. Participating in this collaboration benefits the STS Project by providing peers for developing and testing software and by providing technical expertise from projects with similar requirements and operating needs.

The EPICS architecture (Figure 6.1) is built around the input/output controller (IOC), which provides a run-time process database. The process database is a memory-resident database that defines records and logic for controlling input/output (I/O), executing control algorithms, performing data conversions, checking alarm thresholds, and providing updates to distributed clients. Records can be processed periodically at defined intervals or be event driven. Processing can be synchronous or asynchronous. I/O operations are supported through a device support layer for hardware interfaces and equipment-specific protocols. Existing device support is already available for a wide variety of field buses, embedded

controllers, programmable logic controllers (PLCs), motion control systems, digital and analog I/O devices, and instrumentation.

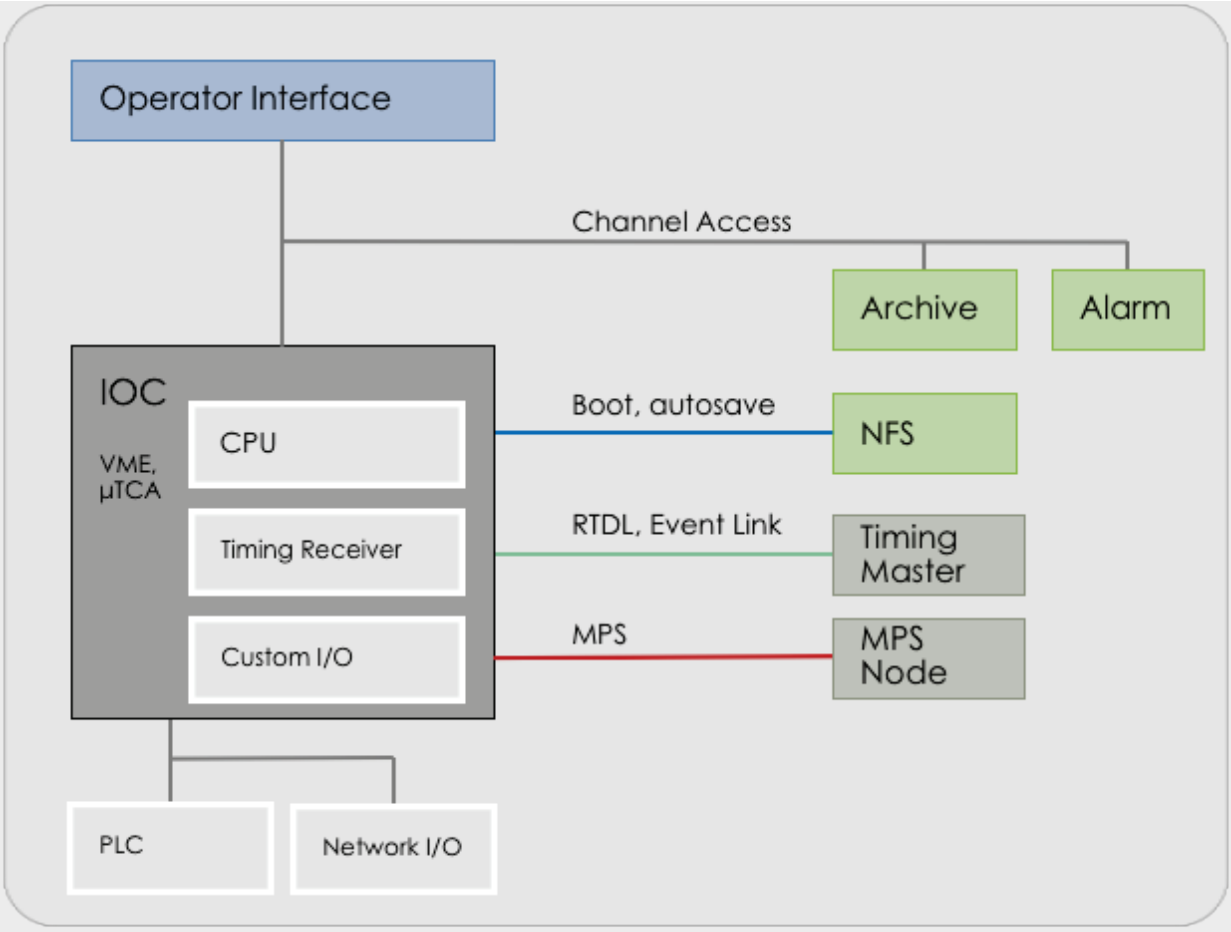

Figure 6.1. Typical EPICS-based control system physical architecture.

EPICS currently supports two network protocols: Channel Access (CA) and PVAccess. CA, the original protocol, is optimized for robust and reliable communication for process control and monitoring. CA is in wide usage with a number of server and client implementations. The newer PVAccess protocol is optimized for efficient network transport of complex data structures. The CA protocol is in use for the existing SNS accelerator, conventional facilities, target, and safety systems. Existing FTS neutron instrument systems use a combination of CA and PVAccess protocols. The use of both CA and PVAccess protocols will continue with STS, with each protocol used where most appropriate.

EPICS supports a variety of client tools for supervisory control, monitoring, automation, and system diagnostics. Existing SNS client tools will continue to be supported with the STS upgrade. SNS is currently using the Control System Studio (CS-Studio) [CSS 2020] suite of graphical user interface (GUI) client tools for many applications. CS-Studio is an international collaboration within the EPICS community to develop a collection of tools to monitor and operate large-scale control systems. For accelerator systems, CS-Studio provides archiving, alarms, diagnostic tools, and some user interface displays. Additionally, Extensible Display Manager (EDM) [SNS 2020] is used for many accelerator system GUIs. For the SNS neutron instrument systems, CS-Studio is the primary user interface tool, providing all user interfaces for scientists to conduct and automate their experiments and for staff to monitor and control the beamline, along with archiving for engineering systems and centralized alarms

for notification of off-normal conditions. STS development will use the CS-Studio suite of software tools for the EPICS client layer.

ORNL NScD and the STS Project include extensive expertise in all aspects of EPICS-based control systems. Staff members are actively contributing to the EPICS collaboration with software development, testing, and organizational management.

6.2 ICS FOR ACCELERATOR SYSTEMS

The ICS scope for the accelerator includes control system hardware, software, and user interfaces for the accelerator systems, including the EPICS-based controls system, PLC–based controls, device integration, timing system, Machine Protection System (MPS), PPS, and the related computing infrastructure. High-level system requirements follow from experiences and lessons learned from the original SNS project [Gurd 2001, Gurd 2003].

Accelerator control system work includes interfacing to new accelerator components and systems, extending and modifying the existing control system to support two target stations, and integrating STS with the existing SNS control system. The SNS original control system design anticipated a future STS, and some interface points are already present. However further additions and modifications will be required to support independent operation of the two target stations. The control systems MPS, PPS, timing, and low-level radio frequency (LLRF) are impacted by the need to support independent operation. Requirements include operation of the FTS only, operation of the STS only, interleaved operation of FTS and STS at the same per-pulse power, and interleaved operation of FTS and STS at different per-pulse power levels. Details are provided in the following subsections.

6.2.1 Accelerator Control System

The existing SNS accelerator control system is an EPICS-based system with over a half million process variables. EPICS IOCs include Versa Module Europa (VME) -based systems running the real-time operating system VxWorks, PC-based systems running Red Hat Linux (controls), and Windows systems (beam instrumentation). The Proton Power Upgrade (PPU) Project will develop Micro Telecommunications Computing Architecture (μTCA) -based systems running real-time Linux for the LLRF systems. Many systems, including cryogenics, target, vacuum, and conventional facilities use Rockwell Automation Allen-Bradley PLCs (ControlLogix and CompactLogix hardware families) with EPICS integration for remote monitoring and control, data archiving, and alarms.

The EPICS-based control system for the SNS accelerator, target, and conventional facilities has been in use since construction of the facility was completed in 2006. The operator interface tools for alarm handling and data archiving have been upgraded to CS-Studio [Geng et al. 2009, Kasemir 2019], and device control applications have been added as the accelerator complex evolved from machine commissioning to routine high-power operation. From 2008 to 2012, a concerted effort was made to improve accelerator reliability, including work to harden the controls system [Hartman 2009]. Figure 6.2 shows the improvement in control system reliability since operations began recording availability data. Some hardware components have been upgraded as part of a general technology refresh or to avoid obsolescence; however, much of the hardware is original. The software tools currently in use are aging. The >2000 display pages in use are based on EDM. Alarms and archiving systems use CS-Studio. More recent versions are available and should be adopted long before STS installation begins, to take advantage of performance and capability improvements. Similarly, accelerator control systems are running relatively old versions of EPICS (3.14), Linux, and VxWorks. Although leaving older hardware and software in place is common for operating facilities, the advent of the PPU and STS projects gives SNS an important opportunity to introduce newer elements and mitigate obsolescence. An infrastructure upgrade plan for

the accelerator control system is anticipated for FY 2020 as part of the SNS operations work. Upgrades will proceed as budget, resources, and outages allow. New systems will be developed using EPICS 7 and the latest CS-Studio tools.

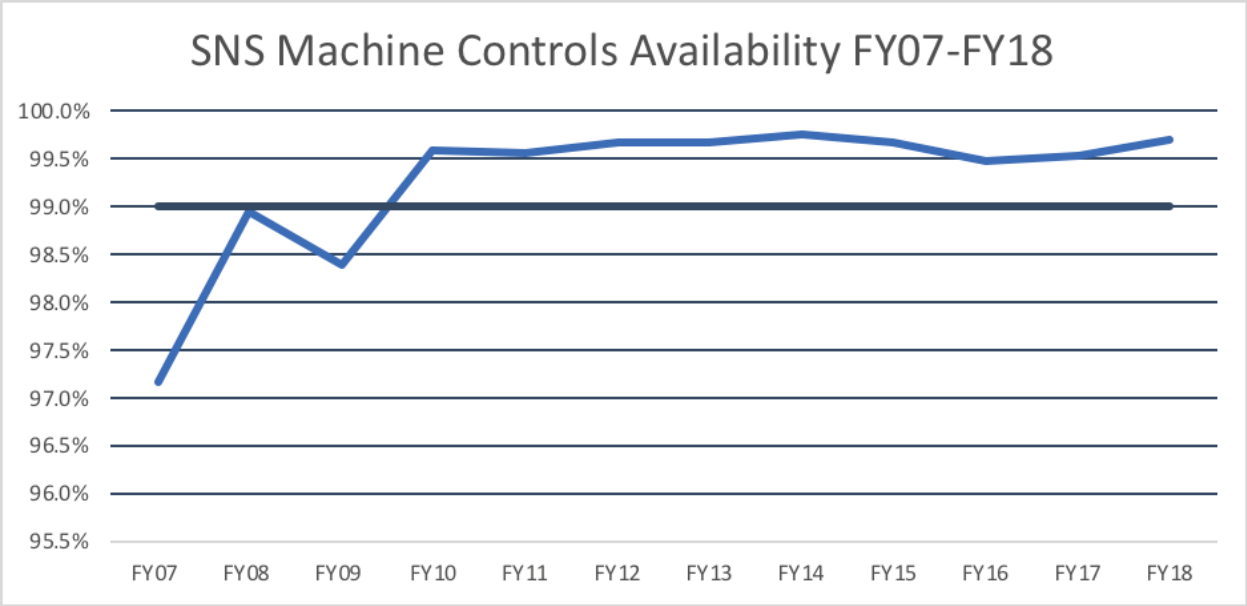

Figure 6.2. Accelerator controls availability compared with the 99% controls goal to achieve 90% for the overall accelerator complex.

6.2.1.1 Accelerator Operating Modes for STS

The SNS accelerator will operate at 60 Hz, which is the same operating frequency used currently. With the STS in operation, the accelerator will typically deliver 45 pulses per second to the FTS and 15 pulses per second at 15 Hz to the STS. The STS will be operating in a “pulse stealing” mode: three pulses will be delivered to FTS and every fourth pulse delivered to the STS. If the STS is offline, the FTS could be operated at 60 Hz/60 pulses per second, 60 Hz/45 pulses per second, or 60 Hz with fewer pulses per second. It is expected that typical operation in this scenario will be 45 pulses per second. If the FTS is offline, the STS will operate at 15 Hz/15 pulses per second or slower. Accelerator operation must support independent power control to each target station. Figure 6.3 shows some anticipated operating modes. The top image shows FTS operation at 60 Hz/60 pulses per second, which is the operating mode prior to STS. The second image shows typical interleaved operation with the FTS operating at 60 Hz/45 pulses per second and the STS operating at 15 Hz/15 pulses per second. The third image shows operation at STS at 15 Hz/15 pulses per second without beam to FTS. The fourth image represents interleaved operation but with reduced power to the STS target.

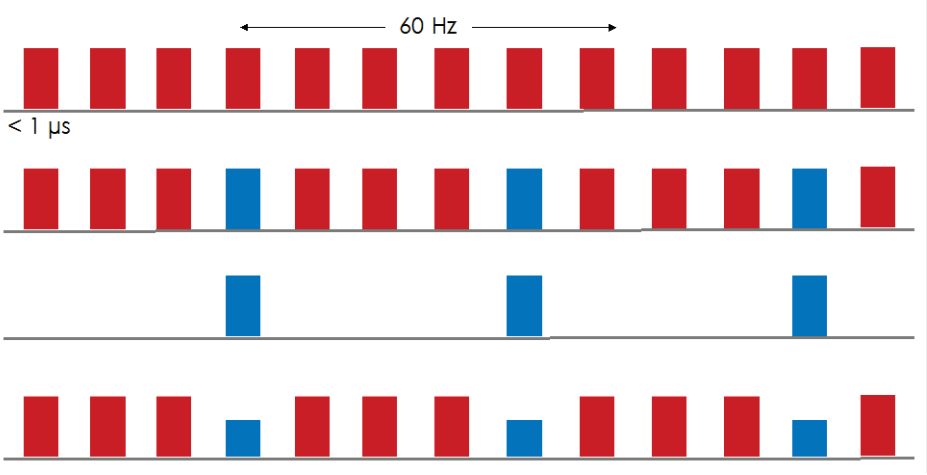

Figure 6.3. Accelerator operating modes with FTS in red and STS in blue.
Bar height represents relative pulse power.

Independent operation of beam power to the two target stations requires the ability to accommodate different beam power pulse-by-pulse through the accelerator chain. The ion source injector current output cannot be changed quickly, nor can the accelerating gradient that determines beam energy. Beam power will therefore be adjusted by modifying the mini-pulse of the proton beam, either by changing the number of mini-pulses within a macro-pulse and/or by adjusting the length of each mini-pulse. Figure 6.4 shows how mini-pulses may be adjusted to vary power within the approximately 1 ms macro-pulse. The top image represents typical SNS operation presently with 1 ms macro-pulses, each consisting of 1 microsecond mini-pulses, to produce a 1.4 MW beam to the FTS. The second image shows three macro-pulses consisting of 1 microsecond mini-pulses to the FTS followed by one macro-pulse to the STS, which would be typical operation with 2.0 MW on the FTS and 0.7 MW on the STS. The third image shows a reduction in beam power by reducing the number of mini-pulses in each macro-pulse. The fourth image shows independent beam power delivered to each target station by varying the length of the mini-pulses to the STS compared with the FTS.

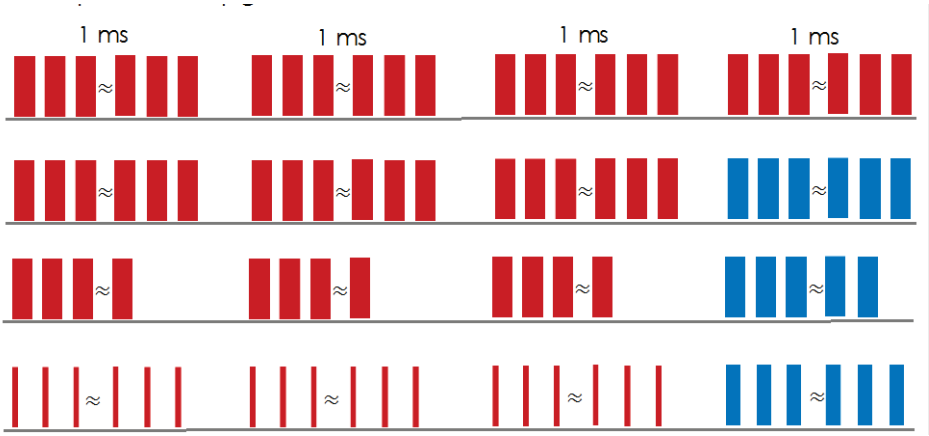

Figure 6.4. Mini-pulse configuration will be used to vary the power between FTS (shown in red) and STS (shown in blue).

To provide this level of control, the LLRF will need to be able to provide different control and feed forward for the different beams going to FTS or STS. An upgrade to the LLRF hardware is being developed as part of the PPU Project and is expected to be available to meet STS LLRF needs after some modification of the firmware and EPICS control.

The injection kickers, used to store the proton beam in the accumulator ring, will need to accommodate different beam “painting” schemes. The waveform generator used to provide the ramping curves to the injection kickers will need to be able to adapt pulse-by-pulse to handle different painting schemes for the FTS beam versus the STS beam. The ring RF bunching system may also require independent control for each style of pulse. The primary subsystems impacted by independent two-target operation are summarized in Table 6.2.

Table 6.2. Control system subsystems impacted by independent two target station operation.

Subsystem	Impact
Linac LLRF	Support different power levels for STS beam vs. FTS beam
MPS	Extension for STS; support independent machine modes
PPS	Extension for STS; support independent operating modes and additional critical devices
Kickers	Variable waveforms
Timing	Extension for STS; support independent operating modes; enhanced requirements for STS instrument timing

6.2.1.2 Accelerator Device Control

Control system support for magnet power supplies, vacuum, and cooling will be extended to support the STS by duplicating existing IOC instances where possible. Added devices will typically be operationally equivalent to those in the existing accelerator installation. It is anticipated that the existing SNS standard Allen-Bradley PLC family will be used for vacuum and cooling systems. Some new device support may be required, for example, for magnet power supplies.

Vacuum controls for the ring-to-second-target (RTST) beam transport line will be similar to those used in the existing ring-to-target-beam-transport (RTBT) line used presently to send beam to the FTS. Vacuum devices requiring control system interface are summarized in Table 6.3. The RTST line will include new magnets with 99 new power supplies. Table 6.4 summarizes the different types of magnets and power supplies needed.

Table 6.3. Vacuum devices and quantities types requiring control system interfaces.

Device type	Quantity
Ion pump	30
Turbo pump (with isolation valve and foreline valve)	1
VAT fast valve	1
Sector gate valve	5
Cold cathode gauge	30
Pirani controller	30
Gauge controller	30

The RTST will also include many new beam instrumentation devices that will be similar to existing devices. These devices are typically controlled with LabVIEW systems, which are within the scope of the Accelerator WBS (S.2). The interface point to the ICS for these devices is CA. Most of the new beam instrumentation devices will require interfaces to the ICS timing system, MPS, and/or PPS. No additional active feedback systems are anticipated for STS. Table 6.5 summarizes new beam instrumentation devices and the required ICS interfaces.

Table 6.4. Magnet power supply types and quantities showing required control system interfaces.

Magnet types	Quantity	Power supply type	Quantity	ICS interfaces	
RTST kickers	5	Similar to existing injection kicker PS; new controls interface in 2020	5	MPS, PPS, timing, waveform monitor	Ramp magnetic field between 60 Hz pulses
RTBT QV09, DCV10	2	New	2	MPS	Provide focusing and trajectory flattening
Quadrupoles	46	New, four variations	34	MPS	Provide focusing
Dipoles	16	New	2	MPS, PPS	Beam transport
Dipole correctors	29	New	53	MPS	Beam trajectory adjustment

Table 6.5. Beam instrumentation devices and quantities, showing control system interfaces.

Device type	Number of devices	Number of crates	ICS interfaces
Beam loss monitor	48	3	MPS
Beam position monitors	24	3	
Beam current monitors	2	2	PPS
Wire scanners	9	3	MPS
View screens	1	1	MPS

The accelerator timing system will be modified to support both single and two target station operations, including beam ramping. Timing needs for the target and timing needs for instruments are discussed in the following subsections. The timing system needs to schedule pulses to the FTS and STS in a consistent and predictable way. Instruments must be able to operate in pulse suppression mode at sub-frequencies (FTS: 30 Hz, 15 Hz, 10 Hz; STS: 7.5 Hz, 3.25 Hz). Pulses will be scheduled in a consistent manner across the existing accelerator 600-pulse super-cycle.

Beam is injected into the accumulator ring using a painting scheme to minimize space charge effects and reduce beam losses. The injection kicker is ramped over 1060 ring turns (~1 ms) with an arbitrary waveform generator used to define the ramping waveform to achieve a uniform beam density. With two different beam flavors, the ability to toggle between two different waveforms on a pulse-to-pulse basis will be required. The injection kicker control and monitoring systems will require upgrades. The kicker waveform monitoring systems, with an interface to the MPS, will also need to be updated to support this capability.

Additional kickers will be added to the RTBT to inject beam into the RTST beam transport line. These will require controls and monitoring, including an MPS interface.

New LLRF hardware will be developed as part of the ongoing PPU Project. The PPU Project will procure and install LLRF hardware for the 28 new cavities in the PPU Project scope. The remaining 96 existing SNS linear accelerator (linac) cavities will be outfitted with the new LLRF hardware as part of the STS Project. The ICS scope for LLRF is to integrate the newly installed systems into the EPICS. The software and configuration will be very similar to the EPICS interfaces developed for the new LLRF under the PPU Project, except that provision must be added for two beam flavors. The LLRF firmware and algorithm development required for STS is under the Accelerator (S.2) WBS scope.

Compared with the LLRF in current use on the accelerator, the new LLRF system will provide extended memory space and computational performance. For example, it can accumulate multiple beam load compensation curves and select them on a per-pulse basis as required to support beam pulses scheduled for the first and second target stations, respectively.

6.2.2 Timing System and Run Modes

The Run Permit System is the combination of timing, messaging, machine protection, and high-level applications used to configure and deliver beam to the target(s). Part of the STS Project is to create a supervisory application that coordinates all of these as well as provides the operator with a consistent user interface. The Run Permit System will be an extension to the existing SNS timing and MPSs [Sibley et al. 2003].

Machine timing (Figure 6.5) is based on two parameters—a 60 Hz clock and the period of one turn around the ring. At each 1/60 second, there is a slot where a beam macro pulse may be injected and accelerated or not. Normally, devices like the RF and kickers are operated every 1/60 of a second, regardless of whether beam is injected, to maintain long-term stability. When the STS is in operation, the machine cycle will still be at 60 Hz with the FTS consuming 45/60 slots and the STS consuming 15/60 slots.

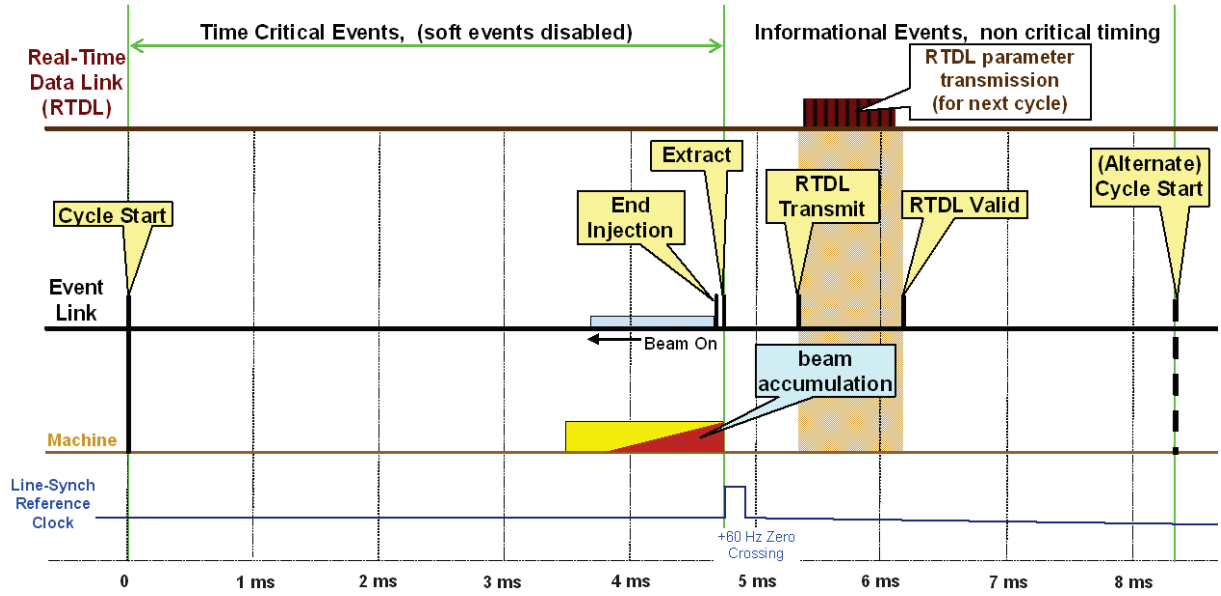

Figure 6.5. Timing sequence for SNS accelerator.

The "turn" is the fundamental unit of time for the mini-pulse and is defined as the time it takes for a beam of velocity βc to travel the full circumference of the ring. *T* is approximately

$$t \approx \frac{C}{c\sqrt{1-\left(1+\frac{E}{E_P}\right)^{-2}}},$$

where *C* is the circumference of the ring (248 m), *c* is the speed of light, *E* is the proton kinetic energy, and E_P is the rest mass energy of a proton.

This relationship is critical to ensure beam is generated, accumulated, and extracted synchronously. The PPU Project will increase the beam energy from 1.0 to 1.3 GeV. Therefore, the time of one turn will decrease proportionately. Figure 6.6 shows the variation of turn period with beam energy.

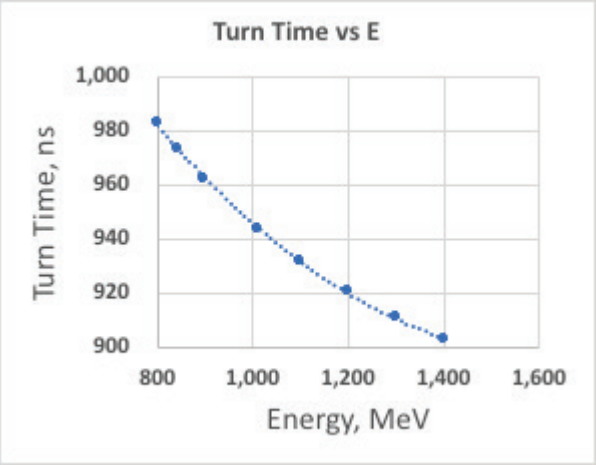

Figure 6.6. Ring revolution period as a function of proton beam kinetic energy.

Beam pulse waveforms are set up by operators based on the desired pulse delay, width, and rise and fall intensity. The parameters define a beam mode "flavor," with up to seven flavors available—flavor 0 is reserved for "no beam." Presently, flavor 1 is reserved for the FTS and flavor 2 is already reserved for STS. Figure 6.7 is a screen shot of the existing flavor 2 (STS) parameter screen. Note that timing is set up in units of "turn," not absolute time.

The "beam gate width" is the maximum time allotted for the pulse waveform to execute. There is presently a separate device, Stanford Instruments DG535, that limits the maximum pulse width and repetition rate. For FTS-only operation, the limit is set to 1 ms/60 Hz. This instrument is incapable of enforcing the variation of pulse width and repetition rates required for simultaneous FTS/STS operation. Therefore, the STS ICS scope includes moving this supervisory function into the timing chassis in the front end.

- FTS only: 60 pulses per second
- FTS only: 45 pulses per second
- STS only: 15 pulses per second
- FTS+STS: 45/15 pulses per second

The timing system distributes two information streams to communicate messages and triggers for real-time operations: the real-time data link (RTDL) and the event link (EL). The RTDL distributes information describing the prior pulse and the plan for the upcoming pulse. Timing receivers decode the RTDL data to configure beam devices for the upcoming pulse or to tag data with the appropriate properties. RTDL data are used by accelerator systems and by the neutron scattering instruments.

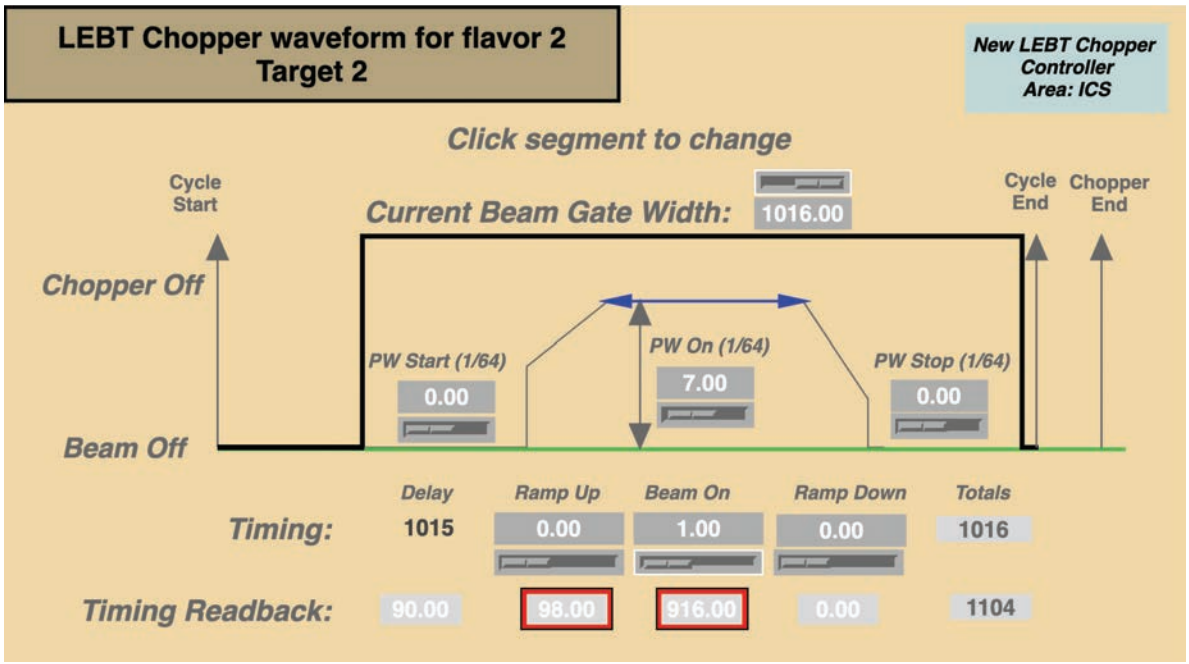

Figure 6.7. Beam width for STS beam can be controlled through existing chopper waveform settings. The chopper controller will remain as-is, with the STS control and timing systems providing configuration and trigger signals for this beam mode.

The EL is used as a real-time clock, phase-locked to the ring RF clock, to generate triggers for beam generation, acceleration, and extraction. The EL is also used to synchronize neutron scattering instrument DAQ with the beam. The STS target will require EL timing information to synchronize the rotation rate of the target with the arrival time of the beam.

The RTDL includes a timestamp derived from a GPS clock. The timestamp has a short-term stability of ±100 ns and a resolution of 1 μs. Experiment DAQ uses EL extraction event #39 as the beam synchronous trigger (TSYNC). Many STS instruments will perform time-resolved experiments requiring accurate synchronization between TSYNC and the wall-clock time provided by the RTDL. Timing accuracy of better than 1 μs will be needed over time scales both short and long. For STS, the GPS and encoder electronics will be upgraded to achieve this goal.

The existing RTDL and EL have more than sufficient unassigned parameters to support the STS needs. Parameters for STS beam and machine modes are already assigned to the existing EL and serve either the FTS or STS beam. One parameter that will need to be added to the RTDL is STS beam charge.

The purpose of the MPS is to shut off the H^- beam if continued operation could harm a component. Some MPS faults are reactionary, like beam loss; and others are preemptive, like machine configuration. The STS MPS design duplicates the MPS inputs and structure used for the RTBT for the FTS machine. The RTST will host an MPS concentrator along with cards with inputs from the magnets, beam loss monitor, beam current monitor, vacuum, and utilities. The RTST MPS will also include a card that will receive MPS inputs from the STS building.

The MPS propagates two types of faults—auto-reset and latched. Auto-resets are transient faults, and it is anticipated that the fault condition will clear. Latched faults are potentially serious faults for which operator acknowledgement and intervention are required before reestablishing beam. The original SNS MPS had dedicated fiber optic outputs for each type of fault. Extending this configuration to the STS

would require two additional cables from the RTST to the front end. The new MPS developed under AIP39 eliminates the need for additional cabling by using a messaging-based shutdown system. The new MPS cards have the capacity to add STS auto-reset and STS latched faults and distinguish them from FTS faults. Because the MPS inhibits or permits beam on a pulse-by-pulse basis, the new MPS will serve STS requirements with minimal modifications to handle inhibiting beam to one target or both.

High-level applications are IOC-level programs and scripts used to set up, control, monitor, and analyze information from SNS equipment. Timing and MPS-related high-level applications include timing configuration, pulse parameter setup, and monitoring. The applications associated with all of these will require modification to accommodate operation with two targets. A new high-level application, Run Permit System, will be developed to integrate beam setup, timing, and MPS-related programs to better address operator awareness and human–machine interface for the two-target facility. The Run Permit System software will also act to prevent the accidental setup of disallowed beam parameters for a given machine state.

6.2.3 Personnel Protection Systems

The existing accelerator PPS is a credited engineered system that enables safe accelerator operation by keeping people and radiation apart. This system includes access controls, interlocks, monitors, and warning devices. The system also includes monitoring of radiation and oxygen levels within the accelerator enclosure. The existing system employs commercial off-the-shelf PLC hardware with code developed by two independent programmers. New systems use safety-rated PLCs and I/O. PPS status is displayed through EPICS for the convenience of operators, but EPICS does not provide any credited safety function. The PPU Project will add a new credited beam power limiting system (BPLS) to ensure accelerator operation does not exceed the design limit of 2.0 MW to the FTS and 0.7 MW to the STS.

The STS Project will expand the accelerator PPS to include the RTST PPS and second target PPS (STPPS) segments. The PPS scope also includes all instrument PPSs (IPPSs), one for each beamline.

The present accelerator PPS is composed of the following quasi-independent operating segments:

- linac
- high-energy beam transport
- ring
- RTBT
- target PPS

Each of those segments must agree that beam operation within its segment is permitted before beam can be enabled in the front end. Requirements include that all areas are clear of personnel, all areas are secure, and there are no faults. The STS Project will add two additional PPS segments, RTST beam transport area and STPPS. Both of these new PPS segments will be based on the existing PPS architecture of redundant safety PLCs.

The RTST will extend from a shielded labyrinth adjoining the RTBT to the target shielding at the second target building. It will have a dedicated access portal adjacent to the RTST truck ramp with equipment for both normal (restricted) and controlled access. The portal will consist of a shielded labyrinth, PPS interlocked doors, badge-operated door locks, and an exchange key access system. The badge reader system will restrict access to the RTST to appropriately trained personnel. Access may be further restricted by Control Room operators as needed. The large truck ramp access doors beside the portal are also interlocked.

Access from the RTST to the RTBT is via a shielded labyrinth with an interlocked door on the RTST side. This door is monitored by both the RTST and the RTBT PPSs. Opening the door will cause a fault in both segments. All doors have emergency exit hardware that is monitored by the PPS—activation of an emergency exit will cause a fault.

The RTST tunnel will have PPS beam shutdown stations located approximately every 90 ft. Each beam shutdown station serves as a search station, emergency stop location, and visual and audible indicator of tunnel status. The PPS will be programmed to enforce a search pattern that must be followed to secure the RTBT tunnel. The RTST PPS includes four to five interlocked area radiation monitors. One monitor will be located in the RTST service building and three will be outside on the RTST berm. An additional monitor tied to the RTBT may be required at the RTST labyrinth wall when the RTST is open for access and beam is running in the RTBT. PPS critical devices will allow access to certain areas to support maintenance activities with independent operation of the two target stations as summarized in Table 6.6.

Table 6.6. Access control to support independent operation and maintenance of the two target stations. Final configuration will be determined after the completion of the safety analysis.

Machine mode	Proposed access provided	Proposed critical device
STS only	FTS target area	DH13 dipole power supply
FTS only	STS target area	RTST kicker power supply, RTST upstream dipole power supply
STS only	RTBT access **not** allowed	N/A
FTS only	RTST (downstream of shielding wall)	RTST kicker power supply, RTST upstream dipole power supply

The RTST PPS will also include a BPLS (Figure 6.8) to monitor beam power to the STS and trip the RTST if power to the STS exceeds 0.7 MW. This system is currently in design for the PPU Project. It is anticipated that the STS will utilize the solution developed by the PPU Project. The two main components are beam charge and beam energy. The charge is derived from an insulated gap beam current monitor, and the beam energy is derived from dipole magnet current measurements. Both signals go to a field programmable gate array (FPGA) –based signal processor for fast calculations. The signal processor provides an “OK” fail-safe signal to a dedicated safety PLC. If the OK signal goes low, the PLC will trip the RTST and therefore the linac PPS to shut off beam. The BPLS also includes extensive self-testing, including an end-to-end test current loop. The system is fault tolerant wherever possible to minimize trips of the PPS.

The STPPS is the supervisory PPS for the second target building. The STPPS performs four major functions:

- Enforce search and secure functions for high- and very high-radiation areas in the second target building
- Provide interlocked area radiation monitoring in key areas of the second target building
- Control the main maintenance shutters to each beamline
- Sum and convey beam shutdown requests from each beamline to the accelerator front end

The number of interlocked high- and very high-radiation areas is to be determined through radiation modeling. However, the basic design for the STS will be modeled on similar areas in the FTS: the basement utility vault and the shutter drive equipment room. Each of these areas contains beam shutdown stations that are also used to sweep the area. Because of the relatively small areas, controlled access is not

supported in the target building. Similarly, the exact placement of interlocked radiation monitors will be determined through radiation modeling.

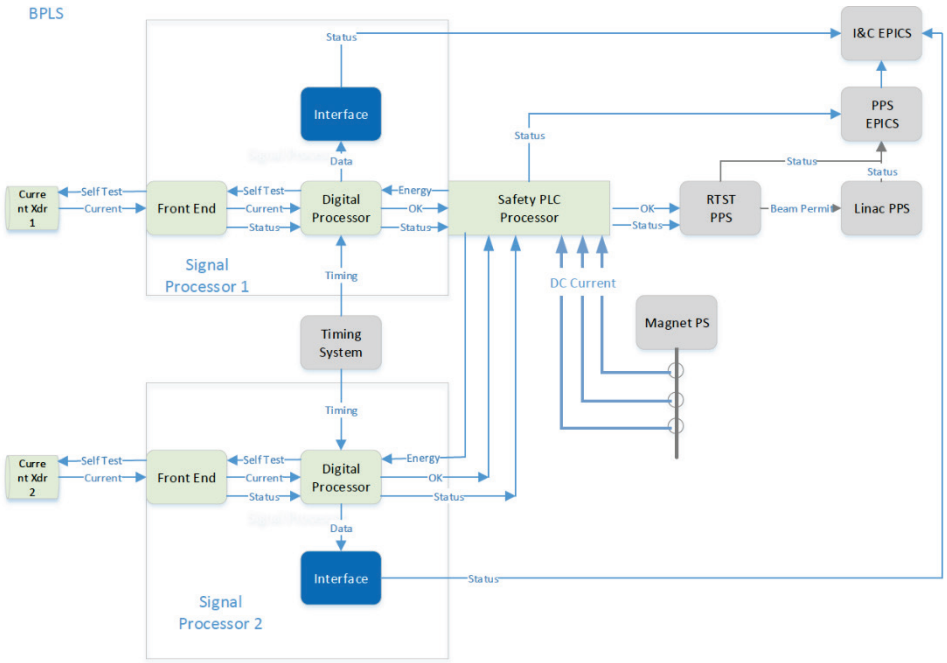

Figure 6.8. Block diagram of beam power limit system.

The STPPS will have an interface to the maintenance shutter controls. Upon the loss of an OK signal from any instrument, the respective shutter will close.

Within the scope of the STS PPS are uninterlocked area radiation monitors used for information only. The FTS uses the Thermoscientific RMS-3, which is now obsolete with no direct manufacturer replacement. Plans at this time are to use monitors from Mirion, which are used in similar applications throughout ORNL.

Each instrument will have an independent IPPS. While an instrument will normally instruct the maintenance shutter to close on a fault, the only credited means of making an instrument area safe is to shut off the proton beam through the STPPS. The STPPS will receive an OK signal from each IPPS. If the signal goes low, the STPPS will assume there is a fault and start a timer before tripping the linac PPS. If an OK signal is not received again before the timer times out, the STPPS will trip the front end and trip the STS extraction kicker via the RTST PPS. Having the maintenance or supplementary shutters insert is one means of setting the OK signal high. The value of the timer is dependent on a conservative estimate of the time during a hypothetical accident before someone could receive an elevated radiation dose. Timers in the FTS IPPS systems vary between 0 and 2 minutes.

IPPSs provide access controls, interlocks, monitoring, and warning devices for each individual beamline. The typical beamline has two shielded enclosures as well as radiation and oxygen monitoring systems. Some beamlines have supplementary shutters to expedite access and sample changeout. The IPPS is the primary control for these shutters. Each IPPS also has a set of dry contacts that can be configured for the individual beamline's needs. Examples from the FTS IPPS include the PPS status used for door controls, robotic control, and motion controls.

In 2015 the SNS Protection Systems Team started an effort to consolidate the different IPPS architectures and functional behavior of the FTS IPPSs. Part of the effort is to define an “ideal” IPPS architecture (Figure 6.9) against which existing systems would be compared and on which future beamline IPPSs would be based. For example, the FTS VENUS beamline currently under construction will use this architecture as its design basis. This ideal beamline IPPS concept will also be used for initial cost estimates for the STS Project.

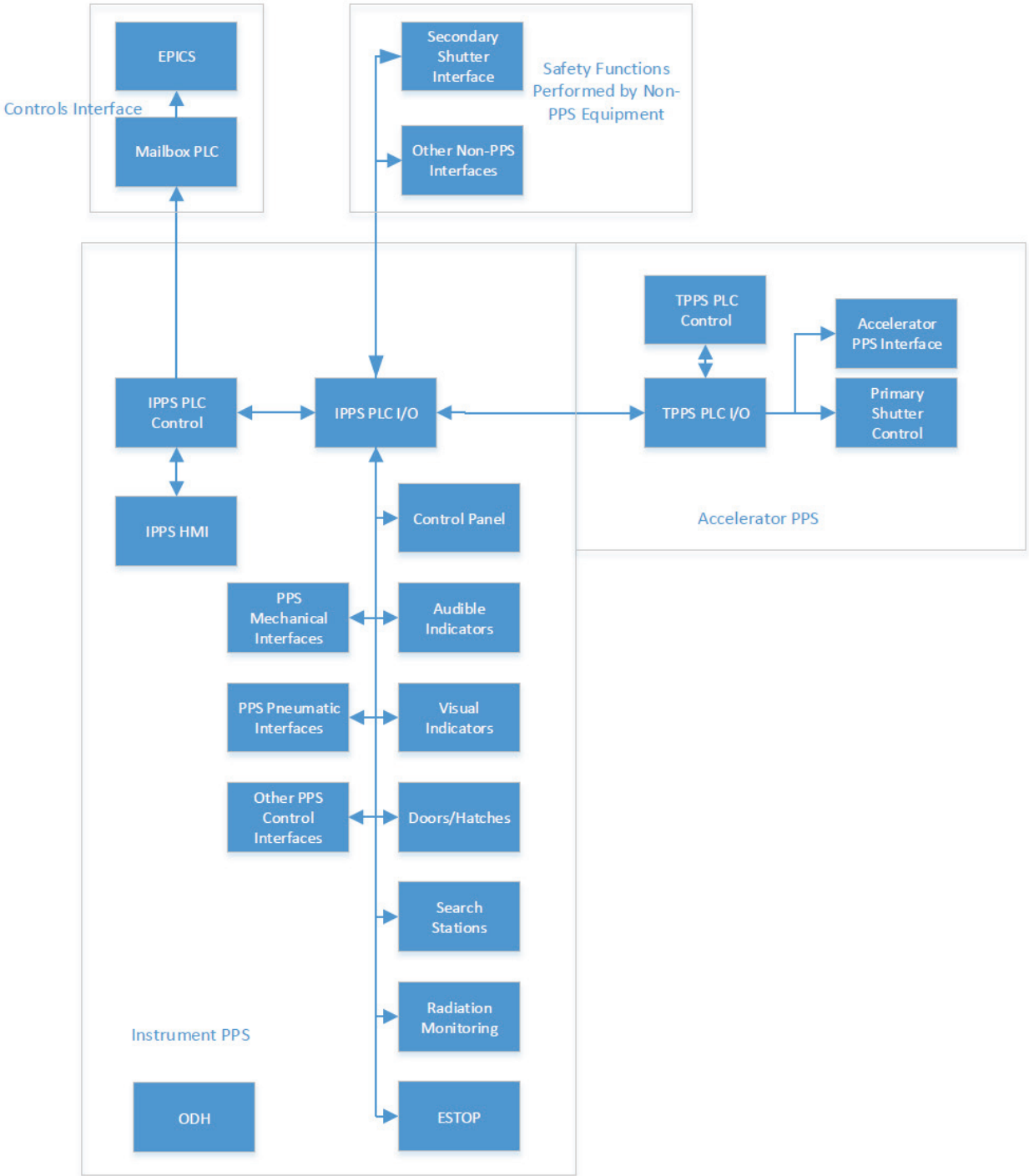

Figure 6.9. The standardized IPPS architecture.

6.2.3.1 Computing and Network

The SNS machine control system uses a private computer network that is segmented to be physically and logically separated from ORNL's business network. A tightly restricted firewall provides a single point of connection with the ORNL network. The accelerator network includes virtual LANs for the accelerator, beam instrumentation, conventional facilities, target, and cryogenic subnetworks [Devan and Williams 2001, Gurd 2004]. The scope required for STS includes adding network devices for the new RSTS accelerator beam transport line; new conventional facilities, including a second Central Utilities Building; and the new target station. The existing machine computing and network infrastructure can be extended to meet this additional scope. The project will provide single-mode fiber optic cables to the new buildings included in the STS Project. This fiber will tie into the existing network. The existing Control Room in the Central Laboratory and Office (CLO) building provides adequate rack space, power, uninterruptible power sources, and cooling capacity to meet the additional computing needs for the accelerator portion of the STS Project. Computing needs for the instruments, including a new server room in the CLO-II, are described in Section 6.4, "ICS for Instruments.

6.3 ICS FOR TARGET SYSTEMS

The ICS scope for the target systems includes control system hardware, software, and user interfaces, including the EPICS-based controls system and PLC-based controls. The process instrumentation and control (I&C) for the target systems will be designed to connect to the existing machine controls system to provide both safety-related and non–safety-related control, equipment protection, and monitoring for the systems shown in the following sections. The target instrumentation will interface to the machine network so that the target systems can be controlled from either the Central Control Room or STS Target Control Room. Target startup and control system maintenance will be performed from the STS Target Control Room. The specification and design of the instrumentation and controls equipment will be like-for-like or as equivalent as possible to existing FTS equipment [Battle et al. 2006]. In addition, enhancements will be incorporated into the STS design based on lessons learned from the FTS operation history. A summary of target functions for the control system is shown in Table 6.7.

Various target systems will provide interlocks to the existing MPS for machine protection, similar to the FTS. The STS control system PLCs will include MPS set points on multiple process parameters that output parallel trips to the two existing MPS trip systems. The MPS parameters in the target controls will include redundant and diverse parameters to trip the proton beam when necessary to prevent damage to the target due to predefined off-normal conditions.

Table 6.7. Summary of Target Control System functions and controller types.

Subsystem	Function	Controller type
Target assembly I&C	Monitor target assembly	PLC
Target assembly motion controls	Synchronize target segments with SNS pulses	TBD
Target assembly timing system	Provide pulse triggers to motion controls	TBD
Target assembly interlock system	Monitor synchronicity and provide input to MPS	PLC
Cryogenic moderator system (CMS) hydrogen system	Monitor and control	PLC
CMS helium system	Monitor and control	PLC
Moderator reflector I&C	Monitor temperature and other system parameters	PLC
Proton beam interface components	Monitor temperature and other system parameters	PLC
Vessel systems I&C	Monitor temperature and other system parameters	PLC
Target utilities	Monitor and control	PLC
Target vacuum systems	Monitor and control	PLC
Target protection systems	Monitor TPS	PLC

6.3.1 Target Assembly

The STS target baseline design is a segmented rotating assembly consisting of tantalum-clad tungsten blocks. The speed and phase of the target's rotation must be synchronized to the proton beam to ensure that each pulse of the beam strikes the target at an appropriate face. The target rotation will be controlled so that it is synchronized to the proton beam using the existing accelerator timing system, which will be extended to the new target station. The timing system's RTDL/EL will specify whether the next beam pulse is scheduled for the FTS or the STS target station. A timing receiver near the target assembly will generate beam-synchronous triggers for controlling the speed and phase of rotation, similar to that required for the neutron choppers used by the neutron scattering instruments. The control system will be designed so that improper rotation (in either speed or phase) or no rotation of the target disk will initiate an interlock to the MPS and/or Target Protection System (TPS) (to be determined based on a safety analysis) to terminate beam.

6.3.2 Target Protection System

The TPS is a credited protection-class system that will monitor the target for abnormal conditions and shut down the proton beam to the STS when necessary. The TPS will have redundant channels consisting of one-of-two voting logic. The TPS parameters (to be determined based on the safety analysis) will be isolated inputs to the Target Control System. These parameters will also trip the beam through the MPS. The TPS electronic circuits will incorporate fail-safe features designed to ensure that a beam shutoff would occur in the event of damage to a circuit, a fire, or a seismic event.

6.3.3 Target Utilities

Controls will be provided for the target utility systems, which consist of the primary cooling water systems, low-level liquid waste (LLLW) system, leak collection system, and helium/nitrogen gas distribution system.

There will be three deionized primary cooling water systems for the STS (Figure 6.10): loop 1—rotating solid target and proton beam window (H_2O); loop 2—reflectors (D_2O); and loop 3—shielding, vessel, moderators, and inserts (H_2O). A deuterium/oxygen recombination system will minimize D_2O losses to the hot-offgas system.

The LLLW system (Figure 6.11) consists of the LLLW collection tanks, filters, ion exchange, sampling, and evaporation systems.

The drain/leak collection systems include hot process vault collection pits, bunker leak collection, bulk shielding liner drain collection, core vessel drain collection, and service cell leak collection. This subsystem also includes liner drain collection of filter/delay and the gas/liquid separator tank cavities

The helium/nitrogen gas distribution system will be used for cover gas in areas exposed to high-energy radiation to minimize the production of activated and corrosive gases.

Instrumentation and controls for protection from special hazards associated with hydrogen, tantalum, activated water or air, and so on will be provided in accordance with applicable codes.

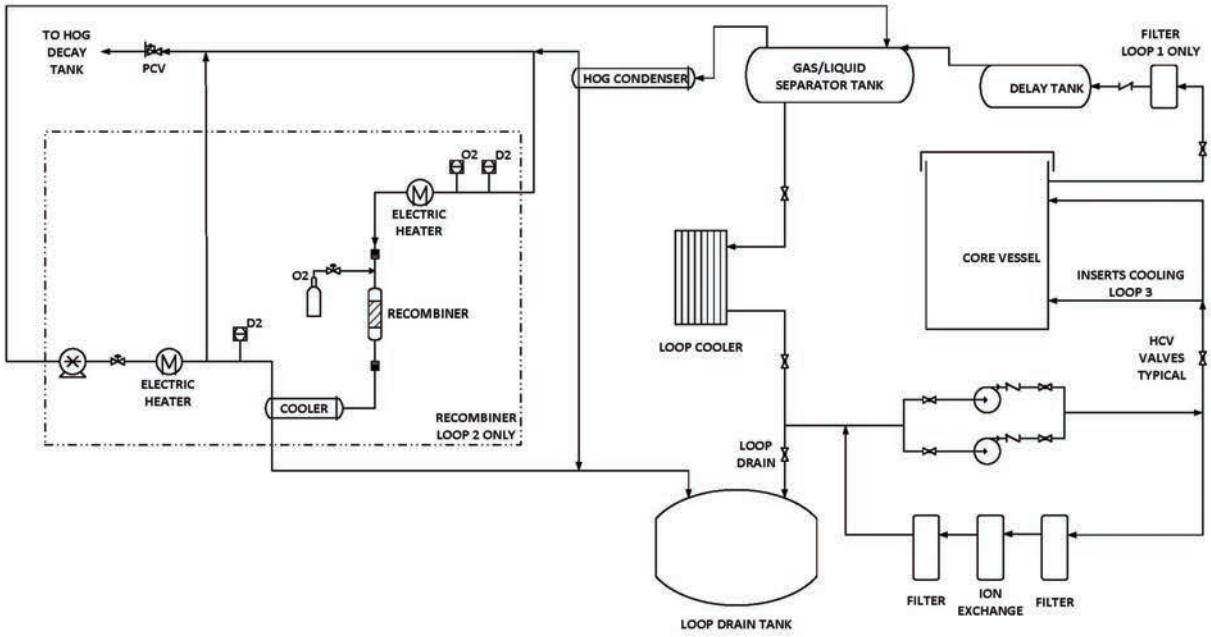

Figure 6.10. Simplified flow diagram—cooling water systems.

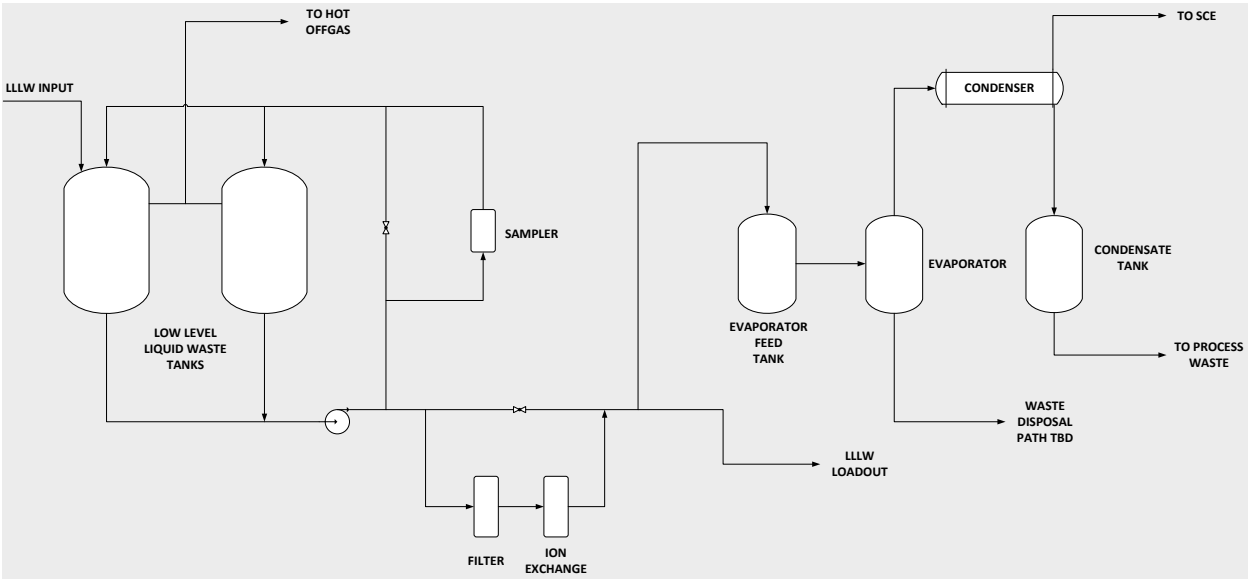

Figure 6.11. Simplified flow diagram—LLLW.

6.3.4 Cryogenics System for the Neutron Moderator

The STS cryogenics moderator system (CMS) will be based on the existing FTS system with some modification for ortho-para converter analysis. The STS CMS subsystems, at a high level, will comprise helium compressors, purification/oil removal systems, a cold box system, and a hydrogen accumulator system (Figure 6.12). All these subsystems for the CMS will require various process monitoring and process control functions, which will include temperature, pressure, speed, and power. One of the process variables that is not widely measured on the FTS CMS is flow. The addition of flow measurement in

several locations will be considered for STS. The control system topology for these subsystems will be a distributed design segregated based on the subsystem to facilitate maintenance.

The ortho-para converter analyzer will be a stand-alone device with local indication and is intended to be implemented initially on the FTS as part of the CMS upgrade for the PPU. However, it is anticipated that some indications will be tied into the control system to read this information remotely at the operator screen.

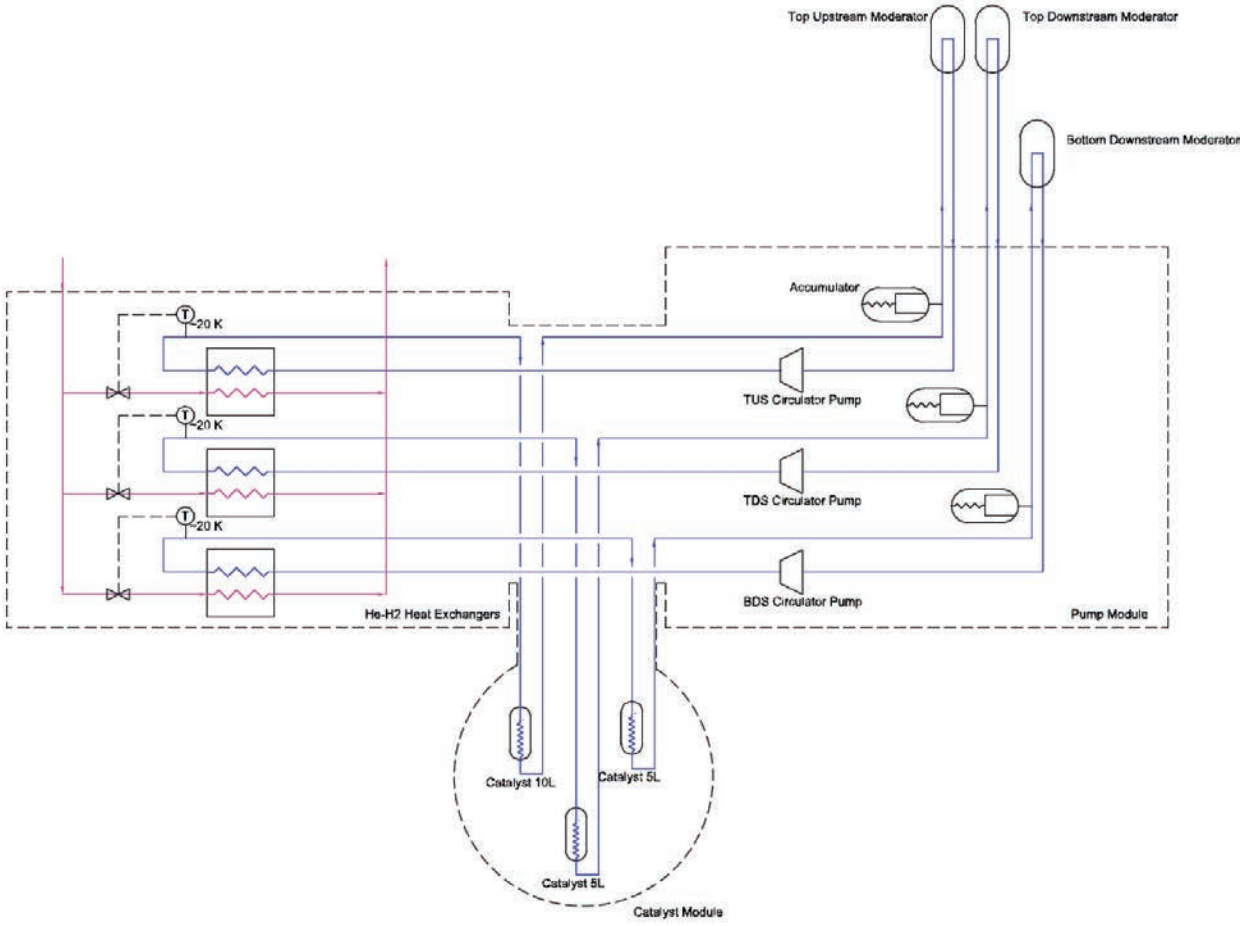

Figure 6.12. Simplified flow diagram—CMS pump/heat exchanger module configuration.

6.3.5 Target Personnel Protection System

The STS PPS is described in Section 6.2.3.

6.4 ICS FOR INSTRUMENTS

The DAQ and control systems for all BES-funded SNS FTS neutron scattering instruments were upgraded during the period from 2013 to early 2019, building on the lessons learned from the original DAQ system of the SNS project [Hartman 2011]. Additionally, three instruments at the High Flux Isotope Reactor (HFIR) are using the same DAQ and control system [Geng et al. 2013], with additional HFIR instruments transitioning now and in the next few years. With these upgrades [Hartman 2013], the DAQ and control system is well positioned for meeting STS instrument needs.

Each beamline has a dedicated private computer network for instrument operation and data collection, with core computing infrastructure serving all of the instruments. Common hardware and software components and tools are used to meet individual instrument needs. This toolkit-based approach helps to ensure a robust, reliable, and maintainable DAQ and control system, with the performance, flexibility, and adaptability to meet instrument needs across the suite of FTS, STS, and HFIR neutron scattering instruments.

The ICS scope for instruments includes

- Design and implementation of custom and commercial electronics for acquiring neutron scattering data
- Development and implementation of software for acquiring, processing, and managing data
- Development and implementation of software and user interfaces for beamline control, data collection, and experiment automation
- Design and implementation of the computing, data storage, and network infrastructure for DAQ, data reduction, and remote user access.

6.4.1 Data Acquisition and Controls Software

The primary functional requirements for STS DAQ and controls software include the following:

- Acquire neutron scattering data from detectors.
- Acquire experiment metadata, including data from high-speed and slow-speed data sources.
- Collate and provide access to experiment data in a format suitable for post-processing (data reduction).
- Provide device control and monitoring for all beamline equipment, including neutron choppers, sample environments, motion control systems, and detector systems.
- Provide user interfaces for operating beam line components and conducting the science experiment.
- Provide software and user interfaces for experiment setup, including experiment planning tools.
- Provide software tools for automating experiment control to allow for unattended operation.
- Provide instrument troubleshooting and monitoring tools such as data archivers and alarm systems.

The STS instrument DAQ and controls software will be built on EPICS, as is common across the SNS accelerator and instruments. EPICS provides a robust framework for instrument controls and DAQ, with reliable network protocols, existing device support for beamline equipment and sample environments, and a collection of tools for user interfaces and experiment automation. Software for the STS will be fully consistent with that used for FTS instruments, building on current capabilities and taking advantage of ongoing life-cycle improvements for the existing FTS instrument software in the coming years.

SNS instruments currently use EPICS with both the CA protocol and the PVAccess protocol. The STS ICS will continue to use both protocols to their full advantage. The baseline design for the STS instrument control system is based on EPICS 7, which combines CA and PVAccess in a single product.

GUIs for STS will be built using the CS-Studio framework, which is currently used for FTS instruments. CS-Studio provides a rich environment for developing client tools to operate the beamlines, automate data collection, and monitor the progress of experiments. For example, the CS-Studio Scan Server provides a batch queuing system for unattended data collection [Kasemir et al. 2013]. Jobs can be submitted to the Scan Server either through GUIs or spreadsheet-like tables, or with Python scripts. In addition to the tools for operating the instruments, CS-Studio provides tools for technical support groups to monitor and troubleshoot the instrument systems. For example, an alarm application provides fault notification of off-normal conditions, and an archiver provides historical data and trends for troubleshooting.

A schematic of the data flow within the existing FTS EPICS-based control software design is shown in Figure 6.13.

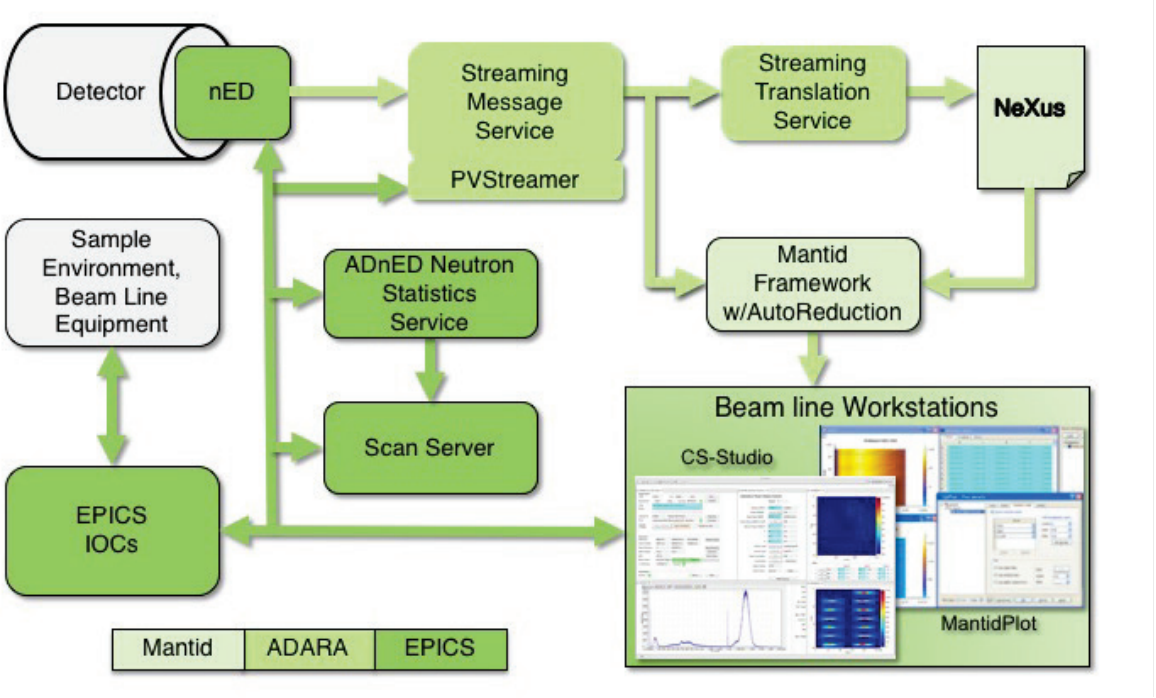

Figure 6.13. Data flow within the instrument data acquisition and control system.

The diagram in Figure 6.13 shows the components of the DAQ and controls system based on EPICS and how it interfaces to the instrument hardware; the Mantid data reduction software; and the ADARA (Accelerating Data Acquisition, Reduction, and Analysis) system, which is responsible for collating and streaming neutron event data and metadata into standard data exchange format for neutron and x-ray scattering experiments (NeXus) data files [NIAC 2020]. NeXus is a standard for neutron and x-ray scattering data. SNS experimental data use NeXus as a schema to organize the complex data in files that are stored in the widely used and interoperable HDF5 data format [HDF Group 2006]. ICS will be responsible for providing the EPICS and ADARA components for the STS, as described in more detail in the following sections.

6.4.1.1 Data Acquisition Software

For STS DAQ, the Neutron Event Detector (nED) [Vodopivec and Vacaliuc 2017] will provide the software interface to the detector hardware. The design of nED is based on the EPICS areaDetector [Rivers 2020] software in use at many synchrotron x-ray beamlines around the world. nED is designed to support acquisition of event-mode neutron scattering data, using areaDetector for counting criteria and online visualization. The areaDetector/nED plugins (ADnED) generate online histograms with regions-of-interest in detector physical orientation, time-of-flight, d-spacing, Q, ΔE, Q/E, signal-to-background ratio, and other transformations to provide counting criteria for data collection. An example of a detector user display is shown in Figure 6.14.

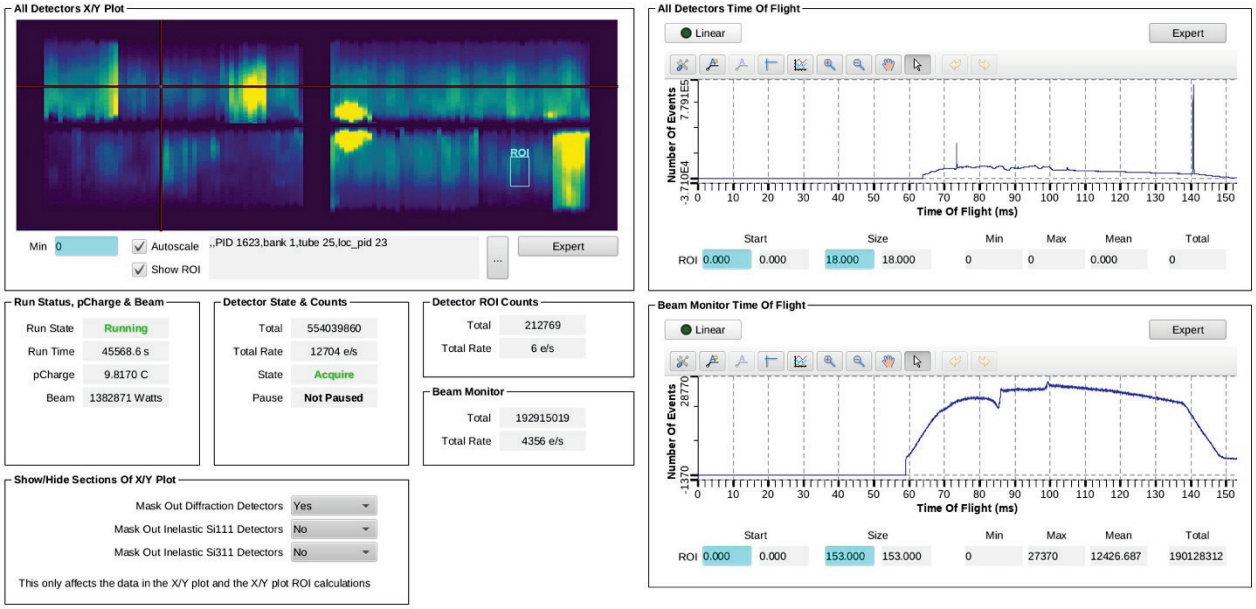

Figure 6.14. Example detector user interface screen showing a 2D intensity plot and 1D time-of-flight plots.

The screenshot in Figure 6.14 shows a 2D representation of the neutron detectors, with a rectangular region of interest that can be used for counting criteria. There are also 1D plots displaying neutron time-of-flight data on the detectors and beam monitors. The plots integrate neutron data over time, showing intensity during an acquisition. An acquisition run typically lasts anywhere from a few seconds to a few hours.

nED also provides an interface for detector configuration, monitoring, and calibration. The software supports all detector types currently in use at SNS, as well as several additional detectors used at beamlines at HFIR. The plug-in design of nED allows extension to support any additional detector types required for STS instruments. This software has been demonstrated to meet data rates more than sufficient for the planned STS instruments. nED has been successfully shown to handle event rates greater than 5 million events per second at operational instruments. The fiber link is capable of 25 million events per second. If higher rates are needed, multiple instances of nED can be run in parallel. nED streams data using the EPICS PVAccess protocol to the ADnED AreaDetector software [Kasemir 2015], and it uses the ADARA protocol to a NeXus file writer for data reduction and archival. The NeXus data file and ADARA protocol are the interface points to the data reduction software.

The ADARA system was developed at ORNL to reliably support neutron event data streaming in a flexible way. There are several software components and a well-documented network protocol. The

Streaming Management Service (SMS) is responsible for aggregating neutron events from various sources into the data stream, such as detector events, beam monitor events, chopper timing events, and other fast metadata. The SMS runs as a Linux daemon service as part of the instrument DAQ software. Also running on each instrument is the Process Variable Streaming Daemon, a CA client, which is responsible for monitoring slow controls metadata (EPICS PVs) and inserting PV value updates as a time-series log into the ADARA data stream. Data related to sample environments, choppers, motion control, and other beamline components are captured as part of the data stream. The SMS sends the aggregated data stream to a central stream translation client, which writes the data stream into a standard NeXus HDF5 data file.

Two existing instruments at the SNS and HFIR are neutron imaging beamlines that perform radiography and tomography experiments using 2D imaging cameras as their primary neutron detector system. An example of such a camera is an Andor charge-coupled device (CCD) or sCMOS camera. These imaging cameras are supported using the EPICS areaDetector software package. The software is responsible for reading out image data, performing statistics and live user display, and writing 2D image files and associated instrument metadata. Several other instruments have other types of CCDs used for sample viewing and neutron beam diagnostics. These are supported in a similar fashion using the areaDetector framework. Imaging capability is not included in the baseline design for the initial STS instruments; however, it is anticipated that the future instrument suite may include a dedicated neutron imaging beamline. This would be supported using the same software framework.

6.4.1.2 Control Software

The EPICS IOC software will be required to interface to a diverse set of hardware and electronics equipment, both commercial and developed in-house. There are several instrument control subsystems typically involved in routine control and experimentation.

Motion Control

All the existing FTS and HFIR instruments have some number of motorized stages to control slits, sample positioning, optics, and detector positions. The majority of stages are controlled by stepper motors in standard NEMA (National Electrical Manufacturers Association) frame sizes and operate at low speed. Positioning requirements are typically in the 10 to 100-micron range, which can be satisfied by general purpose, low-cost linear and rotary stages. Most stages will also have limit switches and home switches that can be fitted with either rotary or linear encoders (quadrature or bidirectional/serial/synchronous interface absolute). In addition, the control system will make use of emergency stop circuits and, where applicable, proximity sensors for equipment protection.

The current standard motor controller for the FTS and HFIR is the Galil DMC-40x0 controller. It is expected that STS instruments will use the same motor controller and that the majority of motor control needs will be very similar to those of existing instruments. Certain specialized motion control systems may require specialized controllers, such as hexapods, piezo stages, and other types of nano-positioning stages. Early STS instrument designs describe the use of small beam sizes and smaller samples compared with what is typical for the FTS, so it is expected that submicron positioning will be required on some instruments. However, the EPICS motor software already provides a wide range of drivers for common controller types, so it is likely that support for these specialized systems already exists (for example, the Newport XPS or the Physik Instrumente brand General Command Set–based controllers).

EPICS will interface to the motor controllers and will provide a means to move and scan each motor in the required fashion. The software will use the well-established EPICS motor record [Peterson 2019]. The motor record is currently in use at HFIR and FTS instruments; it provides a consistent interface to motor

control, allowing the user to perform common motor operations such as moving the motor, stopping, changing speed, and dealing with positioning errors. It provides feedback such as limit switch status. The STS instruments will reuse the existing user interface screens for motion control. An example of such a screen is shown in Figure 6.15.

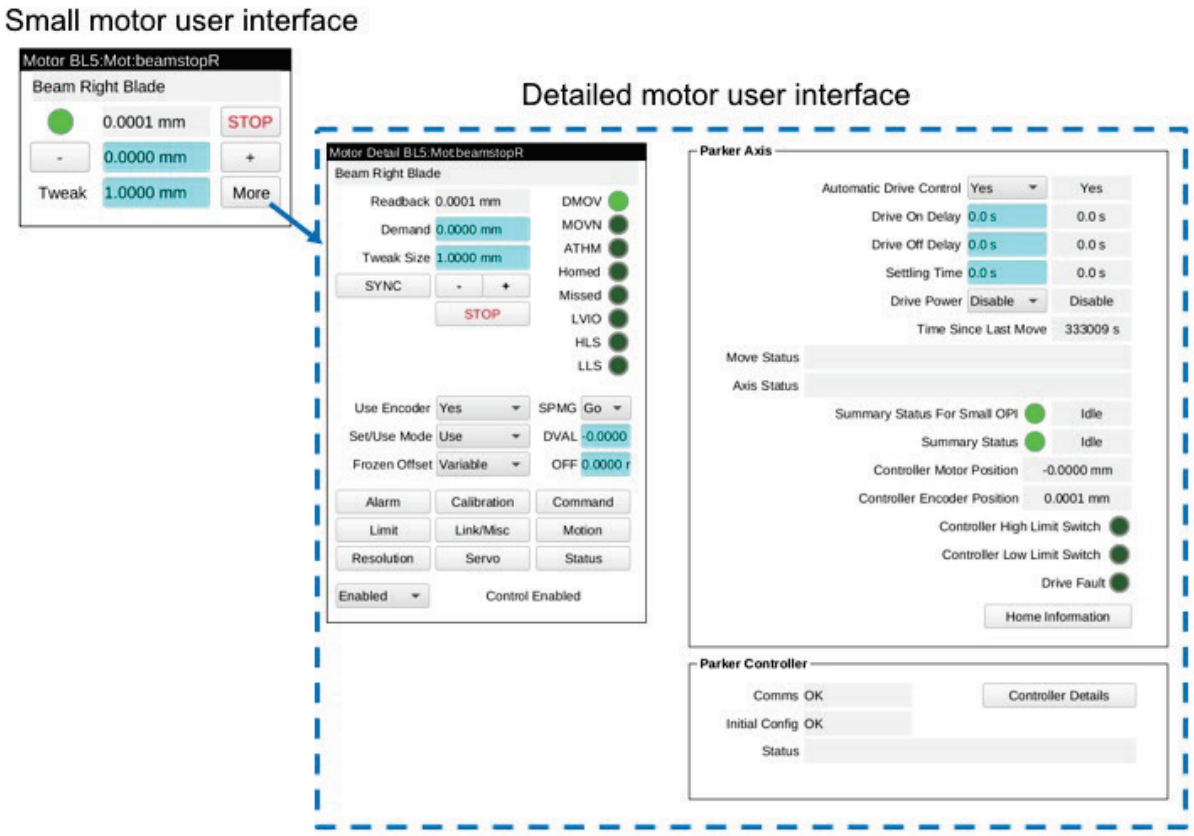

Figure 6.15. Motion control user interface screens.

In addition to general purpose motor control screens, more specialized screens can be provided to aid in scanning, positioning, and feedback. For example, several existing FTS instruments use tables of predefined positions, which can be used to easily move to a predefined position during a scan. This kind of experimental logic is implemented in either EPICS database records or in Python IOCs based on PCASPy [Wang 2017]. For example, the existing alignment scanning interface used at the SNS is shown in Figure 6.16.

The screenshot in Figure 6.16 shows the interface used for aligning a motorized stage. It allows the user to scan a motor in steps and to plot detector counts based on some condition. The software is implemented in Python using the PCASPy IOC framework. It also provides a variety of fitting algorithms to detect peak and edge positions.

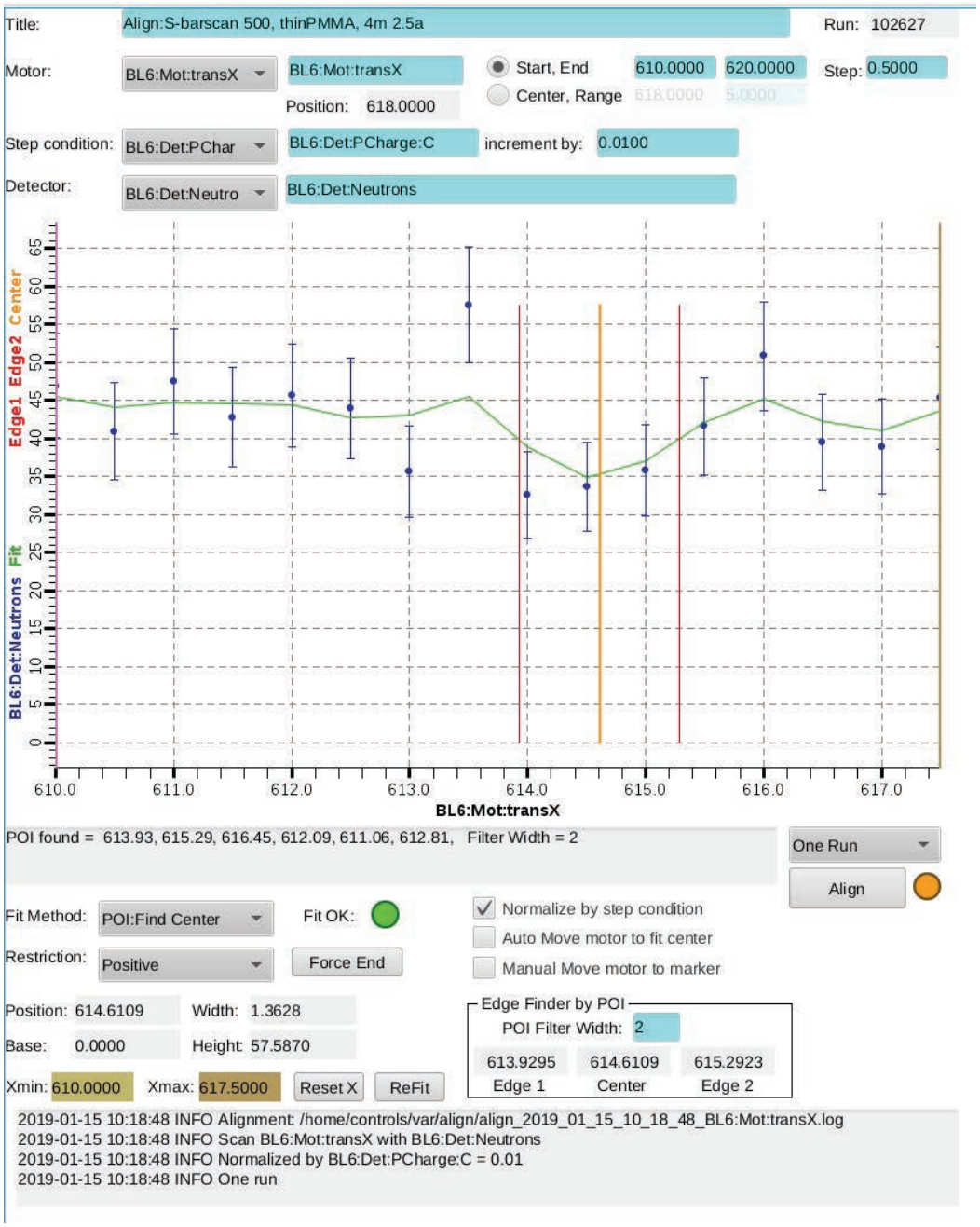

Figure 6.16. User interface screen for alignment of motors, rocking-curve scans, and other scans.

Sample Environment Controls

The EPICS software will provide an interface to the controllers used for sample environment equipment, such as temperature controllers, pressure controllers, power supplies, and general-purpose analog and digital remote I/O systems. The interface to these systems will typically consist of a low-level engineering interface to allow setup and calibration, as well as a high-level user interface to facilitate scanning and experimental logic such as set point ramping and alarm management. There are several categories of sample environments, each requiring very different controllers and software.

Low-temperature experiments tend to be done using a closed-cycle refrigerator or cryostat along with inserts to achieve ultra-low temperatures (<1 K). The existing instruments use the Lakeshore family of temperature controllers. These controllers use an ASCII-based protocol over Ethernet. We have well-established EPICS software for the Lakeshore 336, 350, and 372 low-temperature controllers. For high-temperature experiments, the Eurotherm nanodac controller is used. It uses a Modbus/TCP protocol, for which the SNS has already developed support using the standard EPICS Modbus [Rivers 2019] libraries. It is expected that we will continue using these controllers and the associated software at the STS instruments.

The control software for superconducting magnets will vary depending on the magnet vendor. Typically, a new magnet will be provided with its own control system using LabVIEW running on Microsoft Windows. It is possible to integrate these types of systems into EPICS by using the CA Lab [HZB 2020] LabVIEW-to-EPICS plugin. Some magnets may need have to have custom EPICS software developed for them, which usually will consist of power supply controls and sequence software to control field ramping.

Gas flow, high-pressure and similar types of flow, and ad hoc sample environments can be integrated using a general-purpose process controller such as the Eurotherm nanodac controller. Other types of process controllers can be accommodated as long as they have a suitable type of communication interface/protocol. For example, it is generally easy to develop software in EPICS for devices that use an ASCII-based protocol [PSI 2020] over serial (RS232 or RS485) or TCP/IP, or other well-established protocols to which EPICS already caters, such as Modbus/TCP. Devices that rely on USB or binary closed proprietary protocols will be avoided.

Each instrument will also be provided with a general purpose remote I/O system for ad hoc experiments or for interfacing to hardware that relies on analog or digital I/O. The present FTS instruments use serial-based commercial modules from the ICP-DAS company. These attach to a Moxa serial-to-Ethernet converter. There are a wide range of commercial solutions constantly emerging for network-based I/O; therefore, it is likely that the selection of some of the specific device models for use at the STS can be deferred to a later date.

6.4.1.3 Neutron Chopper Controls

The chopper control systems typically use dedicated controllers that are responsible for rotating and synchronizing the timing of the chopper disks. There are several types of controllers, and the EPICS software has been developed for the current generation of controllers in use at FTS. The controllers use either serial-based or network-based remote protocols, such as Modbus/TCP.

The EPICS software provides a detailed user interface to the chopper controllers to enable routine operation as well as diagnostics and expert control. Figure 6.17 shows an example of one such interface.

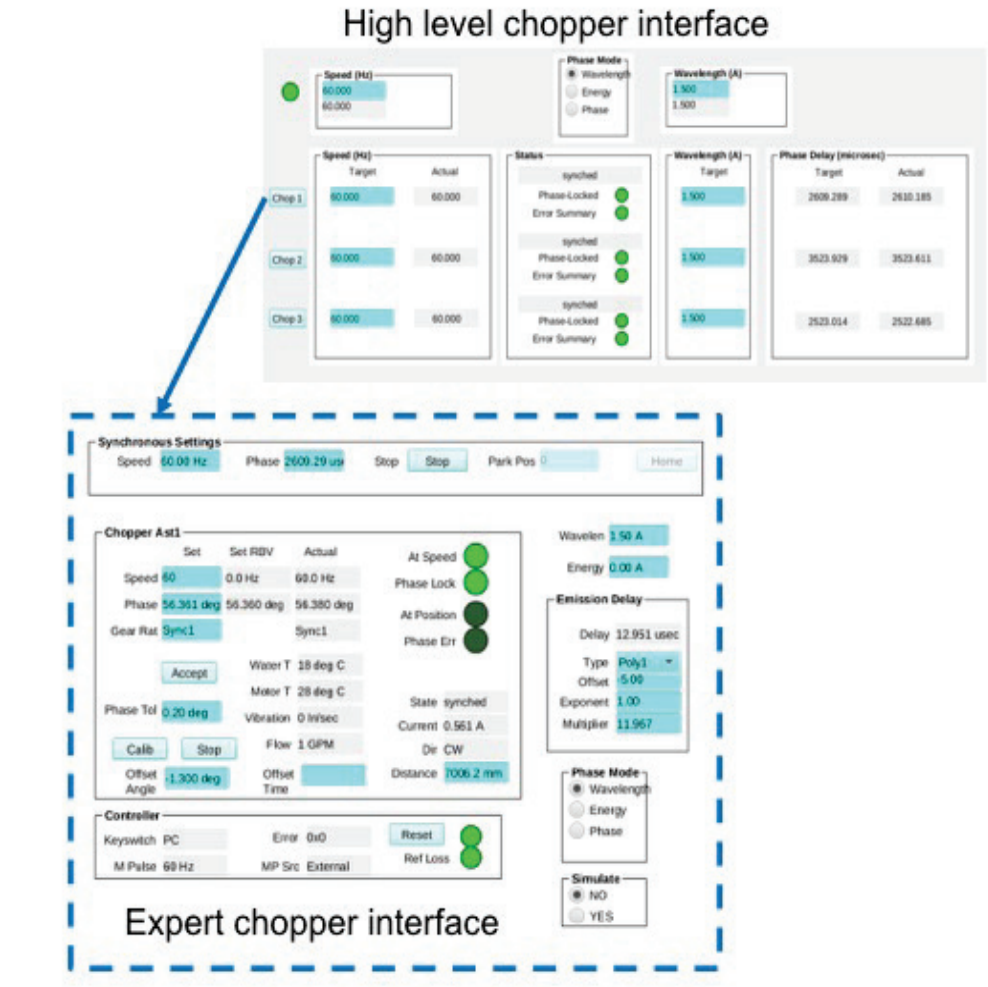

Figure 6.17. Neutron chopper user interface screen.

For the STS instruments, a new generation of choppers is being proposed; therefore, new EPICS interfaces to these choppers will most likely need to be developed. However, the same scheme of separate user and expert screens will be retained.

Control Integration with User Information Systems

The STS instrument user will also be able to use the EPICS software to initially select the experimental proposal number and the specific sample to be measured. A screenshot of the interface for this task is shown in Figure 6.18.

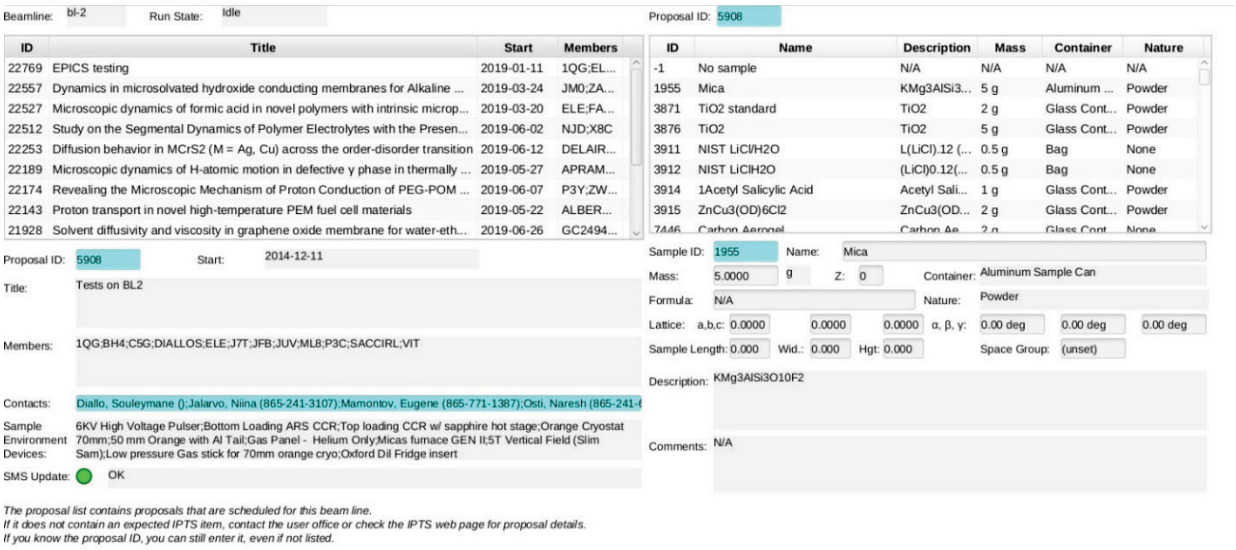

Figure 6.18. User interface screen showing proposal information and sample information from relational databases.

This interface also brings into the control system various metadata for the sample, such as sample mass, chemical formula, density, container, and other parameters. These data can be included in the data stream and in the final data set, which can then be used to facilitate automated data reduction. This eliminates the need for users to enter the same data into multiple systems.

In summary, while it is anticipated that some new features will be required for the STS, such as new device drivers and instrument-specific experimental tools, the reuse of most of the EPICS software components is expected for the future STS. The STS instrument controls will also benefit from new features and improvements made as part of routine operational support and ongoing development in the coming years.

6.4.2 Data Acquisition Hardware

The main functional requirements for the STS DAQ hardware include the following:

- Acquire and timestamp neutron events from the detectors.
- Acquire and timestamp neutron events from the beam monitors.
- Acquire and timestamp the top-dead centers (TDCs) from the choppers.
- Acquire and timestamp time-critical signals for mode control in the sample environment.
- Preprocess the neutron data where appropriate to optimize the throughput.
- Packetize events data and associate them with their corresponding beam frames.
- Provide the synchronization signaling to the choppers.
- Provide signals for the sample environment mode control.

Current FTS DAQ hardware (Figure 6.19) deployed at the FTS instruments is implemented with a standard fan-out, concentrate-in approach. All modules use FPGAs. The nED software, which resides on the DAQ Linux server, is responsible for sending commands and configuration to downstream modules, receiving command responses, and capturing neutron events and metadata [Vodopivec et al. 2019]. Metadata include chopper TDCs, beam monitor counts, and additional inputs that require synchronization with accelerator timing. nED communicates with the detector electronics via the optical communication card (OCC), an FPGA-based commercial-off-the-shelf PCIe carrier with a custom FPGA mezzanine card

(FMC) attached. The FMC has an optical transceiver interface that allows the FPGA to communicate with the data system packetizer and timing interface (DSP-T) via a 2.125 Gb fiber link (1.7 Gb effective bandwidth). The DSP-T receives accelerator timing via two fiber optic inputs, one for EL and one for RTDL. The DSP-T distributes timing to the downstream modules via the copper timing and control interface, and to the choppers, beam monitors, and other equipment via the fiber timing loop.

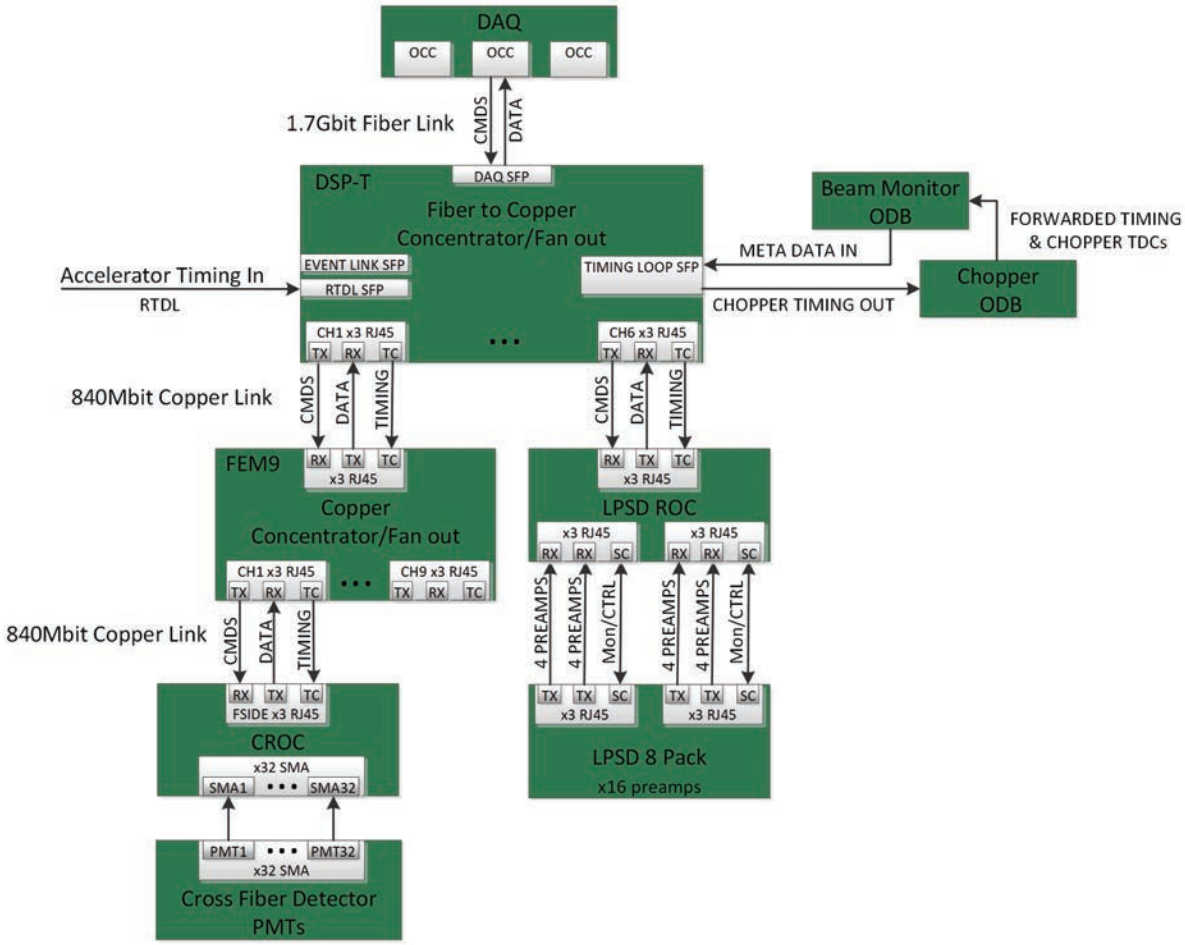

Figure 6.19. Block diagram of instrument data acquisition hardware.

The fiber timing loop is essentially a 106.25 MHz 16-bit parallel-to-serial I/O interface that is serialized via fiber transceivers and sent to an optical distribution board (ODB). The ODB has 16 outputs that are equivalent to the DSP-T's 16 outputs and contain various timing and synchronization signals. In addition, the ODBs have 16 inputs capable of receiving metadata or forwarding timing information from the outputs via jumpers. The last ODB in the chain closes the loop, transmitting all metadata inputs to the DSP-T. Commands and configuration parameters from nED are sent to the downstream modules via six DC-coupled low-voltage differential signaling (LVDS) interfaces on the DSP-T. All downstream commands are replicated or fanned out on each of the six DSP-T channels. The FEM9 is a copper concentrator/fanout module that receives the timing, configuration, and commands and in turn fans them out to all nine of its LVDS channels. Read-out card (ROC) modules receive the timing signals and commands and respond via the upstream LVDS links. The upstream links are used for both command response and data and are capable of link rates of 840 Mb/s and data rates of 640Mb/s. This equates to 10 million four-word events/s. The FEM9 fans-in or concentrates the command responses and neutron events and then sends these aggregated packets to the DSP-T. The DSP-T then concentrates each of its six inputs

and the metadata channel and forwards these packets on to nED via the OCC fiber link, which is capable of transmitting 25 million four-word events/s.

Currently demonstrated data rates for the existing DAQ hardware are sufficient to meet the expected data rates of all STS instruments. Anticipated detector types and data rates are shown in Table 6.8. DAQ hardware and software for linear position-sensitive tube detectors (LPSDs) is currently fully supported at FTS instruments. The CHESS instrument design calls for approximately 50% more detectors than any existing FTS instrument installation, but meeting that requirement is not anticipated to present a difficulty. The SiPM scintillator detectors will require additional development effort. It is anticipated that similar SiPM-based detectors will be deployed to HFIR instruments before they are deployed to STS. DAQ hardware and software interfaces to these detectors will likely be developed to support the HFIR installation and will be available for use to the STS Project.

Table 6.8. Preliminary detector technologies and estimates of data rates for proposed initial suite of STS instruments.

Instrument	Flux at sample	Flux on sample	Sample size	Solid angle coverage	Spatial resolution	Rate capability, total and individual	Type	Quantity
	(n/mm^2/s)	(n/s)	(mm)	(sr)	(mm)	(n/s)		
CHESS	75 K	7.5 M	10	6.2	20	1 M, 6 K	LPSD ^{3}He tubes	160 8-packs (1.5 m × 1 in.)
SANS1	700 K	70 M	10	0.65	3	1 M, 100 K	Scintillator SiPM Anger cameras (30×30 cm)	25
QIKR	2 M	80 M	20×2		1x2	20 K	Slanted-scintillator SiPM pixelated camera	1 (20 cm × 40 cm)
EWALD	7.5 M	2 M	0.5	5.7	0.3	200 K, 10 K	Scintillator SiPM Anger cameras (1×12 cm)	37
VERDI	400 K	40 M	3–20	2.9	10	700 K, 4 K	LPSD ^{3}He tubes	224×8 packs (1 m × 1cm)

6.4.2.1 Data Acquisition Hardware Timing

The timing needed for proper DAQ operation is provided by the accelerator timing system. Three timing sources are used for the DAQ timing: the ~32 MHz, ±2.5 ppm variable RF clock source; the 10 MHz, ±25 ppm crystal clock; and the GPS timing source. The RF clock is used as the carrier for the EL optical fiber channel, and the 10 MHz clock is used as the carrier for the RTDL optical fiber channel. The 10 MHz clock is extracted from the RTDL and distributed to the DAQ modules for common-clock event timestamping. The GPS timing source is used at the accelerator timing systems to timestamp the main synchronization DAQ signal (TSYNC). The TSYNC is timestamped with the current Coordinate Universal Time (UTC) with a resolution of 1 μs. The timestamp is sent to the DAQ hardware through the RTDL. The timestamping resolution in the DAQ modules is 100 ns, resulting from the 10 MHz counting clock. The timestamp cross-module inaccuracy is very small if the common 10 MHz clock is used by all DAQ modules in the system.

However, the error can be up to tens of microseconds for long frames if local clocks at the DAQ modules are used. This timestamping scheme provides continuous timestamping in UTC seconds and nanoseconds with a 100 ns resolution within the acquisition frame and 1 μs resolution between the acquisition frames.

The TSYNC pulse period is set to an integer number of the accelerator turns closest to 16.666667 ms. For higher energy resolution, the accelerator timing system is providing longer acquisition frames selectable by the sub–60 Hz enabling signals sent to the DAQ hardware via the EL. The sub–60 Hz frame rates are 30 Hz, 20 Hz, 15 Hz, 10 Hz, 5 Hz, 2 Hz, and 1 Hz.

The same accelerator timing system EL/RTDL will provide timing information to the STS instruments (Figure 6.20). These instruments will typically operate at 15 Hz, matched to the 15 Hz beam pulse on the STS target. However, sub–15 Hz frame rates will be available for the instruments at 7.5 and 3.25 Hz to provide longer bandwidth as needed. FTS instrument DAQ will typically operate at 60 Hz (with 45 pulses per second) but will fully support operating at sub–60 Hz frame rates. At the lower frame rates for the FTS instruments, the timing system needs to efficiently accommodate the missing pulses directed to STS.

The accelerator timing system will need to provide sufficient data to deterministically synchronize DAQ and chopper systems with the beam to both the STS and FTS. Accelerator metadata, such as beam charge per pulse, will need to be accounted per target station to provide accurate counting criteria and normalization data for the instruments at the FTS and STS.

STS choppers will need to be phase-locked to the 15 Hz STS beam. However, to provide more accurate control, a 60 Hz timing trigger from the accelerator timing system will be used. Each chopper will be provided a 60 Hz reference trigger and a 15 Hz (or sub-frequency) synchronization trigger. This approach is similar to that used to support sub-frequency operation at FTS instruments today.

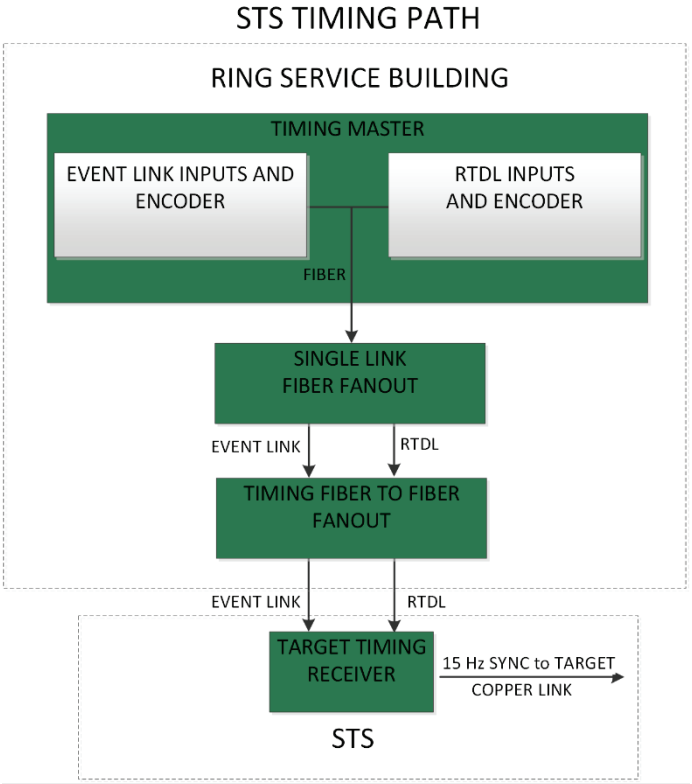

Figure 6.20. Timing distribution network.

6.4.2.2 Ongoing Development

One of the biggest challenges hardware designers face is planning for obsolescence. This can be particularly problematic in long–life-cycle products. Hardware for scientific user facilities definitely falls in this category. Ongoing development, as part of SNS and HFIR operations, is currently under way to provide an upgrade path for existing instruments. These developments will be available for the STS Project.

To address obsolescence with the existing detector ROC for FTS instruments and provide options for planned detector expansions at existing instruments, a redesign is currently under way. The new design is a modular approach, which provides an upgrade path for existing instruments. The modular approach also provides increased flexibility to support detector readout for STS instruments.

The FMC specification, a widely adopted VMEBus International Trade Association (VITA) standard, addresses this issue by providing a pinout specification for the FMC connector. FMC connectors come in two flavors, high pin count and low pin count. See Figure 6.21 for more details on the standard.

The modular ROC is an FPGA-based carrier board with four FMC connectors. Three of the connectors are of the low-pin-count type and one is a high-pin-count type. The idea behind the modular ROC is to create a standardized set of FMC modules that meet the requirements of the different detector technologies deployed at the SNS and HFIR. The FMCs create flexibility, allowing for reverse compatibility with the existing infrastructure and opportunities to test and deploy new designs. On the digital side, STS hardware will use the FPGA's built-in multi-gigabit transceivers, which allow easy replacement of the currently deployed DC-coupled LVDS links (link rate of 840 Mb/s) with 2.125 Gbit/s AC-coupled copper or 6 Gbit/s fiber. This capability has already been successfully demonstrated in the lab. Even greater speeds are within reach presently and are expected to increase in the coming years. The carrier itself can also be upgraded as technology evolves without the need to redesign the various FMCs. A modular concentrator design will follow the modular ROC. Ultimately, it is intended that all of the DAQ hardware for FTS and STS instruments will follow this modular model.

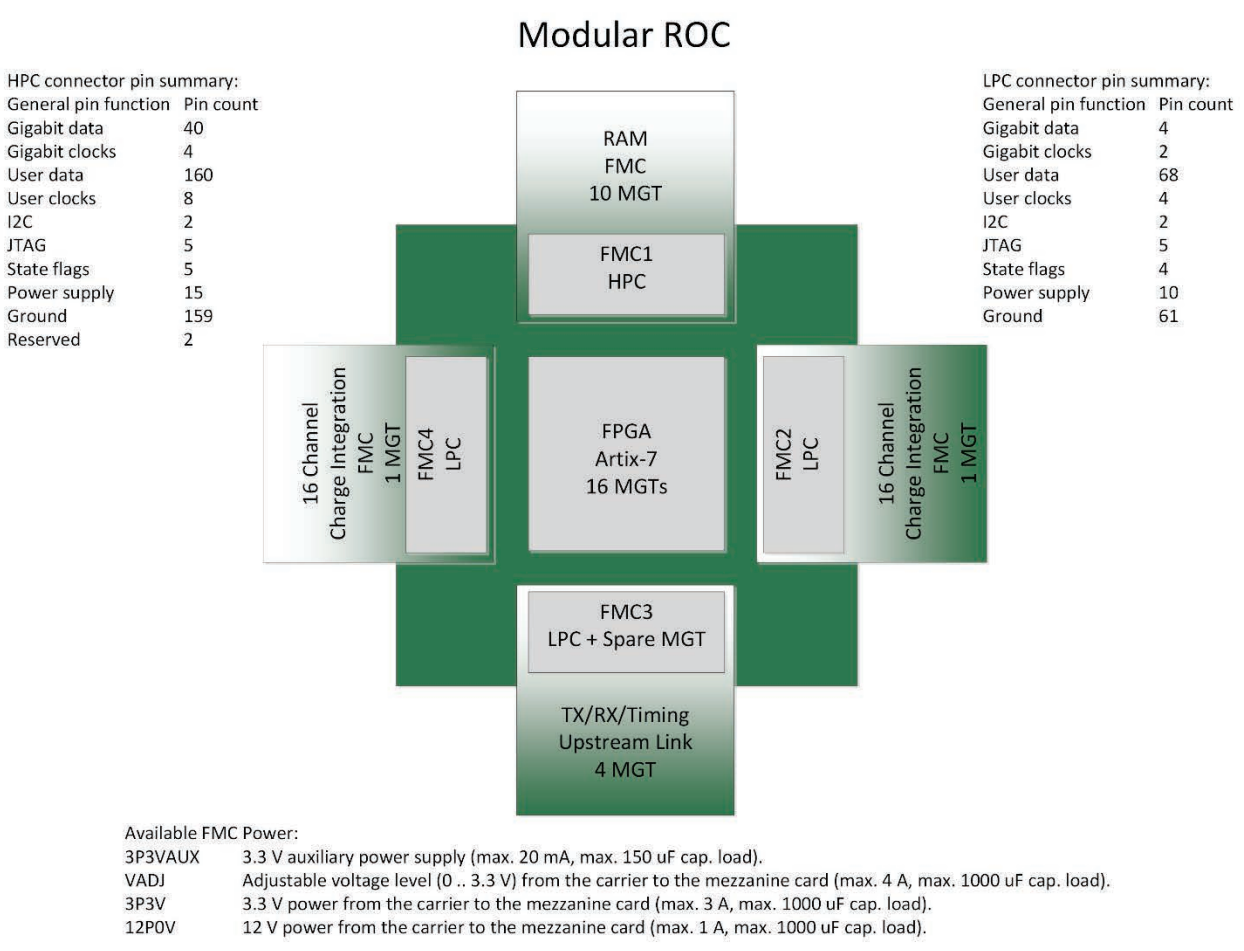

Figure 6.21. Block diagram of a modular detector read-out card design currently under way.

6.4.3 Computing and Network Infrastructure

The existing computing infrastructure for the instruments includes high-reliability systems for DAQ and high-performance systems for data reduction and data analysis.

SNS and HFIR users currently have access to 45 high-performance workstations (with a cumulative 1928 processing cores and 16 terabytes of RAM) for users to reduce and analyze experiment data. During an experiment, users have access to a dedicated workstation for each beamline. A cluster of workstations is also made available for remote access by users for continued analysis after the experiment. These workstations all include common software for data reduction and analysis. Remote login is available through secure shell (ssh) or using a ThinLinc client (either as an application or through a standard web browser) for a full desktop interface.

The computing infrastructure includes 3.5 petabytes of data storage—with more than 2 petabytes on a high-performance storage system (HPSS) for experiment data. Long-term data archival is provided through an agreement with the Oak Ridge Leadership Computing Facility to provide access to its HPSS tape library. Data directories that are not modified in more than 3 years are migrated to offline data storage on this tape system. The data sets can typically be restored to disk within one business day if needed.

The STS Project will include additional computing infrastructure as required to support the STS and the initial STS instruments. It is anticipated that the full suite of STS instruments will approximately double the computing and data storage requirements compared with the FTS only. The STS Project will include computing infrastructure to support the future buildout of the full instrument complement; and it will include sufficient computing, networking, and data storage to fully support instrument operation for the initial suite of instruments included in the project. An “edge computing” model, with dedicated computing resources provided for each instrument, will be used to provide advanced computing and data processing needs. A typical edge computing cluster will likely include CPUs and GPUs to enable machine learning techniques or other advanced computing tools co-located with (or located nearby) and dedicated to each instrument.

The STS Project will include a new server room in the CLO-II building. This server room will include raised-floor cooling and sufficient rack space, power, and UPSs to support the computing and data storage needs for the additional instruments made available by STS. Sufficient single-mode fiber will be provided to interconnect this new server room with the existing server rooms in the CLO and the STS instrument buildings and to the core ORNL network.

6.4.4 Instrument-Specific Needs and Challenges

The initial suite of instruments proposed for the STS Project has been defined. For the most part, DAQ and instrument control needs can be met with existing technologies. Additional development will be required to fully meet some specific instrument needs; however, no major risks have been identified. Some technical challenges are present, but they are manageable.

The STS neutron beamlines will be longer than a typical FTS beamline, and sample sizes at some STS instruments are expected to be small. These characteristics present challenges with positioning and alignment of neutron beam optics and positioning of samples. Additional instrumentation may be required to monitor the positions of beam optics devices. If active control or feedback of beam optics is required, then additional development will be necessary.

The STS instruments will have an increased focus on in operando and time-resolved measurements and multi-modal measurements. These are capabilities that are being developed and used today at the FTS instruments. For example, pulsed-electrical field experiments are being conducted on TOPAZ at the FTS. The DAQ system can acquire electric field waveforms as part of the experiment data stream. A capability has been developed for the Magnetism Reflectometer to support polarization state switching at rates up to several kilohertz. For each acquired neutron event, the acquisition system can identify the state of the polarizer, the state of the analyzer, and, for example, the state of an electric field applied to the sample. The technology to support these techniques continues to be developed and will be available for STS instruments. The modular design of EPICS allows integration of a diverse range of equipment. This capability facilitates multi-modal measurements. The wide range of timescales, combined with the increased use of multi-modal measurements, is anticipated to push the resolution and accuracy requirements beyond the existing SNS accelerator timing system capability. Upgrades or enhancement of the timing system are expected to be part of the STS scope. Specific requirements will be derived from the instrument systems design.

The CHESS instrument will use rep-rate multiplication to acquire up to 20 incident energies within each frame. Rep-rate multiplication presents a challenge in providing online displays to visualize the data in Q vs. energy during an experiment. However, based on experience with existing direct geometry spectrometers operating at higher data rates, doing so should be achievable even with the computer hardware presently available.

Some instruments in the final selection may present unique challenges related to sample environments. As these designs move forward, additional controls software effort will be required to meet these needs.

6.4.5 Instrument PPS and Shutter Control

Instrument systems for STS will include a maintenance shutter in the bunker and operational shutter(s) downstream. Maintenance shutters will have three functional positions: open, gamma blocking, and neutron absorbing. The gamma blocking mode will be used during maintenance outages. The neutron absorber position is intended to reduce activation of failed downstream components during beam operation.

Each beamline will have operational shutters for daily experimental needs. Operational shutters will be used to allow personnel access for sample changes and other access to the sample area. Shutters may include beam guide components and require precise positioning.

IPPSs for STS instruments are described in Section 6.2.3.

6.5 ICS FOR CONVENTIONAL FACILITIES AND CUB-II CONTROLS

The ICS scope for conventional facilities includes control systems for utilities and technical building automation systems. The distributed controls architecture will be EPICS; and the controls design will include all controller hardware up to the process field devices, e.g., instrumentation, variable-frequency drives, motor control centers, and others. The control system will consist of hardware controllers including PLCs, BACnet controllers, and Modbus interfaces. The design will include all software engineering for the various hardware controllers and EPICS systems. Control design effort will also include consulting on instrumentation selection to ensure compatibility for the PLC interfaces. Programming and connection of PLCs to the machine control system shall be completed and the control system commissioned to ensure proper operation.

System software and firmware will provide the following functions:

- Control sequences to support the operations of the technical equipment.
- Proportional-integral-derivative (PID) control to enable faster and closer control to system set points.
- Adaptive tuning to adjust PID loop constants to ensure that control system response remains accurate and reliable over a wide range of dynamic operating conditions.
- Monitoring to read the values of measured variables, to read control loop set points, to monitor control signals to actuators, and to indicate the status of equipment, alarms and overrides.
- Energy management, including optimum start/stop, variable air change rates in laboratories, duty cycling, supply air temperature reset, supply air static pressure reset, demand limiting, and time totalization.
- Data management, including continuous database updating, alarm reporting, trend logging, and report generation.
- System programming to add, delete, or change points, set points, schedules, control algorithms, report formats, and so on.

- System software to enable building operators to graphically monitor and control building operations and provide the functions listed. Graphics will include site plans, overall building plans, floor plans and individual system graphics.

The controls scope will include all PLCs, controller hardware, technical network switches, and controls enclosures to house ICS equipment. The installation, functional testing, and full integration to verify proper operation using EPICS will be performed once all field equipment installation and wiring are complete. The cable design from PLCs to field devices will be included in the controls design, but installation, termination, and cable/connector material cost will not be included in the controls scope.

The control documentation will include design requirements documentation, PLC enclosure layout drawings, detailed I/O wiring to field instrumentation drawings, integration testing procedures, and functional system design documents.

The existing SNS conventional facilities control system is completely integrated with the SNS machine control system [Munro et al. 2001]. The same building blocks are used as for the rest of the ICS: supervisory controls are EPICS based, standard SNS controllers are used for local controls, the machine network is used for communications, and so on. All SNS control rooms can monitor conventional facilities processes.

Conventional facilities data are archived via the same system used for the accelerator and target. Conventional facilities controls are supported and maintained as part of the broader accelerator control system. The integration of conventional facilities controls with accelerator and target controls has proved highly beneficial to SNS operation, and the same approach will be used for STS.

A list of major equipment to be controlled for STS conventional facilities is provided in Table 6.9.

Table 6.9. Major equipment to be controlled by ICS conventional facilities controls.

Building	System or equipment	Quantity
CUB II	Tower water (cooling tower)	2 cells
	Condenser water (cooling tower)	4 cells
	Chillers	4
	Boilers	2
	Air compressors	2
	Air handling unit	1
CEF II	Confinement exhaust fan systems (primary confinement exhaust, secondary confinement exhaust, hot offgas, and RTST tunnel)	7 fan systems
RTST Tunnel	Air handling unit	1
	Deionized (DI) water system (for magnets)	1
RTST Service Bldg.	Air handling unit	1
	DI water system (for power supplies)	1
	Confinement makeup air systems	4
Target Building II	Air handling units (secondary confinement exhaust recirculation, target, 40M, 50M)	8
	Heating, ventilation, and air conditioning (HVAC) for cryogenic moderator equipment rooms	2

Table 6.9. Major equipment to be controlled by ICS conventional facilities controls (continued).

Building	System or equipment	Quantity
	Fan coil units	16
	Confinement high-efficiency particulate air filter banks	11
	DI water systems	2
	Sensible chilled water systems	3
40M Bldg.	Fan coil units	23
50M Bldg.	Fan coil units	21
90M Bldg.	Air handling units	2
	Sensible chilled water system	1
Site-wide	Electrical power monitoring (interface to ORNL supervisory control and data acquisition system)	
CLO II	None [HVAC controls by others; integration with ICS not required]	
Shop Building	None [HVAC and water controls by others; integration with ICS not required]	

The planned controls architecture for two typical conventional facilities control applications is shown in Figure 6.22. With reference to the figure:

- For control of an air handling unit (AHU): A soft IOC (a server-based IOC located in the CLO Central Equipment Room) will handle supervisory control. An application-specific controller (ASC) will handle local control of the AHU. The ASC will be located in an enclosure adjacent to the AHU to minimize cabling. The ASC will be connected to the machine network via an Ethernet cable running to the nearest communication room.

- For control of a deionized water system: A soft IOC will be used for supervisory control. Local control will be implemented using an SNS-standard PLC. Provided that access and the environment are suitable, the PLC will be located in an enclosure close to the equipment to minimize cabling. The PLC will be connected to the machine network via an Ethernet cable running to the nearest communication room.

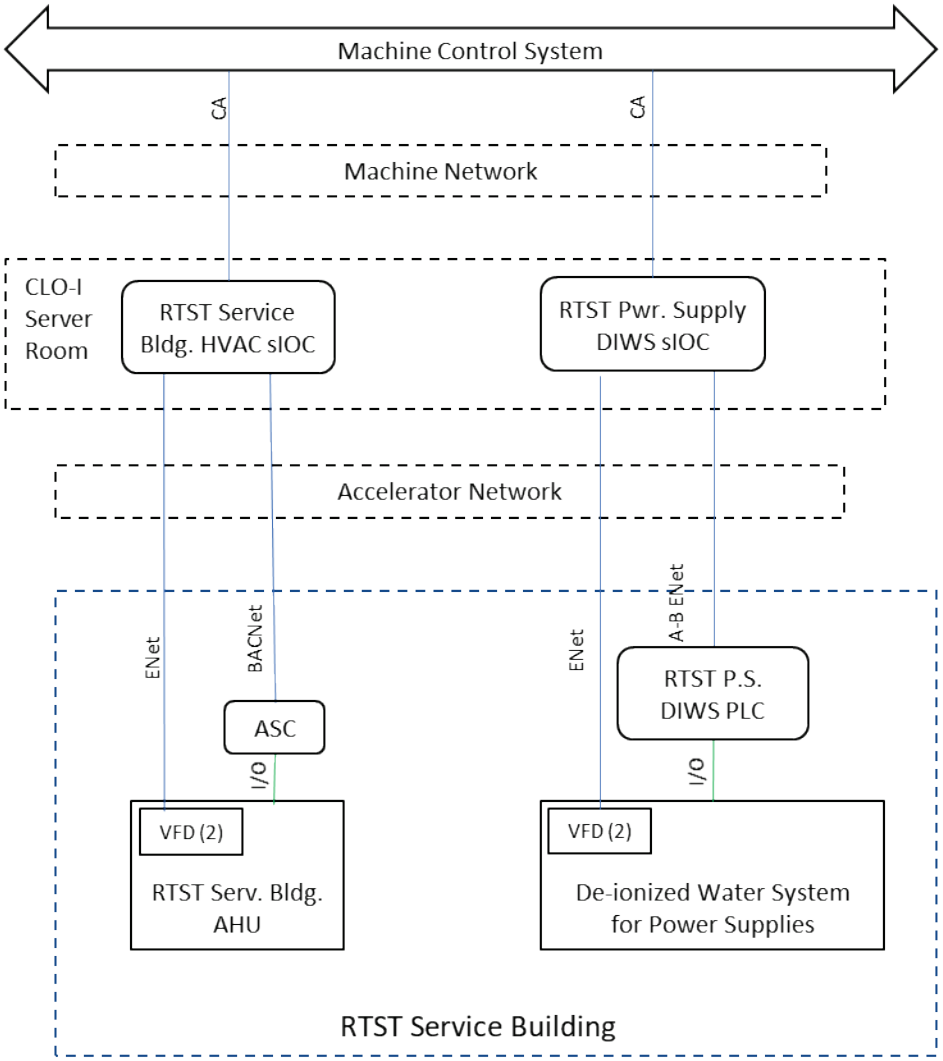

Figure 6.22. Typical conventional facilities control architecture.

6.6 INFORMATION SYSTEMS

The original SNS construction project made extensive use of relational database applications for project management. These included databases for cables, electrical power distribution trees, equipment tracking, magnet calibration, naming standards, and device configuration. The overall success of these tools was uneven, but the experience of the SNS Project and subsequent large-scale accelerator construction projects validated the need for such software tools during construction and in operation.

As an operating facility, SNS continues to use database applications for information management that are both commercial off-the-shelf and developed in-house. These include InforEAM products for asset management and work planning; an electronic logbook; and a suite of tools for users, including proposal submittal, publication tracking, and sample tracking.

The STS Project will leverage this existing experience, along with the experience of similar construction projects, to use information management systems to effectively manage the project. Specific applications are still to be determined.

6.7 REFERENCES

Battle, R. E., B. DeVan, and J. K. Munro Jr. 2006. "SNS Accelerator facility target safety and non-safety control systems," in *NPIC and HMIT 2006: 5th American Nuclear Society International Topical Meeting on Nuclear Plant Instrumentation Control and Human Machine Interface Technology*, Albuquerque, NM, USA, November 12–16, 2006.

CSS (Control System Studio) 2020. Control System Studio website, controlsystemstudio.org. Accessed February 2020.

DeVan, W. R., and E. L. Williams, Jr. 2001. "Plans for the Spallation Neutron Source Integrated Control System Network," in *Proc. 8th Int. Conf. on Accelerator and Large Experimental Physics Control Systems (ICALEPCS'01)*, San Jose, CA, November 2001, paper TUAP055.

EPICS (Experimental Physics and Industrial Control System) 2020. EPICS website, https://epics-controls.org. Accessed February 2020.

Geng, X., X. H. Chen, and K.-U. Kasemir 2013. "First EPICS/CSS based instrument control and acquisition system at ORNL," in *Proc. 14th Int. Conf. on Accelerator and Large Experimental Physics Control Systems (ICALEPCS'13)*, San Francisco, CA, USA, October 2013, paper TUPPC078, pp. 763–765.

Geng, X., S. M. Hartman, and K.-U. Kasemir 2009. "Alarm rationalization: Practical experience rationalizing alarm configuration for an accelerator subsystem," in *Proc. 12th Int. Conf. on Accelerator and Large Experimental Physics Control Systems (ICALEPCS'09)*, Kobe, Japan, October 2009, paper WEP109, pp. 606–608.

Gurd, D. P. 2004. "Accelerator control and global networks—State of the art," in *Proc. 22nd Linear Accelerator Conf. (LINAC'04)*, Lübeck, Germany, August 2004, paper FR201.

Gurd, D. P. 2001. "Management of a large, distributed control system development project," in *Proc. 8th Int. Conf. on Accelerator and Large Experimental Physics Control Systems (ICALEPCS'01)*, San Jose, CA, USA, November 2001, paper TUDI002.

Gurd, D. P., W. R. DeVan, L. Dalesio, L. Hoff, and S. A. Lewis 2003. "First experience with handover and commissioning of the SNS control system," in *Proc. 9th Int. Conf. on Accelerator and Large Experimental Physics Control Systems (ICALEPCS'03)*, Gyeongju, Korea, October 2003, paper MO202.

Hartman, S. M. 2009. "Control system availability for the Spallation Neutron Source," in *Proc. 12th Int. Conf. on Accelerator and Large Experimental Physics Control Systems (ICALEPCS'09)*, Kobe, Japan, October 2009, paper THP010, pp. 691–693.

Hartman, S. M. 2013. "SNS instrument data acquisition and controls," in *Proc. 14th Int. Conf. on Accelerator and Large Experimental Physics Control Systems (ICALEPCS'13)*, San Francisco, CA, USA, October 2013, paper TUPPC076, pp. 755–758.

Hartman, S. M. 2011. "System design towards higher availability for large distributed control systems," in *Proc. 13th Int. Conf. on Accelerator and Large Experimental Physics Control Systems (ICALEPCS'11)*, Grenoble, France, October 2011, paper THBHMUST03, pp. 1209–1211.

HDFGroup. 2006. "What is HDF5," http://www.hdfgroup.org. Accessed February 2020.

HZB (Helmholtz Zentrum Berlin) 2020. "CA Lab (LabVIEW + EPICS)," https://www.helmholtz-berlin.de/zentrum/locations/it/software/exsteuer/calab/index_en.html. Accessed February 2020.

Kasemir, K.-U. 2019. “CS-Studio alarm system based on Kafka,” in *17th Int. Conf. on Accelerator and Large Experimental Physics Control Systems (ICALEPCS’19)*, New York, USA, October 2019, paper WESH2001.

Kasemir, K.-U., X. H. Chen, and E. T. Berryman 2013. “CSS scan system,” in *Proc. 14th Int. Conf. on Accelerator and Large Experimental Physics Control Systems (ICALEPCS’13)*, San Francisco, CA, USA, October 2013, paper FRCOAAB01, pp. 1461–1464.

Kasemir, K.-U., G. S. Guyotte, and M. R. Pearson 2105. “EPICS V4 evaluation for SNS neutron data,” in *Proc. 15th Int. Conf. on Accelerator and Large Experimental Physics Control Systems (ICALEPCS’15)*, Melbourne, Australia, October 2015, pp. 947–949. DOI:10.18429/JACoW-ICALEPCS2015-WEPGF105.

Munro, J. K., J. E. Cleaves, E. L. Williams, D. J. Nypaver, K. U. Kasemir, and R. D. Meyer 2001. “Use of EPICS For high-level control of SNS conventional facilities,” in *Proc. 8th Int. Conf. on Accelerator and Large Experimental Physics Control Systems (ICALEPCS’01)*, San Jose, CA, USA, November 2001, paper TUAP030.

NIAC (NeXus International Advisory Committee) 2020. “About the NeXus Data Format,” https://www.nexusformat.org. Accessed February 2020.

Peterson, K. 2019. “EPICS: Motor Record and Device Driver Support,” https://epics.anl.gov/bcda/synApps/motor/. Accessed February 2020.

PSI (Paul Scherrer Institute) 2020. “What is Stream Device?” http://epics.web.psi.ch/software/streamdevice/. Accessed February 2020.

Rivers, M. 2020. “areaDetector: EPICS Software for Area Detectors,” University of Chicago, cars9.uchicago.edu/software/epics/areaDetector.html. Accessed February 2020.

Rivers, M. 2019. “modbus: Driver Support for Modbus Protocol under EPICS Release 3.0, http://cars9.uchicago.edu/software/epics/modbusDoc.html. Accessed February 2020.

Sibley, C., A. Jones, D. Thompson, and E. Bjorklund 2003. “Implementation and integration of the SNS timing and Machine Protection Systems,” in *Proc. 9th Int. Conf. on Accelerator and Large Experimental Physics Control Systems (ICALEPCS’03)*, Gyeongju, Korea, October 2003, paper MP546.

SNS (Spallation Neutron Source) 2020. SNS Controls EDM, https://controlssoftware.sns.ornl.gov/edm/. Accessed February 2020.

Vodopivec, K., J. E. Breeding, and J. W. Sinclair 2019. “The Linux device driver framework for high-throughput lossless data streaming applications,” in *17th Int. Conf. on Accelerator and Large Experimental Physics Control Systems (ICALEPCS’19)*, New York, USA, October 2019, paper MOPHA156.

Vodopivec, K., and B. Vacaliuc 2017. “High throughput data acquisition with EPICS,” in *Proc. 16th Int. Conf. on Accelerator and Large Experimental Physics Control Systems (ICALEPCS’17)*, Barcelona, Spain, October 2017, pp. 213–217. DOI:10.18429/JACoW-ICALEPCS2017-TUBPA05.

Wang, Q. 2017. “PCASPY Documentation,” Rev. 2e57546c, https://pcaspy.readthedocs.io/. Accessed February 2020.

7. ENVIRONMENT, SAFETY, AND HEALTH AND QUALITY ASSURANCE

DOE Order (O) 420.2C, *Safety of Accelerator Facilities*, dated July 21, 2011, applies to all DOE accelerator facilities or modules thereof while "unambiguously confirming the fundamental and operative distinctions between accelerator facilities and nuclear facilities."

The DOE *Integrated Safety Management Policy* (DOE P 450.4A) commits DOE to conducting work safely and efficiently in a manner that ensures protection of workers, the public, and the environment. This Policy serves as a foundation for the DOE Integrated Safety Management (ISM) Program, consistent with 48 CFR 970.5223-1. The ISM process encompasses a work-planning approach that integrates safety into work planning, establishes a set of agreed-upon standards for performance of work, and provides performance-based measures to determine agreed-upon levels of safety.

At ORNL, UT-Battelle Policy commits to the support of the DOE mission and national priorities and mandates that work will be performed in "an effective manner that is protective of all individuals and the environment."

7.1 ENVIRONMENT

7.1.1 Environmental Management System

At ORNL, environmental excellence is demonstrated through implementation of high-level policies that clearly delineate expectations for continual improvement, pollution prevention, and compliance with regulations and other requirements. Specifically, the UT-Battelle Environmental Policy for ORNL requires "implementing work processes and equipment that abate hazards, operating in a manner that protects and restores the environment, and integrating sustainability (including pollution prevention) into planning and decision-making." Furthermore, environmental principles are to be systematically integrated "into management and work practices at all levels." In accordance with DOE O 436.1, *Departmental Sustainability* (DOE 2011), UT-Battelle has implemented an environmental management system (EMS), modeled after and in conformance with the International Organization for Standardization (ISO) 14001 (ISO 2015), to measure, manage, and control environmental impacts. The EMS encompasses a continuing cycle of planning, implementing, evaluating, and improving processes and actions to achieve environmental goals. The EMS is designed to fully comply with all applicable requirements and to continually improve environmental performance. Through the UT-Battelle Standards-Based Management System (SBMS), the EMS establishes environmental policy and translates environmental laws, applicable DOE orders, and other requirements into laboratory-wide subject area documents (procedures and guidelines).

7.1.2 Integration with the Integrated Safety Management System

The objective of the UT-Battelle Integrated Safety Management System (ISMS) is to systematically integrate environment, safety, and health (ES&H) requirements and controls into all work activities and to ensure protection of the workers, the environment, and the public. The UT-Battelle EMS and the ISMS are integrated to provide a unified strategy for the management of resources, the control and attenuation of risks, and the establishment and achievement of the organization's ES&H goals. Under the ISMS, the term "safety" also encompasses ES&H, including pollution prevention, waste minimization, and resource conservation. Therefore, the guiding principles and core functions in the ISMS apply both to protection of the environment and to safety. Figure 7.1 depicts the relationship between the EMS and the ISMS. The UT-Battelle EMS is consistent with the ISMS and includes all the elements in the ISO 14001:2015 standard.

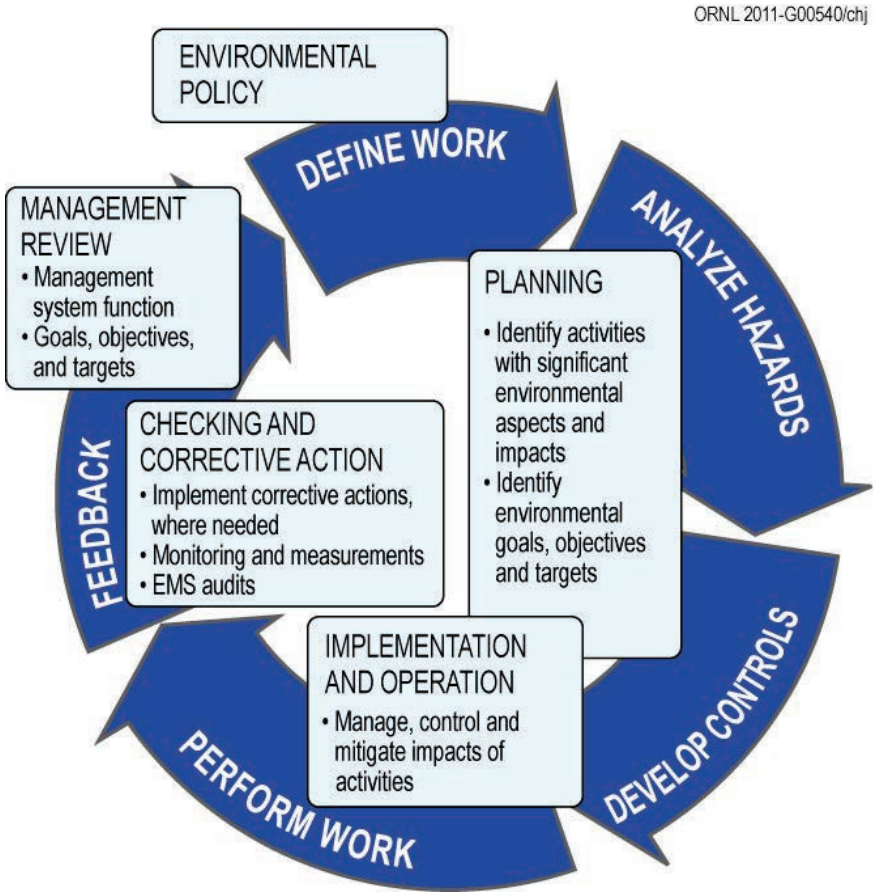

Figure 7.1. The relationship between the UT-Battelle Environmental Management System and the Integrated Safety Management System.

7.1.3 National Environmental Policy Act/National Historic Preservation Act

The National Environmental Policy Act (NEPA) provides a means to evaluate the potential environmental impact of proposed federal activities and to examine alternatives to those actions. The procedures call for a review of each proposed project, activity, or facility to determine the potential for impacts to the environment. Compliance with the National Historic Preservation Act at ORNL is achieved and maintained in conjunction with NEPA compliance. The scope of proposed actions is reviewed in accordance with the Oak Ridge Reservation (ORR) cultural resource management plan (Souza et al. 2001).

The NEPA documentation for construction and operation of SNS shows that approval for the project and/or activity was granted by a record of decision (ROD) issued June 30, 1999 (DOE 1999a). The ROD was based on the analysis contained in the final environmental impact statement (FEIS; DOE 1999).

As described in the FEIS (DOE 1999), the proposed action was to construct and operate SNS, a state-of-the-art, short-pulse spallation neutron source comprising an ion source, a linear accelerator (linac), a proton accumulator ring, a liquid mercury target, and a suite of neutron scattering instruments. Furthermore, the facility would be designed to operate at a proton beam power of 1 MW yet be economically upgradeable to 4 MW. The respective upgrades were identified as follows:

1. Adding a second target station with its own set of instrumentation.

2. Increasing the proton beam power to 2 MW by doubling the ion source output.

3. Increasing the proton beam power to 4 MW by adding a second ion source, modifying the linac, and adding a second proton accumulator ring.

It was recognized that implementation of the upgrades would depend on the need for the upgrades and the availability of future funding. However, the FEIS (DOE 1999) analyzed both the base 1 MW facility and the fully upgraded 4 MW configuration. The 4 MW case is a bounding case beyond the scope of the upgrade proposed here.

Based on analysis found in the FEIS (DOE 1999), DOE decided to proceed with construction and operation of a state-of-the-art SNS facility at the preferred location, ORNL in Oak Ridge, Tennessee; and the ROD for the construction and operation of the SNS was issued in the Federal Register on June 30, 1999 (DOE 1999a). Although construction and operation of the STS itself was covered in the original EIS, a supplement analysis will be prepared to address the proposed clearing and development of an adjacent greenfield area located beyond the bounds of the original project footprint. Furthermore, the supplement analysis will also include a brief comparison of potential impacts identified in the original EIS with actual operational impacts since SNS operation commenced.

7.1.4 Air Quality Program

7.1.4.1 Construction and Operating Permits

The Clean Air Act (CAA), passed in 1970 and subsequently amended in 1977 and 1990, serves as the foundation for the national air pollution control effort. This legislation led to development of comprehensive federal and state regulations to limit air emissions. These comprehensive regulations encompass four major regulatory programs: the national ambient air quality standards, state implementation plans, new source performance standards, and National Emission Standards for Hazardous Air Pollutants (NESHAPs). Radioactive and nonradioactive airborne discharges from DOE Oak Ridge facilities are subject to regulation by the US Environmental Protection Agency (EPA) and the Tennessee Department of Environment and Conservation (TDEC) Division of Air Pollution Control.

The State of Tennessee conveys clean air requirements that are applicable to ORNL. New projects are governed by construction permits until the projects are converted to operating status. The sitewide Title V Major Source Operating Permits include requirements that are generally applicable to large operations such as national laboratories (e.g., asbestos and stratospheric ozone), as well as specific requirements directly applicable to individual air emission sources. Source-specific requirements include Rad-NESHAPs (see Section 5.4.3), requirements applicable to sources of ambient air criteria pollutants, and requirements applicable to sources of other hazardous (nonradiological) air pollutants. On August 2, 2017, the State of Tennessee issued Title V Major Source Operating Permit 571359 to DOE and UT-Battelle operations at ORNL (Minor Modification #3: October 17, 2018). This permit was issued pursuant to the Tennessee Air Quality Act and fulfills requirements of Title V of the Federal CAA (42 USC 7661a-7661e) and the federal regulations promulgated thereunder at 40 CFR Part 70 (*Federal Register*, Vol. 57[140], July 21, 1992, pp. 32295–32312). As currently issued, the permit addresses specifically boilers located at the existing SNS and the central exhaust facility. As conceptual and preliminary designs develop, potential air emission sources associated with the STS project will be identified, and acquisition of construction air permits and/or modifications to the operating permit will be implemented.

Clean Air Act Permitting Requirements for Any New Stationary Emergency Use Generators

Emergency generators are viewed as new stationary engines and are regulated under 40 CFR 60 Subpart IIII for compression ignition engines and Subpart JJJJ for spark ignition engines. Tenn. Comp. R. & Regs. 0400-30-38 and 39 allow for engines to be listed on the facility Title V Operating Permit as insignificant activates provided each engine's potential to emit (PTE) is less than 5 tons per year of criteria pollutants and/or 1,000 pounds of hazardous air pollutants (HAPs). However, as an insignificant activity, in this case generally applicable requirements of Subparts IIII and JJJJ still apply (e.g., manufacturing specifications, fueling requirements). If the specific engine has the PTE greater than 5 tons of criteria pollutants and/or 1,000 pounds of HAPs, construction permitting will be required before purchase and installation.

7.1.5 Radioactive Emissions to the Atmosphere

The SNS STS will release short-lived, accelerator-produced radionuclides into the atmosphere. STS air emissions will be permitted by TDEC, as delegated by EPA.

Radioactive releases from DOE facilities are regulated under 40 CFR 61, *National Emission Standards for Hazardous Air Pollutants,* Subpart H, which is also incorporated in Tennessee Air Pollution Control Regulation 1200-3-11-.08, "Emission Standards for Emissions of Radionuclides Other than Radon from Department of Energy Facilities" (TDEC 2018). Subpart H §61.92 states that "Emissions of radionuclides to the ambient air from Department of Energy facilities shall not exceed those amounts that would cause any member of the public to receive in any year an effective dose equivalent of 10 mrem/year." Subpart H §61.93(a) requires the following: "To determine compliance with the standard, radionuclide emissions shall be determined and effective dose equivalent values to members of the public calculated using EPA-approved sampling procedures, computer models CAP–88 [Clean Air Act Assessment Package-1988]. . . ."

It is assumed that STS radioactive emissions will be comparable with those currently discharged by SNS (Alvarez, Mobley, and Trotter 2008). However, a specific source term will be developed, and a CAP-88 determination will be performed for the modeled STS releases in accordance with Subpart H §61.93(c)(4)(f):

> To determine whether a release point is subject to the emission measurement requirements of paragraph (b) or (c) of this section, it is necessary to evaluate the potential for radionuclide emissions for that release point. In evaluating the potential for a release point to discharge radionuclides into the air for the purposes of this section, the estimated radionuclide release rates shall be based on the discharge of the effluent stream that would result if all pollution control equipment did not exist but facility operations were otherwise normal.

Such releases without pollution control equipment are referred to as "unabated releases," while those with pollution control equipment are called "abated releases." Based on preliminary calculations and process knowledge, unabated releases from the STS have the potential to exceed an effective dose equivalent of 10 mrem/year [5]; therefore, Subpart H §61.93(e) requires the following:

> Radionuclide emission measurements in conformance with the requirements of paragraph (b) or (c) of this section shall be made at all release points that have a potential to discharge radionuclides into the air in quantities that could cause an effective dose equivalent in excess of 1% of the standard. All radionuclides that could contribute greater than 10% of the potential effective dose equivalent for a release point shall be measured. With prior EPA approval, DOE may determine these emissions through alternative

> procedures. For other release points that have a potential to release radionuclides into the air, periodic confirmatory measurements shall be made to verify the low emissions.

The STS emission monitoring requirement will be met under Subpart H §61.93(c).

(1) Effluent flow rate measurements shall be made using the following methods:

(i) ANSI/HPS N13.1, *Sampling and Monitoring Releases of Airborne Radioactive Substances from the Stacks and Ducts of Nuclear Facilities* (HPS 2011), shall be used to determine velocity and volumetric flow rates for stacks and large vents.

(ii) The frequency of the flow rate measurements shall depend on variability of the effluent flow rate. For variable flow rates, continuous or frequent flow rate measurements shall be made. For relatively constant flow rates only periodic measurements are necessary.

(2) Radionuclides shall be directly monitored using the following methods:

(i) ANSI/HPS N13.1 (HPS 2011) shall be used to select monitoring or sampling sites.

(ii) The effluent stream shall be directly monitored continuously with an in-line detector … following the guidance presented in ANSI/HPS N13.1 (HPS 2011).

(iii) Radionuclides shall be collected and measured using procedures based on principles of measurement described in Appendix B, Method 114, of this part [40 CFR 61].

STS emission monitoring will be conducted by in-line, gross gamma counting as prescribed in Appendix B, Method 114, Method G-4, “Gross Gamma Counting” [40 CFR 61].

> *Principle*. The sample is counted with a gamma detector, usually a thallium-activated sodium iodine crystal. The detector is coupled to a photomultiplier tube and gamma rays above a specific threshold energy level are counted.
>
> *Applicability*. Gross gamma measurements may be used to measure emissions of specific radionuclides only when it is known that the sample contains a single radionuclide or the identity and the isotopic ratio of the radionuclides in the effluent stream are well known. When gross gamma measurements are used to determine emissions of specific radionuclides, periodic measurements using methods G-1 or G-2 should be made to demonstrate that the gross gamma measurements provide reliable emissions data. This method may be applied to analysis of gaseous radionuclides directly in an effluent stream by placing the detector directly in or adjacent to the effluent stream by placing the detector directly in or adjacent to the effluent stream ….

The STS will demonstrate that gross gamma measurements provide reliable radionuclide-specific emissions data using Method 114, Method G-1, “High-Resolution Gamma Spectrometry.”

> *Principle*. The sample is counted with a high resolution gamma detector, usually either a Ge (Li) or a high purity Ge detector, connected to a multichannel analyzer or computer. The gamma emitting radionuclides in the sample are measured from the gamma count rates in the energy regions characteristic of the individual radionuclide. Corrections are made for counts contributed by other radionuclides to the spectral regions of the radionuclides of interest.

> *Applicability*. This method is applicable to the measurement of any gamma-emitting radionuclide with gamma energies greater than 20 keV. It can be applied to complex mixtures of radionuclides. … The method can also be applied to the analysis of gaseous gamma-emitting radionuclides directly in an effluent stream.

The STS radioactive release requirements under NESHAPs will be met using an in-line detector (40 CFR 61). The STS releases will be short-lived, gaseous or gaseous-like radionuclides that would be best monitored by an in-line detector. The source term will be developed and modeled based on known accelerator conditions.

Water Quality Program

The purpose of the Clean Water Act (CWA) is to restore, maintain, and protect the integrity of the nation's waters, and the Act serves as a foundation for comprehensive federal and state programs developed to protect the nation's waters from pollutants. Of specific note, EPA has established limits on specific pollutants allowed to be discharged to US waters by municipal sewage treatment plants (STPs) and industrial facilities. EPA has implemented the National Pollutant Discharge Elimination System (NPDES) permitting program to regulate compliance with these pollutant limitations. EPA has delegated authority for implementation and enforcement of the NPDES program to the State of Tennessee.

Recently, under authority of the Tennessee Water Quality Control Act of 1977 (Tennessee Code Annotated [TCA] 69-3-101 et seq.) and the delegation of authority from EPA under the Federal Water Pollution Control Act, as amended by the CWA of 1977 (33 USC 1251, et seq.), the State of Tennessee issued (renewed) the NPDES permit, TN 0002941, on May 1, 2019, with an effective date of June 1, 2019. The permit includes requirements for discharging wastewaters from the two ORNL on-site wastewater treatment facilities and from more than 150 category outfalls (outfalls with nonprocess wastewaters such as cooling water, condensate, groundwater, and stormwater) and for the development and implementation of a water quality protection plan. As conceptual and preliminary designs develop, potential outfalls associated with the STS project will be identified, and acquisition of NPDES permits and/or modifications to the current permit will be implemented.

Of special note, since the STS project will involve clearing, grading, or excavation in an area of disturbance of one or more acres, the project will need to acquire coverage under the State General NPDES Permit for Stormwater Discharges from Construction Activities.

Safe Drinking Water Act

In addition to regulation of surface waters, EPA has also delegated authority to the state for administering compliance with the Federal Safe Drinking Water Act. The TDEC Division of Water Resources is charged with general supervision over construction and operation of public water works systems and is authorized to adopt and enforce rules and regulations governing the location, design, construction, continuous operation, and maintenance of these facilities. It also conducts an enforcement program that requires water suppliers to meet requirements of the Safe Drinking Water Act with respect to water quality monitoring and information reporting—specifically, TCA §§ 68-221-701 et seq.—and to set out the procedures to be followed by the department in carrying out the department's primary enforcement responsibility under the Federal Safe Drinking Water Act. The TDEC Division of Water Resources regulates ORNL's water distribution system, which has been designated a "nontransient, noncommunity" water system by the TDEC Division of Water Supply. TDEC's Water Supply rules, Chapter 0400-45-01, "Public Water Systems" (TDEC 2019), set limits for biological contaminants and for chemical activities and chemical contaminants.

The City of Oak Ridge supplies potable water to the ORNL water distribution system and meets all regulatory requirements for drinking water. The water treatment plant, located on ORR north of the Y-12 Complex, is owned and operated by the City of Oak Ridge.

The Division of Water Resources is charged with general supervision with respect to construction and operation of public water works systems, and is authorized to adopt and enforce rules and regulations governing the location, design, construction, continuous operation, and maintenance of these facilities. Furthermore, it conducts an enforcement program that requires water suppliers to meet requirements of the Safe Drinking Water Act with respect to water quality monitoring and information reporting.

Radioactive Contamination of Groundwater

In the FEIS (DOE 1999), it was recognized that operation of SNS might result in neutron activation of soils in the shielding berm surrounding the linac and accumulator ring. The resulting contamination of berm soils by radionuclides would create the potential for infiltrating water to transport radionuclides from the berm to saturated groundwater zones nearby. The stakeholders expressed concern about this potential. In response to this concern, SNS implemented engineering controls and a site-specific groundwater monitoring program (Bonine, Ketelle, and Trotter 2017).

Engineering Controls

SNS implemented engineering controls focusing on both facility design and facility construction features to minimize the mobility of activation products in the site hydrologic system. Specifically, the shielding berm (Figure 7.2) was designed and constructed to isolate radionuclide contamination generated by the SNS particle beam and to provide radiation protection for outside areas around the beam and ring tunnel. The activation of berm soils was minimized by beam loss control and passive shielding. Furthermore, the berm was constructed of compacted native soils and was engineered to isolate activation products by minimizing the amount of water infiltrating the berm. The construction of the berm using compacted indigenous clay rendered it relatively impermeable to water (the Darcy permeability of the compacted clay was much less than 1e-05 cm/s). In addition, a flexible membrane liner coupled with a drainage net was included in the design to provide an additional degree of control against water penetration.

These same engineering controls (or equivalent ones) will be incorporated into the design and operation of the STS.

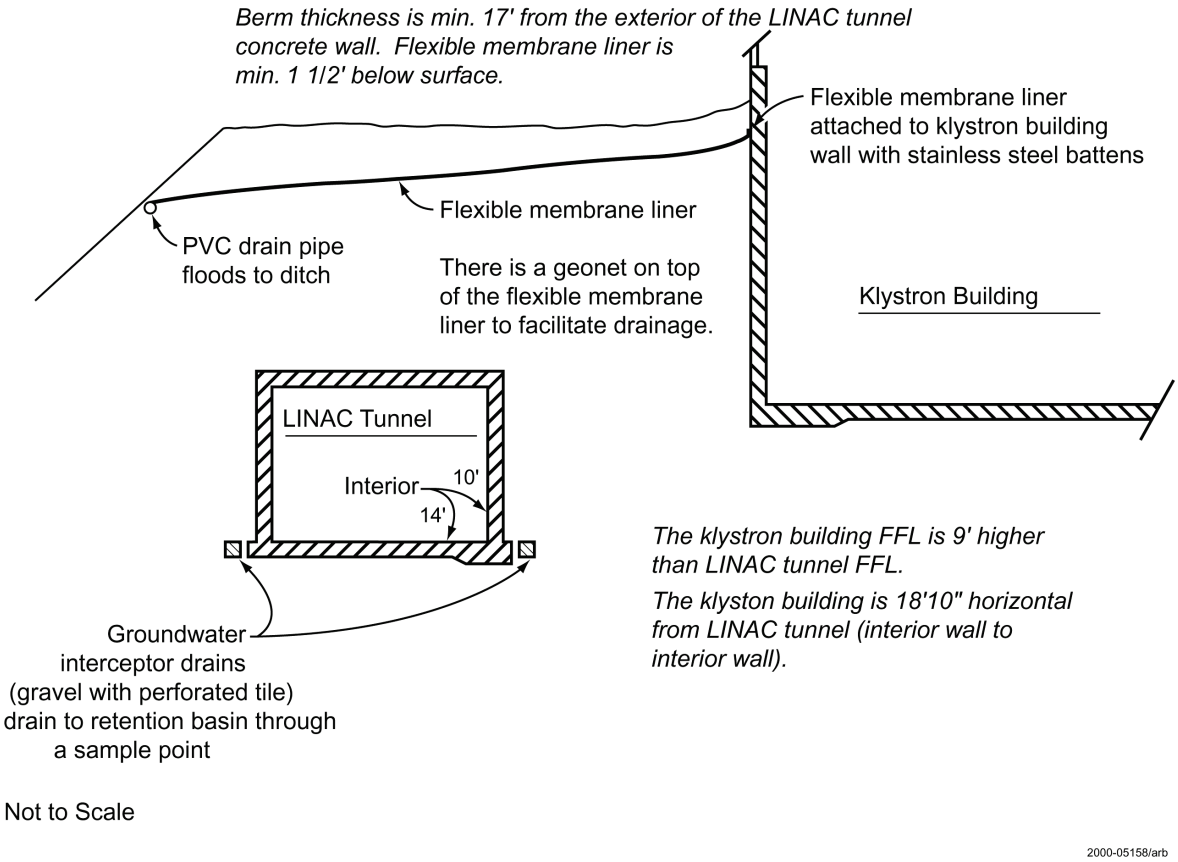

Figure 7.2. Typical berm cross section.

Groundwater Monitoring Program

In addition to the use of engineering controls, a groundwater monitoring program was implemented to ensure that any releases of radiological contaminants from the facility would be detected, tracked, and evaluated to identify any unacceptable impacts to groundwater or surface water.

The SNS site is located atop Chestnut Ridge, northeast of the main ORNL facilities. The site slopes to the north and south, and small stream valleys, populated by springs and seeps, lie on the ridge flanks. Surface water drainage from the site flows into Bear Creek to the north and White Oak Creek to the south.

The site is a hydrologic recharge area underlain by geologic formations that form karst geologic features. Groundwater flow directions at the site are based on the generally observed tendency for groundwater to flow parallel to geologic strike (parallel to the orientation of the rock beds) and via karst conduits that break out at the surface in springs and seeps located downgrade of the SNS site. A sizable fraction of infiltrating precipitation (groundwater recharge) flows to springs and seeps via the karst conduits.

The ability to accurately model the fate and transport of neutron activation products generated by beam interactions with the engineered soil berm is complicated by multiple uncertainties resulting from a variety of factors, including hydraulic conductivity differences in earth materials found at depth, distribution of water-bearing zones, fate and transport characteristics of neutron activation products, diffusion and advection, and presence of karst geomorphic features on the site. These uncertainties led to the initiation of the groundwater surveillance monitoring program at the SNS site.

A total of seven seeps/springs and surface water sampling points (seeps/springs S-1, S-2, S-3, S-4, S-5, and SP-1 and surface-water point SW-1) are routinely monitored as analogues to, and in lieu of, groundwater monitoring wells. Locations were chosen based on hydrogeological factors and proximity to the beamline. Figure 7.3 shows the locations of the specific monitoring points sampled as part of the monitoring program.

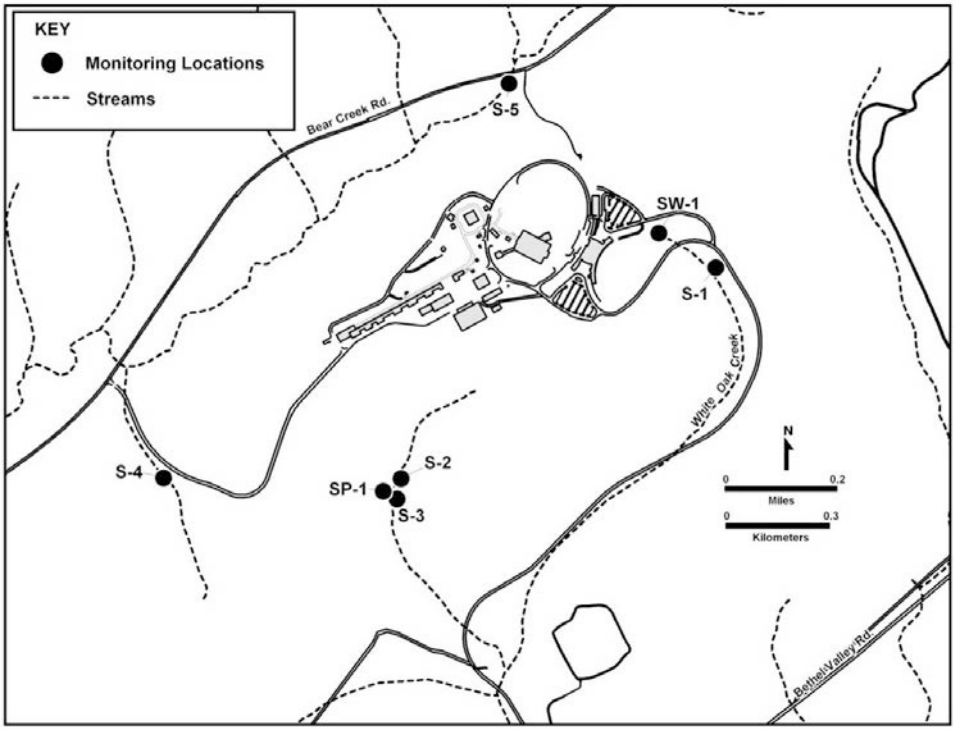

Figure 7.3. Groundwater monitoring locations at the SNS site.

The SNS groundwater monitoring program was implemented in 2004. From 2004–2006, a 2-year baseline program was conducted before commencement of accelerator operations. Subsequently, with the commencement of accelerator operations in April 2006, the baseline groundwater monitoring program was completed and an operational groundwater monitoring program commenced. As of 2014, there have been no adverse impacts to groundwater quality as a result of accelerator operations at SNS. Furthermore, the current monitoring program is robust and more than adequate to support construction and operation of the STS.

7.2 WASTE MANAGEMENT

The STS will generate numerous types of waste from normal operations and maintenance activities. Similar to the waste management plan prepared for the SNS Project in 2006 (Trotter 2006), an STS-specific waste management plan will be prepared to address the entire life cycle for all waste streams before generation. Furthermore, based on process knowledge, all waste streams envisioned to be generated by the STS have identified paths to disposal.

7.2.1 Disposition Mapping

To address the entire life cycle of STS operational and maintenance waste streams, the *STS Waste Management Plan* shall incorporate the use of disposition mapping (DOE 2000). “Disposition” is an

inclusive term that refers to “those activities that follow generation of a waste and which constitute completion of the life cycle of management of the waste, including, but not limited to, stabilization, deactivation, disposal, decommissioning, dismantlement, and/or reuse” (adapted from DOE O 430.1B) (DOE 1998).

DOE headquarters (DOE HQ) has addressed planning for low-level waste (LLW) and mixed LLW (MLLW). The ROD for DOE’s waste management program for LLW and MLLW was issued February 18, 2000 (DOE 2000). The decisions contained therein serve as the programmatic bases for the current master LLW and MLLW disposition maps maintained at DOE HQ. There were four decisions addressing LLW treatment and disposal and MLLW treatment and disposal.

1. DOE decided that each site would perform minimal treatment on its LLW, although each site could perform additional treatment as would be useful to decrease overall costs. However, it was noted that this decision did not preclude DOE’s use of commercial treatment facilities, consistent with DOE regulations and policies.

2. DOE decided to establish regional LLW disposal at two DOE sites: the Hanford Site and the Nevada Test Site (NTS). In addition to disposing of their own LLW, the Hanford Site and NTS will receive and dispose of LLW generated and shipped (by either truck or rail) by other sites which meets the waste acceptance criteria. Although the decision acknowledged that DOE will continue, to the extent practicable, on-site disposal at ORR, current disposition maps show the majority of ORR-generated LLW going to NTS.

3. DOE decided to conduct regional MLLW treatment at numerous sites, inclusive of ORR, as would be consistent with the current site treatment plans. This decision does not preclude DOE’s use of commercial treatment facilities, consistent with DOE regulations and policies.

4. DOE decided to establish regional MLLW disposal operations at two DOE sites: the Hanford site and NTS. In addition to managing their own MLLW, the Hanford site and NTS will receive and dispose of MLLW generated and shipped (by truck or rail) by other sites, consistent with permit conditions and other applicable requirements. Once again, this decision does not preclude DOE’s use of commercial disposal facilities, consistent with current DOE regulations and policies.

Hazardous waste planning is also addressed by DOE HQ. However, the treatment and/or disposal of hazardous waste is well understood, and numerous commercial treatment and/or disposal options are available. Therefore, in the ROD for DOE’s waste management program for non-wastewater hazardous waste, issued August 5, 1998 (DOE 1998), DOE states its decision to continue the use of offsite facilities for the treatment of major portions of the non-wastewater hazardous waste generated at DOE sites. Concurrently, DOE recognized that ORR may treat some of its own non-wastewater hazardous waste on-site, where capacity is available in existing facilities and where treatment is economically favorable. This decision serves as the programmatic basis for the current master hazardous waste disposition map maintained at DOE HQ.

Sanitary/industrial waste is typically not included in DOE HQ planning initiatives because treatment and/or disposal of sanitary/industrial waste is well understood and occurs at all DOE facilities. Typically, the treatment and/or disposal of sanitary/industrial waste is regulated by state programs administered by the state of the respective DOE facility. Sanitary/industrial waste generated on ORR consists of recyclable materials such as metals and nonrecyclable materials such as glass, paper, and wood. Nonrecyclable materials are disposed of in state-permitted land disposal units (sanitary/industrial landfills).

Regardless of waste categorization, the STS will aggressively implement pollution prevention principles to prevent and/or reduce the amount of waste generated. As delineated in the Pollution Prevention Act of 1990, the STS will apply the following four principles with respect to all operations:

1. Pollution should be prevented and reduced at the source whenever feasible.

2. Pollution that cannot be prevented should be recycled in an environmentally safe manner whenever feasible.

3. Pollution that cannot be prevented or recycled should be treated in an environmentally safe manner whenever feasible.

4. Disposal or other release to the environment should be used only as a last resort and should be conducted in an environmentally safe manner.

Furthermore, the STS embraces the ORNL Pollution Prevention Policy, whereby

> we are committed to providing a safe and healthful working environment for all staff, guest scientists and engineers, and visitors; protecting the general public and the environment from unacceptable ES&H risks; operating in a manner that protects and restores the environment; and integrating pollution prevention into planning and decision-making.

Therefore, the STS will follow ORNL pollution prevention guidelines.

7.2.2 Radioactive Low-Level Waste

Low-level radioactive waste is radioactive waste that is not high-level radioactive waste, spent nuclear fuel, transuranic waste, by-product material (as defined in Section 11[e]2 of the Atomic Energy Act of 1954 [42 USC 2011 et seq.]), or naturally occurring radioactive material (adapted from the Nuclear Waste Policy Act of 1982, as amended). Furthermore, "radioactive waste produced as a result of operations of DOE accelerators is low-level waste and shall be managed in accordance with DOE O 435.1, *Radioactive Waste Management*, and [DOE M 435.1-1], and all applicable Federal or State requirements" (DOE M 435.1-1, p. IV-1). Typical examples of STS waste streams in this category include dry active waste (e.g., air filters, plastic cables, hoses and piping, floor sweepings, mops, wipes), radioactive scrap metal (e.g., metal filters, motors, pumps, and piping), resins and trapping materials (i.e., filters and ion-exchange resins), remotely handled miscellaneous solids (e.g., dry active waste, irradiated hardware, radioactive scrap metal, and resins/trapping material), wastewaters (condensate and cooling waters), and organic liquids (oils) generated during STS maintenance and operations.

At present, dry active waste and radioactive scrap metal generated by STS will be transported directly to commercial facilities and/or the Nevada National Security Site (NNSS) for ultimate disposition. Radioactive scrap metal may undergo recycling and reuse when feasible. Resins/trapping material and remotely handled LLW may be temporarily stored for decay and/or transported directly to commercial facilities and/or NNSS for storage for decay and/or disposal. STS process wastewaters will undergo on-site treatment at either the ORNL Wastewater Treatment Complex or the LLW Evaporator Facility. LLW organic liquids will be managed as MLLW.

The STS LLW management approach is consistent with the February 18, 2000, DOE ROD for management of LLW and MLLW (DOE 2000) and agrees with current waste disposition practices at ORNL.

7.2.3 Mixed Low-Level Waste

MLLW comprises both hazardous and low-level radioactive waste. It is managed according to requirements established under the Resource Conservation and Recovery Act (RCRA) for hazardous waste and the Atomic Energy Act of 1954 for its radioactive components. The hazardous component of MLLW is subject to either EPA or state hazardous waste regulations promulgated under RCRA. The STS will not generate any hazardous or low-level radioactive waste for which the hazardous component is regulated under the Toxic Substances Control Act (TSCA).

STS operations and maintenance will typically generate four MLLW waste streams (1) miscellaneous solids, (2) organic liquids, (3) remotely handled miscellaneous solids, and (4) remotely handled organic liquids. At present, both miscellaneous solids and organic liquids will be transported to commercial facilities and/or NNSS for treatment and/or disposal. At present, NNSS has a mixed waste disposal unit located within the Radioactive Waste Management Complex in Area 5 of the NTS. In addition, there are commercial facilities that can support treatment and/or disposal of MLLW.

The STS MLLW management approach is consistent with the February 18, 2000, DOE ROD for management of LLW and MLLW (DOE 2000) and agrees with current waste disposition practices at ORNL.

7.2.4 Hazardous Waste

Hazardous waste comprises nonradioactive waste exhibiting the characteristics of ignitability, corrosivity, reactivity, or toxicity, as defined by the EPA's regulations implementing RCRA, or waste that the EPA has listed under RCRA as hazardous waste. In addition, DOE manages some state-regulated hazardous wastes and hazardous wastes regulated under TSCA as hazardous wastes. STS maintenance and operations should not generate TSCA waste; therefore, the management of TSCA hazardous waste is not addressed in this plan. Conversely, STS maintenance and operations will generate RCRA hazardous waste. Typical examples of waste streams in this category include miscellaneous solids (e.g., lamps and wipes) and miscellaneous liquids (e.g., oils, plating solutions, and solvents). STS hazardous waste disposition will focus on use of commercial treatment and/or disposal.

The commercial treatment and/or disposal of hazardous waste is consistent with DOE's August 5, 1998, ROD on treatment of non-wastewater hazardous waste, which specified continued use of off-site facilities for treatment of major portions of non-wastewater hazardous waste generated at DOE sites (DOE 1998). However, DOE does acknowledge that ORR may treat some of its own non-wastewater hazardous waste on-site where capacity is available in existing facilities and where such treatment is economically favorable. Thus, the STS hazardous waste management approach is consistent with the applicable DOE ROD and current waste disposition practices at ORNL.

7.2.5 Sanitary/Industrial Waste

Sanitary/industrial waste comprises both liquid and solid wastes. Liquid wastes typically consist of industrial and/or sanitary wastewaters that are routed to the ORNL sanitary sewer system. All such wastewaters comply with the respective waste acceptance criteria for the STP. The STS cooling tower waters will be discharged to an on-site sediment/retention pond, which discharges to the headwaters of White Oak Creek. All liquid discharges, both those routed to the STP and those routed to the on-site sediment/retention pond, are permitted under existing NPDES permits.

The solid wastes are nonhazardous, nonradioactive solid wastes from areas or systems free of potential activation or surface contamination. Typical examples of waste streams in this category include dry solids

(e.g., air supply filters, plastic cables, hoses and piping, floor sweepings), resins and trapping materials (ion-exchange resins), and nonrecyclable scrap metal (e.g., aerosol cans) generated during STS maintenance and operations. In addition to potentially nonrecyclable scrap metal, a significant quantity of recyclable scrap metal will result from maintenance and operations.

At present, the State of Tennessee regulates a subcategorization of sanitary/industrial waste known as "special wastes." Special wastes include sludges, bulky wastes, pesticide wastes, medical wastes, industrial wastes, liquid wastes, exempted hazardous wastes, friable asbestos wastes, combustion wastes, and other solid wastes that are difficult or dangerous to manage. Presently, approved special waste streams that could be disposed of in the reservation landfill include empty hazardous material containers, empty aerosol cans, fiberglass, glass, and empty pesticide containers. Special waste streams requiring evaluation and approval include ion-exchange resins and filters from the Central Utilities Building's de-ionized water supply, filters from the tunnel confinement or purge ventilation exhaust system, filters and ion-exchange resins from the target cooling loop deionized water supplies, and used oil filters from nonactivated systems. Miscellaneous maintenance materials that are not contaminated with oils or solvents from the front-end system, warm linac, or klystron gallery are also in this category. Process knowledge and/or sampling and analysis may be used for categorizing and characterizing solid waste.

7.3 SAFETY AND HEALTH

The safety of all personnel is recognized as a primary concern of all project participants at ORNL. Unsafe conditions and unsafe behavior can result in injuries and deaths as well as impact schedules, cause financial losses, and damage professional reputations. Because of this, it is our goal that all project participants plan, manage, and execute their respective operations with the ultimate goal of conducting their operations injury-free on a daily basis.

The Worker Safety and Health program description discusses ORNL's approach to the development, management, and implementation of the worker safety and health program at ORNL. This program description documents the ORNL processes for compliance with worker safety and health regulatory requirements, including 10 CFR 851, *Worker Safety and Health Program*, and provides cross-references to implementing systems, programs, and subject areas. It describes how ORNL integrates worker safety and health requirements with other related worker protection activities and the ORNL ISMS program description. The program description illustrates the ORNL framework for effective worker protection and the integration of safety- and health-related functional areas including construction safety, fire protection, explosives safety, pressure safety, firearms safety, industrial hygiene, biological safety, occupational medicine, motor vehicle safety, and electrical safety.

7.3.1 Construction Safety

All construction activities on Chestnut Ridge in support of the STS shall comply with the most recent version of the *Oak Ridge National Laboratory/Chestnut Ridge Facilities Project Safety, and Health Plan* (ORNL 2019). The safety of all personnel is recognized as a primary concern to all project participants at ORNL. Unsafe conditions and unsafe behavior can result in injuries and deaths, as well as impact schedules, cause financial losses, and damage professional reputations. Because of this, the goal is that all project participants plan, manage, and execute their respective operations with the ultimate goal of conducting their operations injury-free on a daily basis.

It is the responsibility of the respective contractor to adhere to the requirements of the *ES&H Plan* (ORNL 2019). Each contractor shall incorporate safety into the planning of each task, ensure the safety of its personnel, provide all safety devices necessary for its employees, establish a safe and drug-free work environment, and confirm that its equipment meets applicable safety standards. Each contractor is

responsible for any actions of its personnel that could endanger other participants or otherwise expose them to potential hazards on the project site.

The ISMS shall be used to achieve these goals. The system is a practical approach to the prevention of accidents with an emphasis on line-management responsibility for safety. A central premise is that work planning starts with a focus on the nature of the job to be performed and assessment of the hazards involved in each step. Through the use of self-assessment and feedback from the line organizations, continuous improvement in each contractor's safety process is expected. Project participants are required to supervise and direct activities using their best management skills and technical expertise. Each contractor will be solely responsible for all work means, methods, techniques, sequences, and procedures. This includes all safety precautions and programs in connection with the work, as well as coordination of all portions of the work. Each lower-tier subcontractor is likewise required to be responsible for all safety precautions and programs in connection with the work under the subcontractor's contractual agreement.

Furthermore, contractors will be selected based on past documented performance indicators. Contractors not demonstrating exceptional past performance in safety will not be invited to participate in STS-sponsored work. A copy of the most current *ES&H Plan* (ORNL 2019) will be provided to all contractors and subcontractors.

7.4 FACILITY SAFETY

The STS will have a safety evaluation in accordance with DOE G 420.2-1A, *Accelerator Facility Safety Implementation Guide for DOE 420.2B, Safety of Accelerator Facilities.* As noted in the guide, "Accelerator projects that go through formal project management reviews as required by DOE O 413.3B, *Program and Project Management for the Acquisition of Capital Assets*, normally submit an HA [hazard analysis] as part of the critical decision (CD) process." In accordance with this method, a preliminary hazard analysis report was prepared in parallel with development of the conceptual design (McManamy et al. 2019). A hazard analysis report and a final safety assessment document will be developed in parallel with development of preliminary and final designs for the project. As was done for the FTS, a systematic evaluation will be performed using safety experts and the design teams to identify hazards, credible impacting events, initiators of events, assumptions used in estimating impacts, consequences of events, and the controls required to reduce risks. This will be done for the accelerator upgrades, operation of the FTS at up to 2 MW, and operation of the STS with new instruments at up to 700 kW. One of the principal differences between the FTS and the STS is the proposed use of a compact tungsten target. Such a target has the decay heat concentrated in a small volume that can reach elevated temperatures and has a potential release mechanism by the vaporization of the tungsten in steam. A preliminary evaluation of the radiological consequences of releases for the conceptual tungsten target will be prepared.

Furthermore, the Accelerator Readiness Review (ARR) program delineates a structured approach for ensuring that commissioning and/or routine operations are conducted safely. The program reflects requirements of DOE O 420.2C, *Safety of Accelerator Facilities*, July 2011. According to the order, an accelerator safety program must include the following elements: an approved accelerator safety envelope; a safety assessment document; clearly defined roles and responsibilities for accelerator activities, including those for training and procedures; an unreviewed safety issue process; an ARR program; and a current listing/inventory of accelerators under this order (inclusive of exemptions or equivalencies under the order). As the STS moves forward, the ARR program will be fully implemented.

7.4.1 Natural Phenomena Hazards

DOE Standard 1020-2012, *Natural Phenomena Hazards Analysis and Design Criteria for DOE Facilities* August 2012, provides criteria and guidance for the analysis and design of facility structures, systems, and

components (SSCs) that are necessary to implement the requirements of DOE O 420.1C, *Facility Safety*, December 2012, and to ensure that the SSCs will be able to effectively perform their intended safety functions under the effects of natural phenomena hazards (NPHs). This standard also provides criteria and guidance for the use of industry building codes and voluntary consensus standards in the NPH analysis and design of SSCs in DOE facilities. In particular, it provides criteria and guidance for the following.

Establishing the performance requirements for SSCs in terms of parameters that define failure of their safety functions (e.g., design basis flood water level relative to the location of an SSC that is vulnerable to inundation, the state of SSC deformation under various NPH loads, and limit states under dynamic loads) and grading the SSCs into more than one NPH design category based on the consequences of SSC failure when subjected to NPH events:

- Calculating NPH demands on SSCs resulting from NPH events in terms of parameters that define failure of their safety functions

- Designing (or, for existing facilities, design evaluation) SSCs to ensure their ability to maintain required functionality when subjected to demands of NPH events

This standard will be used for the analysis and design of the STS. At present, the assumptions listed in Table 7.1 are used here to categorize the current accelerator/target facilities.

Table 7.1. Assumed seismic design categories used for new facilities associated with the STS.

Building	Risk	Seismic design category (SDC)	Limit state	ASCE 7–10 risk category
Lab/office/maintenance/experiment support facility	PC-1	SDC-1	A (?)	II
Central Utility Building (including cooling towers)	PC-1	SDC-1	A (?)	II
R2T2 support building	PC-1	SDC-1	A (?)	II
Modulator support	PC-1	SDC-1	B (?)	II
Central Exhaust Facility	PC-1	SDC-1	B (?)	II
R2T2	PC-2	SDC-2	C (?)	IV
STS (e.g., monolith, hot cell)	PC-3	SDC-3	D	NA
STS Instrument Hall	PC-2	SDC-2	C (?)	IV
Satellite and 90M instrument buildings (including tunnels)	PC-2	SDC-2	C (?)	IV

7.5 RADIATION SAFETY

The STS Project places safety of the workers, the public and the environment above all other considerations. The presence of direct radiation resulting from beam operations and residual radiation resulting from activated materials are two of the most important nonindustrial safety hazards at the SNS STS site. A major consideration for the design, construction, and operation of this facility is to reduce radiation exposures to the workers, the public, and the environment to levels as low as reasonably achievable (ALARA). In compliance with 10 CFR 835.1001 and 1002, the STS facility design objective is to limit prompt radiation in continuously occupied areas to less than 0.25 mrem/h and as far below that level as is reasonably achievable. Iterations of extensive modeling calculations based on conservative beam-loss predictions are used to optimize shielding. The adequacy of installed shielding and the

magnitude and characteristics of radiation produced by routine operations are assessed to the extent practical during low-power operations. Fault studies are conducted as part of commissioning. Areas that are not occupied full-time and that have dose rates above the nominal design objective may have access restricted at an appropriate level. A high-integrity automatic protective system, the Personnel Protection System (PPS), excludes workers from areas with dangerous radiation levels in accordance with DOE O 420.2C. During normal operations, real-time radiation monitors and ongoing periodic radiation surveys ensure that radiation levels in accessible areas are well characterized and within expected ranges, and they provide verification that access is controlled in accordance with 10 CFR 835. Active real-time radiation detectors with beam shut-off capability through the PPS are placed in potentially occupied areas where credible beam-spill accidents could produce unacceptable radiation levels.

The majority of worker dose is expected to result from exposure to activated materials. Materials included in designs are chosen to minimize activation and the generation of hazardous/mixed waste. The accelerator and associated systems are designed and will be operated to minimize activation and worker exposure to activated materials. Localized and general area shielding will be employed as necessary to reduce the dose received from activated equipment and items. Personnel exposure to liquid and gaseous activated materials (including cooling water, dust, air, and mercury) will be minimized through appropriate combinations of confinement, differential pressure, holding for decay, flushing, local shielding, and protective equipment. Personnel who will potentially be exposed to radiation will wear appropriate dosimetry, including extremity and neutron dosimeters as appropriate. Work control documents, including radiological work permits (RWPs), will be used to designate appropriate controls for workers who might be exposed to hazards or hazardous conditions. Some activated structures and materials being removed from beam-accessible areas or awaiting repair will be stored for decay, or access to the area will be appropriately restricted. These items will be shielded so that dose rates in nearby occupied areas meet the STS area design dose rate criteria or access to the affected area will be appropriately restricted. It is also important to protect materials stored outdoors from deterioration so that activated components do not develop removable contamination, so it is STS policy that radioactive components and materials stored outside are protected from the elements.

When the beam is off, an access-control system will restrict and control entry to the beam tunnel and other areas containing potentially highly activated equipment and materials. RWPs for work in radiological areas will ensure proper authorization and training before access. Most users and visiting scientists will be restricted to the experiment floor/mezzanine areas of the Target Building and public-access areas of the facility. Configuration control plays a prominent role in ensuring radiation safety at the SNS. Shielding configurations, monitor locations, and PPS access are carefully controlled by procedures and approved at an appropriate level. Periodic radiation surveys monitor shielding effectiveness. Active radiation monitors considered important to safety are placed in accordance with supporting calculations, and removed only with an equivalent level of supporting information. As a credited engineering control safety system, all aspects of the PPS are under strict configuration control. This SNS Radiation Safety policy is an extension of the ORNL SBMS Radiation Protection Program and is implemented in the SNS Operations Procedures Manual.

7.5.1 Shielding Policy

The SNS facility minimizes exposures to radiation to ALARA levels—well below regulatory limits—and this approach will also be used in design and construction of the STS. The STS will use engineered controls as the primary method to maintain radiation exposures in occupied areas to ALARA levels in accordance with 10 CFR 835.1001 and 10 CFR 835.1002. Administrative procedures, appropriate area classifications and restrictions, and compliance with ORNL SBMS subject areas are additional components in the project’s defense-in-depth strategy to further limit radiation exposures. In addition to normal operating conditions, fault and accident conditions will be considered for shielding design and

selection. Bulk shielding surrounding the proton and neutron beam confinements (including concrete, iron, soil, and other materials) will be designed to maintain radiation exposures at an ALARA level in all areas, considering the expected occupancy levels. Additional physical barriers (e.g., locked doors, fences, etc.) will be incorporated in areas surrounding the shielding to ensure that occupancy in these areas is controlled as necessary. ALARA design reviews will be part of the approval process for major changes in design or operations. Trained personnel will confirm the continuing adequacy of the workplace radiological controls as part of periodic area radiological surveillances. Shielding designs (drawings and calculations), including proposed major modifications to existing area shielding, will be reviewed and approved by both management and technical representatives. STS facility shielding will be under configuration control, and movable shielding will be locked or labeled as appropriate to prevent unauthorized changes that might significantly reduce worker safety. Visual inspections will confirm the proper installation of approved shielding and barriers. Controlled low-intensity beam- and fault-studies will be used as appropriate to verify the effectiveness of area shielding designs. The STS will protect workers and the public from the hazards of nonionizing radiation by implementing the ORNL SBMS subject area “Lasers” and the procedure “Working with Nonionizing Radiation” in the “Occupational Hazard Controls” subject area. The effectiveness of the STS design and implementation for shielding and access control will be demonstrated by achieving the following performance goals.

- Radiation exposures at the SNS facility will be ALARA, as implemented by the SNS ES&H director.
- The annual radiation dose due to normal operations at the SNS STS site boundary will not exceed 25 mrem from all pathways.
- Beam faults at the SNS STS will not lead to an integrated dose greater than 25 mrem per year at the site boundary.
- No member of the public or untrained visitor will unintentionally access a radiological area.
- No one who is not trained as a radiological worker will receive more than 100 mrem in any calendar year while on the SNS STS site.

7.6 FIRE PROTECTION SAFETY

The identification and control of fire-related hazards are well-defined processes, both within industry and the DOE complex. Extensive regulation and guidance have been established using national consensus codes and standards. In addition to applicable codes and standards established on the national and state levels, DOE provides further guidance in specific orders and technical standards. In general, the codes focus on elimination of ignition sources, minimization of combustible/flammable materials, establishment of early warning fire detection, confinement of higher hazard areas, and installation of fire suppression systems based on the value of the facility and the safety of the respective occupants.

Based on operational experiences with accelerators throughout the DOE complex, most fires are electrically initiated by equipment failures. In addition to the evaluation of this risk, additional hazards associated with fire, life safety, and property protection will be considered in the design, construction, and operation of the STS. These include the construction methods and materials, use and storage of hazardous materials, storage of combustible materials, and natural phenomena.

For the STS project, a comprehensive fire protection program will be implemented to ensure regulatory compliance and produce a fire-safe work environment in which to conduct research. The program will address the response to fire, management of fire protection for emergencies, prevention and control of fire hazards (experimental and temporary flammable gas systems, facility natural gas service, flammable

atmospheres, cutting and welding, materials of construction and transient fire loads, and ignition control), maintaining the integrity of facility fire safety features, and fire hazards analyses and evaluations.

7.7 QUALITY ASSURANCE

DOE has established quality assurance (QA) requirements for DOE activities through DOE O 414.1D, April 2011, and passed these requirements to UT-Battelle LLC through its contract to operate ORNL.

The ORNL Quality Management System (QMS) is the overarching quality management document. It describes the UT-Battelle approach to the integration of quality principles, practices, and safety into all activities at ORNL. The program is based upon the elements of ISO-9000 and is implemented through the ORNL SBMS.

The STS Project QA and validation process (QA&VP) provides a description of how the elements of the ORNL QMS and SBMS are implemented within the STS project using a graded application appropriate to the scope and potential risks of project activities. Many processes are used directly from the ORNL SBMS, where appropriate and sufficient. Project procedures or instructions may be written to document or provide guidance for processes performed solely within the project for the project.

Appendix B of this plan contains a matrix of implementing processes (both SBMS and STS Project).

STS Project activities encompass the design, build, fabrication, and commissioning of facilities and instruments for the STS addition to the SNS facility. The facilities and equipment involved range from the relatively simple to the very complex. The equipment costs range from minor to major budget items. Some of the equipment is quite benign, while other items involve significant hazards such as radiation, cryogenics, high magnetic fields, or lethal electrical or mechanical exposure to personnel.

The QA&VP describes quality program controlling elements used to prevent, mitigate, or correct risks identified in designing, building, and commissioning the STS. A graded application of these provisions will be implemented through ORNL, division, and STS project implementing procedures and instructions.

7.8 REFERENCES

Alverez, J. L., M. H. Mobley, and S. M. Trotter 2008. *Spallation Neutron Source Air Effluent Exhaust Stack Emissions Monitoring*, SNS 102010203-ES0001-R00, February.

Bonine, T. M., R. H. Ketelle, and S. M. Trotter 2017. *Operational Groundwater Monitoring Plan for the Spallation Neutron Source Site*, SNS 102040000-ES001-R02, January.

DOE (Department of Energy) 2011. *Departmental Sustainability*, DOE O 436.1, May 2.

DOE (US Department of Energy) 1999. *Final Environmental Impact Statement (FEIS), Construction and Operation of the Spallation Neutron Source*, DOE/EIS-0247. Available online at https://www.energy.gov/nepa/downloads/eis-0247-final-environmental-impact-statement.

DOE (US Department of Energy). 1999a. "Record of Decision for the Construction and Operation of the Spallation Neutron Source," *Federal Register*, Vol. 64 (125): pp. 35140–35142, June 30, 1999. Available online at https://www.energy.gov/sites/prod/files/nepapub/nepa_documents/RedDont/EIS-0247-ROD-1999.pdf.

DOE (US Department of Energy) 2000. "Record of Decision for the Department of Energy's Waste Management Program: Treatment and Disposal of Low-Level Waste and Mixed Low-Level Waste; Amendment of the Record of Decision for the Nevada Test Site," DOE/EIS-0200, *Federal Register*, Vol. 65(38), pp. 10061–10066, February 25, 2000. Available online at https://www.energy.gov/sites/prod/files/nepapub/nepa_documents/RedDont/EIS-0200-ROD-2000.pdf.

DOE (US Department of Energy) 1998. "Record of Decision for the Department of Energy's Waste Management Program: Treatment of Non-wastewater Hazardous Waste," *Federal Register*, Vol. 63(150): pp. 41810–41813m August 5, 1998. Available online at https://www.energy.gov/sites/prod/files/nepapub/nepa_documents/RedDont/EIS-0200-ROD-01-1998.pdf.

HPS (Health Physics Society) 2011. *Sampling and Monitoring Releases of Airborne Radioactive Substances from the Stacks and Ducts of Nuclear Facilities*, ANSI/HPS N13.1, Health Physics Society, 2011.

ISO (International Organization for Standardization) 2015. *Environmental Management Systems*, ISO 14001:2015, International Organization for Standardization, Geneva, Switzerland.

McManamy, T. J., J. R. DeVore, R. M. Harrington, et al. 2019. *Second Target Station (STS) Project Preliminary Hazard Analysis Report*, STS-S01030000-ES0002, R00, Oak Ridge National Laboratory, April 30.

ORNL (Oak Ridge National Laboratory) 2019. *Oak Ridge National Laboratory/Chestnut Ridge Facilities Project Safety, and Health Plan*, SNS 102030000-ES0007-R07, Oak Ridge National Laboratory, Oak Ridge, Tennessee, September 2019.

ORNL (Oak Ridge National Laboratory) 2019. *Oak Ridge Reservation Annual Site Environmental Report*, DOE/ORO-2512, Oak Ridge National Laboratory, September.

Souza, P. A., G. D. DuVall, and M. J. Hart 2001. *Cultural Resource Management Plan, DOE Oak Ridge Reservation, Anderson and Roane Counties, Tennessee*, DOE/ORO/2085, US Department of Energy, Washington, DC.

TDEC (Tennessee Department of Environment and Conversation) 2018. "Emission Standards for Emissions of Radionuclides Other than Radon from Department of Energy Facilities," TDEC Rules, Division of Air Pollution Control, Chapter 1200-03-11-.08, pp. 93–98, revised effective September

2018. Available online at https://publications.tnsosfiles.com/rules/1200/1200-03/1200-03-11.20180904.pdf.

TDEC (Tennessee Department of Environment and Conversation) 2019. "Public Water Systems," TDEC Rules, Division of Water Resources, Chapter 0400-45-01, revised effective February 17, 2019. Available online at https://publications.tnsosfiles.com/rules/0400/0400-45/0400-45-01.20190217.pdf.

Trotter, S. M. and J. R. DeVore 2006. *Spallation Neutron Source Waste Management Plan (SNS 102030000-TR0002-R02*, Oak Ridge National Laboratory, March.